

ADVANCED AND CONTEMPORARY STUDIES IN ENGINEERING



Editor:
Assoc. Prof. Mehmet Sait CENGİZ



**ADVANCED AND
CONTEMPORARY STUDIES
IN ENGINEERING**

Editor:

Assoc. Prof. Mehmet Sait CENGİZ



Advanced and Contemporary Studies in Engineering

Editor: Assoc. Prof. Mehmet Sait CENGİZ

Editor in chief: Berkan Balpetek

Cover and Page Design: Duvar Design

Printing : December -2023

Publisher Certificate No: 49837

ISBN: 978-625-6585-69-0

© Duvar Yayınları

853 Sokak No:13 P.10 Kemeraltı-Konak/İzmir

Tel: 0 232 484 88 68

www.duvar yayinlari.com

duvarkitabevi@gmail.com

TABLE OF CONTENTS

Chapter 1.....7	7
The Effects of Using Superplasticizer and Pozzolans at Different Ratios on the Rheological Properties of Self-Compacting Cement Paste	
<i>Fethi İŞSEVER, M. Hulusi ÖZKUL, Sadık VAROLGÜNEŞ</i>	
Chapter 2.....33	33
Formation Mechanisms and Deposition Processes of Pyroclastic Rocks	
<i>Abdullah SAR, Mehmet Ali ERTÜRK</i>	
Chapter 3.....50	50
Effects of Operating Parameters on NOX Emissions in Diesel Engines	
<i>Adem TÜYLÜ, Kubilay HAN, Yasin AKIN</i>	
Chapter 5.....64	64
In-Situ Hydrogen Peroxide and Hydrogen Production in Wastewater Treatment with Fenton-Fenton Like Oxidation	
<i>Ayşe Elif ATEŞ, Sinan ATEŞ</i>	
Chapter 4.....77	77
Modeling the COD removal of DMSO-Containing Wastewater from the Pharmaceutical Industry Using Photo-Fenton Oxidation with the Response Surface Method	
<i>Ayşe Elif ATEŞ</i>	
Chapter 6.....88	88
Energy Management Strategies and Techniques in Hybrid and Electric Vehicles	
<i>Bayram KILIÇ, Emre ARABACI</i>	
Chapter 7.....97	97
ENVIRONMENTAL BIOTECHNOLOGY PROCESSES IN THE TREATMENT OF LIVESTOCK WASTES	
Büşra YAYLI ₁ İlker KILIÇ ₂	
Chapter 8.....112	112
Environmental Impact Assessment Of Laying Hen Production Systems Through Life Cycle Assessment	
Büşra YAYLI, İlker KILIÇ	

Chapter 9.....132

Material Strength Tests With Electrical Approach
Emrah KAPLAN, Dursun EKMEKCI

Chapter 10 152

Effects of the Use of Nanofluids in Solar Collectors on Thermal-
Hydraulic Performance
Fatma OFLAZ

Chapter 11.....162

The Effect of Using Wire Coil Inserts on Heat Transfer
Enhancement in Tube Flow
Fatma OFLAZ

Chapter 12.....173

Urban Climate Change Resilience
Gökhan KARA, Esmâ Gül EMECEN KARA

Chapter 13.....186

Investigation Of Chaotic Behavior In A 3D Nonlinear System With
Exponential Function
Haris CALGAN, Metin DEMİRTAS

Chapter 14.....196

Investigation of the Phase Development of NBT, KBT and BT
Lead-Free Piezoelectric Ceramics
Hatice Şule ÇOBAN TETİK

Chapter 15.....210

SMALL HORIZONTAL AXIS WIND TURBINE: A CASE STUDY
Kemal ERMİŞ, Mehmet ÇALIŞKAN, Murat KARABEKTAŞ

Chapter 16.....230

The Role of Sensors and Encoders in Exoskeleton Technologies
Melih CANLIDİNÇ, Mustafa GÜLEŞEN

Chapter 17.....242

Effects of Climate Change on Water Resources,
Soil Resources and Weather Events
Sümeyye ADALI, Melike YALILI KILIÇ

Chapter 18.....254

The Rehabilitation Of Open Solid Waste
Dumping Areas
Fatma ALFARRA, Mirac Nur CİNER, H. Kurtulus Ozcan

Chapter 19	284
Criteria for Determining Parameters in Metal Powder Production by Gas Atomization <i>Mustafa GÜLEŞEN, Osman Selim KİBAR</i>	
Chapter 20	296
The Response Of Soil Properties To Global Climate Change <i>Fatma Olcay TOPAÇ</i>	
Chapter 21.....	311
Modeling and Simulation of Fuzzy Logic MPPT Method for Photovoltaic DC/DC Boost Converter <i>Yasemin ÖNAL</i>	
Chapter 22.....	328
Results and Suggestions Regarding Cutting Forces, Surface Roughness And Tool Wear In Turning Inconel 718 With Different Cutting Tools <i>Abdullah ALTIN</i>	
Chapter 23.....	337
Contact Mechanics of Functionally Graded Orthotropic Materials: Semi-Analytical Solution for Rigid Punch Loading <i>Erdal ÖNER, Ahmed Wasfi Hasan AL-QADO</i>	
Chapter 25.....	348
Blockchain Technology and Consensus Algorithms <i>İrfan SARIYILDIZ, Mehtap KÖSE ULUKÖK</i>	
Chapter 25.....	357
A Review on the Design, Modeling and Optimization of Fused Deposition Process Printing Parameters <i>Melih SAVRAN</i>	
Chapter 27	385
Analyzing and Fixing the Grasshopper Optimization Algorithm <i>Okkes Tolga ALTINOZ</i>	
Chapter 27.....	396
Health Problem Pre-Application System Recommendation for International Transportation Personnel and Passengers and Evaluation of The Proposed System <i>Orhan GÖNEL, Bengisu OLGUN BEKMAN</i>	

Chapter 28.....414

Detection and Recognition of Allergic Fruit with
Deep Learning Models
Sevinç AY

Chapter 29.....424

A Comparative Study on Signal Processing for Harmonics
Sıtkı AKKAYA

Chapter 30.....439

Numerical Analysis of the Effects of
Different Fin Geometries on the Performance of
Thermoelectric Modules in Channel Configurations
Ali TAŞKIRAN, İhsan DAĞTEKİN, Celal KISTAK, Nevin ÇELİK

Chapter 31.....459

Energy Saving Potentials in Compressed Air Systems
Ergün KORKMAZ

Chapter 32.....491

Investigation of the Effect of Hole Diameter and Aspect Ratio on
Elastic Buckling Strength and Determination Buckling Coefficients for
Thin Plate Structural Parts in Aerospace Industry with Finite Elements Method
Mert SUBRAN, Fatih KARPATI

Chapter 33.....507

Energy Consumption of Headlights in Electric Vehicles While Driving
Çiğdem CENGİZ, Metin KAYNAKLI

Chapter 34.....527

R-SHINY App As An Interface For Topic Modeling: Rtoptech
Ahmet ALBAYRAK, Muammer ALBAYRAK

Chapter 1

The Effects of Using Superplasticizer and Pozzolans at Different Ratios on the Rheological Properties of Self-Compacting Cement Paste

Fethi İŞSEVER¹

M. Hulusi ÖZKUL²

Sadık VAROLGÜNEŞ³

INTRODUCTION

Self-compacting concrete (SCC) has a unique property that enables it to spread to small-formed and tightly reinforced elements whilst retaining its homogeneity, without the requirement of compression. This makes SCC well-suited for high-performance concrete structures, which typically use conventional vibro-compacted concrete. The concept of SCC was introduced for underwater concrete applications in the early 1980s (Okamura, 1997). Self-compacting concrete (SCC) finds application in precast concrete, on-site poured concrete, or fibre-reinforced concrete (Skarendahl & Petersson, 2000). Moreover, SCC takes the form of cement pastes or mortars in a variety of structural and soil improvement applications, such as soil grouting or filling concrete cracks (Lacerda, da Silva, Alva, & de Lima, 2018; Tullini & Minghini, 2016; Vasumithran, Anand, & Sathyan, 2021). As SCC has a less porous structure with a more uniform interfacial transition zone (ITZ) than traditional concrete, it has fewer pores.

Moreover, cement paste provides several benefits pertaining to labour and worker safety, workability, segregation, ease and duration of production, energy efficiency, sound insulation and durability (Ramanathan, Baskar, Muthupriya, & Venkatasubramani, 2013). It is also employed in the restoration of historical constructions, precast engineering, and filling tile joints (Vasumithran et al., 2021).

¹ Asst. Prof.; Bingöl University Faculty of Engineering and Architecture, Department of Civil Engineering. fissever@bingol.edu.tr ORCID No: 0000-0002-8394-7026

² 2Prof. Dr.; Beykent University Faculty of Engineering and Architecture, Department of Civil Engineering. hulusi.ozkul@beykent.edu.tr ORCID No: 0000-0002-6453-8956.

³ 3Asst. Prof.; Bingöl University Faculty of Engineering and Architecture, Department of Civil Engineering. fissever@bingol.edu.tr ORCID No: 0000-0001-9580-9889

Chemical admixtures utilized in the production of self-compacting concrete comprise a blend of various admixtures, mainly superplasticizers and viscosity-regulating admixtures. Superplasticizer admixtures are employed to deliver high fluidity and lower the water/binder ratio. Viscosity regulating admixtures are used to prevent segregation such as sweating and precipitation, to ensure uniformity of the concrete, and to reduce the shear yield stress (Bürge, 1999). Most concrete structures currently in use have standard strength. However, due to the practical constraints, there is limited scope for the application of conventional concrete. Hence, there is a need to innovate low-bonding, normal-strength and high-flowability concrete, which can be implemented not only in regular constructions but also in specialized buildings. This development has the potential to significantly reduce construction timeline and labor costs. This has also paved the way for the discovery and application of Polycarboxylate-based superplasticizers (Kong & Lee, 2021).

Upon examination of the working principles of superplasticizers, it becomes evident that the latest generation of superplasticizers, containing lengthy polymer chains, amass on the surface of fine particles. Consequently, the electrical impulse and steric effect are utilized, ensuring the distribution of cement grains (Uchikawa, Hanehara, & Sawaki, 1997; Yoshioka, Sakai, Daimon, & Kitahara, 1997). While traditional superplasticizers are derived from sulfone naphthalene formaldehyde or sulfonated melamine formaldehyde, newer superplasticizers consist of copolymers in which a carboxylic group is present in the main chain and a polyethylene glycol group is connected to the side chain (Houst et al., 1999). Viscosity-regulating admixtures or fine aggregate, or both, may offer increased resistance to segregation, settling, and compressibility. The fine material content (less than 90 μ m), which includes cement, is deliberately increased beyond a certain threshold to improve resistance to weathering (Özkul, Dogan, Çavdar, Sağlam, & Parlak, 2000; Özkul, Doğan, Çavdar, Sağlam, & Parlak, 1999). Mineral admixtures, finely ground materials blended with cement mortar and concrete, are used to achieve specific engineering properties (ASTM_C125-13a, 2013). These materials may be added during mixing or the clinker production stage. Subsequently fine grinding may be employed for both natural and processed manufactured materials used as mineral admixtures. Numerous studies have researched materials that act as mineral admixtures, reducing the cement quantity used (Ardalan, Joshaghani, & Hooton, 2017; Choudhary, Gupta, Alomayri, Jain, & Nagar, 2021; Choudhary, Gupta, & Nagar, 2020; Dadsetan & Bai, 2017; Güneyisi, Gesoğlu, Al-Rawi, & Mermerdaş, 2014; Mendes & Dutra, 2004; Princen & Kiss, 1989; Ramanathan et al., 2013; Sadrmomtazi, Gashti, & Tahmouresi, 2020; Sharbatdar, Abbasi, & Fakharian, 2020). Cement paste features non-Newtonian fluid with Bingham attributes; its fresh

properties are evidently grain size-sensitive (H.-y. Cheng, Wu, Zhang, & Wu, 2020). These observations can be applied as references for cement paste and mortars.

Various techniques have been devised to quantify the rheological characteristics of self-consolidating concretes. These include filling capacity, separation resistance, ability to pass through hindrances (Özkul et al., 1999) and viscosity and shear yield stress. These rheological properties can be gauged in cement paste, mortar and concrete employing the viscometer tool in conformity with the Bingham model (Nornberg, Peterson, & Billberg, 1997). Using this methodology, the forces opposing shear at different rotational velocities ($\dot{\gamma}$) are measured through torque (τ). Shear yield stress (τ_0) and viscosity (η) values are derived using the linear correlation between shear resistance and rotational speed (Mendes & Dutra, 2004; Princen & Kiss, 1989):

$$\tau = \tau_0 + \eta \cdot \dot{\gamma}$$

Torque resistances (T, torque) at varying rotational speeds were measured using the Mettler RH180 Rheomat viscometer instrument in this study, which is also applicable to cement paste. The slope of the linear relationship plotted between torque and rotational speed (N) yields the magnitude (H), indicative of viscosity, whereas the point of intersection between this line and the moment axis corresponds to the magnitude (G) related to the slip threshold. The mathematical expression for this scenario is as follows:

$$T = G + H \cdot N$$

Factorial Design Method

Thanks to this method, it is feasible to attain the most favorable ratios with less testing material and in a shortened time frame, foregoing the need for numerous experiments (C.-S. Cheng, 2016; Montgomery, 2017). This experimental method employed three variables. It is known as the “star method” or “cube method”. As per the method, central values are positioned at three distinct points on the cube, as shown in Figure-1. Material ratios increase as one moves away from these points. Three values are positioned at the midpoints, resulting in 8 binary combinations in total using factorial design. Six extreme values are identified by selecting from the midpoints towards the extremes. The experiments are then validated by repeating the mean values three times. The central composite design is depicted as a cube in Figure 1, where the vertices signify low and high levels of every variable, with endpoints outside the cube and midpoints at its center. The subsequent equations are derived by passing surfaces

for each feature using the test outcomes. Khayat et al (Khayat, Ghezal, & Hadriche, 1999) applied the same method successfully to concrete.

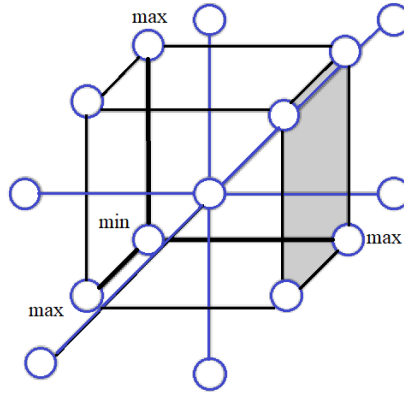


Figure 1: Factorial Design Method

In this study, the effects of mineral admixture/binder (M/B), chemical admixture/binder (SP/B), water/binder (W/B) ratios on cement paste properties were investigated using rheological measuring instruments. Experiments made are Spread, Yield Shear Stress and Viscosity measurement experiments.

MATERIALS and METHOD

Materials

- **Portland Cement (PC)**

In all experiments, ordinary Portland Cement of PC 42.5 class (CEM I, TS-EN 197-1) was used (TS-EN-197-1, 2012).

Table 1: Physical and Mechanical Properties of Cement

Chemical Proportion (% weight)									
total SiO ₂	dissolved SiO ₂	CaO	Al ₂ O ₃	Fe ₂ O ₃	SO ₃	MgO	free CaO	K ₂ O	LOI*
23.0	19.8	63.3	4.5	4.0	2.3	0.9	0.7	0.5	2.0
Cement Mixed Oxides (Bogue) (% weight)									Lime Standard
C ₃ S		C ₂ S		C ₃ A		C ₄ AF		96.5	
50.3		23.4		5.0		12.1			
Physical and Mechanical Properties						Compressive Strength			
Specific gravity	Blaine Fineness m ² /kg	Le Chatelier mm	Setting times		7 days MPa	28 days MPa			
			Initial	Final					
3.07	307	1	2h 45m	4h 10m	42	51			

* Loss on Ignition

- **Fly Ash (FA)**

The fly ash used was obtained from the Lignite Thermal Power Plant, which is in Orhaneli district of Bursa, in the Karıncalı region.

Table 2: Properties of fly ash supplied from Bursa Orhaneli Thermal Power Plant

Cement Oxides	SiO ₂	CaO	MgO	Fe ₂ O ₃	Al ₂ O ₃	Na ₂ O	K ₂ O	SO ₃	
Proportion as weight %	34.8	26.3	1.7	3.9	19.4	2.7	1.9	6.3	
Blaine Fineness (m ² /kg)							303		
10µm-40µm materials (%)							42.6		
D _{median} (µm)							29		
Specific Gravity							2.4		
Efficiency Factor, EF (C=350 kg/m ³)							0.43		

- **Silica Fume (SF)**

Silica fume was obtained from Etibank Ferro-Chrome factories in Antalya. Chemical composition of Silica Fume is given in Table-3. The density and unit weight of silica fume are 2.32 g/cm³ and 245 kg/m³, respectively. Residue of silica fume on 45 µm sieve is 4.8%.

Table 3: Oxide ratios of silica fume

Oxide	SiO ₂	Al ₂ O ₃	Fe ₂ O ₃	CaO	MgO	SO ₃	K ₂ O	Na ₂ O	LOI
SF	85.96	0.66	0.32	0.7	4.93	0.61	-	-	2.66

- **Superplasticizers**

In the experiment, Sika Viscocrete was utilized, which is a new generation chemical admixture founded on Polycarboxylate ether. (Specific Gravity: 1.10 20 °C; dissolved solid material: %33.88, Ph 6.8±0.6)

- **Mix Proportions and Specimen Preparation**

Cement paste mixtures were mixed in a mortar mixer with a 3 dm³ capacity in two stages over a total of 3.5 minutes. Firstly, the Cement Paste was mixed slowly for 2 minutes in the mixer. It was then mixed by hand for 15 seconds to prevent cement from sticking to the mixing bowl's walls. After 1 minute of rapid mixing with the machine, the mixture was left to settle for 3 minutes before being subjected to another 30 seconds of mixing with the machine. The measurements were then taken. The experiment was conducted in two stages: firstly, measurements were taken using a viscometer, followed by the measurement of spreading values.

For the spreading test, a Kantro mini slump-expansion method was used. The experiment utilized a truncated cone with a diameter of 39 mm at the base, 19 mm at the top, and a height of 57.5 mm. Finally, the two perpendicular diameters of the spreading material were measured, and the resulting average was recorded. The study was replicated at intervals of 6, 30, 60, 90, and 120 minutes to monitor the gradual decline in spreading over time.

Başlık ile; yazar isimleri (orta, times new roman, 10 punto), Kurum, Ülke bilgileri (orta, times new roman, 10 punto) ve iletişimdeki yazarın e-posta adresi alt satıra (10 punto) yazılmalıdır.

- **Testing Procedures**

The factorial design method was used to find the mixture compositions in this study. In Table 5 and Table 6, the mixture composition of each experimental set is given.

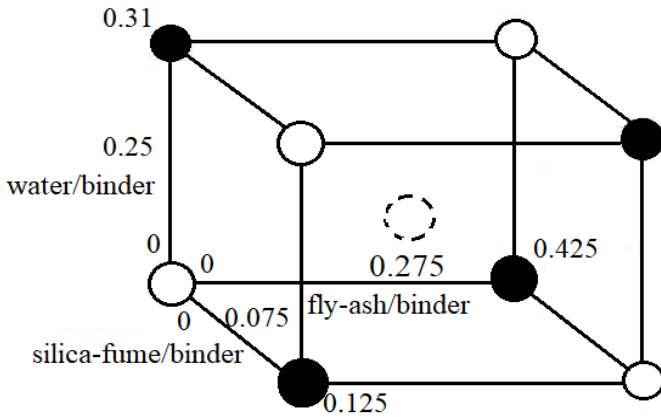


Figure 2: Mixing ratios applied in experiments according to FDM

Before starting the experiments, cement paste control samples (CPK) were poured first (Table 5). After these mixtures, the optimum mixture values used in the experimental program were obtained (Table 6).

Table 4: Rheological Measurements of Cement Paste Experiment for Control Samples

Proportion	Amounts
Cement	Nuh PC 42.5
Fly Ash	% 0-27.5-42.5
Silica Fume	% 0-7.5-12.5
Superplasticizers	Viscocrete 1
Reading Times	06-30-60-90-120 minutes
Reading RPMs	10-30-50-70-90-110-130-150 rpm
Mix	First by machine Second by hand
Experiment Equipment	Mini slump Coni
Dimensions	(mm)
Top Diameter	19.0
Bottom Diameter	39.0
Height	57.5

Table 5: Mixing Proportions with Control Measurements for Factorial Design

Experiment	Cement				Superplasticizer					
	Nuh PC 42.5		Fly Ash		Silica Fume		Viscocrete		w=Water + admixture	
	%	gr	%	gr	%	gr	%	gr	(w/c)	gr
CPK1	72.5	725	27.5	275			1.25	12.5	0.25	250
CPK2	72.5	725	27.5	275			1.25	12.5	0.31	310
CPK3	72.5	725	27.5	275			0.75	7.5	0.28	280
CPK4	72.5	725	27.5	275			1.75	17.5	0.28	280
CPK5	100.0	1000	0	0			1.25	12.5	0.28	280
CPK6	57.5	575	42.5	425			1.25	12.5	0.28	280
CPK7	92.5	925			7.5	75	1.25	12.5	0.25	250
CPK8	92.5	925			7.5	75	1.25	12.5	0.31	310
CPK9	92.5	925			7.5	75	0.75	7.5	0.28	280
CPK10	92.5	925			7.5	75	1.75	17.5	0.28	280
CPK11	100.0	1000			0	0	1.25	12.5	0.28	280
CPK12	87.5	875			12.5	125	1.25	12.5	0.28	280

Table 6: Mixing ratios of the Main Measurements

Experiment	Cement						Superplasticizer			
	Nuh PC 42.5		Fly Ash		Silica Fume		Viscocrete		w=Water+admixture	
	%	gr	%	gr	%	gr	%	gr	(w/c)	gr
CP1	100.0	1000					1.00	10.0	0.26	260
CP2	100.0	1000					1.20	12.0	0.26	260
CP3	100.0	1000					1.50	15.0	0.26	260
CP4	80.0	800	20.0	200			1.00	10.0	0.26	260
CP5	65.0	650	35.0	350			1.00	10.0	0.26	260
CP6	80.0	800	20.0	200			1.20	12.0	0.26	260
CP7	65.0	650	35.0	350			1.20	12.0	0.26	260
CP8	80.0	800	20.0	200			1.50	15.0	0.26	260
CP9	65.0	650	35.0	350			1.50	15.0	0.26	260
CP10	95.0	950			5.0	50	1.00	10.0	0.26	260
CP11	90.0	900			10.0	100	1.00	10.0	0.26	260
CP12	95.0	950			5.0	50	1.50	15.0	0.26	260
CP13	90.0	900			10.0	100	1.50	15.0	0.26	260
CP14	100.0	1000					1.00	10.0	0.30	300
CP15	100.0	1000					1.50	15.0	0.30	300
CP16	80.0	800	20.0	200			1.00	10.0	0.30	300
CP17	65.0	650	35.0	350			1.00	10.0	0.30	300
CP18	80.0	800	20.0	200			1.50	15.0	0.30	300
CP19	65.0	650	35.0	350			1.50	15.0	0.30	300
CP20	95.0	950			5.0	50	1.00	10.0	0.30	300
CP21	90.0	900			10.0	100	1.00	10.0	0.30	300
CP22	95.0	950			5.0	50	1.50	15.0	0.30	300
CP23	90.0	900			10.0	100	1.50	15.0	0.30	300

RESULTS AND DISCUSSIONS

Plastic viscosities and yield shear stresses of CPs were measured considering that they have Bingham body properties. In the measurements made with the Viscometer (Rheomat) test device, the averages of the forward and reverse readings were measured between (6-120) minutes and at (10-150) RPM speeds.

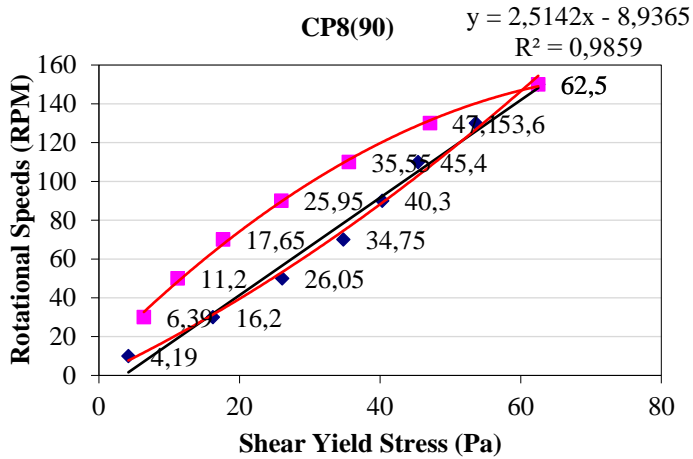


Figure 3: Rheomat measurement graph for the 90th minute of the CP8 sample

For this, threshold shear stress τ_0 and viscosity η_{pl} data, known as Bingham constants, were considered in all test result evaluations. Cement paste tests were evaluated in four sections. These are:

- I. Superplasticizer effect for varying proportions of Viscocrete
- II. Water effect
- III. Effect of Mineral Admixture and binders
- IV. Correlations between above relations.

In the evaluations, the first readings, which are the sixth minute readings, were neglected as they contradicted Bingham behavior and distorted the linear part. Viscosity was found from the slope of the linear part, and SYS values were found from the point where the curve cuts the shear axis.

Effects of Fresh Concrete Properties

- **Effects on Shear Yield Stress (SYS)**
 - **Superplasticizer Effect**

In CPs without admixtures and FA added CPs, SYS decreases when the ratio of other materials is kept constant (W/B= 0.26, C/B=100%) and SP is increased (Figure 4a, b). If the amount of both W and FA is too high, the SYS values take small values (Figure 4c). This indicates that there is near to segregation. It has been found that the appropriate rate for FA in this combination is about 20%. Optimum SYS values in terms of workability and consistency are obtained with 20% FA, 1.2% SP and 26% water.

When the amount of SP increased in SF-doped CP, the SYS value decreased, albeit slightly. However, it was observed that the viscosity tester could not measure when the SF ratio was high, and the SP and water ratios were low. This shows that due to the very fine structure of the SF, it needs a large amount of water to get wet (Figure 4d).

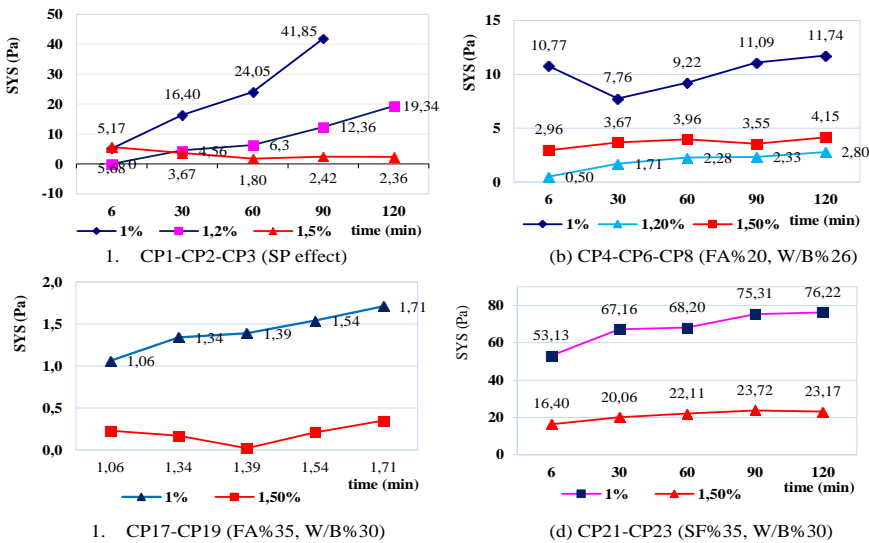


Figure 4: SYS changes in CP caused by SP effect

- **Water Effect**

In CP without mineral admixtures, when the value of SP was kept constant and the W/B ratio increased, the SYS value decreased. This rate of decrease was approximately 10 times. However, when the SP ratio increases from 1% to 1.5%, there is no point in increasing the water. Figure 5 (a, b)

While the SP ratio was low in FA added mixtures, there was an insignificant decrease in SYS when the amount of water was increased. In other words, the

desired yield could not be obtained by increasing the water. In addition, if both the FA ratio and the SP ratio are high, as in the CP16 experiment, segregation occurred in the CP and water vomiting was observed. Figure 5 (c)

It was observed that in the experiments with high SF ratio, low water and SP admixtures, a consistency that was too dense to be measured in SF-added CP and viscosity and spread measurements could not be made. When SF is in very fine-grained structure, it was beneficial to have both water and SP ratios as high as possible. For Figure 5 (d) SF, appropriate ratios of 5% SF/B, 30-32% W/B, 1.5-2% SP would be appropriate.

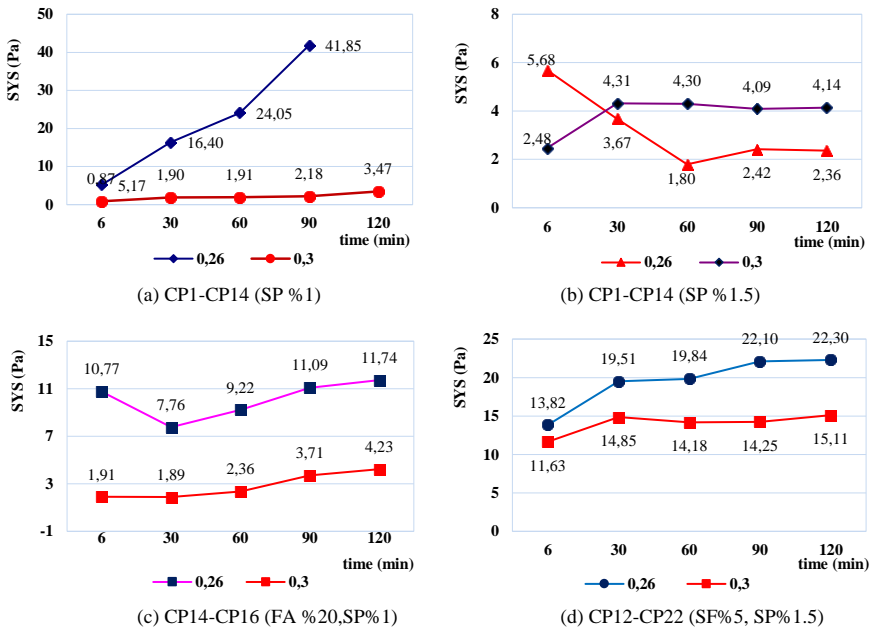


Figure 5: SYS changes in CP caused by water effect

- *Pozzolan Effect*

In pure CP experiments, it was observed that SYS decreased in general when the FA/B ratio was increased from 20% to 35%. It was observed that SYS values decreased by an average of 5 times when the FA ratio was kept constant at W/B=26%, and SP=1.5% in FA added mixtures and the FA ratio was increased from 20% to 35%. Figure 6 (a) and (b)

It was observed that in the experiments with high SF ratio, low water and SP admixtures, a consistency that was too dense to be measured in SF-added CP and viscosity and spread measurements could not be made. When SF is in very fine-grained structure, it was beneficial to have both water and SP ratios as high as

possible. For Figure 5 (d) SF, appropriate ratios of 5% SF/B, 30-32% W/B, 1.5-2% SP would be appropriate Figure 6(c).

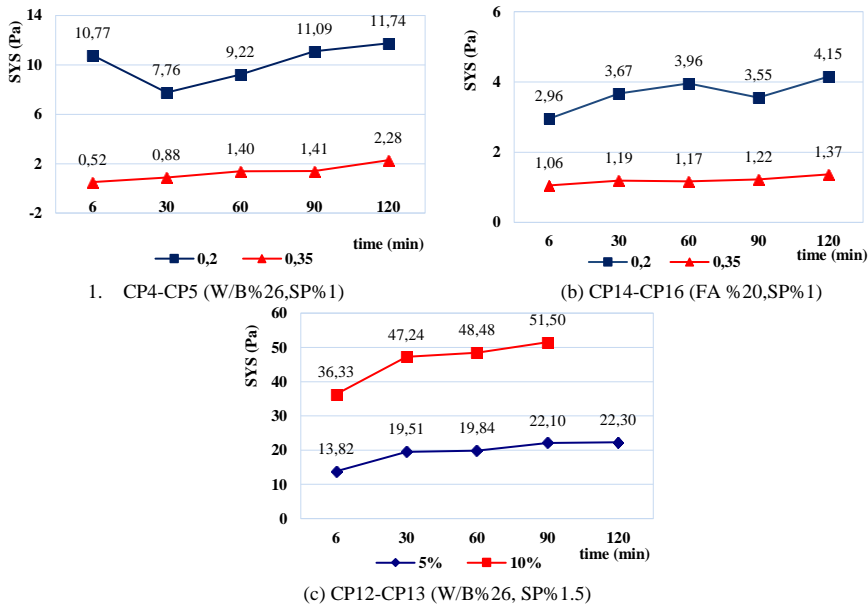


Figure 6: Change of SYS with the effect of mineral admixtures in CP

• *Effects on Viscosity*

Viscosity is the most important rheological property in determining the homogeneity of CP and thus of concrete. Therefore, it is desirable that the viscosity be above a certain ratio. In the experiments carried out, it has been seen that SP gives a better behavior to CP than water for viscosity. Because water, besides being effective in reducing SYS, also reduces the viscosity below the desired values, causing segregation and deterioration of homogeneity. Although separations were observed when the SP was applied more than the required dose, an excellent machinability was obtained when the SP/B ratio was well adjusted. In other words, the more advantageous aspect of SP than water is that it prevents segregation while increasing the workability. In addition, the processing time of CP has increased.

- Superplasticizer Effect

In the CP experiments without mineral admixtures (control samples), it was observed that the viscosity increased as the SP ratio increased. Figure 7 (a).

It was observed that increasing the SP ratio (1-1.2-1.5%) in CP with FA did not improve the viscosity, on the contrary, when the SP ratio increased with the water ratio, undesired separation became inevitable. Naturally, when FA and other admixtures are used at optimum values, very good consistency and workability are provided in CP. Figure 7(b, c)

In admixtures with SF, when the SP ratio increased from 1% to 1.5%, the viscosity did not change much. For these experiments, the reason for this is that SF is already a material that requires a lot of water and SP on its own. Figure 7 (d).

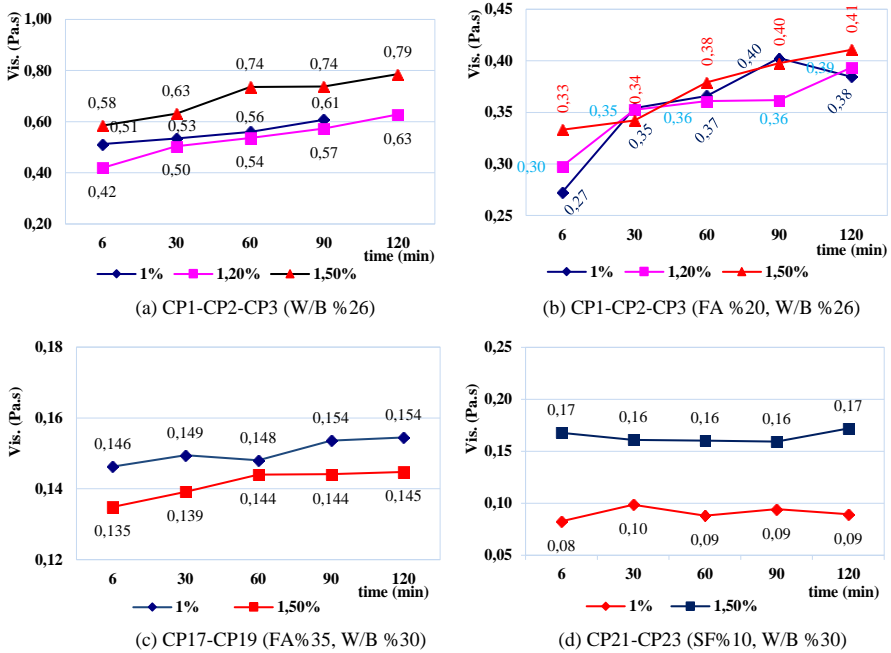


Figure 7: Effects of SP on viscosity in CP

- Water Effect

In CP without mineral admixtures, viscosity decreases enormously when water increases (26-30%). It can be said that among all binders, the material that interacts best with water is cement. However, in general, the viscosity increases rapidly over time, as water decreases the viscosity. Figure 8 (a, b, c).

Water, which already has the ability to reduce viscosity in CP mixtures with FA, also decreases when it is processed with a coarser grained material than cement.

In SF, although the viscosity decreased when the amount of water was increased, this did not decrease over time and preserved its value. Figure 8(d).

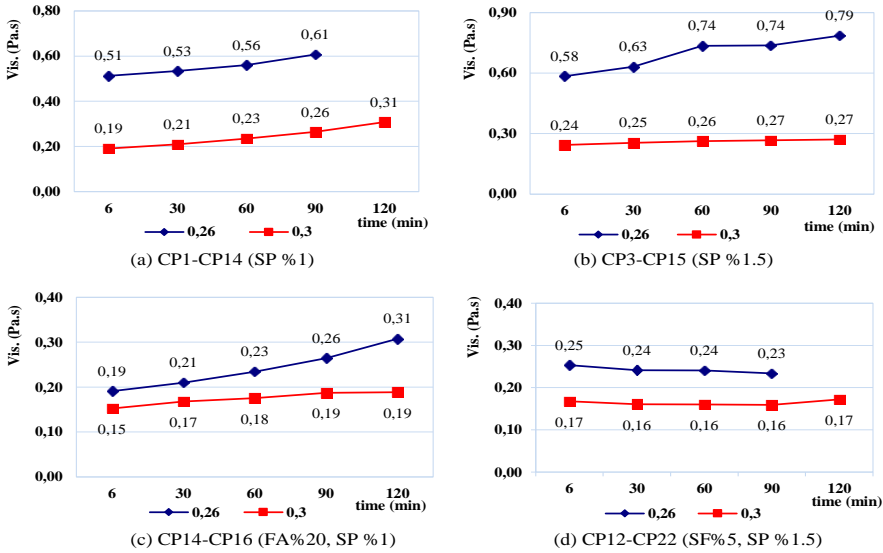


Figure 8: Effect of water effect on viscosity in CP

- *Pozzolan Effect*

In FA added CP, the viscosity increases with the amount of FA (20-35%) at low water (26%) and SP ratios, that is, it shows the desired behavior. On the other hand, when FA increases, viscosity decreases in mixtures with high water and SP content. Figure 9 (a, b) It is observed that the viscosity decreases very little when the SF increases.

All evaluations were obtained because of the comparison of the specified experiments with other experiments. Viscosity increases from 6 to 120 minutes because of the recovery of some of the mixtures over time, and the condensation of some of the mixtures over time, since they already have a normal consistency, in almost all experiments, in other words, they go towards the viscous state. The amount of this increase varies from mixture to mixture. It has been observed that time alone is not as effective as SYS for viscosity.

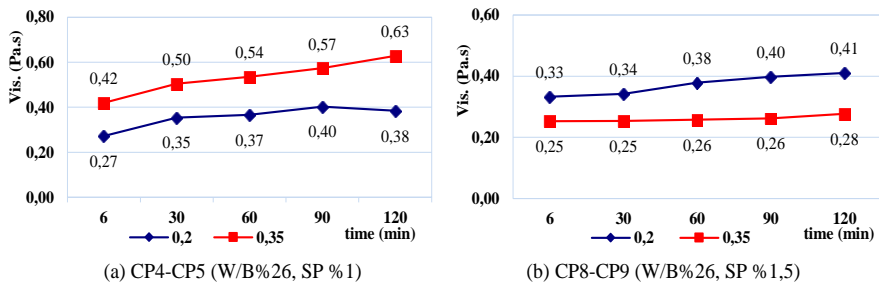


Figure 9: Effect of SF on viscosity in CP

- **Evaluation of Spread Test Results**

Slump-scattering experiments were performed for CP mixtures using slump cones. For each mixture, the spreading diameter, and the time to reach 100 mm were measured in seconds.

- **Superplasticizer Effect**

In the examinations made with mini slump spreading experiments, it was understood that the use of SP increased the spread and maintained this spread regularly for 120 minutes. While no measurement could be made after the 30th minute in control samples, this problem was overcome with the use of SP, in addition, it was observed that viscosity and homogeneity were preserved. It has been determined that the use of SP together with FA ensures that the spread is smooth and uniform in all directions. When the time to reach a diameter of 100 mm in CP was examined, it was observed that the use of SP shortened the time to reach. Thus, it is understood that fresh material will settle into the mold more quickly in concrete pouring at construction sites Figure 10(b).

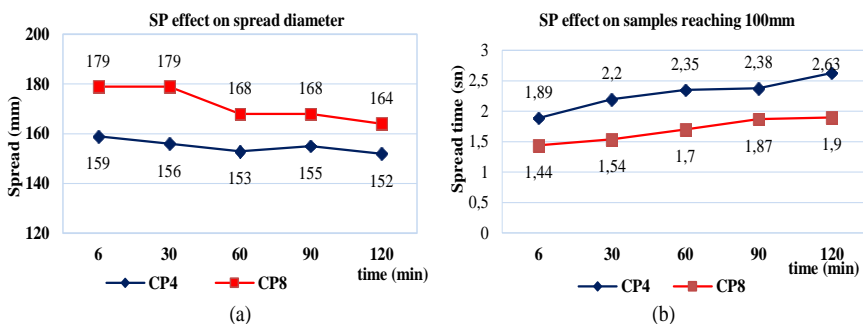


Figure 10: SP effect on CP4-CP8 spread diameter and time to reach 100 mm diameter

- **Water Effect**

When the effect of water on the spreading in CP was examined, it was observed that the spreading increased with the increase in water. The diameter difference between the samples was maintained at almost the same rate from the 6th minute to the 120th minute. Figure 11 (a). When the time to reach 100 mm was examined, it was understood that the amount of water accelerated the spread, and this speed was maintained for 120 minutes. Figure 11 (b).

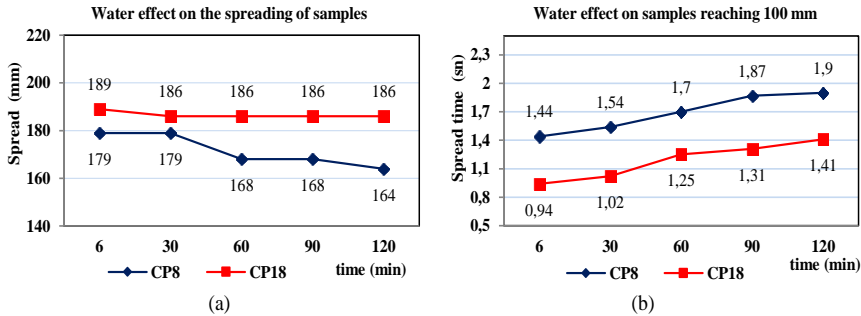


Figure 11: W/B effect on CP8-CP18 spread and time to reach 100mm

- **Pozzolan Effect**

While examining the pozzolan effect in the diffusion experiments for CP, the effect of FA was examined first. While the use of FA was more effective in the first minutes of the mixture, the effect of the use of FA on the spread decreased as time progressed. The effect of using 35% FA instead of 20% FA decreased rapidly after 30 minutes. Figure 12 (a). For the time to reach 100 mm, the use of water reduced the time by approximately 40%, which was true for all 5 measurements over 120 minutes. Figure 12 (b).

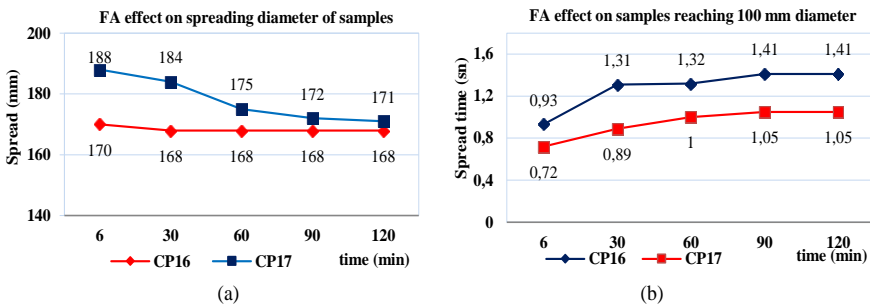


Figure 12: FA effect on CP16-CP17 spread and time to reach 100 mm diameter

Increasing the amount of Silica Fume greatly reduced the spread. Increasing the SF/B ratio from 5% to 10% prevented measurements after a certain time in

many mixtures. Despite the use of the highest amount of water and SP, both the final spread and the results of reaching a diameter of 100 mm could not be measured after the 90th minute, even in the CP22-CP23 samples. Figure 13 (a). Figure 13 (b)

While there was a directly proportional difference in the spreading diameter measurements depending on the time, there was a rapid slowdown in reaching 100 mm between the 6th and 30th minutes.

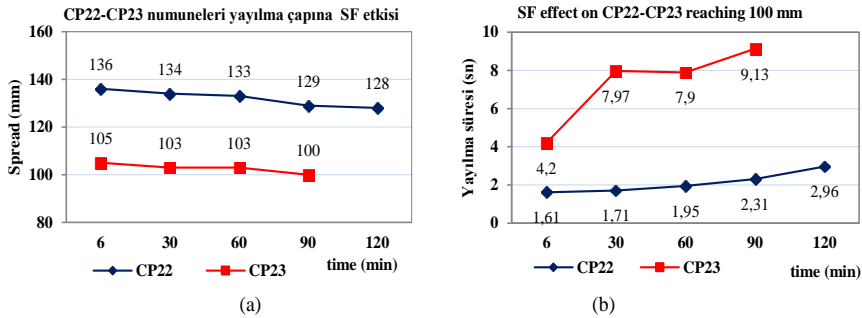


Figure 13: SF effect on CP spread and time to reach 100 mm diameter

Analysis of Correlations between Fresh Cement Paste Properties

- ***Correlation between Viscosity-Shear Yield Stresses***

In general, a directly proportional relationship is determined between viscosity and SYS. SYS increased over time in control samples made with cement only. Especially after the 60th minute, the increase accelerated. The viscosity increase rate was not as much as SYS. However, the machinability loss was not much (Figure 14-a, b).

In FA-added CP mixtures, when the ratios of W/B=26% and SP/B=1% were constant while the FA ratio increased from 20% to 35%, both SYS and viscosity values decreased. The decrease of the viscosity and the SYS revealed that the homogeneity of the material did not deteriorate, and the workability was preserved (Figure 14-c, d).

In FA-added samples, when both W/B and FA ratios are maximum, and SP kept constant while FA increased, the decrease of viscosity is less, and the decrease of SYS is slightly higher. A situation with good workability has occurred (Figure 14-e, f).

In SF-added mixtures, when W/B 30% and SP kept constant at 1.5% while SF increased from 5% to 10%, SYS increased while viscosity decreased. This shows that the workability was reduced (Figure 14-g, h).

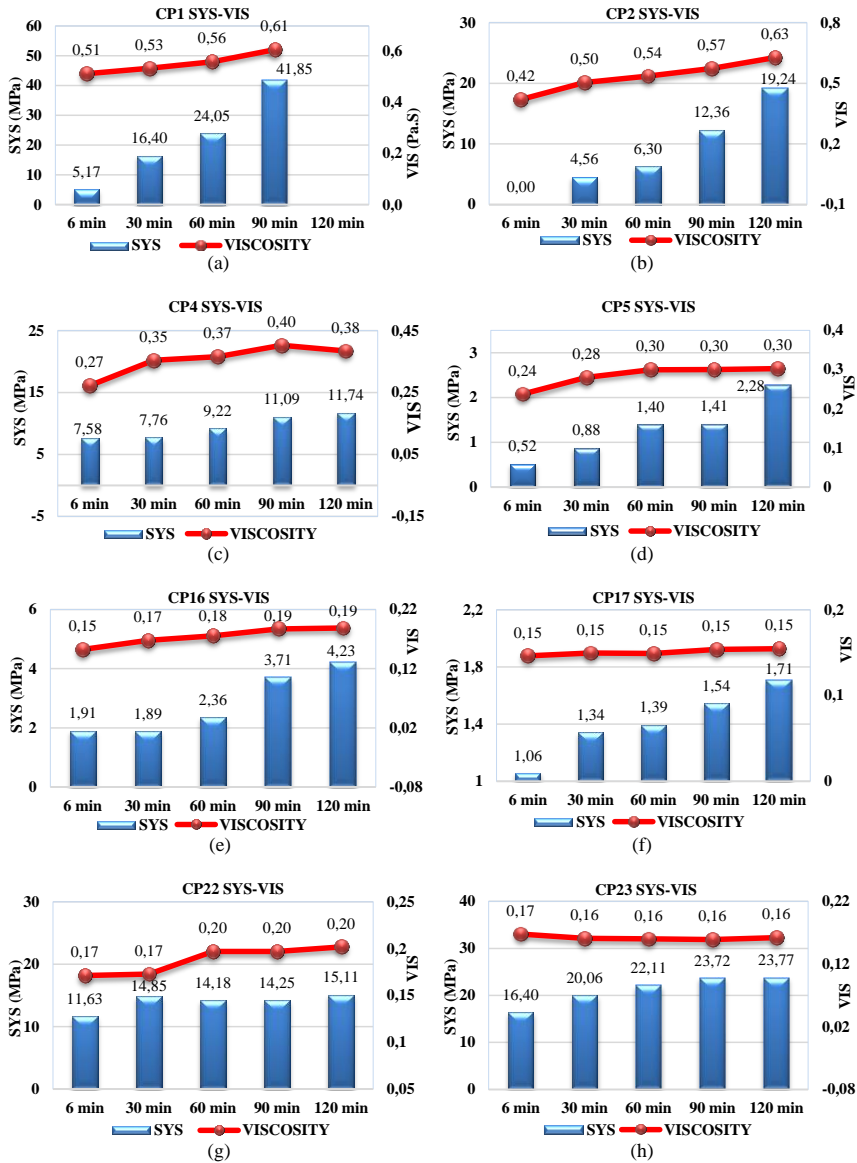


Figure 14: Correlation between Vis-SYS

- ***Correlation between Viscosity-Spread***

In general, a direct proportional relationship was observed between viscosity and SYS in the study. SYS increased over time in control samples made with cement only. Especially after the 60th minute, the increase accelerated. The viscosity increase rate was not as much as SYS. However, the machinability loss was not much (Figure 15-a, b)

In FA added CP mixtures, when the ratios of W/B=26% and SP/B=1% were kept constant and the FA ratio was increased from 20% to 35%, both SYS and viscosity values decreased. The decrease in the viscosity value and the decrease in the SYS value revealed that the homogeneity of the material was not deteriorated, and the workability was preserved. (Figure 15-c, d)

In FA added samples where both W/B and FA ratios are maximum, when W and SP are kept constant and FA ratio is increased, the decrease in viscosity is less and the decrease in SYS is slightly higher. A situation with good workability has occurred. (Figure 15-e, f)

In mixtures with SF, when W/B 30% and SP were kept constant at 1.5%, SF ratio increased from 5% to 10%, SYS increased, and viscosity decreased. This showed that the workability was reduced. (Figure 15-g, h).

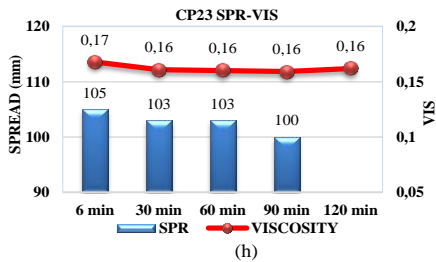
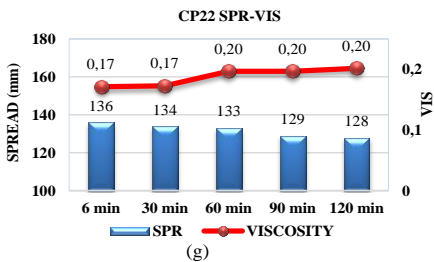
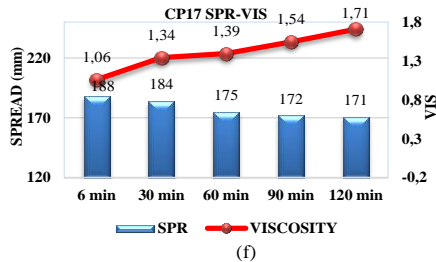
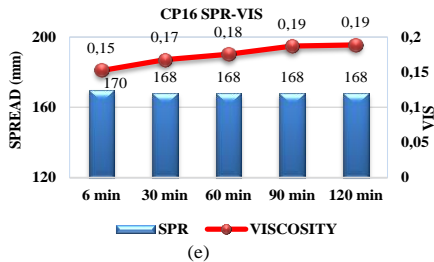
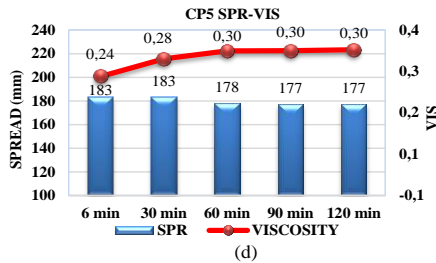
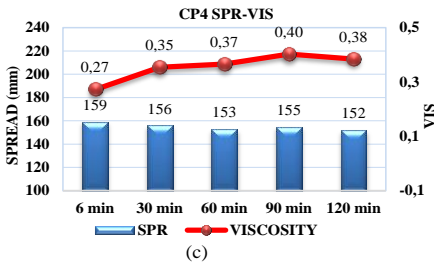
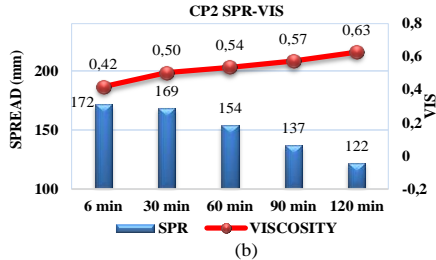
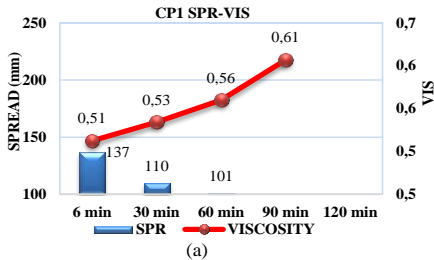


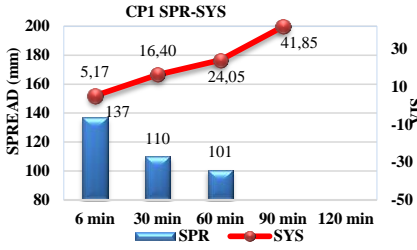
Figure 15: Correlation between Vis-Spread

- ***Correlation between Shear Yield Stress-Spread***

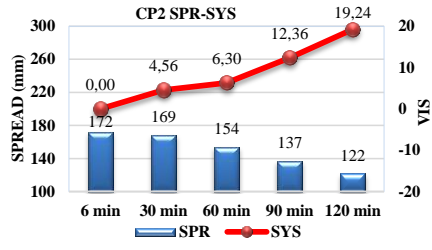
In the samples without mineral admixtures, the W/B ratio kept constant while the mineral admixture ratio increased, and the viscosity values decreased. Especially in the 120th minute, it has decreased from 41.85 Pa.s to 19.24 Pa.s. The spreading could not be measured after the 60th minute in the sample with a low SP ratio. The SP ratio was very effective in both features, and the interaction between cement-SP was strong (Figure 16-a, b).

In FA-added samples, FA increased while the W/B and SP were constant, and the viscosity decreased approximately 14 times at the beginning and five times at the end. On the other hand, the spreads increased remarkably (Figure 16-c, d).

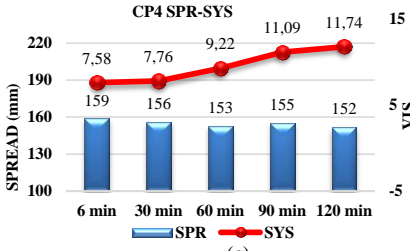
In FA-added samples, when FA increased while W/B was 30% at the upper limit and SP was kept constant at 1% at the lower limit, the viscosity decreased, and the spread increased. While the FA ratio was low in viscosity and high in spreading, the difference between the 6th and 120th minutes was more pronounced (Figure 16-e, f). It was seen that the increase of mineral admixture caused an increase in viscosity and a decrease in spread (Figure 16-g, h).



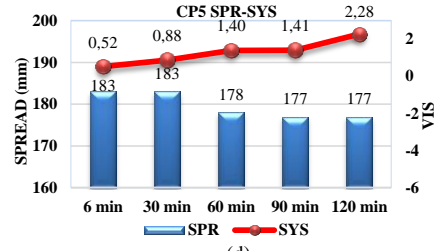
(a)



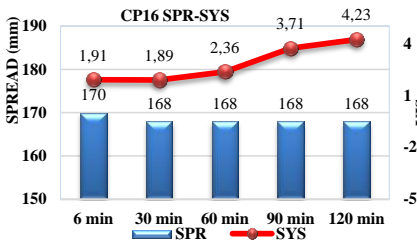
(b)



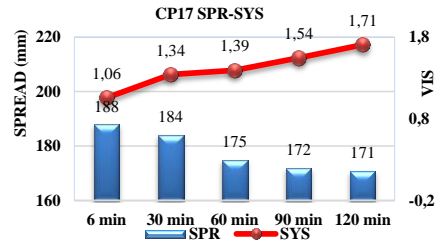
(c)



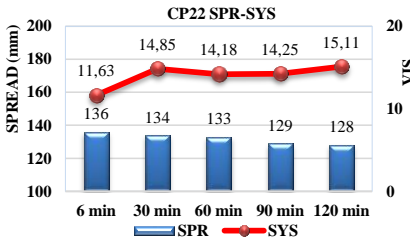
(d)



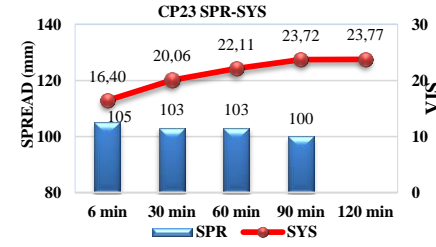
(e)



(f)



(g)



(h)

Figure 16: Correlation between SYS-spread

CONCLUSION

The following conclusions can be drawn from this study.

- A significant and slightly directly proportional relationship was observed between viscosity and shear yield stress in cement pastes. The use of silica fume instead of fly ash showed an effect increasing both viscosity and SYS in cement pastes.
- When SYSs were compared, it was observed that CPs with SF had higher values than those with FA. It has been revealed that SYS approaches zero in mixtures where both FA and SF CPs are very high and SYS is very low, and even takes negative values in mixtures with FA. It can be stated that this type of CP is normally considered Newtonian except for the Bingham behaviour representation.
- In general, the most effective mixing parameters in fly ash pastes were FA/B and W/B. SP/B was also found to be more effective on the spreading rate and shear threshold but did not deteriorate the viscosity. A very low viscosity value indicates segregation and segregation in the mixture.
- In experiments with CP, it was observed that the use of pozzolan (FA, SF) and SP improved all the rheological properties of the building material. Accordingly, it was observed that especially the machinability and consistency properties improved with the decrease of SYS values to a certain extent. Therefore, it has been determined that pumpability has also improved, thus contributing to the reduction of energy use, which is the most important factor today.
- It can be accepted that the use of FA together with SP is very effective in reducing water use, and the use of SF in the right proportions to balance this will make the SYS and viscosity values more balanced.
- It has been observed that the "Response surface" method, which is applied to the experimental data designed with the "Factorial Design Method" method, can be successfully applied in the estimation of the rheological parameters of self-compacting cement pastes.
- It is thought that it will be useful to examine the correlations between the fresh state properties and the hardened CP properties by conducting strength and durability tests in future studies.
- A study can be made in which the cost analysis of both the chemical and mineral admixtures used and the materials poured, and the cost analysis of the work can be done by pouring the classical CP and making a cost analysis.

REFERENCES

- Ardalan, R. B., Joshaghani, A., & Hooton, R. D. (2017). Workability retention and compressive strength of self-compacting concrete incorporating pumice powder and silica fume. *Construction and Building Materials*, 134, 116-122.
- ASTM_C125-13a. (2013). Standard Terminology Relating to Concrete and Concrete Aggregates. In (Vol. C125-13a). West Conshohocken, PA, USA: ASTM.
- Bürge, T. (1999). Viscocrete. *Latest Development, Madrid, Spain*.
- Cheng, C.-S. (2016). *Theory of Factorial Design*: Chapman and Hall/CRC.
- Cheng, H.-y., Wu, S.-c., Zhang, X.-q., & Wu, A.-x. (2020). Effect of particle gradation characteristics on yield stress of cemented paste backfill. *International Journal of Minerals, Metallurgy and Materials*, 27(1), 10-17.
- Choudhary, R., Gupta, R., Alomayri, T., Jain, A., & Nagar, R. (2021). *Permeation, corrosion, and drying shrinkage assessment of self-compacting high strength concrete comprising waste marble slurry and fly ash, with silica fume*. Paper presented at the Structures.
- Choudhary, R., Gupta, R., & Nagar, R. (2020). Impact on fresh, mechanical, and microstructural properties of high strength self-compacting concrete by marble cutting slurry waste, fly ash, and silica fume. *Construction and Building Materials*, 239, 117888.
- Dadsetan, S., & Bai, J. (2017). Mechanical and microstructural properties of self-compacting concrete blended with metakaolin, ground granulated blast-furnace slag and fly ash. *Construction and Building Materials*, 146, 658-667.
- Güneyisi, E., Gesoğlu, M., Al-Rawi, S., & Mermerdaş, K. (2014). Effect of volcanic pumice powder on the fresh properties of self-compacting concretes with and without silica fume. *Materials and Structures*, 47(11), 1857-1865.
- Houst, Y., Flatt, R., Bowen, P., Hofmann, H., Maeder, U., Widmer, J., . . . Buerge, T. (1999). New superplasticizers: From research to application. In *Modern concrete materials: binders, additions and admixtures* (pp. 445-456): Thomas Telford Publishing.
- Khayat, K., Ghezal, A., & Hadriche, M. (1999). Factorial design model for proportioning self-consolidating concrete. *Materials and Structures*, 32(9), 679-686.
- Kong, T.-W., & Lee, H.-S. (2021). The Rheology of Cement Paste Using Polycarboxylate-Based Superplasticizer for Normal Strength-High Fluidity Concrete. *Journal of the Korean Recycled Construction Resources Institute*, 9(3), 276-286.
- Lacerda, M. M. S., da Silva, T. J., Alva, G. M. S., & de Lima, M. C. V. (2018). Influence of the vertical grouting in the interface between corbel and beam in

- beam-to-column connections of precast concrete structures—An experimental analysis. *Engineering Structures*, 172, 201-213.
- Mendes, P. R. S., & Dutra, E. S. (2004). Viscosity function for yield-stress liquids. *Applied Rheology*, 14(6), 296-302.
- Montgomery, D. C. (2017). *Design and analysis of experiments*: John Wiley & sons.
- Nornberg, J., Peterson, Ö., & Billberg, P. (1997). *Effect of new generation superplasticizers on the properties of fresh concrete*, *Superplasticizers and Other Chemical Admixtures in Concrete*. Paper presented at the Proceedings.
- Okamura, H. (1997). Self-compacting high-performance concrete. *Concrete international*, 19(7), 50-54.
- Özkul, M., Dogan, A., Çavdar, Z., Sağlam, A., & Parlak, N. (2000). *Effects of self compacting concrete admixtures on fresh and hardened concrete properties*. Paper presented at the Proceedings.
- Özkul, M., Doğan, A., Çavdar, Z., Sağlam, A., & Parlak, N. (1999). Properties of fresh and hardened concretes prepared by new generation superplasticizers. In *Modern Concrete Materials: Binders, Additions and Admixtures* (pp. 467-474): Thomas Telford Publishing.
- Princen, H., & Kiss, A. (1989). Rheology of foams and highly concentrated emulsions: IV. An experimental study of the shear viscosity and yield stress of concentrated emulsions. *Journal of colloid and interface science*, 128(1), 176-187.
- Ramanathan, P., Baskar, I., Muthupriya, P., & Venkatasubramani, R. (2013). Performance of self-compacting concrete containing different mineral admixtures. *KSCE journal of Civil Engineering*, 17(2), 465-472.
- Sadrmomtazi, A., Gashti, S. H., & Tahmouresi, B. (2020). Residual strength and microstructure of fiber reinforced self-compacting concrete exposed to high temperatures. *Construction and Building Materials*, 230, 116969.
- Sharbatdar, M. K., Abbasi, M., & Fakharian, P. (2020). Improving the properties of self-compacted concrete with using combined silica fume and metakaolin. *Periodica Polytechnica Civil Engineering*, 64(2), 535-544.
- Skarendahl, Å., & Petersson, Ö. (2000). *Report 23: Self-Compacting Concrete—State-of-the-Art Report of Rilem Technical Committee 174-SCC* (Vol. 23): RILEM publications.
- TS-EN-197-1. (2012). Cement – Part 1: Composition, specification and conformity criteria for common cements. In *Cement – Part 1: Composition, specification and conformity criteria for common cements* (Vol. TS EN 197-1). Ankara: Turkish Standards Institute.

- Tullini, N., & Minghini, F. (2016). Grouted sleeve connections used in precast reinforced concrete construction—Experimental investigation of a column-to-column joint. *Engineering Structures*, *127*, 784-803.
- Uchikawa, H., Hanehara, S., & Sawaki, D. (1997). The role of steric repulsive force in the dispersion of cement particles in fresh paste prepared with organic admixture. *Cement and Concrete Research*, *27*(1), 37-50.
- Vasumithran, M., Anand, K., & Sathyan, D. (2021). Effects of fillers on the rheology of cement grouts. *Materials Today: Proceedings*, *46*, 5153-5159.
- Yoshioka, K., Sakai, E., Daimon, M., & Kitahara, A. (1997). Role of steric hindrance in the performance of superplasticizers for concrete. *Journal of the American Ceramic Society*, *80*(10), 2667-2671.

Chapter 2

Formation Mechanisms and Deposition Processes of Pyroclastic Rocks

Abdullah SAR¹
Mehmet Ali ERTÜRK²

ABSTRACT

The pyroclast is defined as crumbs thrown out of volcanic vents, regardless of the origin of the grains and their eruption patterns. Pyroclastic rocks are formed by the transport, accumulation and consolidation of pyroclastic material produced by a volcanic eruption by air or water. Pyroclastic eruptions are examined in four sections: Hawaiian-type, Stromboli-type, Vulcano-type and Plinian-type eruptions, according to magma density, viscosity, temperature, gas content and chimney height. While Hawaiian eruptions with the lowest eruption intensity are represented by basaltic lavas, Plinian eruptions with the highest eruption intensity are represented by dacitic lavas with high viscosity. Pyroclastic eruptions are deposited as debris, flows and turbulence deposits. The sizes and shapes of the debris tanks formed after the explosive rise of gas and tephra from the chimney reflect the eruption column height, speed and direction of atmospheric winds. As a result of the spreading of the rising column, the crumbs fall to the ground due to gravity and thus form "debris depots". The formation of flow depots, which are formed due to the pyroclastic mass with high grain density flowing along the surface, is controlled by gravity, and the pyroclastic material is hot and sometimes fluid. Pyroclastic material: The reservoirs are transported by a widespread, turbulent, low-grain density gas-grain cloud across the surface with turbulent motion.

Keywords: Pyroclast, Pyroclastic rocks, Pyroclastic eruptions, Pyroclastic Eruption Deposites

¹ Arş. Gör Dr., Fırat University Engineering Faculty Department of Geological Engineering. asar@firat.edu.tr
ORCID No: 0000-0002-9752-7807

² Dr. Öğr. Üyesi; Fırat University Engineering Faculty Department of Geological Engineering.
erturkmae@gmail.com ORCID No: 0000-0003-1197-9202

INTRODUCTION

Pyroclastic rock is formed by the transport, accumulation and consolidation of pyroclastic material produced by a volcanic eruption by air or water (Sun et al., 1987, 2001; Chang et al., 2009; Huang et al., 2010; Wang et al., 2019; Zhou et al., 2022). Regarding classification, pyroclastic rocks are located in the transition zone between volcanic and sedimentary rocks (Sun et al., 1987, 2001; Chang et al., 2009; Zhou et al., 2022). Although it has the characteristics of volcanic and sedimentary rocks, it has a complex lithology. (Sun et al., 1987, 2001; Chang et al., 2009; Huang et al., 2010; Wang et al., 2019; Yuan et al., 2021). The mineral composition and cementation mode are different from the other two species (Sun et al., 2001; Huang et al., 2010; Wang et al., 2019; Yuan et al., 2021). Pyroclastic rocks are mainly composed of pyroclastic material with some sediments or lava materials (Chang et al., 2009; Huang et al., 2010; Wang et al., 2019; Zhou et al., 2022). Physically, these rocks can be described as hard, semi-plastic or plastic (Sun et al., 1987, 2001; Chang et al., 2009; Huang et al., 2010; Wang et al., 2019; Zhou et al., 2022). Typically, pyroclastic rocks consist of a combination of rock debris, crystal debris, and volcanic glass debris (Huang et al., 2010; Wang et al., 2019).). Pyroclastic rocks can also form from amorphous cooled molten mud, as pyroclastic material is subjected to rapid changes in pressure and temperature as lava advances towards the surface (Sun et al., 1987, 2001; Chang et al., 2009; Wang et al., 2019; Zhou et al., 2022).

Pyroclast is defined as fragments of grains thrown out from volcanic vents, regardless of their origin and eruption form (Schmid, 1981). Pyroclastic clasts are clasts formed directly by volcanic means. Volcanic materials that have been involved in sedimentation processes are defined as volcanoclastic. Hydroclastic clasts are a type of pyroclasts formed from steam eruptions where magma-water interaction occurs, rapid cooling, and mechanical graining of lavas in contact with water or water-saturated sediments (URL-1).

ERUPTION TYPES

Pyroclastic eruptions are divided into Hawaiian (Figure 1a), Stromboli (Figure 1b), Vulcano (Figure 1c), and Plinian (Figure 1d) eruptions.

Hawaiian-Type Eruptions

Hawaiian eruptions are one of the types of volcanic eruptions named after Hawaiian volcanoes. These are among the calmest eruptions, characterized by intense eruptions of fluid basaltic lavas due to their low gas content. The volume of materials ejected in Hawaiian eruptions is less than half that in other eruptions. The continuous production of small amounts of lava creates the large shape of a

shield volcano. Eruptions are not centred on the main summit as in other volcanic types but generally occur in cracks radiating from outside the centre and in chimneys around the summit (URL-2).

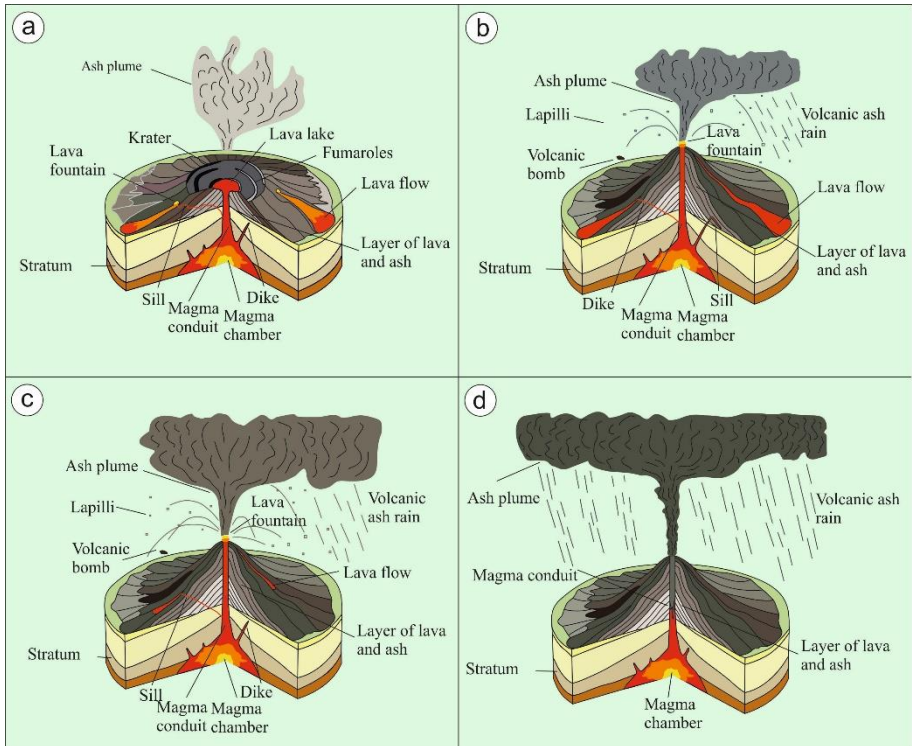


Figure 1: Pyroclastic eruption types **a.** Hawaii-type eruption, **b.** Stromboli-type eruption, **c.** Vulcano-type eruption, **d.** Plinien-type eruption (URL-2).

Hawaiian eruptions begin as an eruption line along cracks called "fire curtains." These are cut off over time as lava accumulates in the crevices. Central vent eruptions, meanwhile, take the form of large lava fountains that can reach hundreds of meters high. Particles in lava fountains often cool in the air before falling to the ground, accumulating volcanic cinders. However, when the air is concentrated, especially with volcanic fragments, it does not cool quickly enough due to the surrounding temperature. The pieces fall hot to the ground and form cinder cones (URL-2)..

If eruption rates are high enough, they can produce splatter-fed lava flows. Hawaiian eruptions are often extremely long-lasting; Pu'u O'o, a cinder cone of Kilauea, has erupted continuously since 1983. Another feature of Hawaiian

volcanoes is active lava lakes. Currently, there are only 5 of these lakes in the world. Kilauea's Kupaianaha crater is one of them.

The flows in the Hawaiian eruptions are basaltic, and their structural character is divided into two types. Pahoehoe lavas are fairly smooth lava flows that can be wavy or rope-shaped. A'a lava flows are denser and more viscous than Pahoehoe lavas and tend to be transported more slowly. Flows can be measured between 2-20 meters thick. A'a lavas are so thick that their outer shell cools from the inside, like a rock mass that protects it from cooling and isolates the heat inside. Pahoehoe lavas can turn into A'a lavas as their viscosity increases, but A'a lavas never turn into Pahoehoe flows (URL-2)..

Hawaiian eruptions are responsible for several specific volcanological formations. Small volcanic particles are formed and carried by the wind, quickly cooling the inside of teardrop-shaped glassy fragments known as Pele's tears (URL-2).. Especially during strong winds, these pieces can take the form of long striped hairs known as Pele's hair (Figure 2).

Stromboli-Type Eruptions

Stromboli eruptions are one of the types of volcanic eruptions named after the Stromboli volcano, which has been erupting continuously for centuries. Stromboli eruptions are triggered by the explosion of gas bubbles within magma. These gas bubbles within the magma coalesce and accumulate into large bubbles called gas slugs. These grow large enough to rise throughout the lava column. Once they reach the surface, differences in air pressure cause the bubbles to burst with a loud noise. Due to the high gas pressure associated with lavas, sustained activity usually consists of episodic explosive eruptions accompanied by distinctive high eruptions (URL-2). During an eruption, these explosions occur every few minutes.

The term stromboli is used to describe a variety of volcanic eruptions, ranging from small volcanic eruptions to large eruption columns. True stromboli eruptions are characterized by the explosive eruption of short-term and moderately viscous lavas. Eruption columns can reach heights of hundreds of meters (URL-2). The lavas formed by these eruptions are partly a form of high-viscosity basaltic lavas, and their final product is mostly scoria (Figure 3).

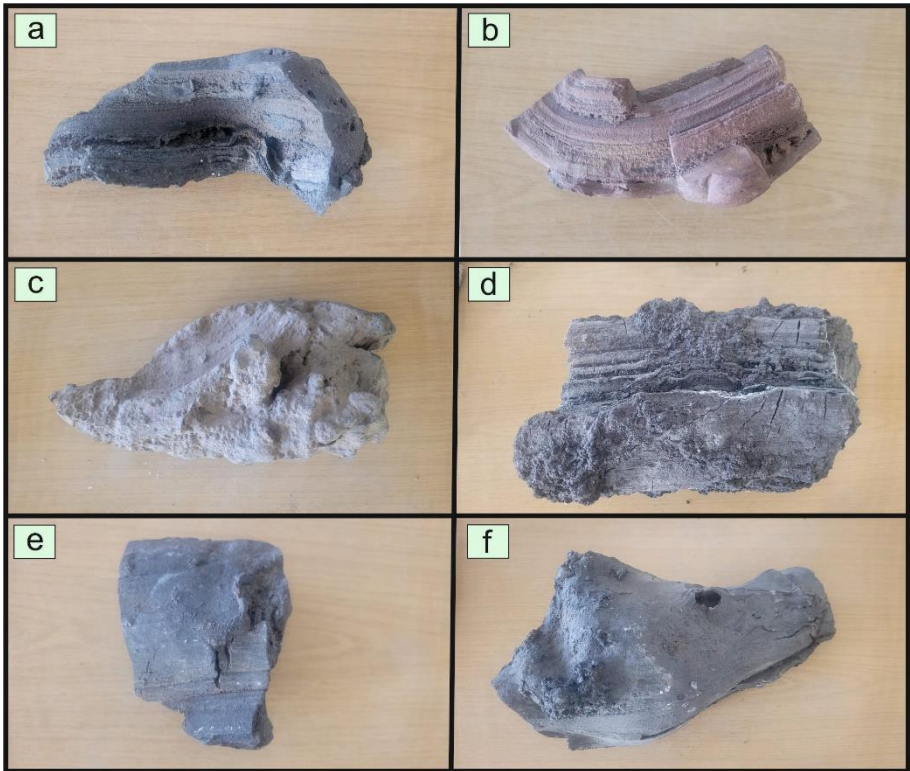


Figure 2: Samples of pyroclastic Pele's hair

Strombolian eruptions eject volcanic bombs and lapilli fragments (Figure 4) that travel in a parabolic orbit before falling into a region around the crater. The continuous accumulation of small fragments forms cinder cones formed entirely by combining basaltic pyroclasts. Stromboli eruptions are similar to Hawaiian eruptions, but there are some differences. Stromboli eruptions are louder and do not have a continuous eruption column. Pele's hair does not produce some volcanic products associated with Hawaiian volcanism, such as Pele's tears (Figure 2), and produces less molten lava flows (URL-2).

Vulcano-Type Eruptions

Vulcanian eruptions are one of the types of volcanic eruptions named after the Vulcan volcano, which gave the word volcano its name. In Vulcan-type eruptions, separating gases from the magma is difficult due to their high viscosity. Similar to Stromboli eruptions, an increase in high gas pressure is observed in these eruptions. However, unlike Stromboli eruptions, the lava pieces ejected in vulcano-type eruptions are not aerodynamic. This is due to the high viscosity of

the magma. They are much more explosive than stromboli-type eruptions, with eruption columns reaching 5 to 10 km (URL-2).

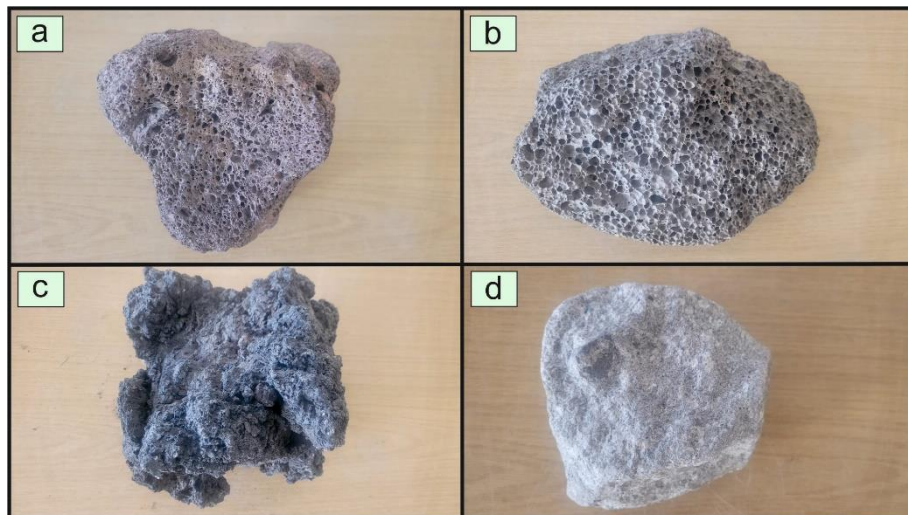


Figure 3: Samples of pyroclastic scoria

Vulcanian deposits are andesitic or dacitic rather than basaltic. Initial volcanic activity involves a series of short-lived eruptions lasting from a few minutes to several hours, typically ejected volcanic bombs and blocks. These eruptions erode the lava domes that preserve the magma underneath and break it apart with numerous and continuous eruptions. Therefore, early signals of future Vulcanian eruptions are lava dome growth. As lava domes collapse, pyroclastic material forms on the volcano's slopes (URL-2).

Deposits close to the crater contain large volcanic blocks and bombs (Figure 4), particularly commonly called "bread crust bombs". They are formed by rapidly cooling the ejected lava's outer surface into a glass or fine-grained shell. However, cooling and void formation continue inside. The centre of the piece expands, cracking the outer surface. However, Vulcanian deposits consist of fine-grained ash. This ash is partially dispersed, and its abundance indicates high gas pressure within the magma and a high degree of fragmentation (URL-2).

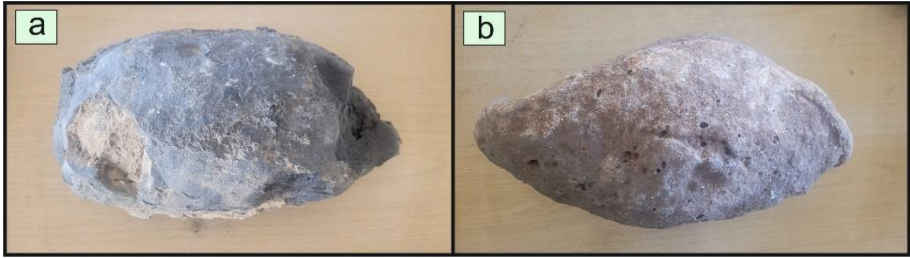


Figure 4: Samples of pyroclastic bomb

Plinian-Type Eruptions

In Plinian-type eruptions, the process begins in the magma chamber, where dissolved volatile gases accumulate in the magma. Gases rise along the magma channel, accumulate and form a void. These bubbles coalesce and burst when they reach a certain size (approximately 75% of the total volume of the magma conduit). Narrow sections of the channel put pressure on the gases that shape the eruption column. The gas content in the magma column controls the eruption rate, and low-strength surface rocks disintegrate under the eruption pressure, forming a conical outlet structure (URL-2)..

Large-diameter eruption columns are a distinctive feature of Plinian eruptions. They reach an altitude of between 2 and 45 km in the atmosphere. These highly explosive eruptions are associated with rhyolitic or dacitic lavas, rich in volatile content, and are typically seen in stratovolcanoes. Eruptions can continue for days, with longer-lasting eruptions more commonly associated with felsic volcanoes (URL-2). Although associated with felsic magma, Plinian eruptions can also occur in basaltic volcanoes.

Plinian eruptions are similar to Vulcanian and Strombolian eruptions, except for distinct explosive eruptions. Continuous eruption columns shape plinian eruptions. These eruptions are similar to the Hawaiian eruption type. Both types of eruptions form continuous eruption columns fueled by the growth of bubbles that are transported at approximately the same speed as the surrounding magma (URL-2)..

Regions affected by Plinian eruptions are exposed to dense pumice (ash) clouds, affecting an area of 0.5 to 50 km³. The most dangerous eruption feature is pyroclastic flows, which occur when material transported down the mountain slope at a speed of approximately 700 km per hour collapses.

PYROCLASTIC ERUPTION DEPOSITES

Pyroclastic deposits, formed due to magma or rock's disintegration by explosive volcanic activity, are divided into three groups according to their

origin, transportation and storage methods. These are (i) debris, (ii) flow, and (iii) turbulence (Helvacı and Erkül, 2001).

Spill Deposit

The sizes and shapes of the debris tanks formed after the explosive rise of gas and tephra from the chimney reflect the eruption column height, speed and direction of atmospheric winds. As a result of the spreading of the rising column, the crumbs fall to the ground due to gravity and thus form "debris depots". Larger pieces fly out of the chimney due to explosions, and the pieces called "ballistic crumbs or clasts" are unaffected by the wind. Pyroclastic flows partially form other fine-grained pyroclastic debris depots. They are formed by separating from the upper part. These depots are called "debris depots derived from the ash cloud" (Helvacı and Erkül, 2001).

Debris deposits that form overburden layers generally have equal thickness, except for areas with high slope topography. Although poor sorting is generally observed in pyroclastic deposits, debris deposits show good sorting due to their separation in air during transportation. In some cases, they show planar lamination or layering due to the change of the eruption column. However, they do not present erosion, cross-bedding or load structures in the underlying layers. It originates from debris tanks near the chimney (Helvacı and Erkül, 2001).

Flow Deposit

These deposits are formed due to the pyroclastic mass with high grain concentration flowing along the surface. Their formation is controlled by gravity, and the material is hot and, in some cases, fluid. They generally show topography-controlled settlements that fill valleys and depression areas (Helvacı and Erkül, 2001). When the internal structure of pyroclastics is examined, it is seen that they are generally massive and poorly sorted. Poor sorting in flow tanks is due to high grain concentration and is not related to turbulence. The dominant flow mechanism is generally laminar. When each flow unit overlaps, it appears as a layer. In pyroclastic flow reservoirs, sometimes, after the flow stops, "fossil fumarole chimneys" or gas outlet chimneys are formed due to the separation of fine ash-sized material by the gas effect. Structures formed as a result of the enrichment of heavy crystalline, lithic and larger vesicular pieces in vents are one of the most important data in distinguishing primary pyroclastic deposits from epiclastic flows formed as a result of the flow of volcanic material (Helvacı and Erkül, 2001).

Pyroclastic flows settle at high temperatures. Pyroclastic flows are also mechanisms that preserve temperature well. Therefore, hot pyroclastic flows may

be at approximately magmatic temperature during their movement and shortly after their emplacement. Conditions such as the height of the material ascending in the eruption column, the amount of cold air mixed during the upward movement of the eruption column, the total volume of the flow, and the amount of air engulfed during column collapse determine the settlement temperature of pyroclastic flows. Data showing settlement at high temperatures are important in distinguishing pyroclastic flow deposits from epiclastic stack flow deposits (Helvacı and Erkül, 2001). These data:

(a) Charred piece of wood,

(b) Pink colour or magnetite (or other metal) resulting from thermal oxidation of iron

dark colour due to the crystallization of microliths (iron/manganese oxide minerals),

(c) Welded tuff zone or zones,

(d) Thermal residual magnetism (Hoplitt and Kellogg, 1979)

The reservoirs of pyroclastic flows are diverse, reflecting sedimentation regimes and different types of eruptions. Most pyroclastic flow reservoirs consist of more than one flow unit. Each flow unit is considered a pyroclastic flow reservoir. Three main types of flow deposits are defined in current volcanic deposits.

- Block and ash flow tanks,
- Basaltic slag flow tanks and
- Pumex flow deposits or ignimbrites.

Block and ash flow deposits are unsorted depots controlled by topography, with an ash matrix containing lithic, non-vesicular blocks of congeneric origin that can exceed 5 m in diameter. Some of these blocks have radial cracks, indicating they were hot-settled. Clasts generally have the same magma type and present monolithological features. A flow unit may be reverse-graded within itself. Although not very common, gas escape structures and charred pieces of wood can be found. These sediments' homogeneous clast composition, hot blocks' location, and gas escape structures are important field data in distinguishing them from other epiclastic deposits. Basaltic slag flow tanks are unsorted and topographically controlled tanks made of vesicular lapilli and ashes in basalt-andesite composition in varying amounts up to 1 m in diameter.

In some cases, they may contain large and cognate non-vesicular lytic clasts. Reverse grading of large clasts is common within flow units, and a fine-grained base level can sometimes be found at the base of the flow unit. Gas escape chimneys and charred pieces of wood can be seen. Welding is not seen.

Pumex flow deposits, or ignimbrites, are typically poorly sorted and massive deposits containing varying amounts of ash and rounded pumex lapilli and occasionally block up to 1 m in diameter. Within flow units, lithic clasts show normal grading, while large pumex fragments may be reversely graded. However, ungraded yield units are generally common. Fine-grained basement levels are located at the base of flow units.

Pyroclastic flows occur in different tectonic and volcanic locations and very different volumes. Small (and medium) volume streams generally range from rhyolite to basalt in composition. However, large-volume flows are mostly composed of rhyolite to dacite. The different types of pyroclastic clasts in pyroclastic flow deposits relate to how the flows develop. Although small-volume flows are found to be predominantly pumice, small-volume flows produced by dome collapse or explosions associated with dome formation generally contain poorly porous products of domes. Medium to large volume flows generally comprise materials with high vesicle content, originating from magma that forms vesicles quickly.

In the relationship of pyroclastic flows with topography, pyroclastic flows flow entirely from the upper slope and can be preserved in the lower parts of the valleys where they can first thicken, away from the source (Gorshkov, 1959; Taylor, 1958). In areas with flat topography, small-volume pyroclastic flows may be confined to valleys. On the volcano's upper slopes, pyroclastic flows flow down from the centres of the volcano, leaving large pieces of rock with traces of hard and high water on either side of the valley or the upper edges of the meandering channel due to the flowing action. Pyroclastic flows spread in fan-like lobes like lahars beyond the mountain slopes (Helvacı and Erkül, 2001).

Pyroclastic and turbulent flow reservoirs are composed of crystals, glass shards, pumice and lithic fragments in highly variable proportions, depending on the roots and magma composition of the flows. In some deposits, many crystals and their lithic composition may be xenoliths (Helvacı and Erkül, 2001). Flow reservoirs derived from lava flows, dome collapse, or eruption cessation. They contain a mixture of partially vesicular, partially vesicular, or fully vesicular lithic clasts. In the definition of ash flow tuffs, ash size intervals (2 mm) components are more than 50%. This forms the dough that will hold varying amounts of pumice lapilli or lithic lapilli together. Glass fragments, the most common ash-sized grains, are often accompanied by small amounts of pumice shards. Ash or lapilli-sized pumice pieces are characterized by long, subparallel planar vesicles that are either spherical or a few millimetres to micrometres in diameter. Flat pumice is thought to develop due to the rapid rise of magma-containing vesicles from the chimney, where the vesicles extend (Helvacı and

Erkül, 2001). Crystals are another component close to the ash size. Compared to phenocrysts in lavas, those in ignimbrite are generally fractured. The fact that the crystals in the pumas lapilli or blocks are generally unbroken indicates that the breakage occurred during eruption or transport. Considering that twisted mica lavas, "boudin" feldspar tablets, and slightly separated fractures in the crystal were filled with glass, the fracture may have continued during compaction. Crystal dominance is approximately 0-50% in ignimbrites. And its equivalent in the same composition may be greater than the amount in the lava flow. Crystals are generally more abundant in the matrix than in pumice or lapilli bombs. This is strong evidence of preferential concentration in the matrix compared to crystalline glass fragments during transport (Hay, 1959; Walker, 1972; Sparks and Walker, 1977).

Since most large-volume pyroclastic flow deposits are calc-alkaline dacite-rhyolite, common phenocrysts are quartz, sanidine, plagioclase and small amounts of amphibole, pyroxene, phonolite. In peralkalic rhyolites, anorthoclase replaces two feldspars (Helvacı and Erkül, 2001). Lithic clasts rarely exceed 5% in medium (too large) volume and some small-volume pumiceous pyroclastic flows. There are three main sources for liquid clasts:

The crust formed on the chamber walls in slowly cooling and crystallizing magma (Schnincke, 1973). Rocks coming from the chimney walls. Rock clasts collected along the line of pyroclastic flows. From the first two sources, information about the depth of the magma reservoir can be obtained if the regional stratigraphy is known well enough. Felsic, calc-alkaline, and alkaline magma eruptions formed most medium and large-volume ignimbrites. Additionally, they show vertical compositional zoning due to post-eruption zoning in the initial magma chamber.

In pyroclastic flow deposits, graded basement zones are revealed by irregular arrangements of large clasts, alternation of coarse (fine) grained levels, rough orientation of long or plate-like grains and color-composition changes. Many features, including graded bedding, are evidence of settlement by high-density laminar currents. The gradation in a single yield unit can be normal, reverse, symmetrical or repetitive. Pumex clasts should be reverse graded, while lithic clasts may be normally graded due to large density differences.

In the textural analysis of pyroclastic flow deposits, it is important to know the relative amounts of crystals, rock fragments and pumice (Walker, 1971; Sparks, 1976). Because grain size distribution, sorting and other parameters of these three materials may be different from the sorting in the eruption column during flow, for example, lithic clasts may derive from magmatic stopping, disintegration of magma chamber walls, or disintegration of the plug or dome

within the vent. They may also have been collected from the ground during the flow. The grain size distribution of crystal clasts is a function of primary phenocryst size in the magma and fracture during explosive eruption. Furthermore, different mineral types have different grain size ranges (e.g. Feldspar vs Magnetite). Pumex has low mechanical strength, and the reason for the dominance of pumex dust in the fine-grained fraction of the sediment may be the decrease in grain size during eruption and flow (Walker, 1972).

Grain size vertical gradation is highly variable, although not always in pyroclastic flow deposits. Vertical grading of large grain sizes is common, except for the fine-grained bottom level of pyroclastic flow deposits. For example, pumex grains should be reverse-graded (Sparks et al., 1973, Sparks, 1976). However, they can also be graded normally. They can also be graded alternately, especially at the base level. The largest pumice grain size may be three times greater in the upper part of the stream than in the lower part.

In some cases, excessive concentration of pumice grains is found in the upper part of the flow unit. However, they have also been observed near the base (Crowe et al., 1978). In terrestrial deposits, the largest grain size of pumice and lithics decreases with distance. There are two processes in forming turbulence reservoirs where grain gradations are observed. The first is very intense turbulent pyroclastic flow, and the second is laminar flow. Here, a wide range of pyroclastic flow types occur, from high grain density to low grain density. This requires a process from complex grain flow to fluidized, laminar, and more turbulent flow. As grain size decreases in reservoirs formed by turbulence, the differences between flow and turbulence reservoirs decrease with the development of laminar flow where friction is low (Helvacı and Erkül, 2001). In pyroclastic flows, fluidization is necessary to transport large grains. It is natural for large amounts of fine-grained material to be removed in turbulent flows, and this causes fluidization to decrease. However, the removal of fine-grained material occurs not only during turbulence but also during pyroclastic flow processes. There is no change in the flow pattern during the fine grain removal process that develops with pyroclastic flow.

Segregation and washing of grains lead to reducing fine-grained vitric clasts and enriching crystalline lithic clasts in pyroclastic flow deposits. It occurs during flow in the chimney and the spray cone. Grains with low speed are not carried high in the atmosphere and are not carried away by the current. Others escape upstream as the current moves. These developments led to the formation of different types of fine-grained "Fallout tephra" with a lower crystal/glass ratio than pumice (Sparks and Walker, 1977).

Pyroclastic flows occur by several different mechanisms. According to observations made on current volcanoes, these are mainly divided into two main groups. (1) lava-dome or lava-flow collapse, (2) eruption column collapse.

Turbulence Deposit

Pyroclastic deposits are transported by turbulent movement along the surface with a widespread, turbulent and low-grain density gas-grain cloud. Pyroclastic turbulence can occur in many different ways. Volcanic basement turbulence reservoirs constitute only one of these and are formed due to "phreatomagmatic" eruptions. Pyroclastic turbulence deposits are known to be deposited in three situations. These are (1) "phreatomagmatic" and "phreatic" eruptions, (2) pyroclastic flows and (3) pyroclastic eruptions (Helvacı and Erkül, 2001).

These eruptions form base turbulence, a low ash cloud that spreads circularly in all directions from the explosion's location or the "Phreatomagmatic"/"Phreatic" eruption column. Basement turbulence resulting from the interference of magma and water is "cold and wet" in many cases. No charring of trees was observed during the Taal 1965 eruption. In the area where ash adheres to objects, the ash is mixed with water rather than steam. Accordingly, in turbulence, the temperature should be below 100 °C. However, some "phreatomagmatic" eruptions have created hot pyroclastic turbulence reservoirs (Helvacı and Erkül, 2001). Basement turbulence is associated with the forming of small volcanic craters called maars, tuff rings, and tuff cones. These are common in basaltic volcanisms where there is no groundwater intrusion, surface water or seawater by the basaltic magma that forms basaltic slag cones. Large volcanoes with fundamental turbulence are known. Basic turbulence reservoirs are common products in andesitic caldera lakes and other stratovolcanoes (Helvacı and Erkül, 2001).

Thin, layered pumice and ash deposits are found with different pyroclastic flow deposits. If they are located at the base of the flow unit, they are called base turbulence. If they occur in the upper part, they are called ash cloud turbulence. These types of turbulence have a different formation mechanism compared to base turbulence. They can be considered hot and dry compared to base turbulence tanks. Base turbulence tanks are densely located in front of the flow body (Helvacı and Erkül, 2001). There are several ways in which they can form:

- (a) low-concentration explosion,
- (b) separation from the head of the moving pyroclastic flow and
- (c) collapses that develop earlier and are smaller than the edge of the vertical eruption column.

Ash cloud turbulence is the low-intensity flow in a gas and ash cloud. The rising ash cloud consists of material separated from the moving pyroclastic flow that will form the base. However, most of the ash that rises as a cloud is later stored as ash debris. Sometimes, the turbulent ash cloud separates from the moving pyroclastic flow and proceeds independently.

Turbulence reservoirs associated with magmatically erupted debris reservoirs are formed directly by the collapse of the eruption column without pyroclastic flow (Helvacı and Erkül, 2001). This type of turbulence is also called bottom turbulence.

According to the above descriptions, pyroclastic turbulence reservoirs can be divided into three types:

- Basic turbulence,
- Bottom turbulence and
- Ash clouds are turbulence reservoirs.

Basement turbulence creates layered, laminated and sometimes massive deposits consisting of pyroclastic clasts made of vesicular and non-vesicular lithic clasts, ash, crystals and small amounts of foreign lithic fragments (Helvacı and Erkül, 2001). Some lithic debris forms bomb traces close to the chimney. The debris formed due to the "Phreatic" steam eruption consists of fragments of the previous explosion (accessory lithic) or very few basement fragments. As a result of excessive fragmentation due to water-magma intrusion, the fragments are generally smaller than 10 cm. Although they suddenly thin out as they move away from the crater, they form thick deposits (> 100 m) around the craters. It is generally thin in alternating deposits of stratovolcanoes (Helvacı and Erkül, 2001). Uniform bedding and dune structures may be common. Uniformly stratified turbulence tanks near the stack can be difficult to distinguish from ash debris tanks. Additionally, enlarged lapilli may be commonly seen. Basement turbulence creates layered sediments less than 1 m thick and is typically seen at the base of a pyroclastic flow unit. It is made up of ash, vesicle fragments, crystals and lithic crumbs in different proportions depending on the components in the eruption column (Helvacı and Erkül, 2001). It is richer in denser components than the pyroclastic flow deposits with which it is found. Carbonized wood chips and gas vents may be present (Helvacı and Erkül, 2001). Ash cloud turbulence reservoirs are layers thinner than 1 m above pyroclastic flow units. The layers are in one direction, showing crushing and swelling structures, and can be found in thinly separated lenses. Grain size and proportions of components depend on the type of adjacent pyroclastic flow. Ash cloud turbulence reservoirs may contain small gas vents.

CONCLUSION

✓ The pyroclast is defined as crumbs thrown out of volcanic vents, regardless of the origin of the grains and their eruption patterns.

✓ Pyroclastic rocks are formed by the transport, accumulation and consolidation of pyroclastic material produced by a volcanic eruption by air or water.

✓ Pyroclastic eruptions are examined in four sections: Hawaiian-type, Stromboli-type, Vulcano-type and Plinian-type eruptions, according to magma density, viscosity, temperature, gas content and chimney height.

✓ Pyroclastic eruptions are deposited as debris, flows and turbulence deposits.

REFERENCES

- Chang, L., Cao, L., and Gao, F. (2009). *Handbook of Igneous Rock Identification*, Geological Publishing House, Beijing, pp. 95–115.
- Crowe, B.M., Linn, G.W., Heiken, G. and Bevier, M.L. (1978). Stratigraphy of Bandelier Tuff in the Pajarito Plateau; Applications to waste management. Los Alamo Sci. Lab., New Mexico, Informal Rpt., LA- 7225, 1-57.
- Gorshkov, G.S. (1959). Gigantic eruption of the volcano Bezymianny. Bull. Volcanol., 20, 77-109.
- Hay, R.L. (1959). Formation of the crystal-rich glowing avalanche deposits of St. Vincent, B. W. I. J. Geol. 67, 540-562.
- Helvacı ve Erkül, (2001). Volkaniklastik Kayaçların Oluşumu, Genel Özellikleri ve Sınıflaması, Dokuz Eylül Üniversitesi Mühendislik Fakültesi Jeoloji Mühendisliği Bölümü, Ders Notları.
- Hoplitt, R.P. and Kellogg, K.S. (1979). Emplacement temperatures of unsorted and unstratified deposits of volcanic debris as determined by paleomagnetic techniques. Geol. Soc. Amer. Bull. Part I, 90, 633-642.
- Huang, Y., Wang, P., Shao, R. (2010). Porosity and permeability of pyroclastic rocks of the Yingcheng Formation in Songliao basin. J. Jilin Univ. (Earth Sci. Ed.), 40 (2), 227–236.
- Schmincke, H.-U. (1973). Magmatic evolution of tectonic regime in Canary, Madeira and Azores Island Groups. Geol.Soc. Amer.Bull., 84, 633-648.
- Sparks R.S.J. and Walker, G.P.L. (1977). The significance of vitric-enriched air-fall ashes associated with crystal-enriched ignimbrites. J. Volcanol. Geotherm. Res., 2, 329-341.
- Sparks R.S.J., Self, S. and Walker, G.P.L. (1973). Products of ignimbrite eruption. Geology, 1, 115-118.
- Sparks R.S.J. (1976). Grain size variations in ignimbrites and implications for the transport of pyroclastic flows. Sedimentology, 23, 147-188.
- Sun, S., Li, J., Zhu, Q., and Wei, H. (1987). History and present situation of classification and nomenclature of pyroclastic rocks in China and abroad. Earth Sci.—J. Wuhan Coll. Geol. 12 (6), 571–577.
- Sun, S., Liu, Y., Zhong, R., Bai, Z., Li, J., Wei, H., and Zhu, Q. (2001). Classification of pyroclastic rocks and trend of volcanic sedimentology: a review. Acta Petrol. Mineral., 2 (3), 313–317+328.
- Taylor, G.A. (1958). The 1951 eruption of Mount Lamington, Papua. Austr. Bur. Min.Resour. Geol. Geophys. Bull., 38, 1-117.
- Walker, G.P.L. (1971). Grain size characteristics of pyroclastic deposits. J. Geol. 79, 696-714.

- Walker, G.P.L. (1972). Crystal concentrations in ignimbrites. *Contr. Mineral. Petrol.* 36, 135-146.
- Wang, Y., Wang, J., Wang, Q., Sui, F., Shi, H., Xu, Y. (2019). Diagenesis of volcanoclastic rocks and its control over reservoir performance: a case study of the Carboniferous system in Chepaizi area, Junggar basin. *J. China Inst. Min. Technol.*, 48 (2), 405–414.
- Yuan, Y., Rezaee, R., Yu, H., Zou, J., Liu, K., Zhang, Y. (2021). Compositional controls on nanopore structure in different shale lithofacies: a comparison with pure clays and isolated kerogens. *Fuel*, 303, 121079.
- Zhou, J., Liu, B., Shao, M., Yin, C., Jiang, Y., and Song, Y. (2022). Lithologic classification of pyroclastic rocks: A case study for the third member of the Huoshiling Formation, Dehui fault depression, Songliao Basin, NE China. *Journal of Petroleum Science and Engineering*, 214,110456.
- URL-1 Vikipedi, *Piroklastik* *Kayaçlar*
https://tr.wikipedia.org/wiki/Piroklastik_kaya%C3%A7 adresinden 10
Aralık 2023 tarihinde alınmıştır.
- URL-2 Wikipedia, *Types* *of* *volcanic* *eruptions*.
http://en.wikipedia.org/wiki/Types_of_volcanic_eruptions adresinden 10
Aralık 2023 tarihinde alınmıştır.

Chapter 3

Effects of Operating Parameters on NO_x Emissions in Diesel Engines

Adem TÜYLÜ¹

Kubilay HAN²

Yasin AKIN³

INTRODUCTION

Diesel engines are preferred in the automotive sector, particularly in heavy-duty vehicles, due to their high torque output and low fuel consumption. Although electric vehicles are becoming more widespread, internal combustion engine vehicles continue to be used due to issues such as battery life and deficiencies in charging station infrastructure. Internal combustion engines release various exhaust gases that have adverse effects on the environment and human health. Among these emissions, hydrocarbons (HC) and carbon monoxide (CO) are primary concerns for Otto engines, while nitrogen oxides (NO_x) and particulate matter are major issues for diesel engines. The negative effects of NO_x emissions include respiratory problems and lung diseases in humans, as well as the formation of acid rain through chemical interactions with water, oxygen, and other compounds in the atmosphere. Legal regulations restrict these harmful emissions, with the upcoming Euro VII emission standards, expected to be effective by 2025, aiming for even stricter limits (Demir et al., 2023; Calam et al., 2022; Syed and Renganathan, 2022; Mulholland et al., 2022; Bögrek et al., 2021).

In diesel engines, the relatively high levels of NO_x emissions stem from the operational conditions of the engine. Diesel engines operate with fuel-lean mixtures compared to Otto engines and have higher compression ratios. Consequently, more oxygen is involved in the combustion in diesel engines, leading to higher combustion temperatures. These two factors contribute to the high levels of NO_x emissions in diesel engines. However, operational parameters of diesel engines, fuel quality, and emission reduction technologies installed in

¹ Arş. Gör. Adem TÜYLÜ Sakarya University Of Applied Sciences Faculty of Technology Mechanical Engineering, ademtuylu@subu.edu.tr ORCID No: 0000-0001-9828-1573

² Arş. Gör. Kubilay HAN Sakarya University Of Applied Sciences Faculty of Technology Mechanical Engineering, kubilayhan@subu.edu.tr ORCID No: 0000-0003-1472-2832

³ Arş. Gör. Yasin AKIN Sakarya University Of Applied Sciences Faculty of Technology Mechanical Engineering, yasinakin@subu.edu.tr ORCID No: 0000-0003-3201-379X

the exhaust system have significant effects on the amount of NO_x emissions released in the exhaust gases. Improvements in the fuel, such as the addition of various fuel additives, the use of alternative fuels, and the utilization of low-nitrogen diesel fuel can reduce NO_x emissions from diesel engines through pre-combustion enhancements. Additionally, post-combustion NO_x emissions are reduced through the Selective Catalytic Reduction (SCR) technology installed in the exhaust system before being released into the ambient air (Çelebi et al., 2021; Tüylü, 2021; Tüylü vd., 2019; Koebel et al., 2000; Haşimoğlu and İcingür, 2000).

In this study, the types and formation mechanisms of NO_x emissions were first explained. Subsequently, the effects of operational parameters influencing the combustion process on NO_x emissions, particularly focusing on reducing effects, were discussed. Studies in the literature on the reduction of NO_x emissions with operational parameters were comprehensively evaluated in subheadings.

NO_x EMISSIONS IN DIESEL ENGINES

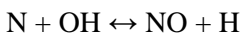
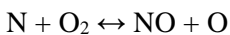
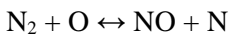
The most influential factors in the formation of NO_x emissions in diesel engines are cylinder oxygen concentration and cylinder temperatures. NO_x emissions begin to form when cylinder temperatures exceed 1800 K. NO_x includes various nitrogen oxide compounds such as NO, NO₂, N₂O, N₂O₅, and NO₃. Approximately 95% of diesel engine NO_x emissions consist of nitrogen monoxide (NO), with the remaining 5% composed of other compounds (Varatharajan and Cheralathan, 2012; Chen et al., 2018).

NO_x FORMATION REACTIONS

As explained above, the vast majority of NO_x emissions consist of NO emissions. In this section, the mechanisms and reactions for the formation of nitric oxide (NO) and nitrous oxide (N₂O) are described.

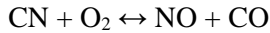
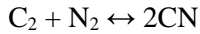
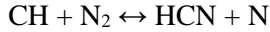
Thermal NO Formation

This mechanism is the primary source of NO_x emissions. It occurs when nitrogen (N) and oxygen (O₂) react at cylinder temperatures above 1800 K. These reactions are known as the Zeldovich mechanism (Varatharajan and Cheralathan, 2012).



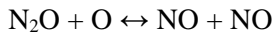
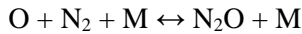
Prompt NO Formation

It represents the formation of NO in the combustion process where the mixture is fuel-rich, and temperatures are relatively low inside the cylinder. The reactions for Prompt NO formation are provided below (Varatharajan and Cheralathan, 2012).



NO and N₂O Formation Reactions

The reactions below take place in conditions where the cylinder pressure is high, and the cylinder filling is low, at high air/fuel ratios during the combustion process. Oxygen atoms react with nitrogen gases (N₂) to form N₂O. The N₂O formed in the initial reaction can later react with oxygen to produce NO (Varatharajan and Cheralathan, 2012).



REDUCTION METHODS OF NO_x EMISSIONS IN DIESEL ENGINES

Exhaust Gas Recirculation (EGR)

EGR (Exhaust Gas Recirculation) is one of the most effective methods for reducing NO_x emissions from diesel engines. It involves recirculating exhaust gases containing inert, high heat capacity CO₂, and H₂O (water vapor) into the intake air. This results in a change in the characteristics of the intake air, leading to a reduction in NO_x emissions. The addition of these compounds to the intake air decreases the O₂ content in the intake air. Additionally, these compounds with high heat capacity cause a reduction in peak combustion temperatures. The decrease in cylinder O₂ concentration and post-combustion peak temperatures due to EGR results in the reduction of NO_x emissions. However, it should be noted that the application of EGR leads to an increase in particulate matter emissions and a deterioration in engine performance.

EGR can be implemented through internal and external systems. Many modern diesel engines are equipped with turbochargers. Internal EGR involves the inclusion of burned exhaust gases in the next cycle by modifying intake and exhaust timings, valve opening and closing times, and valve duration. This is achieved through the manipulation of valves, employing variable valve activation

technology. In cold EGR applications, exhaust gases are subjected to intercooling before being introduced into the intake air (Figure 1). In hot EGR applications, exhaust gases are mixed with the intake air without undergoing any cooling process. Cold EGR is more effective and efficient compared to hot EGR but is also more costly (Pradeep et al., 2007; Haşimoğlu et al., 2002).

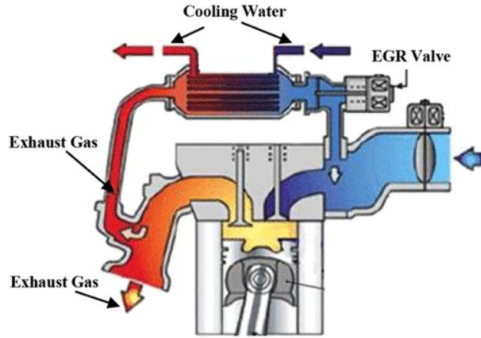


Figure 1. EGR scheme (Lou et al., 2022)

When implementing EGR, the percentage of EGR can be calculated using the following equation (Pierpont et al., 1995). Since the ambient % CO₂ is relatively small and is considered as zero in the equation, the EGR ratio is calculated by dividing the percentage of CO₂ in the intake air by the percentage of CO₂ in the exhaust air.

$$\frac{\%CO_{2(\text{intake})} - \%CO_{2(\text{ambient})}}{\%CO_{2(\text{exhaust})} - \%CO_{2(\text{ambient})}} \times 100$$

In conclusion, Exhaust Gas Recirculation (EGR) reduces NO_x emissions by lowering peak temperatures in the combustion process through the high heat capacity compounds H₂O and CO₂, and by reducing the amount of O₂ introduced into the cylinder. However, EGR can lead to increases in other emissions, particularly particulate matter, and a deterioration in engine performance. Therefore, EGR is applied by optimizing parameters such as engine load, turbocharging, intake air temperature, etc., in a combined and coordinated manner (Maiboom et al., 2008; Hountalas et al., 2008).

NO_x Emission Reduction through Combustion Strategies

Combustion strategies with low-temperature combustion (LTC) such as Homogeneous Charge Compression Ignition (HCCI), Reactivity Controlled Compression Ignition (RCCI), and Premixed Charge Compression Ignition

(PCCI) result in combustion at lower temperatures compared to traditional diesel engines (Figure 2). Particularly, in the HCCI strategy, combustion occurs with fuel-lean mixtures and at lower temperatures, providing an opportunity to simultaneously reduce soot and NO_x emissions (Kutluata, 2002; Dong et al., 2018; Krishnamoorthi et al., 2019). Creating a homogeneous fuel-air mixture in combustion strategies can be achieved by making changes in fuel injection timings. In addition to the main fuel injection timing in traditional diesel engines, pilot, early, and late fuel injections (Figure 3) are used to create a homogeneous charge (Zhao, 2007).

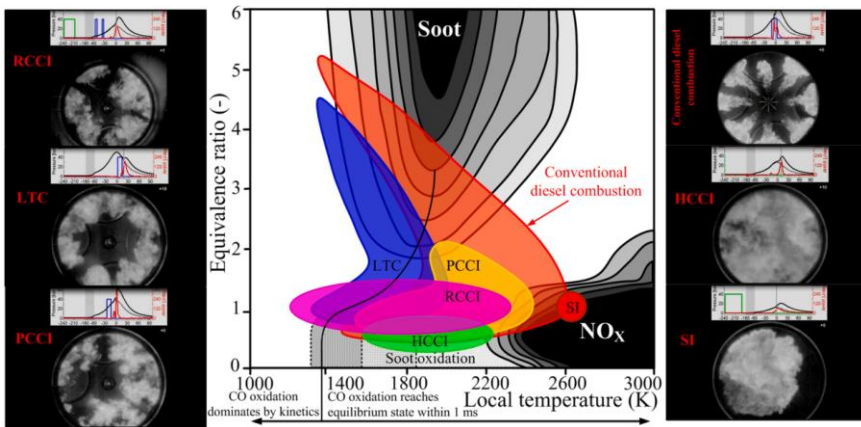


Figure 2. Low temperature combustion (LTC) strategies operating ranges (Duan vd., 2021)

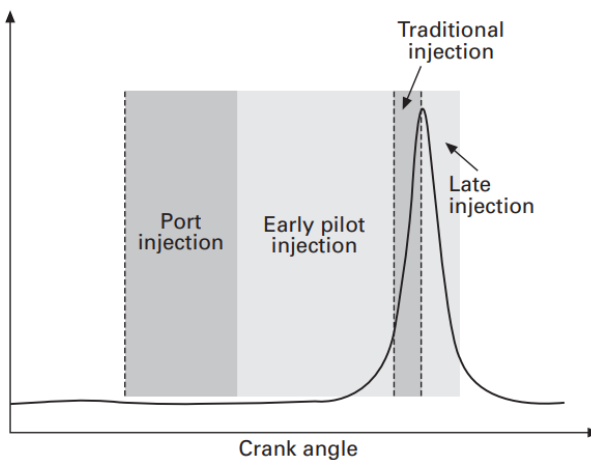


Figure 3. Fuel injection timing types for homogeneous fuel-air mixture (Zhao, 2007)

Effect of Fuel Injection Strategies on NO_x Emissions

One of the parameters that significantly influences the reduction of NO_x emissions in diesel engines is fuel injection strategies. Particularly, performing multiple fuel injections per cycle results in notable reductions in NO_x emissions compared to a single main injection scenario. Moreover, the multiple injection strategy has the potential to simultaneously reduce both NO_x and soot emissions without compromising engine performance (Tow et al., 1994; Sindhu et al., 2018). On the other hand, delaying the fuel injection timing, in other words, reducing the advance leads to a decrease in ignition delay resulting in a reduction in NO_x emissions (Shundoh et al., 1992; Cheng et al., 2016).

In numerical studies, Wang et al. (2007) investigated the effects of fuel injection advance and multiple injection strategies on engine performance and emissions. They found that in single, 3-stage, and 5-stage injection strategies with the same start of fuel injection, as the number of stages increased, NO_x emissions decreased. In other words, multiple injections resulted in lower NO_x emissions compared to a single injection. Additionally, they noted that reducing the injection advance from -10 CA to 5 CA for fuel spray strategies resulted in NO_x emission reduction. In conclusion, multiple injections and reducing fuel injection advance have a mitigating effect on NO_x emissions.

Effect of Fuel Injection Pressure on NO_x Emissions

In diesel engines, as the fuel injection pressure increases the diameter of the fuel particles sprayed from the injector decreases leading to a reduction in the penetration areas within the cylinder. As the injection pressure increases, a relatively homogeneous fuel-air mixture is formed in the cylinder, resulting in a decrease in ignition delay. Therefore, an increase in injection pressure leads to a reduction in NO_x emissions (İçingür and Altıparmak, 2003). However, studies using biodiesel as fuel in diesel engines have shown different trends in NO_x emissions in response to increasing injection pressure (Jindal et al., 2010; Deokar and Harari, 2021).

Effect of Intake Air Characteristics on NO_x Emissions

The physical and compositional characteristics of intake air play a crucial role in diesel engine performance and emissions. The effects of intake air temperature, pressure, and oxygen content on combustion and emissions have been investigated through experimental and numerical studies. Jeevahan et al. (2019) examined the influence of intake air oxygen (O₂) concentration on the performance and emissions of a single-cylinder diesel engine. They adjusted the intake air O₂ concentration to 21%, 23%, 25%, and 27% under normal conditions.

Under full-load conditions, they observed NO_x formations of 2435 ppm when the intake air O₂ concentration was 21% and 5599 ppm when it was 27%. They noted that the improvement in combustion and the increase in post-combustion temperatures with higher oxygen concentration led to increased NO_x emissions.

Li et al. (1997) conducted experimental studies on a direct-injection, water-cooled diesel engine to investigate the effects of intake air pressure and oxygen concentration on engine performance and emissions. To clearly observe the effects of these two factors on emissions and performance, they maintained the engine speed at 1800 rpm, intake air temperature at 300 K, and the injected fuel quantity per cycle at 30.2 mg/cycle. They set the intake air pressure to 1.1 bar, 1.5 bar, and 2 bar, and the oxygen concentration in the inhaled air to 21%, 19.5%, and 18.8%. They diluted the oxygen concentration in the inhaled air to 19.5% by adding carbon dioxide to the intake air. Similarly, by adding argon and nitrogen gases to the intake air, they reduced the normal 21% oxygen concentration to 18.8%. They found that increasing intake air pressure led to a decrease in NO_x emissions, and they associated this decrease with the decrease in ignition delay due to increased inhaled air pressure. On the other hand, adding inert gases to the intake air resulted in reduced oxygen concentrations, leading to a decrease in NO_x emissions. Particularly, under operating conditions with an intake air pressure of 2 bar and an oxygen concentration of 18.8%, they achieved significant reductions in NO_x emissions.

Increasing intake air temperatures in diesel engines through various methods lead to higher peak temperatures at the end of combustion. The increase in peak temperature values has an enhancing effect on NO_x emissions (Haraldsson et al., 2002; Gowthaman and Sathiyagnanam, 2018).

Effect of Air-Fuel Ratio on NO_x Emissions

The air-fuel ratio (AFR) is one of the most influential parameters affecting combustion and emissions in internal combustion engines. As indicated by the equation below (Chatlatanagulchai et al., 2010), excess air coefficient (λ) denotes whether the mixture in the cylinder is fuel-rich, fuel-lean, or stoichiometric. There are many publications in the literature that discuss the changes in emissions according to the excess air coefficient. NO_x emissions are observed to be at their maximum when $\lambda=1.1$, and they decrease when λ is below or above 1.1 (Figure 3). The trends in NO_x emissions can be explained by the combustion efficiency of fuel-rich and fuel-lean mixtures, which leads to a decrease in combustion temperatures.

$$\lambda = \frac{(\text{Air/Fuel})_{\text{actual}}}{(\text{Air/Fuel})_{\text{theoretical}}}$$

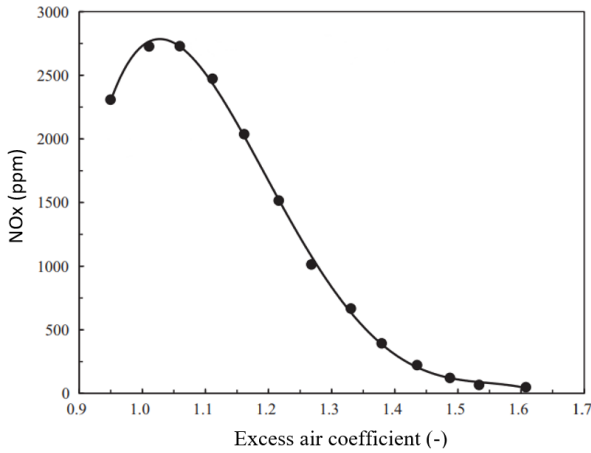


Figure 3.4 Change of NO_x emissions according to excess air coefficient (Li et al., 2015)

Shu et al. (2019) have presented a graph illustrating the variations in NO_x emissions in a turbocharged diesel engine under operating conditions of 50% and 100% loads, and engine speeds of 1000 rpm and 1500 rpm, with respect to the excess air coefficient. In the graph, it is observed that NO_x emissions reach their maximum level when λ is 1.1. In cases where λ decreases to 1 and increases to 1.5, NO_x emissions exhibit a decline.

Effect of Compression Ratio on NO_x Emissions

In diesel engines, the compression ratio can be increased or decreased by implementing various structural changes. Alterations in the compression ratio directly impact the physical properties of the air drawn into the cylinder. Researchers have found in their studies that increasing the compression ratio has an augmenting effect on NO_x emissions. Although the ignition delay time decreases as a result of an increased compression ratio, it has been argued that the rise in peak combustion temperatures following the compression ratio increase contributes to an elevation in NO_x emissions (Al-Dawody and Bhatti, 2014; Khatri et al., 2019; Aydın, 2021).

Effect of Engine Load on NO_x Emissions

In diesel engines, the amount of load is adjusted by making changes to the injected fuel quantity into the cylinder. When there is an increase in engine load,

the corresponding rise in post-combustion temperatures leads to an increase in NO_x emissions. Experimental studies conducted by Zhu et al. (2010) and Sinay et al. (2018) observed increases in NO_x emissions correlated with percentage increases in engine load.

Effect of Water Injection on NO_x Emissions

Studies in the literature, such as those conducted by Ishida et al. (1997), Hountalas et al. (2006), Tauzia et al. (2010) on water injection into the intake manifold, and direct water injection into the cylinder, as implemented by Ayhan and Ece (2020), have demonstrated significant reductions in NO_x emissions. On the other hand, water injection into the intake manifold is a relatively costly method. Water injection strategies that prove highly effective in reducing NO_x emissions in diesel engines also pose various risks, including the potential for corrosion in engine components.

CONCLUSION

In diesel engines, NO_x emissions are formed as a result of combustion reactions. Similar to other emissions, NO_x emissions have adverse effects on the environment and human health. Reduction of NO_x emissions in diesel engines is achieved through improvements in pre-combustion fuel characteristics, combustion process parameters during engine operation, and post-combustion emission reduction technologies in the exhaust system. In this work, the roles of engine operating parameters in reducing NO_x emissions are elucidated.

Exhaust Gas Recirculation (EGR), intake air physical properties, fuel injection strategies, combustion strategies, Air-Fuel Ratio (AFR), compression ratio, engine load, and water injection applications are identified as highly influential engine operating parameters on NO_x emissions. While there are studies demonstrating the reduction of NO_x emissions through the application of individual engine operating parameters, recent research indicates simultaneous changes in multiple parameters to achieve emission reductions. It is understood that these approaches aim to compensate for deteriorations in engine performance or other emissions that may occur when NO_x emissions are reduced with a single parameter. The optimization of engine operating parameters by considering both engine performance and emissions is apparent in these studies.

REFERENCES

1. Al-Dawody, M. F., & Bhatti, S. K. (2014). Effect of variable compression ratio on the combustion, performance and emission parameters of a diesel engine fuelled with diesel and soybean biodiesel blending. *World Applied Sciences Journal*, 30(12), 1852-1858.
2. Aydın, H. (2021). An innovative research on variable compression ratio in RCCI strategy on a power generator diesel engine using CNG-safflower biodiesel. *Energy*, 231, 121002.
3. Ayhan, V., & Ece, Y. M. (2020). New application to reduce NO_x emissions of diesel engines: Electronically controlled direct water injection at compression stroke. *Applied Energy*, 260, 114328.
4. Böğrek, A., Haşimoğlu, C., Calam, A., & Aydoğan, B. (2021). Effects of n-heptane/toluene/ethanol ternary fuel blends on combustion, operating range and emissions in premixed low temperature combustion. *Fuel*, 295, 120628.
5. Calam, A., Halis, S., Aydoğan, B., & Haşimoğlu, C. (2022). Combustion characteristics of naphtha and n-heptane fuels in an auto-ignited HCCI engine at different lambda values and engine loads. *Fuel*, 327, 125183.
6. Chatlatanagulchai, W., Yaovaja, K., Rhienprayoon, S., & Wannatong, K. (2010). Air-fuel ratio regulation with optimum throttle opening in diesel-dual-fuel engine (No. 2010-01-1574). SAE Technical Paper.
7. Chen, H., Xie, B., Ma, J., & Chen, Y. (2018). NO_x emission of biodiesel compared to diesel: Higher or lower?. *Applied Thermal Engineering*, 137, 584-593.
8. Cheng, X., Li, S., Yang, J., & Liu, B. (2016). Investigation into partially premixed combustion fueled with N-butanol-diesel blends. *Renewable energy*, 86, 723-732.
9. Çelebi, S., Haşimoğlu, C., Uyumaz, A., Halis, S., Calam, A., Solmaz, H., & Yılmaz, E. (2021). Operating range, combustion, performance and emissions of an HCCI engine fueled with naphtha. *Fuel*, 283, 118828.
10. Demir, U., Çelebi, S., & Özer, S. (2023). Experimental investigation of the effect of fuel oil, graphene and HHO gas addition to diesel fuel on engine performance and exhaust emissions in a diesel engine. *International Journal of Hydrogen Energy*.
11. Deokar, A. J., & Harari, P. A. (2021). Effect of injection pressure, injection timing and nozzle geometry on performance and emission characteristics of diesel engine operated with thevetia peruviana biodiesel. *Materials Today: Proceedings*, 47, 2622-2626.

12. Dong, S., Wang, Z., Yang, C., Ou, B., Lu, H., Xu, H., & Cheng, X. (2018). Investigations on the effects of fuel stratification on auto-ignition and combustion process of an ethanol/diesel dual-fuel engine. *Applied energy*, 230, 19-30.
13. Duan, X., Lai, M. C., Jansons, M., Guo, G., & Liu, J. (2021). A review of controlling strategies of the ignition timing and combustion phase in homogeneous charge compression ignition (HCCI) engine. *Fuel*, 285, 119142.
14. Gowthaman, S., & Sathiyagnanam, A. P. (2018). Analysis the optimum inlet air temperature for controlling homogeneous charge compression ignition (HCCI) engine. *Alexandria engineering journal*, 57(4), 2209-2214.
15. Haraldsson, G., Tunestål, P., Johansson, B., & Hyvönen, J. (2002). HCCI combustion phasing in a multi cylinder engine using variable compression ratio. *SAE Transactions*, 2654-2663.
16. Haşimoğlu, C., Ur, Y. I. I., & Ogut, H. (2002). Dizel motorlarında egzoz gazları resirkülasyonunun (EGR) motor performansı ve egzoz emisyonlarına etkisinin deneysel analizi. *Turkish J. Eng. Env. Sci*, 26, 127-135.
17. Haşimoğlu, C., & İcingür, Y. (2000). Dizel Motorlarında Azot Oksit (Nox) Kontrol Yöntemleri. *Selçuk-Teknik Dergisi*, 1(2).
18. Hountalas, D. T., Mavropoulos, G. C., & Binder, K. B. (2008). Effect of exhaust gas recirculation (EGR) temperature for various EGR rates on heavy duty DI diesel engine performance and emissions. *Energy*, 33(2), 272-283.
19. Hountalas, D. T., Mavropoulos, G. C., Zannis, T. C., & Mamalis, S. D. (2006). Use of water emulsion and intake water injection as NOX reduction techniques for heavy duty diesel engines (No. 2006-01-1414). *SAE Technical Paper*.
20. Ishida, M., Ueki, H., & Sakaguchi, D. (1997). Prediction of NOx reduction rate due to port water injection in a DI diesel engine. *SAE transactions*, 1468-1478.
21. İcingür, Y., & Altıparmak, D. (2003). Effect of fuel cetane number and injection pressure on a DI Diesel engine performance and emissions. *Energy conversion and management*, 44(3), 389-397.
22. Jeevahan, J., Poovannan, A., Sriram, V., Durai Raj, R. B., Maghwaran, G., & Britto Joseph, G. (2019). Effect of intake air oxygen enrichment for improving engine performance and emissions control in diesel engine. *International Journal of Ambient Energy*, 40(1), 96-100.

23. Jindal, S., Nandwana, B. P., Rathore, N. S., & Vashistha, V. (2010). Experimental investigation of the effect of compression ratio and injection pressure in a direct injection diesel engine running on Jatropha methyl ester. *Applied thermal engineering*, 30(5), 442-448.
24. Khatri, D., Goyal, R., Darad, A., Jain, A., Rawat, S., Khan, A., & Johnson, A. T. (2019). Investigations for the optimal combination of zinc oxide nanoparticle-diesel fuel with optimal compression ratio for improving performance and reducing the emission features of variable compression ratio diesel engine. *Clean Technologies and Environmental Policy*, 21, 1485-1498.
25. Koebel, M., Elsener, M., & Kleemann, M. (2000). Urea-SCR: a promising technique to reduce NO_x emissions from automotive diesel engines. *Catalysis today*, 59(3-4), 335-345.
26. Krishnamoorthi, M., Malayalamurthi, R., He, Z., & Kandasamy, S. (2019). A review on low temperature combustion engines: Performance, combustion and emission characteristics. *Renewable and Sustainable Energy Reviews*, 116, 109404.
27. Kutluata, A. (2002). Homojen Karışımli Sıkıştırılmalı Ateşlemeli Motorların Çok Boyutlu Modellenmesi (Doctoral dissertation, Fen Bilimleri Enstitüsü).
28. Li, J., Chae, J. O., Park, S. B., Paik, H. J., Park, J. K., Jeong, Y. S., ... & Choi, Y. J. (1997). Effect of intake composition on combustion and emission characteristics of DI diesel engine at high intake pressure (No. 970322). *SAE Technical Paper*.
29. Li, W., Liu, Z., Wang, Z., Xu, Y., & Wang, J. (2015). Experimental and theoretical analysis of effects of N₂, O₂ and Ar in excess air on combustion and NO_x emissions of a turbocharged NG engine. *Energy Conversion and Management*, 97, 253-264.
30. Lou, D., Kang, L., Zhang, Y., Fang, L., & Luo, C. (2022). Effect of Exhaust Gas Recirculation Combined with Selective Catalytic Reduction on NO_x Emission Characteristics and Their Matching Optimization of a Heavy-Duty Diesel Engine. *ACS omega*, 7(26), 22291-22302.
31. Maiboom, A., Tauzia, X., & Hétet, J. F. (2008). Experimental study of various effects of exhaust gas recirculation (EGR) on combustion and emissions of an automotive direct injection diesel engine. *Energy*, 33(1), 22-34.
32. Mulholland, E., Miller, J., Bernard, Y., Lee, K., & Rodríguez, F. (2022). The role of NO_x emission reductions in Euro 7/VII vehicle emission

- standards to reduce adverse health impacts in the EU27 through 2050. *Transportation Engineering*, 9, 100133.
33. Pierpont, D. A., Montgomery, D. T., & Reitz, R. D. (1995). Reducing particulate and NOx using multiple injections and EGR in a DI diesel. *SAE transactions*, 171-183.
34. Pradeep, V., & Sharma, R. P. (2007). Use of HOT EGR for NOx control in a compression ignition engine fuelled with bio-diesel from *Jatropha* oil. *Renewable energy*, 32(7), 1136-1154.
35. Shu, J., Fu, J., Liu, J., Wang, S., Yin, Y., Deng, B., & Becker, S. M. (2019). Influences of excess air coefficient on combustion and emission performance of diesel pilot ignition natural gas engine by coupling computational fluid dynamics with reduced chemical kinetic model. *Energy Conversion and Management*, 187, 283-296.
36. Shundoh, S., Komori, M., Tsujimura, K., & Kobayashi, S. (1992). NOx reduction from diesel combustion using pilot injection with high pressure fuel injection (No. 920461). *SAE Technical Paper*.
37. Sinay, J., Puškár, M., & Kopas, M. (2018). Reduction of the NOx emissions in vehicle diesel engine in order to fulfill future rules concerning emissions released into air. *Science of the Total Environment*, 624, 1421-1428.
38. Sindhu, R., Rao, G. A. P., & Murthy, K. M. (2018). Effective reduction of NOx emissions from diesel engine using split injections. *Alexandria Engineering Journal*, 57(3), 1379-1392.
39. Syed, S., & Renganathan, M. (2022). NOx emission control strategies in hydrogen fuelled automobile engines. *Australian Journal of Mechanical Engineering*, 20(1), 88-110.
40. Tauzia, X., Maiboom, A., & Shah, S. R. (2010). Experimental study of inlet manifold water injection on combustion and emissions of an automotive direct injection diesel engine. *Energy*, 35(9), 3628-3639.
41. Tow, T. C., Pierpont, D. A., & Reitz, R. D. (1994). Reducing particulate and NOx emissions by using multiple injections in a heavy duty DI diesel engine. *SAE transactions*, 1403-1417.
42. Tüylü A., Ayhan V., Cesur İ. (2019). Etanol Fumigasyonunun DI Dizel Motorunda Motor Performans, NO ve İş Emisyonlarına Etkisinin İncelenmesi. *KİTABI, F. B., & II, C. Uluslararası Marmara Fen ve Sosyal Bilimler Kongresi (BAHAR 2019)*.
43. Tüylü, A. (2021). Kısmi homojen dolgulu direkt enjeksiyonlu bir dizel motorunun deneysel ve numerik olarak incelenmesi (Master's thesis, Sakarya University Of Applied Sciences).

44. Varatharajan, K., & Cheralathan, M. (2012). Influence of fuel properties and composition on NO_x emissions from biodiesel powered diesel engines: A review. *Renewable and sustainable energy reviews*, 16(6), 3702-3710.
45. Wang, D., Zhang, C., & Wang, Y. (2007). A numerical study of multiple fuel injection strategies for NO_x reduction from DI diesel engines. *International Journal of Green Energy*, 4(4), 453-470.
46. Zhao, H. (2007). *HCCI and CAI engines for the automotive industry*. Elsevier
47. Zhu, L., Zhang, W., Liu, W., & Huang, Z. (2010). Experimental study on particulate and NO_x emissions of a diesel engine fueled with ultra low sulfur diesel, RME-diesel blends and PME-diesel blends. *Science of the Total Environment*, 408(5), 1050-1058.

Chapter 5

In-Situ Hydrogen Peroxide and Hydrogen Production in Wastewater Treatment with Fenton-Fenton Like Oxidation

Ayşe Elif ATEŞ¹

Sinan ATEŞ²

1- INTRODUCTION

Purifying water and reusing it as both industrial and drinking water is of great importance in preventing water scarcity. However, with increasing industrialization in recent years, efforts to provide clean energy production during wastewater treatment are increasing. Biogas, biodiesel, and hydrogen energy can be given as examples of clean energy (Hu, L., 2023: 177). Due to the rapid increase in population, the need for energy and water has increased globally, and accordingly, energy and water reserves are facing difficulties in meeting the need (Wang, Y., 2023: 307). In addition, the fact that polluting gases due to industrialization accelerate climate change and that the need for water and energy will increase in the next 30 years has encouraged researchers to develop methods that can solve both crises simultaneously (Sun, J., 2022: 168) (Hu, L., 2023: 177). However, the studies carried out are generally on a laboratory scale and are in the testing phase for use in large-scale industries. The priority in the studies is generally to provide energy supply from renewable energy. Here, when choosing a renewable energy supply system, variables such as the geological, meteorological, material and social situation of the region should be taken into consideration. Researchers generally recommend adding energy storage systems to the process to improve the system (Cheng, S., 2021: 46).

Hydrogen energy has been one of the important fields of study in recent years, both in terms of its ability to be obtained during water treatment and as renewable energy. The important advantages of hydrogen energy are that it is storable, has a high calorific value, and does not create polluting gases. Despite these advantages, the fact that hydrogen fuel cannot be produced directly is a significant disadvantage. Generally, gasification, electrolysis, and reforming of

¹ Res. Asst.. Gör.; İstanbul Üniversitesi-Cerrahpaşa Mühendislik Fakültesi Çevre Mühendisliği Bölümü, ayseelif.ates@iuc.edu.tr ORCID No: 0000-0001-5391-7478

² İstanbul Üniversitesi-Cerrahpaşa Mühendislik Fakültesi Çevre Mühendisliği Bölümü, sinanates89@gamil.com ORCID No: 0000-0003-0967-2367

fossil fuels are used in the production of hydrogen energy (Chen, Y.,2022: 81) (Hoang, A. T., 2022: 47) (Zhang, H., 2022:104). Although it is challenging to use these methods in the production of hydrogen energy, they have been turned into an advantage by researchers because they are methods used in water purification. Hydrogen energy production processes integrated with water treatment are advanced oxidation processes and include methods using hydrogen peroxide (H_2O_2), ozone (O_3), electrolysis and ultraviolet lamps (Liu, C., 2023: 52). In these advanced oxidation systems, pollutants are oxidized as a result of electron transfer or chemical interaction. In addition, studies have shown that electrochemical methods are more effective in oxidizing pollutants. This can be said to be due to the higher number of radicals formed during the process. Electro-Fenton and Photoelectro-Fenton oxidation methods are advanced oxidation processes frequently used in wastewater treatment because H_2O_2 is produced by cathodic reduction (Behrouzeh, M.,2022: 15). In studies conducted in the literature, Electro-Fenton oxidation's low operating costs and high wastewater treatment efficiencies are among its critical advantages. It is also one of the advanced oxidation processes that can be used on an industrial scale (Campos, S., 2023:169). However, although wastewater treatment can be done by Electro-Fenton oxidation, desalination cannot be done. It is seen that the electrodialysis method is widely used in the literature for desalination (Jia, Y., 203:48).

Fenton Oxidation

It is stated in the literature that the redox potential of the hydroxyl radical ($\bullet OH$) formed as a result of the reaction in advanced oxidation processes is 2.8V. Compared to other advanced oxidation processes, Fenton oxidation provides the formation of more hydroxyl radicals through the decomposition of H_2O_2 . In addition, the formation of hydroxyl radicals in this process is rapid and easy to operate (Liu, Y., 2021: 404). In Fenton oxidation, H_2O_2 is a chemical usually added externally. However, transportation and storage of H_2O_2 is a costly and risky process, which limits the use of this process on large scales. To overcome this disadvantage, researchers provide oxygen activation so that H_2O_2 can be produced in situ during Fenton oxidation. Thus, the process can be carried out in a less costly and safe manner without reducing the hydroxyl radicals that will be produced during Fenton oxidation (Asghar, A., 2015: 87) (Yang, Z., Zhang, X., 2019: 250) (Pi, L., 2020: 189) (Zhou, W., 2019: 225).

By integrating oxygen activation into electrochemical, photochemical and chemical methods, H_2O_2 can be produced in situ. These processes can operate homogeneously or heterogeneously. In electrochemical methods, oxygen is

reduced to H₂O₂ by taking electrons from the cathode. In photocatalytic oxidation, photoelectrons coming from semiconductor materials under UV light activate oxygen. This situation is directly affected by oxygen activation and environmental conditions in the on-site production of H₂O₂ (Pi, L., 2020: 189) (Liu, Y., 2021: 404). Although iron-containing chemicals are generally used as catalysts in Fenton and Fenton-like oxidation processes where H₂O₂ is produced on-site, different catalysts that do not contain iron are also used. However, iron-containing catalysts are frequently used in studies due to their low cost and high growth efficiency (Bokare, A. D., 2014: 275) (Su, P., 2019. 245).

H₂O₂ PRODUCTION IN THE FENTON OXIDATION PROCESS

Iron, a zero-valent metal, is frequently preferred in Fenton and Fenton-like oxidations due to its low cost and ease of application. In Fenton oxidation, which is carried out with the on-site production of H₂O₂, the iron required for the reaction to occur is provided. Other zero-valent metals used in the studies are Al, Zn, Mg and Cu (shown in Figure 1). In addition, by using iron electrodes in Electro-Fenton oxidation, the necessary iron is given to the environment in situ and the reaction takes place. Fenton and Fenton-like oxidation occurs under acidic environment (pH=2-4) conditions (Liu, Y., 2021: 404) (Liu, Y., 2019: 671).

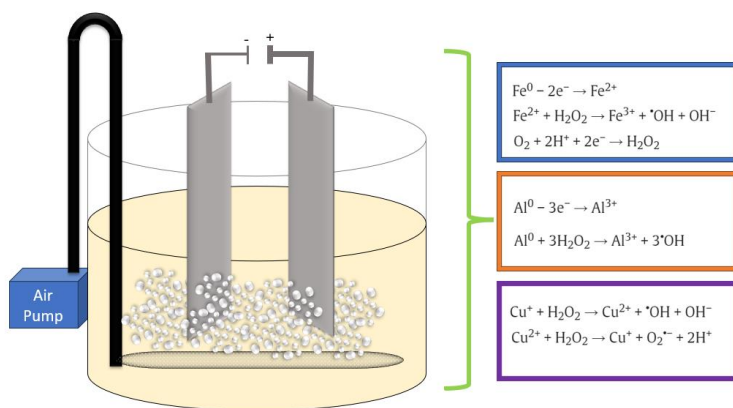


Figure 1: Reactions of zero-valent metals in in-situ production of H₂O₂

Studies have shown that the reduction capacity of zero-valent copper is weaker compared to iron and aluminum. However, considering the redox potential, it has been explained in these studies that it is thermodynamically possible to produce H₂O₂ in situ with the presence of sufficient oxygen in the environment. In addition, when copper is used, super oxide radicals (O₂^{•-}) are

formed along with hydroxyl radicals, unlike other zero-valent metals, with the activation of oxygen (Wen, G., 2014: 275) (Liu, Y., 2021: 404). Another advantage of using copper in the treatment of wastewater is that it dissolves in wide pH ranges and high efficiency results can be obtained in neutral pH conditions. Another advantage of using copper in the treatment of wastewater is its stability and its ability to dissolve in wide pH ranges, resulting in highly efficient results in neutral pH conditions (Dong, G., 2014: 66).

To enhance the efficiency of Zero-Valent Metals (ZVMs) in O₂ activation, bi-metals consisting of two metals with different redox potentials are synthesized. This can expedite O₂ reduction in aqueous solutions by establishing corrosion cells. Incorporating Fe⁰ was found to notably enhance the activity of Al⁰ for O₂ activation. Additionally, Fe⁰ doped with Cu⁰ accelerated the degradation of organic contaminants, exhibiting greater reactivity compared to Fe⁰ alone (Fan, J., 2015: 263) (Fan, J., 2016: 23). Detailed equations for the reactions in Fenton and Fenton-like oxidation processes are provided below (Liu, Y., 2021: 404).

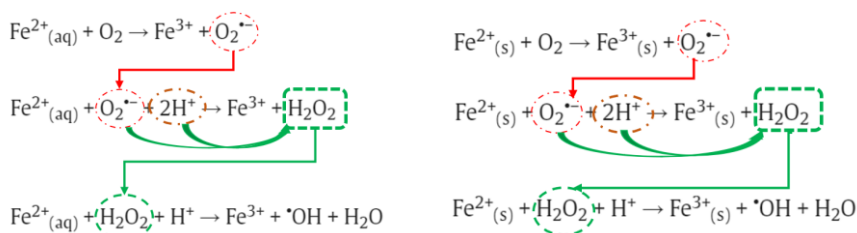
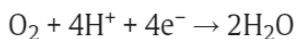
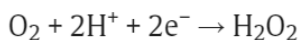


Figure 2: Production of H₂O₂ in Electro-Fenton oxidation of Fe²⁺ (aq and s) and its use in the reaction

The Electro-Fenton/Fenton-like process involves activating O₂ electrochemically, generating H₂O₂ on the cathode surface through the 2-electron O₂ reduction pathway. This process employs Fe-based catalysts, both homogeneous and heterogeneous, for the catalytic breakdown of H₂O₂ into hydroxyl radicals (•OH) through the electrode reaction. The Fenton process, rooted in electrochemical O₂ activation, is versatile, with classifications like electro-catalysis activation of O₂, fuel cell activation of O₂, and corrosion cell activation of O₂. O₂ reduction on the cathode surface can yield H₂O through the direct 4-electron pathway or H₂O₂ through the 2-electron pathway, depending on the cathode material's type and characteristics (Liu, Y., 2021: 404).



The crucial role of cathode material selectivity in facilitating the in-situ generation of H₂O₂ on the cathode surface is evident in various advanced oxidation processes, particularly in electro-Fenton/Fenton-like systems. To achieve this, a diverse array of cathode materials has been harnessed, including noble metals, metal alloys, and carbon-based materials. Carbon-based materials, with their distinctive attributes such as high stability, low toxicity, cost-effectiveness, and pronounced selectivity toward the 2-electron pathway of oxygen (O₂) reduction, have emerged as pivotal candidates for in-situ H₂O₂ generation (Zhuang, S., 2019:253) (Liu, Y., 2021: 404). In electro-Fenton/Fenton-like processes, O₂ in the solution can be obtained from O₂ gas, air aeration, or generated in-situ on an anode through water electrolysis. Two main methods supply Fenton catalysts: direct addition of homogeneous catalysts (Fe²⁺ or Fe³⁺) or immobilization of iron on electrode materials for O₂ reduction and H₂O₂ generation, acting as a source for catalytic breakdown into hydroxyl radicals (•OH) (Liu, H., 2007: 41) (Yang, S., 2018:8). These processes, offering cost savings and reduced risks of H₂O₂ handling, maintain Fenton catalyst activity by reducing ferric ions (Fe³⁺) to ferrous ions (Fe²⁺) at the cathode. However, challenges like high energy consumption and the need for supporting electrolytes hinder practical implementation (Liu, Y., 2021: 404).

The production of H₂O₂ is calculated with the faradic current efficiency formula given in the equation below (Garza-Campos, B., 2018:269) (Zhang, C., 2015: 160).

$$CE = \frac{nFC_{H_2O_2}V}{\int_0^t I dt} \times 100$$

C_{H₂O₂}= H₂O₂ concentration, mol/L

F=Faraday constant (96,485 C/mol)

n=Number of electrons transferred during the reduction of oxygen to H₂O₂.

V= Volume (L)

I= current (A)

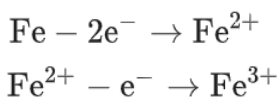
t= time (s)

H₂ PRODUCTION IN THE FENTON OXIDATION PROCESS

Water electrolysis, commonly known as water splitting, is a primary method for hydrogen (H₂) production within the context of a futuristic sustainable energy system. Water electrolysis is a fundamental process that entails the decomposition of water into its constituent elements, H₂ and oxygen, and holds significant promise for a diverse range of energy applications, encompassing

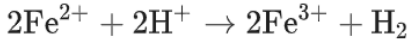
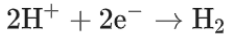
electricity generation, transportation, heating, and chemical production. This process hinges on the orchestrated movement of electrons within a closed circuit. An electrolysis unit comprises key components, including an anode, a cathode, an electrolyte, and a power supply (refer to Figure 1 for a schematic representation). The field of electrolyzer technology recognizes three primary types: polymer electrolyte membrane electrolyzers, alkaline electrolyzers, and solid oxide electrolyzers, each offering distinct advantages and applications in the realm of sustainable energy systems. (Aydin, M. I., 2021:279) (Tak, S., 2022:47).

In a conventional water electrolysis process driven by electricity, the transformation of water occurs, leading to the generation of oxygen gas at the anode electrode and H₂ at the cathode electrode (Yi, S., 2023:91). This fundamental electrochemical process serves as a versatile method for H₂ production, playing a crucial role in the realm of sustainable energy. Alternatively, there exists another method based on the oxidation of iron, which presents a distinctive approach with potential advantages over the traditional water electrolysis process. This iron oxidation process is characterized by its reduced energy requirements compared to standard electrolysis. The utilization of iron oxidation as an alternative pathway for water electrolysis highlights the diverse strategies employed to harness H₂ as a clean and renewable energy source. Ferrous ion may be produced using the iron oxidation process (Nuengmatcha, P., 2023). When ferrous ion is exposed to anode potential, it can be converted to ferric ion (Hu, L., 2023:177).



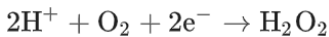
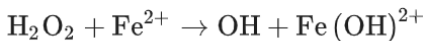
Contrasted with the energy demand of the oxygen evolution reaction, the preceding electrochemical reaction demands a remarkable 69% less energy, underscoring its energy efficiency and potential as an economically viable process for H₂ production. This noteworthy reduction in energy consumption opens avenues for more sustainable and cost-effective approaches to electrolytic H₂ generation. Delving into the specifics of the chemical reaction occurring on the cathode electrode of an electrolyzer utilizing the iron oxidation process provides valuable insights into the mechanisms driving this energy-efficient reaction. The elucidation of this electrochemical reaction not only contributes to our understanding of the fundamental processes involved but also sheds light on the distinctive features that make the iron oxidation-based electrolysis method a

promising contender in the landscape of H₂ production technologies (Hu, L., 2023:177).



In contrast to the conventional water electrolysis method, the chemical reaction described above boasts a noteworthy 38% reduction in energy consumption for H₂ production. This substantial decrease in energy requirements not only positions the process as a more environmentally sustainable alternative but also introduces the possibility of harnessing renewable energy sources, such as solar energy systems, to power this H₂ generation technique. The pivotal role of H₂O₂ in the formation of a Fenton-type reagent at the anode adds a layer of complexity to the electrochemical processes involved. As long as a sufficient supply of H₂O₂ is maintained, the anode becomes a site for the continuous generation of the Fenton-type reagent, accentuating the self-sustaining nature of the electrochemical system. This intricate interplay of chemical reactions and renewable energy integration highlights the multifaceted potential and versatility of the described H₂ production method in the realm of sustainable energy technologies. Iron ions can be obtained electrochemically. via contrast, H₂O₂ is created via an electro-Fenton process by an electrochemical reaction involving the cathodic reduction of dissolved oxygen (Brillas, E., 2020:250).

The electro-Fenton technique is a highly recommended advanced oxidation method for wastewater treatment applications. Furthermore, the oxidizing power of H₂O₂ can be increased by adding Fe to treated wastewater (Shokri, A., 2023:172) (Hu, L., 2023:177).



In the literature, The rate of H₂ production is calculated based on Faraday's law (Hu, L., 2023:177) (Shen, Y., 2021: 47).

$$\dot{m}_{\text{H}_2} = \frac{q \times M}{2F \times t_{\text{cell}}}$$

q= electrical charge

M= molar mass of H₂

F = Faraday constant (96,485 C/mol)
 t_{cell} = overall operation time of the cell

H₂ production efficiencies in light and dark conditions have been compared in the literature. In this study, it is seen that H₂ production increases with increasing voltage. Additionally, H₂ production increases when the system operates in bright conditions. In the study, the H₂ production rate increases approximately 10 times as the voltage increases from 1.7V to 2.5V(Aydin, M., 2022: 256).

RESULT

In comparison to the traditional water electrolysis approach, the chemical reaction elucidated above not only manifests a significant 38% reduction in energy consumption for the production of H₂ but also establishes itself as a compelling option for environmentally sustainable practices (Navarro-Solís, I., 2010:35). This marked decrease in energy requirements not only signifies the method's potential for reduced environmental impact but also opens up avenues for exploring renewable energy sources, with a particular emphasis on solar energy systems, as viable power inputs for this H₂ generation technique (Hu, L., 2023:177).

The intricate dynamics of H₂O₂ in facilitating the formation of a Fenton-type reagent at the anode introduce a nuanced layer to the underlying electrochemical processes. The continuous generation of the Fenton-type reagent at the anode, contingent upon maintaining an ample supply of H₂O₂, underscores the inherent self-sustaining nature of the electrochemical system (Liu, Y., 2021: 404) (Liu, Y., 2019: 671). This complex interplay of chemical reactions and the integration of renewable energy sources not only showcases the method's multifaceted potential but also underscores its adaptability and versatility within the realm of sustainable energy technologies (Fan, J., 2015: 263) (Fan, J., 2016: 23) (Dong, G., 2014: 66). The synergistic relationship between energy efficiency, environmental impact, and renewable energy integration positions this H₂ production method as a promising contributor to the ongoing pursuit of sustainable and clean energy solutions. Furthermore, due to limitations in the environment, the sector is compelled to adequately treat wastewater for reuse. In the studies carried out, if H₂O₂ is used in the treatment of wastewater, on-site production can be carried out to reduce the cost and overcome the difficulties in storing and transporting the chemical (Wen, G., 2014: 275) (Liu, Y., 2021: 404) (Liu, Y., 2019: 671). One of the important reasons why advanced oxidation methods using H₂O₂ are widely used is that

high treatment efficiencies can be achieved in the treatment of resistant industrial wastewater (Hu, L., 2023:177). New studies enable the production of H₂ energy, which is a renewable energy, while producing H₂O₂ on site. Although H₂ production seems possible in studies, studies on its use as energy in the industry are quite new and storage and usage technologies are being developed (Aydin, M. I., 2021:279) (Lu, Y., 2011:36).

REFERENCES

1. Asghar, A., Raman, A. A. A., & Daud, W. M. A. W. (2015). Advanced oxidation processes for in-situ production of hydrogen peroxide/hydroxyl radical for textile wastewater treatment: a review. *Journal of cleaner production*, 87, 826-838.
2. Aydin, M. I., Selcuk, H., & Dincer, I. (2022). A photoelectrochemical reactor for ion separation and hydrogen production. *Energy*, 256, 124641.
3. Aydin, M. I., Karaca, A. E., Qureshy, A. M., & Dincer, I. (2021). A comparative review on clean hydrogen production from wastewaters. *Journal of Environmental Management*, 279, 111793.
4. Behrouzeh, M., Parivazh, M. M., Danesh, E., Dianat, M. J., Abbasi, M., Osfouri, S., ... & Akrami, M. (2022). Application of Photo-Fenton, Electro-Fenton, and Photo-Electro-Fenton processes for the treatment of DMSO and DMAC wastewaters. *Arabian Journal of Chemistry*, 15(11), 104229.
5. Brillas, E. (2020). A review on the photoelectro-Fenton process as efficient electrochemical advanced oxidation for wastewater remediation. Treatment with UV light, sunlight, and coupling with conventional and other photo-assisted advanced technologies. *Chemosphere*, 250, 126198.
6. Bokare, A. D., & Choi, W. (2014). Review of iron-free Fenton-like systems for activating H₂O₂ in advanced oxidation processes. *Journal of hazardous materials*, 275, 121-135.
7. Campos, S., Lorca, J., Vidal, J., Calzadilla, W., Toledo-Neira, C., Aranda, M., ... & Salazar, R. (2023). Removal of contaminants of emerging concern by solar photo electro-Fenton process in a solar electrochemical raceway pond reactor. *Process Safety and Environmental Protection*, 169, 660-670.
8. Cheng, S., Zhao, G., Gao, M., Shi, Y., Huang, M., & Marefati, M. (2021). A new hybrid solar photovoltaic/phosphoric acid fuel cell and energy storage system; Energy and Exergy performance. *International Journal of Hydrogen Energy*, 46(11), 8048-8066.
9. Chen, Y., Feng, L., Mansir, I. B., Taghavi, M., & Sharma, K. (2022). A new coupled energy system consisting of fuel cell, solar thermal collector, and organic Rankine cycle; generation and storing of electrical energy. *Sustainable Cities and Society*, 81, 103824.
10. Dong, G., Ai, Z., & Zhang, L. (2014). Total aerobic destruction of azo contaminants with nanoscale zero-valent copper at neutral pH: promotion effect of in-situ generated carbon center radicals. *Water research*, 66, 22-30.

11. Fan, J. H., Liu, X., & Ma, L. M. (2015). EDTA enhanced degradation of 4-bromophenol by Al₀-Fe₀-O₂ system. *Chemical Engineering Journal*, 263, 71-82.
12. Fan, J., Wang, H., & Ma, L. (2016). Oxalate-assisted oxidative degradation of 4-chlorophenol in a bimetallic, zero-valent iron-aluminum/air/water system. *Environmental Science and Pollution Research*, 23, 16686-16698.
13. Garza-Campos, B., Morales-Acosta, D., Hernández-Ramírez, A., Guzmán-Mar, J. L., Hinojosa-Reyes, L., Manríquez, J., & Ruiz-Ruiz, E. J. (2018). Air diffusion electrodes based on synthesized mesoporous carbon for application in amoxicillin degradation by electro-Fenton and solar photo electro-Fenton. *Electrochimica Acta*, 269, 232-240.
14. Hoang, A. T., Huang, Z., Nižetić, S., Pandey, A., Nguyen, X. P., Luque, R., ... & Le, T. H. (2022). Characteristics of hydrogen production from steam gasification of plant-originated lignocellulosic biomass and its prospects in Vietnam. *International journal of hydrogen energy*, 47(7), 4394-4425.
15. Hu, L., Yan, G., Chauhan, B. S., Elbadawy, I., Abouelela, M., Marefati, M., & Salah, B. (2023). Development and evaluation of an electro-Fenton-based integrated hydrogen production and wastewater treatment plant coupled with the solar and electro-dialysis units. *Process Safety and Environmental Protection*, 177, 568-580.
16. Jia, Y., Wu, X., Xu, S., Zhang, Y., & Wang, S. (2023). Experimental investigation on dyeing wastewater treatment and by-product hydrogen with a reverse electro-dialysis flocculator. *International Journal of Hydrogen Energy*, 48(50), 19022-19032.
17. Liu, C., Chu, Y., Wang, R., & Fan, J. (2023). Preparation of lotus-leaf-like carbon cathode for the electro-Fenton oxidation process: Hydrogen peroxide production, various organics degradation and printing wastewater treatment. *Journal of Water Process Engineering*, 52, 103596.
18. Liu, H., Wang, C., Xiangzhong, Xuan, X., Jiang, C., & Cui, H. N. (2007). A novel electro-Fenton process for water treatment: reaction-controlled pH adjustment and performance assessment. *Environmental science & technology*, 41(8), 2937-2942.
19. Liu, Y., & Wang, J. (2019). Reduction of nitrate by zero valent iron (ZVI)-based materials: A review. *Science of the Total Environment*, 671, 388-403.
20. Liu, Y., Zhao, Y., & Wang, J. (2021). Fenton/Fenton-like processes with in-situ production of hydrogen peroxide/hydroxyl radical for degradation

- of emerging contaminants: Advances and prospects. *Journal of Hazardous Materials*, 404, 124191.
21. Lu et al., Y. Lu, L. Zhao, L. Guo, (2011) Technical and economic evaluation of solar hydrogen production by supercritical water gasification of biomass in China, *Int. J. Hydrogen Energy*, 36 (2011), pp. 14349-14359
 22. Navarro-Solís, I., Villalba-Almendrea, L., & Alvarez-Gallegos, A. (2010). H₂ production by PEM electrolysis, assisted by textile effluent treatment and a solar photovoltaic cell. *International Journal of Hydrogen Energy*, 35(20), 10833-10841.
 23. Nuengmatcha, P., Kuyyogsuy, A., Porrawatkul, P., Pimsen, R., Chanthai, S., & Nuengmatcha, P. (2023). Efficient degradation of dye pollutants in wastewater via photocatalysis using a magnetic zinc oxide/graphene/iron oxide-based catalyst. *Water Science and Engineering*.
 24. Pi, L., Cai, J., Xiong, L., Cui, J., Hua, H., Tang, D., & Mao, X. (2020). Generation of H₂O₂ by on-site activation of molecular dioxygen for environmental remediation applications: A review. *Chemical Engineering Journal*, 389, 123420.
 25. Shen, Y., Li, X., Wang, N., Li, L., & Hoseyni, A. (2021). Introducing and investigation of a pumped hydro-compressed air storage based on wind turbine and alkaline fuel cell and electrolyzer. *Sustainable Energy Technologies and Assessments*, 47, 101378.
 26. Shokri, A., & Nasernejad, B. (2023). Treatment of spent caustic wastewater by electro-Fenton process: Kinetics and cost analysis. *Process Safety and Environmental Protection*, 172, 836-845.
 27. Su, P., Zhou, M., Lu, X., Yang, W., Ren, G., & Cai, J. (2019). Electrochemical catalytic mechanism of N-doped graphene for enhanced H₂O₂ yield and in-situ degradation of organic pollutant. *Applied Catalysis B: Environmental*, 245, 583-595.
 28. Sun, J., Yan, G., Abed, A. M., Sharma, A., Gangadevi, R., Eldin, S. M., & Taghavi, M. (2022). Evaluation and optimization of a new energy cycle based on geothermal wells, liquefied natural gas and solar thermal energy. *Process Safety and Environmental Protection*, 168, 544-557.
 29. Tak, S. S., Shetye, O., Muley, O., Jaiswal, H., & Malik, S. N. (2022). Emerging technologies for hydrogen production from wastewater. *International Journal of Hydrogen Energy*, 47(88), 37282-37301.
 30. Yang, S., Verdaguier-Casadevall, A., Arnarson, L., Silvioli, L., Colic, V., Frydendal, R., ... & Stephens, I. E. (2018). Toward the decentralized

- electrochemical production of H₂O₂: a focus on the catalysis. *Acs Catalysis*, 8(5), 4064-4081.
31. Yang, Z., Zhang, X., Pu, S., Ni, R., Lin, Y., & Liu, Y. (2019). Novel Fenton-like system (Mg/Fe-O₂) for degradation of 4-chlorophenol. *Environmental Pollution*, 250, 906-913.
 32. Yi, S., Lin, H., Abed, A. M., Shawabkeh, A., Marefati, M., & Deifalla, A. (2023). Sustainability and exergoeconomic assessments of a new MSW-to-energy incineration multi-generation process integrated with the concentrating solar collector, alkaline electrolyzer, and a reverse osmosis unit. *Sustainable Cities and Society*, 91, 104412.
 33. Zhang, C., Zhou, M., Yu, X., Ma, L., & Yu, F. (2015). Modified iron-carbon as heterogeneous electro-Fenton catalyst for organic pollutant degradation in near neutral pH condition: characterization, degradation activity and stability. *Electrochimica Acta*, 160, 254-262.
 34. Zhang, H., Sun, X., Hao, S., & Dong, S. (2022). A solar-rechargeable bio-photoelectrochemical system based on carbon tracking strategy for enhancement of glucose electrometabolism. *Nano Energy*, 104, 107940.
 35. Zhuang, S., Liu, Y., & Wang, J. (2019). Mechanistic insight into the adsorption of diclofenac by MIL-100: Experiments and theoretical calculations. *Environmental Pollution*, 253, 616-624.
 36. Zhou, W., Meng, X., Gao, J., & Alshawabkeh, A. N. (2019). Hydrogen peroxide generation from O₂ electroreduction for environmental remediation: A state-of-the-art review. *Chemosphere*, 225, 588-607.
 37. Wang, Y., Liu, L., Yang, X., Suib, S. L., & Qiu, G. (2022). Removal of As (V) from wastewaters using magnetic iron oxides formed by zero-valent iron electrocoagulation. *Journal of Environmental Management*, 307, 114519.
 38. Wen, G., Wang, S. J., Ma, J., Huang, T. L., Liu, Z. Q., Zhao, L., & Xu, J. L. (2014). Oxidative degradation of organic pollutants in aqueous solution using zero valent copper under aerobic atmosphere condition. *Journal of Hazardous Materials*, 275, 193-199.

Chapter 4

Modeling the COD removal of DMSO-Containing Wastewater from the Pharmaceutical Industry Using Photo-Fenton Oxidation with the Response Surface Method

Ayşe Elif ATEŞ¹

INTRODUCTION

The global need for high-quality water, which is required for drinking, sanitation, irrigation, and industrial reasons, has steadily increased. Water treatment and reuse have become a major problem in recent years, needing high requirements (Larsson, D. J., 2007:148). The pharmaceutical business has issues associated with high-value, low-volume multiproduct facilities that generally operate as batch processes that mix and treat effluents. There are also dedicated batch, semibatch, and continuous process factories involved in the manufacture of bulk medicines. These plants use a variety of reactants, (homogeneous) catalysts, solvents, solids, and water, all of which are processed with specialized equipment. The kind of impurity, rather than the purity level of the medicine, influences the fundamental cost of the drug in such units. In the pharmaceutical industry, ultrapure water is used to wash the solid cake numerous times or as an extractant or solvent in and of itself. This water is not reused due to tight rules outlined in authorized drug master file (DMF) etiquettes (Gadipelly, C., 2014:53). Pharmaceutical residues in the aquatic environment offer challenges in terms of existence, consequence, and toxicity (Dalrymple, O. K., 2007:82) (Guillette Jr, L. J., 2000:40) (Orlando, E. F., 2004:112) .When dealing with this issue, the recovery of high-value API and pharmaceutical medications from dilute streams, rather than treatment, should be explored (Gadipelly, C., 2014:53). Water is an important raw component for the pharmaceutical and chemical industry; constant and high-quality water supplies are essential for a variety of processes such as production, material processing, and cooling. Safe-for-consumption water, process water, feedwater for utilities, water recycling, wastewater, water from byproduct treatment, water from desalination, and water for irrigation are all types of water that require treatment for water management. Because the quantities are small and various

¹ Res. Asst.. Gör.; İstanbul Üniversitesi-Cerrahpaşa Mühendislik Fakültesi Çevre Mühendisliği Bölümü, ayseelif.ates@iuc.edu.tr ORCID No: 0000-0001-5391-7478

products are generated from the same reactors and separators, a unique treatment is not tried because the wastewater flowing from the pharmaceutical unit varies in content and concentration. Water reuse saves money by lowering recycling costs and feedwater demands while balancing operational expenses involved with the waste reused procedure (Mompelat, S., 2009:35) (Klavarioti, M., 2009:35) (Khetan, S. K., 2007:107) (Kessler, R. 2010). Over the past decade, a plethora of research articles has emerged, shedding light on the treatment of a diverse range of contaminants, including pharmaceuticals (PhPs), endocrine-disrupting chemicals (EDCs), and various home consumer products (PHCPs). Most of these studies have predominantly focused on addressing effluents emanating from tertiary wastewater treatment plants (WWTPs) (Vieno, N., 2007:41) (Larsson, D. J., 2007:148) (Goossens, H., 2007:44) (Kümmerer, K., 2009:75) (Van der Aa, N. G. F. M., 2011:63). However, the efficacy of treating these contaminants at their source presents a compelling alternative that not only has the potential to minimize costs and environmental impact but also opens avenues for the recovery of valuable compounds. Despite the considerable volume of research in this domain and the emergence of numerous studies in recent years, there remains a gap in the literature, as existing works do not offer a comprehensive overview of the composition of pharmaceutical wastewater and the array of treatment technologies available (Gadipelly, C., 2014:53).

As part of this study, pharmaceutical industry wastewater containing DMSO (C_2H_6OS) underwent purification through photo-Fenton oxidation. The refinement study involved generating 3D graphics through response surface modeling. Previous literature has primarily focused on the treatment of overall wastewater combining process wastewater from various sources within the industry. However, this study specifically investigated the treatment of process wastewater resulting from the production of penicillin and its derivative drugs using Photo-Fenton oxidation.

Material and Method

After the pharmaceutical industry process wastewater was obtained, chemical oxygen demand (COD), biological oxygen demand (BOD_5), Total Nitrogen (TN), Total Phosphorus (TP), Oil Grease, total suspended solids (TSS), pH were analyzed for characterization and stored at $+4^\circ C$ in the laboratory (shown in Table 1) (Rice, E. W., 2012:10).

Table1: Characterization of raw pharmaceutical industry wastewater containing DMSO

Parameter	Unit	Value
COD	mg/L	189.600
BOD ₅	mg/L	993
TN	mg/L	215
TP	mg/L	0,45
Oil Grease	mg/L	31
TSS	mg/L	118
pH	-	6,5

Since the DMSO content causes intense foam after the chemicals to be added for the Fenton reaction, the wastewater was aerated for 2 hours before the Photo-Fenton oxidation. For Photo-Fenton oxidation, the wastewater pH was adjusted to approximately 3 using 0.1 N H₂SO₄. For the process, 250 ml sample was used and FeSO₄ and H₂O₂ were added at variable concentrations determined in response surface modelling. The variables used for response surface modeling are given in Table 2.

Table 2: Actual values and coded values used in response surface modeling

Variable	Unit	Actual Value				Coded Value			
		Low	High	-Alpha	+Alpha	Low	High	-Alpha	+Alpha
Time (A)	Min.	45	75	30	90	-1	1	-2	2
FeSO ₄ (B)	g/L	1.5	2.5	1	3	-1	1	-2	2
H ₂ O ₂ (C)	g/L	3	5	2	6	-1	1	-2	2

A schematic representation of the process setup is given in Figure 1. It was stirred under UV light for 1 hour to ensure that the Fenton oxidation reaction occurred at high yields. A 40W UV-A lamp was used as UV light. At the end of 1 hour, the pH was adjusted to >7.5 using 0.1 N NaOH to terminate the reaction. The chemicals used in the study are Merck brand. After the study, the samples were centrifuged at 2000 rpm for 4 minutes and the COD removal efficiency was calculated by taking the upper phase.

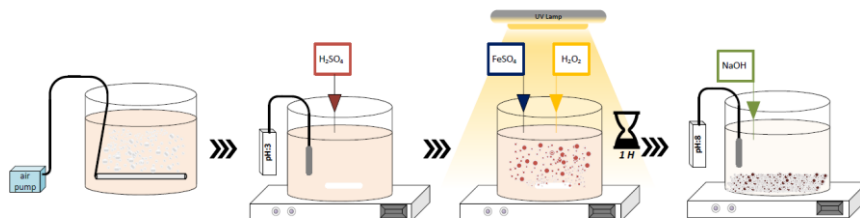


Figure 1: Scheme of treatment of DMSO-containing pharmaceutical industry wastewater by Photo-Fenton oxidation

RESULT AND DISCUSSION

FeSO₄ and H₂O₂ concentrations and time were determined as variables. The ranges of these variables were chosen according to studies in the literature. In the study, the FeSO₄ concentration is between 1-3 g/L and the H₂O₂ concentration is between 3-6 g/L. The duration was 90 minutes and samples were taken at different times. Additionally, a 40w UV-A lamp was used for Photo-Fenton. Studies were carried out at constant pH value (pH = 3). Modeling of COD removal from raw pharmaceutical industry wastewater was done with RSM. The experimental design and COD removal efficiencies required for RSM in the study are given in Table 3.

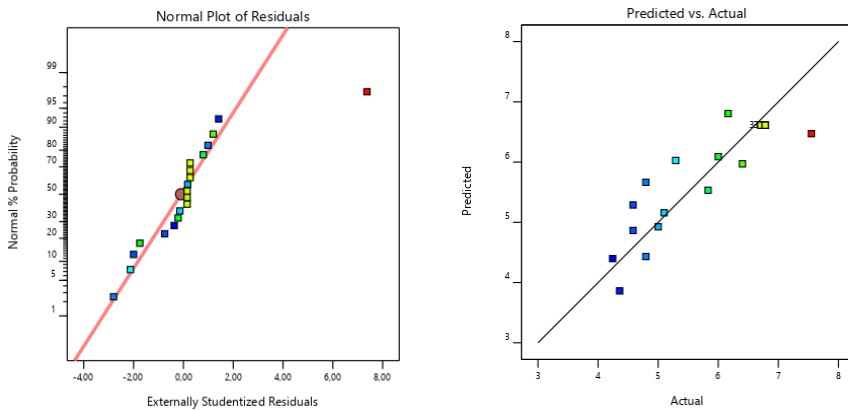


Figure 2: Normal Plot of residuals and Predicted vs Actual

Table 3: Actual values and coded values used in the experimental study for response surface modelling

Run	Actual Value			Coded Value			COD removal efficiency (%)
	A:Time (min)	B:FeSO ₄ (g/L)	C:H ₂ O ₂ (g/L)	A	B	C	
1	45	1,5	5	-1	-1	+1	25
2	60	1	4	0	-2	0	23
3	45	2,5	5	-1	+1	+1	36
4	60	2	4	0	0	0	45
5	75	1,5	5	+1	-1	+1	28
6	60	2	4	0	0	0	46
7	60	2	4	0	0	0	45
8	45	1,5	3	-1	-1	-1	18
9	75	1,5	3	+1	-1	-1	21
10	60	2	4	0	0	0	46
11	75	2,5	5	+1	+1	+1	38
12	45	2,5	3	-1	+1	-1	26
13	60	2	4	0	0	0	45
14	60	2	6	0	0	+2	34

15	90	2	4	+2	0	0	57
16	60	2	2	0	0	-2	19
17	60	3	4	0	+2	0	41
18	30	2	4	-2	0	0	21
19	75	2,5	3	+1	+1	-1	23
20	60	2	4	0	0	0	46

The model formulation obtained in the surface response modeling probe is given in equation 1. The equation expressed in coded factors allows us to make predictions about the response based on specific levels of each factor.

COD removal=+6,61+0,4017A+0,3848B+0,4175C-0,3528 B²-0,4789 C²
Eq (1)

Table 4: Adequacy of the model tested

Source	Sequential p-value	R ²	Lack of Fit p-value	Adjusted R ²	Predicted R ²	
Linear	0,0428	0,3908	<0.0001	0,2765	0,0994	Suggested
2FI	0,9778	0,3997	<0.0001	0,1226	-0,8757	
Quadratic	0,0133	0,7850	<0.0001	0,5915	-0,7371	Suggested
Cubic	0,3865	0,8824	<0.0001	0,6275	-23,0793	Aliased
Source	Sum of Squares	df	Mean Square	F-value	p-value	
Mean vs Total	663,19	1	663,19			
Linear vs Mean	7,74	3	2,58	3,42	0,0428	Suggested
2FI vs Linear	0,1768	3	0,0589	0,0644	0,9778	
Quadratic vs 2FI	7,63	3	2,54	5,97	0,0133	Suggested
Cubic vs Quadratic	1,93	4	0,4820	1,24	0,3865	Aliased
Residual	2,33	6	0,3884			
Total	683,00	20	34,15			

Table 5: ANOVA results of the study according to the quadratic model

Source	Coefficient estimate	Sum of Squares	df	Mean Square	F-value	p-value	
Model		15,55	9	1,73	4,06	0,0198	S
Intercept				6,61			
A-Time	0,4017	2,58	1	2,58	6,06	0,0335	S
B-FeSO ₄	0,3848	2,37	1	2,37	5,56	0,0400	S
C-H ₂ O ₂	0,4175	2,79	1	2,79	6,55	0,0284	S
AB	-0,0963	0,0742	1	0,0742	0,1741	0,6853	NS
AC	0,0524	0,0220	1	0,0220	0,0516	0,8249	NS
BC	0,1004	0,0807	1	0,0807	0,1894	0,6726	NS
A ²	-0,2361	1,40	1	1,40	3,29	0,0997	NS
B ²	-0,3528	3,13	1	3,13	7,35	0,0219	S
C ²	-0,4789	5,77	1	5,77	13,54	0,0042	S

Residual		4,26	10	0,4258			
Lack of Fit		4,25	5	0,8500	515,65	<0.0001	S
Pure Error		0,0082	5	0,0016			
Cor Total		19,81	19				

In ANOVA analysis, a P-value less than 0.05 indicates that the value is significant (S), while a P-value greater than 0.1 indicates that it is not significant (NS). Accordingly, when table 5 is examined, it is seen that A, B, C, B², C² are significant.

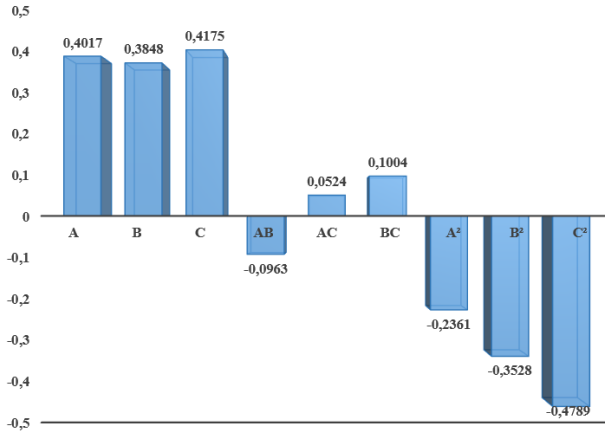
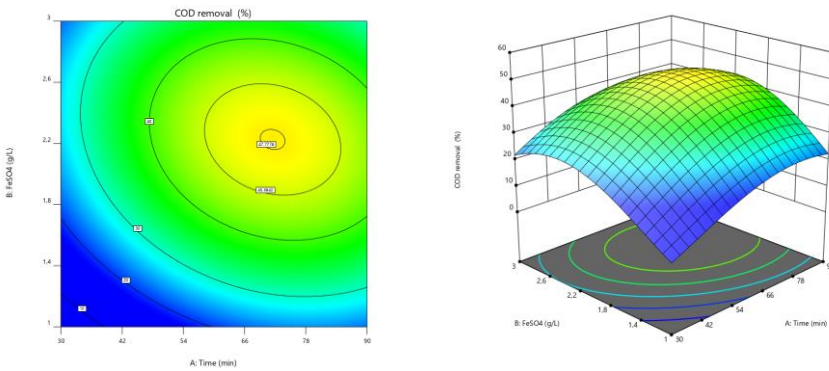
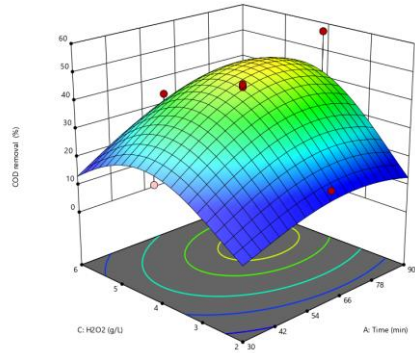
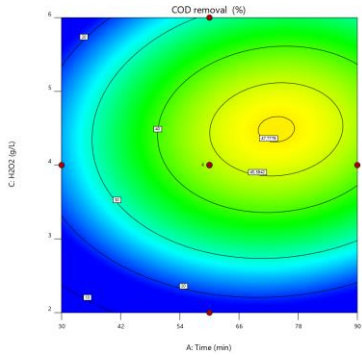


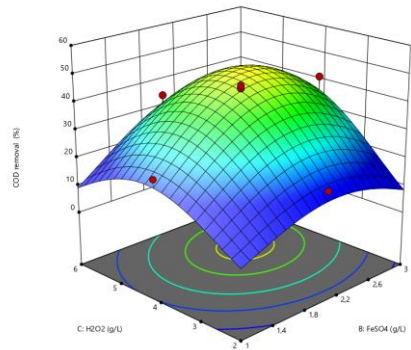
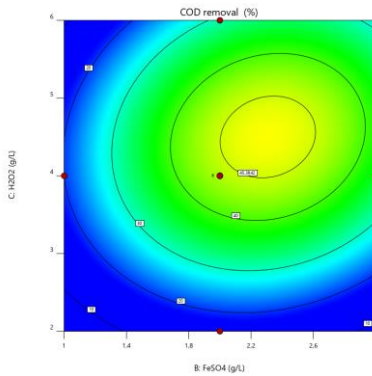
Figure 3: Graphical representation of the quadratic model and the coefficient of determination (R²) for model terms associated with Chemical Oxygen Demand removal.



a.



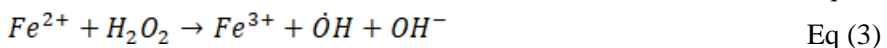
b.



c.

Figure 4: Graphs of COD removal efficiency from raw pharmaceutical industry wastewater of H_2O_2 and $FeSO_4$ concentrations and time variables, a.) $FeSO_4$ (mg/L)- Time (min.), b.) H_2O_2 (mg/L)- Time(min.), c.) H_2O_2 (mg/L)- $FeSO_4$ (mg/L)

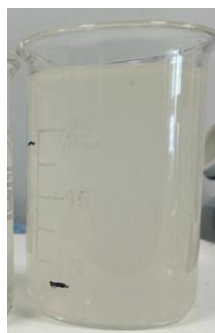
The use of UV lamps with Fenton oxidant increases the optical reduction of ferric ion. It is also an agent that increases the photolysis of hydrogen peroxide. Photo-Fenton oxidation is one of the widely used methods for the degradation of different organic pollutants in wastewater. This is due to the formation of hydroxyl radicals resulting from both the photolysis of hydrogen peroxide and the reduction of iron ions in acidic environments (pH2-4). In literature studies, it was stated that the amount of iron ions was recovered under UV light and did not decrease during the reaction (Eq 2-6).





When graph 4_{a,b} is examined, COD removal efficiency increases with increasing time, regardless of the FeSO₄ and H₂O₂ concentration. However, increasing the time from 30 to 90 did not cause a significant increase in the yield. In addition, the low FeSO₄ concentration reduced the treatment efficiency. This is because the concentration required for the reaction with H₂O₂ cannot be achieved. Although high concentration increases the purification efficiency, being above the optimum H₂O₂/FeSO₄ ratio causes coagulation. In the H₂O₂- FeSO₄ graph in figure 4_c, it can be seen that the efficiency decreases at concentrations other than the optimum ratio. The optimum H₂O₂/ FeSO₄ concentration was determined as 2. In addition, the highest purification efficiency, 46%, was reached after 60 minutes, and running the process for 90 minutes for the reaction increases the cost. The inert of the chemicals in the wastewater reduced the treatment efficiency. However, in the study where Photo-Fenton oxidation was used for DMSO degradation, it was observed that although the Total organic carbon (TOC) removal efficiency was low, the degradation of DMSO was at high efficiency (Behrouzeh, M., 2022:15) (de Luna, M. D. G., 2013: 232).

As seen in Figure 5, after adding FeSO₄ and H₂O₂ for photo-Fenton oxidation, an intense amount of foam was formed. In addition, figure 5_c shows that the foam decreases after the process but does not disappear completely. When Figures 5_a and 5_c are compared, color appeared in the wastewater after Photo-Fenton oxidation. In this case, a different treatment process must be applied for color removal after the process. The Photo-Fenton oxidation process alone was not found suitable because the low purification efficiency and the color caused after the process were due to the high amount of solvent.



a.

b.

c.

Figure 5: Wastewater images before and after Fenton oxidation a.) raw wastewater, b.) Before Photo-Fenton oxidation, c.) After Photo-Fenton oxidation

CONCLUSION

In the study, COD removal by Photo-Fenton oxidation in crude pharmaceutical industry wastewater containing DMSO was modeled with RSM. In the study, wastewater was aerated for 2 hours before Photo-Fenton oxidation. This is because aeration-free Photo-Fenton oxidation causes dense foam when chemicals are added. At the end of the study, the optimum $\text{H}_2\text{O}_2/\text{FeSO}_4$ ratio was found to be 2 at pH 3. In addition, the highest treatment efficiency, 46% COD removal, was achieved after 60 minutes. Although the increase in efficiency does not contradict the literature, oxidation should be tried after at least 5 hours of ventilation to increase the efficiency. In addition to the UV process applied as a hybrid with Fenton oxidation, it is recommended to add an electro process and try it in future studies as Photo-Electrofenton oxidation will increase hydroxyl radicals. Since the increase in the power of the UV lamp is another factor that increases hydroxyl radicals, a lamp with a higher power should be used instead of a 40w lamp.

REFERENCES

1. Behrouzeh, M., Parivazh, M. M., Danesh, E., Dianat, M. J., Abbasi, M., Osfouri, S., ... & Akrami, M. (2022). Application of Photo-Fenton, Electro-Fenton, and Photo-Electro-Fenton processes for the treatment of DMSO and DMAC wastewaters. *Arabian Journal of Chemistry*, 15(11), 104229.
2. Dalrymple, O. K., Yeh, D. H., & Trotz, M. A. (2007). Removing pharmaceuticals and endocrine-disrupting compounds from wastewater by photocatalysis. *Journal of Chemical Technology & Biotechnology: International Research in Process, Environmental & Clean Technology*, 82(2), 121-134.
3. de Luna, M. D. G., Colades, J. I., Su, C. C., & Lu, M. C. (2013). Comparison of dimethyl sulfoxide degradation by different Fenton processes. *Chemical engineering journal*, 232, 418-424.
4. Gadipelly, C., Pérez-González, A., Yadav, G. D., Ortiz, I., Ibáñez, R., Rathod, V. K., & Marathe, K. V. (2014). Pharmaceutical industry wastewater: review of the technologies for water treatment and reuse. *Industrial & Engineering Chemistry Research*, 53(29), 11571-11592.
5. Guillette Jr, L. J., Crain, D. A., Gunderson, M. P., Kools, S. A., Milnes, M. R., Orlando, E. F., ... & Woodward, A. R. (2000). Alligators and endocrine disrupting contaminants: a current perspective. *American Zoologist*, 40(3), 438-452.
6. Goossens, H., Ferech, M., Coenen, S., Stephens, P., & European Surveillance of Antimicrobial Consumption Project Group. (2007). Comparison of outpatient systemic antibacterial use in 2004 in the United States and 27 European countries. *Clinical infectious diseases*, 44(8), 1091-1095.
7. Kessler, R. (2010). *INDUSTRY ISSUES: pharmaceutical factories as a source of drugs in water*.
8. Khetan, S. K., & Collins, T. J. (2007). Human pharmaceuticals in the aquatic environment: a challenge to green chemistry. *Chemical reviews*, 107(6), 2319-2364.
9. Kümmerer, K. (2009). Antibiotics in the aquatic environment—a review—part I. *Chemosphere*, 75(4), 417-434.
10. Klavarioti, M., Mantzavinos, D., & Kassinos, D. (2009). Removal of residual pharmaceuticals from aqueous systems by advanced oxidation processes. *Environment international*, 35(2), 402-417.

11. Larsson, D. J., de Pedro, C., & Paxeus, N. (2007). Effluent from drug manufactures contains extremely high levels of pharmaceuticals. *Journal of hazardous materials*, 148(3), 751-755.
12. Mompelat, S., Le Bot, B., & Thomas, O. (2009). Occurrence and fate of pharmaceutical products and by-products, from resource to drinking water. *Environment international*, 35(5), 803-814.
13. Rice, E. W., Bridgewater, L., & American Public Health Association (Eds.). (2012). *Standard methods for the examination of water and wastewater* (Vol. 10). Washington, DC: American public health association.
14. Orlando, E. F., Kolok, A. S., Binzcik, G. A., Gates, J. L., Horton, M. K., Lambright, C. S., ... & Guillette Jr, L. J. (2004). Endocrine-disrupting effects of cattle feedlot effluent on an aquatic sentinel species, the fathead minnow. *Environmental health perspectives*, 112(3), 353-358.
15. Van der Aa, N. G. F. M., Kommer, G. J., Van Montfoort, J. E., & Versteegh, J. F. M. (2011). Demographic projections of future pharmaceutical consumption in the Netherlands. *Water Science and Technology*, 63(4), 825-831.
16. Vieno, N., Tuhkanen, T., & Kronberg, L. (2007). Elimination of pharmaceuticals in sewage treatment plants in Finland. *Water research*, 41(5), 1001-1012.

Chapter 6

Energy Management Strategies and Techniques in Hybrid and Electric Vehicles

Bayram KILIÇ¹
Emre ARABACI²

INTRODUCTION

Energy policies of developing countries aim at economic growth, energy security and climate action together. Energy, which is the most fundamental input of production, is a necessary condition for societies to survive. The use of energy occurs in the direct manufacture of a product or in supporting the production process. While these processes occur, some problems arise, such as the decrease in natural resources, environmental pollution, climate change and high energy costs.

However, considering the current state of existing energy resources, it is a fact that the increasing energy demand in the world cannot be met forever. In addition to the decrease in conventional energy resources, the problem of global warming, which is one of the most important environmental problems, necessitates the efficient and effective use of renewable energy sources and currently produced energy. To increase energy efficiency, currently implemented regulations include measures such as burning fuels efficiently in combustion processes, performing thermal insulation in facilities and systems, using applications that will increase heat transfer efficiency, using heat recovery systems, and automatic control applications. In addition to these applications, especially in newly installed systems, it is required that the machines have high technologies, have thermal insulation, create energy efficiency monitoring systems, keep emission values to a minimum and pay attention to combined heat and power production.

The decrease in available energy resources day by day has increased the tendency towards alternative energy sources in energy production and use. Today, energy saving is seen as an alternative energy source. Energy savings in production and use are extremely important for environmental problems as well

¹ Assoc.Prof.; Burdur Mehmet Akif Ersoy University, Technical Sciences Vocational School, Department of Electricity and Energy, Burdur, Turkey, bayramkilic@mehmetakif.edu.tr ORCID No: 0000-0002-8577-1845

² Assoc. Prof.; Pamukkale University, Faculty of Technology, Automotive Engineering Department, Denizli, Turkey, earabaci@pau.edu.tr ORCID No: 0000-0002-6219-7246

as economic gains. Energy saving should not be about reducing energy production and use, but about reducing the energy consumed per product. For this, losses must be minimized or even eliminated by performing a good energy analysis.

Energy management in electric vehicles is achieved through various strategies and techniques. These strategies are used to increase the vehicle's efficiency, extend range, and maximize battery life (Kural, 2015). Figure 1 shows the types of energy management strategies for electric vehicles (Yuzheng et al., 2022).

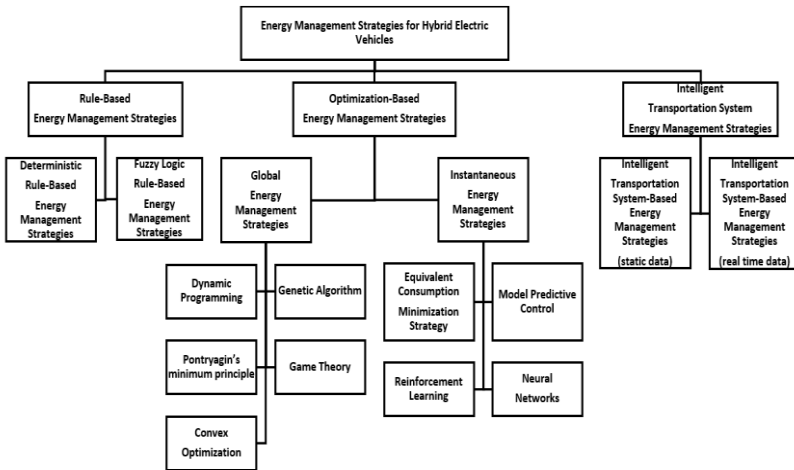


Figure 1. Types of energy management strategies for electric vehicles

REGENERATIVE BRAKING IN ELECTRIC VEHICLES

Various technologies are used to ensure efficient use and energy saving of electric vehicles and development studies are continuing. Regenerative braking is one of the most important of these technologies. Regenerative braking is an energy recycling system that converts the kinetic energy generated during vehicle braking into electrical energy and recovers it in the batteries. This system both increases energy efficiency and improves braking performance (Altındemir, 2008).

Regenerative braking follows the following processes:

- **Braking Start:** When the driver presses the brake pedal or deceleration factors come into play, the vehicle's speed begins to decrease. Meanwhile, the movement of the wheels creates the kinetic energy of the vehicle.
- **Role of Electric Motors:** Electric motors enable the movement of the vehicle and also produce electrical energy by working as generators during braking.

- Conversion of Kinetic Energy: During braking, electric motors convert the kinetic energy coming from the moving wheels into electrical energy.
- Storage of Electrical Energy: Electrical energy produced by regenerative braking is sent as recovery to batteries or energy storage systems. This energy meets the energy needs of the receivers in the vehicle.

Figure 2 shows the flow chart of regenerative braking. According to this scheme, 4 conditions must be met for regenerative braking to occur. The first thing checked in the braking data is the speed at which you press the brake pedal. The first condition is met if the driver presses the brake pedal slower than a predetermined speed P_v . In the second stage, the amount of pedal pressing is checked. The second condition is met if the driver presses the brake pedal less than a predetermined amount of movement P_x . In the third stage, the battery charge rate (State of Charge) is checked. It is desirable that the charge level of the electric vehicle's battery should not fall below 50% and should not exceed 70%. If the battery charge is below 50%, the third stage occurs. Finally, it is checked whether the torque capacity of the electric motor is sufficient. Regenerative braking occurs if the torque value that the electric motor can produce when the driver presses the brake pedal is sufficient to meet the desired braking acceleration.

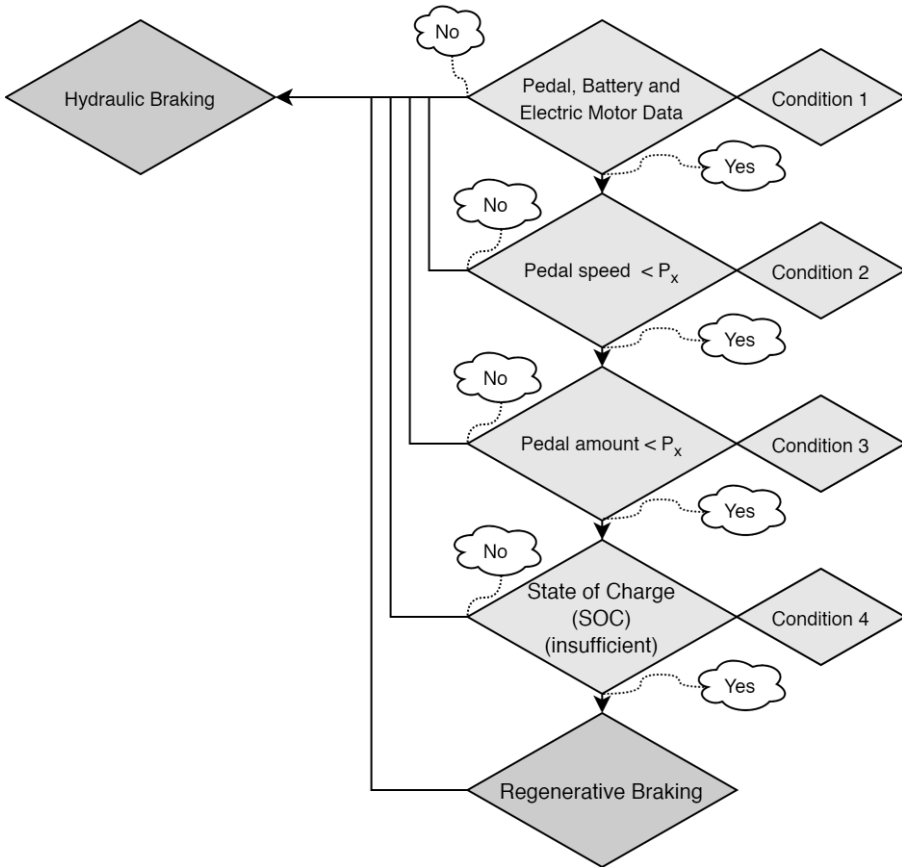


Figure 2. Regenerative Braking Flow Chart

There are many advantages to using regenerative braking in hybrid and electric vehicles. Regenerative braking reduces energy losses by increasing energy efficiency as it enables the recovery of the energy generated during braking. Converting kinetic energy into electrical energy in regenerative braking provides both shorter braking distances and lower wear. As a result, it contributes to the long life of brake components. In addition, regenerative braking contributes to increasing vehicle range as it reduces the use of stored energy in hybrid and electric vehicles (Denton, 2020).

Although regenerative braking is an important process that increases the energy efficiency of hybrid and electric vehicles, it may not provide the same level of efficiency at all speeds and conditions. The efficiency of regenerative braking may decrease, especially at low speeds and under heavy load conditions. Therefore, studies on the constraints continue.

SPEED AND ROAD SLOPE OPTIMIZATION

Factors such as driving speed and road slope affect the vehicle's energy consumption and therefore the vehicle's range. Different strategies can be used to increase the energy efficiency of electric vehicles and optimize vehicle range. One of these strategies is speed and road grade optimization. Optimizing the speed of electric vehicles and the road slope on the planned route can result in less energy consumption. This method guides the driver or automation system to determine the most efficient driving strategies or routines.

Speed optimization involves controlling the speed to ensure that the hybrid and electric vehicle travels a given route with the lowest energy consumption. In electric vehicles, energy consumption increases as speed increases. Therefore, using optimum speed saves energy. Additionally, choosing a speed appropriate to traffic flow and road conditions also increases driving safety. In speed optimization, the most efficient speed of the electric vehicle can be calculated by taking into account the speed requests from the driver or the speed limits on the route.

The impact of road slopes on electric vehicles significantly affects energy consumption. While more energy is required when going uphill, kinetic energy can be recovered when going downhill. Road slope optimization analyzes the route of the vehicle and the profile of the road and provides energy consumption control by reducing the speed in areas requiring high energy and increasing the speed in regions requiring low energy (Erjavec, 2012).

Intelligent navigation and automation systems are implemented to use speed and road grade optimization in real-time. These systems analyze the route of the vehicle, determine the most efficient speed and guide the driver or automation system. Some systems detect slope changes on the road using map data and adjust the speed accordingly.

By applying speed and road slope optimization, the energy efficiency of electric vehicles is increased, thus extending the range of the vehicle and reducing the negative environmental impact. This provides a more sustainable transportation option. It is thought that with the use of advanced sensor technologies and artificial intelligence algorithms, speed and road slope optimization will further develop and its use will become widespread in the future.

THERMAL MANAGEMENT IN ELECTRIC VEHICLES

The effective use of thermal management processes in electric vehicles is one of the most important factors that determine the performance, efficiency and battery life of electric vehicles. Thermal management in electric vehicles

consists of a set of strategies and technologies aimed at controlling the heat dissipation and temperature of vehicle components, especially batteries. Thermal management is crucial for the sustainability and safety of electric vehicles. The performance and reliability of electric vehicles depend on effective temperature control. Overheating or overcooling batteries can shorten their lifespan, reduce performance, and even pose safety risks. Therefore, thermal management in electric vehicles minimizes undesirable consequences by ensuring that batteries remain at optimized operating temperatures (Halderman and Martin, 2011).

The main purpose of battery cooling systems used in electric vehicles is to prevent batteries from overheating. For this purpose, the temperature of the batteries is controlled by using liquid cooling or air cooling systems in electric vehicles. These systems provide temperature control in batteries and also extend battery life. In addition, exposing batteries to very low temperatures in cold weather may slow down chemical reactions and reduce the performance of batteries. For this reason, heating systems are also used in electric vehicles. These systems ensure that batteries and other components are kept at operating temperatures. In addition to the use of heating and cooling systems in electric vehicles, the use of thermal insulation in the interior of the vehicle is extremely important in terms of temperature control. In this way, energy efficiency is increased while the vehicle interior temperature is maintained. Figure 3 shows an example flow chart for the battery cooling process.

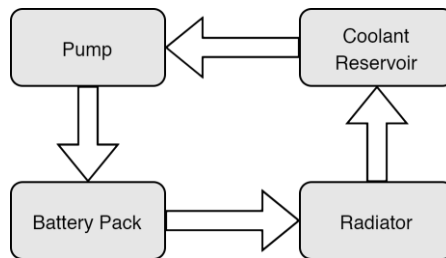


Figure 3. Flow diagram of battery cooling process

The high power and extreme acceleration demands that can be expected from electric vehicles may cause batteries to overheat. Thermal management strategies attempt to balance the temperature of batteries by controlling their power demands. Correct thermal management strategies increase vehicle performance while extending battery life.

As electric vehicles become more widespread, thermal management technologies will continue to develop. Thanks to advanced sensors, artificial intelligence and automation systems, smarter and more effective thermal management strategies can be developed. As a result, thermal management in electric vehicles plays a critical role in energy efficiency, reliability and battery life. By using correct thermal management strategies, the temperature of the batteries is controlled while the performance and safety of the vehicle are increased. This is an important element that makes electric vehicles more sustainable and user-friendly (Husain, 2011).

ROUTE PLANNING FOR ELECTRIC VEHICLES

Route planning plays a critical role to use electric vehicles efficiently and effectively. Route planning aims to ensure that the electric vehicle reaches the planned destination quickly, safely and using energy efficiently. The optimal route should be determined by taking into account factors such as the range of electric vehicles, charging infrastructure, and fast charging points. This method is used to save energy, increase range and provide the user with a better driving experience (Khajepour et al., 2014).

Range limitations of electric vehicles make route planning important. Route planning ensures that the electric vehicle reaches the planned distance smoothly by optimizing its energy consumption. Additionally, consideration of charging infrastructure and fast charging points ensures long-distance travel is hassle-free. When planning a route, many variables that affect the vehicle's performance, range and energy consumption, such as range, road slope, traffic condition, weather conditions and charging infrastructure, are taken into account. When determining the optimal route for electric vehicles, data including road slope, traffic conditions, weather conditions and location of charging stations are collected along the route. By analyzing this data, the optimal route is created (Mi and Masrur, 2017).

Route planning can be further optimized with smart navigation systems and artificial intelligence algorithms. More dynamic and effective route planning can be made by taking into account factors such as the current status of vehicle parameters, traffic conditions and weather forecast in real-time. An example representation of the road network is given in Figure 4 (Mariem et al., 2022).

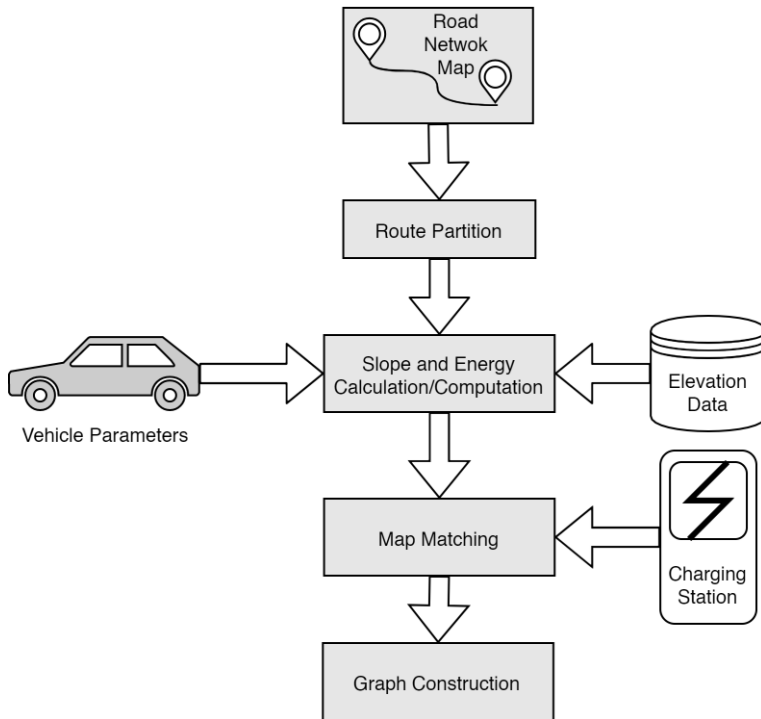


Figure 4. Illustrate the road network

CONCLUSION

Energy management in electric vehicles plays a critical role in terms of sustainability and vehicle efficiency. Technological advances and the development of energy management strategies will shape the future of electric vehicles. Energy management not only increases the performance and efficiency of vehicles, but also contributes to an environmentally friendly transportation future.

REFERENCES

1. Altındemir, E. (2008). Hibrid elektrikli taşıtlarda rejeneratif frenleme. Yüksek lisans tezi, İstanbul Teknik Üniversitesi Fen Bilimleri Enstitüsü.
2. Denton, T. (2020). *Electric and hybrid vehicles*. Routledge.
3. Erjavec, J. (2012). *Hybrid, electric, and fuel-cell vehicles*. Cengage Learning.
4. Halderman J., and Martin, T. (2011). *Hybrid and Alternative fuel vehicles*. Pearson Prentice Hall.
5. Husain, I. (2011). *Electric and hybrid vehicles: design fundamentals*. CRC press. Scientific Studies on the Edge of Global Warming
6. Khajepour, A., Fallah, M. S., and Goodarzi, A. (2014). *Electric and Hybrid Vehicles: Technologies, Modeling and Control-A Mechatronic Approach*. John Wiley & Sons.
7. Kural, E. (2015). Hibrid Elektrikli Araçlar İçin Enerji Yönetim Sistemleri. Doktora Tezi, İstanbul Teknik Üniversitesi Fen Bilimleri Enstitüsü.
8. Mariem, S., Lilia, R., Mohamed, A. D., Yasmine, A., Lasaad, B., Lamjed, B. S. (2022). Optimal Electric Vehicles Route Planning with Traffic Flow Prediction and Real-TimeTraffic Incidents, Journal of Electrical and Computer Engineering Research, 2 (1), 1-12.
9. Mi, C., and Masrur, M.A. (2017). *Hybrid electric vehicles: principles and applications with practical perspectives*. John Wiley & Sons.
10. Yuzheng, Z., Xueyuan, Li., Qi, Liu., Songhao, Li., and Yao, Xu. (2022). Review article: A comprehensive review of energy management strategies for hybrid electric vehicles, Mechanical Sciences, 13, 147-188.

Chapter 7

ENVIRONMENTAL BIOTECHNOLOGY PROCESSES IN THE TREATMENT OF LIVESTOCK WASTES

Büşra YAYLI¹
İlker KILIÇ²

1. Introduction

Organic wastes generated from various activities are thrown into the environment, stored, incinerated, or used inefficiently without an effective transformation process. As a result, waste cannot be thoroughly degraded and threatens the environment, ecosystem, and human health, although it has an essential place in national economies. Uncontrolled storage and decomposition of waste lead to the formation of gases such as CH₄ and CO₂, which are harmful to human health; odor, flies, and pathogens are formed, and the hygiene conditions of the environment deteriorate. Nitrate accumulation resulting from decomposition can cause deterioration of soil structure and microbiology and pose a threat to humans and other living things through vegetable and fruit consumption and drinking water as a result of nitrate mixing with surface and groundwater [1, 2].

Due to the increase in the world population, the livestock sector has grown and caused the accumulation and formation of animal waste that causes environmental pollution in developed and developing countries. These wastes are very harmful to the environment and difficult to dispose of. In recent years, environmental waste caused by livestock and animal waste has become one of the most critical environmental problems. Manure, wet organic, and animal wastes are non-resident pollution sources from the livestock industry. It reaches surface waters or groundwater, deteriorating the water quality and making it unusable [3].

Livestock industry waste can also be used in fertilizer and feed production areas. Thus, the evaluation of wastes in the livestock industry both reduces environmental pollution and ensures economic recovery of these wastes. However, applying waste directly to agricultural fields or streams without any

¹ Research Assistant.; Bursa Uludag University Faculty of Agriculture Department of Biosystems Engineering. busrayayli@uludag.edu.tr ORCID No: 0000-0002-0198-3550

² Prof. Dr.; Bursa Uludag University Faculty of Agriculture Department of Biosystems Engineering. ikilic@uludag.edu.tr ORCID No: 0000-0003-0087-6718

fermentation process negatively affects the product productivity of the soil as well as environmental pollution [3].

Nitrate accumulation resulting from decomposition can cause deterioration of soil structure and microbiology and threaten humans and other living things through vegetable and fruit consumption and drinking water due to nitrate mixing with surface and groundwater. Biotechnological methods find an essential area of use in the evaluation and elimination of wastes at the point of environmental protection.

Biotechnology has recently enabled modern tools and approaches in various fields such as agriculture, food, healthcare, and environmental protection. Suppose there is not a very serious pollution burden in treating hazardous wastes and controlling pollution. In that case, applying environmental biotechnology techniques using living organisms can offer solutions. This paper examines environmental biotechnological applications that can be applied in evaluating, removing, and treating farm animal manure.

2. Uses Areas of Environmental Biotechnology in Livestock Wastes Treatment

2.1. Treatment of wastes

Excessive nutrient accumulation occurs in soils where unreasonable or excessive fertilizer is applied. This situation causes heavy metal pollution in the ground, creating a toxic effect on living things in the ecosystem. At the same time, it disrupts the soil's flora and affects the soil's biological and biochemical reactions. Thanks to bioremediation methods, highly toxic pollutants are transformed into less harmful forms thanks to the metabolic activities of microbes (such as transformation, mineralization, and immobilization) [4]. Bioremediation is a process that includes the capacity to clean the environment by removing pollutants in water and soil through degradation, detoxification, and retention by macro and microorganisms such as plants, bacteria, earthworms, and fungi [5]. Bioremediation is a more permanent method because pollutants do not transform from one phase to another but are changed into harmless end products such as carbon dioxide and water through biological activities.

In bioremediation methods, two approaches, in-situ and ex-situ, are based on transporting or removing wastes to a different location for pollutant removal. In in-situ application, the contaminated material is cleaned on-site. Bioventing, biostimulation, biodegradation, biosparging, and bio-augmentation are in-situ methods. In the ex-situ process, pollutant removal is carried out by physically

removing the contaminated material from its location. Land farming, composting, bioreactors, and soil biopiles are examples of ex-situ bioremediation methods. The ex-situ bioremediation method, the remediation technologies that cannot be applied in the soil environment, gives faster and more effective results than the in-situ method [6].

The bioremediation method is called phytoremediation if plants are used to remove pollutants in soil and water. If plants are used to remove heavy metals from the soil with the phytoremediation method, the plants must be removed from the soil. Plants and macro and micro creatures are used in bioremediation applications. In the studies conducted, it is thought to be a valuable alternative for the treatment of heavy metal pollution in the soil, with its features such as accumulating heavy metals in the tissues of earthworms, contributing to the development of plants by increasing plant nutritional elements in the soil, providing aeration of the soil and supporting microbial activity [7]. However, there needs to be more information on how and by which methods the heavy metals in earthworms can be removed from the soil since heavy metals in their bodies can be mixed back into the soil after they die. There is a need for further research on this subject.

Microorganisms are also used in the bioremediation method. Microorganisms are transferred to the soil, and conditions are controlled to optimize their metabolic activity and growth. Environmental factors such as temperature, pH, and inorganic nutrients such as nitrogen and phosphorus are modified for optimization. With another method, by looking at the microorganismic structure of the soil, microorganisms transfer nutrients to the area where waste is in the soil. Thus, microorganisms existing in the soil are activated. Creatures such as fungi and bacteria are also microorganisms used in bioremediation. Thanks to mycelial structure and fungal enzymatic systems, fungi are more suitable for the bioremediation method. Thanks to their biochemical capacities and morphologies, fungi play an essential role as decomposers, including organisms in soil and water [8].

In cases of excessive pollutant loads, natural microorganisms may be unable to clean pollutants. In such cases, studies are being conducted on genetically modified microorganisms (GEMs).

2.2. Bioenergy Products From Livestock Wastes

2.2.1. Biomass

The world's most important energy source is oil, but as oil reserves gradually decrease, alternative energy sources have become even more critical. Biomass

is all organic materials of plant and animal origin that are not fossils. Biomass energy is obtained from all natural materials of animal and plant origin, the main components of which are carbohydrate compounds. Biomass production from animal waste can be converted into liquid and gaseous fuels due to biotransformation processes, and it can also be used for heating and electricity generation. An economic study of the energy that can be obtained should be conducted when agricultural biomass resources are characterized to determine their chemical and physical properties. If the feasibility and operation of the process are economical, biofuel can be produced by applying thermochemical methods to agricultural biomass. If the techno-economic evaluation is not applicable due to the examination, it can be used in applications such as compost, animal feed, soil improver, and natural fertilizer [9].

In addition, minimizing gas emissions from animal waste, pathogens, microorganisms associated with waste, and odor supports its conversion into useful energy sources and helps reduce environmental impacts. It will be achieved by increasing the energy production from biomass by applying advanced technologies to convert electricity, liquid, gas, or unprocessed solid fuels from raw biomass into suitable energy carriers [10].

As the number and weight of animals increase, the amount of waste generated also increases, which is related to the biomass energy potential. Since biomass resources of animal origin are generally rich in CH_4 and CO_2 , biogas production involving anaerobic digestion is prioritized. The products resulting from biogas production are also converted and used for electricity and heat generation, as valuable fertilizer, and even as biofuel.

Physical, biochemical, and thermochemical processes can be used in biomass conversion processes. Physical methods such as grinding, drying, pelletizing, and accumulation can be applied in bioconversion [11]. Applying physical techniques before thermochemical or biochemical processes increases the applicability of biomass.

Thermochemical conversion processes to convert biomass into products are gasification, pyrolysis, and combustion. The most commonly used chemical processes in biomass conversion are combustion, gasification, pyrolysis, fermentation, and transesterification [12].

The combustion process is applied to convert the chemical energy in biomass into mechanical, electrical, or heat energy. Materials with more than 50% moisture content are not preferred because they must be dried before combustion. Especially since the moisture content of animal manure is usually more than 50%, the combustion process is not applied. It is also undesirable because it creates problems in terms of low energy efficiency and air pollution.

The gasification process is applied to obtain gas from carbon-containing materials to produce fuel. It is carried out by heating the biomass in the anaerobic environment at 700-1000°C. With the gasification technique from biomass, a gaseous fuel can be obtained with a high efficiency to be used in oil-fired turbines that provide power and heat. Using gas fuel obtained by gasification of biomass can be expanded by making small arrangements in places where natural gas is used [13].

Pyrolysis of biomass is a thermochemical process carried out in the absence of oxygen and at high temperatures to break down organic molecules to obtain gas. The classical working range of pyrolysis is between 300-600°C. It can be realized in 3 ways according to the change of these temperatures and heating rates: slow, fast, and flash. The most well-known pyrolysis process is biochar production, which is realized by slow pyrolysis. The main objective of fast pyrolysis is to obtain a high amount of liquid from biomass. Flash pyrolysis occurs at very high temperatures within milliseconds compared to other pyrolysis types.

Bioethanol and biogas are produced as a result of the fermentation of biomass in an oxygen-free environment. Since the transesterification process produces biodiesel from biomass, this process is examined under biofuel.

2.2.2. Biogas

Biogas, a clean energy source, is obtained due to the anaerobic treatment of some specially grown plants, agricultural, and organic wastes, especially animal manure, with suitable bacteria [2]. In parallel with the interest in energy recovery from waste, interest in anaerobic biotechnology has also increased. Biogas production is the breakdown of organic substances containing biodegradable substances under anaerobic conditions by successive multistage reactions [14]. Biogas applications, which have significant advantages, especially in regions with intensive agricultural production, attract considerable interest in agriculture waste management worldwide due to their environmental and economic benefits. After biogas production in biogas plants, the remaining organic wastes can be used in agriculture as high-quality fertilizer by composting [15].

Biogas production is based on the formation of methane gas (CH₄) and carbon dioxide (CO₂) as the end product as a result of the breakdown of organic matter [16]. One m³ of biogas provides a heat value in the range of 4700-5700 kcal and has the equivalent of 0.62 liters of kerosene, 1.46 kg of charcoal, 3.47 kg of wood, 0.43 kg of butane gas, 12.3 kg of dung and 4.70 kWh of electrical energy [17].

Biogas production factors include temperature, pH, organic matter loading rate, MRS (microorganism retention time), C/N, toxicity, and hydraulic feeding time [18]. Depending on the operating temperature in biogas plants, the hydraulic waiting time varies between 20 and 120 days. The C/N ratio in wastes producing biogas from animal manure varies between 15/1 and 30/1. If the C/N ratio provides 15/1 to 30/1, there is no need to adjust the livestock manure separately. C/N calculations are always based on dry matter. The optimum C/N ratio can be achieved by mixing different organic substances. Mineral ions, heavy metals, and detergents have a toxic effect by inhibiting the growth of microorganisms in anaerobic treatment. While small amounts of mineral ions (sodium, potassium, calcium, magnesium, ammonium, and sulfur) improve the growth of bacteria, heavy metals create a toxic effect [18].

Biogas production occurs in 3 stages: Fermentation and hydrolysis, acetic acid formation, and methane formation (Figure 1). During the fermentation and hydrolysis phase, the first phase of biogas production, bacterial groups called fermentation and hydrolysis bacteria break down carbohydrates, proteins, and fats, the three essential elements of organic matter. Organic substances transform into CO₂, acetic acid, and soluble volatile organic substances. Since most volatile organic substances in the last group are volatile fatty acids, this stage is called the formation phase of volatile fatty acids. In the acetic acid formation stage, acetogenic (acid-forming) bacterial groups, which are released as a result of the first stage and convert volatile fatty acids into acetic acid, are activated, and some acetogenic bacteria convert volatile fatty acids into acetic acid and hydrogen. Another group of acetogenic bacteria uses the released carbon dioxide and hydrogen to form acetic acid. However, the acetic acid formed this way is less than the first pathway. In the methane formation stage, methane-forming bacteria use CO₂ and H₂ to produce methane (CH₄) and water (H₂O). In contrast, another group of methane-forming bacteria uses the acetic acid released from the second stage to produce CH₄ and CO₂. Of all the methane produced, 30 percent is made in the first pathway and 70 percent in the second.

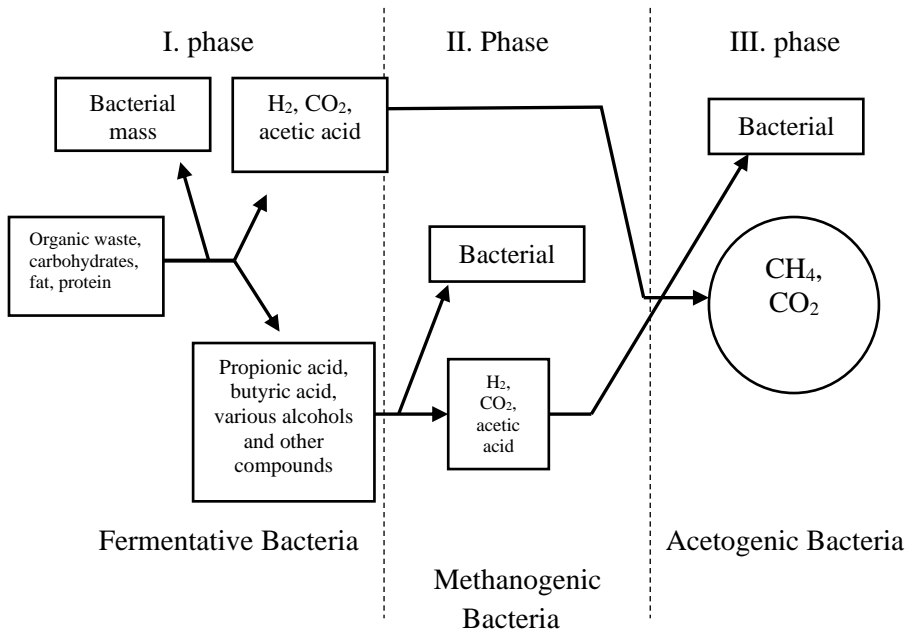


Figure 1. Biogas production stages [3]

Qi et al. [19], examined a biogas system in Northern China where pig manure and vegetable waste were used together and found that there was a decrease in the emissions of air pollutants such as H_2S , SO_2 , NO_2 , NH_3 , CO , and C_2H_4 released into the atmosphere with the use of the system, and also that manure and vegetable waste were released into the atmosphere. It has been determined that harmonious service provides a 32.4% increase in efficiency.

White et al. [20], conducted a study on a small-scale biogas system in cattle farms in Ontario. They found that the system could produce 120 MW of electricity and that changes in the feedstock used in biogas production affected the biogas yield between 10-80%.

In the study conducted by Kurt [15], the animal fertilizer production results of Düzce province were examined, and the annual animal manure production amount was 369,421.188 tons, the biomass calorific value was 10,266.95 TEP (ton equivalent oil), the biogas amount was 10,323,786 m^3 , and the biomass and bioenergy potential. It has been determined that research and development studies on energy production from biomass should be disseminated, and technological designs should be made.

2.2.3. Composting

The composting process is the biological decomposition of organic materials under aerobic or anaerobic conditions into CO_2 and H_2O together with a humus-

like substance that is harmless to health [21, 22]. The compost material should have high biodegradability and organic matter content, contain ideal concentrations of trace nutrients that plants can benefit from, and be free from harmful substances. The moisture content of the compost produced should be 65%, nitrogen content should be 1.8-2%, and pH value should be around 7. Since the organic matter in the compost increases the soil's maximum water-holding capacity, it prevents soil erosion by ensuring that the earth absorbs water in high amounts of rainfall [22]. The composting process aims to convert biodegradable organic materials into stable end products and reduce waste volume, eliminating undesirable organisms such as pathogens and fly eggs that may be present in solid waste, eliminating existing or potential odor problems, maintaining maximum macronutrient (N, P, K) and micronutrient (Zn) content, obtain products that have fertilizer value and can be used as soil conditioners [23].

Different methods are applied in composting, windrow composting, passively aerated piles, aerated static piles, and composting in reactors. Composting is faster than mixing the heap because the composting process is faster when plenty of air reaches the microorganisms. During composting in reactors, it should be ensured that the raw material continues to be in contact with oxygen. The most essential difference between open field and bioreactor composting is the use of enzymes in bioreactors. The most important advantage of this method, known as enzymatic composting, is that it saves time.

Aerobic composting is an odorless process and is widely preferred in compost production. It has advantages such as short fermentation time and elimination of pathogenic microorganisms and disadvantages such as the need for continuous oxygen supply and moisture control. There must be enough oxygen to provide aerobic conditions for decomposition without creating an odor problem. Anaerobic composting is a process that takes a long time to complete and may require external heat in some cases. Bad odor formation is observed. Biogas can be obtained as a by-product during anaerobic conversion [24].

Common factors affecting composting in all forms are grain structure, C/N ratio, pH, temperature, aeration, and water content [25]. Moisture is essential for the growth and reproduction of microorganisms in the compost. The moisture content is approximately 40-45% in the lower range. The upper range is determined by keeping the pores open so oxygen can reach the microorganisms. The optimal pH of the bacteria used in composting is 6-8. When the environment starts to warm up during the process, the pH drops to 4 -

5 with the organic acids secreted by the bacteria. With the transition to the thermophilic phase, the pH value of the environment increases again to 8.

Microorganisms used in composting feed on organic materials. Heat is generated during this activity. The increase in temperature in the environment also causes pathogenic organisms to die. For pathogen removal, the compost temperature must be above 60°C for 2 or 3 days [25]. Breaking down solid wastes with small grain structures provides more surface area for microorganism activity. In this case, the reaction time can be shortened. The optimum C/N ratio for composting is between 25-35. If this ratio exceeds 35, biological activity slows down, and the duration of the process is prolonged. If it is below 25, ammonia is released, and microorganisms are damaged.

2.2.4. Biodiesel

Biofuel can be converted from biomass of plant and animal origin and is the only renewable energy source that can be converted into liquid biofuels such as ethanol and biodiesel. It is an environmentally safe fuel that can be used in various diesel engines and generally without any modification to the machines, offering an alternative to fossil fuels. Similar processes are followed to obtain biodiesel from animal waste and vegetable waste. Pork, beef, and poultry solid fats and oils are animal-derived materials that can be converted into biodiesel.

Compared to traditional fuels, interest in using agricultural products has started to increase due to their advantages, such as being both renewable and having lower environmental emission rates. Esterification and transesterification methods are used in biodiesel production. Non-toxic and biodegradable biodiesel is produced by combining animal fat, vegetable oil, or recycled cooking oil with methanol or ethanol using the transesterification process.

In biodiesel production in the transesterification process of animal-derived biomass, fat-based triglycerides consist of three fatty acids attached to a glycerol moiety. The triglycerides in the reaction react with alcohols such as methanol or ethanol and a catalyst to produce esters and glycerol at the end of the three-step response (Figure 2) [26, 27]. Although acidic catalysts, essential catalysts, or enzymes can be used in transesterification, important catalysts are generally used [28]. Animal fats, which are subjected to the process before the transesterification process, provide efficiency during the process by filtering impurities. Transesterification is the most widely used process in biodiesel production and is considered the best option because this process is relatively simple compared to other methods.

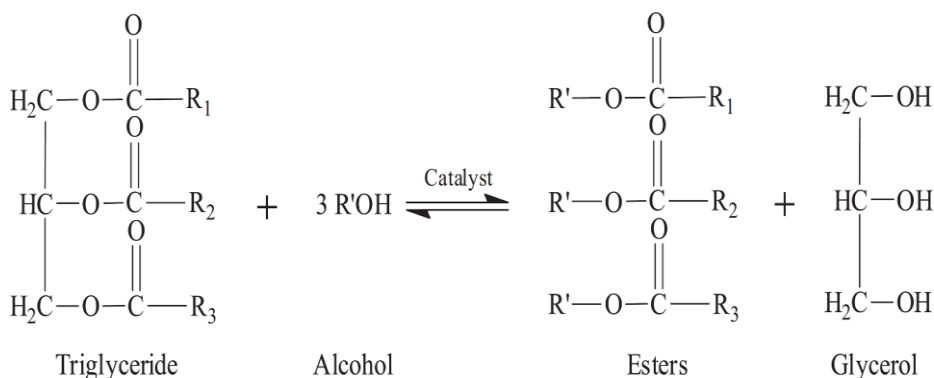


Figure 2. Transesterification Reaction [27]

The type and amount of oils used as raw material sources in biodiesel production are essential. Because the types and ratios of fatty acids in the oil used show the fuel quality of the biodiesel produced, saturated and unsaturated fatty acids can affect the cetane number of biodiesel. Since the cetane number of saturated fatty acids is higher, it has better ignition properties. The viscosity of biodiesel can also be related to the length of the fatty acid. Short chain lengths reduce viscosity and provide good fuel flow in cold weather.

Biodiesel production is a preferable alternative for recycling animal wastes into valuable products without contributing to environmental pollution, especially in cases where proper disposal cannot be provided. In addition, considering the significant impact of animal wastes on greenhouse gas emissions, the mitigation effect of climate change effects through conversion is substantial. However, it may lead to additional resources and energy consumption in case of incorrect practices or insufficient care in collecting, storing, and disposing of animal wastes. During and after the biodiesel production process, by-products and by-products may cause negative impacts on water and soil pollution when the process is not controlled correctly.

2.3. Biosensor Applications

Biosensors are another biotechnology used to determine environmental pollution and control environmental conditions. Thanks to the developed biosensors, it is possible to detect waste and predict pollution in the ecosystem.

The main field of study in developing biosensors is the perception and response of living things to changes in the ecological system. Living things must perceive changes in their environment and adapt to change to continue

their lives. This sensing mechanism has formed the basis for developing biosensors (in artificial conditions) in the laboratory [29, 30].

In biosensors used in the agricultural field, animal and plant cells are used as recognizers. Biosensors in agriculture can generally be used to measure pesticide use, artificial fertilizer, foul odor, and plant and animal diseases [31]. One of the biosensors used in agriculture is the electronic nose. An electronic nose is a smart device that detects and identifies volatile compounds and odors that mimic the human nose. There are various studies on the use of electronic noses in agricultural applications. Some of the studies include the detection of *Salmonella enteric* pathogen in poultry manure, the use of maturity detection in fruits, the determination of the freshness of beef, the collection and classification of aroma signals from wheat of different ages [32, 33, 34]. Electronic noses monitor and analyze the odors emitted into the atmosphere from animal waste and waste management systems from animal housing facilities. Determination of pathogens and microorganisms in animal-derived fertilizer content will help ensure quality and safety in production.

Thanks to biosensor technologies, enzymes, microorganisms, and antibodies are used to detect heavy metals, pathogens, toxins (aflatoxins), and organic pollutants created by animal waste. In enzyme-based biosensors, enzymes catalyze the reaction by selecting the relevant substrate among thousands of chemicals. If adverse conditions occur in the responses, it may cause the enzyme activity to deteriorate and the determination to fail.

Antibody-based biosensors (Immunosensors) are biosensors using antibodies as receptors. Antibodies are protein-structured substances that immune system cells produce against foreign organisms such as viruses, bacteria, or their protein products. The most crucial advantage of antibody-based biosensors is that they are immunogenic. The most critical benefit is that the target must not be purified before detection. Immunosensors can be developed to determine hormones, drugs, viruses, bacteria, and pesticides.

Living organisms such as bacteria, algae, and fungi have a high potential for use in biosensors. Microbial biosensors must be able to establish a specific connection between the biological structure and the measurable signal, and particular forms with selectivity towards the target analyte must be used. Microorganism-based biosensors are advantageous compared to enzyme-based biosensors because they are created using living cells, are easy to obtain, are cheaper, provide more stability than enzymes, and have intracellular sensing mechanisms.

Different microbial sensors have been developed today for the detection of environmental pollutants such as heavy metals, toxic gases, drugs, endocrine

disruptors, and physicochemical parameters such as biochemical oxygen demand, which determines how fast the oxygen present in water is used by microorganisms in water [35]. In addition, some cold-adapted organisms are widely used in the food industry to prevent microbial contamination and increase the preservation of cell tissues by freezing and preserving the texture and flavor of frozen foods [36].

4. Conclusion

Reducing waste generation is of great importance in solving the environmental problems that are increasing globally today. Considering the pressure of the livestock sector on the environment, technological methods to be used in this field have essential advantages in protecting both the environment and human health. Animal manure and animal wastes generated in animal production facilities cause air, water, and soil pollution in production areas. Treatment of these wastes by technological methods is essential for environmental health. The application of biotechnological processes in agriculture is very economically and environmentally significant.

In this study, the main methods used in treating animal wastes were examined, the studies carried out worldwide were reviewed, and it was determined that the biotechnological techniques applied in treating animal wastes have high removal efficiency. The studies to be used in this field have the potential to be used successfully.

References

1. Yu, H. W., Samani, Z., Hanson, A., & Smith, G. (2002). Energy recovery from grass using two-phase anaerobic digestion. *Waste Management*, 22, 1-5.
2. Deviren, H., İlkılıç, C., & Aydın, S. (2017). Usable Materials in the Production Biogas and Using Fields of Biogas. *Batman University Journal of Life Sciences*, 7 (2/2), 79-89.
3. Şenol, H., Elibol, E. A., Açıklı, Ü., & Şenol, M. (2017). Potential of producing biogas and electric energy from poultry animals in Turkey. 2016. *BEU Journal of Science*, 6(1), 1-11.
4. Gangola, S., Joshi, S., Kumar, S., & Pandey, S. C. (2019). *Comparative analysis of fungal and bacterial enzymes in biodegradation of xenobiotic compounds*. Smart bioremediation technologies (pp. 169-189). Academic Press.
5. Ojuederie, O. B., & Babalola, O. O. (2017). Microbial and plant-assisted bioremediation of heavy metal polluted environments: A review. *International Journal of Environmental Research Public Health*, 14, 1–26.
6. Baker, K. H., & Herson, D. S. (1994). *Bioremediation*. McGraw – Hill, New York.
7. Kara, E., Taciroğlu, B., & Sak, T. (2016). Using Earthworms to Remove Heavy Metal in Soil. *KSU Journal of Natural Sciences*, 19(2), 201-207.
8. Deshmukh R., Khardenavis A. A., & Purohit H. J. (2016). Diverse metabolic capacities of fungi for bioremediation. *Indian journal of microbiology*, 56(3), 247-264.
9. Saleem, M. (2022). Possibility of utilizing agriculture biomass as a renewable and sustainable future energy source. *Heliyon*, 8(1), e08905.
10. Rosillo-Calle, F., De Groot, P., Hemstock, S. L., & Woods, J. (Eds.). (2015). *The biomass assessment handbook: Energy for a sustainable environment*. Routledge.
11. Üçgül, İ., & Akgül, G. (2010). Biomass Technology. *Journal of YEKARUM*, 1(1), 3-11.
12. Noor, S., Latif, A., & Jan, M. (2011). Overview of biomass conversion technologies. *Science Vision*, 16.
13. Mutlu, N., Tolay, M., Karaca, C., & Öztürk, H. H. (2019). Developments in Biomass Gasification Technology. *Journal of Agricultural Machinery Science*, 15(2), 53-59.
14. Bayrak, E. H., Yokuş, S. K. & Pehlivan, E. (2014). Biogas production from sludge of sewage treatment plant in Turkey. *Electronic Journal of Occupational Improvement and Research*, 2(1), 84-93.

15. Kurt, A. (2021). Evaluation of biogas and compost availability potential of agricultural and animal origin in Duzce province. *Journal of Yalvac Academy*, 6(1), 14-26.
16. Yüksekdağ, M., Gökpınar, S. & Yelmen, B. (2020). Treatment Sludges and Disposal Applications in Wastewater Treatment Plants. *European Journal of Science and Technology*, (18), 895-904.
17. Çelikkaya, H. (2016). *Biyogaz*. Fırat Kalkınma Ajansı. Retrieved December 2, 2023, from https://fka.gov.tr/sharepoint/userfiles/Icerik_Dosya_Ekleri/FKA_ARAST_IRMA_RAPORLARI/BİYOGAZ.pdf
18. Gülen, J. & Çeşmeli, Ç. (2012). General knowledge about biogas and usage areas of by products. *Erzincan Journal of Science and Technology*, 5(1), 65-84.
19. Qi, X., Zhang, S., Wang, Y., & Weng, R. (2005). Advantageous of the integrated pig biogas- vegetable greenhouse system in North China. *Ecological Engineering*, 34, 175-185.
20. White, A. J., Kirk, D. W., & Graydon, J. W. (2011). Analysis of small-scale biogas utilization systems on Ontario cattle farms. *Renewable Energy*, 36(3), 1019-1025.
21. Epstein, E. (1997). *The Science of composting*. Technomic Publishing Co. Inc, USA, 383-415.
22. Orkun, M. O., Güngör, E. B. Ö. & Erdin, E. (2011). Investigation of compost application respect of potential soil pollution. *Katı Atık ve Çevre*, 83, 60-67.
23. Öztürk, İ., Arıkan, O., Altınbaş, M., Alp, K., & Güven, H. (2016). Katı Atık Geri Dönüşüm ve Arıtma Teknolojileri. *Union of Municipalities of Turkey*. Retrieved November 8, 2023, from https://www.researchgate.net/publication/320549122_Kati_Atik_Geri_Donusum_ve_Aritma_Teknolojileri_El_Kitabi
24. Ogejo, J. A. (2018). *Compost Bedded Pack Dairy Barns*. Virginia State University. Retrieved November 10, 2023, from <https://digitalpubs.ext.vt.edu/vcedigitalpubs/7988474469263459/MobilePagedReplica.action?pm=2&folio=1#pg1>
25. Dudu, Ü. & Nazilli, G. E. (2018). Compositing of Organic Solid Wastes with Biotechnological Methods in Aerobic Conditions. *Turkish Journal of Scientific Reviews*, 11(2), 47-50.
26. Baskar, G., Kalavathy, G., Aiswarya, R., & Selvakumari, I. A. (2019). *Advances in bio-oil extraction from nonedible oil seeds and algal*

- biomass*. In *Advances in eco-fuels for a sustainable environment* (pp. 187-210). Woodhead Publishing.
27. Pereira, C. O., Portilho, M. F., Henriques, C. A., & Zotin, F. M. (2014). SnSO₄ as catalyst for simultaneous transesterification and esterification of acid soybean oil. *Journal of the Brazilian Chemical Society*, 25, 2409-2416.
 28. Dunford, N. T. (2007). *Biodiesel production techniques*. Oklahoma Cooperative Extension Service.
 29. Malhotra, S., Verma, A., Tyagi, N., & Kumar, V. (2017). Biosensors: principle, types and applications. *International Journal of Advance Research and Innovative Ideas In Education*, 3(2), 3639-3644.
 30. Tüylek, Z., (2021). Biosensor and Biochip Applications in Biotechnology. *International Journal of Life Sciences and Biotechnology*, 4(3), 468-490.
 31. Boz, B., Paylan, İ. C., Kizmaz, M. Z., & Erkan, S. (2017). Biosensors and Their Using Areas in Agriculture. *Agricultural Machinery Science*, 13(3), 141-148.
 32. Balasubramanian, S., Panigrahi, S., Louge, C. M., Marchello, M., Doetkott, C., Gu, H., Sherwood, J., & Nolan, L. (2005). Spoilage identification of beef using an electronic nose system. *Transactions of the ASAE*, 47(5), 1625-1633.
 33. Zhang, H., & Wang, J. (2008). Identification of stored-grain age using electronic nose by ANN. *American Society of Agricultural and Biological Engineers*, 24(2), 227-231.
 34. Kızıl, Ü., Genç, L., Genç, T. T., Rahman, S., & Khaitza, M. L. (2015). E-nose identification of Salmonella enterica in poultry manure. *British Poultry science*, 56(2), 149-156.
 35. Gupta N., Renugopalakrishnan V., Liepmann D., Paulmurugan R., & Malhotra, B.D. (2019). Cell-based biosensors: recent trends, challenges and future perspectives. *Biosensors and Bioelectronics*, 141(1), 111435.
 36. Kırkıncı, S. F., Maraklı, S., Aksoy, H .M., Özçimen, D., & Kaya, Y., (2021). Antarctica: A review of Life Sciences and Biotechnology Researches. *International Journal of Life Sciences and Biotechnology*, 4(1), 158-177.

Chapter 8

ENVIRONMENTAL IMPACT ASSESSMENT OF LAYING HEN PRODUCTION SYSTEMS THROUGH LIFE CYCLE ASSESSMENT

Büşra YAYLI¹
İlker KILIÇ²

1. Introduction

Egg production is easy and economical, the protein content is high, and the fat content is low despite being an animal protein. The vast consumption area can be consumed quickly and is offered to the consumer at a more affordable price than other animal-derived proteins in retail sales. For these reasons, the increasing demand for eggs has played an active role in developing the egg poultry sector. Developments such as the widespread use of industrial egg poultry and automation in the poultry house have also significantly accelerated the realized production potential.

China is the largest producer of chicken eggs in the world, providing 36.4% alone in 2021. In the same year, 6.8% was supplied by America, 7.5% by India and 7% by Indonesia. Turkey supplies approx.1.2% of the world's egg production with 1 243 633 tons of eggs, ranking it 10th. In the world of egg export, after the Netherlands (351 224 tons), Turkey ranks second with 221 215 tons [1]. In the first ten months of 2023, 16 million 975 thousand eggs were produced. In the January-October period, chicken egg production increased by 4.0% compared to the same period of the previous year [2]. According to 2021 data, 121 302 869 laying hens and 4975 commercial laying hen houses in Turkey. In the same period, 19 billion 788 million eggs were produced in the commercial egg sector, and 239 eggs were produced per person [3]. Turkey is a significant producer and exporter with its egg potential. Today, the technical and technological developments in the egg industry have progressed at the same level as in European countries. As the egg is one of the essential export

¹ Research Assistant.; Bursa Uludag University Faculty of Agriculture Department of Biosystems Engineering. busrayayli@uludag.edu.tr ORCID No: 0000-0002-0198-3550

² Prof. Dr.; Bursa Uludag University Faculty of Agriculture Department of Biosystems Engineering. ikilic@uludag.edu.tr ORCID No: 0000-0003-0087-6718

products and its consumption increases, the production potential mostly made by intensive enterprises also increases the amount of waste to be generated.

Along with the increase in egg production, waste and emissions such as manure, urine, and gas outputs appear in addition to the product obtained. In cases where these cannot be controlled within the enterprise, they affect the employees' efficiency, animal welfare, and health. At the same time, if they reach the environment, they cause various environmental problems. To develop prevention and control strategies against ecological effects, it is essential first to determine which effects they cause and their effect sizes. Life cycle assessment, a holistic system to assess the environmental performance of products or services, is a reliable analysis used for multiple purposes. Life cycle assessment evaluates ecological impacts by qualitatively and quantitatively defining the use of raw materials, energy requirements, emissions, and wastes released to the environment throughout the life cycle of a product, process, or activity [4].

2. Environmental Effects of Laying Hens Productions

Consumption of resources and raw materials such as feed production, water, and land use throughout the egg production process (cradle-to-grave); The coal, fuel, and electricity consumptions used in the operating process; and the manure and urine from chickens are the main factors causing environmental problems. The overall environmental impacts caused by pollutants from laying poultry can be described as follows:

Climate change: It causes climate change with the emissions of greenhouse gases that cause global warming (especially CO₂, CH₄, and N₂O, which are the most critical greenhouse gases) to the atmosphere. It is expressed in kg CO₂, which is the equivalent of CH₄ and N₂O gases, according to the emission factors determined by the IPPC. For a 100-year timeline, methane (CH₄) has an estimated global warming potential of 27-30 times CO₂, and nitrous oxide (N₂O) has 273 times that of CO₂ [5]. The concept of carbon footprint is also an effective method to determine the impact of a product or service on climate change and uses these equivalences in calculations.

Energy use: In egg farming, energy use includes a significant share before production, during the production period, and in the stages after production. Diesel fuel use, coal use, and electricity consumption of machinery, tools, and equipment used during production in the poultry house are evaluated in energy use. Energy uses are usually expressed in MJ.

Water use: In the rearing of layer hens, the amount of water used to grow the product is the stage of feed production that causes the most water consumption. In addition, the water consumed by chickens in the poultry house and the water

used for cleaning are evaluated within the water use. The water consumed is calculated as m³, ton, or liter. The concept of water footprint has emerged to determine the water consumption and the extent of pollution in the water in the formation of production or product.

Acidification and eutrophication: The most crucial gas emission in poultry farming originates from ammonia (NH₃). NH₃ gas emission causes acidification and eutrophication [6, 7]. Acidification is the emission of gases that harm the environment by reacting with other compounds such as sulfur dioxide (SO₂), nitrogen oxides (NO_x), and ammonia (NH₃) arising from various sources in the air and returning to the surfaces as acid rain [8, 9, 10]. In acidification, the reference gas is expressed in terms of SO₂. The primary sources of eutrophication are emissions of NO₃⁻ (nitrate) and PO₄⁻³ (phosphate) in water and NH₃ (ammonia) in air. Eutrophication can be measured by reference gases NO₃⁻ or PO₄⁻³ equivalents.

Nitrification and denitrification: N gas in nitrogenous compounds in the air is first converted to NH₄ by bacteria and released into the soil. Bacteria in the soil first convert NH₄ (ammonium) to NO₂ (nitrite) and then to NO₃ (nitrate), and this is called nitrification. NO₃ leaks from the soil, leaching with surface waters and underground drinking water, causing NO₃ accumulation. The process of reducing NO₃ to N gas by microorganisms is called denitrification. NO₃, gaseous by denitrification, causes environmental effects such as the greenhouse effect, global warming, acid rain, and ozone degradation.

Land use: In general, as in all aquaculture, while most land use is realized in feed production in laying hen farming, the operation structure established on a specific land also causes land use. The m² equivalence is used as the reference unit.

3. Life Cycle Assessment (LCA)

The rapid increase in consumption and the increasing population over time, the decrease in resources, the concern of being unable to meet future needs, and the potential environmental effects it creates have revealed the concept of life cycle analysis in which ecological sustainability is evaluated. Life cycle analysis is an all-purpose analysis that enables the calculation, evaluation, and reporting of the effects, risks, and their interactions throughout the entire life cycle of an activity or product. In various studies, the definition of life cycle analysis has been made:

Guinee [11], stated that life cycle assessment is a generally accepted method for evaluating the environmental impacts of a product throughout its life cycle.

According to Baumann and Arvidsson [12], life cycle assessment is a systematic methodology that deals with the material and energy flows used in processes such as raw material input, production, use, and waste generation related to a product or process and their environmental impacts.

According to Gulli [13], Life cycle assessment is a quantitative analysis that can be used with other models to identify and evaluate potential environmental impacts during the life cycle of a process or product, to improve production methods, and to predict the behavior of various production cycles, including agricultural production.

According to the International Organization for Standardization (ISO), life cycle assessment is the collection of inputs and outputs throughout the life cycle of a product system and the assessment of its potential environmental impacts.

The life cycle assessment methodology has been standardized with ISO 14040:2006 and ISO 14044:2006, a series of environmental management standards created by the International Organization for Standardization [14].

The phases within which a product, service, or process's life cycle analysis will be presented with four different approaches: 'cradle to grave,' 'cradle to gate,' 'cradle to cradle,' and 'gate to gate.'

According to ISO standards, life cycle analysis consists of four stages. These;

- Definition of aim and scope
- Inventory analysis
- Impact assessment
- Interpretation

3.1. Definition of Aim and Scope

The first stage of life cycle analysis is defining the aim and scope. The aim and scope of the product, service, or process to be analyzed should be clearly stated. While LCA analysis can be applied for short-term studies, it can also be used for long-term studies. The target public to which the research results will be presented may vary. Factors such as working time, target audience, and databases suitable for the study influence choosing the LCA type. The available database is selected for the data and standards used in the study. The database chosen may change depending on the geographical region where the study is conducted, the content, and the purpose of the study.

The defined functional unit is taken as a basis in the life cycle assessment while limiting the scope. A reference is an operating unit that reveals the environmental effects of a production system or a service. Wiedemann and McGahan [15] stated that the definition of an available unit is "a reference unit

that enables the comparison of inputs and outputs in production and different system operations in a similar structure." The functional unit is determined by considering the environmental impact categories and the aim of the research. [16, 17].

The production or process must be limited while estimating in the life cycle assessment. In determining the system boundaries, which stages and processes of the life cycle of the product or service will be included, which will be excluded, and their justifications are taken into account [18].

3.2. Life Cycle Inventory

In the inventory analysis phase, which is the third part of the life cycle analysis, the limits and product system of the work whose purpose and scope are determined are defined. The life cycle Inventory step includes data on raw material inputs, resource use, energy requirements, liquid and solid waste, atmospheric emissions, and leakage to aquatic environments. Additionally, it aims to collect qualitative and quantitative data, to express the product outputs as a result of production numerically, to obtain and evaluate all the data-related data, and to determine the calculation procedures. The inventory phase of the life cycle is the primary phase for analyzing the method. The data's details, accuracy, and consistency directly affect the accuracy of the results in determining the impact categories and the results for the future stages. In the ISO-14044:2006 standard, the formation steps of inventory analysis are specified as obtaining the data, calculating the data, and distributing the data (allocation) (Figure 1).

3.2.1. Obtaining Data

Data collection is the most challenging and long-time phase of life cycle analysis. Qualitative or quantitative data collected, measured, calculated, or estimated for each process of inputs and outputs at the working system boundaries are obtained. Local or global sources are used if data cannot be accepted or reached. The main headings in which the data can be classified can be listed as follows:

- energy inputs, raw material inputs, auxiliary inputs, and other physical inputs
- products, by-products and wastes
- air, water, and soil emissions
- other environmental degradations

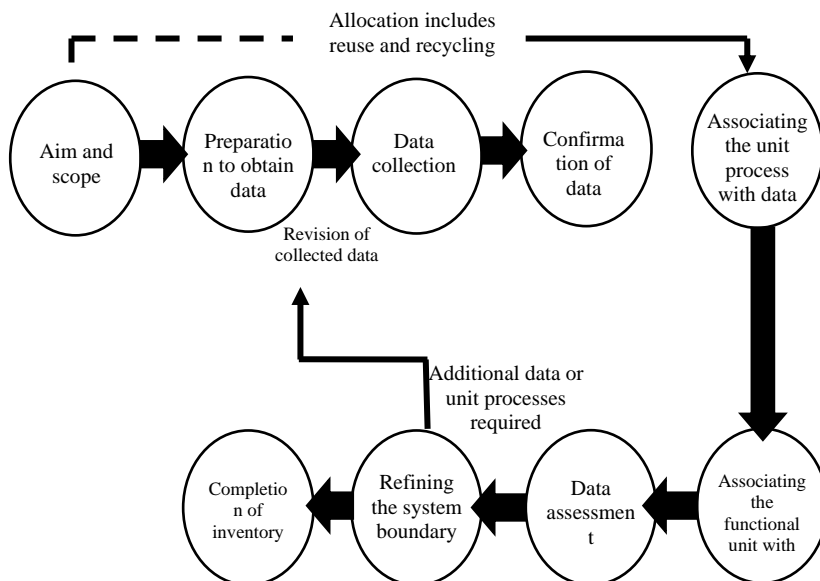


Figure 2. Flow chart of life cycle inventory assessment

3.2.2. Calculation of Data

At this stage of the inventory analysis, the calculation methods should be clearly stated, and the same calculation procedures should be applied consistently throughout the study. Data needs to be validated to ensure data quality in computation. Validation of data is related to being consistent with each other and making comparative analysis. Calculations of inputs and outputs should be made by creating flow charts in unit processes, considering the study's unit function. Based on its purpose, system boundaries can be revised according to the sensitivity analysis of essential inputs and outputs in processing data obtained in life cycle analysis.

3.2.3. Allocation

This stage includes data distribution to the relevant processes. Distribution should be avoided if the unit process is split into two or more sub-stages, by-products are produced, and the production process is expanding. Suppose data allocation cannot be avoided in the production process. In that case, it must be distributed in a way that reflects the fundamental physical relationship between different products or functions. If the physical connection between the development or processes cannot be established in the distribution, it is done by

decoupling it with other relationships. For example, the economic value of the products is allocated among the by-products in proportion.

3.3. Life Cycle Impact Assessment

As stated in ISO [14], since life cycle assessment is a relative approach based on unit function, it differs from other techniques such as environmental performance assessment, environmental impact assessment, and risk assessment in this respect. At this stage of the life cycle analysis, the potential effects of the inventory data collected for system inputs (raw material, energy, water, and resource uses) and system outputs (product, waste, by-products) on humans and ecology are evaluated. There are some compulsory and optional elements to carry out an impact assessment. Required factors include defining impact categories and category indicators, impact classification (classification), and characterization.

3.3.1. Identification of impact categories and indicators

In the life cycle assessment, impact categories indicate environmental problems (climate change, acidification, eutrophication) related to the production system or process examined to reflect the purpose and scope of the work done (Table 1). Each impact category has a specific environmental mechanism, and impact indicators vary according to the types defined within these ecological mechanisms.

Table 1. Environmental Impact Categories and Units

Impact Category	Unit
Climate Change	kg CO ₂ eq
Ozone Depletion	kg CFC-11 eq
Terrestrial Acidification	kg SO ₂ eq
Freshwater Eutrophication	kg P eq
Marine Eutrophication	kg N eq
Human Toxicity	kg 1,4-DB eq
Photochemical Oxidation Formation	kg NMVOC
Particulate Matter Formation	kg PM10 eq
Terrestrial Ecotoxicity	kg 1,4-DB eq
Freshwater Ecotoxicity	kg 1,4-DB eq
Marine Ecotoxicity	kg 1,4-DB eq
Ionizing Radiation	kBq U235 eq
Agricultural Land Use	m ² a
Urban Area Use	m ² a

Natural Area Transformation	m ²
Water Consumption	m ³
Metal Consumption	kg FE eq
Fossil Consumption	kg oil eq

3.3.2. Impact classification

Classifications are grouped by associating the determined impact categories and indicators with the data collected during the life cycle inventory analysis. For example, SO₂ (sulfur dioxide) gas emissions cause acidification. Therefore, SO₂ is classified in the acidification effect category.

3.3.3. Characterization

Whichever data obtained in the inventory analysis contributes to the same impact category, these data are multiplied by specific coefficients and converted into a standard unit, revealing the total impact of that impact category. The characterization stage enables comparison between inventories within the same impact category. E.g., CO₂, CH₄, and N₂O are the most important greenhouse gases that cause climate change. Calculating the effects of these gases on climate change in kg CO₂ equivalents over the standard unit characterizes their impact on climate change.

After the compulsory stages in the life cycle impact assessment are carried out, optional steps can also be carried out within the scope of the study on the inventory data. These stages are normalization, grouping, weighting, and data quality analysis [14].

3.3.4. Normalization

An inventory analysis tool eliminates the units by dividing the impact indicators by a selected reference value and comparing them between different impact categories [19]. For the reference to be determined, reference values such as the sum of inputs and outputs for a specific area globally, regionally, nationally, or locally, the sum of inputs and outputs per capita for one particular area, and the information and outcomes of the alternative scenario presented to the product system can be selected.

3.3.5. Grouping

Impact categories within the defined purpose and scope of the work are assigned to one or more predefined groups. The grouping stage provides ease of interpretation and evaluation of impact categories for studies to be carried out in certain areas. For example, when examining the chemicals of a service that

cause environmental pollution in the aquatic environment, grouping them as water emissions provides ease of monitoring and evaluating the impact category.

3.3.6. Weighting

At this stage of the life cycle analysis, different impact categories are graded according to their values using numerical values. Weighting the impact categories with the weighting process reveals which class has a more significant impact. The same indicators or normalized indicator results can differ depending on the country, region, organization, or society where the weighting process is performed.

3.3.7. Data quality analysis

Additional information and techniques may be needed to understand better and demonstrate the importance, uncertainty, and sensitivity of inventory analysis results. Different analyses are used to reveal the accuracy of the data to carry out the purpose and scope of life cycle analysis. Gravity Analysis is applied to identify the data that contributes the most to the result. Uncertainty Analysis is applied to reveal uncertainties in data and calculations. Sensitivity Analysis is used to decide how changes in data and methodological choices affect the inventory results.

3.4. Life Cycle Interpretation

Interpretation is the final stage of life cycle analysis. The data, findings, and results obtained in the inventory analysis and impact assessment step are evaluated by the purpose and scope of the study and suggestions presented. Regarding the purpose of the study, interpretations should be made using the definitions of system functions, functional units, and system boundaries, using the data obtained and within the limitations determined by sensitivity analysis. There are some points to be considered in the interpretation phase of an LCA study [14]:

- According to the findings obtained from the inventory analysis and impact assessment phase, it is necessary to determine and emphasize the critical issues that affect the study.
- The evaluation should involve the subject and ensure the results are sensitive and consistent.
- In the interpretation phase, the final work should be concluded, and the precautions and limitations that can be taken for the current situation should be put forward.

4. Standardization of Life Cycle Assessment

The environmental concept of life cycle assessment (LCA) was developed from the idea of a detailed environmental assessment of products in Europe and the USA in the late 1960s and early 1970s [20]. The Society of Environmental Toxicology and Chemistry (SETAC) published the first guideline for life cycle assessment in 1993, describing the procedures for life cycle assessment. In the international standards developed and accepted in the late 1990s, recommendations and requirements were put forward for various methodological issues that should have been included in the directive published by SETAC [21].

Another organization working on life cycle analysis is UNEP (United Nations Environment Development). In 1996, a guiding guide was published titled "Life Cycle Assessment: What it is, and what to do about it." SETAC and UNEP are currently working in collaboration with the Lifecycle Initiative. This cooperation ensures that the public interest is a scientifically provided global forum by establishing a consensus (governments, companies, scientific organizations, and non-governmental organizations).

The first national standard on life cycle assessment was established by ISO on May 15, 1997, with the title "ISO-14040: Environmental management - Life cycle assessment - Principles and framework". This standard explains the general framework, principles, and requirements for carrying out and reporting life cycle assessment studies and specifies relevant definitions. However, this published standard needs to mention a detailed structuring of the life cycle assessment. To under-define the methodology and eliminate the deficiencies, new standards were established that clarified the stages of the lifecycle review.

These standards are "ISO 14041:1998 Environmental management - Life cycle assessment - Goal and scope definition and inventory analysis", "ISO 14042:2000 Environmental management - Life cycle assessment - Life cycle impact assessment", and "ISO 14043:2000 Environmental management - Life cycle assessment - Life cycle interpretation" titles. ISO 14041, ISO 14042, and ISO 14043 standards were cancelled in 2007. It was revised as "ISO 14040:2006 Environmental management - Life cycle assessment - Principles and framework" in 2007 and the standards titled "ISO 14044:2006 Environmental management — Life cycle assessment — Requirements and guidelines" entered into force as the last standard published up to date. In the year 2018, the standard ISO 14044 Environmental Management - life cycle assessment - requirements and guidelines - Amendment 1", and by 2020, "Environmental Management-life

cycle assessment - requirements and guidelines - Amendment 2" headers with improvements have been made, but yet are not provided with free access. It is applied based on ISO 14040 and 14044 standards in every study on life cycle assessment conducted nationally or internationally. Other ISO standards that can help in the life cycle analysis and the standards published by the Turkish Standards Institute (TSE) based on the ISO 14040 standard are given in Table 2.

Table 2. ISO and TSE standards related to life cycle assessment

Standards	Current Status
ISO 14040:1997 Environmental management – Life cycle assessment – Principles and framework	Withdrawn
ISO 14041:1998 Environmental management - Life cycle assessment - Goal and scope definition and inventory analysis	Withdrawn
ISO 14042:2000 Environmental management - Life cycle assessment - Life cycle impact assessment	Withdrawn
ISO 14043:2000 Environmental management - Life cycle assessment-Life cycle interpretation	Withdrawn
ISO/TR 14049:2000 Environmental management-Life cycle assessment-Examples of application of ISO 14041 to goal and scope definition and inventory analysis	Withdrawn
ISO 14040: 2006 Environmental management - Life cycle assessment - Principles and framework	Current
ISO 14044:2006 Environmental management - Life cycle assessment - Requirements and guidelines	Current
ISO 14044:2006 / Amd 1: 2017 Environmental management — Life cycle assessment — Requirements and guidelines — Amendment 1	Current
ISO 14044:2006 / Amd 2: 2020 Environmental management — Life cycle assessment — Requirements and guidelines — Amendment 2	Current
ISO 14045:2012 Environmental management - Eco-efficiency assessment of product systems -Principles, requirements and guidelines	Current
ISO/TR 14047:2012 Environmental management- Life cycle assessment-Illustrative examples on how to apply ISO 14044 to impact assessment situations	Current
ISO/TS 14048:2002 Environmental management -- Life cycle assessment -- Data documentation format	Current
ISO 14049:2012 Environmental management - Life cycle assessment - Illustrative examples on how to apply ISO 14044 to goal and scope definition and inventory analysis	Current
TS EN ISO 14041:2003 Environmental management- Life cycle assesment-Goal and scope definition and inventor analysis	Withdrawn
TS EN ISO 14042:2002 Environmental management- Life cycle assessment-Life cycle impact assessment	Withdrawn
TS EN ISO 14043:2003 Environmental management - Life cycle assessment - Life cycle interpretation	Withdrawn
TS EN ISO 14040:2007 Environmental management – Life cycle assessment – Principles and framework	Current
TS EN ISO 14044/A1: Environmental management – Life cycle assessment – Requirements and guidance-Amendment 1	Current
TS EN ISO 14044/A2: Environmental management - Life cycle assessment - Requirements and guidelines - Amendment 2	Current

5. Life Cycle Analysis (LCA) Software

There is a lot of computer software used in life cycle assessment studies. The most widely used software is Simapro and GaBi.

5.1. SimaPro Software

SimaPro software was developed in 1990 by PRe Consulting, a Dutch company. This software makes a comprehensive environmental assessment of products or services, and their environmental performance is evaluated. SimaPro provides the determination and definition of the sustainability targets of the products or services for which their ecological performance is determined, as well as sustainable product development and analysis. It is software widely used in over 80 countries by many international and local industrial organizations, consultancy companies, academia, and research centers such as Unilever, Heineken, and BASF [22] SimaPro software has an integrated structure of various databases and various applications for impact assessment analysis. These evaluations are as follows [23]:

- Monitoring corporate and product sustainability performance

- Carbon footprint assessment

- Water footprint assessment

- Product design and eco-design

- Environmental product declaration

- Environmental reporting

- Determination of key performance indicators

Simapro has a rich library with international databases in computer software. New databases can be included as versions are updated. Simapro contains various databases:

- Agri-footprint

- Ecoinvent

- European and Danish Input/Output database

- Industry data library: PlasticsEurope, ERASM, World Steel

- US Life Cycle Inventory database

- AGRIBALYSE

- Environmental Footprint database

- EXIOBASE

- Quantis World Food LCA Database

- DATASMART LCI package

- ESU World Food LCA database

- IDEA Japanese Inventory database

- Social hotspots database

- WEEE LCI database

5.2. GaBi Software

GaBi, another software used for life cycle analysis, was developed by the German company Thinkstep firm. The life cycle inventory data of the GaBi program, which has been used for more than 25 years, is produced by ISO 14044, ISO 14064, and ISO 14025 standards. It offers alternative scenarios by evaluating the effects on the environment to determine the production, waste, distribution, and recycling stages of a product or system and its sustainability from the perspective of the life cycle. The GaBi program covers automotive, building and construction, chemicals and petroleum, consumer products, education, electronics, food and agriculture, food and beverage, textiles, and energy; it is applied in many industrial areas [24].

5.3. Umberto Software

Umberto life cycle assessment software developed by the German company IFU Hamburg. Umberto is an all-purpose software with resource efficiency and process optimization that enables the calculation of life cycle analysis. With this software, the LCA analysis provides the most comprehensive integrated cost analysis to increase environmental effectiveness and reveal the climatic effects by determining the CO₂ balance of products or companies by calculating the environmental impacts throughout the product's life cycle [25].

5.4. OpenLCA Software

OpenLCA, another life cycle analysis program, is a free and open-access LCA software that emerged in 2006 due to discussions by Andreas Ciroth, Michael Srocka, and Jutta Hildenbrand. It has been managed by a company named GreenDelta, located in Berlin, since its inception [26].

6. LCA studies on Egg Production

Studies on LCA predict the potential environmental impacts of the egg production process and integrate improvement and control methods into the process. Inputs such as feed, electricity and water consumption, and land use were considered in the LCA application in egg production. Feed production, laying hen activities, manure management, transportation, and retailing processes have significantly benefited LCA-applied egg production systems [27, 28, 29, 30, 31]. When the studies are examined, the feed production process is where the most emissions originate in egg production. Climate change is the hotspot among environmental problems in the egg production process.

De Vries and De Boer [32], examined the production of chicken, beef, eggs, milk, and pig meat to compare the environmental impacts of different livestock farms in their study. They stated that the differences between ecological effects were affected by feed efficiency, enteric CH₄ emission rates in monogastric and ruminant animals, and reproduction rates. The study shows that egg production generally causes less environmental impact than other livestock.

Dekker et al. [33], conducted a study in the Netherlands to compare the ecological effects per 1 kg of eggs produced using life cycle assessment between single and multi-layer cage systems, free-range systems, and organic systems. It has been determined that global warming potential, energy use, phosphorus use, nitrogen, and phosphorus supplements have the lowest environmental impact in free-range systems and organic farming systems. Land use, nitrogen, and phosphorus deficiency were the weakest in battery cage systems. It was shown that the system in which acidification has the most minor effect was multi-layer battery cage systems.

Leinonen et al. [34], in a study they conducted in England, evaluated the environmental effects of 1 kilogram of egg with life cycle analysis from four different egg production systems: battery cage systems, free-run systems, free-range systems, and organic systems. As a result of the study, the number of chickens required for 1 kg egg production is the highest in organic production systems and the lowest in battery cage systems. Similarly, the feed consumption per chicken was highest in organic production systems and lowest in caged systems. It is stated that these general differences in production also affect the differences in environmental effects between systems. Feed production, processing, and transportation account for 54-75% of energy use and 64-72% of the global warming potential of systems. While electricity consumption (ventilation, automatic feeding, and lighting) creates the second most significant impact on energy use, gas and fuel use constitute 7-14% of the total energy use. It has been stated that the most critical contributor to acidification and eutrophication potential are caused by manure.

Pelletier et al. [28], in a study conducted in the Midwestern United States, determined the carbon footprint by evaluating greenhouse gas emissions along the intensive egg production and supply chain with life cycle analysis. According to the study results, feed production and use significantly contributed to the supply process emissions. They stated that feed production constitutes the largest share of emissions in egg production.

The potential environmental impacts of a laying hen farm in Bursa were evaluated by Kilic and Karaman [35], through life cycle analysis. The study obtained 3.3 kg/day of feed and 3.52 kg of water consumed per viol egg

produced, 1.08 m² of land use, and 2.64 kg of manure was released. As a result of the study, they concluded that the gas that contributes the most to acidification and eutrophication is NH₃, and the gas that contributes the most to global warming is CH₄.

In a study in Iran, Ghasempour and Ahmadi [31], examined the environmental effects of 1 kg egg production from 1000 chicks for 420 days. As a result of the analysis, it has been determined that the energy input for 1 kg egg production is 30/09 MJ and 4/07 kg CO₂ equivalent, creating a global warming potential, and the information that causes the environmental impact is from the feed.

In a study by Pelletier [36], five laying hen breeding systems (battery cage system, enriched cage system, free-range system, free-run system, and organic system) operating in Canada were applied in egg production and their environmental effects on the life cycle. Compared with the analysis. As a result of the data and evaluations obtained in the life cycle inventory and impact assessment stages, non-organic systems showed very similar environmental performance. It has been observed that the use of resources and emissions in organic egg production are lower in organic farming systems compared to other systems.

Abín et al. [37], conducted a study in Spain that determined the environmental effects of an intensive farm with 55.000 laying hens through life cycle analysis using the Simapro program. According to the study's results, the most severe environmental impact was natural area transformation, followed by terrestrial toxicity and aquatic ecotoxicity. While feed production is the most important source of adverse environmental effects, the exchange process of newly arrived chickens and old ones creates less impact. They stated that its contribution to reducing the environmental impacts of urban land use and metal consumption resulting from the change of laying hens is remarkable.

Estrada-Gonzalez et al. [38], focused on an eco-efficient approach to life cycle analysis with a door-to-door approach in a semi-technological egg production farm. The study revealed 5.58 kg CO₂/kg of egg emission per egg produced, indicating that the climate change category is a hotspot in egg production. They stated that implementing an eco-efficient plan focusing on energy use could result in a 49.5% reduction in total energy consumption and a 56.3% savings in environmental impacts.

7. CONCLUSION

Considering the world's population growth rate and our country, the need for protein from animal products will increase, and a deficit will occur. In order to

close this gap, there will be an increase in industrial enterprises that produce more eggs per unit area. This change in cultivation systems also brings environmental effects. In order to achieve sustainable production, environmental impacts must be predicted, and necessary precautions must be taken. When the studies in the literature are examined, it has been seen that the environmental effects of egg poultry production systems can be predicted successfully. Therefore, as a result of the study, it was concluded that the life cycle assessment method is beneficial in determining the environmental impacts of egg poultry production systems.

References

1. FAO, (2021). Food and Agriculture Organization of the United Nations, *Crops and livestock products*. Retrieved October 13, 2023, from <https://www.fao.org/faostat/en/>
2. TUIK, (2023). Turkish Statistical Institute, *Livestock Statistics*. Retrieved October 13, 2023, from <https://data.tuik.gov.tr/Bulten/Index?p=Kumes-Hayvanciligi-Uretimi-Ekim-2023-49416>
3. YUM-BİR, (2021). *Yumurta Üreticileri Merkez Birliği, Yumurta Tavukçuluğu Verileri*. Retrieved November, 14, 2023, from <https://www.yum-bir.org/UserFiles/File/Veri-2021.pdf>
4. Berlin, J. (2002). Environmental life cycle assessment (LCA) of Swedish semi-hard cheese. *International Dairy Journal*, 12, 939-953.
5. EPA, (2023). United States Environmental Protection Agency, *Greenhouse gas emissions: understanding global warming potentials*. Retrived November 16, 2023, from [https://www.epa.gov/ghgemissions/understanding-global-warming-potentials#:~:text=Methane%20\(CH4\)%20is%20estimated,uses%20a%20different%20value](https://www.epa.gov/ghgemissions/understanding-global-warming-potentials#:~:text=Methane%20(CH4)%20is%20estimated,uses%20a%20different%20value)
6. Cowling, E. B., Erisman, J. W., Smeulders, S. M., Holman, S. C., & Nicholson, B.M. (1998). Optimizing air quality management in Europe and North America: justification for integrated management of both oxidized and reduced forms of nitrogen. *Environmental Pollution*, 102, 599–608.
7. Mollenhorst, H., & De Boer, I. J. M. (2004). Identifying sustainability issues using participatory SWOT analysis: A case study of egg production in the Netherlands. *Outlook on Agriculture*, 33, 267-276.
8. Audsley, A., Alber, S., Clift, R., Cowell, S., Crettaz, R., Gaillard, G., Hausheer, J., Jolliet, O., Kleijin, R., Mortensen, B., Pearce, D., Roger, E., Teulon, H., Weidema, B., & Van Zeijts, H. (1997). *Harmonisation of environmental life cycle assessment for agriculture*. Final Report, Concerted Action AIR3-CT94-2028. European Commission, DG VI Agriculture, 139(1).
9. Basset-Mens, & C., Werf, VDHMG. (2003). Environmental assessment of contrasting pig farming systems in France. *Life Cycle Assessment in the Agri-food Sector Proceedings from the 4th International Conference*, 6-8 October, 2003, Bygholm, Denmark.
10. Kilic, I., & Amet, B. (2017). Estimation of Carbon Footprint of a Dairy Cattle Operation: Bursa Case Study. *Journal of Agricultural Faculty of Gaziosmanpasa University*, 34(Supplementary Issue), 134-142.

11. Guinée, J. B. (2002). *Handbook on Life Cycle Assessment: Operational Guide to the ISO Standards*. Institute for Environmental Sciences, The Netherlands.
12. Baumann, H., & Arvidsson, R. (2015). *Life Cycle Assessment (LCA): Encyclopedia of Polymeric* Berlin, Germany.
13. [13] Gulli, A. (2017). *A Comparative Analysis of Feed and Environmental Factors on Broiler Growth in the United States*. Master's Thesis, University of Arkansas, Bachelor of Science in Chemistry, USA.
14. ISO, (2006). International Organization for Standardization, ISO-14044:2006, *Environmental Management - Life Cycle Assessment - Requirement and Guidelines*. Retrieved October 10, 2023, from <https://www.iso.org/standard/38498.html#:~:text=ISO%2014044%3A2006%20specifies%20requirements,and%20critical%20review%20of%20the>
15. Wiedemann, S., & McGahan, E., (2011). *Environmental Assessment of an Egg Production Supply Chain Using Life Cycle Assessment*. Australian Egg Corporation Limited, Sydney. Retrieved from December 1, 2023, from http://www.freeranger.com.au/uploads/7/4/2/0/7420102/aecl_carbon_footprint.pdf
16. De Boer, I. J. M. (2003). Environmental impact assessment of conventional and organic milk production. *Livestock Production Science*, 80, 69–77.
17. Thomassen, M. (2003). *Life cycle assessment at commercial organic dairy farms. Comparison of three methodologies: LCA, ecological footprint-analysis and an adjusted nutrient balance*, Master's Thesis, Animal Production Systems Group, Wageningen University, The Netherlands.
18. Tillman, A. M., Ekvall, T., Baumann, H., & Rydberg, T. (1993). Choice of system boundaries in life cycle assessment. *Journal of Clean Production*, 2, 21-29.
19. Demirer, G. N., (2011). *Yaşam Döngüsü Analizi, Sürdürülebilir Üretim ve Tüketim Yayınları-I*. Retrieved October 14, 2023, from <https://rec.org.tr/wp-content/uploads/2017/02/yda.pdf>
20. Hunt, R. G., & Franklin, W. E. (1996). LCA - How it came about - Personal reflections on the origin and the development of LCA in the USA. *The International Journal of Life Cycle Assessment*, 1(1), 4-7.

21. Russell, A., Ekvall, T., & Baumann, H. (2005). Life cycle assessment - introduction and overview. *Journal of Cleaner Production*, 13(13), 1207-1210.
22. Metsims, (2005). Retrieved November 18, 2023, from <https://www.metsims.com/tr/>
23. Simapro, (2021). *About SimaPro*. Retrieved November 18, 2023, from <https://simapro.com/about/>
24. Sphera, (2021). Retrieved November 18, 2023, from <http://www.gabi-software.com/turkey/index/>
25. iPoint, (2021). *Umberto-know the flow*. Retrieved October 19, 2023, from <https://www.ifu.com/en/>
26. openLCA, (2021). *Why we started the development of openLCA*. Retrieved November 19, 2023, from <http://www.openlca.org/>
27. Li, Y., Allacker, K., Feng, H., Heidari, M. D., & Pelletier, N. (2021). Net zero energy barns for industrial egg production: An effective sustainable intensification strategy?. *Journal of Cleaner Production*, 316, 128014.
28. Pelletier, N., Ibarburu, M., & Xin, H. (2013). A carbon footprint analysis of egg production and processing supply chains in the Midwestern United States. *Journal of Cleaner Production*, 54, 108-114.
29. Xin, H., Gates, R. S., Green, A. R., Mitloehner, F. M., Moore, P. A., & Wathes, C. M. (2011). Environmental impacts and sustainability of egg production systems. *Poultry Science*, 90 (1), 263–277.
30. Xin, H., Gates, R. S., Green, A. R., Mitloehner, F. M., Moore, P. A., Wathes, C. M., Moore Jr., P. A., & Wathes, C. M. (2011). Environmental impacts and sustainability of egg production systems. *Poultry Science*, 90 (1), 263–277.
31. Ghasempour, A., & Ahmadi, E. (2016). Assessment of environment impacts of egg production chain using life cycle assessment. *Journal of Environmental Management*, 183, 980–987.
32. De Vries, M., & De Boer, I. J. M. (2010). Comparing environmental impacts for livestock products: A review of life cycle assessment. *Livestock Science*, 128, 1-11.
33. Dekker, S. E. M., De Boer, I. J. M., Vermeij, I., Aarnik, A. J. A., & Groot Koerkamp, P. W. G. (2011). Ecological and economic evaluation of Dutch egg production systems. *Livestock Science*, 139, 109-121.
34. Leinonen, I., Williams, A. G., Wiseman, J., Guy, J., & Kyriazakis I. (2012). Predicting the environmental impact of chicken systems in the United Kingdom through a life cycle assessment: Egg production systems. *Poultry Science*, 91, 26-40.

35. Kilic, I., & Karaman, S. (2014). Life cycle assessment of a laying hen farm. *Mediterranean Agricultural Sciences*, 27(2), 107-112.
36. Pelletier, N. (2017). Life cycle assessment of Canadian egg products, with differentiation by hen housing system type. *Journal of Cleaner Production*, 152, 167-180.
37. Abín, R., Laca, A., Laca, A., & Díaz, M. (2018). Environmental assesment of intensive egg production: A Spanish case study. *Journal of Cleaner Production*, 179, 160-168.
38. Estrada-Gonzalez, I. E., Taboada-González, P. A., Guerrero-Garcia-Rojas, H., & Marquez-Benavides, L. (2020). Decreasing the Environmental Impact in an Egg-Producing Farm through the Application of LCA and Lean Tools. *Applied Sciences*, 10(4), 1352.

Chapter 9

Material strength tests with electrical approach

Emrah Kaplan¹
Dursun Ekmekci²

Abstract – This review article discusses the important connections between mechanical analysis methods and electrical measurement methods in materials. In particular, it focuses on how conductivity, resistance and capacitance measurement methods can be used to determine the mechanical properties of materials. The role of these methods in evaluating material durability and elastic properties is considered. Additionally, electrical investigation of mechanical tests is examined as an important approach that allows material testing processes to obtain more detailed and precise results. This study also highlights the advantages and potential contributions of using electrical methods in bullet proofness analysis. This review aims to make a significant contribution to the existing literature by emphasizing the importance of the electrical approach in material durability tests. It demonstrates the potential of how the electrical approach can be used to evaluate mechanical properties of materials quickly and precisely.

Keywords – *Electrical measurements, mechanical properties, ballistic resistance, material testing methods*

I. INTRODUCTION

Material strength and durability are one of the main properties that determine the performance of a material. Accurate evaluation of the mechanical properties of materials is of critical importance in many industries such as industrial design, construction, automotive, aerospace and defence [1].

Properties of materials such as electrical conductivity, resistance and capacitance can provide important information about their mechanical durability. Electrical measurement methods are important tools widely used in materials science and engineering in the characterization and performance

¹ Department of Electrical and Electronics Engineering, Gümüşhane University, Turkey

² Department Department of Mechanical Engineering, Gümüşhane University, Turkey

*(dursunekmekci@gumushane.edu.tr) Email of the corresponding author

improvement of materials. Electrical measurement methods can also be used without applying impact or load to examine material strength and durability. This potential is important for predicting the long-term performance of materials and assessing their suitability for specific applications [2]. Additionally, it should be noted that electrical approaches enable fast, economical and repeatable measurements.

This article specifically examines the relationship between electrical measurement methods and the mechanical durability of materials. The role, advantages and limitations of electrical methods in the process of evaluating the mechanical properties of materials will be discussed and their potential impact in industrial applications will be discussed. The ability of electrical approaches to provide greater insight into material strength and durability highlights the importance of research in this area. This review article aims to provide a guide for researchers and industry professionals in the field of materials science and engineering on how mechanical testing as well as electrical measurement methods can be used in materials characterization.

II. MECHANICAL ANALYSIS METHODS IN MATERIALS

They are common methods used to study different mechanical properties and behaviors of materials in both commercial and military fields. Which method to choose depends on the properties and material type you want to measure. Commonly used destructive and non-destructive analysis methods are given in Fig 1.

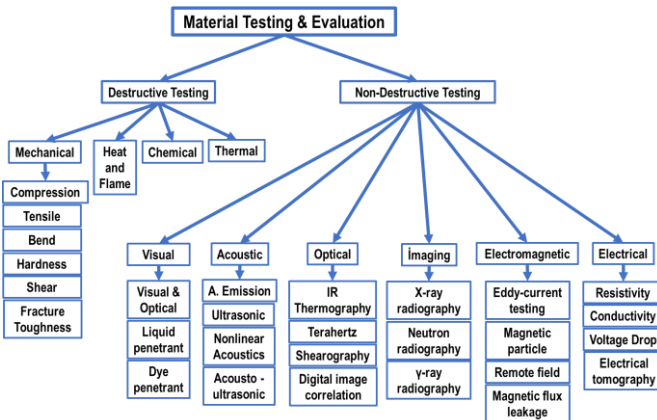


Fig. 1 Commonly used material testing methods

This review focuses on mechanical and electrical methods. In these tests, the stress (load) value applied to the material is associated with deformation (shape

change). The data obtained as a result of these tests is used to determine important mechanical properties of the material, such as elastic modulus, yield strength, and tensile strength. It is used to measure stress, strain rate and elastic/plastic zone in the plastic deformation of the material [3]. The tensile test shown in Fig. 2 is the most common test used to measure mechanical properties. It is a widely used test to examine the mechanical behavior of a material. This curve shows the elastic behavior of the material, its plastic deformation and the moment of final fracture.

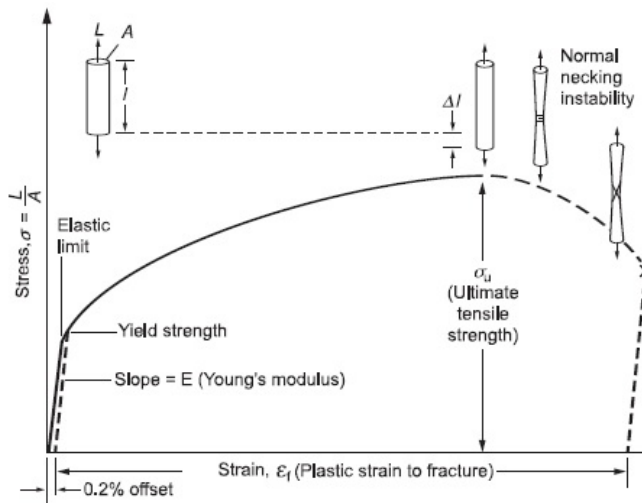


Fig. 2 Tensile stress-strain curve. Reprinted from [4]

Hardness tests are used to evaluate the material's properties such as resistivity, durability and wear resistance. There are different methods such as Rockwell, Brinell and Vickers hardness tests. In these tests, the tensile force applied to a material sample is used to determine the properties of the material such as breaking strength, modulus of elasticity and tensile strength. Compression tests are used to determine the compressive force applied to a material sample and its properties such as compressive strength, modulus of elasticity and tensile strength. Impact tests are used to measure the impact resistance of a material. In these tests, a standard impact is applied to the material and the energy absorption ability, crack resistance and fracture behavior of the material are evaluated. There are different methods such as Charpy and Izod impact tests. Fatigue tests are used to evaluate how a material behaves when subjected to repetitive loading. In these tests, repetitive stresses are applied to the material sample and the properties of the material, such as

fatigue strength and fracture behavior, are determined. The thermal behavior of the material can affect its mechanical properties. Therefore, thermal analysis methods are used to study the thermal behavior of the material. Additionally, changes in the temperature of the material may occur during plastic deformation. The temperature profile of the material can be examined using thermal cameras or temperature sensors [5], [6]. When the material undergoes plastic deformation, changes in its magnetic properties may occur. Magnetic field measurements can be used to detect these changes and monitor the intensity of plastic deformation. Acoustic emission tests capture sound waves emitted by micro-cracks or other signs of plastic deformation occurring in the material. These audio signals can be used to evaluate the presence and intensity of plastic deformation on the material [7].

III. ELECTRICAL MEASUREMENT METHODS

Electrical methods are an effective tool used in material characterization and these methods are used to monitor electrical changes due to mechanical effects on the material [8]. In this way, it is possible to determine and analyze the plastic deformation, crack formation and similar mechanical changes of the material. Additionally, these methods offer the possibility of testing before and after impact, thus providing comprehensive information about the durability and changing properties of the material. These electrical tests allow analysis without applying a bullet or other impact, which is a great advantage for evaluating the material's potential applications such as armor steels. However, specific mechanical tests that require direct measurement of mechanical properties are also used and generally provide more accurate results. Therefore, while electrical methods play an important role in material characterization, combining them with mechanical testing for a complete evaluation is often the preferred approach.

A. *Electrical Resistance Measurement*

Resistivity is a physical property that measures the electrical resistance of a material. Resistance (ρ), on the other hand, is a characteristic feature of a material independent of geometry and size, and is an important parameter expressed according to the electrical resistance (R) and volume (V) of the material. Resistance is calculated by the formula given below and is a fundamental tool in both electrical and mechanical characterization of the material. In this context, the product of the parameters W (width) and L (length) expresses the volume of an object. In addition to evaluating the electrical behavior of the material, this property also plays a critical role in understanding

the structural and mechanical properties of the material. Using current (I), voltage probe range and cross-sectional area of the sample, the ρ value (resistance) of the sample is determined (Fig. 3). Material cross-section and resistance values are calculated with the help of Eq. (1) and Eq. (2).

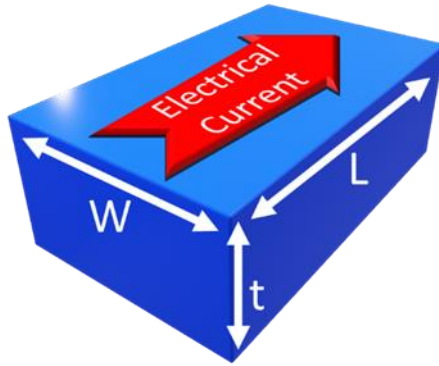


Fig. 3 Diagram and formula about resistivity: This diagram, which shows the definition of material resistivity, visualizes the resistivity formula. A: Cross-sectional area, t: Material thickness

$$A = W * t \quad (1)$$

$$R = \rho * (L/A) \quad (2)$$

Electrical resistivity can provide information about the material's conductivity, density, and internal structural properties. In their research, Miyajima et al. reported the changes in the resistance of commercially pure aluminum and discussed the relationship between resistance and crystal defects [9]. Again, in different studies and researches important results have been obtained to understand the complex electrical behaviour of various materials which occur after physical effects applied on them such as, shape memory alloys [10], [11], metals [12], concrete parts [13], [14], carbon fiber reinforced plastics [15], [16], ceramic matrix composites [17], uniaxial rock [18], nanocomposites [19], conductive fabrics [20], wearable electronics [21] and even carbon nanotube threads [22], [23].

Each of the four different basic methods described below offers a different approach to the process of measuring the electrical properties of materials and includes different measurement techniques. The aim of these methods is to precisely and reliably evaluate the electrical properties of the material, such as resistance, conductivity and contact resistance. Different analysis approaches

can be achieved with four different resistance measurement methods. The four-point resistance measurement method (Fig. 4) allows the resistance value to be determined precisely without being affected by parasitic effects, especially since it does not include any probe resistance. Four probes are used during measurement: While two probes carry current, the other two probes measure electrical voltage. As shown in Fig. 4, since the current i is assumed to be zero, the voltmeter only measures the material resistance and the material resistance (R_2) is calculated with high accuracy by Ohm's law. With the help of this sensitive and repeatable method, electromechanical property characterization of materials is also carried out [13], [15], [17], [19]. Since the voltmeter impedance is very high, negligible current flows through it and no voltage drops on contacts B and C. In this case, since $i = 0$, the loop Eq. (3) turns into Eq. (4). Therefore, the Voltmeter only shows the voltage falling on R_2 and we obtain the material resistance (R_2) value according to Ohm's law [24].

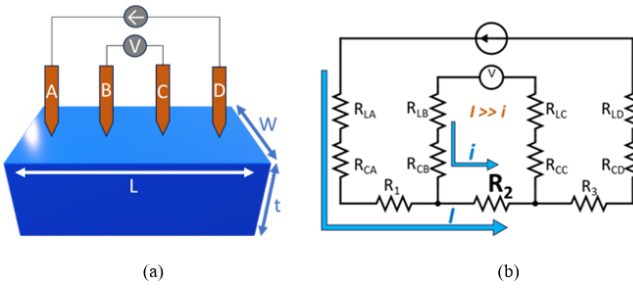


Fig. 4 Four-point electrical resistance measurement technique: (a) Diagram of the measurement set consisting of the sample material, a current source and a voltmeter in contact with the four probes. (b) The electrical equivalent circuit of the measurement setup (R_L : Lead resistance, R_C : Contact resistance, R_2 : Sample resistance, V : Measured voltage between probes B and C)

$$V = I * R_2 + i * (R_{LB} + R_{CB} + R_2 + R_{CC} + R_{LC}) \quad (3)$$

$$V = I * R_2, R_2 = V/I \quad (4)$$

As in the example study whose results are shown in Fig. 5, one-way pressure and strain rates can be determined by electrical resistance measurement [25]. Therefore, in order to indirectly measure the mechanical properties of a material and/or the deformation occurring in that material, four-point resistance measurements of the material under a certain mechanical stress or uniaxial pressure can be repeated [26]. As a result of these measurements, changes in the

electrical resistance of the material can be determined and mechanical properties can be determined accordingly. These graphs highlight the critical role of electrical resistivity measurements in predicting the mechanical properties of igneous rocks. These two graphs support the main findings of the paper by providing a visual representation of the relationship between electrical resistivity and rock mechanical properties.

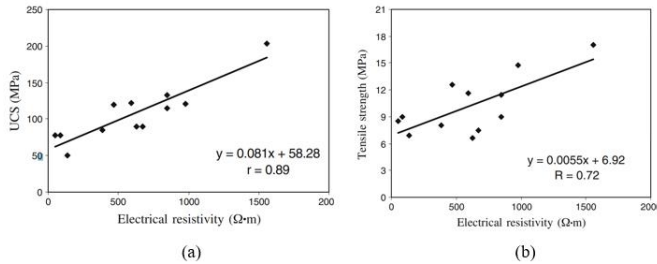


Fig. 5 A study proving the relation between mechanical effect and electrical resistance in materials; (a) The relationship between uniaxial compressive strength (UCS) and electrical resistance, (b) Relationship between tensile strength and electrical resistance. Reprinted from [25]

Conductivity measurements can vary depending on the structure of the material, and these measurements can be used to predict mechanical properties or evaluate application suitability. Changing microstructure or mechanical deformations can have effects on conductivity, and these changes can be detected thanks to these measurements. Within this logic, different measurements have been made on materials such as alloys [27]–[31], composites [30], [32] and superconductors [33], and the connection between mechanical properties and conductivity has been examined. The results of a study using graphene nanoparticles show that the addition of graphene nanoplatlets to pure Fe powders can help us understand the relationship between material microstructure, hardness and electrical conductivity [34]. Contact resistance measurement is important to ensure efficient energy transfer in electrical circuits and connections. This measurement is used to determine the resistance between two points and provides information about sources of resistance in the contact (surface contamination, oxidation, etc.). It is also a method used when characterizing the electromechanical properties of different materials [15], [35], [36]. This method provides information about mechanical properties by evaluating the contact resistance on the material surface. Due to its advantages, it is a widely used method in many industrial and research fields. Electrical conductivity spectroscopy is a technique that examines the electrical

behavior of a material depending on the frequency range. Measurements made at different frequencies provide information about parameters such as structural changes of the material, surface properties, carrier densities and carrier mobility. Electrical conductivity spectroscopy is a method used both as a general material characterization tool and in the evaluation of mechanical properties. It has a wide range of applications with the advantages of high sensitivity, resolution and non-destructive measurement.

B. Measurement of Dielectric Properties

Dielectric properties include parameters such as a material's electrical insulation performance, its effect on high-frequency signals, and its dielectric constant. Dielectric measurement is used to determine the electrical properties of materials, not their mechanical properties. However, in some cases, changes in the dielectric properties of the material can indirectly provide information about mechanical properties. For example, the dielectric constant of a polymer material can provide information about the material's mechanical stiffness or modulus of elasticity. Studies in which mechanical and dielectric properties were investigated together on different materials have also been published [37]–[39].

C. Voltage Drop Method

The voltage drop technique, unlike resistance measurement, uses the movement of electrical current across the material surface. Cracks or defects in the material block the path of electrical current and therefore a voltage drop occurs [40], [41]. This voltage drop is measured to determine the location and size of cracks or defects [42]. While resistance measurement is usually done homogeneously throughout the material, the voltage drop technique offers a more sensitive method to detect such defects on the surface of the material and perform a detailed analysis.

D. Capacitance Measurement

Capacitance is the ability of a material to store electrical charge and can vary depending on various physical parameters. As the amount of moisture in the material increases, capacitance generally increases. Denser materials generally have a lower capacitance. The effect of density on mechanical properties depends on factors such as the compressibility and strength of the material. Therefore, information about mechanical properties can be obtained indirectly by measuring capacitance on the material. In a study, the effect of carbon nanotube (CNT) dispersion on both mechanical properties and electrical

capacity in cement-based materials was investigated. The study found that CNT content affects the mechanical strength and modulus of elasticity of the material and demonstrated that capacity is related to these mechanical properties, describing the interaction between mechanical and electrical properties [43].

A more complex version, electric capacitance tomography (ECT) [44], [45], is an imaging technique that creates cross-sectional images of the distribution of dielectric material through capacitance measurements and image reconstruction [46]. Widely used in different industries, this method provides important information about material distribution and has different system variations that offer unique advantages in terms of precision and variable processing speeds. The system shown in Fig. 6 is an ECT system and includes an impedance analyzer, a multi-electrode sensor, a switch unit, and a computer. This system utilizes a switch configuration to minimize fixed capacity. Although it offers high resolution and sensitivity, it is slower than other types of ECT due to the low data acquisition speed of the impedance analyzer [47]. Consequently, since there may be an indirect relationship between the capacitance value and material mechanical properties, both types of properties should be measured separately and used together to understand the overall performance of the material.

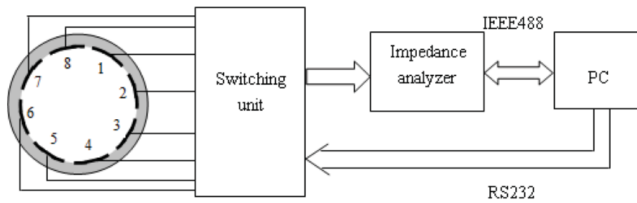


Fig. 6 Schematic representation of the impedance analyzer based ECT system.
Reprinted from [47]

E. *Electrical Tomography*

Electrical resistivity tomography (ERT) is an internal imaging technique used in various fields. It applies a low level of electrical current or voltage to determine the internal electrical resistance distribution of the object through electrodes. Computers process this electrical data and create an image that shows the internal structure of the object. ERT is an environmentally friendly, non-invasive, real-time monitoring technique and is used in many areas such as groundwater monitoring, mineral deposit observation and industrial process control [48]–[50]. Therefore, this technique also has the capacity to provide information about the internal mechanics of materials. In Fig. 7, the concrete

block sample with an insulating material (with different structure and properties) in the middle was analyzed in three dimensions with the ERT technique.

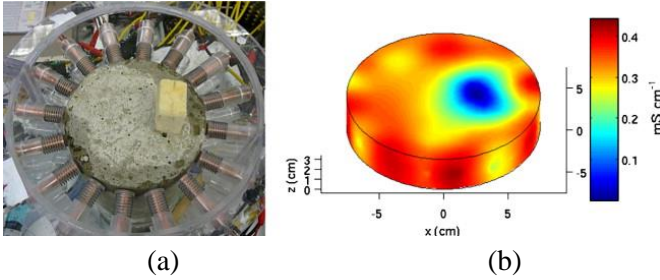


Fig. 7(a) Concrete block sample with an insulating material in the middle and (b) 3D analyzed image using the ERT technique. Reprinted from [48]

IV. ELECTRICAL INVESTIGATION OF MECHANICAL TESTS

A. *Electrical and Mechanical Property Relationship for Metals and Alloys*

The relationship between mechanical and electrical properties of metal materials is a complex issue and various factors come into play [29]. By alloying metals, we can significantly change both their mechanical and electrical properties. Adding specific elements onto a metal material allows you to customize conductivity, resistance, and mechanical behaviour. Mechanical and electrical properties can be interconnected based on the fundamental physical properties of the material. Some key relationships and factors to consider are examined in this section. Electrical conductivity shows how well a material can conduct electrical current. Electrical resistance is the opposite of conductivity and represents the resistance of a material to electric current. Metals generally have high electrical conductivity due to the abundance of free electrons in their atomic structures [34]. High conductivity is associated with low resistance. Mechanical impact/deformation can affect the crystal structures of a metal. Excessive deformation can lead to defects and displacements, which can increase resistance [51]. However, structures that act contrary to general expectations and show a decrease in resistance have also been investigated [52]. Therefore, structural changes in the material can be examined by examining the increase in resistance value. There are studies on structures whose electrical conductivity does not change despite deformation due to their flexibility [21]. It is aimed to make flexible sensors and electronic circuits with materials with this elastic ability. Both mechanical and electrical properties can be temperature dependent. Mechanical properties that will change include yield strength, ductility, and toughness. These changes can affect the material's ability to

withstand extreme deformation. For some metals, electrical resistance increases as temperature increases, while for others it decreases [23]. These changes can affect the material's behavior in electrical circuits. In a study conducted on an aluminum alloy, it was observed that mechanical properties and electrical conductivity changed depending on the aging temperature [31]. An increase in resistance due to temperature was observed in the filament produced for 3D circuit production, and a thermometer was also produced with a 3D printer by taking advantage of this feature [53]. The tensile behavior of metals is a fundamental mechanical property. Deformation due to mechanical stress can affect the electron configuration and crystal structure of the material, which in turn can affect the electrical resistance [36]. Electrical sensors known as strain gauges are used to measure mechanical stress in materials. These devices can indirectly provide information about mechanical stresses by sensing mechanical stresses and deformations. At high frequency, electric current is usually concentrated on the surface of a conductor, known as the surface effect [54]. Significant heat release occurs due to surface effect [55]. This can affect both electrical and mechanical properties in applications related to high-frequency signals or power transmission. At very low temperatures some metals can become superconducting, in which case the electrical resistance is zero. Superconducting materials can change mechanical properties when they transition to a superconducting state.

B. Electrical Properties of Impact-resistant Metals and Alloys

The relationship between the mechanical and electrical properties of metals is complex and depends on various factors such as material composition, temperature and mechanical loading conditions. These relationships are important to understand in engineering applications such as the design of electrical connections, conductors, and other electrical components where both mechanical and electrical performance are critical [56].

Materials that have bullet-proof properties such as armor and have high resistance to impact are generally metals or composite materials. The electrical properties of such materials may vary depending on the type and structure of the material used. Here are the typical electrical properties of such materials. Many metals are good electrical conductors. This allows electric current to be easily conducted through these metals. Metals such as copper (Cu) are particularly effective in terms of electrical conductivity. The electrical resistances of these materials can vary depending on the type of metal or composite material used. Generally, high strength materials are found to have low resistance. Many impact-resistant and bullet-proof materials are resistant to

corrosion. This ensures long-term stability of the electrical properties. Such materials are resistant to impact and mechanical stress and keep electrical connections strong. This again ensures the stability of the electrical properties. Shockproof materials are not generally used for insulation purposes because they are good conductors of electricity. However, electrical insulation can be achieved by combining it with some special coatings or insulating materials. Fig. 8 shows the measured characteristic points of the 12-layer composite at 24 J on the impact force-displacement curve and the high-speed camera images of the characteristic points. The electrical properties of such materials may vary depending on the design objectives and the specific properties of the material used. Particularly in electronic or military applications, determining electrical properties is an important part of the material selection and design process. It is therefore important to consider the electrical requirements when choosing the most suitable material for a particular application.

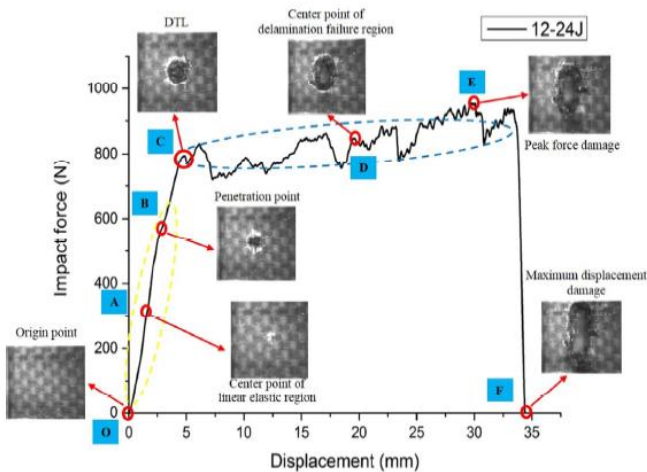


Fig. 8 Impact force-displacement performance graph obtained as a result of impact tests performed on a 12-layer composite and high-speed camera images of these measured points [57]

C. *Non-destructive Evaluation of Mechanical Properties of Materials*

Electrical measurements are an important tool for damage detection, for example in fiber reinforced polymer (FRP) materials [7]. In carbon fiber reinforced polymers such as CFRP, carbon fibers provide electrical conductivity, so it is possible to monitor the state of the material under load. When a matrix filling material such as carbon black is used in materials such as GRP, voltage and damage monitoring can be performed using the direct current

method. Direct current electrical resistance, alternating current capacitance and loss characteristics change as a result of applied load or voltage. These measurements can be used to evaluate the condition of composite parts even when the components are in use, and these methods are considered a non-destructive evaluation technique. However, more fundamental studies are required to better understand the effect of alternating current electrical properties on the material [58].

D. Intensity Measurement of Mechanical Impact

It may be possible to indirectly measure the effect of mechanical action on a material by using electrical methods, especially through piezoelectric sensors. In fact, the data obtained here is intended to measure the magnitude of the impact applied to that material rather than the change in the material caused by the impact. At this point, piezoelectric materials produce an electrical charge in response to mechanical stress or deformation. This feature makes them suitable for purposes of sensing and measuring mechanical effects or vibrations in a variety of applications. These sensors are made of piezoelectric materials (e.g., quartz crystals, piezoceramics) that produce an electrical charge when subjected to mechanical stress [59]. The amount of charge produced is proportional to the force or impact applied to the material.

In some cases, mechanical effects can lead to pressure changes. Electrical pressure sensors can detect these pressure changes and convert them into electrical signals [60]. This information can be used to extract the force or intensity of mechanical action. These electrical methods indirectly measure the effects of mechanical effects by detecting changes in electrical properties or signals caused by the impact. Data obtained from these sensors can provide valuable information about the mechanical behavior of materials, especially to external forces or vibrations.

E. Armor Material Testing Process

The results of bullet resistance tests determine the performance and durability of the tested material. The following analyzes are performed on the material after the bullet impact. If the bullet has penetrated the material, this is called "penetration" and the bullet proof level is considered as failed. If the bullet has not penetrated the material, the speed at which the bullet remains in the material is determined. This data shows how much energy the material absorbs. It is also evaluated whether the bullet damages the material. Holes, cracks or deformations on the material are observed and recorded. The results show how much protection the material provides against which types of

projectiles and according to which standards [61]. Evaluation results can be used in performance enhancing processes such as changing material structure or components. These results are critical for the development of military equipment, ballistic vests or armor, and civilian security applications. In Fig. 9, the European EN 1522/1523 standard is taken into consideration for the target plate used in ballistic tests, the distance between the accelerometers and the gun, and the bullet speed. Before the tests, the bullet speed was adjusted by the amount of gunpowder in the cartridge case and it was tried to be kept at 820 ± 10 m/s for the 7.62 Ball type bullet and 830 ± 10 m/s for the 7.62 AP type bullet [62].

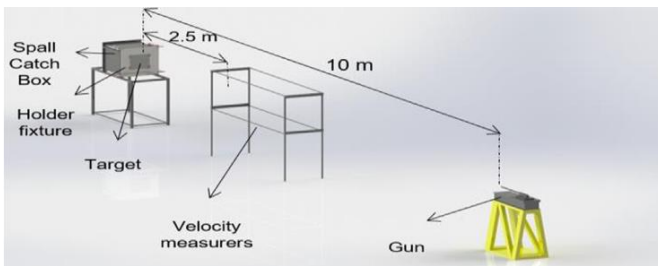


Fig. 9 The mechanism where ballistic tests applied to armor steels are performed

In bullet proof tests, various mechanical measurement methods are used to evaluate the material's resistance to bullet or ballistic threats. Mechanical measurement methods commonly used in these tests. They form the basis of bullet proof tests. In these tests, impacts are simulated in which the material is struck at a certain speed and angle. The behavior of the material under the influence of impact is observed and recorded.

V. CONCLUSION

Electrical measurements can often be made quickly. Especially when automatic data collection systems are used, processes can be accelerated and more data can be obtained. These devices are suitable for real-time monitoring, which can increase the ability to understand rapidly changing properties of the material. Particularly for simple devices, investment costs are low and maintenance requirements are usually limited. This can reduce long-term costs. Bullet proof tests performed by electrical methods offer a versatile and effective way to measure the material's resistance to ballistic threats and impacts. These tests provide valuable information about the material's mechanical strength and structure by precisely monitoring changes in the material's electrical properties.

Additionally, these electrical tests can be performed without damaging the structure of the material, allowing tests to be performed while maintaining the inviolability of the material. Therefore, electrical tests offer the opportunity to perform analysis without applying a bullet or other impact and can make a positive contribution to the evaluation of potential materials for armor construction. As a result, electrical methods generally have the advantage of making rapid measurements and obtaining data at low cost, but it is always necessary to evaluate the cost, especially for a specific application, and to verify measurements made by electrical measurement by common mechanical measurements.

REFERENCES

1. Dobrzański LA. Significance of materials science for the future development of societies. *J Mater Process Technol* 2006;175:133-148.
2. Bjørheim F, Siriwardane SC, Pavlou D. A review of fatigue damage detection and measurement techniques. *Int J Fatigue* 2022;154:106556.
3. Vargas ALM, Blando E, Hübler R. Elasto – Plastic materials behavior evaluation according to different models applied in indentation hardness tests. *Measurement* 2019;139:134-139.
4. Gray GTR, Maudlin PJ, Hull LM, Zuo QK, Chen SR. Predicting material strength, damage, and fracture The synergy between experiment and modeling. *J Fail Anal Prev* 2005;5:7-17.
5. Yildiz RA. Evaluation of fracture toughness and Charpy V-notch test correlations for selected Al alloys. *Eur Mech Sci* 2022;6:1-8.
6. Marar K, Eren Ö, Çelik T. Relationship between impact energy and compression toughness energy of high-strength fiber-reinforced concrete. *Mater Lett* 2001;47:297-304.
7. Walther F, Eifler D. Cyclic deformation behavior of steels and light-metal alloys. *Mater Sci Eng A* 2007;468–470:259-266.
8. Cross JO, Opila RL, Boyd IW, Kaufmann EN. Materials characterization and the evolution of materials. *MRS Bull* 2015;40:1019-1034.
9. Miyajima Y, Komatsu S, Mitsuura M, Hata S, Nakashima H, Tsuji N. Change in electrical resistivity of commercial purity aluminium severely plastic deformed. *Philos Mag* 2010;90:4475–4488.
10. Ferčec J, Anžel I, Rudolf R. Stress dependent electrical resistivity of orthodontic wire from the shape memory alloy NiTi. *Mater Des* 2014;55:699–706.
11. Gonzalez CH, Quadros NF, Araújo CJ, Morin M, Guénin G. Coupled stress-strain and electrical resistivity measurements on copper based shape memory single crystals. *Mater Res* 2004;7:305-311.
12. Kuczynski GC. Effect of elastic strain on the electrical resistance of metals. *Phys Rev* 1954;94:61-64.
13. Azarsa P, Gupta R. Electrical resistivity of concrete for durability evaluation: A review. *Adv Mater Sci Eng* 2017;2017:8453095.
14. Taylor MA, Arulanandan K. Relationships between electrical and physical properties of cement pastes. *Cem Concr Res* 1974;4:881-897.
15. Todoroki A, Suzuki K, Mizutani Y, Matsuzaki R. Electrical resistance change of CFRP under a compression load. *J Solid Mech Mater Eng* 2010;4:864-874.

16. Todoroki A, Yoshida J. Electrical resistance change of unidirectional CFRP due to applied load. *JSME Int J A-Solid M* 2004;47:357-364.
17. Morscher GN, Baker C, Smith C. Electrical resistance of SiC fiber reinforced SiC/Si matrix composites at room temperature during tensile testing. *Int J Appl Ceram* 2014;11:263-272.
18. Chen G, Lin Y. Stress-strain-electrical resistance effects and associated state equations for uniaxial rock compression. *Int J Rock Mech Min Sci* 2004;41:223-236.
19. Khodabakhshi F, Simchi A. The role of microstructural features on the electrical resistivity and mechanical properties of powder metallurgy Al-SiC-Al₂O₃ nanocomposites. *Mater Des* 2017;130:26-36.
20. Bera TK, Mohamadou Y, Lee K, Wi H, Oh TI, Woo EJ, Soleimani M, Seo JK. Electrical impedance spectroscopy for electro-mechanical characterization of conductive fabrics. *Sensors* 2014;14:9738-9754.
21. Han Y, Lu WF. Structural design of wearable electronics suitable for highly-stretched joint areas. *Smart Mater Struct* 2018;27:105042.
22. Abot JL, Alesh T, Belay K. Strain dependence of electrical resistance in carbon nanotube yarns. *Carbon* 2014;70:95-102.
23. Starkova O, Mannov E, Schulte K, Aniskevich A. Strain-dependent electrical resistance of epoxy/MWCNT composite after hydrothermal aging. *Compos Sci Technol* 2015;117:107-113.
24. Minagawa H, Miyamoto S, Kurashige I, Hisada M. Appropriate geometrical factors for four-probe method to evaluate electrical resistivity of concrete specimens. *Constr Build Mater* 2023;374:130784.
25. Kahraman S, Yeken T. Electrical resistivity measurement to predict uniaxial compressive and tensile strength of igneous rocks. *Bull Mater Sci* 2010;33:731-735.
26. Tan S, Long S, Yao X, Zhang X. An improved material model for loading-path and strain-rate dependent strength of impacted soda-lime glass plate. *J Mater Res Technol* 2021;15:905-1919.
27. Bodyakova A, Tkachev M, Pilipenko A, Belyakov A, Kaibyshev R. Effect of deformation methods on microstructure, texture, and properties of a Cu-Mg alloy. *Mater Sci Eng A* 2023;876:145126.
28. Mishnev R, Shakhova I, Belyakov A, Kaibyshev R. Deformation microstructures, strengthening mechanisms, and electrical conductivity in a Cu-Cr-Zr alloy. *Mater Sci Eng A* 2015;629:29-40.
29. Salazar-Guapuriche MA, Zhao YY, Pitman A, Greene A. Correlation of strength with hardness and electrical conductivity for aluminium alloy 7010. *Mater Sci Forum* 2006;519-521:853-858.

30. Vandersluis E, Ravindran C, Bamberger M. Mechanisms affecting hardness and electrical conductivity in artificially-aged B319 aluminum alloy. *J Alloys Compd* 2021;867:159121.
31. Zhang P, Li Y, Liu Y, Zhang Y, Liu J. Analysis of the microhardness, mechanical properties and electrical conductivity of 7055 aluminum alloy. *Vacuum* 2020;171:109005.
32. Payakaniti P, Pinitsoontorn S, Thongbai P, Amornkitbamrung V, Chindapasirt P. Electrical conductivity and compressive strength of carbon fiber reinforced fly ash geopolymeric composites. *Constr Build Mater* 2017;135:164-176.
33. Kopera L, Kováč P, Melišek T. Electromechanical characterization of selected superconductors. *Supercond Sci Technol* 2008;21:115001.
34. Altuntas O, Ozer M, Altuntas G, Ozer A. Investigation of the microstructure, hardness and electrical conductivity properties of Fe/Graphene compacts. *Mater Sci Technol* 2023;39:2670-2679.
35. Wieczorek L, Howes VR, Goldsmid HJ. Electrical contact resistance and its relationship to hardness. *J Mater Sci* 1986;21:1423.
36. Yamaguchi K, Busfield JJC, Thomas AG. Electrical and mechanical behavior of filled elastomers I The effect of strain. *J Polym Sci B Polym Phys* 2003;41:2079-2089.
37. Cho E, Chiu LLY, Lee M, Naila D, Sadanand S, Waldman SD, Sussman D. Characterization of mechanical and dielectric properties of silicone rubber. *Polymers* 2021;13:1831.
38. Haddour L, Mesrati N, Goeriot D, Tréheux D. Relationships between microstructure, mechanical and dielectric properties of different alumina materials. *J Eur Ceram Soc* 2009;29:2747-2756.
39. Li X, Yin X, Zhang L, Cheng L, Qi Y. Mechanical and dielectric properties of porous Si₃N₄-SiO₂ composite ceramics. *Mater Sci Eng A* 2009;500:63-69.
40. Zhao Q, Zhang K, Zhu S, Xu H, Cao D, Zhao L, Zhang R, Yin W. Review on the electrical resistance/conductivity of carbon fiber reinforced polymer. *Appl Sci* 2019;9:2390.
41. Horstmann M, Gregory JK, Schwalbe KH. The ac potential drop method: measuring the growth of small surface cracks during fatigue. *Mater Test* 1993;35:212-217.
42. McCullough KYG, Fleck NA, Ashby MF. Uniaxial stress-strain behaviour of aluminium alloy foams. *Acta Mater* 1999;47:2323-2330.
43. Danoglidis PA, Konsta-Gdoutos MS, Shah SP. Relationship between the carbon nanotube dispersion state, electrochemical impedance and

- capacitance and mechanical properties of percolative nanoreinforced OPC mortars. *Carbon* 2019;145:218-228.
- 44.Rao SM, Zhu K, Wang CH, Sundaresan S. Electrical capacitance tomography measurements on the pneumatic conveying of solids. *Ind Eng Chem Res* 2001;40:4216-4226.
- 45.Chaniecki Z, Dyakowski T, Niedostatkiewicz M, Sankowski D. Application of electrical capacitance tomography for bulk solids flow analysis in silos. *Part Part Syst Charact* 2006;23:306-312.
- 46.Asencio K, Bramer-Escamilla W, Gutiérrez G, Sánchez I. Electrical capacitance sensor array to measure density profiles of a vibrated granular bed. *Powder Technol* 2015;270:10-19.
- 47.Chen D, Yang W, Deng X. Comparison of three electrical capacitance tomography systems. *IEEE Int Conf Imaging Syst Tech* 2010;11476349.
- 48.Karhunen K, Seppänen A, Lehtikoinen A, Monteiro PJM, Kaipio JP. Electrical resistance tomography imaging of concrete. *Cem Concr Res* 2010;40:137-145.
- 49.Cultrera A, Serazio D, Zurutuza A, Centeno A, Txoperena O, Etayo D, Cordon A, Redo-Sanchez A, Arnedo I, Ortolano M, Callegaro L. Mapping the conductivity of graphene with electrical resistance tomography. *Sci Rep* 2019;9:10655.
- 50.Bukhary T, Huisman JA, Wang H, Zimmermann E, Vereecken H, Lazarovitch N. Electrical resistivity tomography (ERT) measurements during water flow in a date palm stem segment. *Comput Electron Agric* 2023;212:108084.
- 51.Wu X, Jia H, Fan J, Cao J, Su C. Study on the effect of cold deformation and heat treatment on the properties of Cu-Ag alloy wire. *Micromachines* 2023;14:1635.
- 52.Glushko O, Cordill, MJ. Electrical resistance decrease due to grain coarsening under cyclic deformation. *JOM* 2014;66:598-601.
- 53.Kwok SW, Goh KHH, Tan ZD, Tan STM, Tjiu WW, Soh JY, Ng ZJG, Chan YZ, Hui HK, Goh KEJ. Electrically conductive filament for 3D-printed circuits and sensors. *Appl Mater Today* 2017;9:167-175.
- 54.Swain A, Abdellatif E, Mousa A, Pong PWT. Sensor technologies for transmission and distribution systems: A review of the latest developments. *Energies* 2022;15:7339.
- 55.Cabrini M, Carrozza A, Lorenzi S, Pastore T, Testa C, Manfredi D, Fino P, Scenini F. Influence of surface finishing and heat treatments on the corrosion resistance of LPBF-produced Ti-6Al-4V alloy for biomedical applications. *J Mater Process Technol* 2022;308:117730.

56. Stadler F, Antrekowitsch H, Fragner W, Kaufmann H, Pinatel ER, Uggowitzner PJ. The effect of main alloying elements on the physical properties of Al–Si foundry alloys. *Mater Sci Eng A* 2013;560:481-491.
57. Du Z, Chen C, Wang X. The mechanism of stab resistance of carbon fiber reinforced polymer. *Eng Fail Anal* 2022;142:106817.
58. Kupke M, Schulte K, Schüler R. Non-destructive testing of FRP by d.c. and a.c. electrical methods. *Compos Sci Technol* 2001;61:837-847.
59. Safaei M, Sodano HA, Anton SR. A review of energy harvesting using piezoelectric materials: state-of-the-art a decade later (2008–2018). *Smart Mater Struct* 2019;28:113001.
60. Kalsoom T, Ramzan N, Ahmed S, Ur-Rehman M. Advances in sensor technologies in the era of smart factory and industry 4.0. *Sensors* 2020;20:6783.
61. Alwan FHA, Prabowo AR, Muttaqie T, Muttaqie T, Muhayat N, Ridwan R, Laksono FB. Assessment of ballistic impact damage on aluminum and magnesium alloys against high velocity bullets by dynamic FE simulations. *J Mech Behav Mater* 2022;31:595-616.
62. Bekci ML, Canpolat BH, Usta E, Güler MS, Cora ÖN. Ballistic performances of Ramor 500 and Ramor 550 armor steels at mono and bilayered plate configurations. *Eng Sci Technol an Int J* 2021;24:990-995.

Chapter 10

Effects of the Use of Nanofluids in Solar Collectors on Thermal-Hydraulic Performance

Dr. Fatma OFLAZ¹

Abstract

The use of nanofluids in solar collectors includes a technology that aims to increase the efficiency of collectors. Nanofluids consist of liquid particles at the nanometer scale, and their properties enable more efficient heat conduction. The high thermal conductivity, low viscosity, and chemical stability properties of nanofluids allow for increased heat transfer in solar collectors, improving temperature control, and, as a result, increasing efficiency. These features, when utilized in the liquid cooling systems of solar collectors, effectively cool the panel and optimize performance by controlling temperature increases. The implementation of these technologies can contribute to making solar collectors more effective, efficient, and durable, thereby encouraging the wider adoption of solar energy systems. However, it is crucial to keep in mind that each technology has its advantages and disadvantages. Therefore, factors such as the features, cost implications, and environmental impacts of the chosen technology should be considered. This study includes detailed examinations of the use of nanofluids in solar collectors. The research aims to provide valuable insights for future studies in the field of solar energy by thoroughly exploring these applications. The characteristics, cost implications, and environmental impacts of these technologies have been examined to consider both their advantages and disadvantages. The comprehensive analysis of nanofluids in solar collectors may pave the way for advancements and innovations in the future, encouraging the development of more effective, efficient, and durable solar energy systems.

Keywords

Solar collectors, Nanofluids, Thermal and hydraulic performances

1. Introduction

The use of fossil fuels, greenhouse gas emissions, and environmental issues such as climate change have led many countries to review their

¹ Firat University, Automotive Engineering

Email: fteber@firat.edu.tr, ORCID NO: 0000-0002-9636-5746

energy policies and shift toward renewable energy sources (Sait et al. 2022). Solar energy plays a significant role in this context and has numerous advantages. Solar energy, unlike fossil fuels, does not emit harmful gases directly into the environment and does not contribute to the release of greenhouse gases into the atmosphere. With this feature, it provides an effective solution in the fight against climate change and air pollution. Solar energy is considered an unlimited source of energy. Advances in solar energy technologies have reduced costs and made solar energy projects more economical (Elhenawy et al. 2023). This situation provides long-term cost advantages. For these reasons, many countries are working to integrate solar energy into their national energy portfolios. Shaping energy policies and investments in this direction can contribute to a sustainable energy future. Among the existing renewable resources, solar energy is recognized as an attractive option due to its availability and abundance. As shown in Figure 1, solar energy can be used for a multitude of applications in homes, industry, and transportation.

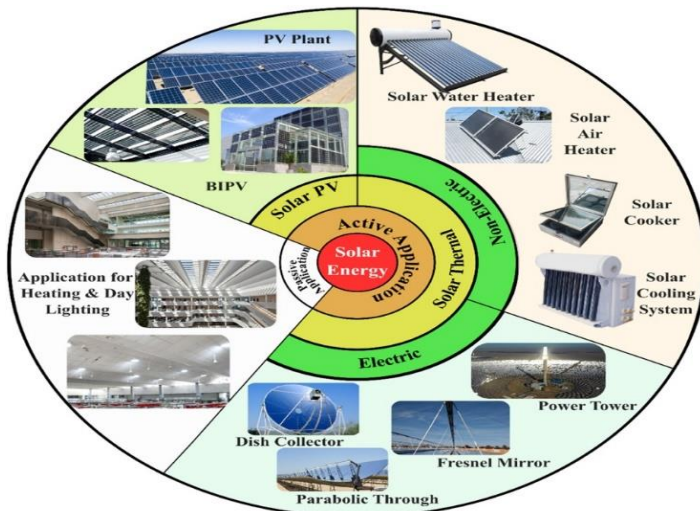


Fig. 1. Applications of solar energy (Sadhu et al. 2015).

2. Solar Thermal Collectors

Solar collectors are devices that capture sunlight and convert it into usable heat or electricity. There are several types of solar collectors, each designed for specific applications. Flat-plate solar collectors (FPSC) are devices that capture solar energy and convert it into heat, commonly used for hot water production or heating systems (Murtadha and Hussein 2022). They consist of a flat absorber plate mounted within a frame as shown in Figure 2 (Abu-zeid, Elhenawy, and Bassyouni 2024). This plate typically

contains metal or another thermally conductive material and is painted in a dark color to enhance heat absorption by better capturing sunlight. The absorber plate is a surface that absorbs sunlight, and it is covered by a glass or plastic cover. This cover allows sunlight to enter while minimizing heat loss inside. The heated liquid on the absorber plate is often circulated through a network of pipes or a serpentine arrangement. This liquid, commonly water or another heat-transfer fluid, absorbs the solar energy's heat and is then transferred to a storage tank or a heat exchanger. Flat-plate solar collectors find applications in various settings, including homes for hot water production, swimming pool heating, industrial processes, and space heating systems. They are particularly effective in low and medium-temperature applications. Due to their simple design and cost-effectiveness, flat-plate solar collectors are widely used in solar energy harvesting systems.

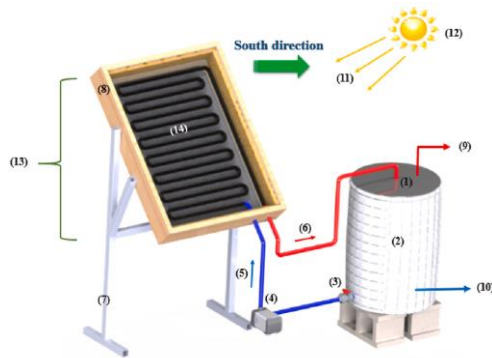


Fig. 2. The flow diagram of the Flat-plate solar collectors (FPSC) (Abu-zeid, Elhenawy, and Bassyouni 2024).

Evacuated Tube Solar Collectors (ETSCs) are solar energy harvesting devices designed to capture and convert sunlight into usable heat. These collectors are known for their efficiency, especially in cold and overcast conditions. ETSCs consist of a series of parallel rows of cylindrical tubes, as shown in Figure 3 (Ghaderian and Sidik 2017). Each tube is made of high-quality glass or other transparent materials. The tubes are typically arranged in a manifold, and the entire collector is mounted within a frame. The absorber coating on the inner surface of the outer tube is designed to maximize the absorption of solar radiation while minimizing heat radiation losses. Common materials for this coating include aluminum nitride or other selective coatings. Within each evacuated tube, there may be a heat pipe or a U-shaped metal tube containing a working fluid usually a low-boiling-point liquid like water, methanol, or ethanol. This fluid absorbs the heat generated by the absorber coating. ETSCs are commonly used for

space heating, domestic hot water production, industrial processes, and other applications that require medium to high-temperature heat. Comparison of ETSC performance of different nanofluids is shown in Table 1.



Fig. 3. The experimental set up of evacuated tubes solar collector (Ghaderian and Sidik 2017).

Table 1. Comparison of ETSC performance of different nanofluids

Study	Nanofluid/water	Volume Concentration	Performance
Mahbulul et al. (Mahbulul et al. 2018)	SWCNT	0.05 – 0.2	16.4
Sharafeldin et al. (Sharafeldin and Gróf 2019)	WO ₃	0.014 – 0.042	19.3
Dehaj et al. (Dehaj and Mohiabadi 2019)	CeO ₂	0.015 – 0.035	34.7
Gan et al. (Gan et al. 2018)	TiO ₂	0.5	45.3
Iranmanesh et al. (Iranmanesh et al. 2017)	GNP	0.025–0.1	65.5
Sabiha et al. (Sabiha et al. 2015)	SWCNT	0.050 – 0.2	71.7

Parabolic Trough Collectors (PTSCs) have a unique parabolic shape resembling a large trough and are designed to capture solar energy and convert it into heat for various applications. The collector is typically long and curved, with a reflective surface that focuses sunlight onto a receiver. PTSCs are mounted on a tracking system that allows them to follow the

sun's movement throughout the day (Ahmad et al. 2024). This tracking capability maximizes the amount of sunlight captured and enhances overall efficiency. The heat-transfer fluid in the receiver tube absorbs the concentrated solar energy and reaches high temperatures.

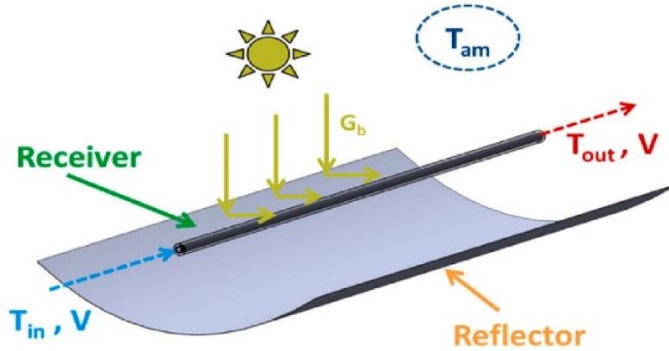


Fig. 4. Typical parabolic trough collector (Bellos and Tzivanidis 2018).

This fluid is then used to produce steam, which can drive a turbine connected to an electricity generator or be used directly for industrial processes. PTSCs are widely used to generate electricity in large-scale solar power plants (Ahmad et al. 2024). They can also be utilized for industrial process heat, desalination, and other applications requiring high-temperature heat.

3. Use of Nanofluids in Solar Collectors to Increase Thermal Performance

Nanofluids are engineered liquids containing nanoparticles, usually on the nanometer scale, dispersed in a base liquid (Choi 1995). Compared to traditional liquids, nanofluids have features such as improved thermal conductivity, stability, efficiency, and direct absorption of solar radiation (Qiu et al. 2020). By using nanofluids as heat transfer fluids in solar collectors, heat absorption and transfer can be made more efficient. For this purpose, a considerable amount of research has been conducted to investigate the improvement of heat transfer properties through the use of nanofluids in solar systems. Ajeena et al. (Ajeena, Farkas, and Víg 2023) examined the effects of the hybrid nanofluid prepared using ZrO_2 -SiC particles and water on the performance change in a flat plate solar collector. The solar collectors showed maximum thermal efficiency of 75.21% when the volume fraction was 0.1% and the mass flow rate was 0.041 kg/s. They found that the addition of nanofluid leads to a 31.64% increase in thermal efficiency. Sundar et al. (Syam Sundar et al. 2021) used $NDCo_3O_4$ /water

hybrid nanofluid in FPSC, at a weight concentration of 0.15%, the Nusselt number (Nu) exhibited an approximately 21.23% increase, and the friction factor showed a 1.13 times increase. The absorber's efficiency was found to be 11% higher when compared to water. Li et al. (Li, Zeng, and Lei 2020) added SiC-MWCNT nanoparticles to an ethylene glycol-based liquid to produce hybrid nanofluids. They evaluated the stability, thermal, and optical efficiencies of the nanofluids used in Direct Absorption Solar Collectors (DASCs). They found that the nanofluid at a mass concentration of 1% increased the efficiency by 97.3%. Kiliç et al. (Kiliç, Menlik, and Sözen 2018) investigated the effects of using a nanofluid obtained by mixing TiO₂ with pure water at a weight concentration of 2% on the thermal performance of a Flat-Plate Solar Collector (FPSC). The results indicated that the TiO₂/water nanofluid outperformed pure water, with instantaneous efficiencies of 48.67% and 36.20%, respectively. The effects of using Al₂O₃, CuO, SiO₂, TiO₂ nanofluids at different flow rates and nanoparticle volumes in a flat plate solar collector on heat transfer, entropy change and pressure drop were examined (Alim et al. 2013). The results showed that CuO nanofluid exhibited the best performance as shown in Figure 5. CuO nanofluid increased the heat transfer coefficient by 22.15% and reduced entropy formation by 4.34% compared to water.

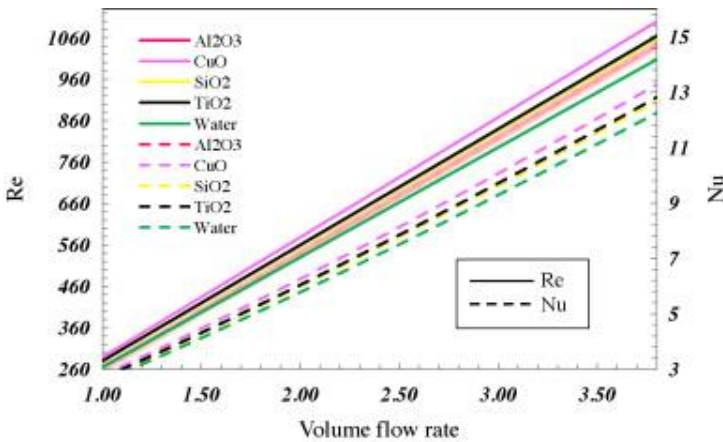


Fig. 5. Effect of volumetric flow rate of different nanofluids on Nusselt and Reynolds numbers (Alim et al. 2013).

4. Conclusions

In this study investigating the effects of using nanofluids in solar collectors, the following results were obtained.

- Nanofluids with superior thermal properties compared to conventional fluids in solar collectors increase heat transfer by facilitating more effective absorption and transport of heat.

- Parameters that determine the thermal conductivity of the nanofluid, such as particle size, particle shape, mass concentration, volume concentration, agglomeration, sedimentation, create a complex effect on the thermal conductivity of the nanofluid. Therefore, it is important to carefully evaluate these factors and conduct further studies in the use of nanofluids in solar collectors.

- In solar collectors, heat transfer is typically sensitive to the viscosity of the fluid. Nano-fluids are produced by adding surfactants to the solution to ensure the stability of nanoparticles. However, an excess of surfactant can increase the viscosity of the nanofluid. High viscosity makes it difficult for the fluid to flow easily, leading to a decrease in heat transfer and, consequently, a reduction in the thermal performance of solar collectors.

- The biggest challenges in using nanofluids in solar collectors are ensuring long-term stability and reducing high pumping power.

- More theoretical and experimental studies are needed to better evaluate the results of using nanofluids in solar collectors.

5. References

1. Abu-zeid, Mostafa Abdel-rady, Yasser Elhenawy, and Mohamed Bassyouni. 2024. "Results in Engineering Performance Enhancement of Flat-Plate and Parabolic Trough Solar Collector Using Nanofluid for Water Heating Application." *Results in Engineering* 21(October 2023): 101673. <https://doi.org/10.1016/j.rineng.2023.101673>.
2. Ahmad, Asim et al. 2024. "Parabolic Trough Solar Collectors: A Sustainable and Efficient Energy Source." *Materials Science for Energy Technologies* 7(July 2023): 99–106. <https://doi.org/10.1016/j.mset.2023.08.002>.
3. Ajeena, Ahmed M., Istvan Farkas, and Piroska Víg. 2023. "Performance Enhancement of Flat Plate Solar Collector Using ZrO₂-SiC/DW Hybrid Nanofluid: A Comprehensive Experimental Study." *Energy Conversion and Management: X* 20(July): 100458. <https://doi.org/10.1016/j.ecmx.2023.100458>.
4. Alim, M. A. et al. 2013. "Analyses of Entropy Generation and Pressure Drop for a Conventional Flat Plate Solar Collector Using Different Types of Metal Oxide Nanofluids." *Energy and Buildings* 66: 289–96. <http://dx.doi.org/10.1016/j.enbuild.2013.07.027>.
5. Bellos, Evangelos, and Christos Tzivanidis. 2018. "Analytical Expression of Parabolic Trough Solar Collector Performance." *Designs* 2(1): 1–17.
6. Choi, Stephen U.S. 1995. "Enhancing Thermal Conductivity of Fluids with Nanoparticles." American Society of Mechanical Engineers, Fluids Engineering Division (Publication) FED 231: 99–105.
7. Dehaj, Mohammad Shafiey, and Mostafa Zamani Mohiabadi. 2019. "Experimental Investigation of Heat Pipe Solar Collector Using MgO Nanofluids." *Solar Energy Materials and Solar Cells* 191(April 2018): 91–99. <https://doi.org/10.1016/j.solmat.2018.10.025>.
8. Elhenawy, Yasser et al. 2023. "Experimental and Numerical Simulation of Solar Membrane Distillation and Humidification – Dehumidification Water Desalination System." *Renewable Energy* 215(March): 118915. <https://doi.org/10.1016/j.renene.2023.118915>.
9. Gan, Yong Yang et al. 2018. "Thermal Conductivity Optimization and Entropy Generation Analysis of Titanium Dioxide Nanofluid in Evacuated Tube Solar Collector." *Applied Thermal Engineering* 145(August): 155–64.
10. Ghaderian, Javad, and Nor Azwadi Che Sidik. 2017. "An Experimental Investigation on the Effect of Al₂O₃/Distilled Water

- Nanofluid on the Energy Efficiency of Evacuated Tube Solar Collector.” *International Journal of Heat and Mass Transfer* 108: 972–87. <http://dx.doi.org/10.1016/j.ijheatmasstransfer.2016.12.101>.
11. Iranmanesh, Soudeh et al. 2017. “Thermal Performance Enhancement of an Evacuated Tube Solar Collector Using Graphene Nanoplatelets Nanofluid.” *Journal of Cleaner Production* 162: 121–29. <http://dx.doi.org/10.1016/j.jclepro.2017.05.175>.
 12. Kiliç, Faruk, Tayfun Menlik, and Adnan Sözen. 2018. “Effect of Titanium Dioxide/Water Nanofluid Use on Thermal Performance of the Flat Plate Solar Collector.” *Solar Energy* 164(April 2017): 101–8. <https://doi.org/10.1016/j.solener.2018.02.002>.
 13. Li, Xiaoke, Guangyong Zeng, and Xinyu Lei. 2020. “The Stability, Optical Properties and Solar-Thermal Conversion Performance of SiC-MWCNTs Hybrid Nanofluids for the Direct Absorption Solar Collector (DASC) Application.” *Solar Energy Materials and Solar Cells* 206(1): 110323. <https://doi.org/10.1016/j.solmat.2019.110323>.
 14. Mahbubul, I. M. et al. 2018. “Carbon Nanotube Nanofluid in Enhancing the Efficiency of Evacuated Tube Solar Collector.” *Renewable Energy* 121: 36–44.
 15. Murtadha, Talib K., and Ali Adil Hussein. 2022. “Optimization the Performance of Photovoltaic Panels Using Aluminum-Oxide Nanofluid as Cooling Fluid at Different Concentrations and One-Pass Flow System.” *Results in Engineering* 15(August): 100541. <https://doi.org/10.1016/j.rineng.2022.100541>.
 16. Qiu, Lin et al. 2020. “A Review of Recent Advances in Thermophysical Properties at the Nanoscale: From Solid State to Colloids.” *Physics Reports* 843: 1–81. <https://doi.org/10.1016/j.physrep.2019.12.001>.
 17. Sabiha, M. A. et al. 2015. “Energy Performance of an Evacuated Tube Solar Collector Using Single Walled Carbon Nanotubes Nanofluids.” *Energy Conversion and Management* 105: 1377–88. <http://dx.doi.org/10.1016/j.enconman.2015.09.009>.
 18. Sadhu, Moumita, Suprava Chakraborty, Niladri Das, and Pradip Kumar Sadhu. 2015. “Role of Solar Power in Sustainable Development of India.” *TELKOMNIKA Indonesian Journal of Electrical Engineering* 14(1): 34–41.
 19. Sait, Hani Hussain et al. 2022. “Non-Catalytic Valorization of Date Palm Seeds.” *Energies*: 1–13.
 20. Sharafeldin, M. A., and Gyula Gróf. 2019. “Efficiency of Evacuated Tube Solar Collector Using WO₃/Water Nanofluid.” *Renewable Energy* 134: 453–60.

21. Syam Sundar, L. et al. 2021. "Efficiency Analysis of Thermosyphon Solar Flat Plate Collector with Low Mass Concentrations of ND-Co₃O₄ Hybrid Nanofluids: An Experimental Study." *Journal of Thermal Analysis and Calorimetry* 143(2): 959–72. <https://doi.org/10.1007/s10973-020-10176-1>.

Chapter 11

The Effect of Using Wire Coil Inserts on Heat Transfer Enhancement in Tube Flow

Dr. Fatma OFLAZ¹

Abstract

Various active and passive methods can be employed to optimize heat transfer. Passive methods increase heat transfer without requiring an additional energy source, providing energy savings, reducing costs, and improving the performance of thermal systems. Adding wire inserts to the heat transfer surface, used as one of the various passive methods to enhance the heat transfer rate, alters fluid flow, increases turbulence, and thereby enhances the thermo-hydraulic performance of the heat transfer surface. The ease of installation and low cost associated with this method make it a preferred choice in numerous applications. It is essential to consider flow conditions simultaneously when evaluating the effects of added wire inserts on heat transfer. Wire inserts disrupt the flow pattern, thereby enhancing heat transfer in laminar flow. In turbulent flow, these inserts attempt to promote turbulence to increase heat transfer. It is crucial to take economics into account when evaluating the effect of inserts on heat transfer by assessing their cost, ease of assembly, and long-term performance benefits. This study includes a detailed review of numerical and experimental research aimed at enhancing heat transfer using wire inserts in laminar and turbulent flows.

Keywords

Heat transfer enhancement, Wire insert, Friction factor, Nusselt number, Thermal Performance Factor

1. Introduction

The increasing energy demand has made the need for lower-cost, easily producible, and energy-efficient heat exchangers an important issue. Heat exchangers are devices that transfer the temperature of a fluid to another fluid. This plays a crucial role in various applications such as heat recovery from industrial facilities, heating, cooling, and many others. Lower-cost heat

¹ Firat University, Automotive Engineering
Email: fteber@firat.edu.tr, ORCID NO: 0000-0002-9636-5746

exchangers can make production processes more economical and reduce energy costs. This can help businesses gain a competitive advantage. Heat exchangers that are easy to produce can be quickly integrated into industrial applications, enabling businesses to respond more swiftly. Highly energy-efficient heat exchangers allow for the more effective use of energy. This is crucial for many industries to achieve sustainability goals and use energy resources more efficiently. Additionally, the use of energy-efficient exchangers can reduce environmental impacts and lower carbon footprints. Therefore, research and development focused on advanced and low-cost heat exchangers play a critical role in achieving sustainability and efficiency goals in the energy sector. Increasing the surface area, altering the properties of the fluid, changing the flow of the tube, utilizing nanomaterials, and increasing turbulence by adding wire inserts to the heat transfer surface are ways to increase the heat transfer efficiency of a heat exchanger (Tavousi et al. 2023). This article aims to conduct a comprehensive evaluation of the effects of wire inserts on heat transfer performance by examining numerous experimental and numerical studies. The study presents a detailed examination of studies to determine the wire coil inserts that exhibit the highest thermal performance.

2. Important Definitions

Additional parts of a thermal system, such as wire coils, are evaluated for performance using the thermal performance factor (η), which is a function of friction and heat transfer coefficients. The following equation describes the thermal performance factor:

$$\eta = \frac{Nu/Nu_0}{(f/f_0)^{1/3}} \quad (1)$$

Nu , f represent the insert configuration and Nu_0 , f_0 represent without insert configuration.

the Nusselt Number,

$$Nu = \frac{hD}{k} \quad (2)$$

The value of the fluid's Reynolds number plays a significant role in determining the flow regime of the fluid. Low Reynolds numbers represent laminar flow, while high Reynolds numbers indicate turbulent flow. The Reynolds number is calculated as below:

$$Re = \frac{UD}{\nu} \quad (3)$$

The friction factor, which is a measure of head loss or pumping power, is typically determined by the fluid's Reynolds number (Re) and the flow regime of the fluid.

$$f = \frac{\Delta P}{\frac{1}{2}\rho U^2 \frac{L}{D}} \quad (4)$$

3. The Effect of Using Wire Inserts on Enhancing Heat Transfer

The laminar boundary layer is a layer that forms when a fluid flows smoothly and regularly. The use of wire inserts disrupts this smooth flow and increases the density of the boundary layer. This increase in density leads to a more effective development of thermal and hydrodynamic boundary layers (Bahiraei, Gharagozloo, and Moayedi 2020). Additionally, the use of wire inserts adds extra geometry to the heat transfer surface, thereby providing more surface area. This additional surface area increases the contact between the fluid and the heat transfer surface, enhancing heat transfer efficiency. Studies (Behabadi and Varma 1998; Promvongse 2008) have observed that the use of wire coils throughout the flow creates a secondary flow and causes a separate flow as shown in Fig. 1. Secondary flow and separated flow significantly increased heat transfer while causing acceptable friction.

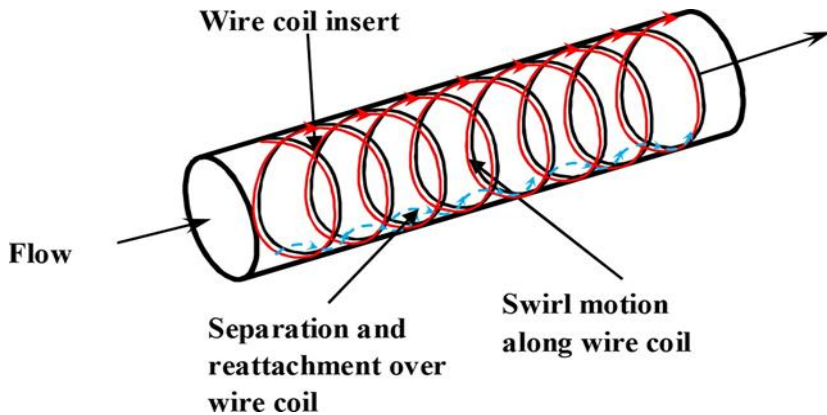


Fig. 1. Flow mechanism in wire coil insert (Behabadi and Varma 1998).

3.1 Experimental Studies

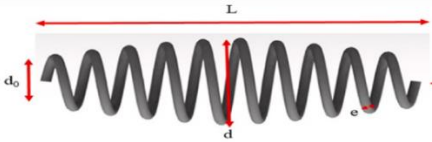
Oflaz et al. (Oflaz, Keklikcioglu, and Ozceyhan 2022) examined the synergistic effects of newly designed conical wire inserts used in conjunction with nanofluids. They noticed that the spacing ratio between conical wire inserts inserted into the tube at regular intervals affected the Nusselt number and friction factor. They found that, in the case of using wire inserts, the Nusselt number increased by 2.43 times compared to the situation where conical wire inserts were not used. They achieved the best thermal performance with a spacing ratio

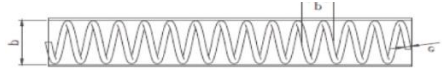
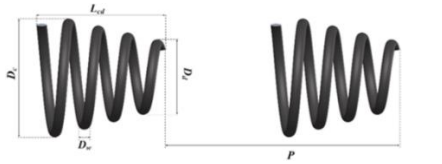
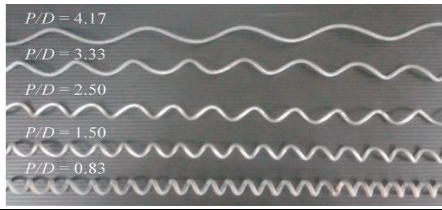
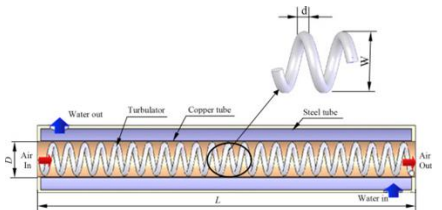

corresponding to the most densely placed conical wire inserts, obtaining a value of 1.75. Keklikcioğlu et al. (Keklikcioğlu and Ozceyhan 2018) investigated the thermo-hydraulic performance of coiled wire inserts with equilateral triangular cross-sections by placing them at a distance of 1 mm from the inner tube wall. They investigated the effect of coiled-wire inserts placed at a certain distance from the inner wall of the tube on heat transfer. They achieved a 1.67 times increase in thermal performance compared to a smooth tube, with a heat transfer rate showing an increase of 11-18%. Sing et al. (Singh and Sarkar 2021) found that the use of conical wire coils and nano-fluids increased the Nusselt number by up to 171% in their study conducted using nano-fluids and conical wires of various types. The diverging (D type) wire coil was found to have the highest increase in heat transfer among all coil arrangements, with values for the $h/\Delta p$ ratio ranging from 1.94 to 4.64. The study showed that the thermal performance factor obtained through the use of conical wires and nanofluids being greater than 1 is promising for future applications. Rajabi et al. (Rajabi et al. 2023) investigated the effect of coiled wire inserts of varying lengths placed inside a tube on the condensation heat transfer coefficient and pressure drop. Reddy et al. (Chandra Sekhara Reddy and Vasudeva Rao 2014) used TiO_2 nanofluid and helical wire coil inserts together to assess heat transfer performance of heat exchanger. Experiments were conducted in the Reynolds number range from 4000 to 15,000 and at two different volume concentrations. In experiments using helical wire coil inserts, the heat transfer coefficient and friction factor increased by 13.85% and 10.69%, respectively. Akyürek et al. (Akyürek et al. 2018) examined the heat transfer and pressure drop properties under turbulent conditions by using wire coils with two different pitches together with different volumes of Al_2O_3 -water nanofluid. It has been shown that adding 25mm and 39mm pitch wire coils to pure water at different Reynolds numbers increases the Nusselt number by 51.6% and 24.64%, and the total heat transfer coefficient by 12.69% and 8.03%, on average, compared to water without inserts. In another study examining the effects of different pitch and spring rates of spring tape inserts on thermo-hydraulic properties under turbulent flow conditions, the highest thermohydraulic performance value was obtained as 2.8 (Bhattacharyya et al. 2019). Hong et al. (Hong et al. 2018) evaluated the thermal performance of wire coils at constant heat flow in turbulent flow and Reynolds number of 6000 to 20,000. The outcomes demonstrated that the Nusselt number of wire coils increased by 1.46–2.49 times, and the friction factor increased by 8.36–18.62 times compared to a plain tube. Jung-Yang San et al. (San, Huang, and Chen 2015) investigated the effects of different coil diameters/tube diameters and varying pitch/diameter ratios on wire coil inserts using water and air as the

working fluids on circular tubes. Keklikcioglu et al. (Keklikcioglu and Ozceyhan 2016) investigated the increase in heat transfer resulting from the disruption of the laminar boundary layer with coiled-wire inserts placed at distances of 1 and 2 mm from the inner wall of the tube. Coiled wire inserts exhibited the highest thermal performance, reaching up to 1.82, depending on the coil pitch and clearance. In another study (Ahmadi, Sarmadian, and Shafae 2019), the effect of coiled wire inserts with different wire diameters and coil pitches placed inside a horizontal condenser on the increase in condensation heat transfer was investigated. The results showed that the coiled wire inserts with a 1.5 mm wire diameter and a 10 mm coil pitch exhibited the best performance among all inserts, with an increased heat transfer coefficient of up to 107% compared to a plain tube. Du et al. (Du et al. 2018) investigated the effect of wire coils on the increase in heat transfer rate using air as the working fluid and different arrangements of wire coils. In cases where wire coils were used, the Nusselt number was found to be 1.74-2.26 times higher compared to a plain tube, while the friction factor showed an increase of 4.18-10.68 times compared to a plain tube. Numerous studies have been conducted with different flow conditions and arrangements of wire inserts to enhance heat transfer rate and improve thermal performance (Berbish and Ali 2017; Agrebi et al. 2016; Eiamsa-ard, Kongkai-paiboon, and Promvong 2011; Keklikcioglu and Ozceyhan 2017). Literature reviews indicate that wire inserts significantly positively impact heat transfer performance in many thermal applications. This suggests that the use of wire inserts can increase heat transfer or improve the performance of thermal systems, thereby enhancing energy efficiency. In cases where wire inserts are applied, higher Nusselt numbers and lower thermal resistances are generally observed. This phenomenon is associated with the ability of wire inserts to alter the fluid flow, increasing turbulence and thus improving heat transfer. Additionally, the low cost and easy installation features of wire inserts contribute to their preference in many applications.

The literature studies related to wire inserts with high performance used in heat exchangers are given in Table 1.

Table 1. Literature studies of wire inserts used in heat exchangers

Study	Geometry	Re	η
Oflaz et al. (Oflaz, Keklikcioglu, and Ozceyhan 2022)	conical wire inserts 	3300–21000	1.75

Wang et al. (Wang et al. 2023)	<p>helical coiled wire insert</p> 	4200-14000	1.21
Keklikcioğlu et al. (Keklikcioğlu and Ozceyhan 2022)	<p>conical wire coils</p> 	4627 - 25099	1,62
Azmi et al. (Azmi et al. 2021)	<p>wire coil inserts</p> 	2000-12000	1.72
Şahin et al. (Şahin et al. 2015)	<p>coiled turbulators</p> 	3000-17000	1.95-2.28
Singh et al. (Singh and Sarkar 2021)	<p>conical wire coil</p> 	9000-45000	1.39

3.2 Numerical Studies

Abbaspour et al. (Abbaspour et al. 2021) used two different turbulators to assess heat transfer performance. The numerical experiments were conducted in the Reynolds number range of 4000 to 10000. The results demonstrated that reducing the helical pitch of a wire coil by 37.5% increased the average Nusselt number by approximately 143%, and an increase of 300% in the wire coil diameter led to an approximately 131% increase in the average Nusselt number. Sharifi et al. (Sharifi et al. 2020) used Computational Fluid Dynamics (CFD) and GA-ANN methods to identify the most effective wire inserts in heat exchangers. Heat transfer and friction coefficients were examined for twelve different wire

coil configurations placed inside the tubes at various Reynolds numbers. The results supported that the proper selection of wire inserts significantly enhanced heat transfer efficiency. Padmanabhan et al. (Padmanabhan et al. 2020) used the ANSYS CFX method to evaluate the performance of using helical inserts in double-pipe heat exchangers. The results show that the pitch interval of helical inserts directly affects the heat conduction. The heat transfer coefficient increased by 63.91% and 31.39% for helical inserts with 5 and 15 mm pitch, respectively. Many researchers have carried out studies to investigate the performance of heat transfer using Finite Element Analysis and Computational Fluid Dynamics (CFD) for wire inserts with different geometric shapes (Feng et al. 2017; Kadam, Patil, and Mohite 2022; Martín Subirana et al. 2023).

4. Conclusions

In this study, the effects of wire inserts in the latest designs used different flow conditions on increasing heat transfer performance were examined by scanning experimental and numerical studies. Studies have shown that the use of wire inserts increases the heat transfer rate while simultaneously increasing the pressure drop. The results obtained are summarized below:

- Placing wire coil inserts within the flow field disrupts the thermal boundary layer, promoting the mixing of the flow. This changes the movement of the fluid and increases turbulence. The interaction of the fluid with wire coil inserts causes increased mixing and higher levels of turbulence, thus increasing heat transfer.
- Wire coil inserts have distinct advantages in many applications due to much smaller pressure drops compared to other turbulators.
- It has been determined that the performance value decreases when the coil pitch increases.
- The increased turbulence and heat transfer advantages associated with the use of wire inserts typically come with some amount of pressure drop. Therefore, in the design process, factors such as energy consumption and pressure drop should also be considered in addition to heat transfer.

5. References

1. Abbaspour, Mohammadreza, Seyed Soheil Mousavi Ajarostaghi, Seyyed A.H. Hejazi Rad, and Mohammad Nimafar. 2021. "Heat Transfer Improvement in a Tube by Inserting Perforated Conical Ring and Wire Coil as Turbulators." *Heat Transfer* 50 (6): 6164–88. <https://doi.org/10.1002/htj.22167>.
2. Agrebi, Senda, Juan P Solano, Ali Snoussi, and Ammar Ben Brahim. 2016. "Local Entropy Generation Rate through Convective Heat Transfer in Tubes with Wire Coil Inserts" 26 (5): 1365–79. <https://doi.org/10.1108/HFF-12-2014-0374>.
3. Ahmadi, Hadi, Alireza Sarmadian, and Maziar Shafae. 2019. "An Experimental Study on Condensation Heat Transfer Characteristics of R-600a in Tubes with Coiled Wire Inserts." *Applied Thermal Engineering* 159 (May): 113889. <https://doi.org/10.1016/j.applthermaleng.2019.113889>.
4. Akyürek, Eda Feyza, Kadir Geliş, Bayram Şahin, and Eyüphan Manay. 2018. "Experimental Analysis for Heat Transfer of Nanofluid with Wire Coil Turbulators in a Concentric Tube Heat Exchanger." *Results in Physics* 9: 376–89. <https://doi.org/10.1016/j.rinp.2018.02.067>.
5. Azmi, W. H., K. Abdul Hamid, A. I. Ramadhan, and A. I.M. Shaiful. 2021. "Thermal Hydraulic Performance for Hybrid Composition Ratio of TiO₂-SiO₂nanofluids in a Tube with Wire Coil Inserts." *Case Studies in Thermal Engineering* 25 (November 2020): 100899. <https://doi.org/10.1016/j.csite.2021.100899>.
6. Bahiraei, Mehdi, Khashayar Gharagozloo, and Hossein Moayedi. 2020. "Experimental Study on Effect of Employing Twisted Conical Strip Inserts on Thermohydraulic Performance Considering Geometrical Parameters." *International Journal of Thermal Sciences* 149 (August 2019): 106178. <https://doi.org/10.1016/j.ijthermalsci.2019.106178>.
7. Behabadi, M A Akhavan, and H K Varma. 1998. "HEAT TRANSFER AUGMENTATION BY COILED WIRE INSERTS DURING FORCED CONVECTION CONDENSATION OF R-22 INSIDE HORIZONTAL TUBES" 24 (4): 635–50.
8. Berbish, M A Sharafeldeen N S, and M A Moawed R K Ali. 2017. "Experimental Investigation of Heat Transfer and Pressure Drop of Turbulent Flow inside Tube with Inserted Helical Coils." *Heat and Mass Transfer* 53 (4): 1265–76. <https://doi.org/10.1007/s00231-016-1897-z>.
9. Bhattacharyya, Suvanjan, Ali Cemal Benim, Himadri Chattopadhyay, and Arnab Banerjee. 2019. "Experimental Investigation of Heat Transfer

- Performance of Corrugated Tube with Spring Tape Inserts.” *Experimental Heat Transfer* 32 (5): 411–25.
<https://doi.org/10.1080/08916152.2018.1531955>.
10. Chandra Sekhara Reddy, M., and Veeredhi Vasudeva Rao. 2014. “Experimental Investigation of Heat Transfer Coefficient and Friction Factor of Ethylene Glycol Water Based TiO₂ Nanofluid in Double Pipe Heat Exchanger with and without Helical Coil Inserts.” *International Communications in Heat and Mass Transfer* 50: 68–76.
<https://doi.org/10.1016/j.icheatmasstransfer.2013.11.002>.
 11. Du, Juan, Yuxiang Hong, Shuangfeng Wang, Wei-biao Ye, and Si-min Huang. 2018. “International Journal of Thermal Sciences Experimental Thermal and Flow Characteristics in a Traverse Corrugated Tube Fitted with Regularly Spaced Modified Wire Coils” 133 (May): 330–40.
<https://doi.org/10.1016/j.ijthermalsci.2018.05.032>.
 12. Eiamsa-ard, Smith, Vichan Kongkaitpaiboon, and Pongjet Promvonge. 2011. “Tube Flow Through Wire Coil Turbulators Thermal Performance Assessment of Turbulent Tube Flow Through Wire” 7632.
<https://doi.org/10.1080/01457632.2011.556381>.
 13. Feng, Zhenfei, Xiaoping Luo, Feng Guo, Haiyan Li, and Jinxin Zhang. 2017. “Numerical Investigation on Laminar Flow and Heat Transfer in Rectangular Microchannel Heat Sink with Wire Coil Inserts.” *Applied Thermal Engineering* 116: 597–609.
<https://doi.org/10.1016/j.applthermaleng.2017.01.091>.
 14. Hong, Yuxiang, Juan Du, Shuangfeng Wang, Si-min Huang, and Wei-biao Ye. 2018. “International Journal of Heat and Mass Transfer Heat Transfer and Fluid Flow Behaviors in a Tube with Modified Wire Coils.” *International Journal of Heat and Mass Transfer* 124: 1347–60.
<https://doi.org/10.1016/j.ijheatmasstransfer.2018.04.017>.
 15. Kadam, Sanjay V., Shubham S. Patil, and Suhas S. Mohite. 2022. “Numerical Analysis of Wire Coil Inserted Corrugated Tube for Laminar Flow.” *Materials Today: Proceedings* 62 (P12): 6837–43.
<https://doi.org/10.1016/j.matpr.2022.05.021>.
 16. Keklikcioglu, Orhan, and Veysel Ozceyhan. 2016. “Experimental Investigation on Heat Transfer Enhancement of a Tube with Coiled-Wire Inserts Installed with a Separation from the Tube Wall ☆.” *International Communications in Heat and Mass Transfer* 78: 88–94.
<https://doi.org/10.1016/j.icheatmasstransfer.2016.08.024>.
 17. ———. 2017. “Entropy Generation Analysis for a Circular Tube with Equilateral Triangle Cross Sectioned Coiled-Wire Inserts.” *Energy* 139:

- 65–75. <https://doi.org/10.1016/j.energy.2017.07.145>.
- 18.—. 2018. “Experimental Investigation on Heat Transfer Enhancement in a Circular Tube with Equilateral Triangle Cross Sectioned Coiled-Wire Inserts.” *Applied Thermal Engineering* 131: 686–95. <https://doi.org/10.1016/j.applthermaleng.2017.12.051>.
- 19.—. 2022. “Heat Transfer Augmentation in a Tube with Conical Wire Coils Using a Mixture of Ethylene Glycol/Water as a Fluid.” *International Journal of Thermal Sciences* 171 (July 2021): 107204. <https://doi.org/10.1016/j.ijthermalsci.2021.107204>.
- 20.Martín Subirana, A., J. P. Solano, R. Herrero-Martín, A. García, and J. Pérez-García. 2023. “Mixed Convection Phenomena in Tubes with Wire Coil Inserts.” *Thermal Science and Engineering Progress* 42 (January): 101839. <https://doi.org/10.1016/j.tsep.2023.101839>.
- 21.Oflaz, Fatma, Orhan Keklikcioglu, and Veysel Ozceyhan. 2022. “Investigating Thermal Performance of Combined Use of SiO₂-Water Nanofluid and Newly Designed Conical Wire Inserts.” *Case Studies in Thermal Engineering* 38 (August): 102378. <https://doi.org/10.1016/j.csite.2022.102378>.
- 22.Padmanabhan, S., Obulareddy Yuvatejeswar Reddy, Kanta Venkata Ajith Kumar Yadav, V. K. Bupesh Raja, and K. Palanikumar. 2020. “Heat Transfer Analysis of Double Tube Heat Exchanger with Helical Inserts.” *Materials Today: Proceedings* 46: 3588–95. <https://doi.org/10.1016/j.matpr.2021.01.337>.
- 23.Promvongse, Pongjet. 2008. “Thermal Performance in Circular Tube Fitted with Coiled Square Wires” 49: 980–87. <https://doi.org/10.1016/j.enconman.2007.10.005>.
- 24.Rajabi, Vahid, Zohreh Mansoori, Hassan Rahimzadeh, Hamed Nasrfard, and Goodarz Ahmadi. 2023. “Experimental Study of Refrigerant Condensation Heat Transfer and Pressure Drop in Horizontal Tubes with Full and Partial Coiled Wire Inserts (CWIs).” *International Journal of Heat and Mass Transfer* 216 (August): 124577. <https://doi.org/10.1016/j.ijheatmasstransfer.2023.124577>.
- 25.Şahin, Hacı Mehmet, Eşref Baysal, Ali Rıza Dal, and Necmettin Şahin. 2015. “Investigation of Heat Transfer Enhancement in a New Type Heat Exchanger Using Solar Parabolic Trough Systems.” *International Journal of Hydrogen Energy* 40 (44): 15254–66. <https://doi.org/10.1016/j.ijhydene.2015.03.009>.
- 26.San, Jung-yang, Wen-chieh Huang, and Chang-an Chen. 2015. “Experimental Investigation on Heat Transfer and Fluid Friction

- Correlations for Circular Tubes with Coiled-Wire Inserts ☆.” *International Communications in Heat and Mass Transfer* 65: 8–14. <https://doi.org/10.1016/j.icheatmasstransfer.2015.04.008>.
27. Sharifi, Khashayar, Morteza Sabeti, Mehdi Rafiei, Amir H. Mohammadi, Ali Ghaffari, Masoud Haghghi Asl, and Hamidreza Yousefi. 2020. “A Good Contribution of Computational Fluid Dynamics (CFD) and GA-ANN Methods to Find the Best Type of Helical Wire Inserted Tube in Heat Exchangers.” *International Journal of Thermal Sciences* 154 (April 2017): 106398. <https://doi.org/10.1016/j.ijthermalsci.2020.106398>.
28. Singh, Sumit Kumar, and Jahar Sarkar. 2021. “Thermohydraulic Behavior of Concentric Tube Heat Exchanger Inserted with Conical Wire Coil Using Mono/Hybrid Nanofluids.” *International Communications in Heat and Mass Transfer* 122 (January): 105134. <https://doi.org/10.1016/j.icheatmasstransfer.2021.105134>.
29. Tavousi, Ebrahim, Noel Perera, Dominic Flynn, and Reaz Hasan. 2023. “Heat Transfer and Fluid Flow Characteristics of the Passive Method in Double Tube Heat Exchangers: A Critical Review.” *International Journal of Thermofluids* 17 (January): 100282. <https://doi.org/10.1016/j.ijft.2023.100282>.
30. Wang, Ning, S.P. Ghouschi, Kamal sharma, Ibrahim Elbadawy, Abir Mouldi, Hassen Loukil, and Ahmed Farouk Deifalla. 2023. “Thermal Performance Enhancement in a Double Tube Heat Exchanger Using Combination of Bubble Injection and Helical Coiled Wire Insert.” *Case Studies in Thermal Engineering* 52 (October): 103722. <https://doi.org/10.1016/j.csite.2023.103722>.

Chapter 12

Urban Climate Change Resilience

Gökhan KARA¹

Esma Gül EMECEN KARA²

1. INTRODUCTION

Climate change can be defined as the change in the behavior of weather events in a certain period depending on the change in the average temperature of the world and the sum of events and their impact that occur as a result. Especially with the positive increase in temperature over the last 50 years, the change in temperature has been incredibly supported by unnatural processes, that is, by humans. Population growth, in parallel with urbanization and industrialization, as well as the use of fossil fuels, have significantly accelerated this process. Today, the 100 least-emitting countries constitute 3% of total emissions, while the 10 largest emitters account for 68% of emissions. From this perspective, countries have great responsibilities regarding limiting the increase in emissions. CO₂, water vapour, methane, ozone, and nitrogen oxides, naturally found in the atmosphere, known as greenhouse gases (GHG), keep our planet's temperature in balance. However, if these gases are released into the atmosphere more than normal, the heat that needs to escape into space remains in the atmosphere, and our planet warms up more than usual. This causes us to face consequences such as drought, lack of usable water, fires, destructive storms, and melting polar ice caps that we experience today. In the report of the Intergovernmental Panel on Climate Change (IPCC), the impact of the human factor on the occurrence of extreme weather events such as heat waves, heavy rains, drought and tropical storms has been emphasized once again. Greenhouse gas emissions are at their highest levels in the last three million years and continue to rise. Our earth is approximately 1.2 °C warmer than it was in the 1800s. If carbon dioxide emissions continue to rise at today's rate, temperatures are expected to increase between 3°C and 5°C by the end of the century.

¹ Prof.Dr.Gökhan KARA İstanbul University-Cerrahpaşa, Engineering Faculty, Maritime Transport Management Engineering Department, Avcılar, İstanbul, Turkey ORCID: 0000-0001-5796-8707. E mail: karagok@iuc.edu.tr

² Assoc.Prof.Esma Gül EMECEN KARA İstanbul University-Cerrahpaşa, Engineering Faculty, Maritime Transport Management Engineering Department, Avcılar, İstanbul, Turkey ORCID: 0000-0001-6963-0965.Email:emeceng@iuc.edu.tr

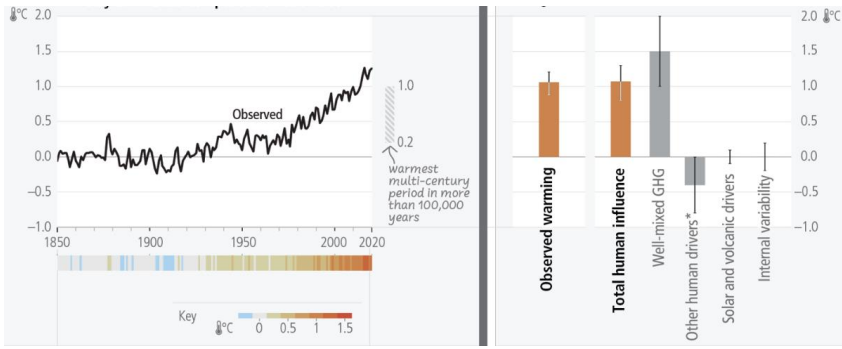


Figure 1. Causes from emissions to global warming (IPCC Report, 2023)

As seen in Figure 1, the temperature, which has shown small oscillations since the 1850s, has increased rapidly in the last 70 years. The figure on the right shows the observed and measured value of the temperature increase between 1850 and 2020 and the temperature change due to natural causes. Global surface temperature (shown as annual deviations from the 1850-1900 average) has increased by approximately 1.1°C since 1850-1900. All of the warming observed between 1850-1900 and 2010-2019 is caused by humans. The total human impact, changes in greenhouse gas concentrations and other human factors (aerosols, change in ozone and land use, solar and volcanic eruptions, and internal climate variability) are shown on the right. The contribution of human activities to global temperature change is clearly seen in the figure.

If we evaluate the consequences of climate change under main headings; the number and intensity of tropical storms will increase further, and such destructive storms will begin to form in higher latitudes due to the change in the temperature of the seas and oceans. As drought increases in some places, the resulting forest fires will increase, production of agricultural products will fall, water resources will decrease, and soil and water-related diseases will emerge. In some regions, floods and soil erosion will occur due to excessive rainfall. Recently in our country, the severity and frequency of natural disasters such as thunderstorms, extreme rainfall, drought, forest fires, etc. has increased. From now on, we will be faced with these unusual events much more frequently in the mid-latitudes, including our country. For example, a pessimistic scenario predicts that the number of extremely rainy days in Istanbul will increase by 60% by the end of the century (Figure 2).

Apart from natural causes, the biggest cause of global warming is humans. Most of the activities generated by people are concentrated in cities. Therefore,

cities play a distinct role in global climate change. The world population is now close to 8 billion, and half of this population lives in cities. In the next 20-30 years, this percentage is expected to rise even further. The concentration of the population in cities shows that cities are the places that will be most affected by the consequences of climate change. According to the United Nations (UN) report, the world population is expected to increase to 10.9 billion by 2100. Cities that consume high amounts of energy naturally emerge as the largest source of global greenhouse gas emissions. When evaluated from this perspective, the importance of climate change studies in urban areas where the multiplier effect is high becomes evident.

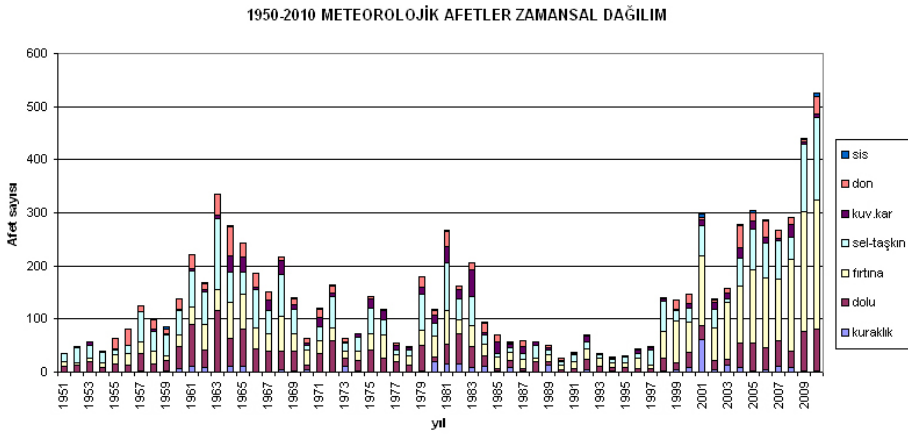


Figure 2. Change over time in the annual total number of hydro-meteorological disasters that occurred in Turkey between 1950 and 2010 (Kadioğlu, 2012).

2. CLIMATE AND URBAN METEOROLOGY

The concept of urban meteorology is that cities create their own atmosphere and climate, depending on the needs of their growing population over the years. Therefore, cities directly affect their own climates, and climates and climate changes directly affect cities. We can see the negative effects of climate change all over the world. As the consequences of the effects are indirectly linked to human life and health, the cities where the impact on humans is most intense are important in this regard. Cities are both areas that emit a lot of emissions and are also the places most affected by its effects. The impact of climate change on cities can be seen directly as meteorological weather events, but indirectly as sociological and psychological events. We can list some of the meteorological and hydro-meteorological disaster risks that cities will be affected by climate change as follows.

2.1 Heat Wave and Heat Island Cities

A heat wave is when weather conditions that exceed the limit value in a region, compared to averages, persist for at least three days (Ünal, et al., 2012). Hot and humid weather is a situation that negatively affects people's comfort and can lead to death. People living in hot cities are more affected by cold weather, and people living in cities with generally cold weather are more affected by hot weather (Curriero et al., 2002; Keatinge et al., 2000). Humid and hot atmospheric conditions, especially in coastal cities during the summer months, cause heart attacks, brain hemorrhages, psychological disorders and serious health problems for the elderly, children and sick people. With global warming, heat waves in our country may become more frequent, longer lasting and more severe (ÇŞB, 2012). When the temperature increase due to urbanization and global warming is combined with a humid heat wave, serious negative effects can occur.

Human-related activities in cities, such as rapid population growth, irregular structuring, the construction of high and frequent buildings with a large surface area, the increase in the number of vehicles using fossil fuels, have a negative impact on the urban atmosphere. The absorption and retention of heat in buildings exposed to solar radiation during the day and the release of this heat to the city atmosphere after sunset causes the city temperature to increase. This phenomenon is called the “heat island” effect.

The city structure and texture should be planned in a way that will benefit from it to the maximum extent, rather than being damaged by the climate and atmospheric effects of that region. Buildings should be designed in accordance with the effects of wind, sunlight duration and surrounding structures. In this direction, all kinds of structures must be built according to scientific meteorological measurements and obtained data (Figure 3).

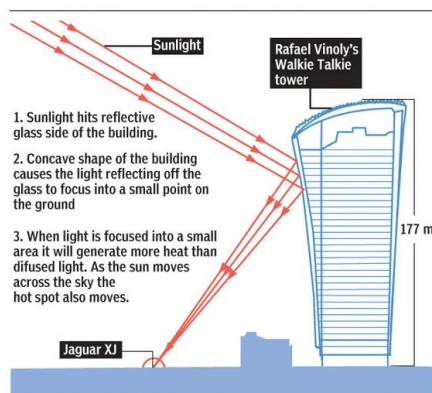


Figure 3. The effect of sunlight reflected from buildings on city temperature.

Heat islands formed in cities are considered as temperature pollution (Gardashov and Kara, 1997). Rapid changes in the urban atmosphere due to structural changes create their own climates on a microscale. In normal conditions, the temperature difference between urban and rural areas averages between 3 and 4 °C. In very hot weather, this difference can go up to 8-9 °C. Therefore, more green spaces are needed in cities (Figure 4).

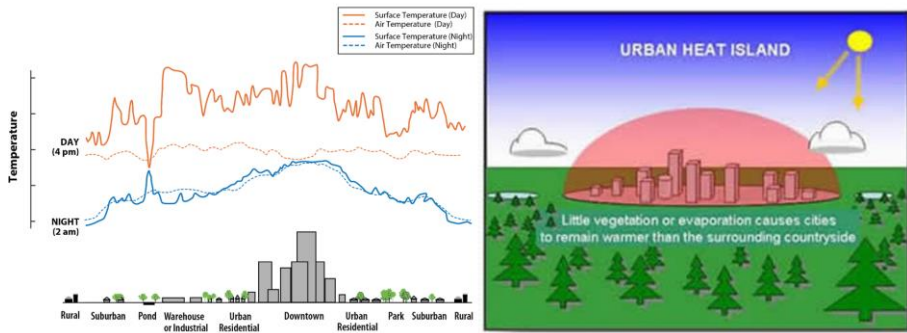


Figure 4. Day and night variation of city temperature due to heat island effect (www.usgs.gov)

Additionally, cooling buildings in hot weather will increase energy consumption. More fossil fuels will be used for energy needs and greenhouse gases will increase, thus warming in the atmosphere will increase and this will have a cyclical negative effect on global climate change.

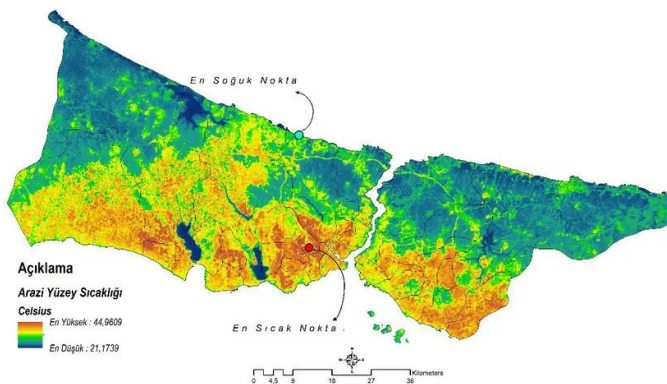


Figure 5. Application of Remote Sensing and GIS in Surface Temperature and Urban Heat Island Detection and Analysis (Khorrami and Gunduz, 2019)

Another effect of the urban heat island is that it changes the regional precipitation regime, especially the city climate (Figure 5). The heat island causes more and heavier rainfall over the city.

2.2 Extreme Precipitation and Urban Flooding

In recent years, there has been a significant increase in heavy rains and subsequent floods. This increase is expected to become stronger with the effects of climate change (Easterling, et al., 2000). Especially in urban disasters, floods rank second after earthquakes. Urban floods occur with short-term extreme precipitation. Even though the amount of precipitation is the same, flash floods occur because the precipitation flows faster in cities than in rural areas. City geometry and artificial materials used in urban environments change surface flows compared to rural areas (Lemonsu and Masson, 2002). The increased frequency of extreme precipitation due to climate change and the insufficient capacity of existing infrastructures in cities cause more negativities to occur. In this regard, cities need to consider the effects of climate change in their risk assessments for future risk levels. Due to climate change or other reasons, lack of precipitation in settlements with a dense urban population will cause water shortage in the dams that supply water to the city and serious problems will occur accordingly.

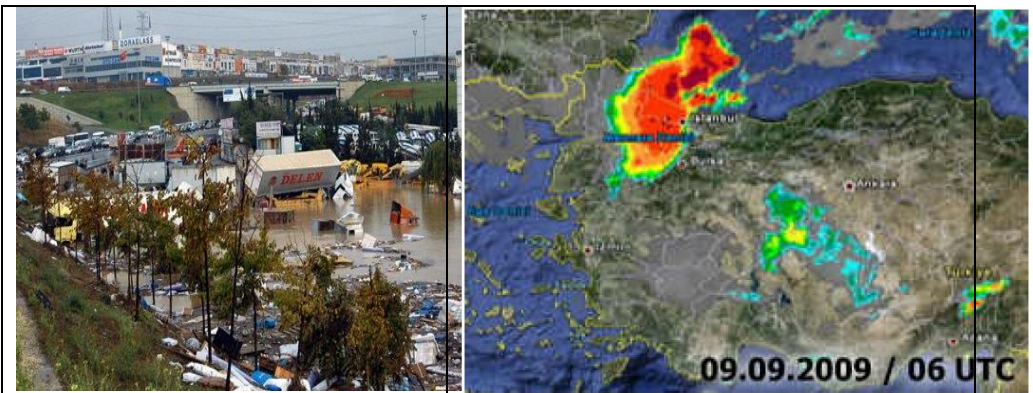


Figure 6a. Flood disaster caused by heavy rain that started at night on Basın Ekspres road in İkitelli.

Figure 6b. Radar image of the General Directorate of Meteorology dated 09.09.2009 (mgm.gov.tr).

A flood occurred on the Basın Ekspres road in İkitelli due to the heavy rain that started at night. 26 people lost their lives after being swept away by flood waters in Istanbul. 5 people lost their lives in the floods that occurred in

2.3 Cities and Snowfall

Although there is a decrease in snowfall due to global climate change, it is a meteorological event that negatively affects urban life. Important problems such as disruption of land, sea and air transportation due to snow accumulation and icing and resulting traffic congestion can weaken the resilience of cities. In this regard, meteorological forecasts must be constantly monitored and precautions must be taken quickly in advance.



Figure 7. Traffic density in Istanbul due to snowfall.

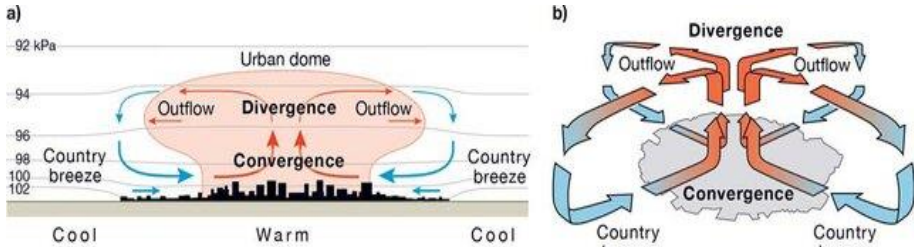
<https://www.aa.com.tr/tr/turkiye/istanbulda-trafik-yogunlugu-yasaniyor/2113475>

2.4 Urban Air Pollution, Fog and Wind

The main cause of air pollution in cities is anthropogenic emissions from buildings, traffic and factories near urban areas. One of the reasons that changes the effect of pollution is fog formation. In general, the frequency of fog formation in cities is 10-20% higher compared to open areas. The concentration of moisture on pollutant particles in cities increases the frequency of fog, and precipitation may also occur when other necessary conditions are available for rainfall.

In addition, when the solar radiation regime of cities is examined, the albedo of the city surface is very important. In cities, buildings, asphalt roads and roofs cause a decrease in surface reflection, an increase in absorbed radiation and surface temperature. A decrease in albedo from 30% to 15% corresponds to an increase in the air temperature by 1.5 °C. When the temperature increases over the city, the direction of the wind will be towards the city center and the hot air will rise. The rising air will move out of the city center and towards the rural

areas at the upper levels. Circulation will continue in this way and the polluted air of the factories, which are generally located outside the city, will be constantly transported to the city center (Figure 8a and Figure 8b). Especially in cities where air pollution is common, air circulation is an important factor in dispersing pollution and providing clean air to the city.



Figures 8a and 8b. Heat island circulation, wind movements and pollution transport in cities (Oke et al., 2017).

It has now become mandatory to know the dominant wind direction and behavior in cities and to take it into account in urban planning. In urban settlements, the height and density of buildings will increase roughness and the speed and direction of the wind will decrease significantly. This will prevent clean air from coming to cities and cause air quality to deteriorate (Figure 9).

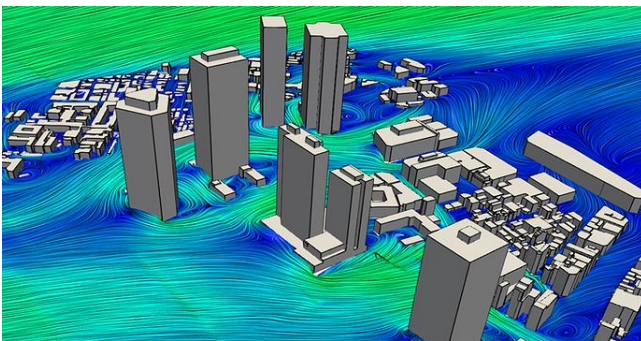


Figure 9. Simulation of wind distribution on buildings in cities (discourse.mcneel.com).

Another meteorological phenomenon that affects both outlying and urban areas is dust storms. Dust storm is the displacement of fine dust particles by the effect of wind. It can be seen frequently in arid and semi-arid regions, both naturally and due to climate change. It generally affects urban areas close to these regions. It is often confused with sandstorms. Sandstorms are horizontal

transport of larger particles such as sand, mostly in deserts and large plains. Excessive heating of the air during the day causes pressure differences and the lower atmosphere to become unstable. This instability causes strong winds in the middle troposphere to direct towards the surface (Figure 10).



Figure10. A dust storm in Australia (mobygeek.com/).

2.5 Sea Level Rise and Storm Surges

Increasing temperatures due to global climate change will cause polar ice caps to melt and sea levels will rise. According to the "very high greenhouse gas emission scenario" (SSP5-8.5), it is estimated that the sea level will rise by 1.0 m in 2100 (IPCC Report, 2021). The rise in sea level will cause coastlines to change and countries to lose land. Its greatest impact will show itself in urban areas located in coastal areas. All physical structures built according to the current situation will lose their functions and features. This will result new investments and high costs. For example; rainwater drainages, capacities of sewage systems, energy infrastructure (natural gas, electricity, etc.). As the sea level rises, the connection of clean water resources near the coasts with the sea will pose a problem. Coastlines should not be filled to expand urban areas and open new areas. Due to increased evaporation, approximately 20% water loss will occur in lakes and rivers. As a result of the recent drought in our country, some of our lakes have already started to dry out and some have even dried up completely.

In addition, due to climate change, winds resulting from more frequent local storms will cause sea levels to rise along the coastlines and damage coastal protection structures (Figure 11). For example; today when the southwest wind blow in the Avcılar-Ambarlı port area, which is an open sea port, ship traffic, ship unloading and loading operations are disrupted and thus time losses occur, which leads to financial losses for the port and ship investors.



Figure 11. Wave formation and breakwater due to high wind speed (www.dw.com).

3. URBAN RESILIENCE SOLUTION SUGGESTIONS/ STRATEGIES WITHIN THE SCOPE OF CLIMATE CHANGE

More frequent extreme precipitation and storms, higher temperatures, rising sea levels, drought and other climate change consequences have significant consequences for the quality of urban life. Additionally, the number of people who have to deal with these consequences is increasing due to increasing urbanization. As a result, cities around the world need to prepare for the impact of climate change on urban life. In this direction, first of all, measurements should be made to determine the current situation and gradual solution strategies should be developed.

In this direction;

- A "Climate Resilient City Research Program" based on scientifically obtained information and studies should be developed,
 - Within the scope of this program, the functioning, adaptation and resilience of urban climate systems should be evaluated; urban air, water, soil and green areas should be analyzed in order to be mapped by conducting temperature, precipitation and wind analyses in the city and its surroundings,
 - A "climate adaptation planning approach" should be created to make the city's infrastructure sustainable and redesigned.

In order to achieve these;

- Meteorological Weather Analysis: Performing weather analysis of the city and its surroundings (modeling city weather events and air quality)
- Hydrology and Water Analysis: The urban water cycle system should be modeled in terms of precipitation, evaporation, storage and discharge (How can pre-storm flooding be predicted and prevented?).

- Urban Planning and Scenarios: Simulating the events that are likely to occur due to climate change with the "climate adaptation planning approach" and reducing the negative consequences in this direction, are required.

Preventing the negative effects of climate change cannot be done at the city level alone. This requires an integrated, multi-layered, long and short-term cooperation with other relevant stakeholders. Thus, efforts to create more climate-resistant cities will be accelerated.

City managers should design and implement policies that will make their cities and the environment healthy, resistant to extreme climate events and increase the well-being of urban residents by analyzing the characteristics, physical structure, environment and human needs of their cities for a sustainable future. In this direction, real experts and scientific outputs need to be given importance for the sustainability of the city, adaptation to climate changes and resilience.

Local governments, which are among the first to respond to disasters such as climate change and extreme weather events, are faced with responsibilities. They are the first institutions to predict, manage and reduce disaster risk. This is achieved by establishing early warning systems and establishing specific disaster/crisis management organization. To understand how meteorological disasters occur, it is important to consider risk factors. Risks are a function of the hazard (e.g. extreme precipitation and flooding, air pollution, sea level rise). In this direction, depending on climate change;

- Determining the meteorological hazards that the city is exposed to and making hazard assessments,
 - Inclusion of all identified hazards and their effects in risk assessments,
 - Regularly updating risk assessments with multi-stakeholder participants,
 - Considering the effects of climate change first in urban risk assessments,
 - Developing clear mechanisms to integrate risks and their impacts.
 - Making all risk assessments easily accessible among other institutions,
 - Establishing a regularly updated data platform that stakeholders can access to exchange risk-related information,
- Making information about hazards and risks publicly available and learning from the experiences of cities with similar risk profiles,
- Benefiting from past disasters to increase resilience and develop measures in this direction, are required

REFERENCES

1. Curriero FC, Heiner KS, Samet JM, Zeger SL, Strug L, Patz JA. 2002: Temperature and mortality in 11 cities of the eastern United States. *Am J Epidemiol*; 155: 80–87.
2. ÇŞB, 2012: Türkiye'nin İklim Değişikliği İkinci Ulusal Bildirimi (Taslak), T.C. Çevre ve Şehircilik Bakanlığı, Nisan 2012, Ankara.
3. Easterling D.R., Meehl, G.A., Parmesan, C., Chagnon S.A., Karl, T.R., Mearns, L.O., 2000: Climate extremes: observations, modeling, and impacts. *Science* 2000; 289: 2068–74.
4. Gardachov R.G., Kara G., (1997) " Kentlerde Hava Kirliliği ve Isı Adası Etkisi", *Doğayı Korumada Kent ve Ekoloji Sempozyumu, Bildiriler Kitabı* , 18-19 Aralık, İ.T.Ü. Mimarlık Fakültesi, 307-313.
5. IPCC, 2023: Climate Change 2023: Synthesis Report. Contribution of Working Groups I, II and III to the Sixth Assessment Report of the Intergovernmental Panel on Climate Change [Core Writing Team, H. Lee and J. Romero (eds.)]. IPCC, Geneva, Switzerland, pp. 35-115, doi: 10.59327/IPCC/AR6-9789291691647.
6. IPCC, 2021: Climate Change 2021: The Physical Science Basis. Contribution of Working Group I to the Sixth Assessment Report of the Intergovernmental Panel on Climate Change [Masson-Delmotte, V., P. Zhai, A. Pirani, S.L. Connors, C. Péan, S. Berger, N. Caud, Y. Chen, L. Goldfarb, M.I. Gomis, M. Huang, K. Leitzell, E. Lonnoy, J.B.R. Matthews, T.K. Maycock, T. Waterfield, O. Yelekçi, R. Yu, and B. Zhou (eds.)]. Cambridge University Press, Cambridge, United Kingdom and New York, NY, USA, In press, doi:10.1017/9781009157896.
7. Keatinge W.R., Donaldson G.C., Cordioli, E., 2000: Heat related mortality in warm and cold regions of Europe: observational study. *BMJ*; 321: 670–73.
8. Kadioğlu, M. 2012. Türkiye’de İklim Değişikliği Risk Yönetimi. Türkiye’nin İklim Değişikliği II. Ulusal Bildiriminin Hazırlanması Projesi Yayını, 172 sf.
9. Khorrami, Behnam & Gunduz, Orhan. (2019). Uzaktan Algılama ve CBS'nin Yüzey Sıcaklığı ve Kentsel Isı Adası Tespit ve Analizinde Uygulanması. ResearchGate. Arşiv Bağlantısı.
10. Oke, T., Mills, G., Christen, A., & Voogt, J. (2017). *Urban Climates*. Cambridge: Cambridge University Press. doi:10.1017/9781139016476
11. Ünal, Y. S., E. Tan ve S. S. Mentés, (2012). Summer heatwave s over western Turkey between 1965 and 2006. *Theor Appl Climatol* DOI 10.1007/s00704-012-0704-0.

12. <https://www.usgs.gov/media/images/urban-heat-islands>

13. <https://www.mgm.gov.tr/>

Chapter 13

Investigation of chaotic behavior in a 3D nonlinear system with exponential function

Haris CALGAN¹
Metin DEMİRTAS²

1- INTRODUCTION

Chaotic behavior introduces a fascinating and complex dimension that challenges our conventional understanding of predictability and order. Unlike systems governed by linear and predictable rules, chaotic systems showcase nonlinear dynamics, wherein small changes in initial conditions can lead to divergent and unpredictable outcomes. This inherent sensitivity gives rise to intricate and seemingly random patterns, often resembling disorder while underlying a deterministic process (Akgul et al., 2016).

Chaotic systems find expression in various scientific disciplines, including physics, biology, economics, and engineering. The weather, for instance, is a classic example of a chaotic system, where minor fluctuations in initial conditions can lead to vastly different weather patterns over time. The study of chaotic systems involves exploring their dynamic behavior through tools such as bifurcation diagrams, Lyapunov exponents, and attractors (Calgan & Gokyildirim, 2023). Bifurcation diagrams illustrate the system's transitions between ordered and chaotic states, while Lyapunov exponents quantify the system's sensitivity to initial conditions. Attractors, such as strange attractors, provide insights into the long-term behavior of chaotic systems.

In the context of a non-equilibrium chaotic system, its dynamic behavior is characterized as hidden dynamic behavior (Liu et al., 2021). The 3D chaotic system stands out as the most basic system capable of generating hidden attractors. Both the non-equilibrium system and conservative system represent distinct categories of chaotic systems, each possessing unique characteristics. When compared to conventional chaotic systems, these types often exhibit more intricate dynamic behaviors (Borah & Roy, 2021). The incorporation of an exponential function imparts a distinctive structural aspect, rendering it a type

¹ Dr.; Balıkesir Üniversitesi Mühendislik Fakültesi Elektrik-Elektronik Mühendisliği Bölümü.
haris.calgan@balikesir.edu.tr ORCID No: 0000-0002-9106-8144

² Prof. Dr.; Balıkesir Üniversitesi Mühendislik Fakültesi Elektrik-Elektronik Mühendisliği Bölümü.
mdtas@balikesir.edu.tr ORCID No: 0000-0003-2622-5286

of specialized chaotic system. In this regards, Ye and Wang presented a 3d system without equilibrium point and with a 0 solution when Lyapunov exponents are summed (Ye & Wang, 2023). However, they investigate the system only in integer-order case.

This work focuses on the investigation of chaotic behavior of 3D chaotic system with exponential terms in fractional-order case. The system dynamics are investigated by means of fractional calculus. The effect of each state's fractional-order is examined individually.

FRACTIONAL-ORDER ANALYSIS OF 3D CHAOTIC SYSTEM WITH EXPONENTIAL TERM

In many real-world phenomena, particularly those exhibiting complexity and memory, conventional calculus falls short. Enter fractional calculus, a mathematical discipline that extends the notion of differentiation and integration to non-integer orders (Demirtas et al., 2019). In contrast to classical calculus, fractional calculus opens the door to a new realm of mathematical tools for understanding phenomena such as fractional-order systems, fractional differential equations, and fractional-order control systems (Ilten & Demirtas, 2016).

In this study, a 3d chaotic system which has an exponential function is investigated by means of fractional calculus. The model in fractional-order form is given as below (Ye & Wang, 2023):

$$\begin{aligned} D_t^q x &= ay \\ D_t^q y &= -x - byz \\ D_t^q z &= cy^2 - e^{-x^2} \end{aligned} \tag{1}$$

where D_t^q denotes fractional-order differentiation or integration based on the q value. The Caputo fractional definition is defined as (Gokyildirim et al., 2023)

$$D_t^q f(t) = \left\{ \frac{1}{\Gamma(n-q)} \left(\frac{d}{dt} \right)^n \int_0^t (t-\tau)^{n-q-1} f(\tau) d\tau \right. \tag{2}$$

where Γ is Euler's gamma function since $n-1 < q < n$. The Laplace transform of the Caputo definition is given by

$$H(s) = L \left\{ \frac{d^q f(t)}{dt^q} \right\} = s^q L \{ f(t) \} \tag{3}$$

By setting integration step (h) = 0.01, $q_1 = q_2 = q_3=1$ (integer-order case), $a=2$, $b=1.2$, $c=0.1$, initial conditions=(0.1, 0.1, 0.1), 2D phase portraits can be obtained as illustrated in **Figure 1**. In order to show chaotic behavior for different bifurcation parameter ‘a’, **Figure 2** is obtained. As illustrated in this figure, when $a \in [0.01,3]$, there are periodical or chaotic behaviors. It is proven by the Figs. 1 and 2 that the chaotic behavior is observed when $a=2$.

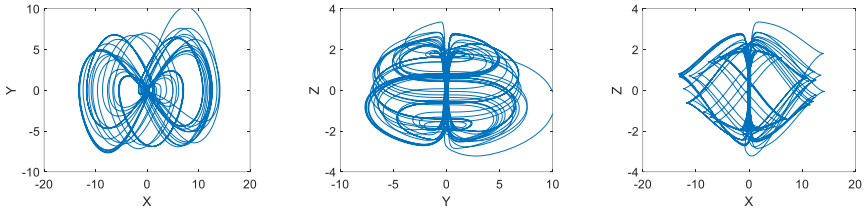


Figure 1: Phase portraits of integer-order chaotic system for $a=2$, $b=1.2$, $c=0.1$

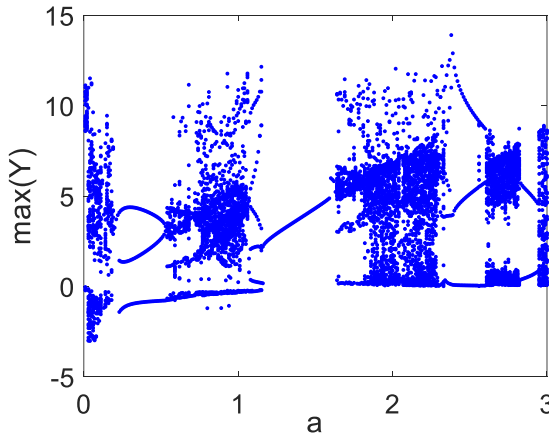


Figure 2: Bifurcation diagram for a when $b=1.2$, $c=0.1$

In order to investigate fractional-order case of the system, FDE.m code of MATLAB program written by Garappa (Garrappa, 2018) is used in this study. This code implements Caputo definition and solves the differential equation with initial conditions. By employing this code bifurcation diagram is obtained as given in **Figure 3**. Note that, the effect of fractional-order value in commensurate order case is evaluated in this figure when $a=2$, $b=1.2$, $c=0.1$. It is shown that chaotic behavior is observed when q is bigger than 0.99. It can be said that richer dynamic is obtained with commensurate fractional-order analysis, yet lower fractional orders can be determined by means of incommensurate fractional-order analysis. **Figure 4** shows the phase portraits of

commensurate fractional-order chaotic system when $q=0.995$, $a=2$, $b=1.2$ and $c=0.1$.

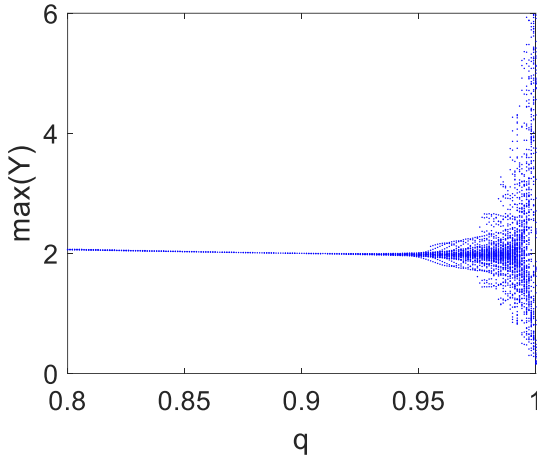


Figure 3: Bifurcation diagram of the commensurate fractional-order chaotic system for q when $a=2$, $b=1.2$, $c=0.1$

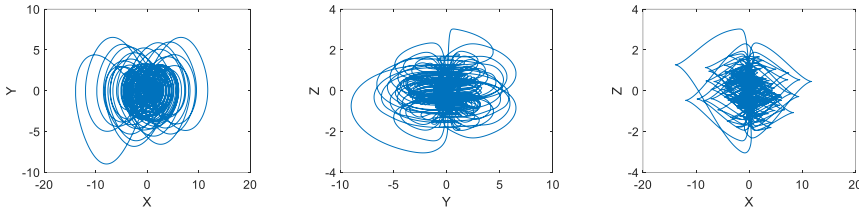


Figure 4: Phase portraits of commensurate fractional-order chaotic system for $q_1=q_2=q_3=0.995$, $a=2$, $b=1.2$, $c=0.1$

For the incommensurate fractional-order analysis, various fractional order parameters are handled. According preliminary trials, it is found that q_3 must be kept integer-order to have chaotic behavior. At the beginning the individual effects of fractional-orders (q_1 , q_2 , q_3) are evaluated, separately by means of bifurcation diagram as depicted in **Figure 5**, **Figure 6** and **Figure 7**. As illustrated in **Figure 5**, chaotic behavior is encountered when q_1 is bigger than 0.95. **Figure 6** shows that lower fractional-order can be used to have chaotic behavior since q_2 is taken into account. **Figure 7** proves the narrow limits q_3 compared to q_1 and q_2 . Therefore, for the next steps, q_3 kept constant at integer order, q_2 is taken as bifurcation parameter and q_1 is decreased step by step.

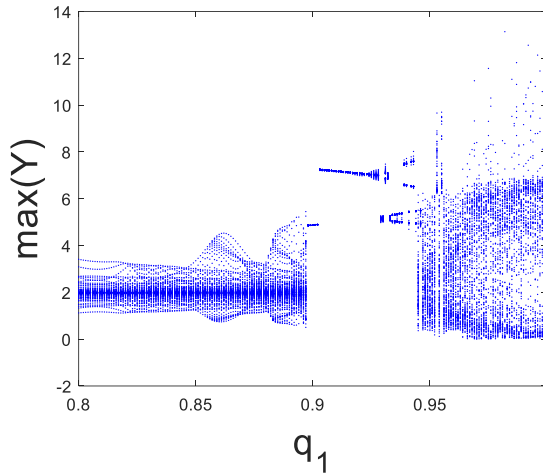


Figure 5: Bifurcation diagram of the commensurate fractional-order chaotic system for q_1 when $q_2=q_3=1$, $a=2$, $b=1.2$, $c=0.1$

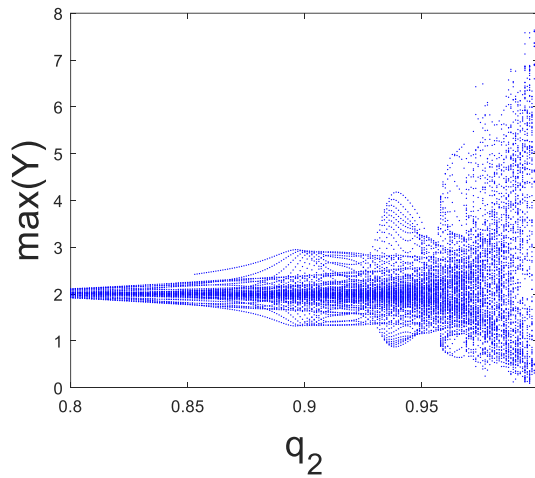


Figure 6: Bifurcation diagram of the commensurate fractional-order chaotic system for q_2 when $q_1=q_3=1$, $a=2$, $b=1.2$, $c=0.1$

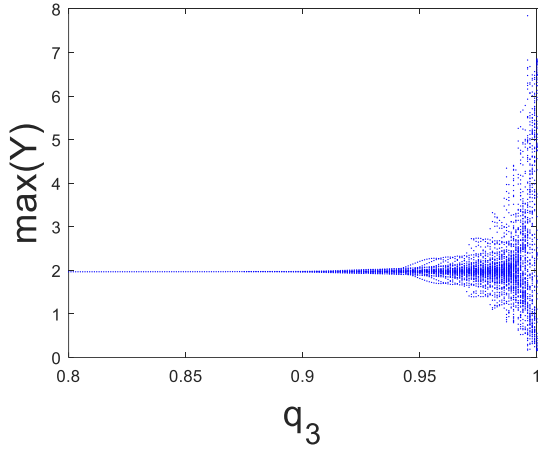


Figure 7: Bifurcation diagram of the commensurate fractional-order chaotic system for q_3 when $q_1=q_2=1$, $a=2$, $b=1.2$, $c=0.1$

As aforementioned, further studies are conducted while q_1 is decreased step by step. Note that, simulation time is taken as 700 s while integration step is 0.01. The limit of bifurcation parameter q_1 is taken in between 0.8-1. Transient behavior (first 100s) is extracted from the dataset and bifurcation figures are obtained. The observed bifurcation diagrams are presented in **Figure 8**, **Figure 9**, **Figure 10**, **Figure 11** and **Figure 12**.

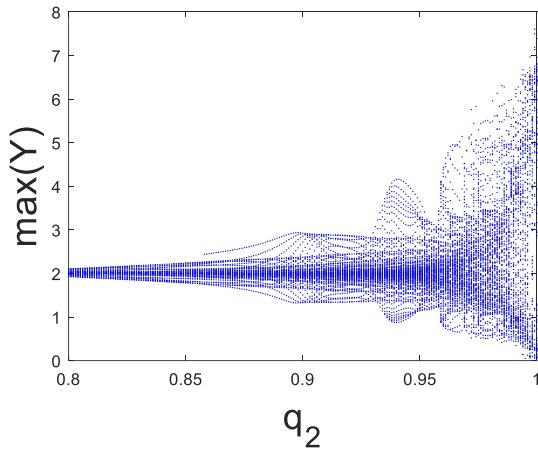


Figure 8: Bifurcation diagram of the commensurate fractional-order chaotic system for q_2 when $q_1=0.99$, $q_3=1$, $a=2$, $b=1.2$, $c=0.1$

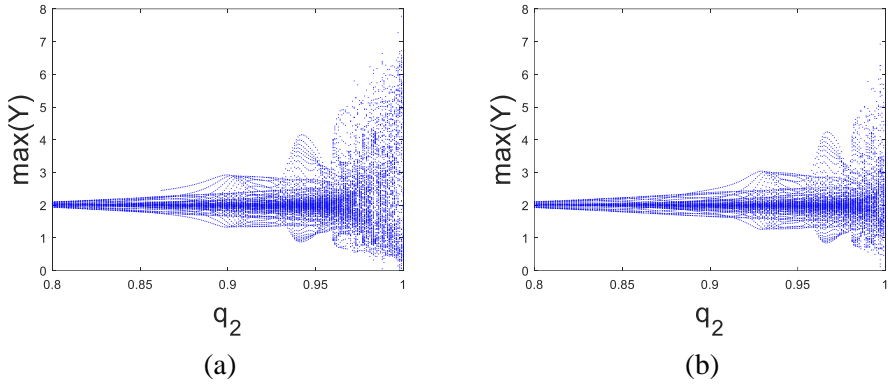


Figure 9: Bifurcation diagram of the commensurate fractional-order chaotic system for q_2 when $q_1=0.98$, $a=2$, $b=1.2$, $c=0.1$, (a) $q_3=1$, (b) $q_3=0.995$.

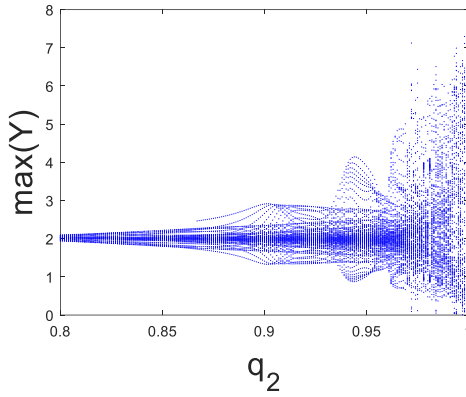


Figure 10: Bifurcation diagram of the commensurate fractional-order chaotic system for q_2 when $q_1=0.97$, $q_3=1$, $a=2$, $b=1.2$, $c=0.1$

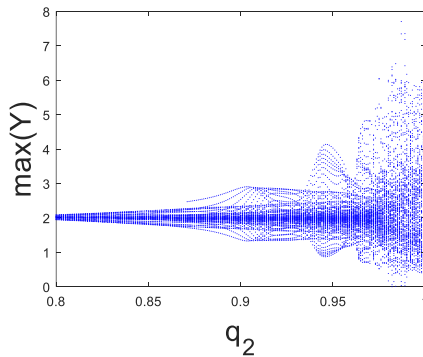


Figure 11: Bifurcation diagram of the commensurate fractional-order chaotic system for q_2 when $q_1=0.96$, $q_3=1$, $a=2$, $b=1.2$, $c=0.1$

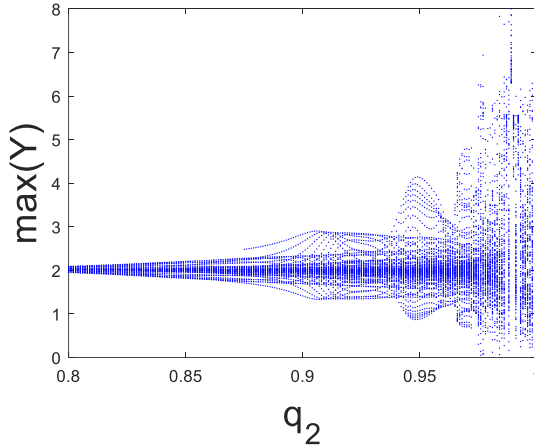
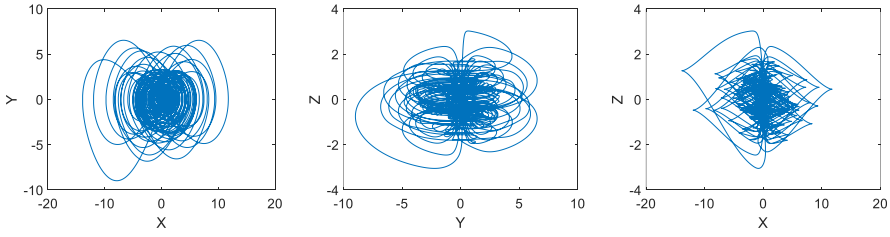


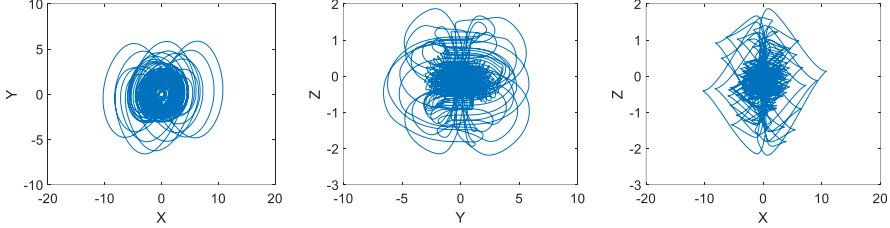
Figure 12: Bifurcation diagram of the commensurate fractional-order chaotic system for q_2 when $q_1=0.95$, $q_3=1$, $a=2$, $b=1.2$, $c=0.1$

It can be inferred from these figures that chaotic behavior strictly depends on q_3 in this chaotic system. Although q_1 does not that effective on chaotic behavior since $0.96 < q_1 < 1$, especially when q_1 equals to 0.95, the dynamic behavior of the system varies. **Figure 8**, **Figure 9a**, **Figure 10**, **Figure 11** and **Figure 12** show that q_2 must be bigger than 0.95 in each condition. Particularly, even small decreasing in q_3 yields the big change in dynamical behavior of the chaotic system as illustrated in **Figure 9b**. Based on this bifurcation diagram q_2 must be at least 0.98 since q_3 decrease from 1 to 0.995.

To show the enrichment of dynamical diversity of the chaotic system with exponential function, two different fractional-order forms are taken into account. For this simulations, the system parameters are set to $a=2$, $b=1.2$, $c=0.1$. Integration step and time are taken as 0.01 and 400s, respectively. Firstly, commensurate-order case is examined while $q_1=q_2=q_3=0.995$. **Figure 13a** shows the phase portraits of commensurate-order case when $q_1=q_2=q_3=0.995$. **Figure 13b** shows the phase portraits of commensurate-order case when $q_1=0.95$, $q_2=0.97$, $q_3=1$. It is obvious in **Figure 13** that chaotic behaviors are obtained in both cases, and however incommensurate fractional-order analysis offers more broaden parameter values.



(a)



(b)

Figure 13: Phase portraits of the chaotic system with exponential function when $a=2$, $b=1.2$, $c=0.1$ (a) $q_1=q_2=q_3=0.995$ (b) $q_1=0.95$, $q_2=0.97$, $q_3=1$

CONCLUSION

This research explores the intriguing dynamics of an incommensurate fractional-order chaotic system with exponential function, shedding light on its unique characteristics and behavior. The system under investigation exhibits fractional-order dynamics with non-integer order, adding a layer of complexity to traditional chaotic systems. Through numerical simulations, the distinctive features of this incommensurate fractional-order chaotic system are unveiled, highlighting its nonlinearity, sensitivity to initial conditions, and the emergence of chaotic attractors. Furthermore, we analyze the system's bifurcation diagrams to quantify its chaotic nature and investigate the impact of parameter variations on its dynamic behavior. The findings contribute to a deeper understanding of fractional-order systems and may have implications for various fields, including implementation of this system into engineering applications.

REFERANSLAR

1. Akgul, A., Calgan, H., Koyuncu, I., Pehlivan, I., & Istanbulu, A. (2016). Chaos-based engineering applications with a 3D chaotic system without equilibrium points. *Nonlinear Dynamics*, 84, 481–495.
2. Borah, M., & Roy, B. K. (2021). Hidden multistability in four fractional-order memristive, meminductive and memcapacitive chaotic systems with bursting and boosting phenomena. *The European Physical Journal Special Topics*, 230(7), 1773–1783.
3. Calgan, H., & Gokyildirim, A. (2023). Synchronization of Incommensurate Fractional-order King Cobra Chaotic System. *Academic Platform Journal of Engineering and Smart Systems*, 11(3), 184–190.
4. Demirtas, M., Ilten, E., & Calgan, H. (2019). Pareto-Based Multi-objective Optimization for Fractional Order PI λ Speed Control of Induction Motor by Using Elman Neural Network. *Arabian Journal for Science and Engineering*, 44(3), 2165–2175.
5. Garrappa, R. (2018). Numerical Solution of Fractional Differential Equations: A Survey and a Software Tutorial. *Mathematics*, 6(2), 16. <https://doi.org/10.3390/math6020016>
6. Gokyildirim, A., Calgan, H., & Demirtas, M. (2023). Fractional-Order sliding mode control of a 4D memristive chaotic system. *Journal of Vibration and Control*, 10775463231166188.
7. Ilten, E., & Demirtas, M. (2016). Off-Line Tuning of Fractional Order PI λ . *Journal of Control Engineering and Applied Informatics*, 18(2), 20–27. <https://hdl.handle.net/20.500.12462/9074>
8. Liu, T., Yan, H., Banerjee, S., & Mou, J. (2021). A fractional-order chaotic system with hidden attractor and self-excited attractor and its DSP implementation. *Chaos, Solitons and Fractals*, 145, 110791. <https://doi.org/10.1016/j.chaos.2021.110791>
9. Ye, X., & Wang, X. (2023). Hidden oscillation and chaotic sea in a novel 3d chaotic system with exponential function. *Nonlinear Dynamics*, 1–10.

Chapter 14

Investigation of the Phase Development of NBT, KBT and BT Lead-Free Piezoelectric Ceramics

Hatice Şule ÇOBAN TETİK¹

ABSTRACT

This study aimed to determine the formation processes of lead-free piezoelectric ceramics NBT, KBT and BT, which have gained prominence in recent years. After mixing the starting powders, the calcination temperatures were determined using TG-DTA analysis, followed by XRD analysis to analyze the phase development. The grain size of the calcined powders was measured and imaged with SEM. The results of the study have yielded a proposed formation mechanism for each phase, providing a comprehensive understanding of the underlying processes. The proposed mechanism for each phase has been meticulously analyzed and presented, offering valuable insights into the complex nature of the phenomenon under investigation. The findings obtained from this study can provide valuable insights and recommendations for future researchers who plan to investigate similar topics.

Keywords: $\text{Na}_{0.5}\text{Bi}_{0.5}\text{TiO}_3$ (NBT), $\text{K}_{0.5}\text{Bi}_{0.5}\text{TiO}_3$ (KBT), BaTiO_3 (BT), lead-free piezoelectric ceramics

INTRODUCTION

Piezoelectric materials play a critical role in various technological applications (Jaffe et al., 1971). The most frequently utilized piezoelectric material, lead zirconate titanate (PZT), has been found to have a detrimental impact on the environment due to its lead content. Therefore, it is imperative to explore and identify an appropriate replacement for PZT that is more environmentally friendly (Cross, 2004; Rödel & Li, 2018)

Sodium bismuth titanate ($\text{Na}_{0.5}\text{Bi}_{0.5}\text{TiO}_3$, NBT) is considered to be a promising lead-free ferroelectric ceramic material as one potential replacement for PZT with perovskite structure at room temperature and was discovered in

¹ PhD Research Assistant; Agri Ibrahim Cecen University, Faculty of Engineering, Department of Computer Engineering / Central Research and Application Laboratory (Assignment)
h.sulecoban@gmail.com ORCID No: 0000-0002-4775-9706

1960 by Smolenskii (1961). The interesting ferroelectric and piezoelectric properties of NBT have triggered extensive studies on its complex perovskite-based crystal structure using a wide range of experimental techniques and simulations. However, to date, the nature of the room-temperature space group and the high-temperature phase transitions are still debated (Reichmann et al., 2015). To date, many methods for the production of NBT have been reported, such as hydrothermal synthesis, sol-gel, reactive nucleation, and citrate method (Kim et al., 2005; Lencka et al., 2000; Rémondière et al., 2007; West & Payne, 2003; Xu et al., 2006). Rémondière et al. (2007) reported that no transient nanocrystalline phase was formed by the sol-gel method. On the other hand, Xu et al. (2006) reported the formation of $\text{Bi}_4\text{Ti}_3\text{O}_{12}$ (BTO) interphase in calcined powders at low temperatures such as 500 and 550 °C, using the citrate method. For NBTs, which are usually produced by solid-state synthesis, a study by Aksel and Jones (2010) reported peaks of small phases during calcination that were not previously reported. These extra peaks were associated with a reaction between Bi_2O_3 and TiO_2 between 500-650 °C. In addition, cases of increase or decrease in piezoelectric properties have been reported in NBT-based systems in case of deviations from stoichiometry (Mishra et al., 2019). The other outstanding lead-free material Potassium Bismuth Titanate- $\text{K}_{0.5}\text{Bi}_{0.5}\text{TiO}_3$ (KBT) was first synthesized by Popper et al. (1957) and later found to have ferroelectric properties with a Curie temperature (T_c) of 370°C by Bührer (1962). The structure of this material is perovskite, and it exhibits tetragonal symmetry at room temperature. However, above 300°C, it passes to a pseudocubic structure with secondary phase transformation (Hiruma et al., 2005). Similarly, in the production of KBT, the solid oxide mixture method is generally used, and an uncontrolled synthesis during production has been reported to cause deviations from stoichiometry, an increase in the proportion of secondary phases, low density, partial sample melting, and poor electrical performances due to high conductivity (König & Suvorov, 2015; Zaremba, 2003). Therefore, its properties still need to be improved, which is possible by chemical modifications of KBT (Rödel et al., 2009). The last one mentioned here is Barium titanate (BaTiO_3 , BT), the first material to produce high performance lead-free piezoelectric ceramics. The dielectric and piezoelectric characteristics of ferroelectric BT are influenced by its stoichiometry, microstructural features, and dopant concentration. These factors play a crucial role in determining the performance of BT-based devices and are, therefore of significant interest to researchers in the field of ferroelectric materials (Uchino, 2018). Although BT is relatively easy to produce compared to others, process conditions (mixing, temperature, etc.) cause problems such as secondary phase

formation in the final powder (Jaffe et al., 1971). To improve piezoelectric properties in NBT-based systems, binary and ternary compositions are used by adding KBT and BT by solid solution technique (Rödel et al., 2009; Takenaka et al., 2008). In the literature, it has been reported that some unwanted phases formed by combining different components are eliminated by the columbite method. The columbite method involves mixing and calcining some starting powders during the formation of complex structures and then adding other starting powders to the system and calcining them again. For example, in the production of $\text{Pb}(\text{Zn}_{1/3}\text{Nb}_{2/3})\text{O}_3\text{-PbTiO}_3$ (PZN-PT) based ceramics, which are leaded piezoelectric ceramics, secondary phase formation called pyrochlore is observed. In order to eliminate this phase, ZnO and Nb_2O_5 were first calcined and then PbO and TiO_2 were added to the system and it was observed that the pyrochlore phases disappeared (Bongkarn et al., 2005; Xia & Yao, 2001). For this reason, it is essential to examine the individual properties of the components used together in order to show how they can behave in the composition. Moreover, the quality of the matrix powder in ceramics depends on the quality of the starting powders, grain size, grain size distribution, grain shape, agglomeration, chemical composition, phase composition, and surface chemistry, and these properties are also critical factors (Rahaman, 2017). Controlling the grain size distribution, grain shape, and homogeneity of the starting powders used in the production of piezoelectric materials are also significant factors for the piezoelectric properties of the materials to be obtained and reproducible. The generally used method is the solid oxide mixture method in which powders of the desired composition are homogeneously mixed and calcined (Uchino, 2018). The purpose of calcination is to (i) remove all kinds of volatile impurities, (ii) perform thermochemical reactions between oxides, and (iii) reduce the final shrinkage after sintering with the reactions that occur (Jaffe et al., 1971).

In this study, a detailed investigation of the phase evolution of NBT, KBT and BT compounds has been carried out. Based on the results, their behaviour in binary, ternary compositions have been predicted. In addition, the ideal powder properties required from the starting powders to exhibit the desired properties of piezoelectric ceramics have also been investigated. The findings were obtained through various analyses and can be helpful in advancing our understanding of these materials. This paper provides a detailed analysis of the composition's phases, focusing on areas that require further development. This is critical for the translation of research into products.

MATERIALS and METHODS

Na₂CO₃ (99.9%), K₂CO₃ (99%), BaCO₃ (99.8%), Bi₂O₃ (99.9%), and TiO₂ (99.7%) were used as starting powders to produce ceramic powders. Due to the moisture absorption properties of these starting powders, they were first dehumidified at 270 °C with a heating rate of 10 °C/min for 24 hours. Then, these powders were stored in an oven at 100 °C. Na₂CO₃, Bi₂O₃, TiO₂ for NBT production, K₂CO₃, Bi₂O₃, TiO₂ for KBT production, and BaCO₃ and TiO₂ for BT production were mixed in an attritor mill for 3 hours with the help of a 5 mm yttria-stabilized zirconia (YSZ) ball in ethanol medium according to the solid oxide mixing method. After mixing, it was dried in an oven at 100 °C for 12 hours to remove the alcohol. Then, the temperatures at which the reactions occurred and ended were determined using thermogravimetric (TG)/differential thermal analysis (DTA) (TA Instruments SDT Q600-Simultaneous Thermal Analysis) with a heating rate of 5 °C/min. According to TG/DTA analysis results, heat treatment was applied at 370-600-800 °C for NBT, 370-620-850 °C for KBT, and 400-885-1050 °C for BT at different temperatures where weight losses occurred. The subsequent phase evolution, phase formation, and crystal structure of these powders after heat treatment at different temperatures were characterized by X-ray diffraction (XRD) (Bruker D2 Phaser). XRD analysis was performed at room temperature between 10°-80° with a 2°/min scan rate and 0.02 steps. Cu K- α (wavelength, 1.5406 Å) was the X-ray radiation source. A matching program was used for phase analysis (DIFFRAC.SUITE EVA-XRD Software/Bruker). The grain size distribution was measured using a Malvern Nano Zetasizer. The powder to be measured was prepared by weighing 0.005 grams and mixing in 10 ml ethanol for 5 minutes in an ultrasonic bath. The grain shapes were coated with Gold-Palladium for 40 seconds and examined with a scanning electron microscope (SEM-Supra) at a voltage of 15 kV with the help of secondary electrons (Secondary electron-SE).

RESULTS AND DISCUSSION

NBT Phase Development

In order to determine the appropriate calcination temperature and investigate the phase formation of NBT powders, a TG-DTA analysis was carried out, and the results are documented in Figure 1a. This analysis involved subjecting the powders to thermal treatment under controlled conditions while monitoring their weight and thermal behavior. The resulting data was then analyzed to obtain insights into the changes in the samples' physical and chemical properties as a function of temperature. Accordingly, weight loss was observed in 3 steps.

In the first step, weight loss is observed between 75 °C-200 °C due to the evaporation of water and some organics in the body. In the second step, weight loss occurred as a result of the decomposition of organics between the temperatures of 200 °C-400 °C and the mass loss in the third step between the temperatures of 500 °C-650 °C was probably due to the irregular form of $\text{Na}(\text{NO}_3)$, $\text{Bi}(\text{NO}_3)_3$ and Ti-complexes. It has been reported that a small amount of $\text{Na}_{0.5}\text{Bi}_{0.5}\text{TiO}_3$ is formed (Chaouchi et al., 2011). After this stage, it was observed that there was no organic content in the powder, with the endothermic peak occurring in the DTA curve. In total, 9.91% (3,64 mg) of mass loss occurred. To examine the formation of the NBT phase, batch experiments were carried out at different temperatures according to the temperatures where weight loss and endothermic peaks were observed according to the TG-DTA analysis. The first heat treatment was carried out at 370°C, the second heat treatment at 600°C, and the final heat treatment at 800°C, which was determined as the calcination temperature. It is known that the highest intensity peak in XRD analysis (Figure 1b) of an ideal material with a perovskite phase is the (110) peak with a 2θ angle between 32-34° (Kumar et al., 2020). After heat treatment at 800 °C, which is the calcination temperature determined accordingly, it was determined that all peaks belong to the perovskite rhombohedral NBT phase (Parija et al., 2012; Pookmanee et al., 2004). XRD analysis results after heat treatment and XRD analysis results of starting powders that make up the NBT phase are given comparatively. In the XRD graph at 370°C, the peaks of Bi_2O_3 appear, which complies with the proposition that it is used as a host. A study by Aksel & Jones, (2010) suggested that Na_2CO_3 and TiO_2 use Bi_2O_3 as a host during NBT formation. The schematic representation of the proposed mechanism for NBT phase development as a result of the analysis is presented in Figure 1c. Here, first of all, the transformation of Na_2CO_3 into Na_2O as carbonates start to move away from the system is shown in the blue circle representing Na_2CO_3 , which is one of the starting materials. Then, the first diffusion reactions by Na_2O and TiO_2 into Bi_2O_3 , which is used as a host, are indicated by red arrows. After the carbonates are removed, and the first diffusions occur, it is thought that Na_2CO_3 and TiO_2 in the system shrink due to the decrease in their amount, while Bi_2O_3 is thought to grow due to the formation of a new phase. This is indicated by the black dashed circles on the figure. All reactions continued with increasing temperature until the final product NBT was formed. The particle size distribution of the NBT powders was examined after calcination, and the graph of the results is shown in Figure 1d. The findings indicated a particle size distribution of 615 nm. The microstructure image of the grains is shown in Figure 1e. The image revealed that the grains were homogeneously distributed and had an equiaxed shape.

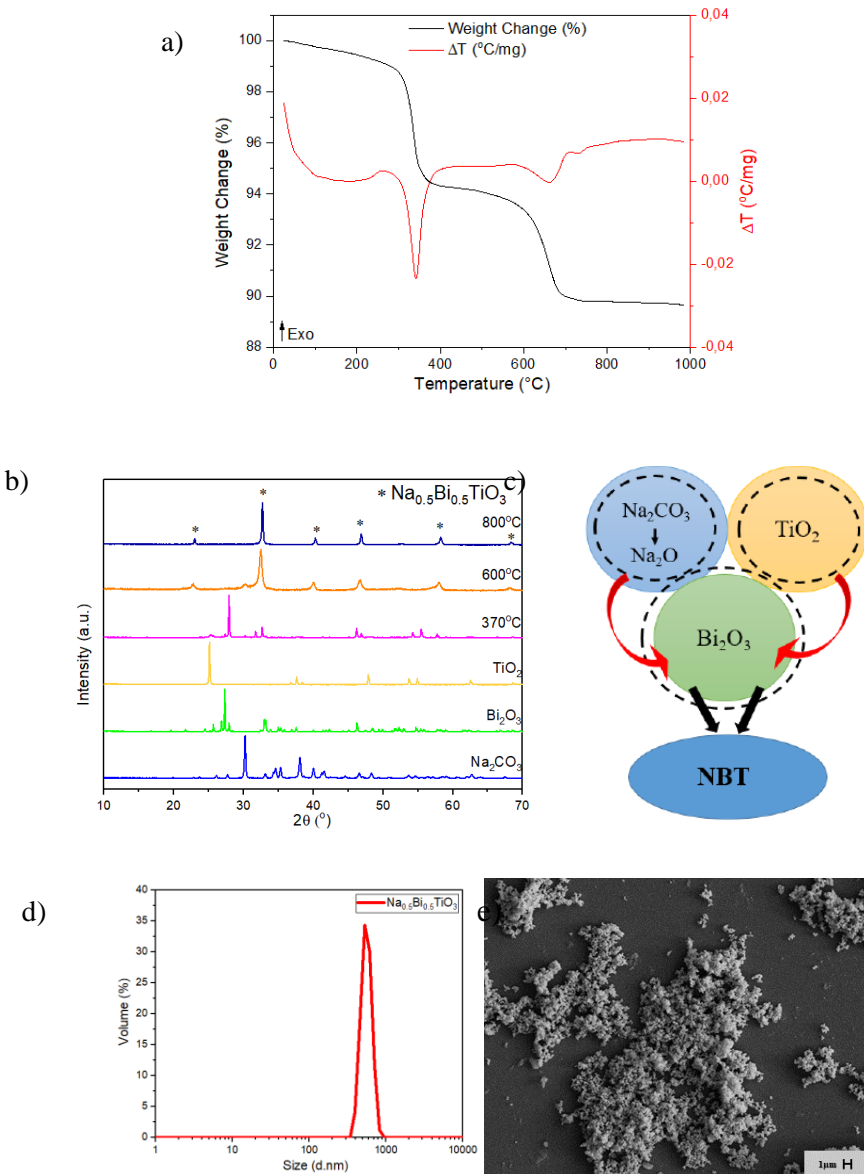


Figure 1: a) TG-DTA analysis of NBT powders b) XRD patterns of starting powders for NBT, and their XRD patterns after mixing and heat treatment at different temperatures c) The schematic representation of the proposed mechanism for NBT phase development d) Particle size distribution and e) SEM image of NBT calcined at 800 °C

KBT Phase Development

TG/DTA analysis was performed after mixing the starting powders K_2CO_3 , Bi_2O_3 , and TiO_2 to obtain the $K_{0.5}Bi_{0.5}TiO_3$ phase which is presented in Figure 2a. Accordingly, weight loss was observed in three steps on the TG graph. Additionally, the endothermic reaction peaks seen in the DTA graph are 100 °C, 210 °C, 320 °C, 620 °C and 745 °C. Alkaline carbonates are one of the powders used to create KBT. These powders tend to absorb moisture, which is called hygroscopic behavior. For this reason, it is known that the weight loss occurring in the first two steps is the loss of water in the structure due to the hygroscopic behavior of alkaline carbonates and the decarbonization of potassium hydrogen carbonate. The weight loss above 400 °C occurs due to the complete removal of carbonates from the system (Kainz et al., 2014). As seen in the graph, 620 °C was the temperature at which the KBT phase started to form. No endothermic or exothermic reactions were observed after 770 °C, and the optimum temperature at which the reactions ended was determined as 850 °C calcination temperature. A total weight loss of 10.83% (3,56 mg) was observed. According to the results of TG-DTA for the production of KBT, heat treatments in the form of batch experiments were applied at temperatures where endothermic reactions were observed and considered important, in order to observe the formation kinetics. It is presented in the same graph as the starting powders in Figure 2b. According to the TG-DTA results, heat treatments were applied at temperatures where endothermic reactions were observed and considered important for observing formation kinetics. XRD analysis was performed at these temperatures and presented in the same graph with the XRD results of the starting powders in Figure 2b. Accordingly, XRD analysis after heat treatment at 370 °C shows more peaks coming from Bi_2O_3 and is thought to be used as a host during reactions as in NBT. According to the XRD results of the heat treatment at 620 °C, it is thought that K_2CO_3 has started to enter the system with the emergence of overlapping peaks, but it is seen that the reactions have not yet ended, and the desired phase has not been reached. According to the XRD analysis after calcination at 850 °C, above the temperature where there is no mass loss and all reactions are over, it is seen that all peaks belong to the perovskite KBT phase with tetragonal symmetry (Zaremba, 2003). A schematic representation of the proposition for the formation of KBT is given in Figure 2c. This figure shows that K_2CO_3 uses Bi_2O_3 as a host together with TiO_2 after its conversion to K_2O . The red arrows indicate the diffusion direction and the black dashed circle indicates the shrinkage. The subsequent formation of the desired phase KBT is also presented with black arrows in the figure. Grain size distribution of starting powders, mixing, grinding, and time are effective

parameters in the formation temperature of a phase. Based on the graph in Figure 2d, the grain size of the KBT powders measures 615nm. In Figure 2e's SEM image, it is observed that the grains are equiaxed and homogeneous.

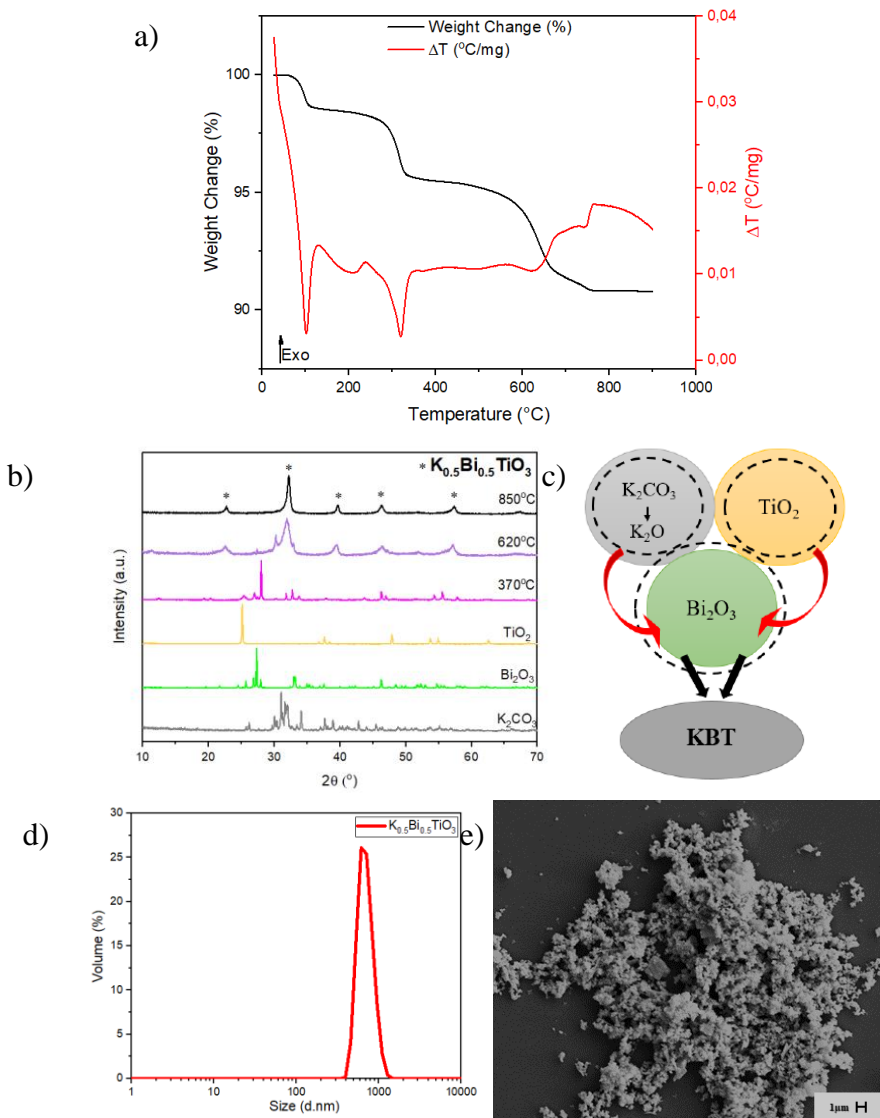


Figure 2: a) TG-DTA analysis of KBT powders b) XRD patterns of starting powders for KBT, and their XRD patterns after mixing and heat treatment at different temperatures c) The schematic representation of the proposed mechanism for KBT phase development d) Particle size distribution and e) SEM image of KBT calcined at 850 $^{\circ}\text{C}$

BT Phase Development

Traditionally, BaTiO₃ is obtained by mixing and reacting BaCO₃ and TiO₂ powders (Herbert, 1985). The TG-DTA analysis at a temperature of 1200 °C determined the mass losses and reaction zones of the starting powders mixture to form the BT phase, as shown in Figure 3a. The first mass loss occurred due to water removal and gave an endothermic peak at about 180 °C. The mass loss between 500-780 °C is known to be due to the start of BaCO₃ degradation (Jung et al., 2010). Therefore it is thought that BaCO₃ started to degrade with an endothermic peak at around 400 °C. BT formation was completed with endothermic-exothermic reactions between 800 °C and 1040 °C. The mass loss in the system was 9.48% (0.77 mg) in the first step, 9.86% (0.81 mg) in the second step, 7.65% (0.62 mg) in the third step, and the total mass loss was 28.08% (2.29 mg). The calcination temperature was determined as 1050 °C, the temperature at which mass losses and reactions are finished. In order to examine the phase formation mechanism, firstly, XRD analysis of the starting powders forming BT was performed. Then, the phase analysis of the powder mixture that will form BaTiO₃ was compared with the XRD analysis of the starting powders after heat treatment at 3 different temperatures, taking into account the temperatures at which mass losses in the TG-DTA analysis and presented in Figure 3b. According to this, it is seen in the XRD graph of the matrix powders heat treated at 400 °C that BT has not yet formed, but BaCO₃ seen 2θ angles at 24°, 27-29°, and 33-35° has entered the system. At 2θ angle 25°, the highest peak of TiO₂ is noticeable (Brzozowski & Castro, 2003; Gomez-Yañez et al., 2000). As a result of the XRD of the heat treatment at 885 °C, BT formation was largely realized, but peaks belonging to the secondary phase Ba₂TiO₄ secondary phase were still observed at 2θ angle between 25-30° and 45-50° (Gomez-Yañez et al., 2000). The fact that the reactions did not end at this temperature in the TG-DTA graph also supports this view. Finally, after calcination at 1050 °C for 2 hours, it was clearly seen that all peaks belonged to the BT phase with tetragonal symmetry in the perovskite structure. The schematic representation of the proposed formation mechanism of the phase evolution of BT is given in Figure 3c. Accordingly, in the XRD analysis performed after 400 °C, first of all, TiO₂ is thought to diffuse into the structure transformed from BaCO₃ to BaO due to the decrease in the intensity of TiO₂ peaks and the similarity of the peaks of BaCO₃ to the initial peak intensities, and it is shown with red arrows on the figure. Then, the diffusion of the formation of the final phase, BT, is also shown with black arrows. Through this study, it has been determined that the BT matrix powder exhibits a particle size distribution of 955 nm, as illustrated in Figure 3d. Furthermore, the SEM image

depicted in Figure 3e reveals an even distribution of grain sizes, indicating a remarkable level of homogeneity within the sample.

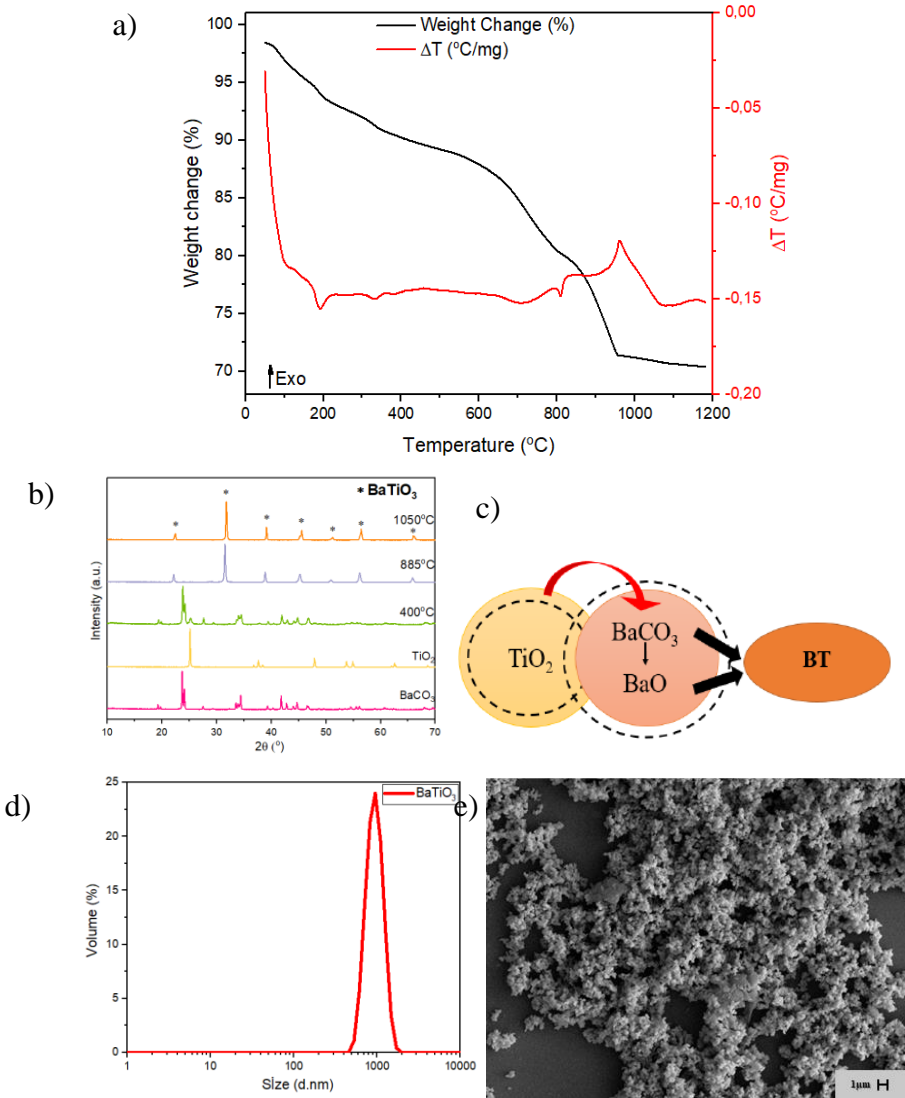


Figure 3: a) TG-DTA analysis of BT powders b) XRD patterns of starting powders for BT, and their XRD patterns after mixing and heat treatment at different temperatures c) The schematic representation of the proposed mechanism for BT phase development d) Particle size distribution and e) SEM image of BT calcined at 1050 $^{\circ}\text{C}$

CONCLUSIONS

As a result, the weight losses of NBT, KBT and BT piezoelectric ceramics at different temperatures during heat treatment and the calcination temperatures required for their production have been determined 800 °C, 850 °C, 1050 °C respectively. On the other hand, the heat treatments applied at different temperatures have illuminated how the reactions that will occur both during phase formation and in the use of starting powders in binary or ternary compositions can proceed. According to the XRD results of these piezoelectric ceramics calcined at the specified temperatures, it was understood that they did not contain any secondary phase and could be obtained without any problems. It was also shown that the powders produced using the solid oxide production method under the specified conditions can meet the desired properties of the ideal powder. The results of this study have the potential to lead to the development of new and innovative technologies in various industries, including energy, electronics, and healthcare.

Acknowledgments

The author would like to express special appreciation to Prof. Dr. Ender Suvacı for his valuable contributions and notable support. Additionally, she is grateful for the funding provided by the Eskisehir Technical University Scientific Projects Commission (Grant No. 1709F504) which made it possible to complete this work.

REFERENCES

1. Aksel, E., & Jones, J. L. (2010). Phase formation of sodium bismuth titanate perovskite during solid-state processing. *Journal of the American Ceramic Society*, 93(10), 3012-3016.
2. Bongkarn, T., Vittayakorn, N., & Rujijanagul, G. (2005). Perovskite Phase Formation, Phase Transition and Ferroelectric Properties of PZN-based Ceramics. *NU. International Journal of Science*, 2(1), 21-32.
3. Brzozowski, E., & Castro, M. S. (2003). Lowering the synthesis temperature of high-purity BaTiO₃ powders by modifications in the processing conditions. *Thermochimica Acta*, 398(1-2), 123-129.
4. Buhner, C. F. (1962). Some properties of bismuth perovskites. *The Journal of Chemical Physics*, 36(3), 798-803.
5. Chaouchi, A., Kennour, S., d'Astorg, S., Rguiti, M., Courtois, C., Marinel, S., & Aliouat, M. (2011). Characterization of sol-gel synthesised lead-free (1-x) Na_{0.5}Bi_{0.5}TiO_{3-x}BaTiO₃-based ceramics. *Journal of alloys and compounds*, 509(37), 9138-9143.
6. Cross, E. (2004). Lead-free at last. *Nature*, 432(7013), 24-25.
7. Gomez-Yañez, C., Benitez, C., & Balmori-Ramirez, H. (2000). Mechanical activation of the synthesis reaction of BaTiO₃ from a mixture of BaCO₃ and TiO₂ powders. *Ceramics International*, 26(3), 271-277.
8. Herbert, J. (1985). *Ceramic dielectrics and capacitors* (Vol. 6). CRC Press.
9. Hiruma, Y., Aoyagi, R., Nagata, H., & Takenaka, T. (2005). Ferroelectric and piezoelectric properties of (Bi^{1/2}K^{1/2}) TiO₃ ceramics. *Japanese Journal of Applied Physics*, 44(7R), 5040.
10. Jaffe, B., Cook, W. R., & Jaffe, H. (1971). The piezoelectric effect in ceramics. *Piezoelectric ceramics*, 7-21.
11. Jung, W.-S., Kim, J.-H., Kim, H.-T., & Yoon, D.-H. (2010). Effect of temperature schedule on the particle size of barium titanate during solid-state reaction. *Materials Letters*, 64(2), 170-172.
12. Kainz, T., Naderer, M., Schütz, D., Fruhwirth, O., Mautner, F.-A., & Reichmann, K. (2014). Solid state synthesis and sintering of solid solutions of BNT-xBKT. *Journal of the European Ceramic Society*, 34(15), 3685-3697.
13. Kim, C.-Y., Sekino, T., Yamamoto, Y., & Niihara, K. (2005). The synthesis of lead free ferroelectric Bi^{1/2}Na^{1/2}TiO₃ thin film by solution-sol-gel method. *Journal of sol-gel science and technology*, 33, 307-314.

14. König, J., & Suvorov, D. (2015). Evolution of the electrical properties of $\text{K}_0.5\text{Bi}_0.5\text{TiO}_3$ as a result of prolonged sintering. *Journal of the European Ceramic Society*, 35(10), 2791-2799.
15. Kumar, D., Yadav, R. S., Singh, A. K., & Rai, S. B. (2020). Synthesis techniques and applications of perovskite materials. *Perovskite Materials, Devices and Integration*.
16. Lencka, M. M., Oledzka, M., & Riman, R. E. (2000). Hydrothermal synthesis of sodium and potassium bismuth titanates. *Chemistry of materials*, 12(5), 1323-1330.
17. Mishra, A., Khatua, D. K., De, A., Majumdar, B., Frömling, T., & Ranjan, R. (2019). Structural mechanism behind piezoelectric enhancement in off-stoichiometric $\text{Na}_{0.5}\text{Bi}_{0.5}\text{TiO}_3$ based lead-free piezoceramics. *Acta Materialia*, 164, 761-775.
18. Parija, B., Badapanda, T., Senthil, V., Rout, S., & Panigrahi, S. (2012). Diffuse phase transition, piezoelectric and optical study of $\text{Bi}_{0.5}\text{Na}_{0.5}\text{TiO}_3$ ceramic. *Bulletin of Materials Science*, 35, 197-202.
19. Pookmanee, P., Rujijanagul, G., Ananta, S., Heimann, R. B., & Phanichphant, S. (2004). Effect of sintering temperature on microstructure of hydrothermally prepared bismuth sodium titanate ceramics. *Journal of the European Ceramic Society*, 24(2), 517-520.
20. Popper, P., Ruddlesden, S., & Ingles, T. (1957). Structure and electrical properties of $\text{Bi}_4\text{Ti}_3\text{O}_{12}$ and its application in dielectrics. *Transactions of the British Ceramic Society*, 56, 356.
21. Rahaman, M. N. (2017). *Ceramic processing and sintering* (Vol. 1). CRC press.
22. Reichmann, K., Feteira, A., & Li, M. (2015). Bismuth sodium titanate based materials for piezoelectric actuators. *Materials*, 8(12), 8467-8495.
23. Rémondière, F., Malič, B., Kosec, M., & Mercurio, J.-P. (2007). Synthesis and crystallization pathway of $\text{Na}_{0.5}\text{Bi}_{0.5}\text{TiO}_3$ thin film obtained by a modified sol-gel route. *Journal of the European Ceramic Society*, 27(13-15), 4363-4366.
24. Rödel, J., Jo, W., Seifert, K. T., Anton, E. M., Granzow, T., & Damjanovic, D. (2009). Perspective on the development of lead-free piezoceramics. *Journal of the American Ceramic Society*, 92(6), 1153-1177.
25. Rödel, J., & Li, J.-F. (2018). Lead-free piezoceramics: Status and perspectives. *MRS Bulletin*, 43, 576-580.
26. Smolenskii, G. (1961). New ferroelectrics of complex composition. IV. *Soviet Physics-Solid State*, 2, 2651-2654.

27. Takenaka, T., Nagata, H., & Hiruma, Y. (2008). Current developments and prospective of lead-free piezoelectric ceramics. *Japanese Journal of Applied Physics*, 47(5S), 3787.
28. Uchino, K. (2018). *Ferroelectric devices*. CRC press.
29. West, D. L., & Payne, D. A. (2003). Microstructure Development in Reactive-Templated Grain Growth of Bi_{1/2}Na_{1/2}TiO₃-Based Ceramics: Template and Formulation Effects. *Journal of the American Ceramic Society*, 86(5), 769-774.
30. Xia, F., & Yao, X. (2001). The role of PbO content on the dielectric and piezoelectric properties of PZN-based Ceramics. *Journal of materials science*, 36, 247-253.
31. Xu, Q., Chen, S., Chen, W., Huang, D., Zhou, J., Sun, H., & Li, Y. (2006). Synthesis of (Na_{0.5} Bi_{0.5}) TiO₃ and (Na_{0.5} Bi_{0.5})_{0.92} Ba_{0.08} TiO₃ powders by a citrate method. *Journal of materials science*, 41, 6146-6149.
32. Zaremba, T. (2003). Application of thermal analysis to study of the synthesis of K_{0.5} Bi_{0.5} TiO₃ ferroelectric. *Journal of thermal analysis and calorimetry*, 74(2), 653-658.

Chapter 15

SMALL HORIZONTAL AXIS WIND TURBINE: A CASE STUDY

Kemal ERMIŞ¹
Mehmet ÇALIŞKAN²
Murat KARABEKTAŞ³

1. INTRODUCTION

Most of the world's energy demand is met from fossil fuel sources. With the increase in population and use of technology, the use of fossil fuels as an energy source is constantly increasing. Using fossil fuels, CO₂ and unhealthy emissions pollute our atmosphere. This increase is rapidly depriving us of livable, clean environmental conditions. Air pollution creates a greenhouse gas effect, causing the world's natural temperature to increase constantly, natural disasters to increase, and balance to be disrupted (Ermiş & Ünal, 2023). It has become clear that the energy needs must be met and this energy production must be done without polluting our atmosphere. The only way to best meet this need is to use renewable energy sources such as the sun, wind, and ocean. One of the best ways is to install wind turbines in windy areas. In recent years, great importance has been given to electricity production from renewable energy sources to reduce environmental pollution, which has increased due to climate changes, and to obtain a more efficient solution. Wind turbines are highly preferred as renewable energy because they do not cause environmental pollution.

Small wind turbines are defined by the International Electrotechnical Commission (IEC 61400-2:2013|IEC Webstore | Rural Electrification, Wind Power, n.d.) for both grid-connected and off-grid applications as having a rotor-swept area equal to or less than 200 m²; that is, they produce electricity at a voltage of less than 1000 V (AC) or 1500 V (DC). Wind energy today constitutes the fastest growing renewable energy source with an annual growth rate of approximately 30%. Over the last 20 years, the size of wind turbines has

¹ Prof. Dr.; Sakarya University of Applied Sciences, Dept. of Mechanical Engineering, Sakarya / Türkiye, ORCID No: 0000-0003-3110-2731

ermis@subu.edu.tr

² Prof. Dr.; Sakarya University of Applied Sciences, Dept. of Mechanical Engineering, Sakarya, Türkiye, ORCID No: 0000-0002-7835-9414

³ Prof. Dr.; Sakarya University of Applied Sciences, Dept. of Mechanical Engineering, Sakarya, Türkiye. ORCID No: 0000-0002-1025-1431

increased from a rotor diameter of approximately 30 m to 150 m; This corresponds to a more than 25-fold increase in power (Schaffarczyk, 2014). Unlike larger utility-scale turbines, microscale/small wind turbines typically have hub heights below 30 m and produce power between 300 W and 10 kW at rated wind speeds. Due to their size, these wind turbines have much greater flexibility in terms of price, maintenance, and location. They can produce wind energy in locations that are much less suitable for direct distribution to the grid system (Ashtine et al., 2016).

Generally, wind turbines are divided into two main types: horizontal and vertical. There are some studies in the literature about wind horizontal turbines. Some of these publications are related to small-scale horizontal axis wind turbine design (Khaled, M., Ibrahim, M. M., Hamed, H. A., & Gawad, n.d.) (Ermis et al., 2022) (Nongdhar et al., 2018) (Umar et al., 2022) (Zidane & Mahmood, 2023), aerodynamic analysis (Suresh & Rajakumar, 2020) (Schaffarczyk, 2014) (Brahimi & Paraschivoiu, 2022) (Saeidi et al., 2013) (Cai et al., 2012) (Tanguilig & Danao, 2017) (Bai et al., 2013) (Liu et al., 2017), optimization and blade performance (Akbari et al., 2022) (Gerhard et al., 2013) (Scappatici et al., 2016) (Pathike et al., 2013) (Muhsen et al., 2019) (Rehman et al., 2018) (Kumar et al., 2018), experimental studies (Abdelsalam et al., 2021) (Lee et al., 2016) (Huang et al., 2015) and review (Karthikeyan et al., 2015) (Tummala et al., 2016).

In this chapter, wind turbine types and their features are examined. The case study on small-scale horizontal axis wind turbine design and installation was carried out at Sakarya University of Applied Sciences, Faculty of Technology, Sakarya province. A small wind turbine designed with 1.5 kW power and three blades was installed in a suitable location. The entire procedure is explained in detail. A static analysis of the wind turbine carrier pole was made using the ANSYS program. Flow analysis of wind turbine blades is done with the ANSYS program.

2. SMALL WIND TURBINE

Wind turbines are mechanical devices that convert the kinetic energy of fast-moving winds into electrical energy. The energy converted is determined by the rotational axis of the blades. Wind energy is an important energy source that is environmentally friendly. In recent years, the use of wind energy has become increasingly important due to the pollution of the atmosphere from the use of fossil fuels. Small wind turbines, also known as urban wind turbines or micro wind turbines, are wind turbines that produce electricity for small-scale use. Small-scale turbines are generally smaller than turbines in wind farms. Small-scale wind turbines use a directly driven generator and use a tail fin to point

downwind, whereas larger turbines have geared drivetrains actively oriented downwind. Small wind turbines often have passive deflection systems as opposed to active ones. They generally produce power between 300 W and 10 kW, some as small as 50 W.

There are many different types of wind turbines, depending on the direction of their rotation axis. They can be divided into two main groups: horizontal axis wind turbines (HAWTs) and vertical axis wind turbines (VAWTs) as shown in Figure 1. Turbines that rotate around a horizontal axis are more common. Vertical-axis turbines are less commonly used. Wind turbines can also be classified according to where they will be used. Onshore, offshore, and even aerial wind turbines have distinct design characteristics.

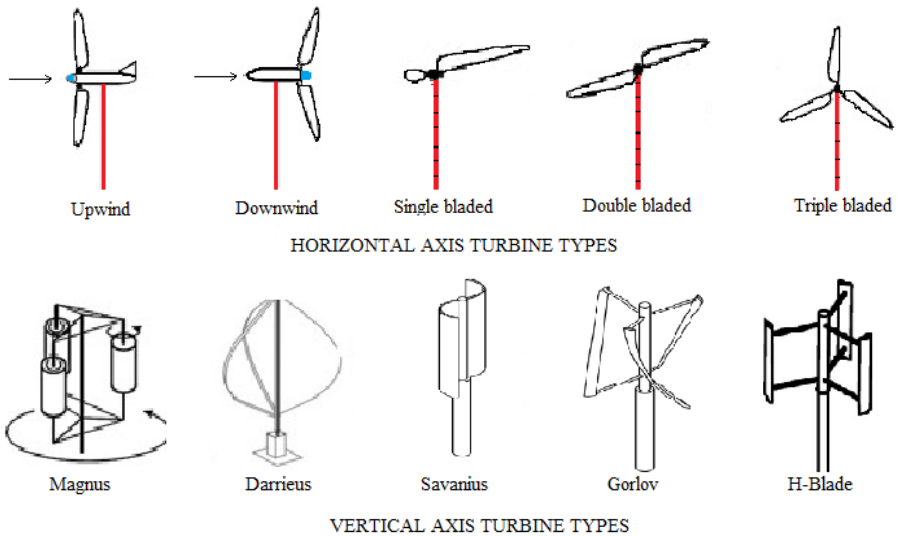


Figure 1: Wind turbine types

Wind turbines have five major components. These are the foundation, tower, rotor, nacelle and generator. Figure 2 shows the typical components of a wind power generator. (*What Is Wind Energy? Definition, Types and More*, n.d.)



Figure 2: The typical components of a wind power generator (Source: bilderzweg - stock.adobe.com)

According to the Global Wind Report, 2022 was another record-breaking year for wind installations, particularly in the fast-growing offshore wind industry, with a total of 94 GW of wind installed worldwide, including 21 GW offshore. The 93.6 GW of new installations in 2021 brings global cumulative wind power capacity to 837 GW, showing year-over-year growth of 12% (Global Wind Report 2022). Global electricity generation by source according to the Announced Pledges Case (APC) is shown in Figure 3. (*Net Zero by 2050 – Analysis - IEA, n.d.*)

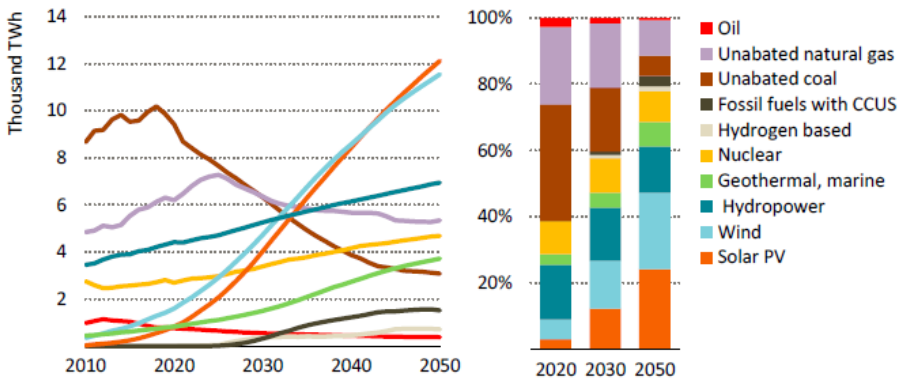


Figure 3: Global electricity generation by source in the Announced Pledges Case (Source: IEA Net Zero by 2050).

The Articulated Commitment Case (APC) assumes that all announced national net zero commitments are met in full and on time, regardless of whether they are already supported by specific policies. Global energy-related and industrial process CO₂ emissions are projected to fall by 30 Gigatonnes in 2030 and 22 Gigatonnes in 2050. Global electricity production will almost double to exceed 50,000 Terawatt-hours by 2050. The share of renewable energy in electricity production will rise to almost 70% by 2050. (*Net Zero by 2050 – Analysis* - IEA, n.d.). It is clearly seen from Figure 3 that the use of solar photovoltaic panels and wind energy will increase between 2020-2050 and will contribute greatly to electrical energy production.

According to Global Wind Energy Council (GWEC) Market Intelligence; wind energy assumes a Compound Annual Growth Rate of ~6.6-7.0% based on a projected Compound Annual Growth Rate (CAGR) for 2021-2026. International Energy Agency (IEA)'s Net Zero Roadmap to 2050 includes wind (35%), solar (33%), hydropower (12%), nuclear (8%), bioenergy (5%), hydrogen-based (2%) reveals the global electricity production mix. By 2050, it will consist of 8,174 GW of wind and 14,878 GW of solar energy; wind produces a slightly higher overall share of global electricity. The rest consists of hydroelectricity, bioenergy, geothermal, tidal/wave, and hydrogen-based production. The wind energy roadmap is shown in Figure 4 (*Global Wind Report 2022 - Global Wind Energy Council, n.d.*).

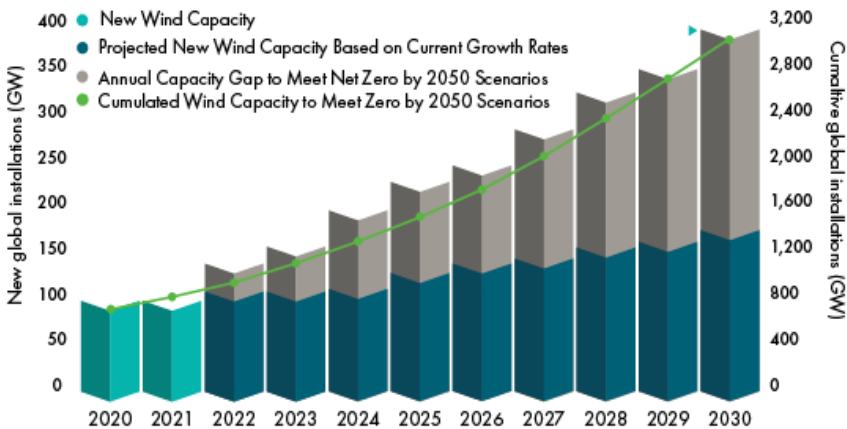


Figure 4: Wind energy roadmap (Source GWEC Market Intelligence; IEA Net Zero by 2050 Roadmap (2021))

A summary of the most important differences between the three turbines are shown in Table 1 (Eriksson et al., 2008).

Table 1: Summary of the most important differences between the three turbines

	H-blade	Darrieus	HAWT
Blade profile	Simple	Complicated	Complicated
Yaw the mechanism needed	No	No	Yes
Pitch mechanism possible	Yes	No	Yes
Tower	Yes	No	Yes
Guy wires	Optional	Yes	No
Noise	Low	Moderate	High
Blade area	Moderate	Large	Small
Generator position	On ground	On ground	On top of the tower
Blade load	Moderate	Low	High
Self-starting	No	No	Yes
Tower interference	Small	Small	Large
Foundation	Moderate	Simple	Extensive
Overall structure	Simple	Simple	Complicated

Small wind turbines generally produce power between 300 W and 10 kW. Table 2 shows the size ranges suited to different small wind applications.

Table 2: Different small wind applications

Market Segment	Size	Applications		
Battery charging, <i>Off-grid</i>	<5 kW	Small remote sites, Area lighting Navigation, Telecommunications, Pumps/irrigation systems, Light seasonal loads		
Residential, Small farm, <i>Grid-connected</i>	1-10 kW	Small Farm, Residential, Small business, Heavy seasonal loads		
According to operating parameters				
Category	Size	rotor radius (m)	Maximum rotor speed (rpm)	Applications
Micro	1 kW	1.5	700	Electric fences, yachts
Mid-range	5 kW	2.5	400	Remote houses
Mini	+20 kW	5	200	Mini-grids, remote communities

3. WIND TURBINE THEORY

The wind is expected to slow down by reducing some of the kinetic energy coming to the wind turbine, but only the air mass passing through the rotor disc slows down. Assuming that the affected air mass remains separate from the air that does not pass and slow down through the rotor disk of the wind turbine, a boundary surface containing the affected air mass can be drawn. This boundary can be extended upstream and downstream as a circular cross-section flow tube

to form a long boundary. As seen in Figure 5, there is no airflow across the boundary and hence the mass flow rate of air flowing through the flow tube will be the same for all positions in the direction of flow along the flow tube. As the air in the flow tube is slowed but not compressed, the cross-sectional area of the flow tube expands to accommodate the slower-moving air.

Estimating the available wind energy at the location where the wind turbine is located is one of the first steps in planning a wind energy project. It describes the wind assessment technique and explains its relationship with energy production (Wais, 2017).

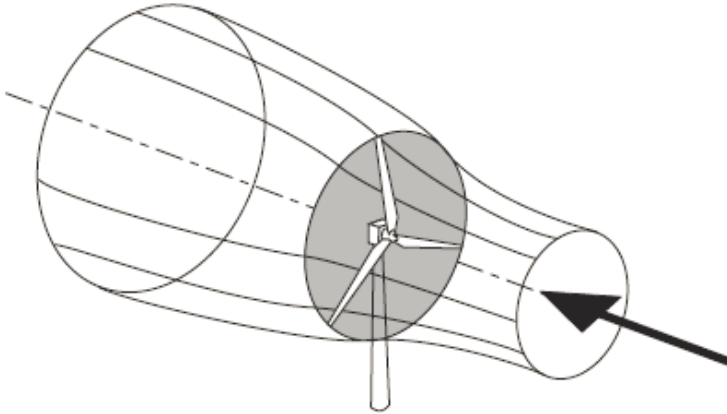


Figure 5: The energy extracting stream tube of a wind turbine

To calculate wind energy statistically, you must first understand the distribution of wind speeds in a certain region. It is critical to correctly determine the probability distribution of wind speed data when calculating wind speed energy in a location. Although various wind speed distribution models are used to fit the wind speed to a certain period, the two-parameter Weibull function is widely used. Furthermore, annual energy production is evaluated according to international standards using the Rayleigh distribution, which is identical to the Weibull distribution and has a shape factor of 2. The approach in question is used to assess a system's power performance characteristics. It offers a consistent process that ensures consistency and precision. At constant velocity u , the available power P_{Av} of the free-air stream flowing mass flow rate \dot{m} through the cross-sectional area A_C is:

$$P_{Av} = \frac{1}{2} \dot{m} u^2 \tag{1}$$

$$\dot{m} = \rho \cdot Q = \rho A_C u \tag{2}$$

$$P_{Av} = \frac{1}{2} \rho A_C u^3 \quad \text{where } A_C = \frac{\pi D^2}{4} \tag{3}$$

where ρ is the air density, Q is the volume flow passing through the given cross-section and D is the turbine rotor diameter.

Factors affecting the available power in the wind stream are air density, area of the wind rotor, and wind speed. It is clearly understood from the equations above that the effect of wind speed on wind power is very large. Since small changes in wind speed cause significant changes in energy production, determining the location of wind turbine installation is important. Since the wind speed changes, the frequency distribution needs to be known. Wind speed distribution determines the available wind energy and the performance of the energy conversion system depending on the location of the wind turbine. The wind speed and frequency, u_i , available wind power, and energy can be estimated by summing the energy corresponding to all possible wind speeds for the period of time by using the following equations.

$$t_i = p(u_i)t_{period} \quad (4)$$

$$P_{Av,i} = \frac{1}{2} \rho A_c \sum_{i=1}^n p(u_i) u_i^3 \quad (5)$$

$$E_{Av,i} = \frac{1}{2} \rho A_c t_{period} \sum_{i=1}^n p(u_i) u_i^3 \quad (6)$$

The above equations can be used to directly determine available wind energy and wind power from data. Statistical calculation of wind energy requires knowing the distribution of wind speeds in a particular region. Correctly determining the probability distribution of wind speed values is very important in evaluating the wind speed energy in a region. Obtaining at least ten years of wind data to determine the wind energy potential of a region increases the reliability of the analysis to be performed. It is quite common to use some probability density functions to reach wind energy potential using short-term data. The most frequently used statistical method in such research is the Weibull probability distribution function. Although different wind speed distribution models are applied to fit the wind speed to a specific time period, the two-parameter Weibull function is considered the most popular technique. It has been widely used by researchers who analyze both wind speed and wind energy for many years. Annual energy production is estimated by applying a Rayleigh distribution similar to the Weibull distribution with a form factor of 2. This process is used to measure the power performance characteristics of a single wind turbine generator system and provides a uniform methodology, ensuring consistency and accuracy in measuring and analyzing the power performance of

wind turbines. The two-parameter Weibull probability density function, $p(u)$ can be written as;

$$p(u) = \frac{k}{c} \left(\frac{u}{c}\right)^{k-1} \exp\left[-\left(\frac{u}{c}\right)^k\right] \quad (7)$$

where u is the wind speed, c is the Weibull scale parameter, and k is the Weibull shape parameter.

To determine the Weibull parameters, the moment method using the average wind speed and standard deviation values was used. Accordingly, the equations giving the Weibull parameters k and c are respectively.

$$k = \left(\frac{\sigma}{u_m}\right)^{-1.086} \quad 1 \leq k \leq 10 \quad (8)$$

$$c = \frac{u_m}{\Gamma\left(1 + \frac{1}{k}\right)} \quad (9)$$

$$u_m = \frac{1}{n} \left[\sum_1^n u_i \right] \quad \text{and} \quad \sigma = \left[\frac{1}{n-1} \sum_1^n (u_i - u_m)^2 \right] \quad (10)$$

where u_m is the average wind speed, σ is the standard deviation, Γ is the gamma function. The average wind speed and standard deviation are respectively.

Once the wind velocities and distribution are known, the total available wind power can be stated as knowing the probability $p(v)$ for which the wind velocity is v and A is the scale parameter (Wais, 2017).

The available wind power as:

$$P_{Av} = \frac{1}{2} \rho A_C k \frac{1}{A^k} \int_0^\infty (u)^{k+2} e^{-\left(\frac{u}{A}\right)^k} du \quad (11)$$

The wind energy as:

$$E_{Av,i} = P_{Av} t_{period} \quad (12)$$

3.1. Turbine blade aerodynamics

The wing sections of modern wind turbines are selected with special airfoils developed to obtain optimum power from the loads occurring on the wing during flow. The aim of developing this special airfoil is to improve the resulting lift force. In their most general form, profiles consist of a combination of two specific curves defined above and below a beamline. Since the upper curve has a more humped form than the lower curve, and the surface length of the upper side of the wing is longer, different fluid velocities occur on both sides. Since the airspeed

at the top of the wing is high, the pressure at the top is lower than at the bottom. Therefore, a pressure difference occurs, and a lifting force is created from the high pressure towards the low-pressure direction. An example profile located in a free stream, with a beamline and an a_h of attack angle between the fluid velocity and the forces acting on it, can be seen in Figure 6. The drag force, F_D , that will occur due to flow is always parallel to the flow direction. The other force generated the lift force, F_L , is in the direction perpendicular to the flow and the drag force. The force that rotates the wind turbine is the result of these two forces. Below are these related equations.

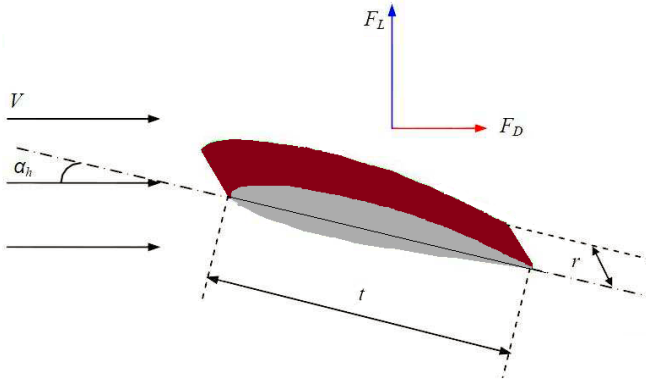


Figure 6: Forces on the airfoil profile

$$F_L = 0,5 C_L \rho A V^2 \quad (13)$$

$$F_D = 0,5 C_D \rho A V^2 \quad (14)$$

where C_L is the lift coefficient, C_D is the drag coefficient, A ($A=t.r$) is the upper surface area of the airfoil and V is the air speed.

For low-velocity flow with a given relative roughness, C_L and C_D must vary with the attack angle (a_h) and the beam-based Reynolds number.

$$C_L = f(a_h Re) \quad \text{and} \quad C_D = f(a_h Re) \quad (15)$$

To determine the profile characteristic, a dimensionless number called the slip number (ε) is defined, which is given by the ratio of the lift force to the drag force.

$$\varepsilon = \frac{C_L}{C_D} \quad (16)$$

C_L , C_D , ε values of the profiles are obtained by experimental methods for a

certain Reynolds number and different angles of attack. These data, traditionally referred to as Polar Curves, determine the quality of the profile. The dimensions of the turbine to be installed to obtain energy from the wind are directly related to the aerodynamic structure. No matter how ideal the system is, there is an upper limit to the energy that can be obtained from the wind. This limit is called the Betz limit. When the Betz limit is calculated, the maximum power coefficient (c_p) is found to be 0.5926. This value is the theoretical upper limit of the energy that can be extracted from the wind under ideal environmental conditions. Under ideal operating conditions, the rotor can only benefit from 2/3 of the freely flowing wind. However, in practical use, it is difficult to reach this limit since the desired ideal working conditions cannot be achieved. The main reasons for this are; Circular waves behind the rotor, a limited number of blades, wing tip losses and aerodynamic drag.

4- CASE STUDY OF SMALL HORIZONTAL WIND TURBINE

In this case study; includes the stresses on the blade, the amount of deformation, and aerodynamic analysis for a horizontal axis 3-blade small horizontal wind turbine (HAWT) established at Sakarya University of Applied Sciences, Faculty of Technology in Sakarya-Turkey as shown in Figure 7. The small wind turbine was established having a 1.5 kW power capacity and 6 meters of hub height.



Figure 7: Picture of the small wind turbine

First of all, the wing design for the semi-drop structure NACA N-11 was made using the SolidWorks program. Polar curves for the N-11 airfoil are shown in Figure 8.

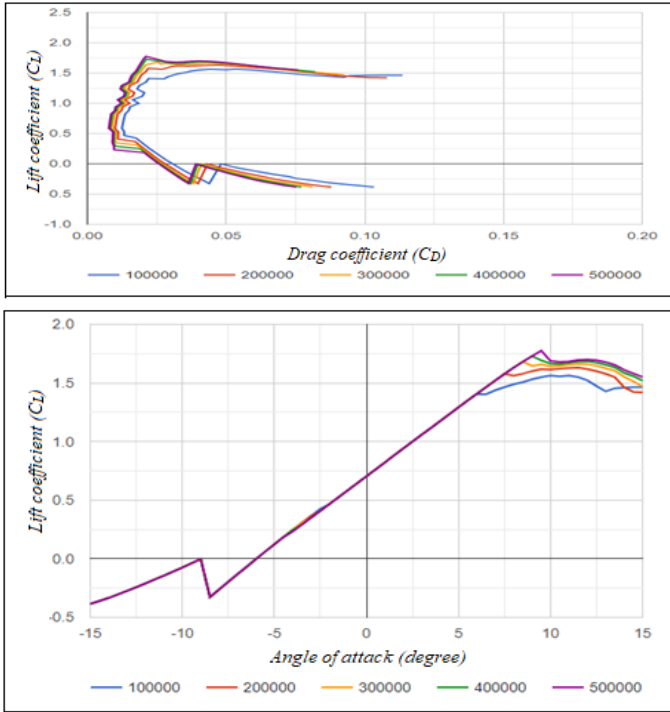


Figure 8: Polar curves for N-11 airfoil for different Reynolds number

For the flow analysis of this wing design, the highest wind speed that occurred in Sakarya province Serdivan district, Sakarya University of Applied Science campus in history was determined from meteorological data and average inputs were taken from these values. For the maximum pressure value obtained using ANSYS Workbench, the amount of stress and total deformation occurring in both the composite material and the airfoil structure and their aerodynamic values were found.

4.1. Wind Turbine Blade Modeling

Wind turbine blade modeling was done on the computer using the SolidWorks program. The dimensions used during the drawing are the N11 airfoil of wind turbine prototype dimensions. To form the airfoil shape, the points of the unit length drop model in the coordinate system were used. Then, by assigning planes along 1 m, drop models with different court lengths were drawn for each plane, and they were combined to create a wing blade shape by entering the wall thickness with the Loft command. To add an airfoil support profile, a plane is created and the support profile the Sketch is drawn on this plane, and the support profile the Sketch drawn on the inner surfaces is created with the add separation

line command. The wind airfoil support profile is created by the joining process. The blade model created can be seen in Figure 9.

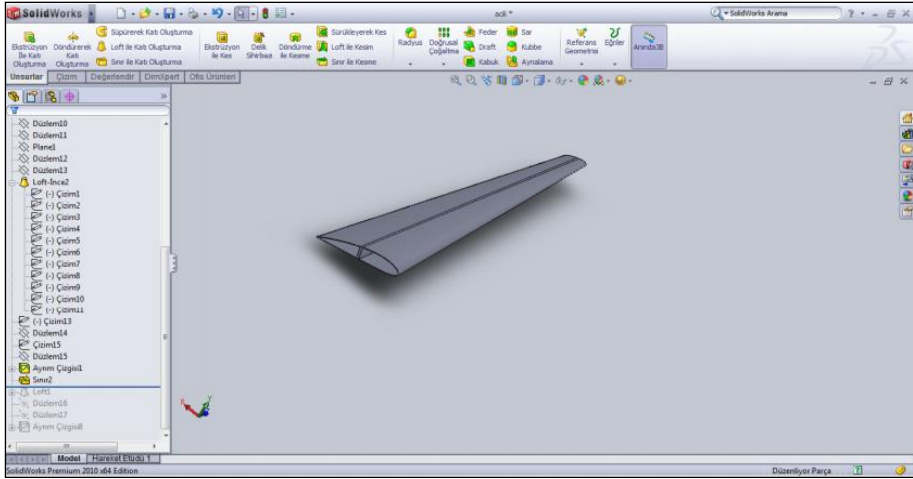


Figure 9: Blade shape with support profile drawn in SolidWorks

4.2. Flow analysis

Before performing flow analysis, the air volume inside the wind turbine blade is modeled. In this modeling, the wind turbine blade in the form of a drop (airfoil) model is placed at point G, as shown in Figure 10.

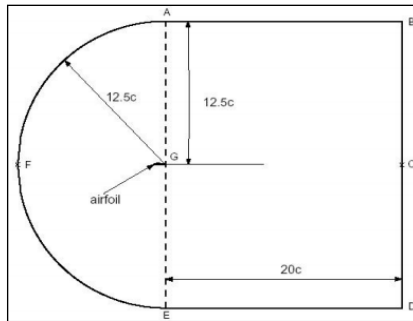


Figure 10: Air volume modeling benchmark

Taking the G point as the criterion, the modeling parameters were measured and measured as shown in Figure 10. The 3D drawing of the air volume, measured by taking its parameters as a criterion, was made in the SolidWorks program. Figure 11 shows how the wind turbine blade is modeled within the air volume. Modeling was made by taking the data in Figure 10 and positioning the wind turbine blade at point G.

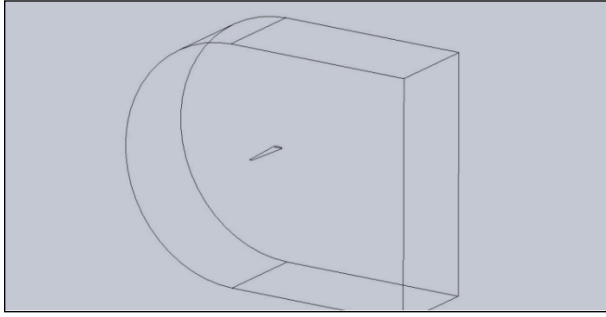


Figure 11: Showing the wing within the modeled air volume

The air volume modeled in the Solidworks program was imported into the ANSYS Workbench flow analysis program. Taking into account the weather data of previous years taken from the archives of the meteorology directorate, the entrance wind speed was accepted as 33.3 km/h, which is the maximum value in the Esentepe region of Sakarya province. The flow of wind in the modeled air volume is given in Figure 12 below.

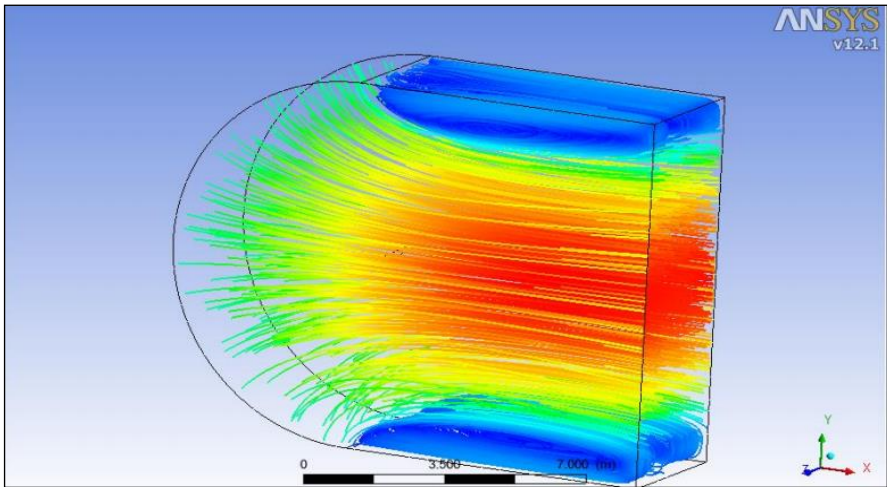


Figure 12: Wind flow in the modeled air volume

The pressures occurring in the wind turbine blade were found with the help of the ANSYS program. The maximum pressure created by the wind on the wing was found to be 3.618 kPa as a result of the analysis, as seen in Figure 13.

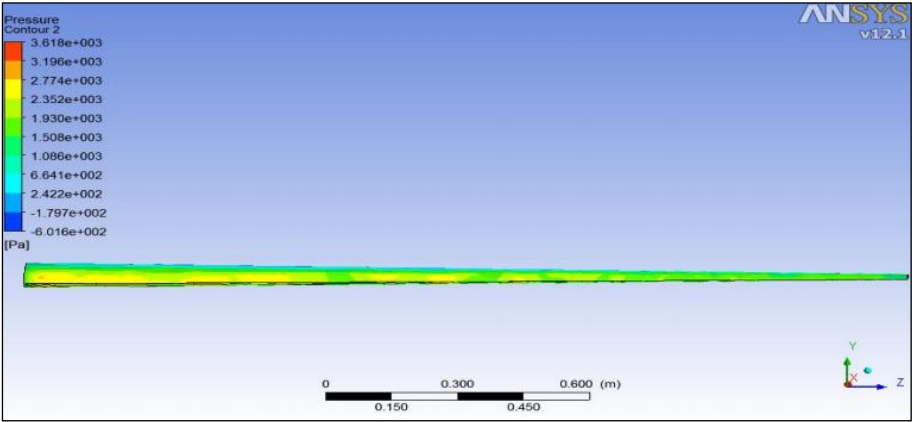


Figure 13: Maximum pressure in the wing section for wind direction

4.3. Wind blade static analysis

Wind blade static analysis the ANSYS program of the blade was made. The properties of the material are defined using the Engineering Data section. In static analysis, total deformation and Equivalent Stress (Von-Mises) were performed. The total amount of deformation was determined to be a maximum of 86.319 mm, as shown in Figure 14, and the maximum Equivalent Stress (Von-Mises) occurring on the wing blade was found to be 380.28 MPa, as shown in Figure 15.

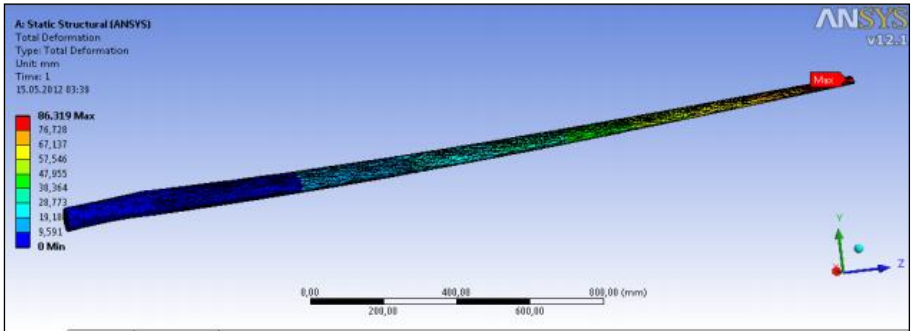


Figure 14: Total deformation analysis of the wing blade

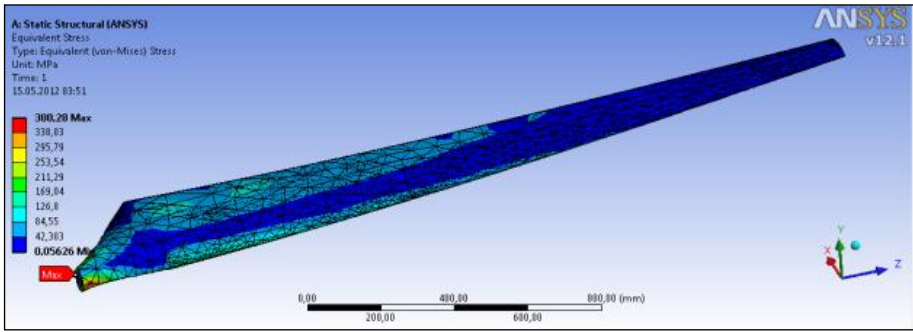


Figure 15: Equivalent Stress (Von-Mises) analysis of the wing blade

Flow analysis was carried out on a wind turbine installed at Sakarya University of Applied Science, Sakarya, with a rated power of 1.5 kW, a height of 6 m, a wing profile of NACA N-11 and a blade length of 1 m. Figure 16 shows wind power and mechanical power according to entry speed. According to data received from meteorology in the region, the wind speed was measured around 10 m/s. According to the graph, wind power at 10 m/s was read as 2750 W and mechanical power as 1121 W. These values coincide with the values we expected.

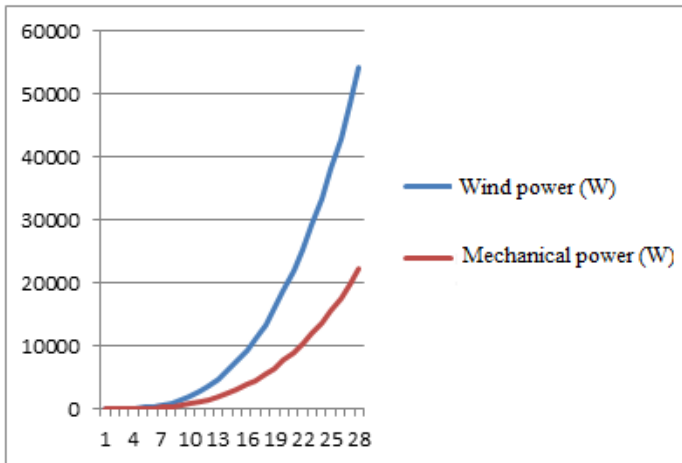


Figure 16: Wind power and mechanical power according to wind speed

As a result of the analysis, the efficiency of the designed turbine was found to be around 40%, as seen in Figure 16.

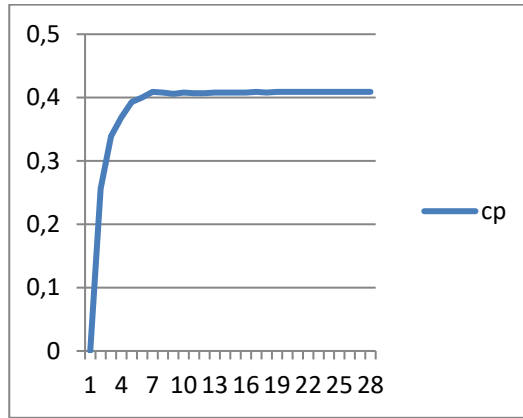


Figure 16: Efficiency (cp, power coefficient) change according to wind speed

5. Conclusions

In this chapter, wind turbine types and their features are examined. Small horizontal wind turbines were investigated by using wind turbine theory details. In the case study, the small wind turbine, having 1.5 kW power capacity, NACA N11 airfoil profile, and 6 meters of hub height was established at Sakarya University of Applied Sciences, Faculty of Technology in Sakarya-Turkey. The entire procedure is explained in detail.

A static analysis of the wind turbine carrier pole was made using the ANSYS program. Flow analysis of wind turbine blade is done with the ANSYS program. Wind turbine blade modeling is explained and The Equivalent Stress (Von-Mises) method and the total deformation of the wind turbine blades were analyzed. The total amount of deformation was determined as a maximum of 86.319 mm and the maximum stress is 380.28 MPa. The wind speed was measured around 10 m/s. According to the graph, wind power at 10 m/s was read as 2750 W and mechanical power as 1121 W. As a result of the analysis, the efficiency of the designed turbine was found to be around 40%.

Acknowledgment

The authors thank Beytullah Başsedir (Mech. Eng.), Caner Doğru (Mech. Eng.), Emre Kum (Mech. Eng.), Mücahit Gündüz (Mech. Eng.), Uğur Kaya (Mech. Eng.) for helping establish the wind turbine.

REFERENCES

- 1- Abdelsalam, A. M., El-Askary, W. A., Kotb, M. A., & Sakr, I. M. (2021). Experimental study on small scale horizontal axis wind turbine of analytically-optimized blade with linearized chord twist angle profile. *Energy*, 216, 119304.
- 2- Akbari, V., Naghashzadegan, M., Kouhikamali, R., Afsharpanah, F., & Yaïci, W. (2022). Multi-Objective Optimization and Optimal Airfoil Blade Selection for a Small Horizontal-Axis Wind Turbine (HAWT) for Application in Regions with Various Wind Potential. *Machines*, 10(8), 687.
- 3- Ashtine, M., Bello, R., & Higuchi, K. (2016). Feasibility of small wind turbines in Ontario: Integrating power curves with wind trends. *Resources*, 5(4), 1–14.
- 4- Bai, C. J., Hsiao, F. B., Li, M. H., Huang, G. Y., & Chen, Y. J. (2013). Design of 10 kW Horizontal-Axis Wind Turbine (HAWT) Blade and Aerodynamic Investigation Using Numerical Simulation. *Procedia Engineering*, 67, 279–287.
- 5- Brahim, T., & Paraschivoiu, I. (2022). Aerodynamic Analysis and Performance Prediction of VAWT and HAWT Using CARDAAV and Qblade Computer Codes. *Entropy and Exergy in Renewable Energy*.
- 6- Cai, X., Zhu, J., Pan, P., & Gu, R. (2012). Structural optimization design of horizontal-axis wind turbine blades using a particle swarm optimization algorithm and finite element method. *Energies*, 5(11), 4683–4696.
- 7- Eriksson, S., Bernhoff, H., & Leijon, M. (2008). Evaluation of different turbine concepts for wind power. *Renewable and Sustainable Energy Reviews*, 12(5), 1419–1434.
- 8- Ermis, K., & Toklu, E. (2022). Design and Establishment of a Small Wind Turbine. *Journal of Engineering Research and Applied Science*, 11(2), 2084–2092.
- 9- Ermiş, K., & Ünal, H. (2023). Investigation of hydrogen production from renewable energy sources. In A. N. (Prof. Dr.) ÖZKER (Ed.), 5th International Black Sea Modern Scientific Research Congress (p. 488). Liberty Academic Publishers, New York, USA.
- 10- Gerhard, T., Sturm, M., & Carolus, T. H. (2013). Small horizontal axis wind turbine: Analytical blade design and comparison with RANS-prediction and first experimental data. *Turbo Expo: Power for Land, Sea, and Air*, 55294, V008T44A005.
- 11- Global Wind Report 2022 - Global Wind Energy Council. (n.d.). Retrieved December 6, 2023, from <https://gwec.net/global-wind-report->

2022/

- 12- Huang, G.-Y., Shiah, Y. C., Bai, C.-J., & Chong, W. T. (2015). Experimental study of the protuberance effect on the blade performance of a small horizontal axis wind turbine. *Journal of Wind Engineering and Industrial Aerodynamics*, 147, 202–211.
- 13- IEC 61400-2:2013 | IEC Webstore | rural electrification, wind power. (n.d.). Retrieved December 4, 2023, from <https://webstore.iec.ch/publication/5433&preview>
- 14- Karthikeyan, N., Kalidasa Murugavel, K., Arun Kumar, S., & Rajakumar, S. (2015). Review of aerodynamic developments on small horizontal axis wind turbine blade. *Renewable and Sustainable Energy Reviews*, 42, 801–822.
- 15- Khaled, M., Ibrahim, M. M., Hamed, H. A., & Gawad, A. F. A. (n.d.). Aerodynamic design and blade angle analysis of a small horizontal-axis wind turbine. *American Journal of Modern Energy*, 3(2), 23–27.
- 16- Kumar, M. S., Krishnan, A. S., & Vijayanandh, R. (2018). Vibrational fatigue analysis of NACA 63215 small horizontal axis wind turbine blade. *Materials Today: Proceedings*, 5(2), 6665–6674.
- 17- Lee, M.-H., Shiah, Y.-C., & Bai, C.-J. (2016). Experiments and numerical simulations of the rotor-blade performance for a small-scale horizontal axis wind turbine. *Journal of Wind Engineering and Industrial Aerodynamics*, 149, 17–29.
- 18- Liu, X., Lu, C., Li, G., Godbole, A., & Chen, Y. (2017). Effects of aerodynamic damping on the tower load of offshore horizontal axis wind turbines. *Applied Energy*, 204, 1101–1114.
- 19- Muhsen, H., Al-Kouz, W., & Khan, W. (2019). Small wind turbine blade design and optimization. *Symmetry*, 12(1), 18.
- 20- Net Zero by 2050 – Analysis - IEA. (n.d.). Retrieved December 8, 2023, from <https://www.iea.org/reports/net-zero-by-2050>
- 21- Nongdhar, D., Goswami, B., Gogoi, P., & Borkataky, S. (2018). Design of Horizontal Axis Micro Wind Turbine for Low Wind Speed Areas. *ADBU Journal of Electrical and Electronics Engineering (AJEEE)*, 2(2), 39–47.
- 22- Pathike, P., Katpradit, T., Terdtoon, P., & Sakulchangsatjatai, P. (2013). A new design of blade for small horizontal-axis wind turbine with low wind speed operation. *Energy Research*, 4(1), 1–7.
- 23- Rehman, S., Alam, M. M., Alhems, L. M., & Rafique, M. M. (2018). Horizontal axis wind turbine blade design methodologies for efficiency enhancement—A review. *Energies*, 11(3), 506.

- 24- Saeidi, D., Sedaghat, A., Alamdari, P., & Alemrajabi, A. A. (2013). Aerodynamic design and economical evaluation of site specific small vertical axis wind turbines. *Applied Energy*, 101, 765–775.
- 25- Scappatici, L., Bartolini, N., Castellani, F., Astolfi, D., Garinei, A., & Pennicchi, M. (2016). Optimizing the design of horizontal-axis small wind turbines: From the laboratory to market. *Journal of Wind Engineering and Industrial Aerodynamics*, 154, 58–68. <https://doi.org/10.1016/J.JWEIA.2016.04.006>
- 26- Schaffarczyk, A. P. (2014). *Introduction to Wind Turbine Aerodynamics*.
- 27- Suresh, A., & Rajakumar, S. (2020). Design of small horizontal axis wind turbine for low wind speed rural applications. *Materials Today: Proceedings*, 23, 16–22.
- 28- Tanguilig, N. R. P., & Danao, L. A. M. (2017). A Hybrid CFD-BEM Analysis of the Aerodynamic Performance of a Cut-Out Hollow Pipe Horizontal Axis Wind Turbine Blade. *SCIENCE DILIMAN*, 29(2), 5–31.
- 29- Tummala, A., Velamati, R. K., Sinha, D. K., Indraj, V., & Krishna, V. H. (2016). A review on small scale wind turbines. *Renewable and Sustainable Energy Reviews*, 56, 1351–1371.
- 30- Umar, D. A., Yaw, C. T., Koh, S. P., Tiong, S. K., Alkahtani, A. A., & Yusaf, T. (2022). Design and optimization of a small-scale horizontal axis wind turbine blade for energy harvesting at low wind profile areas. *Energies*, 15(9), 3033.
- 31- Wais, P. (2017). A review of Weibull functions in wind sector. *Renewable and Sustainable Energy Reviews*, 70, 1099–1107.
- 32- What is wind energy? Definition, types and more. (n.d.). Retrieved December 11, 2023, from <https://www.power-and-beyond.com/what-is-wind-energy-definition-types-and-more-a-e95f3c16c898e889f0757f62ee91038d/>
- 33- Zidane, O. K., & Mahmood, Y. H. (2023). Small Horizontal Wind Turbine Design and Aerodynamic Analysis Using Q-Blade Software. *Baghdad Science Journal*, 20(5), 1772–1778.

Chapter 16

The Role of Sensors and Encoders in Exoskeleton Technologies

Melih CANLIDİNÇ¹

Mustafa GÜLEŞEN²

INTRODUCTION

Sensors are crucial in exoskeletons for gathering vital information from the environment and the user, influencing their functionality significantly. The data required varies depending on the exoskeleton's design, control mechanisms, and operational mode. Different body parts like lower or upper limbs need specific sensory inputs for effective control.

A range of sensors, including force, torque, pressure, muscle and neuronal activity sensors (e.g., EMG, EEG), bending sensors, inertial measurement units (IMU), cameras, and encoders, are integral in exoskeletons. They measure physical properties like position, displacement, rotation, and muscle activation.

In lower limb exoskeletons, extensively researched for their role in gait analysis, sensors ensure the device's synchronization with human movements. Commonly used sensors in these exoskeletons include force, torque, pressure sensors, IMUs, EMGs, and encoders, often in multi-sensor configurations (Amici et al., 2020).

Sensing human motion intention is a shared objective across various exoskeletons, including those for upper limbs and hands. The use of biosensors, which detect biological signals such as EMG, has gained popularity. These are crucial for real-time motion intention recognition, often using advanced control algorithms, sometimes based on machine learning (Tiboni et al., 2019).

Cross-analysis reveals dynamic sensors (pressure, force, torque sensors, and IMUs) are most used in hand and upper limb exoskeletons. EEG is explored for detecting brain activity in lower limb exoskeletons, though challenges remain due to brain signal complexity.

The incorporation of sensors is essential for the control of exoskeletons, especially concerning different types of actuators and power sources. Encoders are frequently used alongside DC, SEA, and Brushless actuators. In systems

¹ Arş. Gör. Dr.; Kütahya Dumlupınar Üniversitesi Mühendislik Fakültesi Makine Mühendisliği Bölümü.
melih.canlidinc@dpu.edu.tr ORCID No: 0000-0002-4011-9490

² Dr. Öğr. Üyesi; Kütahya Dumlupınar Üniversitesi Mühendislik Fakültesi Makine Mühendisliği Bölümü.
feridun.karakoc@dpu.edu.tr ORCID No: 0000-0001-8781-2746

with fluidic actuators, pressure sensors are the preferred choice, whereas force sensors are commonly associated with SEAs, VSAs, and torque motors. Torque sensors are typically utilized in conjunction with specific actuators such as linear motors. Bending sensors are employed in applications involving soft-actuators and torque motors. For systems that include hydraulic cylinders and brushless motors, Inertial Measurement Units (IMUs) are predominantly used.

In summary, sensor selection in exoskeletons is influenced by the type of actuator and power source, with different sensors being more suitable for different configurations.

Bending Sensors

Bending sensors are essential in detecting the magnitude and orientation of bending forces in various applications, notably in exoskeletons and wearable electronic devices. These sensors, fundamental for quantifying bending and indirectly measuring other physical quantities like pressure and stress, are versatile due to their flexibility and adaptability to different positions and angles relative to the human body (Jung et al., 2015). They are particularly useful in applications requiring a mix of joint movements, such as glove-exoskeletons for finger movements (Bin Imtiaz et al., 2021).

A bending sensor typically comprises an elastic part for restoring deflection and a rigid part encased in elastic material. This material can form a "Tubular Active Bending Sensor" or a "Rubber Active Bending Sensor," depending on whether it's a rigid/semi-rigid tube or a rubber film. In artificial pneumatic muscles shown in Figure 1, the elasticity of a rubber film can be achieved using air pressure (Wang, Fei, Chen, 2020). For non-rigid materials, deformation techniques include torsion, compression, shear, and stretching (Aubin et al., 2014).

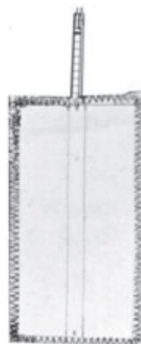


Figure 1: The flex sensor embedded into the inextensible fabric (Wang et al. 2020).

Numerous technologies such as piezoelectric, resistive, optical, and capacitive have been innovated for the creation of bending sensors, which are utilized in wearable devices and specialized applications (Tiboni, 2021). For example, piezoelectric sensors are designed to produce electrical energy upon deformation. Certain models of these sensors are specifically engineered to examine the correlation between the voltage output and the curvature caused by bending. These can be implemented as surface sensors in actuators with limited flexion, and some variants are even tailored to factor in the rate of bending to enhance precision, proving especially beneficial in glove-type exoskeletons.

Resistive bending sensors use a thick resistive material coated on a plastic insulating substrate, with resistance value changing upon deflection by an external force. They are effective as electronic goniometers on body joints for assessing human body segment configurations (Al-Fahaam, 2018).

Dynamic Sensors

Exoskeletons feature dynamic sensors categorized into four primary types according to the physical quantities they measure: Pressure Sensors, Force Sensors, Torque Sensors, and Inertial Measurement Units (IMUs). These sensors are integral in assessing the interactions between the exoskeleton and human limbs.

Pressure Sensors: These sensors are commonly implemented in exoskeletons equipped with fluidic or soft actuators, such as Pneumatic Artificial Muscles (PAMs). They gauge fluidic pressure, which has an indirect connection to dynamic aspects such as force and torque interactions with both the external environment and the user of the exoskeleton. A notable example is the work of Wang et al., (2021), who created a cost-effective, wearable soft sensor system for measuring force in a hip exoskeleton (Figure 2). This system employed a soft pneumatic chamber, translating the dynamic interaction forces into variations in air pressure.

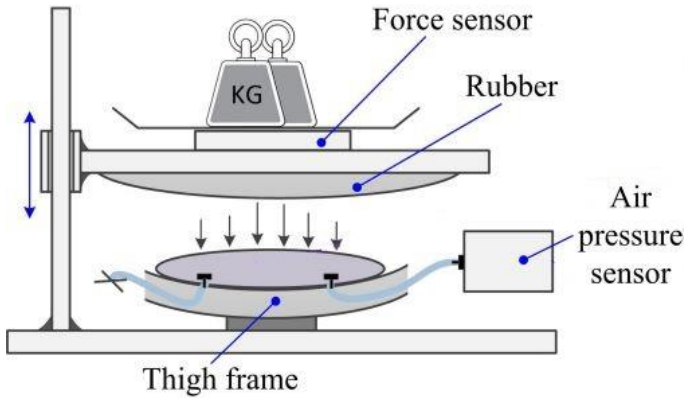


Figure 2: The force and air pressure sensor embedded into the system (Wang et al. 2021).

Force Sensors: These sensors directly measure the force exerted by the user at the interface and are also used for device validation and performance estimation. For example, Hamaya et al. (2021) and Zhang et al. (2021) employed force sensors in various exoskeleton applications, including spasm detection in rehabilitation.

Torque Sensors: Primarily used in lower limb exoskeletons (LLE), they measure torque at the joints. Yu et al. (2020) presented a hip exoskeleton equipped with torque sensors for detecting interface torque. Additionally, Jarrett and Mc Daid (2019) demonstrated using a series elastic actuator as a torque sensor in exoskeletons.

IMU Sensors: Predominantly employed in LLE, IMUs assist in analyzing gait phases. Susanto et al. (2021) utilized an IMU sensor to recognize the pitch angle from the knee joint in a LLE, contributing valuable information about the walking gait cycle.

Multi-sensor systems are common in exoskeletons for comprehensive sensing and control. For example, Kim et al. (2015) developed a modular knee exoskeleton system using force-sensitive resistors, a torque sensor, and an encoder.

Electromyographic (EMG) Sensors

Electromyographic (EMG) sensors, employed in the process of electromyography, play a vital role in evaluating and documenting the electrical behavior of skeletal muscles. This method captures the electrical potential produced by muscle cells during electrical or neurological stimulation. The collected signals are examined for irregularities, levels of activation, or patterns

of muscle recruitment, and these can be linked with the movement's kinematics. There are generally two methods for conducting EMG: needle EMG, which uses a needle attached to an electrode inserted into the muscle, and surface EMG, involving electrodes placed on the skin close to the targeted muscle.

In the context of exoskeletons, EMG is employed to direct the device's motion, blending the movements of the subject and the exoskeleton in an active-assisted approach, or to evaluate the subject's muscle activation patterns during motion. Needle EMG, being invasive, requires experienced medical personnel and is rarely used in conjunction with exoskeletons. In contrast, surface EMG is non-invasive and more adaptable to various contexts.

Needle EMG is more suited for use in prostheses, where subcutaneous, fixed electrode innervation is possible, avoiding the need for skin penetration. However, surface EMG can be affected by artifacts related to skin slippage, electrical resistance, and changes due to atmospheric conditions and hydration. As a result, needle EMG is reserved for precise neurological examinations where high measurement accuracy is essential.

EMG has been applied in several studies involving exoskeletons. For instance, Kiguchi et al. and Rosen et al. (2001) applied a similar approach for an elbow exoskeleton. Li et al. (2019) analyzed an upper limb EMG signal in real-time for a lower limb exoskeleton controller, adjusting for stair height and width (Figure 3). Fleischer et al. (2006) employed EMG in real-time controlled single knee and hand exoskeletons.

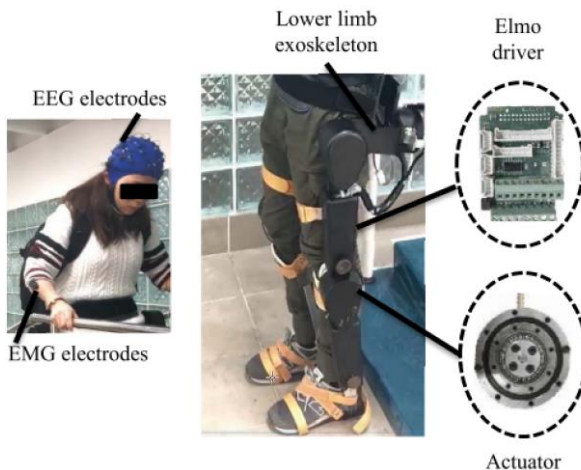


Figure 3: An elastic and air-permeable cap with electrodes were attached to the participant's head to record EEG signals and two collection electrodes of Delsys were attached to the upper forearms to obtain the surface EMG signals (Li et al. 2019).

Electroencephalographic (EEG) sensors

Electroencephalographic (EEG) sensors, used in electroencephalography, track the progression of electrical fields across the skull's surface, mirroring the fluctuation of membrane potentials at the brain's synapses. Originating from neurons on the cortical surface, EEG signals are instrumental in evaluating electrical activity in the brain under both normal and pathological conditions. The form of EEG recordings changes depending on the context, shaped by the origin of the signals and the direction of ionic flows.

Analysis of EEG signals offers a window into brain activity, though the connection with the actual electrical activity of the brain is somewhat indirect. Both the cerebral cortex and deeper brain structures, such as the thalamus, play important roles in producing and regulating this activity. EEG is generally recorded from the scalp using a variety of electrode types (such as scalp-fixed, headset-fixed, and hypodermic needle-fixed) in multi-channel arrangements, necessitating careful placement at standardized locations on the skull.

Numerous research studies have utilized EEG signals to determine the intent behind movements, leading to the development of Brain-Computer Interfaces that facilitate the operation of exoskeletons for both healthy individuals and those with medical conditions, often integrating other methods such as EMG or Functional Electrical Stimulation (Elnady, 2015).

However, the EEG signals tend to differ significantly among individuals, and this difference becomes more pronounced in cases of individuals suffering from neurological disorders such as stroke, Parkinson's disease, or major brain injuries. Therefore, applications that rely on EEG data need to be extensively personalized, incorporating a period for adaptation and learning. In the context of diseases that progress rapidly, like acute and subacute strokes, it is crucial to frequently readjust the EEG parameters to ensure ongoing precision.

Encoders

A rotary encoder, often referred to as a shaft encoder, is an apparatus that translates the rotational position or movement of a shaft or axle into either analog or digital outputs. These devices emit signals indicative of the rotation angle as pulses, which are then converted by a signal conditioning system into formats that are more practical for use. The inherent slack within the shaft of many motors and comparable mechanisms makes it difficult to precisely determine the absolute position using only analog methods such as voltage or potentiometers. Consequently, this situation requires the use of digital inputs or software-driven systems to ensure precise measurements and effective feedback control.

Rotary encoders are primarily of two types: absolute and incremental. Absolute encoders serve as angle transducers, indicating the current shaft position, while incremental encoders provide information on shaft motion, often processed into data like position, speed, and distance. In exoskeletons, encoders are typically used near a rotary motor or a rotary joint (Vantilt et al., 2019). The choice between these locations depends on cost considerations and the rigidity of the transmission between the motor and joint. For accurate monitoring of relative motion between adjacent body segments or exoskeleton segments, encoders are placed around the joint.

In more complex systems, encoders are combined with other sensors to create comprehensive information acquisition systems (Moon, 2019). When the exoskeleton structure is rigid, encoders can measure anticipatory movements and help forecast movement intentions (Moon, 2019). In Figure 4, they are also used in elastic structures in some cases (Marconi, 2019).

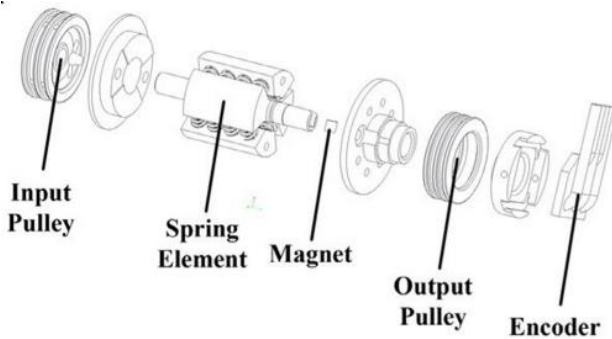


Figure 4: An elastic-encoder module (EEM), of the series-elastic actuation (SEA) architecture (Marconi et al., 2019).

The most common encoder technologies are mechanical, optical, and magnetic. Mechanical encoders, which can be rotary or linear, usually feature a disk with concentric rings that produce an encoding based on a binary code. This system encodes the relative position between a fixed and a moving reference. Multi-turn encoders, under certain design conditions, can track rotary movements exceeding 360 degrees.

DISCUSSION

This study has explored various sensor types and imaging systems and their roles in exoskeleton technologies. Advancements in sensor technologies are aiding our understanding of interactions between exoskeletons and the human

body, enhancing the effectiveness of these devices. Among these sensors, EMG and EEG stand out for their capacity to detect movement intentions and monitor neurological functions. Additionally, rotary encoders and diverse camera systems are increasing the accuracy and adaptability of exoskeleton movements.

The choice of sensors for exoskeletons varies depending on the application's requirements. For instance, EMG and EEG sensors are crucial in rehabilitation-focused exoskeletons for understanding patient muscle and brain activity. Conversely, in industrial or military applications, rotary encoders and advanced imaging systems are preferred to provide the user with greater strength and precision.

Our study also highlights that sensors and imaging systems not only enhance the functionality of exoskeletons but also improve user safety and comfort. These technologies allow for more accurate tracking of body movements, enabling the exoskeleton to move in a more natural and intuitive manner. Furthermore, these sensors can monitor the user's fatigue levels and movement patterns, allowing for device performance to be tailored to individual needs.

In conclusion, sensors and imaging systems play a central role in the future of exoskeleton technologies. Their advancement will not only improve user experience but also enable the use of exoskeletons across a broader range of applications. However, it is important to ensure that these advancements align with ethical and safety considerations. The development of these technologies necessitates careful attention to issues such as user privacy and data security.

CONCLUSION

This study has extensively examined the significance and applications of various sensor types and imaging systems used in exoskeleton technologies. The capabilities of EMG and EEG sensors in detecting movement intentions and monitoring neurological activities have significantly enhanced user interaction and adaptability within these systems. Additionally, rotary encoders and advanced camera systems have increased the precision and adaptability of exoskeletons to user movements.

Considering the varied use cases of exoskeletons, sensor selection is contingent upon the requirements of the application. In rehabilitation-focused exoskeletons, the use of EMG and EEG sensors is vital for understanding users' muscle and brain activities. In industrial and military applications, rotary encoders and advanced imaging systems are preferred to provide users with greater strength and control.

It is evident that sensors and imaging systems not only enhance the functionality of exoskeletons but also improve user safety and comfort. These

technologies enable more accurate tracking of body movements, allowing the exoskeleton to move in a more natural and intuitive manner. Furthermore, they enable exoskeletons to monitor users' fatigue levels and movement patterns, allowing for device performance to be customized to individual needs.

This study demonstrates that sensors and imaging systems play a central role in the future of exoskeleton technologies. Their advancement will not only improve the user experience but also enable the application of exoskeletons across a wider range of uses. However, it is crucial that these technological advancements align with ethical and safety considerations, and that issues such as user privacy and data security are carefully addressed.

REFERENCES

1. Al-Fahaam, H., Davis, S., Nefti-Meziani, S., & Theodoridis, T. (2018). Novel soft bending actuator-based power augmentation hand exoskeleton controlled by human intention. *Intelligent Service Robotics*, 11, 247–268.
2. Amici, C., Ragni, F., Ghidoni, M., Fausti, D., Bissolotti, L., & Tiboni, M. (2020). Multi-Sensor Validation Approach of an End-Effector-Based Robot for the Rehabilitation of the Upper and Lower Limb. *Electronics*, 9, 1751.
3. Aubin, P., Petersen, K., Sallum, H., Walsh, C., Correia, A., & Stirling, L. (2014). A pediatric robotic thumb exoskeleton for at-home rehabilitation: The isolated orthosis for thumb actuation (IOTA). *International Journal of Intelligent Computing and Cybernetics*, 7, 233–252.
4. Bin Imtiaz, M.S., Babar Ali, C., Kausar, Z., Shah, S.Y.A.Y.A., Shah, S.Y.A.Y.A., Ahmad, J., Imran, M.A., & Abbasi, Q.H. (2021). Design of portable exoskeleton forearm for rehabilitation of monoparesis patients using tendon flexion sensing mechanism for health care applications. *Electronics*, 10, 1279.
5. Elnady, A.M., Zhang, X., Xiao, Z.G., Yong, X., Randhawa, B.K., Boyd, L., & Menon, C. (2015). A single-session preliminary evaluation of an affordable BCI-controlled arm exoskeleton and motor-proprioception platform. *Frontiers in Human Neuroscience*, 9, 1–14.
6. Fleischer, C., Wege, A., Kondak, K., & Hommel, G. (2006). Application of EMG signals for controlling exoskeleton robots. *Biomedical Engineering*, 51, 314–319.
7. Garate, V.R., Parri, A., Yan, T., Munih, M., Lova, R.M., Vitiello, N., & Ronsse, R. (2017). Experimental validation of motor primitive-based control for leg exoskeletons during continuous multi-locomotion tasks. *Frontiers in Neurobotics*, 11, 15.
8. Hamaya, M., Matsubara, T., Teramae, T., Noda, T., & Morimoto, J. (2021). Design of physical user—Robot interactions for model identification of soft actuators on exoskeleton robots. *International Journal of Robotics Research*, 40, 397–410.
9. Jarrett, C., & McDaid, A. (2019). Modeling and Feasibility of an Elastomer-Based Series Elastic Actuator as a Haptic Interaction Sensor for Exoskeleton Robotics. *IEEE/ASME Transactions on Mechatronics*, 24, 1325–1333.
10. Jung, J.Y., Heo, W., Yang, H., & Park, H. (2015). A neural network-based gait phase classification method using sensors equipped on lower limb exoskeleton robots. *Sensors*, 15, 27738–27759.

11. Kiguchi, K., Kariya, S., Watanabe, K., Izumi, K., & Fukuda, T. (2001). An exoskeletal robot for human elbow motion support—Sensor fusion, adaptation, and control. *IEEE Transactions on Systems, Man, and Cybernetics - Part B: Cybernetics*, 31, 353–361.
12. Kim, J.H.J.H., Shim, M., Ahn, D.H., Son, B.J., Kim, S.Y.S.Y., Kim, D.Y., Baek, Y.S., & Cho, B.K.B.K. (2015). Design of a Knee Exoskeleton Using Foot Pressure and Knee Torque Sensors. *International Journal of Advanced Robotic Systems*, 12, 112.
13. Li, Z., Yuan, Y., Luo, L., Su, W., Zhao, K., Xu, C., Huang, J., & Pi, M. (2019). Hybrid Brain/Muscle Signals Powered Wearable Walking Exoskeleton Enhancing Motor Ability in Climbing Stairs Activity. *IEEE Transactions on Medical Robotics and Bionics*, 1, 218–227.
14. Marconi, D., Baldoni, A., McKinney, Z., Cempini, M., Crea, S., & Vitiello, N. (2019). A novel hand exoskeleton with series elastic actuation for modulated torque transfer. *Mechatronics*, 61, 69–82.
15. Moon, D.H., Kim, D., & Hong, Y.D. (2019). Intention detection using physical sensors and electromyogram for a single leg knee exoskeleton. *Sensors*, 19, 4447.
16. Moon, D.H.D.H., Kim, D., & Hong, Y.D.Y.D. (2019). Development of a single leg knee exoskeleton and sensing knee center of rotation change for intention detection. *Sensors*, 19, 3960.
17. Rosen, J., Brand, M., Fuchs, M.B., & Arcan, M. (2001). A myosignal-based powered exoskeleton system. *IEEE Transactions on Systems, Man, and Cybernetics - Part A: Systems and Humans*, 31, 210–222.
18. Susanto, S., Simorangkir, I.T., Analia, R., Pamungkas, D.S., Soebhakti, H., Sani, A., & Caesarendra, W. (2021). Real-time identification of knee joint walking gait as preliminary signal for developing lower limb exoskeleton. *Electronics*, 10, 2117.
19. Tiboni, M., Filippini, A., Amici, C., Vetturi, D. (2021). Test-Bench for the Characterization of Flexion Sensors Used in Biomechanics. *Electronics*, 10, 2994.
20. Tiboni, M., Incerti, G., Remino, C., & Lancini, M. (2019). Comparison of signal processing techniques for condition monitoring based on artificial neural networks. *Applied Condition Monitoring*, 15, 179–188.
21. Vantilt, J., Tanghe, K., Afschrift, M., Bruijnes, A., Junius, K., Geeroms, J., Aertbeliën, E., De Groote, F., Lefeber, D., & Jonkers, I., et al. (2019). Model-based control for exoskeletons with series elastic actuators evaluated on sit-to-stand movements. *Journal of Neuroengineering and Rehabilitation*, 16, 65.

22. Wang, J., Fei, Y., & Chen, W. (2020). Integration, Sensing, and Control of a Modular Soft-Rigid Pneumatic Lower Limb Exoskeleton. *Soft Robotics*, 7, 140–154.
23. Wang, S., Zhang, B., Yu, Z., Yan, Y. (2021). Differential Soft Sensor-Based Measurement of Interactive Force and Assistive Torque for a Robotic Hip Exoskeleton. *Sensors*, 21, 6545.
24. Yu, S., Huang, T.H., Yang, X., Jiao, C., Yang, J., Chen, Y., Yi, J., & Su, H. (2020). Quasi-Direct Drive Actuation for a Lightweight Hip Exoskeleton with High Backdrivability and High Bandwidth. *IEEE/ASME Transactions on Mechatronics*, 25, 1794–1802.
25. Zhang, F., Yang, L., & Fu, Y. (2021). Development and Test of a Spasm Sensor for Hand Rehabilitation Exoskeleton. *IEEE*

Chapter 17

Effects of Climate Change on Water Resources, Soil Resources and Weather Events

Sümeyye ADALI¹
Melike YALILI KILIÇ²

Abstract

The extraordinary change in technological developments and anthropological activities in the last century has caused the resources available on earth to face the danger of depletion and the high levels of pollutant emissions released into the atmosphere, especially CO₂. This change in atmospheric chemistry, proportional to the amount of pollutants released, causes climate types to deteriorate long-term and unusual weather events to occur. These significant changes also lead to the degradation and pollution of water and soil environments, enormous natural resources on the planet, and the atmosphere. In this study, the effects of climate change are discussed, and the measures that can be taken to reduce these effects are explained.

Key Words: Climate Change, Drought, Soil Resources, Water Resources, Weather Events.

Özet

Geçtiğimiz son yüzyıl içerisinde teknolojik gelişmeler ve antropolojik faaliyetlerde meydana gelen olağanüstü değişim, dünya üzerinde mevcut olan kaynakların tükenme tehlikesiyle karşı karşıya kalmasına ve başta CO₂ olmak üzere atmosfere salınan kirlenici emisyonlarının yüksek seviyelerde oluşumuna neden olmaktadır. Salınan kirlenici miktarıyla orantılı olarak atmosfer kimyasında yaşanan bu değişim, uzun dönem içerisinde iklim türlerinin bozularak olağandışı hava olaylarının meydana gelmesine neden olmaktadır. Yaşanan bu büyük değişimler ayrıca gezegende atmosferle birlikte en büyük doğal kaynak konumunda yer alan su ve toprak ortamlarının da bozulmasına ve

¹ PhD Student; Bursa Uludag University, Faculty of Engineering, Department of Environmental Engineering, sumeyyeadali00016@gmail.com ORCID No: 0000-0002-5077-7358

² Prof.Dr.; Bursa Uludag University, Faculty of Engineering, Department of Environmental Engineering, myalili@uludag.edu.tr
ORCID No: 0000-0001-7050-6742

kirlenmesine yol açmaktadır. Bu çalışmada günümüzde en büyük küresel felaket niteliği taşıyan iklim değişikliği ve etkileri ele alınarak, bu etkilerin azaltılması konusunda alınabilecek önlemler açıklanmıştır.

Anahtar Kelimeler: İklim Değişikliği, Kuraklık, Toprak Kaynakları, Su Kaynakları, Hava Olayları.

1. INTRODUCTION

As a result of the variation in atmospheric chemistry over time, climate change has occurred many times in the approximately 4.5 billion-year history of the earth. Due to natural climate changes over millions of years, oil, coal, underground, and aboveground riches have emerged in addition to the clean air and freshwater resources humans and other living creatures need today, causing radical changes in human life. Today, rapidly developing technology, population growth, unconscious consumption habits, and anthropogenic activities increase the pressure on the environment and natural resources, leading to climate change (Koncagül et al., 2022). Climate change has become a global crisis due to increased pollutant emissions into the atmosphere over the last 150 years due to these activities that accelerated with the Industrial Revolution. For these reasons, climate change is defined as changes in climate that occur directly or indirectly due to anthropogenic factors that disrupt the composition of the atmosphere, in addition to natural climate change observed over a comparable period (Öztürk, 2002).

Since the First World Climate Conference (1979) until today, the fight against climate change has been carried out by many factors on a local, national, and international scale (Kaymaz and Tut, 2020). The Intergovernmental Panel on Climate Change (IPCC), jointly established by UNESCO and the World Meteorological Organization in 1988, is among the leading efforts in the fight against climate change. As a result of the meetings held in 1996, 2001, 2007, 2014, and 2021, starting from 1989, this panel prepared reports to raise global awareness and inform the public, politicians, relevant institutions, and organizations about climate change. It provides information about the negativities that this change may cause in the medium and long term (Şen, 2022).

The most important indicator of climate change, which has been a critical agenda, especially since the last quarter of the 20th century, is the world average temperatures, which have increased since 1850, when regular meteorological measurements began to be made (Gürkan et al., 2016). Figure 1 shows the annual average temperatures in the world and in Turkey.

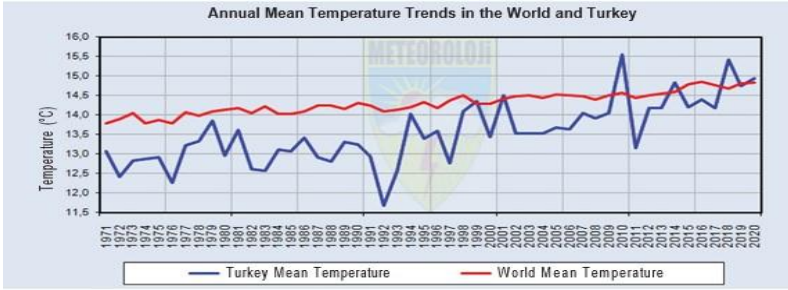


Figure 1. Annual Average Temperatures in the World and Turkey (URL-1, 2023)

During the period 1971-2021, the highest average temperature in Turkey was 15.5°C in 2010, and the lowest average temperature was 11.7°C in 1992. When Turkey's average temperatures are examined, it is reported that there have been positive temperature anomalies since 1994, except for the years 1997 and 2011 (URL-1, 2023).

It is predicted that the temperature increase caused by climate change may cause an increase in the intensity and frequency of natural disasters such as hurricanes, heavy rainfall, floods, and overflows in some parts of the world and may cause more long-lasting severe drought and desertification events in some regions. In our country, it is estimated that climate change will have an impact, especially due to forest fires, weakening of water resources, drought, desertification, and related ecological disruptions (Şen, 2022).

The most significant impact caused by climate change is drought. The drought that will occur in countries such as Turkey, whose primary economic sector is based on agriculture, will result in loss of plant and animal products, increase in plant and animal diseases, decrease in forage crop yield, limited access to forage plants, low product quality, decrease in income of rural producers. The decline in agricultural employment and, in parallel, migration from rural to urban areas, lack of raw materials in agriculture-based industries, food insecurity, erosion, etc. It is stated that it will cause adverse effects (Hazar Kalonya, 2022). 411 million people worldwide are affected by drought, and water stress is common in cities, especially as large cities and crowded populations bring about an increase in water demand (Tuğaç, 2022).

2. CLIMATE CHANGE MODELING STUDIES

It is reported that 75% of carbon dioxide emissions on a global scale originate from urban activities, and these activities include transportation, construction, industrial sector, and fossil fuel-based energy production and

consumption for these sectors (UNEP, 2022). The most important strategies that can be implemented in cities to combat climate change include reducing greenhouse gas emissions and adapting to the current effects of climate change. It is thought that the implementation of climate change adaptation strategies will provide advantages to socially vulnerable groups and low-income neighborhoods in cities against the possible effects of climate change. In this context, carrying out impact, vulnerability, and risk analyses against climate change, preparing Local Climate Change Action Plans to include all sectors in cities, increasing the use of green transportation, compact urbanization, and renewable energy resources, creating green supply systems, financing, and investment for climate actions. Improving opportunities, transitioning to nature-based solutions and green infrastructures, and increasing R&D studies on all these issues are essential tools (Tuğaç, 2022).

The increased severity of weather events caused by climate change causes significant loss of city life and property. It is stated that floods caused by climate change are one of the most common types of disasters, affecting more than 300 thousand people in 1600 cities around the world (WEF, 2022). Today, climate modeling studies are carried out in order to reveal the negativities that may occur due to climate changes. Climate modeling studies are continuing within the General Directorate of Meteorology (MGM) in our country, and the results obtained were last shared in the study titled "Turkey Climate Projections and Climate Change with New Scenarios TR2015-CC" dated 2015 (Gürkan et al., 2016). In the final report of the study, climate projections with 20 km resolution were created for Turkey and its region using the RegCM4.3.4 regional climate model based on HadGEM2-ES, MPI-ESM-MR and GFDL-ESM2M global climate model data and RCP4.5 and RCP8.5 scenarios. Within the scope of the study, the years 1971-2000 were selected as the reference period and climate projections were produced for the period until 2100. According to the results obtained from global model projections, the average temperature increase throughout the country in the 2016-2099 period is expected to be in the range of 1.5-2.5°C according to the RCP4.5 scenario and 2.5-3.5°C according to the RCP8.5 scenario. Although there is no general increase or decrease trend in rainfall, it has been determined that rainfall irregularities tend to increase (Yıldırım and Gürkan, 2016). Analyzing the results of climate change scenarios by reducing them to a regional scale through climate models is of great importance for countries' future planning in the fields of energy, agriculture and water resources management (Deveci et al., 2019).

In terms of combating climate change, protecting areas that may be exposed to climate change, taking necessary precautions against floods and floods in

coastal and river areas, developing unique protection plans against the effects of climate change for residential areas with high population growth, improving agriculture, and industry that are sensitive to climate conditions. Developing protection plans for major economic sectors, such as tourism, finance, etc., is among the essential measures that can be taken to reduce the adverse effects of climate change. Developing protection plans for major economic sectors is among the crucial measures to reduce climate change's adverse effects (Şenerol, 2010). In this study, climate change and its effects are discussed, and various suggestions are presented about the measures that can be taken to combat global climate change.

3. EFFECTS OF CLIMATE CHANGE ON DRINKING WATER

The total amount of water in the world is 1.4 billion km³, 97.5% of which is salt water in the oceans and seas and 2.5% is fresh water in rivers and lakes (Yalılı Kılıç et al., 2008). It is known that 500 thousand km³ of water evaporates from the Earth's surface and mixes with the atmosphere every year. While the continents lose 70 thousand km³ of water through evaporation, they receive 110 thousand km³ of water through precipitation. Approximately 40 km³ of this amount flows into the stream, and only 9000 km³ of this precipitation reaching rivers, seas, and lakes in closed basins can be evaluated technically and economically (Koluman, 2003; Dündar, 2007).

Climate change negatively affects the existing balance between systems and processes in this hydrological cycle. Since one of the most important systems of the hydrological cycle is the atmosphere, changes in atmospheric conditions caused by climate change lead to significant changes in the hydrological processes of basins such as precipitation, evaporation, and flow, both in space and time scales. These changes are not limited to current long-term averages but are also seen in the frequency, magnitude, and spatial distribution of extreme events. Climate change affects water resources not only in terms of quantity but also in terms of quality. The increase in pollution concentrations due to temperature increases and decreases in precipitation and flows will cause the water quality problems experienced even today to become more severe. Therefore, climate change has a restrictive effect on water resources. The main essential effects that climate change will have on water resources are a decrease or increase in surface water potential depending on the regions where the basins are located, a change in the recharge of underground aquifers and, therefore, their levels, change in flood and drought frequencies, seasons and sizes, change in precipitation regime, changes in vegetation and land use. These are listed as erosion problems, changes in the flow regimes of rivers fed by snow water, and

increases in agricultural water requirements (Fıstıkoğlu and Biberöğlu, 2008). When global climate change scenarios are examined, it is predicted that there will be a decrease in precipitation in the coming years and an increase in evaporation (Gündüz, 2023). The combined effect of insufficient water resources, increasing drought, and forest destruction due to climate change increases the risk of fire and may cause the loss of natural vegetation (Hatık, 2015).

With climate change, sea level rise will cause many agricultural areas to be submerged. Changes in planting patterns due to the decrease in water resources will encourage migration from villages to cities and large agricultural areas will be opened to urban settlement. This situation will also bring about changes in plant species and planting areas (Kanber et al., 2010).

The decrease in water resources, one of the most important consequences of climate change, is reaching levels that will prevent sustainable life and its environmental impact. However, it is expected to cause severe problems in water resources, a decrease in agricultural and forest products, energy shortage, and population movement from coastal to inland areas. In order to maintain ecological balance and ensure the sustainable development of humans and other living communities, water resources must be used to meet the needs of all living things today and in the future (Karaman and Gökalp, 2010).

The possible effects of climate change on water resources should be investigated in detail, the management of water resources should be done considering climatic conditions, and the shares of transboundary waters to be allocated to neighboring countries should be determined by considering climate change (Kanber et al., 2010).

The scope and size of the problems experienced today on water resources due to climate change are expected to expand further in the coming period. For this reason, the solution suggestions put forward to reduce or minimize the effects of climate change on water resources will not be different from the solutions to current problems. In terms of protecting water resources, their management with a sustainable integrated basin management approach, in which soil, water, air, and socio-economic structure, which constitute environmental continuity, are considered together, gains importance. This approach also plays a crucial role in adaptation studies to climate change (Fıstıkoğlu and Biberöğlu, 2008).

4. EFFECTS OF CLIMATE CHANGE ON SOIL RESOURCES

Soil resources provide benefits to people in various fields, especially agriculture. For this reason, the demand for land is constantly increasing.

Climate change causes adverse effects such as a decrease in soil fertility, delay in the harvest period of agricultural products, and drought. These adverse effects threaten productivity and sustainability in agricultural activities and safe food. Excessive humidity, precipitation, and temperature changes due to climate change also significantly affect agricultural activities, and cause decreases in product quality and quantity (Akın, 2021). In addition, these changes cause changes in the physiology of plants, causing agricultural pests and pathogens to multiply and survive longer, leading to an increase in foodborne diseases (Akalm, 2014).

As temperatures increase, some agricultural product-growing areas are expected to expand towards the north and higher regions. It is estimated that countries in northern latitudes, such as Canada and Russia, may have the opportunity to engage in agricultural activities in larger areas, negatively affecting developing countries in tropical regions. However, even if climatic conditions improve due to warming weather, some doubts about whether soil conditions will suit intensive agriculture are raised (UNEP, 2006; Akalm, 2014).

The multiplier effect of climate change directly affects the interaction of soil and water resources and can increase or decrease the soil's need for water (Akın, 2021).

Reducing the effects of climate change and protecting water and soil resources are among the important practices to ensure sustainability in agriculture. It is important to urgently implement plans for the effects of climate change on the agricultural system in order to ensure food security and sustainability (Akın, 2021). It is essential to protect and improve the current status of forests, wetlands, marine and coastal ecosystems, meadows, agricultural areas, and peatlands, which can capture and store carbon in reducing the effects of climate change by reducing the release of greenhouse gas emissions (Dudley et al., 2010).

5. EFFECTS OF CLIMATE CHANGE ON WEATHER EVENTS

It shows that extreme weather events, such as heat/cold waves, floods, droughts, typhoons, melting of glaciers, sea level rise, and forest fires, which occur due to climate change and have been seen intensely in recent years, make some ecosystems, and some humans are significantly sensitive to current climate change. Extreme weather events, deterioration of ecosystems, decreased agricultural productivity, problems of access to food and clean water, increased diseases and deaths, and damage to urban infrastructure and settlements cause people's quality of life and welfare to decrease (Demirbas and Aydın, 2020).

Today, there is a great increase in the rate of loss of life and property due to strong winds and floods, especially in the cities of undeveloped and developing countries (Satterthwaite et al., 2007).

According to the IPCC's Second Assessment Report, an increase of approximately 2 C° in global average surface temperature is predicted by 2100 compared to 1990 (IPCC, 1996). Night temperatures are expected to increase significantly during the hot period, especially in large cities, due to the urban heat island effect, and energy consumption for ventilation and cooling will increase accordingly (Türkeş et al., 2000).

The temperature increase caused by climate change is expected to affect air quality in cities negatively (Çobanyılmaz, 2011). It is reported that extreme temperatures prevent concentration at work and cause occupational accidents in all sectors, especially in the agricultural industry, which operates intensively outdoors (Kahraman and Özdemir, 2023).

It is essential to establish appropriate infrastructure systems to prevent the adverse effects of extreme weather events resulting from climate change (Demirbaş and Aydın, 2020).

6. CONCLUSION AND SUGGESTIONS

Climate change, present in our lives as a global disaster with its effects today, will make the world uninhabitable soon. Any small precautions that can be taken to cope with this disaster are essential for humanity to continue its life. At the point of combating climate change:

- In order to reduce the effects of climate change on water resources, a water budget should be made by modeling existing data on a basin basis, and the number of meteorology and flow observation stations should be increased. How the basin will be affected by climate change should be modeled, and future predictions should be made for drinking, irrigation, and energy projects related to water resources.

- The use of fossil energy should be reduced, and the use of renewable energy should be expanded. Energy saving and efficiency studies should be emphasized for all sectors.

- Vehicle and machinery maintenance should be carried out regularly, the use of electric vehicles should be encouraged to reduce greenhouse gases, the use of public transportation in the city should be expanded, and the individual carbon footprint should be reduced.

- Actions against climate change in urban and rural areas should be planned and implemented. At this point, the work farmers and livestock workers can do to combat climate change, especially for soil protection, is

valuable regarding food safety and preventing agricultural greenhouse gas emissions. It seems essential to urgently implement sector-specific work.

- Due to its multi-dimensionality and high-impact power, the fight against climate change requires carrying out work on the basis of inter-societal solidarity and cooperation, as well as global environmental awareness.

REFERENCES

1. Akalın, M. (2014). The climate change impacts on agriculture: adaptation and mitigation strategies for these impacts. Hitit University Journal of Social Sciences Institute, 2, 351-377.
2. Akın, İ. (2021). The effects of water, soil and climate change on the sustainability of safe food and some determinations. Rahva Journal of Technical and Social Studies, 1(1), 13-23.
3. Çobanyılmaz, P. (2011). Determination of vulnerability of cities to climate change: Ankara sample. MSc Thesis, Gazi University Institute of Science and Technology, Ankara.
4. Demirbaş, M., and Aydın, D. (2020). The biggest thread of the 21st century: global climate change. Ecological Life Sciences, 15(4),163-179.
5. Deveci, H., Konukçu, F., and Altürk, B. (2019). Effect of climate change on wheat grown soil moisture profile in thrace district. Journal of Tekirdag Agricultural Faculty, 16(2), 202-218.
6. Dudley, N., Stolton S., Belokurov A., Krueger L., Lopoukhine N., MacKinnon K., Sandwith T. and Sekhran N. (2010). Natural solutions: Protected areas helping people cope with climate change. IUCN/WCPA Coordination Office Publishing, pp. 126.
7. Dündar, M. (2007). International problems causedby water resources. MSc Thesis, KTÜ Social Sciences Institute, Trabzon.
8. Fıstıkoğlu, O., Biberoğlu, E. (2008). Küresel iklim değişikliğinin su kaynaklarına etkisi ve uyum önlemleri. TMMOB İklim Değişimi Sempozyumu, 13-14 Mart, s. 238- 252, Ankara.
9. Gündüz, A. (2023). Temporal and spatial variations in climatological rainfall deficit index was examined in terms of viticulture in Yalova province. BAHÇE 52 (Special Issue 1), 383–390.
10. Gürkan, H., Bayraktar, N., Bulut, H., Koçak, N., Eskioğlu, O., and Demircan, M. (2016). Analyzing of the potential impact of climate change on yield of sunflower (*Helianthus annuus* L.): example of Marmara region. XII. National Agricultural Economics Congress, 25-27 Mayıs, pp. 9-18.
11. Hazar Kalonya, D. (2022). The significance of pastures in climate change mitigation and adaptation processes. The Journal of Environment, Urban and Climate, 1, 128-157.
12. Hatık, S. (2015). The implications of climate change for food security; steps taken by Turkey, EU and international organizations (UN Organizations). EU Specialization Thesis, Ankara.

13. IPCC, 1996. Climate Change 1995, The Science of Climate Change. Contribution of Working Group I to the Second Assessment Report of the Intergovernmental Panel on Climate Change, Houghton J, T., et al., eds., WMO/UNEP. Cambridge University Press, New York.
14. Kanber, R., Baştuğ, R., Büyüктаş, D., Ünlü, M., and Kapur, B. (2010). Küresel iklim değişikliğinin su kaynakları ve tarımsal sulamaya etkileri. Ziraat Mühendisliği VII. Teknik Kongresi, 11-15 Ocak, Ankara.
15. Kahraman, Z., and Özdemir, K.Y. (2023). The effect of temperature increase due to climate change on occupational accidents in the agriculture sector. OKU Journal of The Institute of Science and Technology, 6(3), 1927-1942.
16. Karaman, S., and Gökalp, Z. (2010). Impacts of global warming and climate change over water resources. Tarım Bilimleri Araştırma Dergisi, 3(1), 59-66.
17. Kaymaz, C., and Tut, G. (2020). İklim değişikliği politikalarına yönelik bir çerçeve oluşturma denemesi. Kent ve Çevre Araştırmaları Dergisi, 2(1), 78-98.
18. Koluman, A. (2003). Dünyada su sorununa genel bir bakış. Dünyada Su Sorunları ve Stratejileri, ASAM Yayınları, Ankara.
19. Koncagül, M., Dülger, N.E., and Yinanç, A. (2022). Formation and the effect of musilage in Marmara Sea and in the world. European J. Eng. App. Sci. 5(2), 73-79.
20. Öztürk, K. (2002). Global climatic changes and their probable effect upon Turkey. Gazi University Journal of Gazi Educational Faculty, 22(1), 47-65.
21. Satterthwaite, D., Huq, S., Pelling, M., Reid, H., Lankao, P. R. (2007). Adapting to climate change in urban areas the possibilities and constraints in low- and middle-income nations. International Institute for Environment and Development (IIED), Human Settlements Discussion Paper Series Theme: Climate Change and Cities-1, pp. 112.
22. Şen, Z. (2022). Climate change and Türkiye. The Journal of Environment, Urban and Climate, 1, 1-19.
23. Şenerol, H. (2010). Climate change and effect of Turk's Tourism. MSc Thesis, Balıkesir University Social Sciences Institute, Balıkesir.
24. URL-1, 2023. Environmental indicators. <https://cevreselgostergeler.csb.gov.tr/en/temperature-i-85993> Access: 6.12.2023
25. Tuğaç, Ç. (2022). Climate change crisis and cities. The Journal of Environment, Urban and Climate, 1, 38-60.

26. Türkeş, M., Sümer, U.M., and Çetiner, G. (2000). Küresel iklim değişikliği ve olası etkileri. Çevre Bakanlığı Birleşmiş Milletler İklim Değişikliği Çerçeve Sözleşmesi Seminer Notları, 13 Nisan, Ankara.
27. UNEP, 2006. Global environment outlook 2006. United Nations Environment Programme Year Book, 2006.
28. UNEP, 2022. Cities and climate change. <https://www.unep.org/explore-topics/resource-efficiency/what-we-do/cities/cities-and-climate-change> Access: 10.12.2023
29. WEF, 2022. Biodivercities by 2030: transforming cities' relationship with nature report. Geneva: WEF.
30. Yalılı Kılıç, M., Kestioğlu, K., ve Aydınalp, C. (2008). Atıksuların sulama suyu olarak kullanım olanaklarının değerlendirilmesi. Su Tüketimi Arıtma Yeniden Kullanım Sempozyumu, 3-5 Eylül, İznik, s. 355-366.
31. Yıldırım, M., and Gürkan, H. (2016). Türkiye için iklim değişikliği projeksiyonları. Uluslararası Katılımlı 2. İklim Değişimi ve Tarım Etkileşimi Çalıştayı, 08-09 Kasım 2016, Şanlıurfa.

Chapter 18

THE REHABILITATION OF OPEN SOLID WASTE DUMPING AREAS

Fatma ALFARRA¹

Mirac Nur CİNER²

H. Kurtulus Ozcan³

1. Introduction

The rapid increase in the global population and its consequential increase in economic activity has resulted in significant quantities of waste being produced at the home, municipal, and commercial levels, hence playing a substantial role in the degradation of the environment (Elamin Abbass et al., 2023). The term "waste" is commonly described as any substance or material that becomes useless or unwanted for its owners, maker, or processor, resulting in a loss of its functional worth (Arenibafo, 2023). The waste can be classified based on their respective sources, including municipal solid waste, agricultural waste, biomedical waste, and industrial waste. Municipal solid waste (MSW) is produced as a result of various domestic and business activities, encompassing organic waste, paper, plastic, metal, glass, and miscellaneous substances (Debrah et al., 2021).

Solid waste management (SWM) poses a significant difficulty in the current era. A considerable number of individuals, approximately three billion globally, continue to face the absence of regulated waste management systems. A country's affluence is linked to its level of urbanization, which in turn increases the production of waste (Zoungrana et al., 2022). The management of solid waste has a combination of direct and indirect implications for various aspects of human well-being, including but not limited to health, socioeconomic factors, aesthetics, the environment, and infrastructure. The implementation of environmentally friendly approaches in collecting, transporting, and disposing of solid waste presents a potential resolution for effective solid waste management (Abubakar

¹ MSc; Istanbul University-Cerrahpasa, Engineering Faculty, Department of Environmental Engineering, Avcilar, Istanbul-Turkey; fatma.m.alfarra@hotmail.com. ORCID No: 0009-0007-5240-0793

² Res. Asst.; Istanbul University-Cerrahpasa, Engineering Faculty, Department of Environmental Engineering, Avcilar, Istanbul-Turkey; mirac.ciner@iuc.edu.tr. ORCID No: 0000-0002-9920-928X

³ Prof. Dr.; Istanbul University-Cerrahpasa, Engineering Faculty, Department of Environmental Engineering, Avcilar, Istanbul-Turkey; *Correspondence: hkozcان@iuc.edu.tr. ORCID No: 0000-0002-9810-3985

et al., 2022). Nevertheless, the inadequate management of waste, particularly in developing nations, hinders efficient treatment measures. Consequently, the duration required for waste disposal is substantial, and the inadequately regulated disposal of waste presents a significant peril to both the marine ecosystem and populous urban areas worldwide (Ferronato & Torretta, 2019).

The main purpose of SWM is to efficiently handle the collection, separation, treatment, and dumping of solid waste produced by various metropolitan populations. This purpose aims to ensure that these activities are conducted in a sustainable manner, taking into consideration environmental and social considerations, while utilizing the most economically feasible resources available (Khatiwada et al., 2021). The utilization of waste as both main and secondary raw materials for the manufacturing of consumer products within urban areas needs to be prioritized (OECD, 2021).

The issue of SWM in developing nations is further compounded by the indiscriminate disposal of waste, rendering it a significant environmental contaminant (A. H. Khan et al., 2022). The most popular methods of processing and managing waste in developing nations are landfilling, incineration, open dumping, and composting (Hajam et al., 2023a).

Open burning and dumping are still often used for waste disposal, despite their many negative effects on the environment (Barbhai & Sharma, 2023). Inadequate waste management practices can lead to significant environmental issues. The accumulation of waste in open landfills has deleterious effects on soil contamination and poses a threat to the integrity of the adjacent groundwater (Hasthi et al., 2023). The implementation of effective solid waste management practices has the potential to mitigate or eradicate adverse effects on both the environment and the health of humans. Additionally, it can serve as a catalyst for growth in the economy and enhance overall living standards (Das et al., 2019; Singh Rawat et al., 2020).

This study focuses on the following objectives: assessing the effects of solid waste disposal in open dumps and investigating rehabilitation strategies for open dumping sites in order to mitigate environmental and economic consequences.

2. Global Waste Production

Global production of waste is defined as the cumulative quantity of waste generated via human activities on a global scale within a designated timeframe. This waste might originate from several sources, encompassing municipal, industries, farming, medical centres, and other sectors (Höglund-Isaksson et al., 2020). The production of waste is a significant concern from both an environmental and social standpoint due to its potential to result in a range of

adverse effects, including contamination, the destruction of habitats, and threats to the health of people (Marín-Beltrán et al., 2022).

The generation of waste on a global scale exhibits a consistent upward trend, encompassing developed nations as well as developing nations. Notably, a substantial volume of waste is generated annually in countries belonging to the Organisation for Economic Co-operation and Development (OECD) (Parfitt et al., 2021). The issue of global waste production is of great significance, as evidenced by estimates suggesting that the collective worldwide waste production reached over 20 billion tons in the year 2017. This equates to an average of 2.63 tonnes of waste produced per person annually (Maalouf & Mavropoulos, 2023). MSW production, expressed in kilograms per capita, is illustrated in Figure 1 (URL 1).

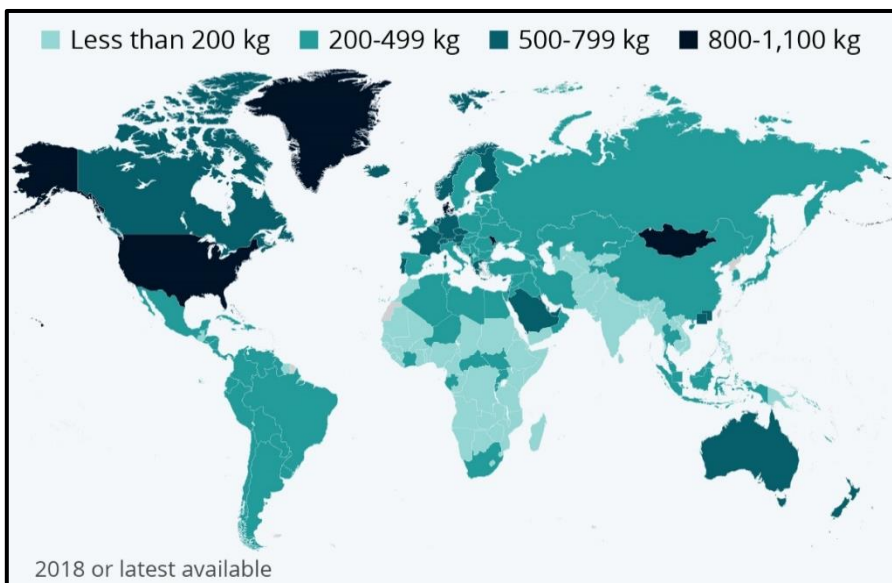


Figure 1. MSW generated per year (in kilograms per capita) (URL 1)

According to projections based on the status quo, it is anticipated that global waste production will reach 46 billion tons in the year 2050 (Mendoza et al., 2022). The quantity of municipal solid waste (MSW) constitutes a relatively smaller part, estimated to be between 2.3 and 3.1 billion tons in the year 2019, and is projected to rise to a range of 2.89 to 4.54 billion tons until 2050 (He et al., 2022). Similarly, based on a report published by the World Bank, it is projected that the yearly production of municipal solid waste could reach a staggering 3.4 billion tons by 2050 (Kaza et al., 2018).

On the other hand, the challenge of accumulating unmanaged plastic waste has become increasingly worrisome. According to estimations, the global production of unmanaged plastic waste ranged from 60 to 99 million tons in 2015. Furthermore, projections indicate that the quantity might potentially triple to reach 155-265 million metric tons annually in 2060 (Lebreton & Andrady, 2019). In developing nations, the majority of waste is primarily derived from household activities and predominantly consists of organic matter derived from plants. The escalating urbanization of communities is a prominent component that is progressively implicated in the generation of trash stemming from industrial and agricultural activities, residual chemicals, and the discharge of hazardous metals (F. F. Robert et al., 2023).

3. Waste Management

The field of solid waste management encompasses the effective management and appropriate disposal of waste materials, with the aim of mitigating adverse effects on both human health and the natural environment (S. Khan et al., 2022). For the purpose of maximizing practical advantage, the waste management hierarchy presents the preferred sequence of steps for waste reduction and management. Landfills are the final resort in waste management; prevention, reduction, recycling, and energy recovery are prioritized in the waste hierarchy (Kabirifar et al., 2020; URL 2) (Figure 2).



Figure 2. Waste hierarchy (URL 2)

Before being processed, MSW must be separated into recyclable, biodegradable, combustible, and non-recyclable categories in order to lessen the

negative effects (Ugwu et al., 2021). The waste materials, including paper, glass, and metals, have the potential to be repurposed in order to reduce the demand for primary resources (David et al., 2019). Furthermore, the process of remediating biodegradable waste involves the conversion of such waste into stable organic molecules, which can serve as an environmentally benign source of energy, such as biogas (Srivastava et al., 2020).

The present condition of waste management in both developed and developing countries is cause for concern, particularly in developing countries, because there is a lack of waste management methods, necessitating the implementation of environmentally sustainable and cost-effective approaches for its management and disposal (Arenibafo, 2023; Debrah et al., 2021; ULUSOY et al., 2023). Several strategies and technological approaches are employed in the field of solid waste management, encompassing incineration, recycling, landfilling, composting, and reduction (Istrate et al., 2020; Karimi, 2023). Nevertheless, the implementation of efficient waste management methods encounters various problems, including insufficient financial resources, inefficient collecting methodologies and equipment, irresponsible disposal procedures, and a lack of educated professionals in managing waste (Kurniawan et al., 2022; Li et al., 2021; Shi et al., 2021).

The current emphasis is on prioritizing reducing waste as the primary approach to address this issue, as opposed to the former emphasis on recovering, recycling, and disposing objectives (Parfitt et al., 2021). In addition to the traditional solid waste management techniques such as volume reduction and landfilling, high-income countries (HICs) are also implementing alternative methods including vermicomposting, sustainable development strategies, and waste-to-energy systems (Alshehrei & Ameen, 2021; Hajam et al., 2023b; Usmani et al., 2020). These waste-to-energy systems encompass various processes such as incineration, pyrolysis, gasification, and anaerobic digestion, as well as the production of biodiesel, biohydrogen, biomethane, bioethanol, and butanol (Barua & Hossain, 2021; S. Y. Lee et al., 2019; Manikandan et al., 2023).

One potential strategy involves the utilization of waste biorefineries, which have the capability to transform municipal solid waste (MSW) into sustainable energy sources, as well as value-added commodities and chemical compounds (Molina-Peñate et al., 2022; Pérez et al., 2020).

4. Open Dumping for Waste Management

Open dumping and landfilling are often employed methods for the management of MSW according to their cost-effectiveness and minimal treatment requirements (Al-Wabel et al., 2022). The utilization of landfills is

suitable for waste that cannot be recycled or incinerated. Nevertheless, it requires vast expanses of land. The leachate generated from the anaerobic and aerobic decomposition of these waste materials contains components that are detrimental to the environment (El-Saadony et al., 2023; Pazoki & Ghasemzadeh, 2020). Accordingly, landfilling becomes the worst option when its negative effects on the environment, human health, the quality of the land, and the groundwater are all taken into account (Blair & Mataraarachchi, 2021; Pires & Martinho, 2019).

Landfilling has witnessed significant expansion in low- and middle-income countries (LMICs) during the past decade. One of the outcomes resulting from this expansion is the emergence of open landfills as a means of solid waste management in various regions across the globe (Idowu et al., 2019). In LMICs, landfilling is a prominent repository for a substantial portion of waste, posing a potential threat to biogas releases caused by the anaerobic decomposition of waste (Chisholm et al., 2021). Additionally, the movement of leachate in these landfills may pollute all surface and groundwater sources. The scenario becomes increasingly concerning in nations that lack protective measures and have landfills situated in close proximity to lakes (Parvin & Tareq, 2021; Zhang et al., 2021). Fortunately, developed countries have started disabling solid waste dumping by stringent regulations, waste reduction, and reuse. In these countries the waste management principle known as "Reduce, Reuse, and Recycle" (often referred to as the '3R') is widely adopted and implemented, making it less probable for this scenario to occur (Batista et al., 2021; Nanda & Berruti, 2021).

5. Composition of MSW

Waste is the byproduct of any human action, be it the routine tasks of daily living or the more involved activities of industries like manufacturing and farming. Waste encompasses a diverse range of components, which exhibit variations among nations and areas, contingent upon the prevailing cultural practices and lifestyles (Elamin Abbass et al., 2023).

The MSW is comprised of several types of waste, including recyclable, organic, combustible, and materials that aren't recyclable. In LMICs, the proportion of substances that decompose in MSW ranged from 46% to 53%. Similarly, the quantity of reusable waste in LMICs was found to be comparatively smaller than that in HICs (UNEP, 2015). MSW, with a high concentration of organic materials, is a major contributor to atmospheric pollution because it releases greenhouse gases (GHG) and leachate, which contaminate groundwater (Cheng et al., 2020; Mor & Ravindra, 2023). Figure 3 shows the composition of MSW on a global scale (Sharma & Jain, 2020).

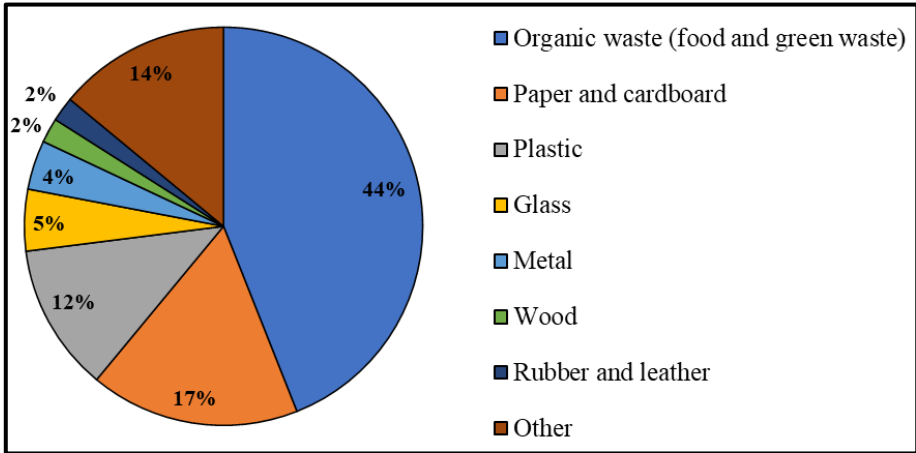


Figure 3. Global MSW Composition (Sharma & Jain, 2020)

6. Environmental Impacts of MSW Open Dumping

The phenomenon of urbanization has led to environmental degradation, posing a significant issue that warrants careful examination (S. Robert et al., 2023). Potential factors contributing to environmental degradation encompass the release of wastewater and effluents, runoff from agriculture, as well as unregulated disposal of solid waste in close proximity to water bodies (Jurado Zavaleta et al., 2021). The impacts on the ecosystem from dumping waste in the open are serious. It causes contamination in a wide variety of environments, from the ocean to the air to the groundwater (Siddiqua et al., 2022).

The practice of open disposal of MSW results in the generation of hazardous compounds that pose risks to both human health and the environment. These compounds, including dioxins and dioxin-like substances (specifically polychlorinated dibenzo-para-dioxins and polychlorinated dibenzofurans), in addition to harmful heavy metals such as nickel and cadmium, are transported into the water, soil, and atmosphere (Roy & Tarafdar, 2022). The contamination of water and soil resources on a worldwide scale is a consequence of various factors, including the transfer of leachates containing toxins, the release of GHG, and the production of odour and dust through open dumping and landfilling practices (Al-Wabel et al., 2022).

This section will cover the negative effects of open dumps for MSW on soil, air, water, and the health of humans.

6.1 Water and Soil Contamination

According to several research, open dumps continue to be the leading cause of water and soil pollution (Alao, 2023; Mekonnen et al., 2020). Additionally, the

unregulated accumulation of MSW at landfills has detrimental consequences for soil quality, leading to a predominance of acidic and sandy conditions, as well as impacting microbial populations (Mouhoun-Chouaki et al., 2019).

An issue arising from the dumping of solid waste is the degradation of organic content inside the waste, resulting in the production of leachate. The very dissolved leachate has the ability to infiltrate into the soil and into water (de Cassia Silva Bacha et al., 2021). Over and above, the process of leaching, whereby organic, inorganic, and other deleterious compounds are released from solid waste and infiltrate the subterranean water, has the potential to result in the contamination of sources of water (Abdel-Shafy et al., 2023).

Moreover, metals including cobalt (Co), cadmium (Cr), copper (Cu), lead (Pb), and zinc (Zn) may contaminate soil at landfills, which can subsequently be taken up by plants and earthworms and pose a threat to both human and environmental health (Aendo et al., 2022; Morita et al., 2021). At the same time, Contamination of surface water sources by heavy element accumulation in soil, such as Cd, Zn, and Pb, may result in biomagnification in the food chain (Gupta et al., 2019).

Another research showed that the disposal of solid waste resulted in a substantial rise in many water parameters, including conductivity, Total Dissolved Solids, hardness, and alkalinity. Additional concerns include malodorous odor, microbiological pollution, and water discoloration. The abundance of nitrogen and phosphorus led to the occurrence of elevated algal blooms in rivers and streams (Mohan & Joseph, 2021).

6.2 Air Pollution

The presence of airborne particulate matter and the accumulation of solid waste from urban areas may lead to the occurrence of contaminants in the air and the generation of smells that are unpleasant (Al-Wabel et al., 2022). As well as the practice of open dumping MSW results in the unregulated generation of landfill gases, predominantly composed of methane and carbon dioxide (Chandra & Ganguly, 2023). Moreover, current numbers imply that over 20 years methane has a global warming potential of 81.2, while carbon dioxide only has a potential of 27.9 during 100 years (IPCC, 2019). The International Panel on Climate Change (IPCC) has also noted in its most recent reports, that the level of methane has risen to above 1000 ppb during a period of the last twenty years (IPCC, 2019).

In light of a substantial rise in methane emissions from MSW, comprehensive investigations have been conducted to analyse the possibility of production from MSW and explore effective methods for converting it into energy forms. These efforts aim to mitigate its release into the environment (Hai et al., 2023;

Naveenkumar et al., 2023; Yang et al., 2023). Increased greenhouse gas emissions are directly attributable to the widespread practice of open waste dumping in developing countries (Ferronato & Torretta, 2019).

Specifically, landfill gases are released when biological waste is decomposed by bacteria in anaerobic environments (US EPA, 2023; Meyer-Dombard et al., 2020). On the other hand, several variables influence how much methane gas is released from an open dumpsite, like the overall amount of garbage dumped, the weather, and the way the waste is collected (Pujara et al., 2023). In a recent report conducted by the United States Environmental Protection Agency (USEPA), it is emphasized that landfill methane emissions in the United States contribute to around 17% of the overall methane production (US EPA, 2022). By 2030 and 2050, developing countries are projected to account for 64 and 76% of global greenhouse gas emissions, up from their 29% share in 2000 (Rafiq et al., 2018).

6.3 Impacts on Human Health

Moreover, the indiscriminate disposal of MSW through open dumping practices has the potential to engender adverse health consequences for individuals residing in close proximity to these dumping sites. Such health risks encompass diseases such as skin and ocular irritation, elevated body temperature, respiratory distress, gastrointestinal disturbances, and a range of other ailments (Dixit et al., 2023).

Open dumping additionally exposes people's health at risk since it can contaminate subterranean water supplies and release gases that can affect nearby populations in ways that can cause cancer.

Moreover, this type of illegal landfill has the potential to trap various creatures and establish favourable conditions for the proliferation of pests, notably mosquitoes, so exacerbating both health and environmental risks (Chireshe et al., 2023).

7. Open Dumping Rehabilitation: A Way to Reduce Environmental and Financial Impacts

Extensive environmental degradation on Earth has prompted significant study efforts toward contamination mitigation and rehabilitation. The rehabilitation procedure encompasses the transformation of polluted areas into gardens and the establishment of nurseries for ornamental plants. The economic benefits of collecting biogas and leachate from the MSW treatment process can be significant for governments. In addition to the economic advantages, the implementation of suitable methods for the extraction of hazardous compounds from MSW has the potential to yield societal benefits. In contrast, the

implementation of suitable waste removal solutions necessitates a larger investment and incurs higher costs for maintenance and operation.

The implementation of rehabilitation solutions for open dumping areas is crucial in addressing the risks to health and the environment that are inherent to these unregulated and filthy waste disposal regions. These sites have the potential to contribute to the contamination of soil and water, the devastation of habitats, and the dissemination of illnesses. Below are a few commonly employed techniques for rehabilitating open dumping sites: landfill mining, soil capping process, landfill gas collection system, bioremediation, revegetation, and phytoremediation.

7.1 Landfill Mining (LFM)

Landfill mining is a method that involves extracting valuable materials from dumping sites. This method has the potential to be a viable alternative for promoting environmental development and managing waste effectively (Zoungrana et al., 2022). LFM entails the removal of waste from a landfill site that has been closed for a lengthy time, typically spanning many years. Throughout this time, the dump has ceased to receive waste and the natural breakdown of waste has significantly decreased (Somani et al., 2020; Zari et al., 2022).

In the current world situation, with its expanding demands for resources, increasing prices of raw materials, dwindling natural reserves for critical commodities, and worsening environmental issues, LFM presents an opportunity for obtaining resources from alternative sources (Jain et al., 2023). Extracting resources from both current and upcoming landfills can result in the utilization of secondary materials and energy, hence minimizing its spatial footprint (Singh & Chandel, 2020). The aforementioned demonstrates that LFM aligns with the EU Roadmap for a Resource-Efficient Europe, which aims to minimize the need to acquire new lands by 2050 (Pitak et al., 2023).

Although there has been growing attention towards LFM and its progress over the past twenty years, the release of dust from mining and landfill mining activities into the environment continues to be a significant problem for public health (Article Author et al., 2019; Cappucci et al., 2020; Qarahasanlou et al., 2022). This is particularly important in cases where old landfills possess the ability to create pollution (H. Lee et al., 2023). The qualities of the mining waste components are influenced by the level of deterioration, kind, and age of the waste. The waste that has been retrieved primarily comprises of soil-like substances, plastic, metal, glass, textile, ceramics, and stones. The predominant

constituent of the extracted waste is a substance resembling soil (Cheela et al., 2023; Han et al., 2024).

7.2 Soil Capping Process

This step would occur as the initial corrective measure that should be implemented while the landfills are finally decommissioned. A landfill cap is a complex structure consisting of multiple layers that are designed to limit the amount of water that seeps into the waste dumped in the landfill. It also helps to minimize the generation of leaches and prevent the unrestricted discharge of landfill gas through the environment. In addition, physically separating waste from organisms such as animals and plants (Ahmed S. et al., 2022).

The choice of capping form for a site is contingent upon various aspects, such as the nature and levels of pollutants, the site's dimensions, the precipitation levels in the location, and the expected later utilization of the land. The hydraulic conductivity (k-value) of components utilized in the building of a hydrodynamic border in waste retention infrastructure is a crucial criterion for assessing the effectiveness of landfill topping layers.

The process of constructing a cover may range from the simplest method of covering mildly polluted soil with one layer of materials to the most complex approach including multiple layers of various materials to separate highly polluted wastes (as shown in Figure 4) (US EPA 2012).

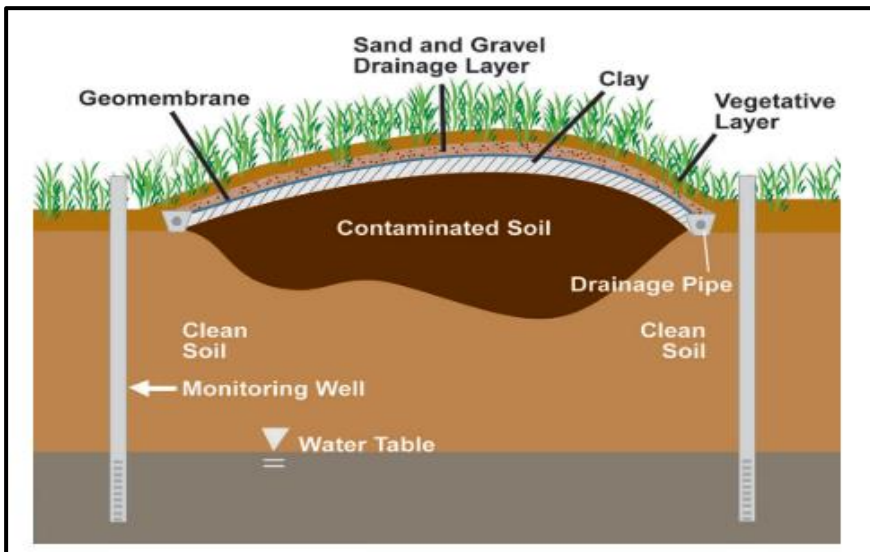


Figure 4. Different layers in landfill capping (US EPA 2012).

7.3 Landfill Gas (LFG) Collection System

Landfills that include a mixture of different types of solid waste produce LFG due to the breakdown of organic materials in the waste through anaerobic degradation. The LFG consists of methane (CH₄) making up around 45 to 60%, carbon dioxide (CO₂) comprising 40 to 60%, and several other small components (Wong & Zawadzki, 2023). The primary objectives of implementing LFG collection are to limit the movement of LFG to areas outside the landfills, decrease discharges on the surface, safeguard groundwater, manage odors, at the same protecting the landfill cover, and create financial resources (Smallwood et al., 2023).

The quantity of LFG that is actually collected is a measure of how efficient a landfill gas collecting system is, and the level of performance that may be attained at any given time is extremely dependent on the landfill's circumstances (Anshassi et al., 2022; Wong & Zawadzki, 2023). In this context, landfills that are closed and covered produce a greater amount of gas for collection than open landfills that are not covered (Borisova et al., 2023).

7.4 Bioremediation

Bioremediation refers to the use of microorganisms or plants to degrade harmful contaminants into carbon dioxide, water, microbial biomass, and less dangerous by-products, which are then removed from the natural (Malik, 2022). In order to achieve optimal bioremediation results, it is crucial that bacteria act in enzymatic degradation of pollutants, converting them into non-toxic substances (Tamang, 2022). Moreover, For the most effective degradation of polluted materials, such as hydrocarbons, chlorinated chemicals, and toxic heavy metals, bioremediation is the approach of choice (Hassan et al., 2022; Malik, 2022). Although microorganisms can not metabolize heavy metals, they may be employed to modify their valence states, therefore converting them into stationary or less hazardous forms (Hassan et al., 2019).

On the other hand, pollutants can lead to a decrease in soil biodiversity. However, microorganisms that can resist contamination have the ability to survive because of their flexible metabolism. This can possibly lead to the creation of new microbial populations (Selvarajan et al., 2022). Additionally, converting current landfills into bioreactor landfills may reclaim important land space and efficiently manage leachate remediation (Sughosh et al., 2021).

According to the study of Muksy & Kolo (2023), one of the major challenges is leachate from landfills, which is hard to remove and causes stratification in waters due to its dangerous circumstances. Furthermore, bioremediation

technologies can be employed for the treatment of the leachate, offering enhanced efficacy as well as economic and environmental benefits (Muksy & Kolo, 2023).

7.5 Revegetation

Revegetation refers to the process of returning plants, whether they are horticulture or native to the area that has been impacted (Stadius, 2019). Native plants can be utilized as treatment agent due to their ability to create a self-sufficient environment, reduce the requirement for fertilizer, pesticides, and water, low upkeep costs, possess inherent adaptability to local conditions, exhibit lasting characteristics, and demonstrate stress tolerance (Song, 2018). Revegetating landfill sites may enhance environmental quality through the promotion of soil formation, augmentation of microbial biomass, improvement of fertility, and reduction of LFG releases (Wen et al., 2023). The conversion of polluted areas into green spaces is important due to its ability to enhance soil performance, provide recreation possibilities, and stimulate the local economy (Pang et al., 2020).

When first preparing to revegetate a site, it is important to handle some practical difficulties. One of them is seedbed preparation, which involves tasks such as levelling the surface, breaking up large clods, and minimizing the prevalence of weeds (Stadius, 2019). Another process incorporating legumes into the mixture provides a rich supply of soil nitrogen. In addition, mulch like straw, wood chips, or plastic sheeting is used to protect planting sites before plants are established. Moreover, watering is essential for revegetation in certain areas to promote the healthy growth of plants and prevent the need for replanting in the event of a dry (DWER, 2018). As well as it is advisable to utilize plant seeds that have been certified as free from weeds in order to prevent the entrance of invasive species that can be challenging to eradicate once they have established themselves. Finally, Grazing management is necessary to prevent over browsing by wildlife and ruminants, which can leave a recently planted site susceptible to invasive species (Saljnikov et al., 2022).

7.6 Phytoremediation.

Phytoremediation methods involve employing plants, such as trees and grassland, to remove contaminants from soil, water, or air. Its landfill site treatment has been extensively researched due to its straightforwardness, low operation and maintenance expenses, and environmentally beneficial nature (Kanwar et al., 2023; Kumar Tyagi & Ojha, 2023; Ramos-Arcos et al., 2019). Furthermore, phytoremediation involves the process of plants absorbing and storing toxins in their leaves, enabling the future collection and elimination of

these pollutants (Hogland et al., 2020). Similarly, plant roots absorb toxins, and these pollutants are broken down by soil microbes through biodegradation. In addition, phytoremediation entails the immobilization of inorganic pollutants in the vicinity of the plant's roots, preventing their migration through the groundwater (Sekhohola-dlamini et al., 2022).

The choice of plants in phytoremediation plays a crucial role in determining the performance of this method. The selected plants must have resistance to high saltiness, ammonium-rich leachate, and have the potential for phytoremediation as well as growth. Appropriate plant types are selected eliminating any edible plant to prevent bioaccumulation. Some examples of these plants include *Bambusa sulfurea*, *Agave sisalana*, *Tradescantia spathacea*, *Chrysopogon zizanioides*, *Chlorophytum comosum*, *Scadoxus multiflorus*, and *Zephyranthes robusta* (Khapre et al., 2022).

8. Monitoring and Control

An important aspect of ecosystem protection for a landfill site is the implementation of a post-closure control and monitoring program. The length of time for post-closure control may vary based on variables such as landfill stabilization methods and the composition of the waste. Thorough management is necessary to prevent obstacles and enhance the likelihood of effectively implementing sustainable disposal solutions. The following are many important steps often involved in such a program:

Landfill Cover Repairs: Consistent upkeep of the landfill cover is crucial in order to avert erosion, reduce infiltration, and manage gas emissions. This may include regular inspections, repairs, and vegetation control (Grossule, 2020).

Leachate Management: The liquid generated inside landfills, known as leachate, needs appropriate management to avert the pollution of groundwater. Post-closure plans often include measures for the installation of leachate collecting and treating systems, along with periodic monitoring to ensure their efficacy (Zahari et al., 2022).

Surface Water Management: The implementation of strategies to regulate the flow of surface water, such as the maintenance of drainage systems and erosion controls, serves to prevent the pollution of adjacent water bodies (Tallaki et al., 2023).

Groundwater Monitoring: The ongoing surveillance of groundwater quality is crucial for the early detection of any possible pollution caused by leachate. Tracking wells are often positioned around the boundaries of the landfill, and samples are frequently collected and examined (Cuciureanu et al., 2020).

Gas Monitoring: Continuous monitoring of landfill gas emissions is essential for ensuring the regulation and effective handling of potentially hazardous gases such as methane. Gas collecting systems are often built and monitoring involves routine testing and maintenance (Scheutz & Kjeldsen, 2019).

Monitoring the stability and settling of the landfill: is necessary to guarantee its over time structural integrity. Periodic inspection and surveys aid in the detection of any problems that could need remedial actions (Pasternak et al., 2023).

Finally, Table 1 provides a concise overview of the control necessary throughout both the active (operational) and passive (post-closure) stages of a landfill (Zahari et al., 2022).

Table 1: Landfill Monitoring Elements

Element	Parameter	Active Phase	Passive Phase
<i>Leachate</i>	Qualitative and Quantitative analysis	Monthly	Phase I: First 5 years (every 6 months) Phase II: Once a year until all work in the landfill site is finished.
<i>Gas</i>	Methane (CH ₄) Carbon dioxide (CO ₂) Oxygen (O ₂)	Monthly	Phase I: First 10 years (every 6 months) Phase II: Once every two years until all activities are finished.
<i>Surface water</i>	Surface water	Phase I: The first year-Monthly Phase II: After the first year-Quarterly	Phase I: First 5 years (every 6 months) Phase II: Once a year until all activities are finished.
<i>Protection layers</i>	Sensors for a barrier layer monitoring system.	Continual	Continual
<i>Structure and cover slope stability</i>	Stability of waste covering layer. Quantity and kind of waste discharged. Monitoring landfill subsidence.	Yearly	Yearly

9. Conclusion

In terms of rehabilitating polluted sites, especially previous landfills, the landfill mining, soil capping process, landfill gas collection system, bioremediation, revegetation, and phytoremediation approaches can all play an

important role and have beneficial effects on the environment and biological diversity.

These approaches may not just rehabilitate biodiversity but also remediate air and water. Furthermore, the right choice of plants that have great potential for remediation of polluted sites, with reduced cost could be an essential part in enhancing the environment.

References

1. Abdel-Shafy, H. I., Ibrahim, A. M., Al-Sulaiman, A. M., & Okasha, R. A. (2023). Landfill leachate: Sources, nature, organic composition, and treatment: An environmental overview. In *Ain Shams Engineering Journal*. Ain Shams University. <https://doi.org/10.1016/j.asej.2023.102293>
2. Abubakar, I. R., Maniruzzaman, K. M., Dano, U. L., AlShihri, F. S., AlShammari, M. S., Ahmed, S. M. S., Al-Gehlani, W. A. G., & Alrawaf, T. I. (2022). Environmental Sustainability Impacts of Solid Waste Management Practices in the Global South. In *International Journal of Environmental Research and Public Health* (Vol. 19, Issue 19). MDPI. <https://doi.org/10.3390/ijerph191912717>
3. Aendo, P., Netvichian, R., Thiendedsakul, P., Khaodhiar, S., & Tulayakul, P. (2022). Carcinogenic Risk of Pb, Cd, Ni, and Cr and Critical Ecological Risk of Cd and Cu in Soil and Groundwater around the Municipal Solid Waste Open Dump in Central Thailand. *Journal of Environmental and Public Health*, 2022. <https://doi.org/10.1155/2022/3062215>
4. Ahmed S., N., Anh, L. H., Thanh, N. T., Thao, P. T. M., & Schneider, P. (2022). Life Cycle Assessment of Substitutive Building Materials for Landfill Capping Systems in Vietnam. *Applied Sciences (Switzerland)*, 12(6). <https://doi.org/10.3390/app12063063>
5. Alao, J. O. (2023). Impacts of open dumpsite leachates on soil and groundwater quality. *Groundwater for Sustainable Development*, 20. <https://doi.org/10.1016/j.gsd.2022.100877>
6. Alshehrei, F., & Ameen, F. (2021). Vermicomposting: A management tool to mitigate solid waste. In *Saudi Journal of Biological Sciences* (Vol. 28, Issue 6, pp. 3284–3293). Elsevier B.V. <https://doi.org/10.1016/j.sjbs.2021.02.072>
7. Al-Wabel, M. I., Ahmad, M., Rasheed, H., Rafique, M. I., Ahmad, J., & Usman, A. R. A. (2022). Environmental Issues Due to Open Dumping and Landfilling. In *Circular Economy in Municipal Solid Waste Landfilling: Biomining & Leachate Treatment* (pp. 65–93).
8. Anshassi, M., Smallwood, T., & Townsend, T. G. (2022). Life cycle GHG emissions of MSW landfilling versus Incineration: Expected outcomes based on US landfill gas collection regulations. *Waste Management*, 142, 44–54. <https://doi.org/10.1016/j.wasman.2022.01.040>
9. Arenibafo, F. E. (2023). The 3Rs(Reduce, Reuse, Recycle) of Waste Management – An effective and Sustainable Approach for Managing Municipal Solid Waste in Developing Countries. *6th International*

- Conference of Contemporary Affairs in Architecture and Urbanism (ICCAUA-2023)*, 383–398. <https://doi.org/10.38027/iccaua2023en0108>
10. Article Author, J., Acker, V., Passel, V., Carlos Hernández Parrodi, J., Lucas, H., Gigantino, M., Sauve, G., Laurence Esguerra, J., Einhäupl, P., Vollprecht, D., Pomberger, R., Friedrich, B., Van Acker, K., Krook, J., Svensson, N., & Van Passel, S. (2019). Integration of resource recovery into current waste management through (Enhanced) landfill mining. *Detritus*, 8. <https://doi.org/10.3929/ethz-b-000426919>
 11. Barbhai, S., & Sharma, P. (2023). Repercussion of Open Dumping Ground in the Vicinity at Mantarwadi, Pune. *IOP Conference Series: Earth and Environmental Science*, 1110(1). <https://doi.org/10.1088/1755-1315/1110/1/012044>
 12. Barua, P., & Hossain, N. (2021). Waste to energy: an overview by global perspective. In *Advanced Technology for the Conversion of Waste into Fuels and Chemicals: Volume 1: Biological Processes* (pp. 1–49). Elsevier. <https://doi.org/10.1016/B978-0-12-823139-5.00011-3>
 13. *Basic Information about Landfill Gas | US EPA*. (2023). <https://www.epa.gov/lmop/basic-information-about-landfill-gas>
 14. Batista, M., Goyannes Gusmão Caiado, R., Gonçalves Quelhas, O. L., Brito Alves Lima, G., Leal Filho, W., & Rocha Yparraguirre, I. T. (2021). A framework for sustainable and integrated municipal solid waste management: Barriers and critical factors to developing countries. *Journal of Cleaner Production*, 312. <https://doi.org/10.1016/j.jclepro.2021.127516>
 15. Blair, J., & Matararachchi, S. (2021). A review of landfills, waste and the nearly forgotten nexus with climate change. In *Environments - MDPI* (Vol. 8, Issue 8). MDPI AG. <https://doi.org/10.3390/environments8080073>
 16. Borisova, D., Kostadinova, G., Petkov, G., Dospatliev, L., Ivanova, M., Dermendzhieva, D., & Beev, G. (2023). Assessment of CH₄ and CO₂ Emissions from a Gas Collection System of a Regional Non-Hazardous Waste Landfill, Harmanli, Bulgaria, Using the Interrupted Time Series ARMA Model. *Atmosphere*, 14(7). <https://doi.org/10.3390/atmos14071089>
 17. Cappucci, G. M., Avolio, R., Carfagna, C., Cocca, M., Gentile, G., Scarpellini, S., Spina, F., Tealdo, G., Errico, M. E., & Ferrari, A. M. (2020). Environmental life cycle assessment of the recycling processes of waste plastics recovered by landfill mining. *Waste Management*, 118, 68–78. <https://doi.org/10.1016/j.wasman.2020.07.048>
 18. Chandra, S., & Ganguly, R. (2023). Assessment of landfill gases by LandGEM and energy recovery potential from municipal solid waste of

- Kanpur city, India. *Heliyon*, 9(4).
<https://doi.org/10.1016/j.heliyon.2023.e15187>
19. Cheela, V. R. S., John, M., Biswas, W., & Dubey, B. (2023). Environmental impact evaluation of landfill mining of legacy waste with on-site sorting using life cycle assessment. *Environmental Science and Pollution Research*, 30(11), 30033–30047. <https://doi.org/10.1007/s11356-022-24210-2>
 20. Cheng, K., Hao, W., Wang, Y., Yi, P., Zhang, J., & Ji, W. (2020). Understanding the emission pattern and source contribution of hazardous air pollutants from open burning of municipal solid waste in China. *Environmental Pollution*, 263. <https://doi.org/10.1016/j.envpol.2020.114417>
 21. Chireshe, A., Shabani, T., & Shabani, T. (2023). Safety and health risks associated with illegal municipal solid waste disposal in urban Zimbabwe. “A case of Masvingo City.” *Safety in Extreme Environments*, 5(3), 243–252. <https://doi.org/10.1007/s42797-023-00080-w>
 22. Chisholm, J. M., Zamani, R., Negm, A. M., Said, N., Abdel daiem, M. M., Dibaj, M., & Akrami, M. (2021). Sustainable waste management of medical waste in African developing countries: A narrative review. *Waste Management and Research*, 39(9), 1149–1163. <https://doi.org/10.1177/0734242X211029175>
 23. Cuciureanu, A., Stanescu, B. A., Cernica, G., & Dinca, S. (2020). ENVIRONMENTAL ASSESSMENT IN THE AREAS OF NON-COMPLIANCE WASTE LANDFILLS IN THE POST CLOSURE PERIOD. *International Symposium “The Environmental and The Industry,” E-SIMI 2020*, 57–58. <https://doi.org/10.21698/simi.2020.ab23>
 24. Das, S., Lee, S. H., Kumar, P., Kim, K. H., Lee, S. S., & Bhattacharya, S. S. (2019). Solid waste management: Scope and the challenge of sustainability. *Journal of Cleaner Production*, 228, 658–678. <https://doi.org/10.1016/j.jclepro.2019.04.323>
 25. David, A., Thangavel, Y. D., & Sankriti, R. (2019). Recover, recycle and reuse: An efficient way to reduce the waste. *International Journal of Mechanical and Production Engineering Research and Development*, 9(3), 31–42. <https://doi.org/10.24247/ijmperdjun20194>
 26. de Cassia Silva Bacha, D., Santos, S., de Alcantara Mendes, R., da Silva Rocha, C. C., Corrêa, J. A., Cruz, J. C. R., Abrunhosa, F. A., & Oliva, P. A. C. (2021). Evaluation of the contamination of the soil and water of an open dump in the Amazon Region, Brazil. *Environmental Earth Sciences*, 80(3). <https://doi.org/10.1007/s12665-021-09401-3>

27. Debrah, J. K., Vidal, D. G., & Dinis, M. A. P. (2021). Raising awareness on solid waste management through formal education for sustainability: A developing countries evidence review. *Recycling*, 6(1), 1–21. <https://doi.org/10.3390/recycling6010006>
28. Dixit, A., Singh, D., & Shukla, S. K. (2023). Assessment of human health risk due to leachate contaminated soil at solid waste dumpsite, Kanpur (India). *International Journal of Environmental Science and Technology*. <https://doi.org/10.1007/s13762-023-04868-y>
29. DWER. (2018). *A Guide to Preparing Revegetation Plans for Clearing Permits*. www.dwer.wa.gov.au
30. Elamin Abbass, O. A., Elhassan, A. M., Abdelgadir, A. E., & Mohamed, M. H. (2023). Detection of Microbiological Activity in Some Collected Water Samples near Dumping Site of Solid Waste, Khartoum North, Sudan. *Tropical Aquatic and Soil Pollution*, 3(1), 69–75. <https://doi.org/10.53623/tasp.v3i1.193>
31. El-Saadony, M. T., Saad, A. M., El-Wafai, N. A., Abou-Aly, H. E., Salem, H. M., Soliman, S. M., Abd El-Mageed, T. A., Elrys, A. S., Selim, S., Abd El-Hack, M. E., Kappachery, S., El-Tarabily, K. A., & AbuQamar, S. F. (2023). Hazardous wastes and management strategies of landfill leachates: A comprehensive review. In *Environmental Technology and Innovation* (Vol. 31). Elsevier B.V. <https://doi.org/10.1016/j.eti.2023.103150>
32. Ferronato, N., & Torretta, V. (2019). Waste mismanagement in developing countries: A review of global issues. In *International Journal of Environmental Research and Public Health* (Vol. 16, Issue 6). MDPI AG. <https://doi.org/10.3390/ijerph16061060>
33. Grossule, V. (2020). Final quality of a sustainable landfill and postclosure management. *Detritus*, 13, 148–159. <https://doi.org/10.31025/2611-4135/2020.13999>
34. Gupta, N., Yadav, K. K., Kumar, V., Kumar, S., Chadd, R. P., & Kumar, A. (2019). Trace elements in soil-vegetables interface: Translocation, bioaccumulation, toxicity and amelioration - A review. In *Science of the Total Environment* (Vol. 651, pp. 2927–2942). Elsevier B.V. <https://doi.org/10.1016/j.scitotenv.2018.10.047>
35. Hai, T., Alenizi, F. A., Alshahri, A. H., Chauhan, B. S., Metwally, A. S. M., & Almujiabah, H. R. (2023). Energy and environmental analyses of a sustainable multi-generation municipal solid waste-to-energy integrated system for hydrogen production. *Process Safety and Environmental Protection*, 177, 307–321. <https://doi.org/10.1016/j.psep.2023.06.030>

36. Hajam, Y. A., Kumar, R., & Kumar, A. (2023a). Environmental waste management strategies and vermi transformation for sustainable development. In *Environmental Challenges* (Vol. 13). Elsevier B.V. <https://doi.org/10.1016/j.envc.2023.100747>
37. Hajam, Y. A., Kumar, R., & Kumar, A. (2023b). Environmental waste management strategies and vermi transformation for sustainable development. In *Environmental Challenges* (Vol. 13). Elsevier B.V. <https://doi.org/10.1016/j.envc.2023.100747>
38. Han, M., Wu, Y., Sun, J., Geng, X., Gao, X., Zhou, T., & Lu, J. (2024). Carbon feasibility of terminating plastic waste leakage by landfill mining: A case study based on practical projects in China. *Science of the Total Environment*, 906. <https://doi.org/10.1016/j.scitotenv.2023.167461>
39. Hassan, A., Pariatamy, A., Ahmed, A., Auta, H. S., & Hamid, F. S. (2019). Enhanced Bioremediation of Heavy Metal Contaminated Landfill Soil Using Filamentous Fungi Consortia: a Demonstration of Bioaugmentation Potential. *Water, Air, and Soil Pollution*, 230(9). <https://doi.org/10.1007/s11270-019-4227-5>
40. Hassan, A., Pariatamy, A., Ossai, I. C., Ahmed, A., Muda, M. A., Wen, T. Z., & Hamid, F. S. (2022). Bioaugmentation-assisted bioremediation and kinetics modelling of heavy metal-polluted landfill soil. *International Journal of Environmental Science and Technology*, 19(7), 6729–6754. <https://doi.org/10.1007/s13762-021-03626-2>
41. Hasthi, S., Budiati, L., & Setiadi, R. (2023). *Study of Waste Management at the Jatibarang Landfill, Semarang City* (pp. 102–111). https://doi.org/10.2991/978-2-38476-072-5_11
42. He, R., Sandoval-Reyes, M., Scott, I., Semeano, R., Ferrão, P., Matthews, S., & Small, M. J. (2022). Global knowledge base for municipal solid waste management: Framework development and application in waste generation prediction. *Journal of Cleaner Production*, 377. <https://doi.org/10.1016/j.jclepro.2022.134501>
43. Hogland, W., Katrantsiotis, C., & Sachpazidou, V. (2020). Baltic Phytoremediation - Soil remediation with plants. *IOP Conference Series: Earth and Environmental Science*, 578(1). <https://doi.org/10.1088/1755-1315/578/1/012003>
44. Höglund-Isaksson, L., Gómez-Sanabria, A., Klimont, Z., Rafaj, P., & Schöpp, W. (2020). Technical potentials and costs for reducing global anthropogenic methane emissions in the 2050 timeframe –results from the gains model. *Environmental Research Communications*, 2(2). <https://doi.org/10.1088/2515-7620/ab7457>

45. Idowu, I. A., Atherton, W., Hashim, K., Kot, P., Alkhaddar, R., Alo, B. I., & Shaw, A. (2019). An analyses of the status of landfill classification systems in developing countries: Sub Saharan Africa landfill experiences. *Waste Management*, 87, 761–771. <https://doi.org/10.1016/j.wasman.2019.03.011>
46. *Inventory of U.S. Greenhouse Gas Emissions and Sinks | US EPA*. (n.d.). Retrieved September 29, 2023, from <https://www.epa.gov/ghgemissions/inventory-us-greenhouse-gas-emissions-and-sinks>
47. IPCC. (2019). *2019 Refinement to the 2006 IPCC Guidelines for National Greenhouse Gas Inventories*. <https://www.ipcc.ch/report/2019-refinement-to-the-2006-ipcc-guidelines-for-national-greenhouse-gas-inventories/>
48. Istrate, I. R., Iribarren, D., Gálvez-Martos, J. L., & Dufour, J. (2020). Review of life-cycle environmental consequences of waste-to-energy solutions on the municipal solid waste management system. In *Resources, Conservation and Recycling* (Vol. 157). Elsevier B.V. <https://doi.org/10.1016/j.resconrec.2020.104778>
49. Jain, M., Kumar, A., & Kumar, A. (2023). Landfill mining: A review on material recovery and its utilization challenges. *Process Safety and Environmental Protection*, 169, 948–958. <https://doi.org/10.1016/j.psep.2022.11.049>
50. Jurado Zavaleta, M. A., Alcaraz, M. R., Peñaloza, L. G., Boemo, A., Cardozo, A., Tarcaya, G., Azcarate, S. M., & Goicoechea, H. C. (2021). Chemometric modeling for spatiotemporal characterization and self-depuration monitoring of surface water assessing the pollution sources impact of northern Argentina rivers. *Microchemical Journal*, 162. <https://doi.org/10.1016/j.microc.2020.105841>
51. Kabirifar, K., Mojtahedi, M., Wang, C., & Tam, V. W. Y. (2020). Construction and demolition waste management contributing factors coupled with reduce, reuse, and recycle strategies for effective waste management: A review. In *Journal of Cleaner Production* (Vol. 263). Elsevier Ltd. <https://doi.org/10.1016/j.jclepro.2020.121265>
52. Kanwar, P., Mina, U., Thakur, I. S., & Srivastava, S. (2023). Heavy metal phytoremediation by the novel prospect of microbes, nanotechnology, and genetic engineering for recovery and rehabilitation of landfill site. In *Bioresource Technology Reports* (Vol. 23). Elsevier Ltd. <https://doi.org/10.1016/j.biteb.2023.101518>

53. Karimi, N. (2023). Assessing Global Waste Management: Alternatives to Landfilling in Different Waste Streams—A Scoping Review. *Sustainability*, 15(18), 13290. <https://doi.org/10.3390/su151813290>
54. Kaza, S., Yao, L., Bhada-Tata, P., & Van Woerden, F. (2018). *What a waste 2.0: a global snapshot of solid waste management to 2050*. https://doi.org/10.1596/978-1-4648-1329-0_ch6
55. Khan, A. H., López-Maldonado, E. A., Khan, N. A., Villarreal-Gómez, L. J., Munshi, F. M., Alsabhan, A. H., & Perveen, K. (2022). Current solid waste management strategies and energy recovery in developing countries - State of art review. In *Chemosphere* (Vol. 291). Elsevier Ltd. <https://doi.org/10.1016/j.chemosphere.2021.133088>
56. Khan, S., Anjum, R., Raza, S. T., Ahmed Bazai, N., & Ihtisham, M. (2022). Technologies for municipal solid waste management: Current status, challenges, and future perspectives. *Chemosphere*, 288. <https://doi.org/10.1016/j.chemosphere.2021.132403>
57. Khapre, A., Khan, S. A., & Kumar, S. (2022). A laboratory-scale phytocover system for municipal solid waste landfills. *Environmental Technology (United Kingdom)*, 43(24), 3670–3681. <https://doi.org/10.1080/09593330.2021.1931470>
58. Khatiwada, D., Golzar, F., Mainali, B., & Devendran, A. A. (2021). Circularity in the Management of Municipal Solid Waste - A Systematic Review. In *Environmental and Climate Technologies* (Vol. 25, Issue 1). Sciendo. <https://doi.org/10.2478/rtuct-2021-0036>
59. Kumar Tyagi, Vinay., & Ojha, C. S. P. (2023). *Landfill Leachate Management*. IWA Publishing.
60. Kurniawan, T. A., Liang, X., O’callaghan, E., Goh, H., Othman, M. H. D., Avtar, R., & Kusworo, T. D. (2022). Transformation of Solid Waste Management in China: Moving towards Sustainability through Digitalization-Based Circular Economy. In *Sustainability (Switzerland)* (Vol. 14, Issue 4). MDPI. <https://doi.org/10.3390/su14042374>
61. Lebreton, L., & Andrady, A. (2019). Future scenarios of global plastic waste generation and disposal. *Palgrave Communications*, 5(1). <https://doi.org/10.1057/s41599-018-0212-7>
62. Lee, H., Coulon, F., & Wagland, S. T. (2023). The influence of humic acid on metal(loid)s leaching in landfill leachate for enhancing landfill mining. *Science of the Total Environment*, 896. <https://doi.org/10.1016/j.scitotenv.2023.165250>
63. Lee, S. Y., Sankaran, R., Chew, K. W., Tan, C. H., Krishnamoorthy, R., Chu, D.-T., & Show, P.-L. (2019). Waste to bioenergy: a review on the

- recent conversion technologies. *BMC Energy*, 1(1).
<https://doi.org/10.1186/s42500-019-0004-7>
64. Li, X., Wang, L., & Ding, X. (2021). Textile supply chain waste management in China. *Journal of Cleaner Production*, 289.
<https://doi.org/10.1016/j.jclepro.2020.125147>
 65. Maalouf, A., & Mavropoulos, A. (2023). Re-assessing global municipal solid waste generation. *Waste Management and Research*, 41(4), 936–947.
<https://doi.org/10.1177/0734242X221074116>
 66. Malik, J. A. (2022). *Advances in Bioremediation and Phytoremediation for Sustainable Soil Management*. Springer.
 67. Manikandan, S., Vickram, S., Sirohi, R., Subbaiya, R., Krishnan, R. Y., Karmegam, N., Sumathijones, C., Rajagopal, R., Chang, S. W., Ravindran, B., & Awasthi, M. K. (2023). Critical review of biochemical pathways to transformation of waste and biomass into bioenergy. In *Bioresource Technology* (Vol. 372). Elsevier Ltd.
<https://doi.org/10.1016/j.biortech.2023.128679>
 68. Marín-Beltrán, I., Demaria, F., Ofelio, C., Serra, L. M., Turiel, A., Ripple, W. J., Mukul, S. A., & Costa, M. C. (2022). Scientists’ warning against the society of waste. In *Science of the Total Environment* (Vol. 811). Elsevier B.V. <https://doi.org/10.1016/j.scitotenv.2021.151359>
 69. Mekonnen, B., Haddis, A., & Zeine, W. (2020). Assessment of the Effect of Solid Waste Dump Site on Surrounding Soil and River Water Quality in Tepi Town, Southwest Ethiopia. *Journal of Environmental and Public Health*, 2020. <https://doi.org/10.1155/2020/5157046>
 70. Mendoza, R. R., Menguins Da Lima, A. M., Aparecida, M., Pimentel, S., & Paulino Da Rocha, E. J. (2022). *World Development and Generation of Waste*. <https://doi.org/10.21203/rs.3.rs-1413201/v1>
 71. Meyer-Dombard, D. R., Bogner, J. E., & Malas, J. (2020). A Review of Landfill Microbiology and Ecology: A Call for Modernization With ‘Next Generation’ Technology. In *Frontiers in Microbiology* (Vol. 11). Frontiers Media S.A. <https://doi.org/10.3389/fmicb.2020.01127>
 72. Mohan, S., & Joseph, C. P. (2021). Potential Hazards due to Municipal Solid Waste Open Dumping in India. In *Journal of the Indian Institute of Science* (Vol. 101, Issue 4, pp. 523–536). Springer.
<https://doi.org/10.1007/s41745-021-00242-4>
 73. Molina-Peñate, E., Artola, A., & Sánchez, A. (2022). Organic municipal waste as feedstock for biorefineries: bioconversion technologies integration and challenges. In *Reviews in Environmental Science and*

- Biotechnology* (Vol. 21, Issue 1, pp. 247–267). Springer Science and Business Media B.V. <https://doi.org/10.1007/s11157-021-09605-w>
74. Mor, S., & Ravindra, K. (2023). Municipal solid waste landfills in lower- and middle-income countries: Environmental impacts, challenges and sustainable management practices. In *Process Safety and Environmental Protection* (Vol. 174, pp. 510–530). Institution of Chemical Engineers. <https://doi.org/10.1016/j.psep.2023.04.014>
 75. Morita, A. K. M., Ibelli-Bianco, C., Anache, J. A. A., Coutinho, J. V., Pelinson, N. S., Nobrega, J., Rosalem, L. M. P., Leite, C. M. C., Niviadonski, L. M., Manastella, C., & Wendland, E. (2021). Pollution threat to water and soil quality by dumpsites and non-sanitary landfills in Brazil: A review. In *Waste Management* (Vol. 131, pp. 163–176). Elsevier Ltd. <https://doi.org/10.1016/j.wasman.2021.06.004>
 76. Mouhoun-Chouaki, S., Derridj, A., Tazdaït, D., & Salah-Tazdaït, R. (2019). A Study of the Impact of Municipal Solid Waste on Some Soil Physicochemical Properties: The Case of the Landfill of Ain-El-Hammam Municipality, Algeria. *Applied and Environmental Soil Science*, 2019. <https://doi.org/10.1155/2019/3560456>
 77. Muksy, R., & Kolo, K. (2023). Experimental Observations and Assessment of Landfill Leachate Bioremediation by Autochthonous Fungi Species and their Effective Geoactivities. *Journal of Ecological Engineering*, 24(1), 312–327. <https://doi.org/10.12911/22998993/156080>
 78. Nanda, S., & Berruti, F. (2021). Municipal solid waste management and landfilling technologies: a review. In *Environmental Chemistry Letters* (Vol. 19, Issue 2, pp. 1433–1456). Springer Science and Business Media Deutschland GmbH. <https://doi.org/10.1007/s10311-020-01100-y>
 79. Naveenkumar, R., Iyyappan, J., Pravin, R., Kadry, S., Han, J., Sindhu, R., Awasthi, M. K., Rokhum, S. L., & Baskar, G. (2023). A strategic review on sustainable approaches in municipal solid waste management and energy recovery: Role of artificial intelligence, economic stability and life cycle assessment. In *Bioresource Technology* (Vol. 379). Elsevier Ltd. <https://doi.org/10.1016/j.biortech.2023.129044>
 80. OECD. (2021). *Towards a more resource-efficient and circular economy The role of the G20*.
 81. Pang, C. C., Lo, W. F., Yan, R. W. M., & Hau, B. C. H. (2020). Plant community composition on landfill sites after multiple years of ecological restoration. *Landscape Research*, 45(4), 458–469. <https://doi.org/10.1080/01426397.2019.1674266>

82. Parfitt, J., Croker, T., & Brockhaus, A. (2021). Global food loss and waste in primary production: A reassessment of its scale and significance. *Sustainability (Switzerland)*, *13*(21). <https://doi.org/10.3390/su132112087>
83. Parvin, F., & Tareq, S. M. (2021). Impact of landfill leachate contamination on surface and groundwater of Bangladesh: a systematic review and possible public health risks assessment. In *Applied Water Science* (Vol. 11, Issue 6). Springer Science and Business Media Deutschland GmbH. <https://doi.org/10.1007/s13201-021-01431-3>
84. Pasternak, G., Zaczek-Peplinska, J., Pasternak, K., Józwiak, J., Pasik, M., Koda, E., & Vaverková, M. D. (2023). Surface Monitoring of an MSW Landfill Based on Linear and Angular Measurements, TLS, and LIDAR UAV. *Sensors*, *23*(4). <https://doi.org/10.3390/s23041847>
85. Pazoki, M., & Ghasemzadeh, R. (2020). *Municipal Landfill Leachate Management*. <http://www.springer.com/series/3234>
86. Pérez, V., Pérez, V., Pascual, A., Rodrigo, A., García Torreiro, M., Latorre-Sánchez, M., Coll Lozano, C., David-Moreno, A., Oliva-Dominguez, J. M., Serna-Maza, A., Herrero García, N., González Granados, I., Roldan-Aguayo, R., Ovejero-Roncero, D., Molto Marin, J. L., Smith, M., Musinovic, H., Raingué, A., Belard, L., ... Muñoz, R. (2020). Integrated innovative biorefinery for the transformation of municipal solid waste into biobased products. In *Waste Biorefinery: Integrating Biorefineries for Waste Valorisation* (pp. 41–80). Elsevier. <https://doi.org/10.1016/B978-0-12-818228-4.00002-2>
87. Pires, A., & Martinho, G. (2019). Waste hierarchy index for circular economy in waste management. *Waste Management*, *95*, 298–305. <https://doi.org/10.1016/j.wasman.2019.06.014>
88. Pitak, I., Denafas, G., Baltušnikas, A., Praspaliauskas, M., & Lukošiušė, S. I. (2023). Proposal for Implementation of Extraction Mechanism of Raw Materials during Landfill Mining and Its Application in Alternative Fuel Production. *Sustainability (Switzerland)*, *15*(5). <https://doi.org/10.3390/su15054538>
89. Pujara, Y., Govani, J., Patel, H. T., Pathak, P., Mashru, D., & Ganesh, P. S. (2023). Quantification of environmental impacts associated with municipal solid waste management in Rajkot city, India using Life Cycle Assessment. *Environmental Advances*, *12*. <https://doi.org/10.1016/j.envadv.2023.100364>
90. Qarahasanlou, A. N., Khanzadeh, D., Shahabi, R. S., & Basiri, M. H. (2022). Introducing sustainable development and reviewing environmental

- sustainability in the mining industry. *Rudarsko Geolosko Naftni Zbornik*, 37(4), 91–108. <https://doi.org/10.17794/rgn.2022.4.8>
91. Rafiq, A., Rasheed, A., Arslan, C., Tallat, U., & Siddique, M. (2018). Estimation of greenhouse gas emissions from Muhammad wala open dumping site of Faisalabad, Pakistan. *Geology, Ecology, and Landscapes*, 2(1), 45–50. <https://doi.org/10.1080/24749508.2018.1452463>
 92. Ramos-Arcos, S. A., López-Martínez, S., Lagunas Rivera, S., González-Mondragón, E. G., de la Cruz Leyva, M. C., & Velázquez-Martínez, J. R. (2019). Phytoremediation of landfill leachate using vetiver (*Chrysopogon zizanioides*) and cattail (*Typha latifolia*). *Applied Ecology and Environmental Research*, 17(2), 2619–2630. https://doi.org/10.15666/aeer/1702_26192630
 93. Robert, F. F., El Hadj Malick, K., Fatoumata, B., Absa, L., Cheikh, D., Mamadou, F., Aminata, T., & Mathilde, C. (2023). Environmental Impacts and Health Risks of Open Landfills in West African Countries: A Systematic Review of the Literature. *Journal of Toxicology and Risk Assessment*, 9(1). <https://doi.org/10.23937/2572-4061.1510053>
 94. Robert, S., Luckins, N., & Menon, R. (2023). Quality deterioration of an Indian urban water source near an open dumping site. *Water Practice and Technology*, 18(5), 1284–1299. <https://doi.org/10.2166/wpt.2023.056>
 95. Roy, D., & Tarafdar, A. (2022). Solid Waste Management and Landfill in High-Income Countries. In *Circular Economy in Municipal Solid Waste Landfilling: Biomining & Leachate Treatment* (pp. 1–23).
 96. Saljnikov, E., Mueller, L., Lavrishchev, A., & Eulenstein, F. (2022). *Advances in Understanding Soil Degradation Innovations in Landscape Research*. <https://link.springer.com/bookseries/16118>
 97. Scheutz, C., & Kjeldsen, P. (2019). Guidelines for landfill gas emission monitoring using the tracer gas dispersion method. *Waste Management*, 85, 351–360. <https://doi.org/10.1016/j.wasman.2018.12.048>
 98. Sekhohola-dlamini, L. M., Keshinro, O. M., Masudi, W. L., & Cowan, A. K. (2022). Elaboration of a Phytoremediation Strategy for Successful and Sustainable Rehabilitation of Disturbed and Degraded Land. *Minerals*, 12(2). <https://doi.org/10.3390/min12020111>
 99. Selvarajan, R., Ogola, H., Kalu, C. M., Sibanda, T., & Obize, C. (2022). Bacterial Communities in Informal Dump Sites: A Rich Source of Unique Diversity and Functional Potential for Bioremediation Applications. *Applied Sciences (Switzerland)*, 12(24). <https://doi.org/10.3390/app122412862>

100. Sharma, K. D., & Jain, S. (2020). Municipal solid waste generation, composition, and management: the global scenario. *Social Responsibility Journal*, 16(6), 917-948.
101. Shi, J., Huang, W., Han, H., & Xu, C. (2021). Pollution control of wastewater from the coal chemical industry in China: Environmental management policy and technical standards. In *Renewable and Sustainable Energy Reviews* (Vol. 143). Elsevier Ltd. <https://doi.org/10.1016/j.rser.2021.110883>
102. Siddiqua, A., Hahladakis, J. N., & Al-Attiya, W. A. K. A. (2022). An overview of the environmental pollution and health effects associated with waste landfilling and open dumping. In *Environmental Science and Pollution Research* (Vol. 29, Issue 39, pp. 58514–58536). Springer Science and Business Media Deutschland GmbH. <https://doi.org/10.1007/s11356-022-21578-z>
103. Singh Rawat, E. S., Chetan Kumar, E., Soni, E. S., Yugal, E., & Prajapat, K. (2020). Solid Waste Management: Treatment & Disposal process. *IJARIE*, 6(0), 2395–4396. www.ijarjie.com
104. Singh, A., & Chandel, M. K. (2020). Effect of ageing on waste characteristics excavated from an Indian dumpsite and its potential valorisation. *Process Safety and Environmental Protection*, 134, 24–35. <https://doi.org/10.1016/j.psep.2019.11.025>
105. Smallwood, T. J., Robey, N. M., Liu, Y., Bowden, J. A., Tolaymat, T. M., Solo-Gabriele, H. M., & Townsend, T. G. (2023). Per- and polyfluoroalkyl substances (PFAS) distribution in landfill gas collection systems: leachate and gas condensate partitioning. *Journal of Hazardous Materials*, 448. <https://doi.org/10.1016/j.jhazmat.2023.130926>
106. Somani, M., Datta, M., Ramana, G. V., & Sreekrishnan, T. R. (2020). Contaminants in soil-like material recovered by landfill mining from five old dumps in India. *Process Safety and Environmental Protection*, 137, 82–92. <https://doi.org/10.1016/j.psep.2020.02.010>
107. Song, U. (2018). Selecting plant species for landfill revegetation: A test of 10 native species on reclaimed soils. *Journal of Ecology and Environment*, 42(1). <https://doi.org/10.1186/s41610-018-0089-9>
108. Srivastava, R. K., Shetti, N. P., Reddy, K. R., & Aminabhavi, T. M. (2020). Sustainable energy from waste organic matters via efficient microbial processes. *Science of the Total Environment*, 722. <https://doi.org/10.1016/j.scitotenv.2020.137927>
109. Staius, C. (2019). Revegetation of the Completed Site. In *Fundamentals of Site Remediation* (pp. 407–437).

110. Sughosh, P., Anusree, N., Prathima, B., & Sivakumar Babu, G. L. (2021). Sustainable Remediation of a Dumpsite. *Indian Geotechnical Conference 2019*, 65–76. <http://www.springer.com/series/15087>
111. Tallaki, M., Bracci, E., & Ievoli, R. (2023). Post-closure Cost Efficiency in Public Versus Private Landfills: The Case of Emilia-Romagna (Italy). *Environmental Management*, 72(4), 850–861. <https://doi.org/10.1007/s00267-023-01809-w>
112. Tamang, R. (2022). *BIOREMEDIATION AS A SUSTAINABLE WASTE MANAGEMENT TECHNIQUE* (pp. 282–290). <https://www.researchgate.net/publication/370221123>
113. URL 1 A World of Waste (Statista) <https://www.statista.com/chart/18732/waste-generated-country/>. Accessed 12 November 2023
114. URL 2 The Waste Hierarchy (NSW EPA)
115. <https://www.epa.nsw.gov.au/your-environment/recycling-and-reuse/warr-strategy/the-waste-hierarchy#:~:text=Waste%20hierarchy,energy%3B%20treat%3B%20dispose%20of%20waste>. Accessed 12 November 2023
116. U.S. Environmental Protection Agency (US EPA). (2012). *A Citizen's Guide to Capping What Is Capping?* www.cluin.org/products/
117. Ugwu, C. O., Ozoegwu, C. G., Ozor, P. A., Agwu, N., & Mbohwa, C. (2021). Waste reduction and utilization strategies to improve municipal solid waste management on Nigerian campuses. *Fuel Communications*, 9, 100025. <https://doi.org/10.1016/j.jfueco.2021.100025>
118. ULUSOY, K., DOĞAN-SAĞLAMTİMUR, N., SEKUŁA, P. M., & STERNIK, A. (2023). Waste Classification and Separation Practices from Türkiye and Selected Countries of the World. *Environmental Research and Technology*. <https://doi.org/10.35208/ert.1252594>
119. United Nations Environment Programme (UNEP). (2015). *Global waste management outlook*.
120. Usmani, Z., Kumar, V., Varjani, S., Gupta, P., Rani, R., & Chandra, A. (2020). Municipal solid waste to clean energy system: A contribution toward sustainable development. In *Current Developments in Biotechnology and Bioengineering: Resource Recovery from Wastes* (pp. 217–231). Elsevier. <https://doi.org/10.1016/B978-0-444-64321-6.00011-2>
121. Wen, Y., Zhao, Y., Guan, Z., & Zhang, X. (2023). Remodeling of Abandoned Land: A Review of Landscape Regeneration and the Reconstruction of Urban Landfill Sites. In *Sustainability (Switzerland)*

- (Vol. 15, Issue 14). Multidisciplinary Digital Publishing Institute (MDPI).
<https://doi.org/10.3390/su151410810>
122. Wong, C. L. Y., & Zawadzki, W. (2023). Emissions rate measurement with flow modelling to optimize landfill gas collection from horizontal collectors. *Waste Management*, 157, 199–209.
<https://doi.org/10.1016/j.wasman.2022.12.018>
123. Yang, M., Chen, L., Wang, J., Msigwa, G., Osman, A. I., Fawzy, S., Rooney, D. W., & Yap, P. S. (2023). Circular economy strategies for combating climate change and other environmental issues. In *Environmental Chemistry Letters* (Vol. 21, Issue 1, pp. 55–80). Springer Science and Business Media Deutschland GmbH.
<https://doi.org/10.1007/s10311-022-01499-6>
124. Zahari, M., Jaafar, I., Ismail, S., Abu Amr, S. S., Aziz, H. A., & Hung, Y. T. (2022). Landfill After-Care Management Plan. In *Solid Waste Engineering and Management* (Vol. 24, pp. 659–706).
<http://www.springer.com/series/7645>
125. Zari, M., Smith, R., Wright, C., & Ferrari, R. (2022). Health and environmental impact assessment of landfill mining activities: A case study in Norfolk, UK. *Heliyon*, 8(11).
<https://doi.org/10.1016/j.heliyon.2022.e11594>
126. Zhang, J., Zhang, J. min, Xing, B., Liu, G. dong, & Liang, Y. (2021). Study on the effect of municipal solid landfills on groundwater by combining the models of variable leakage rate, leachate concentration, and contaminant solute transport. *Journal of Environmental Management*, 292.
<https://doi.org/10.1016/j.jenvman.2021.112815>
127. Zoungrana, A., Hasnine, M. T., & Yuan, Q. (2022). Landfill Mining: Significance, Operation and Global Perspectives. In *Circular Economy in Municipal Solid Waste Landfilling: Biomining & Leachate Treatment* (pp. 25–45).

Chapter 19

Criteria for Determining Parameters in Metal Powder Production by Gas Atomization

Mustafa GÜLEŞEN¹
Osman Selim KİBAR²

INTRODUCTION

Gas atomization is a process that occurs as a result of the collision of the metal melt with a fluid accelerated by the nozzle. It creates a fine droplet distribution by penetrating the high-energy atomization gas into the fluid. It is the result of the transfer of kinetic energy of the gas to the molten metal. Factors such as the size, speed, temperature and cooling rate of the droplets formed by this energy transmission affect the structure and mechanical properties of the powder.

The use of air as a fluid in the gas atomization process started in the early 1920s with the atomization processes of non-ferrous metals such as lead and tin. The atomization process of iron was carried out by R.Z. during the Second World War. Iron powder was obtained by Mannesmann by colliding iron melt with air. Gas atomization method can be applied to many metals such as copper, iron, aluminum, magnesium, high speed steels, stainless steel, intermetallic compounds and ceramics (Gummesson, 1972, Bednow, 1978).

Gases such as argon, nitrogen, helium and air can be used in gas atomization. By mixing gases, production can be made by providing the desired powder properties at low cost.

In atomization processes, powder size decreases with increasing gas velocity. For better energy transmission, a gas jet with laminar flow is desired. In other words, for maximum efficiency, the gas must touch the melt as quickly as possible and with the best contact (Grant, 1978, Donaldsan and Shedeker 1971, Sheikhaliev, et al., 1996).

Different types of nozzles such as flat, convergent, and ultrasonic nozzles are used in the atomization process. Straight pipe mouthpieces are preferred for

¹ Dr. Öğr Üyesi; Kütahya Dumlupınar Üniversitesi, Mühendislik Fakültesi, Makine Mühendisliği Bölümü, mustafa.gulesen@dpu.edu.tr ORCID No:-4827-14

² Makine Yük. Mühendisi: Kütahya Sağlık Bilimleri Üniversitesi, Yapı İşleri ve Teknik Daire Başkanlığı, osmanselim.kibar@ksbu.edu.tr ORCID No: 0000-0002-8452-1406

gas atomization at subsonic speeds, and convergent-divergent pipe mouthpieces are preferred for supersonic gas atomization.

The first aim of gas atomization is to obtain smooth, spherical particles. However, due to the rapid cooling and solidification of aluminum-based alloys, zinc and copper alloys, structures that differ from smoothness and roundness may occur. One of the biggest reasons why spherical powder is desired in buildings is that it gives better results in pressing and sintering processes.

In gas atomization, parameters such as gas type, nozzle, temperature and pressure greatly affect the structure of the powder to be obtained. Studies generally involve changes in these parameters to improve the powder structure.

Gas Atomization

Gas atomization, which is one of the powder metallurgy atomization methods, is the process of impinging gas with increased kinetic energy on the molten metal and transferring its energy, pulverizing it into powder. This method stands out among other atomization methods because it produces higher amounts of spherical powder and particles with homogeneous size distribution. In gas atomization, there are many factors that affect powder morphology such as gas pressure, gas type, nozzle design, melting temperature and cooling rate. When the studies on the subject are examined, it is thought that gas pressure is one of the most important factors affecting powder morphology among these parameters. This study includes the review of studies on the parameters affecting powder structure in gas atomization.

In the study conducted by Gündeş, Yaykaşlı and Özger, Ag92.5Cu7.5 metal powder used in 3D metal printers was produced in the form of rod strips in a wire drawing machine and was produced by the same metal gas atomization method. Pure Cu powder and pure silver powder produced by hydrometallurgy were used in gas atomization, and Ag92.5Cu7.5 powder was obtained by mixing them by mechanical alloying. The products obtained by both production methods were examined with X-ray and scanning electron microscopy. At the same time, the thermal behavior of these products was examined by thermal analysis. In the examination, it was seen that the XRD appearance was a crystal structure. Figure 1 shows the images of Al92.5Cu7.5 obtained with the SEM device. Grain sizes measured in scanning electron microscope images were determined as 10 μm . In thermal behavior analysis, an endothermic peak was observed at 931 $^{\circ}\text{C}$ (Gündeş, et al., 2021).

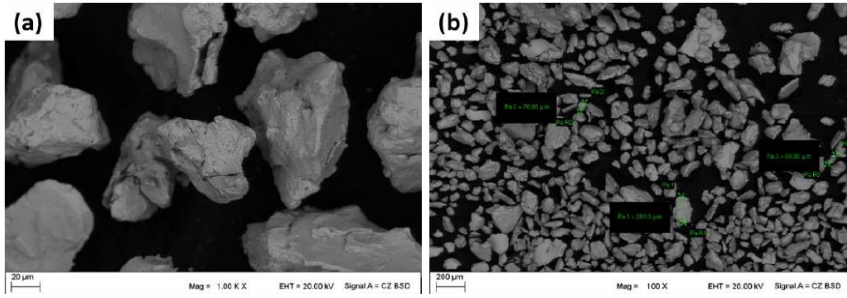


Figure 1: SEM view of Ag92,5Cu7,5 alloy produced by gas atomization (Gündeş, et al., 2021)

Mechanical alloying processes of the powders were carried out for 30, 60 and 120 minutes. Ag and Cu powders are observed in the images obtained during the first 30 minutes. Cold fusion and disintegration were observed after 60 minutes of processing. However, cracks were observed on the powder surfaces. After the 120th minute, it was observed that the powders began to combine and solid solutions were formed (Gündeş, et al., 2021).

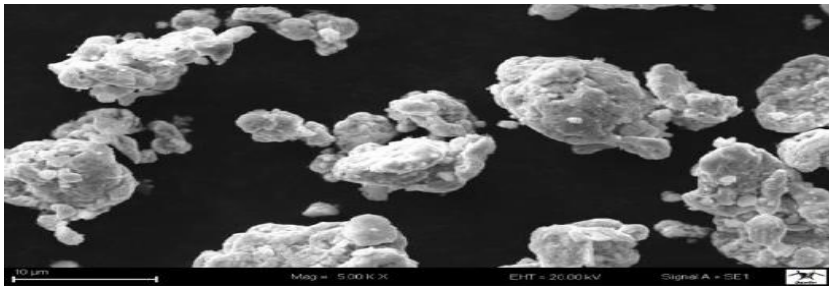


Figure 2: Image of Ag92.5Cu7.5 powder alloy produced by 120 minutes mechanical alloying (Gündeş, et al., 2021)

In the study conducted by Çetin, Akkaş and Boz, the production of AM60 magnesium alloy powder was carried out by the gas atomization method. In the study, the effect of gas pressure parameter on powder shape and size during production was discussed. 820 °C was chosen for the AM60 powder to become molten, and production was completed by applying 5, 15, 25 and 35 bar gas pressure. Argon gas was chosen in the atomization process. SEM was performed to determine powder shapes and XRD, XRF and SEM-EDX analyzes were performed to determine powder contents. In addition, powder size analyzes and hardness tests were performed. As a result of the imaging, the presence of spherical structures along with ligament, rod-like, droplet-shaped, and scaly structures was observed. As the gas pressure was increased, the

structures were observed to change into flakes and spheroids. Figure 3 shows the structural changes in powders with the change of gas pressure. When the powders taken from Bakelite were examined, it was seen that the highest hardness was 73 HV0.025 in production at 35 bar. This hardness value was found to be higher than the hardness of the AM60 alloy in ingot form (67 HV0.025) (Çetin, et al, 2020).

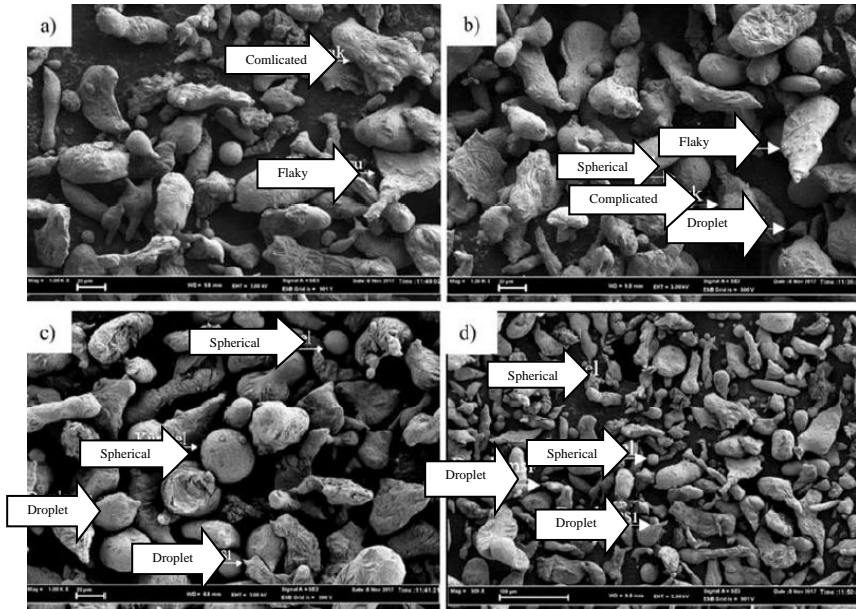


Figure 3: Productions made with a)5, b)15, c)25, d)35 bar pressure (Çetin, et al., 2020)

In the study carried out by Urtekin, Ünal and Özer, bronze and copper powder were produced using water and gas atomization. These bronze and copper powders are intended to be used in self-lubricating bearing pressing. CuSn10 was produced by water atomization method. Cu powder was also produced by gas atomization. The size of the CuSn10 powder produced by water atomization was determined as 41.5 μm , and the powder size of the Cu powder produced by the gas atomization method was determined as 41.9 μm . Figure 4 shows the copper powder obtained by gas atomization, and Figure 5 shows the bronze image obtained by water atomization. A self-lubricating bearing was produced by pressing the resulting powders. This product was subjected to sintering at 780 $^{\circ}\text{C}$ in a protective atmosphere mixed with hydrogen and nitrogen (Urtekin, et al., 2020).

Figure 4: Copper powder produced by gas atomization method (Urtekin, et al., 2020)

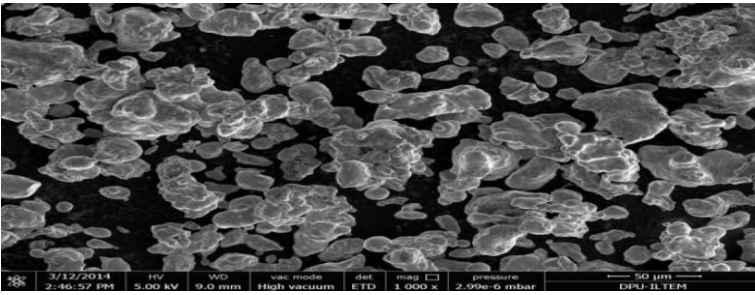


Figure 5: Image of bronze powder produced by water atomization method (Urtekin, et al., 2020)

In the study conducted by Akkaş, Akra, Çetin and Boz, AZ31Mg alloy powder was produced by the gas atomization method. In these productions, the effect of changing the gas pressure parameter on the powder shape and size was examined. In the experiments, the alloy was melted at 790 °C. 5, 15, 25 and 35 bar gas pressure was used. The nozzle diameter is determined as 2mm. XRD and XRF analysis were performed using a scanning electron microscope to see the shape of the powders and the states of the phases occurring in the internal structure. A laser measuring device was also used to determine powder sizes. As a result of production by gas atomization, ligamentous, rod-like, droplet-like, flaky and spherical powder shapes were detected. As the gas pressure increased, an increase in flake and spherical structures was observed. SEM images of powders produced under different gas parameters are shown in Figure 6. The finest powder was obtained at 35 bar, which is the highest pressure. As a result of this study, it was observed that with the increase in gas pressure, the powder size decreased and the powder structures began to take a spherical shape (Akkaş, et al., 2018).

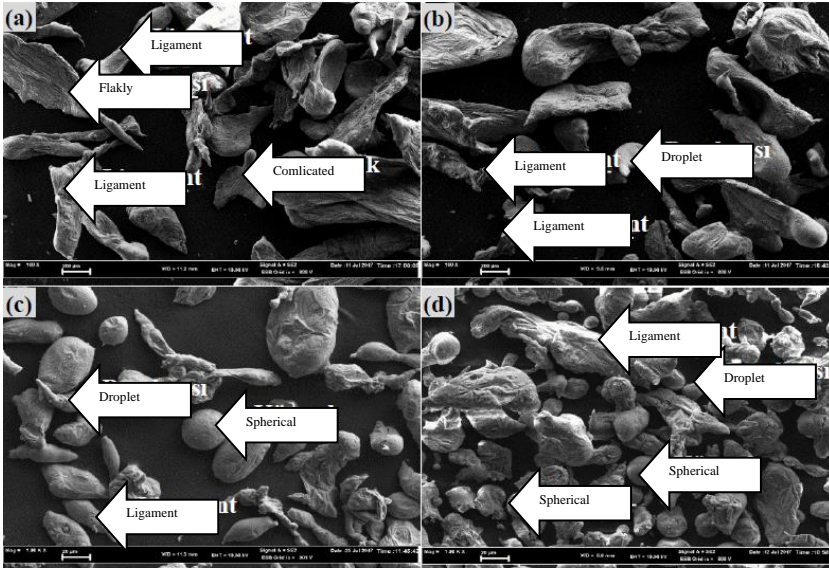


Figure 6: Powder images obtained with a)5, b)15, c)25, d)35 bar gas pressure (Akkaş, et al., 2018)

In the study conducted by Akkaş, Çetin and Boz, Al12Si alloy powder was produced by the gas atomization method. The aim of the study was to examine the effects of changes in temperature, different nozzle diameters and different gas pressure parameters on powder shape and size. As a result of the study, by reducing the nozzle diameter and increasing the gas pressure, the powder size decreased and the powder structures generally had ligamentous, droplet-like, rod-like and complex shapes. The finest powder was obtained at the highest pressure of 35 bar (Akkaş, et al., 2018).

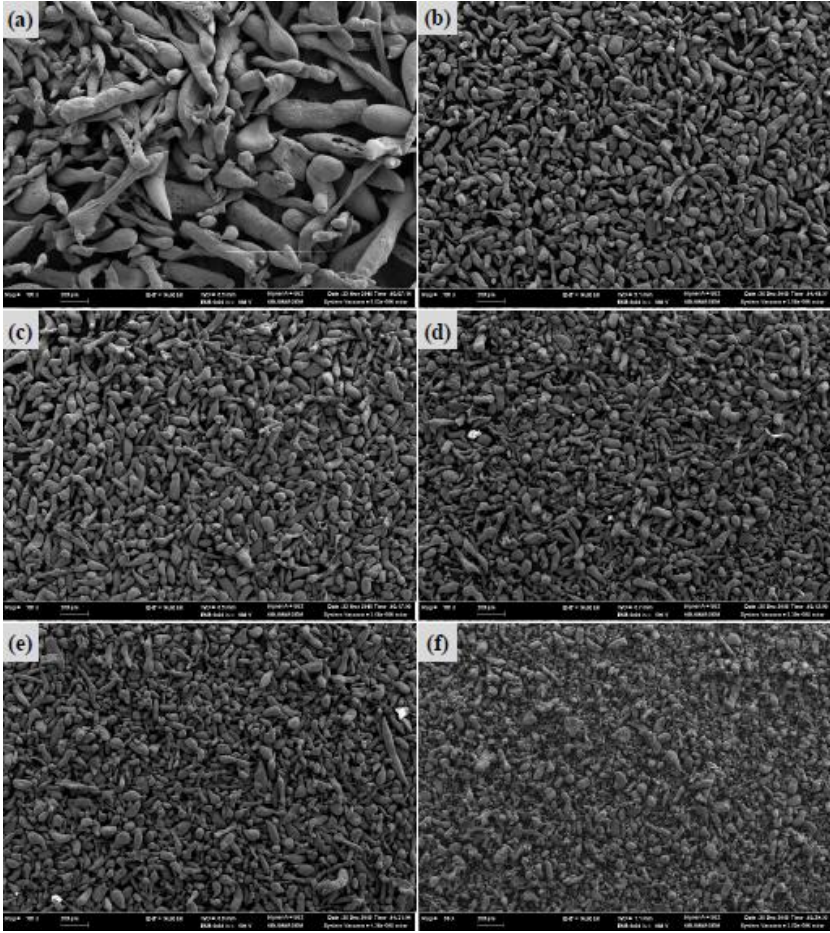


Figure 7: Production images with a)5, b) 10, c)15, d) 20, e)30, f)35 bar gas pressure (Akkaş, et al., 2018)

In the study conducted by Küçük, Öztürk and Kılıçarslan, the recycling of lead, which is among the heaviest metals in nature, was studied. In this study, waste lead was cooled with a cold nozzle gas atomization tower and turned into powder. Powdered lead is considered to be used as a fastener to be used in pipe connections. At the same time, it is aimed to improve the mechanical properties, corrosion and wear resistance of this product and sustainability. A double-sided press was used to press the powders. The pressing process was done with 100 bar pressure. Figure 8 shows the optical microscope image after pressing. The product, shaped by pressing, was subjected to sintering at 240 °C for 15 minutes. Figure 9 shows the optical microscope examination image after sintering. (Küçük, et al., 2018)

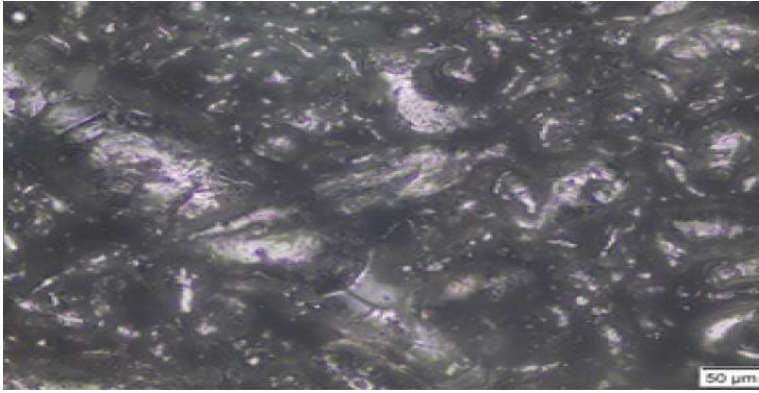


Figure 8: Optical microscope image after pressing (Küçük., et al., 2018)



Figure 9: Optical microscope image after sintering (Küçük., et al., 2018)

In the study conducted by Liu et al., Fe-Si-B-C-P powders were produced by water atomization method. The morphological structures, chemical compositions, phases and magnetic properties of the obtained powders are discussed. Powder structures were generally detected as dendritic and spherical, as shown in Figure 10. Compared to gas atomization, high amounts of oxygen were observed in the powders. It is thought that the Fe content in the material may increase magnetization. It has been stated that water atomization is suitable for industrial applications due to its low cost. (Liu, et al., 2011)

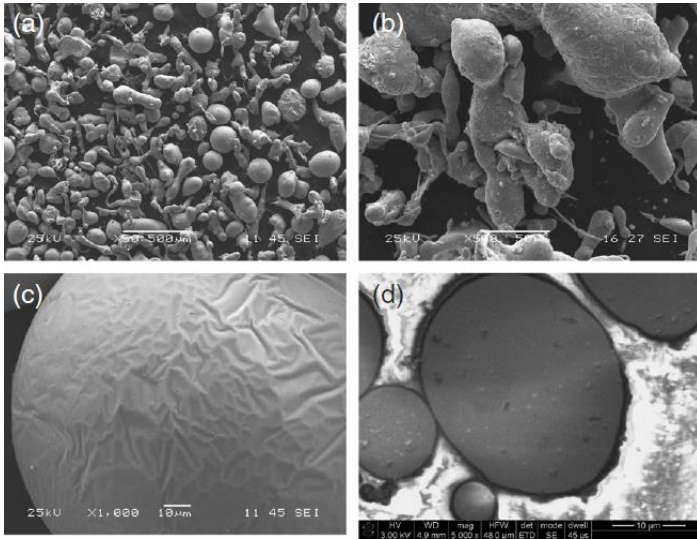


Figure 10: Appearance of Fe-based powders a) General appearance, b)Dendritic powders, c) Spherical powders, d) Microstructure (Liu, et al., 2011)

In the study conducted by Aydın and Ünal, nozzle structure, which is one of the factors affecting the powder structure in powder production by gas atomization, was emphasized. Within the scope of the study, a supersonic nozzle with a circular slot was designed. In the study where tin was used as the metal, excessive heating was applied up to 430 °C and production was carried out with gas pressures of 0.54, 0.9, 1.23, 1.31 and 1.47 MPa. When the powder structures are examined, the powders have a smooth surface and spherical shape, and the average powder size d_{50} is measured to be 11.39 μm . As seen in Figure 11, there are also satellites in the dust. (Aydın and Ünal, 2007)

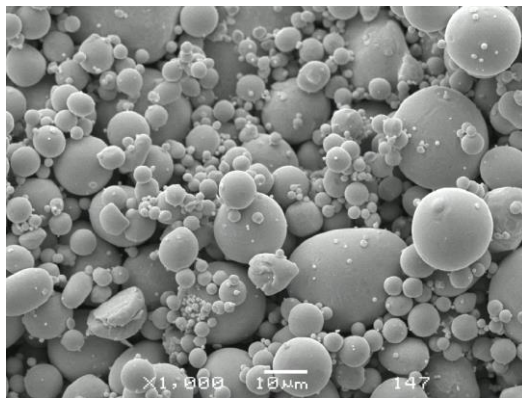


Figure 11: Tin powders produced by gas atomization. (Aydın and Ünal, 2007)

In the research conducted by Akkaş, Çetin and Boz, powders obtained with AM60 metal were examined using the gas atomization method. In this study, nozzles with diameters of 2, 3, 4, and 5 mm were used. In the study where argon gas was used, it was worked at 770 °C and 35 bar gas pressure. It was observed that the general shapes of the powders were rod-like, drop-like, ligamentous, complex and spherical. As shown in Figure 12, it was determined that the powder shapes changed into droplet-like and spherical as the nozzle diameter decreased. (Akkaş, et al., 2018)

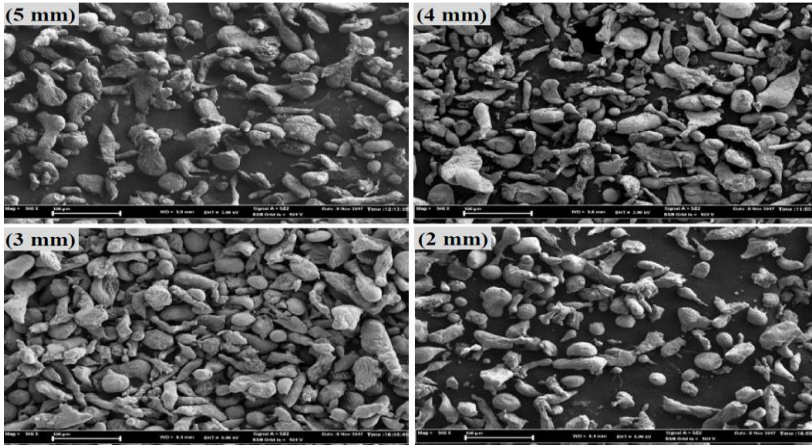


Figure 12: SEM image of AM60 powders (Akkaş, et al., 2018)

RESULT

In order for the sintering and pressing of the products to be more successful, powders with a spherical structure are required. This is one of the most important advantages of the gas atomization method in obtaining spherical powder. Reducing the cost of global powder production is possible by adjusting the optimum parameters of gas atomization variables. It has been observed that as the gas pressure used in atomization processes increases, the powder size decreases and moves from a complex, ligamentous and rod-like structure to a spherical structure. Literature research has shown that gas pressure greatly affects powder structure. At the same time, an increase in hardness values was observed with increasing pressure. However, it has been observed that the effect of pressure on reducing powder size after a certain level is not at the desired rate. However, it has been determined that the effect of gas pressure varies depending on the type of metal used. It has been observed that as the nozzle diameter decreases by a certain amount, the spherical powder in the powder content increases.

REFERENCES

1. Akkas, M., Çetin, T., Boz, M., (2018). Al12Si Powder Production and Characterization by Gas Atomization Method, *Dicle University Journal of Engineering*, 9(2): 795-804.
2. Akkaş, M. Çetin, T., Boz, M. (2018). AM60 Magnesium Alloy Powder Production and Characterization by Gas Atomization Method, *SDU International Journal of Technological Sciences*, 10(3), 1-9.
3. Akkas, M. (2019). Investigation of the Effect of Gas Pressure on AZ31 Mg Powder Production by Gas Atomization Method, *GÜFBED/GUSTIJ*, 9(2): 215-221.
4. Aydın, M., Ünal., (2007). Metal Powder Production with a New Laval Type Nozzle Design and Investigation of the Effect of Production Variables, *Makine Teknolojileri Elektronik Dergisi*, 1, 69-76.
5. Beddow, J.K. (1978), *The Production of Metal Powders by Atomization*, Heyden Press, Philadelphia.
6. Çetin, T. Akkaş, M. and Boz, M. (2019). Investigation of the effect of gas pressure on powder characterization of AM60 magnesium alloy powder produced by gas atomisation method, *Gazi Üniversitesi Mühendislik Mimarlık Fakültesi Dergisi*, 35(2), 967-978.
7. Donaldsan, C.D., and Snedeker, R. S. (1971). A Study of Free Jet Impingement, Part1. Mean Properties of Free and Impinging Jets, *J. Fluid Mech.*, 45(2)281-319.
8. Grant, N.J. (1978). *A Review of Various Atomization Processes*, in: *Rapid Solidification Processing: Principles and Technologies*, pp.230-245, Claitor's Publishing Division, Baton Rouge, LA, USA.
9. Gummeson, P.U. (1972) *Modern Atomizing Techniques*, *Powder Metal*, 15(29),67-94.
10. Gündeş, A., Yaykaşlı H. ve Özger, H., (2021). Comparison of Structural and Thermal Properties of AgCu Alloys Produced by Mechanical Alloying and Newly Developed Gas Atomization Method, *Bitlis Eren Üniversitesi Fen Bilimleri Dergisi*, 10, 1220-1231.
11. Küçük, Ö., Öztürk, B., Kılıçarslan M. F., (2018). Production Of Fittings Materials With Powder Metallurgy Method For Recycling And Sustainability Of Contaminant Plumbic Material With Gas Atomization, *Karadeniz Chemical Science and Technology*, 2, 11-14.
12. Liu, Y., Niu, S., Li, F.i., Zhu, Y., He, Y. (2011). Preparation of Amorphous Fe-based Magnetic Powder by Water Atomization, *Powder Technology*, 213(1-3), 36-40.

13. Sheikhaliev, S. M., and Dunkley, J. J. (1996). A Novel Internal Mixing Gas Atomiser for Fine Powder Production, in: *Advances in Powder Metallurgy and Particulate Materials*, vol.1, Part 1 , pp. 161-170 *MPIF and APMI International*, Princeton, NJ, USA.
14. Urtekin. L, Ünal, R. and Aydın. Ö. (2020). Effect of Powder Processes on Lubricated Bearings, *Dicle University Journal of Engineering*, 11(2), 657-652.

Chapter 20

The response of soil properties to global climate change

Fatma Olcay TOPAÇ¹

INTRODUCTION

Climate change, a global phenomenon, has been an ongoing process since the inception of the Earth. Over the last decade, it has evolved into a prominent subject of both scientific inquiry and political discourse. While discernible cold and hot cycles punctuate the Earth's climatic history, the pace of these alterations has notably accelerated in the past 150-200 years on a global scale (Fauchereau et al., 2003). In the contemporary discourse on environmental sustainability, the focal challenges of climate change and global warming have risen to prominence, demanding immediate attention and concerted efforts. The persistent elevation of greenhouse gases (GHGs) arises from a multifaceted interplay of human-induced activities—such as industrialization, urbanization, and intensive agriculture—and natural phenomena like forest fires, volcanic eruptions, and alterations in vegetation and snow cover. This complex interplay instigates unprecedented alterations in the global environment, encompassing modifications in atmospheric gas composition, spatial and temporal shifts in global temperatures, and variations in precipitation patterns, as underscored by Abbass et al.(2022). Attributed to these combined human and natural factors, the average global temperature has been estimated to have risen by approximately 1 degree Celsius, with a likely range of 0.8 to 1.2 degrees Celsius, compared to the pre-industrial period. To avoid exceeding a 1.5 °C temperature rise, it is imperative to halve net carbon dioxide emissions within the coming decade, with the remaining half mitigated between 2030 and 2050. Climate models indicate that achieving a world with net-zero carbon emissions by 2055 is crucial for a realistic chance of meeting the 1.5 °C target. If this milestone is delayed until around 2070, the global warming objective shifts to 2 °C, resulting in graver consequences for human beings and exceptional climatic conditions, resembling an apocalyptic scenario (Varghese 2023). Minor variations in the overall global temperature can trigger notable environmental anxieties, setting the stage for substantial changes in climate and weather

¹ Prof. Dr.; Bursa Uludağ Üniversitesi Mühendislik Fakültesi Çevre Mühendisliği Bölümü. olcaytopac@uludag.edu.tr ORCID No: 0000-0002-6364-4087

patterns (Figure 1). This phenomenon adds to the worldwide health challenges, resulting in direct or indirect health repercussions caused by extreme weather events and shifts in climate (Baker et al., 2022; Ebi et al., 2021; McMichael, 2015).

Alterations in the atmosphere and oceans hold the potential to significantly transform the biosphere—the delicate living layer of existence on Earth intricately linked to both the atmosphere and hydrosphere. This biosphere serves as the vital fabric sustaining human societies, providing the essential environment within which they thrive. Soil responses to climate change are intricately linked to temperature rises and the occurrence of extraordinary meteorological events. These events encompass intense rainfall, extended periods of drought, unexpected frosts, severe storms, and the escalation of sea levels in coastal regions. These impacts heighten the threats to soils, manifesting in issues including heightened susceptibility to erosion, increased soil compaction, diminished fertility, and a decline in agricultural productivity (Brevik, 2013; Karmakar et al., 2016; Wasan and Wasan, 2023). Put differently, the forthcoming alterations will impact the essential systems and properties of the soil, which play a key role in preserving soil fertility and productivity.

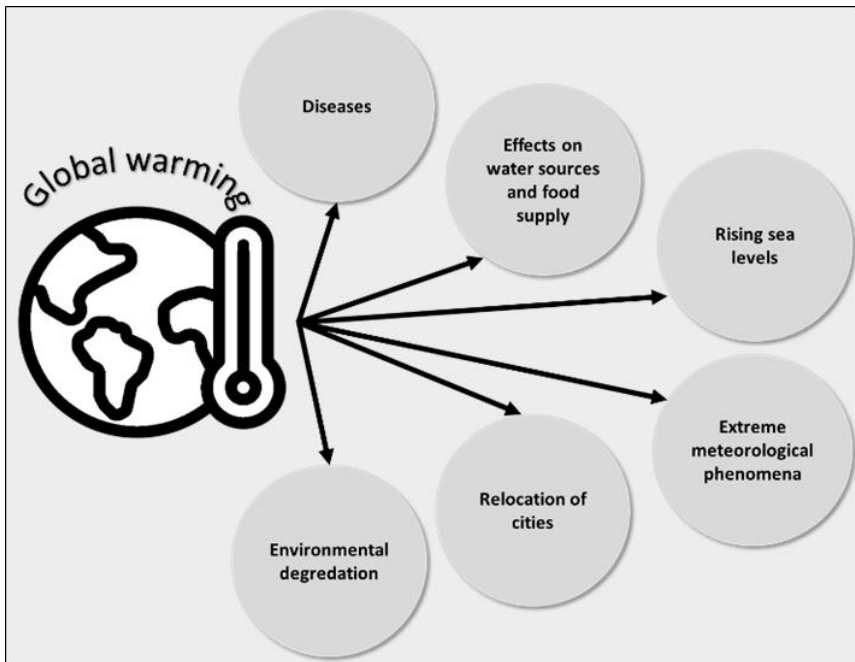


Figure1: Consequences of global warming

Digging deeper into the connection between climate change and soil dynamics reveals a complex set of challenges. Rising temperatures, combined with extreme meteorological conditions create significant threats to soils. Erosion, compaction, reduced fertility, and lower agricultural productivity become real issues, contributing to problems with food security and environmental sustainability. Understanding and addressing these issues requires recognizing how climate and soil interact, and how changes in climate can impact soil. This chapter will explore the effects of climate change on basic soil properties and important biochemical processes, focusing on the interactions between soil and climate.

SOIL C AND N DYNAMICS

There is a widely accepted understanding that elevated CO₂ levels bring about both quantitative and qualitative changes in the release of compounds originating from plant roots. When subjected to elevated levels of carbon dioxide, plants undergo a shift in metabolic resource allocation within root exudates. This entails a diminished allocation of nitrogen-rich metabolites, accompanied by a concurrent increase in the allocation of carbon-rich compounds. This shift leads to heightened microbial activity, subsequently increasing CO₂ production. This phenomenon poses a potential adverse impact on the accumulation of organic carbon in soils, thereby influencing the soil's capacity for sequestration. The observed priming effect resulting from enhanced microbial activity under increased atmospheric CO₂ concentrations represents an enormous negative response on processes of global change, ultimately diminishing the soil's potential for carbon sequestration (Pareek, 2017).

As indicated in Figure 2., elevated temperatures are expected to adversely impact the allocation of carbon to the soil, resulting in decreased levels of soil organic carbon. This phenomenon establishes a positive feedback loop in the global carbon cycle: rising temperatures contribute to an increased release of carbon dioxide from soils into the atmosphere, further amplifying temperature increases (Wan et al., 2011). A study conducted in a semi-arid steppe by Link et al. (2003) revealed that soil warming and drying cycles resulted in a significant reduction of 32% in soil carbon levels within a span of five years. This reduction in soil carbon occurred at a much faster rate than observed declines attributed to enhanced tillage practices.

Given that soil organic matter (SOM) substantially influences the majority of soil functions, a decline in SOM levels may precipitate diminished fertility and biodiversity. Additionally, such reductions in SOM can contribute to the deterioration of soil structure, manifesting as diminished water holding

capacity, heightened susceptibility to erosion, increased bulk density, and consequent soil compaction. Land utilization and strategic management operations fostering the accumulation of SOM serve as effective means to sequester carbon dioxide from the atmosphere, thereby contributing to the mitigation of global warming. The augmentation of water retention capabilities by SOM plays a pivotal role in alleviating the impacts of flooding resulting from intense rainfall events, while concurrently enhancing soil resilience by storing water during periods of drought (Patil and Lamnganbi, 2018).

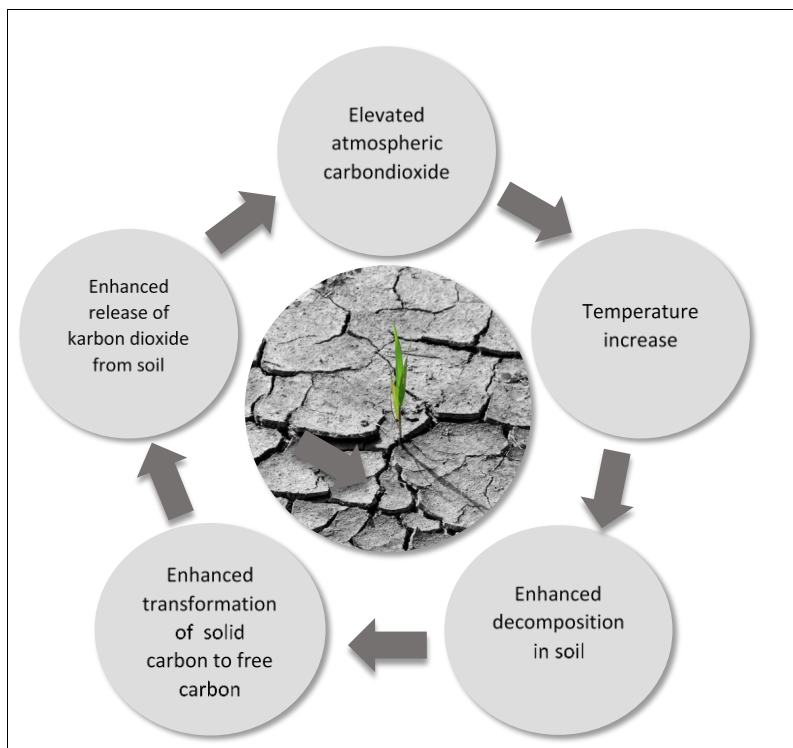


Figure 2: Effect of climate change on soil organic matter.

Elevation in soil carbon-to-nitrogen (C:N) ratio induced by carbon dioxide (CO₂) enrichment necessitates an increased nitrogen (N) demand by decomposing soil organisms, thereby potentially diminishing N mineralization processes. N mineralization represents a pivotal facet in the provision of nitrogen to plants. Consequently, a decline in N mineralization is anticipated to correspondingly diminish the levels of plant-available nitrogen in the soil, thereby exerting a detrimental impact on plant productivity (Brevik, 2013). A research conducted in England has revealed a reduction in carbon storage

capacity within organic matter-rich soils. This decline has been attributed to rising temperatures and diminishing soil moisture, factors associated with global warming and drought conditions, as reported by Ostle et al. (2009).

SOIL EROSION

Soil erosion emerges as a leading catalyst in land degradation, playing a pivotal role in the overall deterioration of landscapes. Its primary impact is felt on the crucial upper layer of fertile soil, integral to the productivity of (agro)ecosystems. This topsoil layer is indispensable for ensuring food security, underscoring its vital role in sustaining agricultural productivity (Abdulle et al., 2022).

The impact of climate change on soil erosion is predominantly affected by shifts in intense precipitation events. Current long-term observations already indicate a rising pattern in global extreme precipitation with projections from climate models foreseeing a continued escalation in the upcoming decades (Papalexioiu and Montanari, 2019). Predictions indicate that a rise in the strength and frequency of precipitation events will likely result in heightened soil erosion. The significance of intensity lies in the ability of rapidly moving raindrops and water to displace larger aggregates and particles. Although fine-textured soils are susceptible to erosion, alterations in precipitation patterns may also pose a risk to soils with a medium texture (Borrelli et al., 2020). However soil erosion does not exhibit a linear correlation with average values of annual precipitation, runoff, and erosion rates. The dynamics of soil erosion, encompassing its rate, type, and extent, are contingent upon the interactive effects of climatic variables, notably the quantity and intensity of precipitation. Additional influential factors include relief, vegetation cover (comprising type, continuity, and density), and the erodibility characteristics inherent in the soil.

According to Varallyay (2010), potential shifts in climate may impart diverse impacts on soil erosion. For instance, heightened precipitation, particularly attributed to intense rainfalls and thunderstorms, may contribute to elevated erosion rates unless counteracted by the protective influence of denser and more enduring vegetation. Conversely, diminished rainfall typically corresponds to a reduction in the erosion rate; however, the evaluation of this diminishing effect necessitates consideration of the concurrent decline in vegetation quality resulting from moisture limitations. As a prevailing trend, decreased precipitation is anticipated to augment wind erosion.

Eekhout and de Vente (2022) conducted an examination of 224 model studies that had explored the effects of climate change on soil erosion, evaluating the robustness of each study through statistical analysis. The results

revealed a global upward trend in soil erosion by the end of the 21st century, with the most significant increases predicted in semi-arid regions. Emphasis was placed on the role of land use change, characterized by agricultural intensification and forest depletion, in amplifying the impact of soil erosion. Conclusions reached included recommendations for reforestation, abandonment of agricultural lands, and implementation of soil conservation practices, all of which were identified as measures that could effectively offset the impact of climate change on soil erosion.

As delineated by de Vente and Eekhout (2021), the prevailing consensus among studies is the expectation of an increase in soil erosion due to imminent climate change. It was further emphasized that the magnitude and significance of these anticipated effects hinge on discrepancies in environmental factors, encompassing climate and land use, as well as methodological considerations like erosion models, bias correction, and climate ensemble, which vary across distinct research investigations.

An additional investigation delved into the escalating patterns of global soil erosion rates, placing emphasis on the discernment of this upward trend. The study highlighted the correlation with annual precipitation levels ranging from 1000 to 1400 mm per year, slopes reaching a maximum gradient of 20%, and a heightened susceptibility of fallow lands to rain-induced soil erosion. Notably, tropical areas, characterized by intricate topography, limited vegetation, and extensive agricultural land utilization, were identified as particularly vulnerable to soil erosion owing to the magnitude and intensity of rainfall during specific temporal intervals (Garcia-Ruiz et al., 2015; Burt et al., 2015).

SOIL TEMPERATURE AND WATER

Global warming leads to an increase in overall air temperatures. This increase in atmospheric temperature can directly influence the surface temperature of the soil. Warmer air temperatures contribute to higher soil temperatures, especially in the upper soil layers. In a research investigation conducted by Reshotkin and Khudyakov (2019), the data collected from meteorological stations situated in diverse natural zones across the European segment of Russia is utilized to illustrate the response of soil temperature to contemporary climate shifts. The most pronounced warming trend was identified at the onset of the 21st century. In the period from 2001 to 2015, the average annual air temperature exhibited an increase of 1.2-1.4°C compared to the period from 1961 to 1990. Across all examined soils and depths, the average annual soil temperature displayed an elevation ranging from 0.5 to 1.0°C. This soil warming phenomenon was evident during both warm and cold periods

throughout the year. In an alternative study, an examination was conducted on the patterns and variations in soil temperatures at depths of 0, 80, 160, and 320 cm, utilizing atmospheric data derived from 30 climate stations situated in Northwest China over the period from 1960 to 2000. The investigation revealed that the disparity between the annual average air temperature and soil temperature within each layer at each station did not exceed 6°C. Results demonstrated the emergence of warming trends at certain stations post the mid-1980s. Notably, minimal warming trends were observed in the western region of Northwest China, while a predominant number of warming trends manifested in the eastern part. Furthermore, positive and statistically significant correlation coefficients between soil and air temperatures were identified at most stations, excluding the winter season, with a confidence level of 95% (Wang et al., 2022).

Global warming can have significant implications for soil moisture dynamics, and the impact on soil moisture levels varies based on regional climate patterns, soil types, and land use practices. Rising temperatures associated with global warming can lead to increased evaporation rates. As temperatures rise, more water is vaporized from the soil surface, potentially leading to drier surface conditions. Global warming has the potential to modify precipitation patterns, causing shifts in the timing, strength, and geographical spread of rainfall. Some regions may experience more intense and less predictable precipitation events, while others may face prolonged periods of drought. These changes can directly impact soil moisture levels. In many regions, global warming is associated with an increased frequency and intensity of drought events. Extended periods of high temperatures and reduced precipitation can lead to soil moisture deficits, negatively affecting vegetation, agriculture, and water resources. Projections for the period spanning 2070 to 2100 indicate a widespread decline in summer soil moisture across the majority of Europe, with particularly noteworthy reductions anticipated in the Mediterranean region. Conversely, an augmentation in summer soil moisture levels is projected for the northeastern part of Europe during the same time frame (Jones et al., 2009).

Understanding the complex interactions between global warming and soil moisture is crucial for developing strategies to adapt to changing environmental conditions. Monitoring soil moisture levels, implementing sustainable water management practices, and incorporating climate-resilient agricultural techniques are important steps in addressing the impacts of global warming on soil moisture.

SOIL ORGANISMS

Among the potential impacts of climate change on soil, the most significant considerations pertain to subterranean biodiversity, encompassing bacteria, microbes, fungi, microscopic invertebrates, and larger invertebrates like earthworms, ants, and termites. The influence of climate change on soil biodiversity is twofold: direct effects stem from alterations in soil temperature and moisture, while indirect effects arise from changes in vegetation communities, productivity, and the rate of organic matter decomposition. Notably, not all soil biota will experience the same degree of impact from climate change.

In an investigation, the response of soil communities to deliberate warming (+4 °C) and increased atmospheric CO₂ levels (800 ppm) was examined within a two-year field experiment carried out in the boreal forest. The initial year of the study aimed to assess the effect of these simulated climate change factors on community composition, wealth of species, diversification and similarity. Surprisingly, in the first year, experimental practices had minimal effects on the fauna. However, during the second year, oribatid mites exhibited responses to both warming and elevated CO₂ levels. Additionally, there was an increase in the richness and diversity of springtails, accompanied by alterations in the composition of the soil community (Meehan et al., 2020).

The modification of microbial soil respiration rates, induced by global phenomena like warming, is a direct consequence of the temperature sensitivity inherent in soil microorganisms and the processes they mediate. DeAngelis et al. (2015) observed that under conditions of a 5-degree Celsius temperature increase in a temperate forest, alterations occurred in the proportional representation of soil bacteria. Furthermore, the community's bacteria-to-fungus ratio demonstrated an increase. Elevated atmospheric CO₂ affects soil microbes by increasing mycorrhizal colonization. CO₂ enrichment is expected to boost mycorrhizal biomass because plants require more nitrogen and phosphorus, which aligns with increased carbon assimilation rates. So, at high CO₂ levels, mycorrhizal biomass increases as C becomes relatively less limiting and soil nutrients become more limiting for plant growth (Drigo et al., 2008).

A study focused on alpine forest ecosystems employed soil column experiments to assess the impact of climate change on soil microbes. The study simulated climate warming and cooling, mimicking temperature changes within the range of ±4.7°C. The findings indicated that warming induced structural alterations in microbial communities across all soil layers. Conversely, cooling did not exhibit a notable influence on the structure of bacterial communities in the various soil layers (0–10 cm, 10–20 cm, and 20–30 cm), but it significantly

impacted fungal communities throughout these layers. The study concluded that variations in soil fungal community structure were primarily driven by soil moisture content and temperature, while soil bacterial community structure exhibited a closer association with overall soil conditions (Fu et al., 2023).

SOIL ACIDIFICATION AND SALINIZATION

Climate change, characterized by global warming and alterations in precipitation patterns, can significantly influence soil acidity. Climate change often brings more intense and frequent rainfall. This increased precipitation can lead to greater leaching of base cations. Elevated temperatures linked to climate change expedite the breakdown of organic material within the soil. This process releases organic acids, further contributing to soil acidity. Faster decomposition can reduce the buffering capacity of the soil, making it more susceptible to changes in acidity (Gelybo et al., 2018; Gupta and Upadhyay, 2023). In the investigation assessing pH variations in Tibetan Plateau grassland areas between 2000 and 2020, alongside temperature, precipitation, and radiation data, findings revealed that climate change induced soil alkalinization at depths of 0-10 cm and soil acidification at depths of 10-20 cm and 20-30 cm. The study determined that, under conditions of climate change, soil alkalinization occurred in 23.71% to 36.84% of the surveyed regions, while soil acidification was observed in 21.43% to 45.52% of the examined areas (Sun et al., 2023).

On the other hand, a rise in temperature combined with reduced rainfall can trigger capillary water movement and the evaporation of groundwater. This process, as highlighted by Varallyay (2007), may give rise to the accumulation of salts in the soil, a phenomenon commonly referred to as salinization. In a study conducted by Khamidov (2022), the salinity dynamics of irrigated lands in the Khorezm region (Uzbekistan) under the influence of climate change were assessed, and projections for salinity increases were made using statistical methods. The results of homogeneity tests indicate that by the year 2100, there will be an increase of 32.5% and 15.1% in areas classified as moderately and highly saline, respectively, while areas classified as slightly saline are projected to decrease by 52.4%. The study concludes that salinity levels across the examined region will significantly increase as a result of climate change.

In a study conducted by Bannari and Al-Ali (2020), the enduring impacts of a 30-year period characterized by escalating temperatures and diminishing precipitation were investigated. The results underscored a positive correlation between these climatic changes and soil salinity, particularly in arid regions where reduced soil leaching occurs. Moreover, the ongoing trend of global warming may intensify salinity concerns in agricultural lands situated in coastal

areas, primarily attributed to the melting of ice sheets and the consequent rise in sea levels. In alignment with these findings, Rahman et al. (2018) observed a noteworthy surge in the salinity rate within coastal agricultural regions, escalating from 1% to 33% over the past 25 years.

CONCLUSION AND RECOMMENDATIONS

In conclusion, this chapter has provided a comprehensive exploration of the multifaceted impacts of climate change on soils. The intricate interplay between rising temperatures, unstable precipitation patterns, and extraordinary weather events has been thoroughly examined, shedding light on the intricate dynamics influencing soil processes. From alterations in soil temperature and moisture content to the consequential changes in soil structure and microbial activity, the effects of climate change resonate across various layers of the soil ecosystem.

The studies discussed highlight the vulnerability of soils to climatic shifts, with implications extending beyond mere changes in physical and chemical properties. Soil erosion, salinization, and shifts in microbial communities underscore the far-reaching consequences that climate change imposes on soil health and fertility. Moreover, the interconnection between soil health and broader environmental considerations, such as agriculture, biodiversity, and ecosystem functioning, emphasizes the urgency of understanding and mitigating these impacts.

The uncertainties inherent in climate change, its impact on long-term soil dynamics, and the complex interactions with agricultural practices all emphasize the importance of continued scientific inquiry. To address these uncertainties and support ambitious goals, future studies may focus on the following areas:

- Investigating how climate change influences soil processes over the long term, including aspects such as nutrient cycling, microbial activity, and soil structure.

- Understanding how climate change interacts with different agricultural practices, such as crop rotation, irrigation methods, and soil management techniques, to identify sustainable and resilient approaches.

- Assessing the consequences of various adaptation options, considering factors such as their effectiveness, economic viability, and environmental sustainability.

- Examining the complex interplay of factors that affect the outcomes of adaptation strategies, including socio-economic factors, technological advancements, and policy changes.

-Investigating how changes in markets, technological advancements, and policy frameworks can impact soil-related adaptation strategies.

By addressing these research areas, scientists can contribute valuable insights that will inform more effective climate change adaptation strategies, particularly in the context of soil processes and agriculture. This knowledge is crucial for developing sustainable practices and policies that can mitigate the adverse effects of climate change on soil health and ensure food security in the face of a changing climate.

REFERENCES

1. Abbass, K., Qasim, M.Z., Song, H., Murshed, M., Mahmood, H., Younis, I. (2022). A review of the global climate change impacts, adaptation, and sustainable mitigation measures. *Environ Sci Pollut Res*, 29, 42539–42559. <https://doi.org/10.1007/s11356-022-19718-6>.
2. Abdulle, Y.A., Hussein, M.F., Mohamed, A.M., Mohamud, A.H., Osman, A.F.I., Mohamuud, B.A., Idiris, F.H. (2022). Effects of soil erosion on crop productivity in Afgoye, lower Shabelle-Somalia. *International Journal of Plant, Animal and Environmental Sciences*, 12, 115-122. <https://doi.org/10.26502/ijpaes.4490136>.
3. Baker, R.E., Mahmud, A.S., Miller, I.F., Rajeev, M., Rasambainarivo, F., Rice, B.L., Takahashi, S., Tatem, A.J., Wagner, C.E., Wang, L. F., Wesolowski, A. , Metcalf, C.J.E. (2022). Infectious disease in an era of global change. *Nat Rev Microbiol*, 20, 193–205. <https://doi.org/10.1038/s41579-021-00639-z>.
4. Bannari, A., Al-Ali, Z. M. (2020). Assessing climate change impact on soil salinity dynamics between 1987–2017 in arid landscape using Landsat TM, ETM+ and OLI data. *Remote Sensing*, 12:2794. <https://doi.org/10.3390/rs12172794>.
5. Borrelli, P., Robinson, D.A., Panagos, P., Lugato, E., Yang, J.E., Alewell, C., Wuepper, D., Montanarella, L, Ballabio, C. (2020). Land use and climate change impacts on global soil erosion by water (2015–2070). *Proc Natl Acad Sci*, 117, 36, 21994–22001. <https://doi.org/10.1073/pnas.2001403117>.
6. Brevik, E.C. (2013).The Potential impact of climate change on soil properties and processes and corresponding influence on food security. *Agriculture*, 3, 3, 398-417. <https://doi.org/10.3390/agriculture3030398>.
7. Burt, T., Boardman, J., Foster, I., Howden, N. (2015). More rain, less soil: Long-term changes in rainfall intensity with climate change. *Earth Surf. Process. Landf.*, 41, 563-566. <https://doi.org/10.1002/esp.3868>.
8. de Vente, J., Eekhout, J. (2021). The impact of climate change on soil erosion: a systematic review. *EGU General Assembly*, EGU21-5008, 19-30. <https://doi.org/10.5194/egusphere-egu21-5008>.
9. DeAngelis, K.M., Pold, G., Topcuoglu, B.D., van Diepen, L.T.A., Varney, R.M., Blanchard, J.L., Melillo, J., Frey, S.D. (2015). Long-term forest soil warming alters microbial communities in temperate forest soils. *Frontiers in Microbiology*, 6, 104. <https://doi.org/10.3389/fmicb.2015.00104>.

10. Drigo, B., Kowalchuk, G.A., Johannes, A.V. (2008). Climate change goes underground: effects of elevated atmospheric CO₂ on microbial community structure and activities in the rhizosphere. *Biology and Fertility Soils*, 44, 5, 667– 679. <https://doi.org/10.1007/s00374-008-0277-3>.
11. Ebi, K.L., Vanos, J., Baldwin, J.W., Bell, J.E., Hondula, D.M., Errett, N.A., Hayes, K., Reid, C.E., Saha, S., Spector, J., Berry, P. (2021). Extreme weather and climate change: Population health and health system implications. *Annual Review of Public Health*, 42,1, 293-315. <https://doi.org/10.1146/annurev-publhealth-012420-105026>.
12. Eekhout, J.P.C., de Vente, J. (2022). Global impact of climate change on soil erosion and potential for adaptation through soil conservation. *Earth-Science Reviews*, 226, 103921. <https://doi.org/10.1016/j.earscirev.2022.103921>.
13. Fauchereau, N., Trzaska, S., Rouault, M., Richard, Y. (2003). Rainfall variability and changes in Southern Africa during the 20th century in the global warming context. *Natural Hazards*, 29, 2, 139–154. <https://doi.org/10.1023/A:1023630924100>.
14. Fu, F., Li, J., Li, Y., Chen, W., Ding, H., Xiao, S. (2023). Simulating the effect of climate change on soil microbial community in an *Abies georgei* var. *smithii* forest. *Front. Microbiol.* 14, 1189859. <https://doi.org/10.3389/fmicb.2023.1189859>.
15. Garcia-Ruiz, J.M., Beguería, S., Nadal-Romero, E., González-Hidalgo, J.C., Lana-Renault, N., Juán, Y.S. (2015). A meta-analysis of soil erosion rates across the World. *Geomorphology*, 239, 160-173. <https://doi.org/10.1016/j.geomorph.2015.03.008>.
16. Gelybo, G., Toth, E., Farkas, C., Horel, A., Bakacsi, Z. (2018). Potential impacts of climate change on soil properties. *Agrochem. Soil Sci.*, 67, 1, 121-141. <https://doi.org/10.1556/0088.2018.67.1.9>.
17. Gupta, S. K., Upadhyay, A. (2023). Impact of climate change on soil properties. *Vigyan Varta*, 4, 12, 122-127.
18. Jones, A., Stolbovoy, V., Rusco, E., Gentile, A.R., Gardi, C., Marechal, B., Montanarella, L. (2009). Climate change in Europe. 2. Impact on soil. A review. *Agron. Sustain. Dev*, 29, 423–432. <https://doi.org/10.1051/agro:2008067>.
19. Karmakar, R. Das, I., Dutta, D., Rakshit, A. (2016). Potential effects of climate change on soil properties: A review. *Science International*, 4, 51-73. <https://scialert.net/abstract/?doi=sciintl.2016.51.73>.

20. Khamidov, M., Ishchanov, J., Hamidov, A., Donmez, C., Djumaboev, K. (2022). Assessment of soil salinity changes under the climate change in the Khorezm region, Uzbekistan. *Int J Environ Res Public Health*, 19, 148794. doi: 10.3390/ijerph19148794.
21. Link, S.O., Smith, J.L., Halverson, J.J., Bolton, H., Jr. (2003). A reciprocal transplant experiment within a climatic gradient in a semiarid shrub-steppe ecosystem: Effects on bunchgrass growth and reproduction, soil carbon, and soil nitrogen. *Glob. Change Biol.*, 9, 1097–1105. <https://doi.org/10.1046/j.1365-2486.2003.00647.x>.
22. McMichael, A.J. (2015). Extreme weather events and infectious disease outbreaks. *Virulence*, 6, 6, 543-5477. <https://doi.org/10.4161/21505594.2014.975022>.
23. Meehan, M.L., Barreto, C., Turnbull, M.S., Bradley, R.L., Bellenger, J.P., Darnajoux, R., Lindo, Z. (2020). Response of soil fauna to simulated global change factors depends on ambient climate conditions. *Pedobiologia*, 83, 150672. <https://doi.org/10.1016/j.pedobi.2020.150672>.
24. Ostle, N. J., Levy, P. E., Evans, C. D., Smith, P. (2009). UK land use and soil carbon sequestration. *Land Use Policy*, 26, S274–S283. <https://doi.org/10.1016/j.landusepol.2009.08.006>.
25. Papalexioiu, S.M., Montanari A. (2019). Global and regional increase of precipitation extremes under global warming. *Water Resour. Res.*, 55, 6, 4901-4914. <https://doi.org/10.1029/2018WR024067>.
26. Pareek, N. (2017). Climate change impact on soils: adaptation and mitigation. *MOJ Ecology & Environmental Science*, 2, 3, 136–139. <https://doi.org/10.15406/mojes.2017.02.00026>.
27. Patil, A., Lamnganbi, M. (2018). Impact of climate change on soil health: A review. *International Journal of Chemical Studies*, 6, 3, 2399-2404.
28. Rahman, A. K. M. M., Ahmed, K. M., Butler, A. P., Hoque, M. A. (2018). Influence of surface geology and micro-scale land use on the shallow subsurface salinity in deltaic coastal areas: A case from southwest Bangladesh. *Environ. Earth Sci*, 77, 423. <https://doi.org/10.1007/s12665-018-7594-0>.
29. Reshotkin, O.V., Khudyakov, O.I. (2019). Soil temperature response to modern climate change at four sites of different latitude in the European part of Russia. *IOP Conf. Ser.: Earth Environ. Sci.*, 368, 012040. <https://doi.org/10.1088/1755-1315/368/1/012040>.

30. Sun, W., Li, S., Zhang, G., Fu, G., Qi, H., Li, T. (2023). Effects of climate change and anthropogenic activities on soil pH in grassland regions on the Tibetan Plateau. *Global Ecology and Conservation*, 45, e02532. <https://doi.org/10.1016/j.gecco.2023.e02532>.
31. Varallyay, G. (2007). Potential impacts of climate change on agroecosystems. *Agriculturae Conspectus Scientificus*, 72, 1, 1-8.
32. Varallyay, G. (2010). The impact of climate change on soils and on their water management. *Agronomy Research*, 8 (Special Issue II), 385–396.
33. Varghese, S. (2023). Future of Climate Change. In: Landes, T., Varghese, S., Sargsyan, K. (eds) *Future Intelligence. Future of Business and Finance*. Springer, Cham. https://doi.org/10.1007/978-3-031-36382-5_7.
34. Wan, Y., Lin, E., Xiong, W., Li, Y., Guo, L. (2011). Modeling the impact of climate change on soil organic carbon stock in upland soils in the 21st century in China. *Agric. Ecosyst. Environ.*, 141, 23–31. <https://doi.org/10.1016/j.agee.2011.02.004>.
35. Wang, Y., Jiang, Z., Zhou, D., and Gong, Z. (2022). Evaluation and analysis of observed soil temperature data over Northwest China. *Open Geosciences*, 4, 1, 1562-1576. <https://doi.org/10.1515/geo-2022-0376>.
36. Wasan, J.P.M., Wasan, K.M. (2023). Effects of climate change on soil health resulting in an increased global spread of neglected tropical diseases. *PLoS Negl Trop Dis*, 17, 6, e0011378. <https://doi.org/10.1371/journal.pntd.0011378>.

Chapter 21

Modeling and Simulation of Fuzzy Logic MPPT Method for Photovoltaic DC/DC Boost Converter

Yasemin ÖNAL¹

Abstract:

Nowadays, in many countries that aim to use clean energy, high amounts of energy are saved with PV panel systems, while gas emission that harm the environment are reduced. However, the performance of the photovoltaic panel system changes with system designs, technological developments and variable environmental conditions such as temperature and irradiation, which reduces the efficiency of the system. To increase the efficiency of the system and to reduce cost of the system, PV panels must be operated at the maximum power point. In this study, modeling and simulation studies of the fuzzy logic MPPT method were carried out to increase the system efficiency by operating the PV panel fed DC/DC boost converter at the maximum power point under variable temperature and irradiation. Modeling, simulation and verification of the method used were carried out in the MATLAB/Simulink program. The simulated circuit consists of PV panel system, DC/DC boost converter, fuzzy logic control block and measurement blocks. Solar irradiation intensity was applied to the panel input as 600W/m^2 , 800W/m^2 and 1000W/m^2 , and the ambient temperature was 25°C . While 380V constant voltage is obtained at the PV panel output, 550V , 620V and 700V are obtained respectively at the boost converter output. Throughout the simulation, system efficiency was achieved at 94.5% and above. The results obtained show that the photovoltaic system with the fuzzy logic MPPT method monitors the maximum power point with high efficiency in changing environmental conditions.

Keywords: MPPT method, PV system, Fuzzy logic algorithms, DC/DC boost converters.

¹ Doç. Dr.; Bilecik Şeyh Edebali University Electric-Electronic Engineering Department, Gulumbe Campus, Bilecik, Turkey, yasemin.onal@bilecik.edu.tr, ORCID ID: 0000-0003-0173-0948

INTRODUCTION

Today's technology is largely dependent on fossil fuels as an energy source for heating, production, transportation and all other activities. However, the use of fossil fuels causes an increase in costs due to the decrease in fuels such as oil and natural gas with limited reserves, and causes harmful emissions and negative effects of greenhouse gases on the environment as a result of burning fossil fuels. Due to the drawbacks of using fossil fuels, renewable energy sources such as wind, solar, geothermal and biomass have begun to be used. Photovoltaic (PV) systems, which convert solar energy into electricity and provide environmentally friendly and sustainable energy production, have an important place among renewable energy sources. However, achieving the maximum power output of PV systems is a challenging process due to the influence of environmental factors such as variable solar irradiation levels and temperature (Benner and Kazmerski, 1999:9).

The current and voltage characteristics and the power and voltage characteristics obtained from the PV panel system have only one maximum power point (MPP). In addition, the location of the MPP changes according to the changing solar irradiation level, temperature level and environmental conditions such as clouds, rain, snow, dust and humidity. The power inequality between sources and load characteristics restricts the maximum power draw from the PV panel system, causing some large power losses. This reduces the efficiency of PV panel systems and increases system costs (Hepzibah and Premkumar, 2020:15).

MPP monitoring in PV systems increases efficiency by ensuring that the panel operates at the optimum operating point. There are many traditional MPPT methods in the literature to achieve this point. Some of these traditional methods are Perturb-and-Observe (P&O) (Jubaer and Zainal, 2015:12; Alik and Jusoh, 2017:12), hill climbing (Saharia and Saharia, 2016:9), incremental conductance (IC) (Safari and Mekhilef, 2010:8) and incremental resistance method (Mei et al., 2010:8). Traditional methods usually use fixed measurement techniques or some optimized algorithms. However, these methods are limited in their ability to provide stable performance under variable weather conditions and variable solar radiation, and the system efficiency is greatly reduced (Dadfar et al., 2019:19).

In order to solve these problems in the literature, artificial neural network (ANN) (Elobaid 2015:21; Fathi and Parian, 2021:11), fuzzy logic (FL) (Nabipour et al., 2017:23; Al Nabulsi and Dhaouadi, 2012:12), artificial intelligence-based methods such as neuro-fuzzy (NF) (Hassan et al., 2017:16) and genetic algorithm (GA) (Joshi and Arora, 2017:24; Hadji et al., 2015:15) have been developed (Seyedmahmoudian et al., 2016:21). The MPPT method using a fuzzy neural

network structure has been developed to increase PV efficiency (Gani, 2021:19). When the results obtained in the study were compared with the incremental conductivity and P&O methods, it was observed that no deviations in MPP occurred under variable irradiation conditions. In another study, the performance, cost, tracking speed, complexity, accuracy, advantages and disadvantages of MPPT methods used in PV systems were examined and the methods were classified (Mao et al., 2020:16). Among artificial intelligence based MPPT methods, the FL method stands out as an important alternative in MPP follow-up thanks to its ability to learn, generalize, make decisions and deal with uncertainties. FL algorithms allow the system to operate more flexibly and optimized under various conditions. The use of FL algorithms in DC/DC boost converter has the potential to achieve more effective and stable performance in MPP tracking by adapting to variable environmental conditions (Nadia, 2018:22).

In this study, simulation studies of the fuzzy logic MPPT method were carried out in order to operate the PWM signals in the PV panel fed DC/DC boost converter at the maximum power point under variable temperature and irradiation and to increase the system efficiency. Modeling, simulation and verification of the method used were carried out in MATLAB/Simulink program. The simulated circuit consists of PV panel system, DC/DC booster circuit, FL control block and measurement blocks. While 380V constant voltage is obtained at the PV panel output, 550V, 620V and 700V voltage are obtained at the boost converter output respectively.

FUZZY LOGIC MPPT METHOD

The existence of uncertainty is expressed in imprecise and nonlinear expressions, and this constitutes the fundamental point of the FL. The general operating structure of the FL method consists of fuzzification, database and rule table creation, fuzzy inference and rinsing stages, as shown in Figure 2.1. These stages include fuzzification of numerical data, creation of a database, definition of rule tables containing uncertainty, fuzzy inference using these rule tables, and finally clarification of the fuzzy results obtained.

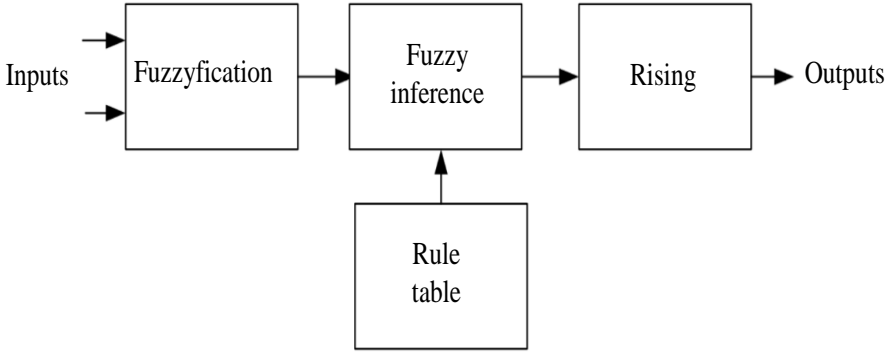


Figure 2.1. Fuzzy logic block diagram

The fuzzification phase is a process in which actual input data is converted into linguistic terms. This transformation occurs by creating a rule base based on control parameters and information obtained from the experiences of experts. The relationships between input and output are formulated through a logical decision-making process based on a rule base, and approximate results are obtained using the fuzzy inference unit. Then, these fuzzy data are converted into real output values to ensure monitor and control of the system, and this transformation occurs by converting linguistic variables into numerical variables. This process means controlling the converter in MPP with analog signals in PV systems. This control can change on the dependence between the output of the fuzzy logic control and the duty ratio of the converter (Bollipo, 2020:20).

The advantages of this algorithm are that it does not require a FL control mathematical model, is suitable for the control and parallel operations of linear or nonlinear systems, and is easy to understand as the control mechanism imitates humans. Based on the fuzzy logic system, the FL MPPT method consists of four separate parts. These sections are fuzzification process, rule table creation, fuzzy inference and rinsing. The input signal, PV power and PV current are measured from the PV panel output and then processed to obtain the signal at the FL output. In the process, the input signal and the output signal are each defined by one or more variables. In general, the algorithm used in the FL MPPT method has two input variables, the system error “ e ”, the change of the system error “ Δe ” and an output variable “ dD ”. These two input variables are defined as in Equation 2.1 and Equation 2.2 (Yilmaz et al., 2018:8).

$$e(k) = \frac{P_p(k) - P_p(k-1)}{I_p(k) - I_p(k-1)} \quad (2.1)$$

$$\Delta e(k) = e(k) - e(k - 1) \quad (2.2)$$

$P_p(k)$ and $I_p(k)$ are the power of the PV panel and the current of the panel, $P_p(k - 1)$ and $I_p(k - 1)$ the previous power and previous current of the PV panel, respectively. In MPP monitoring, the directions of change of power and current determine the path to be followed to reach the optimum operating point. In cases where power and current vary positively, the current may need to be increased to reach the MPP. If the change in power is positive but the change in current is negative, the current may need to be reduced to reach MPP. When the change in power is negative and the change in current is positive, the current may still need to be reduced to reach the MPP. If the changes in power and current are both negative, the voltage may need to be increased to reach MPP. These situations express the complexity and diversity of the decision mechanism in determining the optimum power point in PV systems. The output variable is expressed as the duty cycle step output dD . These two input and output variables are represented as fuzzy subsets. Each fuzzy set has seven basic fuzzy subsets for input and output values that describe linguistic values such as PB, PM, PS, ZO, MS, MM, MB. Figure 2.2 shows the membership function created from fuzzy subsets for inputs error and error change and output.

MPP with zero error in steady state. For this purpose, it aims to reach MPP by increasing or decreasing the operating point as seen in Table 2.1. If the operating point moves away from the MPP, the operating rate can be greatly increased or decreased. The fuzzy system, which includes seven variables for error and error change, contains a total of 49 rules by associating them with these situations in the rules table.

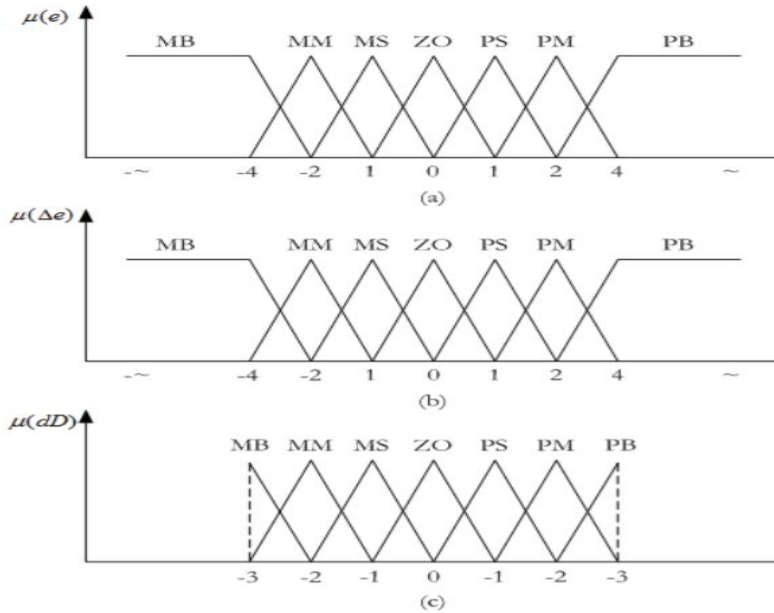


Figure 2.2. Membership functions for (a) FL error, (b) FL error change, and (c) FL output

Table 2.1. Rule table for system error and system error change

$\begin{matrix} e \\ \Delta e \end{matrix}$	ML	MM	MS	ZO	P.S.	P.M.	P.B.
MB	MB	MB	MB	MB	MM	MS	ZO
MM	MB	MB	MB	N.M.	MS	ZO	P.S.
MS	MB	MB	MM	MS	ZO	P.S.	P.M.
ZO	MB	MM	MS	ZO	P.S.	P.M.	P.B.
P.S.	MM	MS	ZO	P.S.	P.M.	P.B.	P.B.
P.M.	MS	ZO	P.S.	P.M.	P.B.	P.B.	P.B.
P.B.	ZO	P.S.	P.M.	P.B.	P.B.	P.B.	P.B.

EQUIVALENT CIRCUIT AND MODELING OF PHOTOVOLTAIC PANEL

One of the most commonly used to reproduce the current-voltage (I-V) characteristic of a PV panel is the one-diode or two-diode equivalent electrical model. The classical single-diode electrical model is often used to obtain the basic characteristics of the PV panel. In this model, a PV panel is represented as an electrical equivalent circuit as shown in Figure 3.1. Other models have been developed to offer a better modeling of the physical phenomena in a PV panel.

Here R_s is the small series resistance and R_{sh} is the large parallel resistance. D ideal diode is a photon current source produced in proportion to I_{ph} is surface temperature and insolation. Current and voltage represent the output voltage and output current of the PV panel, respectively (Tsai, 2008:6).

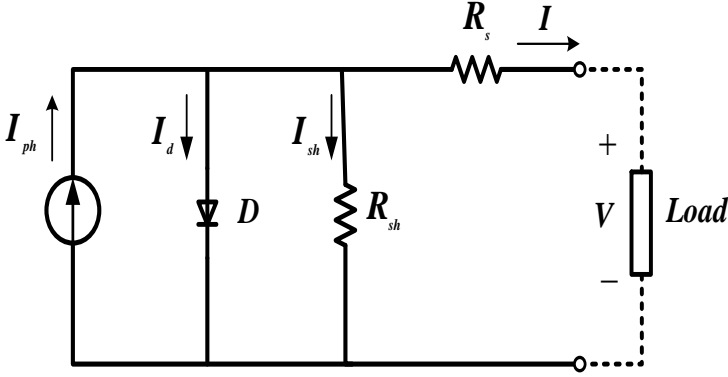


Figure 3.1. The equivalent circuit of a PV panel

The output current as a function of the PV output voltage is expressed as Equation 3.1.

$$I \left(1 + \frac{R_s}{R_{sh}} \right) = n_p I_{ph} - n_p I_{sat} \left(e^{\frac{q \left(\frac{V}{n_s} + R_s I \right)}{AKT}} - 1 \right) - \frac{V - n_s}{R_{sh}} \quad (3.1)$$

q is $1.602176565 \times 10^{-19}$ base charge, K is 1.38×10^{-23} J/K is boltzmann constant, T is the temperature of the PV cell, n_s is the number of cells in series and n_p is the number of cells in parallel. Cell saturation current is given in Equation 3.2.

$$I_{sat} = I_{rr} \left(\frac{T}{T_r} \right)^3 e^{\frac{qE_g}{KA} \left(\frac{1}{T_r} - \frac{1}{T} \right)} \quad (3.2)$$

T is the temperature, E_g is the band energy of each PV cell and T_r is the reference temperature of the PV panel. I_{ph} calculated in Equation 3.3 shows the photon current. I_{sso} is the short circuit current temperature coefficient.

$$I_{ph} = \{I_{sso} + k_i(T - T_r)\}(S_i/1000) \quad (3.3)$$

PSIM package program is used in the design and simulation of power electronic circuits and motor control circuits and provides fast and accurate

results in analog and digital motor control. The output graphics of the PV panel were obtained by using the physical model of the PV panel in PSIM and the resulting graphics are shown in Figure 3.2. Operating conditions such as irradiation intensity and ambient temperature can be changed (Tutorial PSIM, 2019:9). However, many input parameters need to be known. While some of the input parameters can be obtained from manufacturer data sheets, other parameters must be obtained by trial and error. Other parameters of the PV panel such as photon current, diode saturation current, series and parallel resistances and ideality factor are calculated. Parallel resistance The R_{sh} value is entered and the series resistance R_s is automatically calculated using the program.

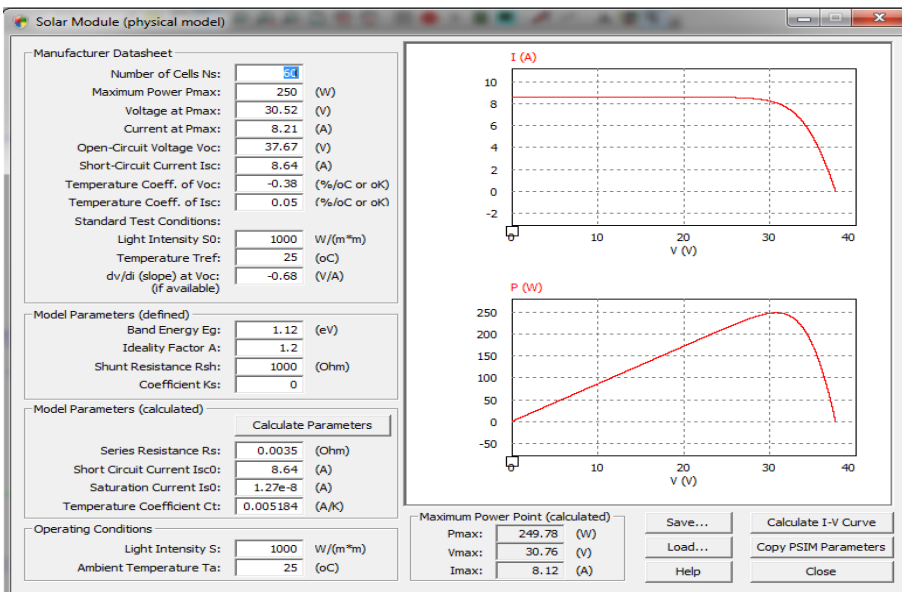
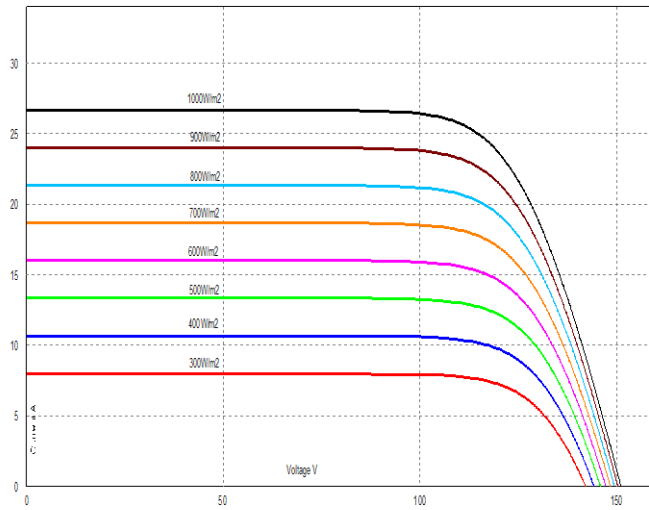


Figure 3.2. PSIM program PV panel physical model

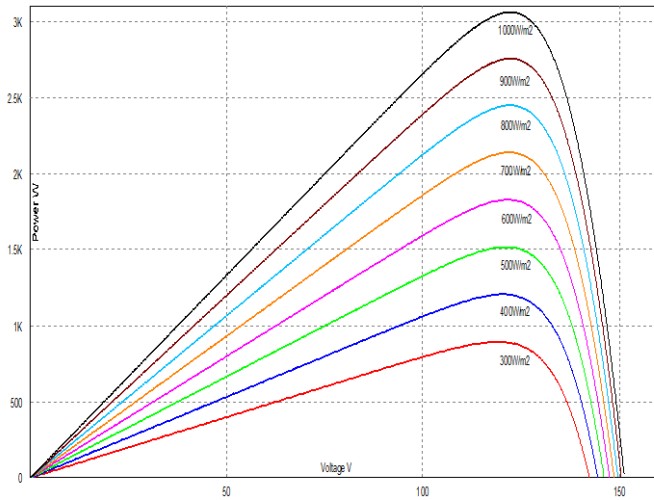
In the process of determining the maximum power point of the PV panel, one of the most critical steps is to determine the power-voltage (P-V) and I-V characteristic curves of the PV panel. While the increase in irradiation generally increases the power and voltage of the PV panel, the increase in temperature has a negative effect on the power and voltage.

In the study, 3×4 PV panel system was created by connecting 4 panels in series and 3 panels in parallel. The output power obtained from the system is 3060 W, open circuit voltage is 151.2 V and short circuit current is 26.85A. I-V and P-V curves for different irradiance values are shown in Figure 3.3. As can be seen from the figure, when the irradiance value decreases and the temperature value is

fixed at 25 °C, the decrease in irradiance greatly reduces the current of the PV panel. However, when the irradiance value decreases, the PV panel voltage changes very little. PV panel system parameters used in the study are given in Table 3.1.



(a)



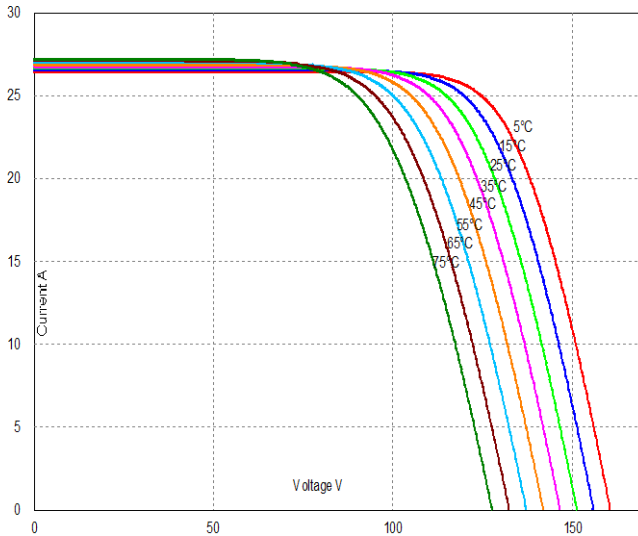
(b)

Figure 3.3 . (a) Variable irradiance I-V characteristic, (b) Variable irradiance P-V characteristic,

Table 3.1. PV panel system parameters

Parameters	Value
Maximum power , P_{max}	3060W
Current at point MPP I_{mpp}	24.96A
Voltage at point MPP V_{mpp}	122.6V
Short circuit current, I_{sc}	26.85A
Open circuit voltage, V_{oc}	151.2V

I-V and P-V curves for different temperature values are shown in Figure 3.4. As can be seen from the figure, when the solar irradiation is constant at $1000W/m^2$ and the panel temperature increases, the voltage of the PV panel decreases. However, when the temperature value increases, the PV panel current changes very little.



(a)

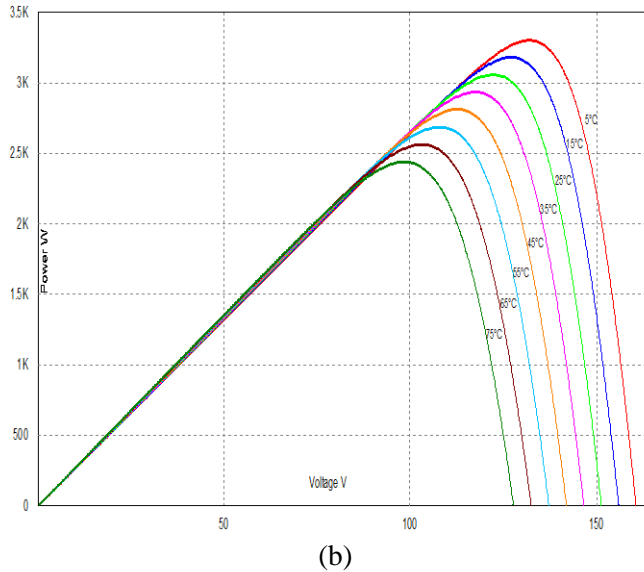


Figure 3.4. (a) Variable temperature I-V characteristic, (b) variable temperature P-V characteristic

SYSTEM SIMULATION AND RESULTS

The simulation of the PV DC/DC boost converter was carried out in the MATLAB/ simulink environment using the FL MPPT algorithm. The power circuit of the PV panel system and DC/DC boost converter is seen in Figure 4.1. In the first stage of modeling, it is necessary to select the PV panel and determine the parameters. At this stage, the PV panel “Soltec 1STH-215p” model was selected. The parameters of the panel are shown in Table 4.1. In order to obtain the desired voltage level and power from the PV panel system, it must be converted into a module. For this purpose, a total of 24 panels were used, 12 panels in series and 2 panels in parallel. The total power of the created panel system is 5115.6 W, current is 15.68 A and voltage is 435.6 V.

Table 4.1. PV panel parameters used in DC/DC boost converter

Panel ID	MPP P_{mpp} (W)	I_{sc} (A)	V_{oc} (V)	MPP I_{mpp} (A)	MPP V_{mpp} (V)
Soltec 1STH-215p	213.15	7.84	36.3	7.35	29

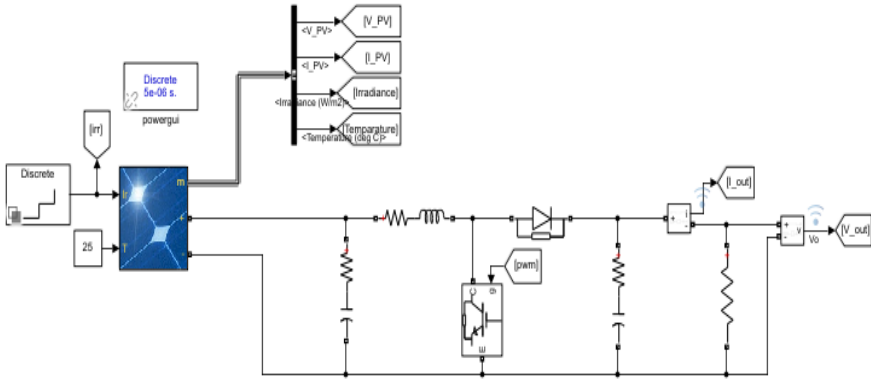


Figure 4.1. PV panel system and DC/DC boost converter power circuit

By connecting a capacitor parallel to the PV panel system output, the voltage produced in the PV panel is transferred to the capacitor. The voltage on the input capacitor is amplified at the DC/DC boost converter output and transferred to the output capacitor and the load. The PWM switching signal of the IGBT used in the boost converter is produced at the output of the FL control circuit and the DC voltage is increased at the output of the boost converter. Current and voltage information of the PV panel was used for the FL control circuit. The power is calculated and its previous value is subtracted from the current value. Then, the error signal was produced by subtracting the previous value from the current value and dividing it. Error and error change were applied as input to the FL block and comparison was made according to the fuzzy logic rules seen in Table 4.2. The signal obtained at the output of the FL block was used to generate the PWM signal.

Table 4.2. Fuzzy logic rule table

$E \backslash \Delta E$	NB	NS	ZE	PS	PB
NB	ZE	ZE	NB	NB	NB
NS	ZE	ZE	NS	NS	NS
ZE	NS	ZE	ZE	ZE	PS
PS	PS	PS	PS	ZE	ZE
PB	PB	PB	PB	ZE	ZE

Figure 4.2 shows FL control and measurement blocks. Here, FL block was created to obtain the duty ratio and DC/DC PWM block was used to obtain PWM signals. The optimum load point required to operate the PV panel in MPP under the environmental conditions must be found, it must be operated at this load point and the active switch in the boost converter must be triggered at this angle value. Solar irradiation applied to the system, temperature, PV panel current I_{PV} and voltage V_{PV} , boost converter output current I_{out} and voltage V_{out} , PV panel ideal power P_{ideal} , PV panel power P_{PV} and boost converter power P_{out} are obtained using the measurement block,

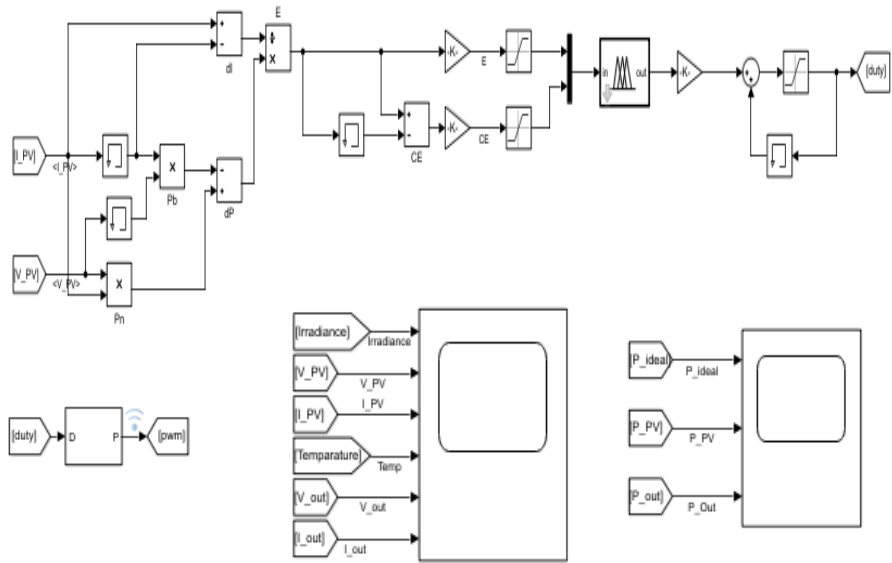


Figure 4.2. FL control and measurement blocks of the PVfed DC/DC boost converter

Current and voltage signals were obtained at the PV panel output and boost converter output from the MATLAB simulation for different irradiance and constant temperature values. Figure 4.3 shows the irradiance and temperature signal shapes. Solar irradiation was changed to 600 W/m^2 at 0s, 800 W/m^2 at 0.5s and 1000 W/m^2 at 1 s, and the temperature value was kept constant at $25 \text{ }^\circ\text{C}$.

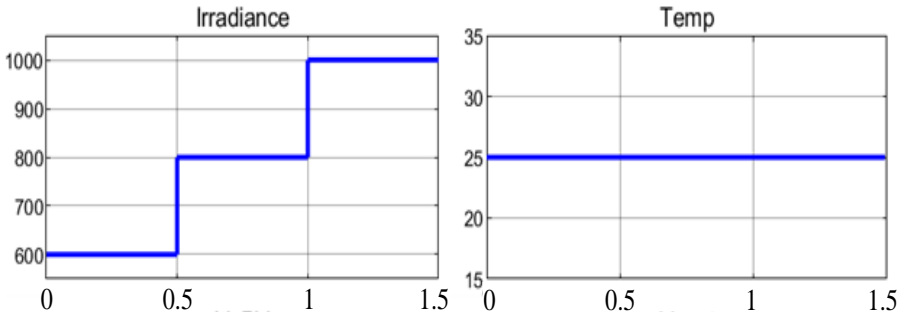


Figure 4.3. Different irradiance and constant temperature signals applied to the PV panel input

Figure 4.4 shows the PV panel voltage and current signals, and the current and voltage signals obtained at the boost converter output. As can be seen in the graphics, 380V constant voltage is obtained at the PV panel output, while 550V, 620V and 700V are obtained at the boost converter output, respectively, depending on the amount of irradiation applied to the panel.

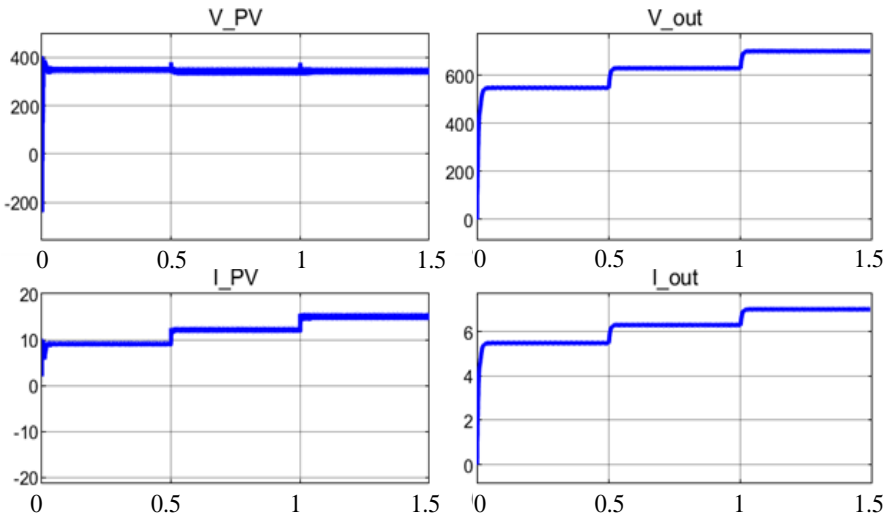


Figure 4.4. PV panel voltage and current signals, boost converter voltage and current signals

Figure 4.5, PV panel ideal power, PV panel power and boost converter output power signals are given. PV ideal power varies between 3000W, 4000W and 5100W, respectively, depending on different irradiation intensity values. The power obtained from the PV panel and the boost converter power follow the ideal power of the PV panel thanks to the FL MPPT algorithm. Additionally, the

efficiency for the system was also calculated. Throughout the simulation, the circuit operates at an efficiency of over 94.5%. Having less fluctuation in the signals is a desired situation for the FL controller, and the desired situation has been achieved. It has been observed that the boost converter works and follows the maximum power point of the FL MPPT method using the FL algorithm.

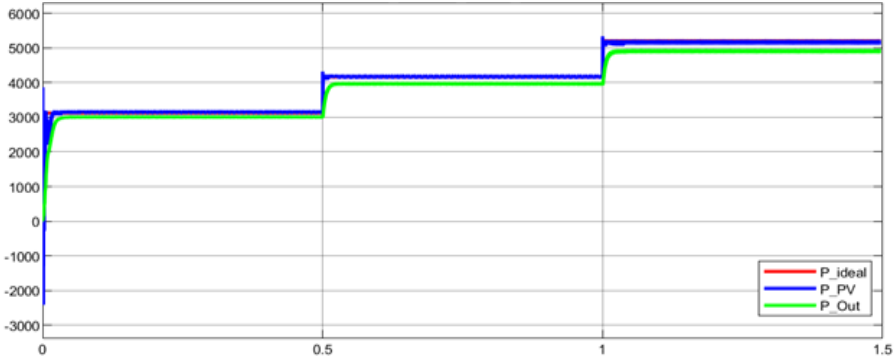


Figure 4.5. PV panel ideal power, PV panel power and boost converter power signals for different irradiance and constant temperature values

RESULTS

In this study, in order to operate the PV panel fed DC/DC boost converter at the maximum power point, the fuzzy logic MPPT method was modeled under three different irradiance severity and simulation studies were carried out. Matlab/Simulink was used for modeling and simulating. The responses of the PV panel system under changing irradiance and constant temperature were observed. The total power of the created panel system is 5115.6 W, current is 15.68 A, and voltage is 435.6 V. While 380V constant voltage is obtained at the PV panel output, 550V, 620V and 700V are obtained respectively at the boost converter output, depending on the amount of irradiance applied to the panel. PV ideal power varies between 3000W, 4000W and 5100W, respectively, depending on different irradiance intensity values. The power obtained from the PV panel and the boost converter power follow the ideal power of the PV panel thanks to the FL MPPT algorithm. The MPP detection efficiency of the FL MPPT method was obtained as 94.5% and above. It proves that in the presence of changes in solar irradiance, the FL MPPT method performs well and extracts the maximum power from the PV panels.

REFERENCES

1. Benner, J. P., and Kazmerski, L. (1999). Photovoltaics gaining greater visibility. *IEEE Spectr.*, 29, 34-42.
2. Hepzibah, A., and Premkumar, K. (2020). ANFIS current–voltage controlled MPPT algorithm for solar powered brushless DC motor based water pump. *Electrical Engineering*, 102(1), 421-435.
3. Jubaer, A., and Zainal, S. (2015). An improved perturb and observe (P&O) maximum power point tracking (MPPT) algorithm for higher efficiency. *Appl. Energy*. 150, 97–108.
4. Alik, R., and Jusoh, A. (2017), Modified Perturb and Observe (P&O) with checking algorithm under various solar irradiation. *Sol. Energy*, 148, 128–139.
5. Saharia, B. J., and Saharia, K. K. (2016). Simulated study on nonisolated DC-DC converters for MPP tracking for photovoltaic power systems. *Journal of Energy Engineering*, 142(1), 04015001.
6. Safari, A., and Mekhilef, S. (2010). Simulation and hardware implementation of incremental conductance MPPT with direct control method using cuk converter. *IEEE T. Ind. Electr.* 58(4), 1154-1161. doi:10.1109/TIE.2010.2048834.
7. Mei, Q., Shan, M., Liu, L., and Guerrero, J. M. (2010). A novel improved variable step-size incremental-resistance MPPT method for FV systems. *IEEE T. Ind. Electr.* 58(6), 2427-2434. doi:10.1109/TIE.2010.2064275.
8. Dadfar, S., Wakil, K., Khaksar, M., Rezvani, A., Miveh, M. R., and Gandomkar, M. (2019). Enhanced control strategies for a hybrid battery/photovoltaic system using FGS-PID in grid-connected mode. *International journal of hydrogen energy*, 44(29), 14642-14660.
9. Elobaid, L. M. Abdelsalam A. K., and Zakzouk E. E. (2015). Artificial neural network-based photovoltaic maximum power point tracking techniques: A survey. *IET Renew. Power Generat.*, 9(8), 1043–1063.
10. Fathi, M., and Parian, J. A. (2021). Intelligent MPPT for photovoltaic panels using a novel fuzzy logic and artificial neural networks based on evolutionary algorithms. *Energy Reports*, 7, 1338-1348.
11. Nabipour, M., Razaz, M., Seifossadat, S., and Mortazavi, S. (2017). A new MPPT scheme based on a novel fuzzy approach. *Renew. Sustain. Energy Rev.*, 74, 1147–1169.
12. Al Nabulsi, A., and Dhaouadi, R. (2012). Efficiency optimization of a DSP-based standalone FV system using fuzzy logic and dual-MPPT control. *IEEE Transactions on Industrial informatics*, 8(3), 573-584.

13. Hassan, S.Z., Li, H., Kamal, T., Arifoğlu, U., Mumtaz, S., and Khan, L. (2017). Neuro-Fuzzy Wavelet Based Adaptive MPPT Algorithm for Photovoltaic Systems. *Energies*, 10, 394.
14. Joshi, P., and Arora, S. (2017). Maximum power point tracking methodologies for solar FV systems—A review. *Renewable and Sustainable Energy Reviews*, 70, 1154-1177.
15. Hadji, S., Gaubert, J. P., and Krim, F. (2015). Theoretical and experimental analysis of genetic algorithms based MPPT for FV systems. *Energy Procedia*, 74, 772-787.
16. Seyedmahmoudian, M., Horan, B., Soon, T. K., Rahmani, R., O, A. M. T., Mekhilef, S., and Stojcevski, A. (2016). State of the art artificial intelligence-based MPPT techniques for mitigating partial shading effects on FV systems—a review. *Renewable and Sustainable Energy Reviews*, 64, 435–455.
17. Gani, A. (2021). Improving dynamic efficiency of photovoltaic generation systems using adaptive type 2 fuzzy-neural network via EN 50530 test procedure. *International Journal of Circuit Theory and Applications*, 49(11), 3922-3940.
18. Mao, M., Cui, L., Zhang, Q., Guo, K., Zhou, L., and Huang, H. (2020). Classification and summarization of solar photovoltaic MPPT techniques: A review based on traditional and intelligent control strategies. *Energy Reports*, 6, 1312-1327.
19. Nadia, A. R., Isa, N. A. M., and Desa, M. K. M. (2018). Advances in solar photovoltaic tracking systems: A review. *Renewable and sustainable energy reviews*, 82, 2548-2569.
20. Bollipo, R. B., Mikkili, S., and Bonthagorla, P. K. (2020). Critical review on FV MPPT techniques: classical, intelligent and optimisation. *IET Renewable Power Generation*, 14(9), 1433-1452.
21. Yilmaz, U., Kircay, A., and Borekci, S. (2018). FV system fuzzy logic MPPT method and PI control as a charge controller. *Renewable and Sustainable Energy Reviews*, 81, 994-1001.
22. Tsai, H. L., Tu, C. S., and Su, Y. J. (2008). Development of generalized photovoltaic model using MATLAB/SIMULINK. In *Proceedings of the world congress on Engineering and computer science*, 1-6.
23. Tutorial, PSIM. How to Use Solar Module Physical Model. Powersim Inc, Accessed on 25 November 2019.

Chapter 22

Results and Suggestions Regarding Cutting Forces, Surface Roughness And Tool Wear In Turning Inconel 718 With Different Cutting Tools

Abdullah ALTIN¹

ABSTRACT

In this study, tool life, cutting forces and surface roughness, which are machinability parameters, were taken into account in evaluating the machinability of Inconel 718 superalloy. In stock removal experiments, silicon nitride based ceramic (KY 2000 RNGN, KY 2100 SNGN), whisker reinforced (Al₂O₃+SiCw) aluminum oxide based ceramic (KY 4300 RNGN, KY 4300 SNGN), CVD coated cementite carbide (KC 935 SCMT, KC 9225). SCMT, SECO 560 RCMT) and uncoated tungsten carbide (SECO 883 RCMM) cutting tools were used. The selected parameters were constant feed ($f=0.20\text{mm/rev.}$), constant depth of cut ($d=2\text{ mm}$), and different cutting speeds ($V=15, 30, 45, 60, 75\text{ m/min.}$ for carbides, ceramics). for $V=150, 200, 250, 300\text{ m/min.}$). An evaluation was made by taking into account the wear patterns on cutting tools and their causes, the cutting forces acting when cutting the material, the resulting surface roughness values and chip shapes. As a result, optimum machining conditions for both ceramic and carbide tools were tried to be determined for Inconel 718 material. In this study, three criteria were taken as basis in determining the effect of cutting variables on tool life. These;

- 1-Tool wear and tool life
- 2- Cutting forces and cutting power
- 3- It is the surface roughness or the quality of the processed surface.

While evaluating the machinability, the surface quality of the processed material was taken as the main criterion to reveal the performance of the cutting tool used. For example, if processing is to be done based on surface quality, a better quality surface was formed in the whisker-reinforced aluminum oxide (Al₂O₃+SiCw) ceramic tool (KYON 4300 SNGN), although the tool life was shorter, at a cutting speed of 150 m/min. On the contrary, in cases where surface quality is considered secondary, $V=250\text{ m/ min.}$ with whisker reinforced

¹ Prof. Dr. Abdullah ALTIN; Yuzuncu Yil University, Van Vocational of Higher School, Mechanical and Metal Technology Department. Van/Turkey, aaltin@yyu.edu.tr ORCID No:0000-0003-4372-8272

aluminum oxide (Al₂O₃+SiCw) ceramic tool (KYON 4300 RNGN). Longer tool life was observed at cutting speed.

Keywords: Machining, optimization, Inconel 718, Surface roughness, Cutting force.

1. Introduction

The most common form of tool failure in the machining of nickel-based superalloys is the notch formed at the depth of cut. This occurs due to the combination of high heat, high work hardness, high stresses of the workpiece and abrasive chips (1,2,3,4,5). Flank edges, cracking and severe damage are other reasons that cause the cutting tool to fail in the machining of nickel-based superalloys. It is reported in welding that large heat gradients have little effect on notch formation in the depth of cut (6). The reason for notch formation is the presence of a hard surface layer formed during processing (7, 4). Notch formation is seen as a result of particles breaking off from the tool material at the depth of cut as a result of welding between the chip and the tool (1, 8). The work hardening layer frequently appears in the form of a crust during machining. In addition, fractures occur on the entire edge of the cutting tool during processing in an environment where a crust has formed (9, 10). At high cutting speeds, tool life is quite limited. Excessive notches are formed as a result of the welding and pull-out processes occurring at the depth of cut. As a result of processing Incoloy 901 with mixed ceramics (4) at a cutting speed of 300 m/min, and Inconel 718 with mixed ceramics, which is another quality (Al+Zr+W), at high cutting speeds, both cutters are cut due to their mechanical strength. A satisfactory tool life was achieved for the tool (11, 12).

2. Materials and Method

To evaluate the machinability of Inconel 718, machining experiments were carried out in two stages. In the first stage, the study on wear and surface quality on cutting tools was carried out in Eskişehir TUSAŞ workshops, and the study on the measurement of cutting forces was carried out in Gazi University TEF Mechanical Training laboratories. The bench, device, hardware features and test method used in these studies are examined below.

3. Experimental Studies and Discussion

The material used in the experimental studies is Inconel 718, a nickel-based superalloy with AMS 5663 specification. This material was heat treated twice during production. These operations are VIM. ((Vacuum induction melting)) + ESR ((Electro slag remelting)). The material was cooled in water by keeping it at

954 oC for one hour. Then, the material was subjected to the precipitation process. During production The purpose of the precipitation process is to give the desired mechanical properties to the material by settling on the grain boundaries of some of the alloying elements (grain boundary) of a hardenable material. For the precipitation process, it was kept at 718 oC for 8 hours, then it was kept at 38 oC/hour until the furnace decreased to 621 oC, and then in the air environment. It is left to cool. The density of the material is 8.470 kg/dm³, its brinell hardness is 388 HBS. Its boiling point is 5660 oC, its melting point is 3410 oC, it has no evaporation pressure, it is a solid and odorless metal that is insoluble in water. It is not harmful to health.

The part name chosen from the Inconel 718 material used for machining experiments is SEAL (air holding comb) and the function of this material is to circulate the fluid between the seals and obtain more efficiency from the aircraft engine. The location of the part within the aircraft engine is shown in Picture 5.4. The diameter of the processed material is 416 mm and its width is 52.8 mm (Figure 5.2.-5.3.). After processing, the material diameter was calculated as 408 mm and the removed chip volume was calculated as 273 cm³.

The experiments were carried out in two stages, in Eskişehir TUSAŞ (Turkish Airplane Industry Inc.) and Gazi University TEF Machinery Training laboratories. In the first stage, a CNC OKUMA 45-LB lathe was used during actual manufacturing at TAI facilities for machining operations to determine the wear on the cutting tools. The part to be processed is the Inconel 718 material called seal, which is located in the aircraft engine and whose function is to ensure greater efficiency by keeping the air entering the aircraft engine. 8 different cutting tools, 4 types of cementite carbide and 4 types of ceramic, were used in the experiments. Cutting parameters were determined with reference to cutting tool catalogs (cutting tool material manufacturers KENNAMETAL and SECO). For carbide tools, five machining operations were performed with each cutting tool, and for ceramic tipped tools, four machining operations were performed. In the experiments, a new cutting edge was used in each new machining process and each cutting edge was given a test code. These codes are marked on the cutting surface of the cutting tool with an acetate pen. In the wear tests at TAI, a chip volume of 273 cm³ was determined for the chip removal process and this amount of chip was removed. In each chip removal process, a sample of the removed sawdust was taken and placed in a separate container for evaluation. Four different holders were used to fasten the cutting tools. Coolant (Simkoll 618 M8) was used in all machining experiments to determine wear and surface roughness. After the machining operations were completed, cutting tool EDS (electron dispersion energy) elemental analysis graphics and wear pictures were taken with

a JSM JOEL 6400 SEM electron scanning microscope in the laboratories of the Mechanical Department of the Faculty of Engineering at Ataturk University. In order for the cutting tool images to be more clearly visible and understandable in SEM, the cutting edges were first coated with gold palladium in a special electrolysis device, and then the wear images were taken by magnifying 30 times in the same SEM device. In order to evaluate the resulting chips, enlarged chip images were taken for each chip sample on an HP 2210 scanner in YYÜ Van MYO Machinery laboratories. A Japanese-made Nikon (Anti-fungus NE Achromat Long Barrel Type) optical microscope with 0.01 mm precision was used to determine the VBB value and VBBMAX values of each cutting tool from the wear pictures taken, and their change graphs depending on the cutting speed were obtained with the Excel program. The changes in the measured surface roughness values and wear values depending on the cutting speed were evaluated by converting them into graphs in Excel, and these graphs were interpreted. During the machining operations at TAI, the surface roughness, brand and model of each machining process. Surtrasonic 3-P, with digital display, recording (recorder feature), detector, nickel-cadmium battery and works with 220 V AC, Ra, Rymax Using a surface roughness measuring device capable of measuring and RTM values, with a filter gap of 0.25 mm, a cut-off length of 0.8 mm and a sampling length of 2.5 mm, 5 measurements were made from different locations and their average was taken into account. Cutting forces were measured with a computer-connected 3-element Kistler dynamometer (type 285543 B model), mounted on a CNC (Johnford 45 LB- 45 KW) lathe in the Machining Department laboratory of Gazi University Faculty of Technical Education, Department of Mechanical Education. During the measurement, For each experiment, the machining program was determined according to the cutting tool tip and rewritten in line with the cutting parameters. In the cutting force measurement at Gazi University, chips were removed only for a short time (approximately 20 seconds). The cutting forces F_f (Feed Force), F_p (Passive Force), F_c (Main Cutting Force) measured in each experiment were recorded on a computer connected to the dynamometer and graphs were obtained. The measurement of each force consisted of 40,000 lines. Then, these force data were displayed graphically on the computer through the Dynaware program. The average of 40,000 lines of data created by the measured forces was obtained through the Excel program and graphs were created based on these average values. The wear values, cutting forces and surface roughness values resulting from all these processes were converted into graphics and compared with the studies in the literature and an evaluation was made. The causes of the problems encountered were investigated and solutions were suggested. By comparing the machinability data with the use

of different tools and considering the machining economy, the results obtained and the machinability of the material under the specified conditions were examined in detail in the "Experimental Findings and Discussion Section".

4. Machining Time and Cutting Tool Life of Tested Inconel 718 Material at Different Cutting Speeds

The machining time of the Inconel 718 material called seal, which was subjected to machining during the experiments, with carbide and ceramic cutting tools, was calculated according to the following formula (110). Accordingly, processing times were different depending on the cutting speed.

$$T_b = \pi \cdot ((d_1 + d_2) / 2) \cdot l \cdot i / 1000 \cdot V \cdot f$$

T_b : longitudinal turning time, min.

d_1 : first outer diameter, mm

d_2 : final outer diameter, mm

l : turning length, mm

V : cutting speed, m/min.

f : feed, mm/rev.

i : number of passes

The tool life of the cutting tools used in the experiments within the 273 cm³ machining time was 86 minutes on average, according to the $V_{BB} = 0.3$ mm criterion at a cutting speed of 15 m/min. According to the extended Taylor tool life ($V \cdot T_n \cdot f^{n_1} \cdot d^{n_2} = C_0$) equation, the n value in uncoated carbide tools was calculated by taking $n = 0.25$, $n_1 = 0.77$, $n_2 = 0.37$ in general use in carbide inserts (21). The tool life obtained as a result of the calculation with the Taylor equation.

$$V \cdot T_n \cdot f^{n_1} \cdot d^{n_2} = C_0 = \text{Constant}$$

$$15 \cdot 86^{0.25} \cdot 0.2^{0.77} \cdot 20^{0.37} = 17.09$$

$V = 30$ m/min. for;

$$30 \cdot T^{0.25} \cdot 0.2^{0.77} \cdot 20^{0.37} = 17.09$$

$$T = 8.13 \text{ min.}$$

In ceramic cutting tools, at a cutting speed of $V = 150$ m/min., the cutting tools lasted for an average of 3 minutes according to the $V_{BB} = 0.3$ mm criterion. According to the extended Taylor tool life ($V \cdot T_n \cdot f^{n_1} \cdot d^{n_2} = C_0$) equation, the n value in ceramic tools was calculated by taking $n = 0.4$, $n_1 = 0.77$, $n_2 = 0.37$ in general use (21).

$$V \cdot T_n \cdot f^{n_1} \cdot d^{n_2} = C_0 = \text{Constant}$$

$$150 \cdot 3^{0.4} \cdot 0.2^{0.77} \cdot 20^{0.37} = 87.11$$

$V=300$ m/min. for
 $300 \cdot T_{0,4} \cdot 0,20,77 \cdot 20.37=87.11$

$T=0.52$ min.

5. Results and Suggestions

In 36 metal removal experiments, $d=2$ mm cutting depth and $f=0.20$ mm/rev. The forward speed was kept constant. Cutting speed, $V=15, 30, 45, 60, 75$ m/min. for carbide tools, $V=150, 200, 250, 300$ m/min. for ceramic tools. is taken as basis. Two different geometries (square and round) are used in both carbide and ceramic tools. The following results were obtained from the evaluation in terms of tool wear, cutting forces and surface roughness.

1- When the cutting speed was increased from the initial value of 15 m/min to 75 m/min in the experiments conducted with carbide cutters, the actual cutting force F_c decreased in all four cutting tools. At cutting speeds of 30, 45 and 60 m/min., the actual cutting force F_c zigzagged, and sometimes an increase and sometimes a decrease was observed in the actual cutting force. As the cutting speed increased, the actual cutting force F_c in coated carbide cutting tools decreased. In uncoated carbide SECO 883, the actual cutting force F_c increased at cutting speeds of $V = 30, 45$ and 60 m/min, and decreased to the lowest level of 345 N at a cutting speed of 75 m/min. When the cutting speed is increased by 500% compared to the initial value, the actual cutting force in F_c is 70.3% in KC 935, 41.4% in KC 9225, 90.5% in SECO 560, 61% in SECO 883, There was a decrease of 5.

2- During machining with round-shaped carbide inserts, vibration occurred in most of the cutting experiments in which the carbide insert was tested due to its round form, and the radial force F_p took values almost close to or higher than the actual cutting force F_c .

3- In machining operations performed with round-shaped carbide cutting tools, a better quality surface was obtained compared to square-shaped carbide cutting tools. Although cutting tools with chip breakers were used in the experiments, the chips were long and continuous. Sawdust is a very difficult chip to break off, and the chip breakers in the cutters were insufficient to break off the chips.

4- SECO 560 and SECO 883 carbide inserts were found to be suitable for Inconel 718 in terms of surface quality and tool life at cutting speeds of $V=30$ and 45 m/min. The other two coated square-shaped cutting tools, KC 935 and KC 9225, caused thermal relaxation in the cobalt phase of the main material under the coating material, due to the high temperature at the cutting edge as a result of the narrow contact area during the processing of Inconel 718. As a result, these

two cutting tools (KC 935 and KC 9225) wore out quickly and were deemed unsuitable due to the plastic deformation of the coating material.

6.Suggestions

-Research topics that are noted in the literature findings but not addressed in this study and are recommended to be studied are as follows:

-Conducting a study on reducing notch formation, the contribution of metal removal at different cutting depths to notch formation,

-The effects of high pressure coolant and normal pressure coolant on chip removal during machining,

-Comparison of the notch formed during the processing of Inconel 718 in a rich oxygen environment and the notch formed in a rich nitrogen and argon environment,

-Determining the coating types that prevent the tool from deteriorating due to the thermal softness in the cobalt phase in the machining of nickel-based superalloys with cemented carbide tools at cutting speeds exceeding 30 m/min.,

-In machining with ceramic and carbide cutting tools, issues such as the effect of the approach angle of the cutting tool on tool life are topics that are useful to be researched.

7. References

- Richards, N., Aspinwall, D., "Use of ceramic tools for machining nickel-based alloys", *Int. J. Mach. tools Manuf.*, 294, 575-588 (1989).
- Ezugwu, E. O., Wang, Z. M., "Performance of PVD and CVD coated tools when machining nickel-based Inconel 718 alloy". IN: N.Narutaki et al. *Progress of Cutting and Grinding 111*, 102-107 (1996).
- Wang, Z. M., Ph.D Thesis, *South Bank University*, London, pp78,79(1997).
- Khamsehazadeh, H., "Behaviour of ceramic cutting tools when machining superalloys", PhD Thesis, pp125 (1991).
- Bhattacharya, S. K., Pashby, I. R., Ezugwu, E. O., "Machining of INCO 718 and INCO 901 superalloys with Sic-whisker reinforced Al₂O₃ composite ceramic tools", *Prod. Eng*, Osaka, 176-181 (1987).
- Moltrecht, K. H., "Tool failure when turning nickel base high temperature alloys", *ASME Technical Paper series no. 637*, Presented at Annual Meeting, Detroit, 1-31 (April 1964).
- Ezugwu, E. O., Pashby, I. R., "High speed milling of nickel-based superalloys". *J.Mater Proc.technol.* 3 , 429-437 (1992).
- Lee, M., Horne, J. G., Tabor, D., "The mechanism of notch formation at dept of cut line of ceramic tools machining nickel-base superalloys", *Proc. 2nd Int Conf*, Wear Materials Dearborn, MI, 460-464 (1979).
- Shaw, M. C., Thurman, A. L., Ahlgren, H. J., "A plasticity problem improving plain strain and plain stress simultaneously: Groove formation in the machining of high temperature alloys", *Trans. ASME (series B), J. Eng. Ind.*, 88-2, 142-146 (1966).
- Choudhury, I. A., El-Baradie, M. A., "Machinability of nickel base super alloys: a general review", *Proc. Advances in Materials and Processing Technologies AMPT'95*, Dublin, Ireland, vol. III, 1405-1413 (1995).
- Suh, N. P., "New theories of wear and their implications for tools materials", *Wear*, vol. 62, 1-20, Abstract INSPEC/ Abstract-FLUIDEX (1980).
- Anon, "Cutting Tool Innovations from Carboloy Systems", *Metal Powder Report No. 39*, 411-412 (July 1984).
- Niemi, R.M., "Integrity prediction", *SME Technical Paper*, Dearbon, Michigan, pp46 (1971).
- Bhattacharya, S. K., Jawaid, A., Lewis, M. H., Wallbank, J., "Wear mechanism of sialon ceramic tools when machining nickel based materials", *Metals Techno.* 10, 71-74 (Dec. 1983).
- Chow, C. B., Liu, Y. H., Miao, H. C., Lo, Z. P., "Investigation on the cutting performance of silicon nitride ceramic tools", *Int. Conf. on Manu. Eng*, Melbourne, Australia, 71-74 (Aug. 1980).

- Reckling, K. S., “New cutting tool tames tough metals”, *Tooling Prod.*, 47, 74-79 (1981).
- Baker, R. D., “High-velocity cutting tools: Application guidelines”, *Proc. Biennial Int. Mach. Tool Tech. Con*, McLean, VA, 487-529 (Sept 1982).
- Ezugwu, E. O., Machado, A. R., Pashby, I. R., Wallbank, J., “The effect of high-pressure coolant supply”. *Lub. Eng.*, 47 9, 751-757 (1990).
- Kramer, B. M., Hartung, P. D., *Proc. Int. Conf. Of Cutting Tool Mat*, Fort Mitchell, KY, 57-74 (1980).
- Focke, A. E., Westermann, F. E., Eemi, A., Yavelak, J., Hoch, M., “Failure mechanism of superhard materials when cutting superalloys”, *Proc. 4th Int.-Am. Conf.*, China, A 268-296 (April 1991).
- Al-Tornachi, M. J. K., Dugdale, D. S., *Proc. 18th MTDR Conf*, 523-528 (1977).
- Itakura, M., Kuroda, H., Omokawa, H., Itani, K., Yamamoto, Y., Ariura, “Wear mechanism of coated cemented carbide tool in cutting of Inconel 718 super heat resisting alloy”, *International Journal of Japanese Society for Precision Engineering* 334, 326-333 (December 1999).
- Prengel, H. G., Jindal, P. C., Wendt, K. H., Santhanam, A. T., Hedge, P. L., Penich, R.M., “A new class of high performance PVD coatings for carbide cutting tools”. *Surface and Coatings Technology* 139, 25-34 (2001).

Chapter 23

Contact Mechanics of Functionally Graded Orthotropic Materials: Semi-Analytical Solution for Rigid Punch Loading

Erdal ÖNER¹

Ahmed Wasfi Hasan AL-QADO²

ABSTRACT

Contact mechanics has consistently been a significant field of study in the realm of elasticity theory, since it has been utilized to address a diverse range of engineering problems. Due to the fact that changing the gradient of material characteristics permits to alter contact stresses and, consequently, to minimize surface-related damages, contact mechanics analysis of functionally graded materials (FGMs) is of major relevance. This study focused on handling the continuous contact problem of a functionally graded (FG) orthotropic layer that is in contact with a rigid foundation. The analysis was conducted using the principles of linear elasticity theory. The solution incorporates the consideration of the body force acting on the layer. In order to apply normal concentrated load to the FG orthotropic layer, a rigid cylindrical punch was used. Over the course of the thickness of the FG orthotropic layer, it was presumed that the elastic stiffness constants exhibited an exponential variation. The Gauss–Chebyshev integration formulas are employed to achieve the numerical solution for the singular integral equation. The main goal of this study is to examine the influence of several factors, such as punch radius, indentation load, and the inhomogeneity parameter of the FG orthotropic layer, on both contact stress and contact length.

Keywords – Contact mechanics, functionally graded materials, orthotropic layer, rigid foundation, theory of elasticity

INTRODUCTION

¹ Assoc. Prof.; Bayburt University Faculty of Engineering, Department of Civil Engineering. eoner@bayburt.edu.tr ORCID No: 0000-0001-7492-3754

² Graduate student; Bayburt University Faculty of Engineering, Department of Civil Engineering. wasfiahmed1997@gmail.com ORCID No: 0000-0002-4609-5047

Contact problems have remained a pivotal area in engineering for over 150 years. In 1882, Hertz initiated a new era in the realm of contact mechanics. Engineering disciplines derive advantages from understanding the contact lengths and stress distributions of materials, since it facilitates the production of materials with more ease and reliability. Contact mechanics found use in many technical contexts, including highways, braking disks, airport superstructures, trains, foundations, grain silos, fuel tanks, and clutches. Functionally graded materials (FGMs) are composite materials consisting of two or more constituent phases, characterized by continuous and smooth spatial gradients in both composition and microstructure. Because of their exceptional thermal, mechanical, optical, and electrical capabilities, FGMs are now extensively utilized in a variety of technical applications. These include tribology, nanotechnology, thermal barrier coatings, and biomechanics.

In the existing body of literature, numerous studies have been conducted to explore the behavior of FGMs in contact mechanics scenarios. These investigations have employed diverse solution methods, geometric conditions, variations in loading, and material distributions.

Singh et al. (2007:155) examined the dynamic response of FG piezoelectric materials subjected to both anti-plane mechanical loading and in-plane electrical loading. Barik et al. (2008:775) explored the static plane contact between FG heat-conducting punch and a rigid insulated half-space. Choi (2009:2703) investigated the contact mechanics involving a FG layer that experiences loading from a flat punch with frictional sliding. Shahzamanian et al. (2010:1591) conducted an analysis of the thermoelastic contact problem associated with a rotating brake disk made of FG material. The study considered the presence of a heat source induced by contact friction. Trubchik et al. (2011:1754) studied the contact problem associated with the layer, examining instances where the elastic properties of the medium vary as arbitrary continuously differentiable functions of its thickness. Volkov et al. (2013:196) investigated a contact problem within the theory of elasticity, specifically addressing the penetration of a circular indenter with a flat base into a compliant FG elastic layer. Nikbakht et al. (2014:92) conducted a study on the elastic contact involving a FG plate of finite dimensions, characterized by a continuous variation of material properties, and subjected to the indentation of a rigid spherical indenter. Çömez (2015:339) examined a contact problem involving the motion of a rigid cylindrical punch and a FG layer. Adıyaman et al. (2016:1753) explored the scenario of a frictionless receding contact in the plane problem,

focusing on an elastic FG layer pressed against two homogeneous quarter planes. Güler et al. (2017:12) studied the frictional contact problem in the plane, focusing on a cylindrical punch interacting with a FG orthotropic medium. Polat et al. (2018:3565) solved the continuous contact problem of a FG layer positioned on an semi-infinite plane, subjected to loading from two distinct blocks. Balci and Dag (2019:267) introduced an analytical method designed for exploring the dynamic frictional contact mechanics between a FG coating and a moving cylindrical punch. Öner and Birinci (2020:2799) explored the discontinuous contact problem involving a FG layer loaded by a rigid block. Çömez and Omurtag (2021:3937) focused on the frictionless plane contact problem between a rigid punch and a FG orthotropic layer situated on a Pasternak foundation within the bounds of linear elasticity theory. Karabulut and Çömez (2023:e202200427) investigated the scenarios of continuous and discontinuous contact in a FG orthotropic layer, positioned over a homogeneous and isotropic layer.

In this study, the continuous contact problem of a FG orthotropic layer resting on a rigid foundation was examined using elasticity theory, while considering the body force exerted by the functionally graded orthotropic layer.

ANALYTICAL FORMULATION OF THE CONTACT PROBLEM

Figure 1 depicts the schematics addressing the considered problem. The orthotropic layer has a thickness denoted by h . The orthotropic layer is considered to have functional grading as part of the assumption. The layer is subjected to a normal force, represented as P , applied through a rigid cylindrical-profile punch. Contact between the punch and the layer occurs within the interval $(-a, +a)$.

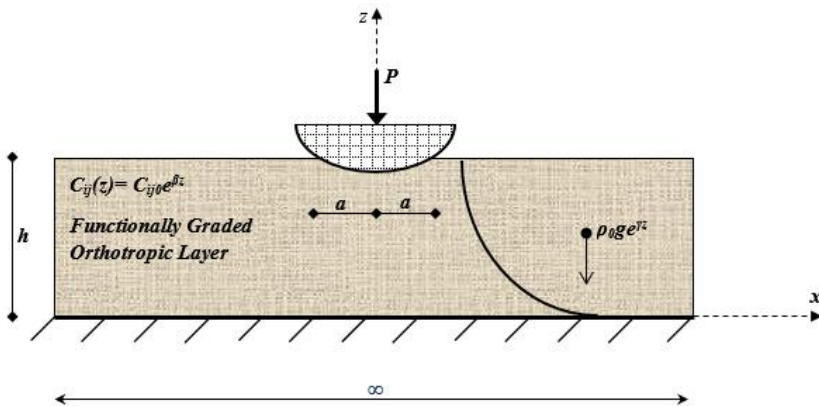


Figure 1: The problem's geometric configuration and loading condition

In Fig. 1, the elastic stiffness constants $C_{ij}(z)$ exhibit exponential variation through the layer's thickness, characterized as follows:

$$C_{ij}(z) = C_{ij0}e^{\beta z} \quad (1)$$

where the inhomogeneity parameter, denoted as β , is featured in the context. The stiffness constants at the bottom surface of the FG layer are denoted by C_{ij0} .

The boundary conditions governing the continuous contact problem presented in Fig. 1 can be expressed in the following manner:

$$\sigma_z(x, h) = \begin{cases} -P(x) & ; \quad (0 \leq x < a) \\ 0 & ; \quad (a \leq x < \infty) \end{cases} \quad (2)$$

$$\tau_{xz}(x, h) = 0 \quad (0 \leq x < \infty) \quad (3)$$

$$\tau_{xz}(x, 0) = 0 \quad (0 \leq x < \infty) \quad (4)$$

$$w(x, 0) = 0 \quad (0 \leq x < \infty) \quad (5)$$

where the contact length is indicated by a and the function $P(x)$ represents the contact stress under the punch.

The boundary conditions (2-5) lead to the derivation of unknown functions in integral form, expressed in terms of the contact stress function $P(x)$. By utilizing the displacement derivative condition associated with the punch profile, the problem is transformed into a singular integral equation, expressed as follows:

$$\frac{\partial}{\partial x} w(x, h) = \frac{x}{R} \quad (6)$$

where R denotes the punch radius. By applying the aforementioned Eq. (6) and conducting the necessary asymptotic analyses, the singular integral equation (SIE) is expressed in the following form:

$$\frac{1}{\pi} \int_{-a}^a p(\zeta) d\zeta \left[\frac{1}{\zeta - x} + A(x, \zeta) \right] = \frac{C_{550} x}{Y R} \quad (7)$$

In the singular integral equation (7), the contact length a remains unknown a priori. A complete solution requires the function $p(\zeta)$ to satisfy the following equilibrium condition.

$$\int_{-a}^a p(\zeta) d\zeta = P \quad (8)$$

Following the essential normalizations and considering that the contact stresses at the ends of the contact area are zero, the index of the integral is

set to -1 (Erdogan et al., 1973:368). Subsequent intermediate operations lead to the reduction of the integral equation and the equilibrium condition into the following system of algebraic equations:

$$\sum_{r=1}^N W_r^N \left[\frac{1}{\lambda_r - \omega_j} + A_1(\omega_j, \lambda_r) \right] \Psi(\lambda_r) = \frac{1}{YR/h} \omega_j \quad (9)$$

$$\frac{\alpha}{h} \sum_{r=1}^N W_r^N \Psi(\lambda_r) = \frac{1}{\pi} \frac{P}{C_{550} h} \quad (10)$$

where

$$\lambda_r = \cos\left(\frac{r\pi}{N+1}\right) \quad (r = 1, \dots, N) \quad (11a)$$

$$\omega_j = \cos\left(\frac{(2j-1)\pi}{2N+2}\right) \quad (j = 1, \dots, N+1) \quad (11b)$$

$$W_r^N = \frac{1 - \lambda_r^2}{N+1} \quad (r = 1, \dots, N) \quad (11c)$$

The $N/2+1^{\text{th}}$ equation in Eq. (9) is satisfied automatically and it is extracted from Eq. (9). Therefore, Eqs. (9) and (10) together provide $N+1$ equations for determining the $N+1$ unknowns. Due to the nonlinearity in the system of equations regarding contact length, it is necessary to employ an iterative procedure for determining the unknown contact length. In the iterative algorithm, an initial value for contact length is chosen, and N unknowns $\Psi(\lambda_r)$ are obtained from Eq. (9). Subsequently, the equation extracted in (9) and the equilibrium condition (10) are validated. If the targeted level of accuracy is not achieved, new values for the contact length are selected. The loop continues until the contact length meets the desired accuracy.

RESULTS AND DISCUSSION

In this section, we present the numerical findings pertaining to the scenario illustrated in Fig. 1, where a rigid cylindrical punch interacts with an orthotropic layer composed of functionally graded (FG) materials. The mechanical characteristics of the orthotropic materials employed in this study are detailed in (Binienda and Pindera, 1994:119).

Fig. 2 illustrates variations in contact length resulting from changes in both punch radius and indentation load. Upon closer inspection of the figure,

it becomes evident that a larger punch radius results in the formation of a correspondingly larger contact surface with the FG orthotropic layer. Consequently, this leads to an augmentation in the contact length in this particular scenario. Another insight gleaned from the figure is that an escalation in the indentation load facilitates deeper penetration of the punch into the FG orthotropic layer, consequently leading to an increase in contact length.

Fig. 3 shows the effect of variation in the inhomogeneity parameter on contact length. As the inhomogeneity parameter for the functionally graded layer increases, indicating a gradual increase in rigidity from the bottom to the top surface of the orthotropic layer, the consequence is a reduction in contact length. Physically, the reduced penetration of the punch on a stiffer surface aligns with the observed outcome.

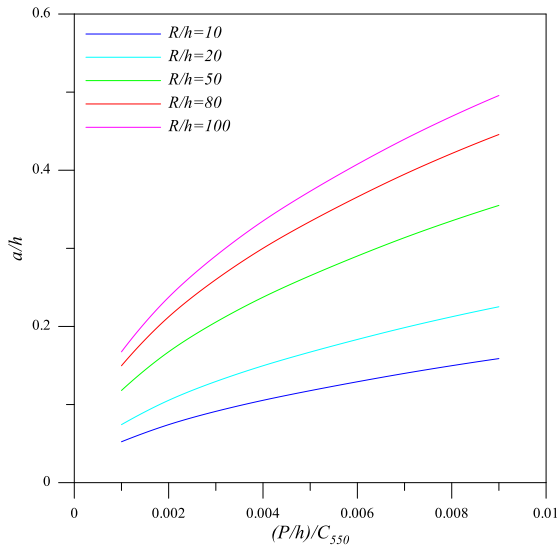


Figure 2: Effect of punch radius and indentation load on contact length (graphite/epoxy (T300/934), $\nu=2$, $h=1$, $\beta=0.5$)

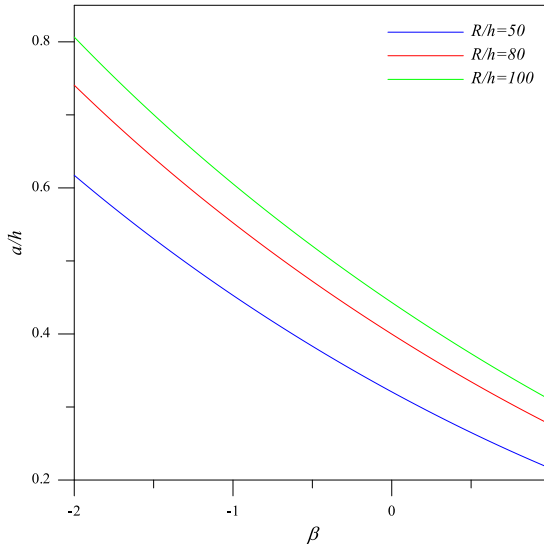


Figure 3: Effect of inhomogeneity parameter on contact length (boron/aluminum (B/Al), $\nu=2$, $h=1$, $(P/h)/C_{550}=0.005$)

Figs. 4-6 depict alterations in the distribution of contact stress under the punch across various dimensionless parameters. Upon examination of these figures, it becomes evident that the highest stress is concentrated along the axis of symmetry, reaching zero at the end of the contact region.

Fig. 4 illustrates the variations in contact stress distribution under the punch resulting from changes in punch radius. Clearly discernible from the figure is the direct relationship between an increase in punch radius and the corresponding increase in contact length. This expanded contact area leads to a dispersion of the load over a wider region, consequently causing a reduction in the peak values of contact stresses.

In Fig. 5, the effect of variations in indentation load on contact stress distribution under the punch is demonstrated. As anticipated, the peak values of stresses exhibit an increase with increase in punch indentation load.

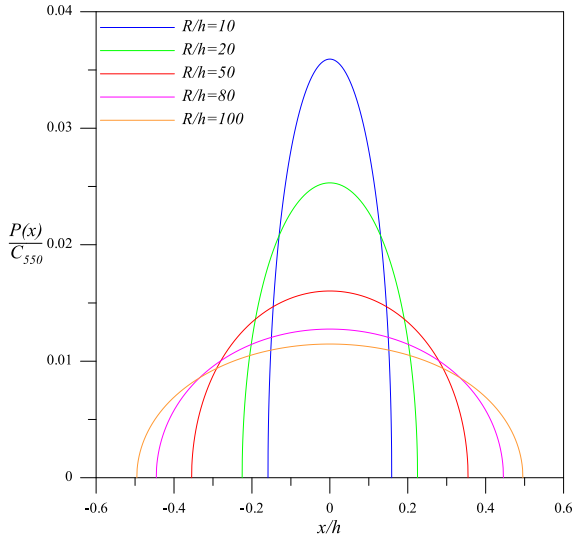


Figure 4: Effect of punch radius on contact stress distribution (graphite/epoxy (T300/934), $\square=2$, $h=1$, $\beta=0.5$, $(P/h)/C_{550}=9 \times 10^{-3}$)

In Fig. 6, the effect of variations in the inhomogeneity parameter of the FG orthotropic layer on contact stress distribution under the punch is illustrated. The figure demonstrates that an increase in the inhomogeneity parameter, signifying enhanced stiffness from the bottom to the top surface, results in a corresponding increase in the peak values of contact stresses.

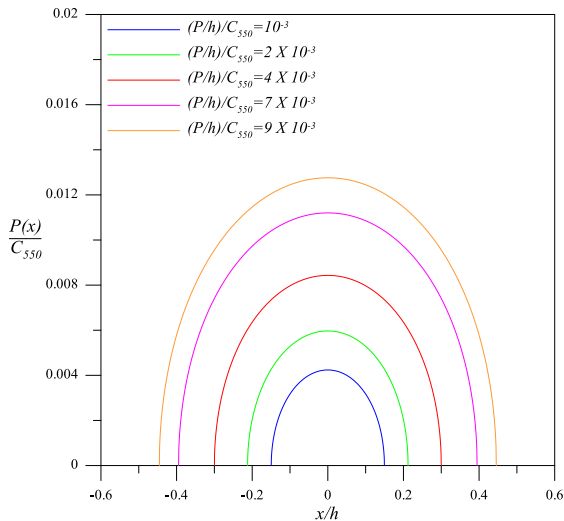


Figure 5: Effect of indentation load on contact stress distribution (graphite/epoxy (T300/934), $\square=2$, $h=1$, $\beta=0.5$, $R/h=80$)

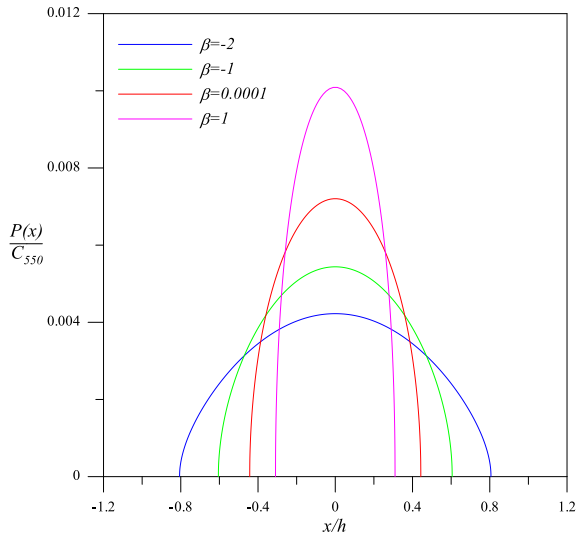


Figure 6: Effect of inhomogeneity parameter on contact stress distribution (boron/aluminum (B/Al), $\nu = 2$, $R/h=100$, $h=1$, $(P/h)/C_{550}=0.005$)

REFERENCES

- Adiyaman, G., Birinci, A., Öner, E., & Yaylacı, M. (2016). A receding contact problem between a functionally graded layer and two homogeneous quarter planes. *Acta Mechanica*, 227(6), 1753–1766.
- Balci, M. N., & Dag, S. (2019). Solution of the dynamic frictional contact problem between a functionally graded coating and a moving cylindrical punch. *International Journal of Solids and Structures*, 161, 267–281.
- Barik, S. P., Kanoria, M., & Chaudhuri, P. K. (2008). Steady state thermoelastic contact problem in a functionally graded material. *International Journal of Engineering Science*, 46(8), 775–789.
- Binienda, W. K., & Pindera, M.-J. (1994). Frictionless contact of layered metal-matrix and polymer-matrix composite half planes. *Composites Science and Technology*, 50(1), 119–128.
- Choi, H. J. (2009). On the plane contact problem of a functionally graded elastic layer loaded by a frictional sliding flat punch. *Journal of Mechanical Science and Technology*, 23(10), 2703–2713.
- Çömez, İ. (2015). Contact problem for a functionally graded layer indented by a moving punch. *International Journal of Mechanical Sciences*, 100, 339–344.
- Çömez, İ., & Omurtag, M. H. (2021). Contact problem between a rigid punch and a functionally graded orthotropic layer resting on a Pasternak foundation. *Archive of Applied Mechanics*, 91(9), 3937–3958.
- Erdogan, F., Gupta, G. D., & Cook, T. S. (1973). Numerical solution of singular integral equations. In G. C. Sih (Ed.), *Methods of analysis and solutions of crack problems: Recent developments in fracture mechanics Theory and methods of solving crack problems*, *Mechanics of fracture* (pp. 368–425). Dordrecht: Springer Netherlands. Retrieved December 19, 2023, from https://doi.org/10.1007/978-94-017-2260-5_7
- Güler, M. A., Kucuksucu, A., Yilmaz, K. B., & Yildirim, B. (2017). On the analytical and finite element solution of plane contact problem of a rigid cylindrical punch sliding over a functionally graded orthotropic medium. *International Journal of Mechanical Sciences*, 120, 12–29.
- Karabulut, P. M., & Çömez, İ. (2023). Continuous and discontinuous contact problem of a functionally graded orthotropic layer indented by a rigid cylindrical punch: Analytical and finite element approaches. *ZAMM -*

Journal of Applied Mathematics and Mechanics / Zeitschrift für Angewandte Mathematik und Mechanik, 103(6), e202200427.

- Nikbakht, A., Fallahi Arezoodar, A., Sadighi, M., & Talezadeh, A. (2014). Analyzing contact problem between a functionally graded plate of finite dimensions and a rigid spherical indenter. *European Journal of Mechanics—A/Solids*, 47, 92–100.
- Öner, E., & Birinci, A. (2020). Investigation of the solution for discontinuous contact problem between a functionally graded (FG) layer and homogeneous half-space. *Archive of Applied Mechanics*, 90(12), 2799–2819.
- Polat, A., Kaya, Y., & Özşahin, T. Ş. (2018). Analytical solution to continuous contact problem for a functionally graded layer loaded through two dissimilar rigid punches. *Meccanica*, 53(14), 3565–3577.
- Shahzamanian, M. M., Sahari, B. B., Bayat, M., Mustapha, F., & Ismarrubie, Z. N. (2010). Finite element analysis of thermoelastic contact problem in functionally graded axisymmetric brake disks. *Composite Structures*, 92(7), 1591–1602.
- Singh, B., Rokne, J., & Dhaliwal, R. (2007). The study of dynamic behavior of functionally graded piezoelectric materials and an application to a contact problem. *Quarterly of Applied Mathematics*, 65(1), 155–162.
- Trubchik, I. S., Evich, L. N., & Mitrin, B. I. (2011). The Analytical Solution of the Contact Problem for the Functionally Graded Layer of Complicate Structure. *Procedia Engineering*, 10, 1754–1759.
- Volkov, S., Aizikovich, S., Wang, Y.-S., & Fedotov, I. (2013). Analytical solution of axisymmetric contact problem about indentation of a circular indenter into a soft functionally graded elastic layer. *Acta Mechanica Sinica*, 29(2), 196–201.

Chapter 24

Blockchain Technology and Consensus Algorithms

İrfan Sarıyıldız^{1*}
Mehtap Köse Ulukök²

Abstract – The emergence of blockchain technology has rapidly ushered in applications across various sectors such as finance, energy, transportation, automotive, and healthcare. The consensus algorithm, which serves as the backbone of blockchain by ensuring transaction validation, chain security, and preventing double-spending, has seen a need for diversification due to blockchain's swift evolution and wide-ranging application. Consensus algorithms have been developed within the distributed architecture of blockchain to secure transaction accuracy and trust. The initial consensus algorithm, Proof of Work (PoW), was energy-intensive with high computational demands. More efficient, energy-saving, and low-computation-power algorithms have emerged for different use cases, mitigating the disadvantages of PoW. While Proof of Stake (PoS), requiring lower energy consumption and computational power, is the most well-known, new consensus algorithms like Proof of Space (PoSpace), Proof of Burn (PoB), and Proof of Importance (PoI) have also been developed. This study, drawing from researchers' scientific publications, aims to elucidate the functioning of the most renowned consensus algorithms in the field, particularly PoW and PoS, and describe the features and use cases of other developed algorithms. The purpose of this paper is to describe the important consensus algorithms. The information provided about these algorithms will help to understand how blockchain technology operates.

Keywords –Blockchain, consensus algorithms, PoW, PoS, hash functions.

I. INTRODUCTION

Financial transactions prior to 1973 were slow, manual, and had low security, conducted through Telegraph, Telephone, Telex (teleprinter exchange), and postal systems. In 1973, with the establishment of the SWIFT system, which had a centralized structure and was controlled from a single center, financial

¹ ¹Department of Software Engineering, Cyprus Science University, KKTC, Mersin 10 Turkey

² ²Department of Software Engineering, Cyprus Science University, KKTC, Mersin 10 Turkey
^{*}(irfansariyildiz@csu.edu.tr) Email of the corresponding author

transactions and the communication of financial data began to be provided faster, more reliably, and standardized compared to the past [1].

Despite updates, the SWIFT system, with its centralized structure, began to fall short of providing the desired efficiency due to emerging needs and limitations inherent in a centralized system. To address this need, in 2008, Blockchain technology was first introduced by Satoshi Nakamoto [2] with the whitepaper titled 'Bitcoin: A Peer-to-Peer Electronic Cash System'.

Advancements in technology have led to an increase in financial transactions, prompting the development of alternative systems to the centralized SWIFT system, which has specific manual approval mechanisms. However, the technological developments that have emerged not only impacted the financial system but also opened opportunities for their use in various fields such as energy, transportation, automotive, healthcare, and more. Unlike traditional systems, this new technology does not require central authority and is defined as a data structure where transactions, once recorded, are immutable.

Although most people are familiar with blockchain technology from its use in the Bitcoin cryptocurrency system, it is also being applied to several other industries. It records transactions in a decentralized, secure ledger that removes the need for middlemen and offers transparency. Because of this, blockchain is being used more and more in sectors other than banking, demonstrating its ability to improve security and transform a variety of operations [3]–[7].

The PoW consensus algorithm, which was first introduced at the inception of blockchain technology, has been widely adopted in various applications. However, due to its significant energy and computational power requirements, experts have developed several alternative consensus algorithms. The purpose was to eliminate the substantial energy and computational power demands of PoW and enable more efficient transaction processing.

Among these alternatives, the most well-known is PoS, which is utilized by Ethereum. However, numerous other consensus algorithms have been created by experts to achieve the goal of more energy-efficient and streamlined transaction processing. Some of these include PoSpace, PoC, PoB, and PoI, among others [8], [9].

The remaining part of this article is organized into four sections. In Section 2, the working principle of blockchain is explained. Section 3 delves into the consensus algorithms and their characteristics as presented in the conducted studies. Finally, Section 4 presents the conclusions drawn from the research.

II. MATERIALS AND METHOD

Unlike centralized technologies, blockchain operates as a decentralized system [10]. This allows blockchain to execute transactions quickly, securely, and openly without relying on a central authority for approval. Blockchain is a distributed database system that secures transactions through cryptographic methods. Transactions in the blockchain are initiated with a crucial starting block called the genesis block. This block is used in finding the block hash, which is crucial for creating subsequent blocks. The transaction process begins between the sender and the recipient. The user initiating the transaction signs it digitally using cryptographic methods, creating, and broadcasting the transaction to the blockchain network [10].

The recipient and other nodes receive the transaction notification, verify its accuracy through cryptographic operations, and if the digital signature is confirmed, the transaction is included in a pool called the “mempool”. Transactions included in the pool are examined by miners based on various parameters. If selected as a candidate for processing, the transaction is moved from the mempool to a temporary transaction pool. When the necessary criteria are met, the node initiating the transaction notifies miners that creating a block has begun. Complex calculations commence based on the block's difficulty level. When a value is found below the target value, the node that found it communicates to other nodes the creation of the block and the specific NONCE value used for the complex mathematical puzzle. After verifying the accuracy of the calculation, other nodes reach a consensus to confirm the block. The transactions within the confirmed block are then executed and recorded in the ledger [10], [11].

While operations using the first algorithm of blockchain, PoW, differ from PoS and other developed consensus algorithms, fundamentally, all algorithms share a common structure where each block contains data from the previous block. This linkage enables blocks to connect to each other, forming a chain. Created through complex and computationally intensive calculations, the blocks aim to establish a decentralized, secure, and transparent database. Initially utilized as the underlying technology for Bitcoin, blockchain has since found applications in various fields, including finance, healthcare, supply chain management, voting systems, and more [6], [12], [13].

PoW, the first consensus algorithm developed for blockchain, involves solving complex mathematical puzzles to verify transactions and create new blocks. These puzzles involve finding the NONCE value, referred to as the 'hash puzzle.' The intricate mathematical puzzle of PoW requires high computational power and energy consumption, making it less environmentally friendly

compared to other algorithms. The flowchart of the PoW consensus algorithm is provided in Fig. 1.

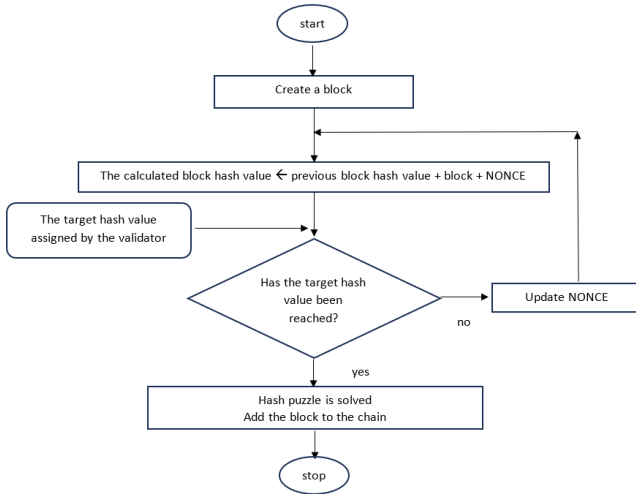


Fig. 1 PoW Consensus Algorithm flowchart

PoS is a consensus algorithm that addresses the energy consumption and computational requirements of PoW. Instead of solving NONCE puzzles, PoS assigns block validation rights based on the number of tokens held by validators. Validators with a higher stake have a greater chance of being selected to verify transactions and create new blocks. The flowchart of the PoS consensus algorithm is presented in Fig. 2.

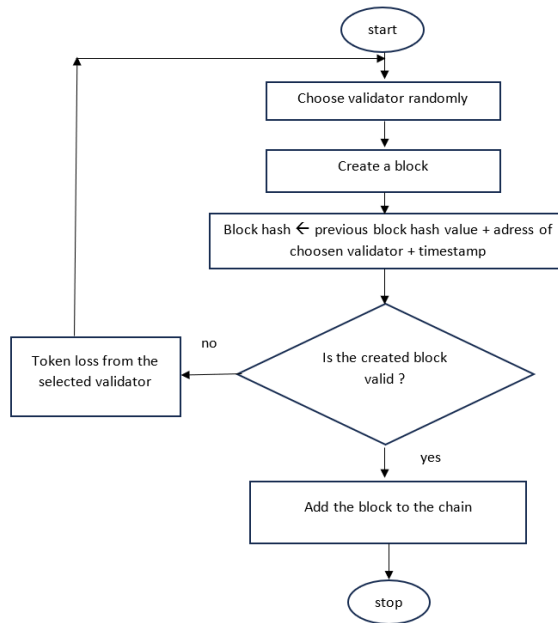


Fig. 2 PoS Consensus Algorithm flowchart

III. CONSENSUS ALGORITHMS AND THEIR FEATURES

A blockchain functions as a distributed database system that enables fast, secure, and transparent transactions without the need for a central authority. It ensures integrity by securing transactions using cryptographic methods. The blockchain begins with the 'genesis block,' which is the first block in the chain. Subsequent transactions are initiated between a sender and a receiver. The sender digitally signs the transaction using cryptographic techniques and broadcasts it to the blockchain network. The receiver and other nodes receive the transaction notification, verify its authenticity using cryptographic operations, and when the digital signature is confirmed, the transaction is included in the transaction pool. Transactions included in the transaction pool are temporarily added to a temporary transaction pool by miners based on various parameters. When the necessary criteria are met, the node initiating the transaction notifies miners that the block creation process has started. Complex calculations begin based on the difficulty level of the block. When a value lower than the target value is found, the node that discovers it notifies other nodes that the block has been created and passes on other required parameters.

Financial transactions have seen a dramatic transformation thanks to the blockchain, which has made them safer, more efficient, and more affordable. The time and expense of transactions can be decreased by using blockchain technology, which allows transactions to be performed instantly. Furthermore,

because blockchain technology makes data modification harder, it improves security and transparency. Financial institutions take use of blockchain's ability to speed up and secure operations by using it to expedite procedures including trade financing, cross-border payments, and settlement.

The blockchain is being used to facilitate efficient and transparent transactions in supply chain management and energy trading. Energy transactions can be carried out peer-to-peer using blockchain technology, cutting out middlemen and transaction fees. Blockchain technology can also monitor energy consumption, ensuring sustainable energy production and consumption. To facilitate precise tracking and trading of renewable energy credits, blockchain is also utilized to maintain certifications of renewable energy.

The blockchain improves openness, decreases bureaucracy, and allows for more effective supply chain management. Blockchain technology makes it possible to track every step of the supply chain, from manufacturing to delivery. This can lessen the possibility of theft, fraud, and counterfeiting. Blockchain is also utilized in transportation payment management to guarantee timely and correct payment to all parties involved. Moreover, decentralized shared transport networks can be established thanks to blockchain technology, enabling passengers to share journeys without the need for middlemen.

In blockchain technology, consensus algorithms are essential to the recording of transactions in a distributed ledger. The PoW algorithm is the first consensus technique utilized in block construction. PoS is another popular consensus algorithm that aims to overcome the computational and energy needs of PoW. There have been numerous other consensus algorithms created in addition to these two well-known ones. The PoSpace, and PoI algorithms are a few of the more popular ones.

A consensus mechanism known as PoSpace is predicated on allocating storage space as evidence of commitment. It is also called as Proof of Capacity (PoC) consensus algorithm. Validators assign a certain amount of storage space to show that they are a part of the network. The greater the area allotted, the greater the likelihood of being chosen for transaction validation and block creation.

The PoI consensus algorithm considers various parameters, including node reputation and activity level. More weight is given to validators who are involved in the blockchain ecosystem, give back to the community, and possess a sizable number of tokens. A validator has a greater chance of being chosen to validate transactions and add new blocks the more significant they are.

IV. CONCLUSION

Blockchain technology's ability to provide quick, safe, and transparent transactions has changed several industries. The consensus algorithm is the

fundamental component of the blockchain's security and integrity, guaranteeing that transactions are legitimate, and the network operates as intended. The PoW is the most well-known consensus mechanism, in which miners confirm transactions by solving challenging mathematical puzzles in exchange for rewards.

PoW does have certain drawbacks, though, such as high energy usage and sluggish transaction rates. The PoS has been created as a substitute consensus algorithm to overcome these problems. PoS uses network stakeholder validators to confirm transactions. This algorithm is a common choice for new blockchain networks since it is faster and more energy-efficient than proof-of-work algorithms. Other consensus algorithms, such as PoSpace, and PoI, exist in addition to PoW and PoS. Since they each have special qualities and uses, they can be used with various kinds of blockchain networks.

Consensus algorithms for blockchains are essential for maintaining the security and integrity of blockchain networks. Blockchain technology is becoming more and more versatile in its applications. It is certain that as technology develops, more creative consensus algorithms will be created to improve the effectiveness and scalability of blockchain networks.

REFERENCES

- S. V. Scott and M. Zachariadis, “Origins and development of SWIFT, 1973-2009,” *Bus Hist*, vol. 54, no. 3, pp. 462–482, 2012, doi: 10.1080/00076791.2011.638502.
- S. Nakamoto, “Bitcoin: A Peer-to-Peer Electronic Cash System.” [Online]. Available: www.bitcoin.org
- S. Alla, L. Soltanisehat, U. Tatar, and O. Keskin, “Blockchain Technology in Electronic Healthcare System Blockchain Technology in Electronic Healthcare Systems,” 2018. [Online]. Available: <https://www.researchgate.net/publication/325542378>
- M. Attaran, “Blockchain technology in healthcare: Challenges and opportunities,” *International Journal of Healthcare Management*, vol. 15, no. 1. Taylor and Francis Ltd., pp. 70–83, 2022. doi: 10.1080/20479700.2020.1843887.
- J. E. Kasten, “Engineering and Manufacturing on the Blockchain: A Systematic Review,” *IEEE Engineering Management Review*, vol. 48, no. 1. Institute of Electrical and Electronics Engineers Inc., pp. 31–47, Jan. 01, 2020. doi: 10.1109/EMR.2020.2964224.
- V. Merlo, G. Pio, F. Giusto, and M. Bilancia, “On the exploitation of the blockchain technology in the healthcare sector: A systematic review,” *Expert Systems with Applications*, vol. 213. Elsevier Ltd, Mar. 01, 2023. doi: 10.1016/j.eswa.2022.118897.
- H. Wan, K. Li, and Y. Huang, “Blockchain: A Review from the Perspective of Operations Researchers,” in *Proceedings - Winter Simulation Conference*, Institute of Electrical and Electronics Engineers Inc., 2022, pp. 283–297. doi: 10.1109/WSC57314.2022.10015500.
- B. Lashkari and P. Musilek, “A Comprehensive Review of Blockchain Consensus Mechanisms,” *IEEE Access*, vol. 9. Institute of Electrical and Electronics Engineers Inc., pp. 43620–43652, 2021. doi: 10.1109/ACCESS.2021.3065880.
- X. Wang et al., “Survey on blockchain for Internet of Things,” *Computer Communications*, vol. 136. Elsevier B.V., pp. 10–29, Feb. 01, 2019. doi: 10.1016/j.comcom.2019.01.006.
- A. A. Monrat, O. Schelén, and K. Andersson, “A survey of blockchain from the perspectives of applications, challenges, and opportunities,” *IEEE Access*, vol. 7. Institute of Electrical and Electronics Engineers Inc., pp. 117134–117151, 2019. doi: 10.1109/ACCESS.2019.2936094.

- M. Beller and J. Hejderup, "Blockchain-based software engineering," in Proceedings - 2019 IEEE/ACM 41st International Conference on Software Engineering: New Ideas and Emerging Results, ICSE-NIER 2019, Institute of Electrical and Electronics Engineers Inc., May 2019, pp. 53–56. doi: 10.1109/ICSE-NIER.2019.00022.
- X. Wang et al., "Survey on blockchain for Internet of Things," Computer Communications, vol. 136. Elsevier B.V., pp. 10–29, Feb. 01, 2019. doi: 10.1016/j.comcom.2019.01.006.
- T. Wang, H. Hua, Z. Wei, and J. Cao, "Challenges of blockchain in new generation energy systems and future outlooks," International Journal of Electrical Power and Energy Systems, vol. 135. Elsevier Ltd, Feb. 01, 2022. doi: 10.1016/j.ijepes.2021.107499.

Chapter 25

A Review on the Design, Modeling and Optimization of Fused Deposition Process Printing Parameters

Melih SAVRAN¹

ABSTRACT

Fused Deposition Modeling (FDM) is an Additive Manufacturing technology that can create complex parts layer-by-layer from 3D computer-aided design (CAD) data. While FDM has advantages, its use in professional settings is limited by the manufactured product's lower mechanical properties. FDM parameters considerably influence the product's properties. Research has been conducted to improve various print quality characteristics, such as mechanical properties, build time, dimensional accuracy, and surface finish of the manufactured parts. However, progress has been slow due to the complexity of the FDM process and conflicting process parameters. This study aims to provide a comprehensive summary of recent studies that have used advanced statistical and experimental design techniques to improve the mechanical properties of printed parts, the effect of process parameters on tensile strength, flexural strength, impact resistance, and existing work on optimizing process parameters.

Keywords: Additive manufacturing, fused deposition modeling, mechanical properties, optimization, process parameters

INTRODUCTION

Additive Manufacturing (AM) technology is a method of manufacturing that creates three-dimensional geometric shapes by adding layers on top of each other using metal, plastic, composites, and organic materials. Unlike traditional methods, AM is a rapidly developing and highly preferred type of production in the industry. It provides ease in the production of complex parts, does not require a mold, uses only as much material as necessary, and allows for rapid prototyping and personalized design. The technology is widely used in many sectors, including medicine, dentistry, aviation and space industry, automotive, jewelry, education, food, and entertainment (Sürmen, 2019).

¹ Res. Asst. PhD.; İzmir Katip Çelebi University, Department of Mechanical Engineering.
mlhsvrn@gmail.com ORCID No: 0000-0001-8343-1073

In order to create a form using additive manufacturing, a 3D model of the form is first created using computer-aided design (CAD) software like CAD, Catia, and Solidworks. Alternatively, a 3D scanning device such as a laser, MRI, optical, or CT scanner can be used to scan an existing form. The 3D model created in the second step is then saved in an appropriate format using a slicer program, most commonly in STL format. There are other recognized formats like .obj, .X3D, and .3MF. In the third step, the saved file is loaded into a slicer software program before printing. In this program, the position of the form on the printer table, its orientation, layer thickness, material type, temperature, printing density, printing speed, supporting base, number of wall layers, and fan settings are adjusted. After these properties are set, the model is sliced and G-codes are generated. Slicer software like Cura, MatterControl, Craftware, Slic3r, and Netfabb Basic, are free and open source. Finally, the prepared file is loaded into the 3D printer, and the printing process is complete (F42 Committee, 2012).

Additive manufacturing, the physical creation of three-dimensional objects by adding layers of digital data, was first developed by Charles Hull in 1984 and patented as Stereolithography (SLA) in 1986 (Gibson et al., 2015). This method involves hardening the liquid photopolymer material layers with ultraviolet laser beams. Subsequently, other methods, such as Selective Laser Sintering (SLS) and Fused Deposition Modeling (FDM) emerged. SLS methods involve hardening powdered raw material with laser beams, while FDM methods involve hardening melted solid polymer material layers with heat.

In 1999, the Wake Forest Institute achieved a significant milestone in the history of additive manufacturing technologies by placing an organ produced with a 3D printer into a human body for the first time (Goldberg, 2018). Since 2006, three-dimensional printers have been developed in line with open information-sharing platforms, and entrepreneurs and producers have created different solutions for different purposes. With open-source sharing among users of additive manufacturing technology, all kinds of data regarding production are accessible worldwide and continue to be developed by users (Şahin and Turan, 2018)

The idea of using cement-based materials in additive manufacturing technologies was first proposed by Pegna in 1997, and this idea has been a guide for concrete printing technologies (Lim et al., 2012). Loughborough University carried out additive manufacturing with concrete material in 2011 (Buswell et al., 2018). Houses built with concrete blocks produced with additive manufacturing technology in China and Andrey Rudenko's castle produced with a 3D printer are the primary examples of additive manufacturing with a concrete printer on a building scale (Fung, 2014; Rudenko, 2014).

Additive manufacturing is a rapidly evolving field constantly under research and study. The most critical areas of interest in additive manufacturing include manufacturing methods, process parameters, analysis, modeling, and parts optimization. The American International Society for Testing and Materials (ASTM) has classified additive manufacturing technologies into seven categories: Stereolithography (SLA), Material Jetting (MJ), Binder Jetting (BJ), Material Extrusion (ME), Powder Bed Fusion (PBF), Laminated Object Manufacturing (LOM), and Directed Energy Deposition (DED). Table 1 discusses different methods of AM, their brief schematics, descriptions, advantages, and disadvantages.

PBF and FDM are two different technologies used in additive manufacturing. While PBF technology is being developed for industrial purposes, FDM technology is growing in popularity for individual use. Material extrusion (ME) technology, which is used in FDM, is considered the most affordable and accessible additive manufacturing method in the World (All3DP, 2019). It is easily scalable and allows for changing print sizes without any additional costs. The use of FDM technology has become widespread due to its low cost and availability of different materials. It can be used in various stages of product development, including pre-prototype, prototype, market product, and mass production design processes, which enables rapid product development and customization.

Depending on the methods used in additive manufacturing, many process parameters affect the results in production. As a natural consequence of having so many process parameters in additive manufacturing, many studies are carried out using different design of experiment, modeling and optimization methods, and approaches to produce better designs in this field. Generally, the most used methods are Taguchi, Anova, Artificial Neural Networks, Regression Analysis, Fuzzy Logic, and Response Surface Method ((Torres et al., 2015);(Laeng et al., 2006);(Liu et al., 2017);(Lee et al., 2005);(Raju et al., 2018);(Mohamed et al., 2015);(Deng et al., 2018);(Srivastava et al., 2018);(Dong et al., 2018)).

Additive manufacturing technologies use different methods and raw materials to achieve the desired physical properties of the final product according to its usage area. The literature suggests several approaches to classify raw materials used in these technologies. They can be classified based on the pre use phase of the raw material, the phase of the raw material in the accumulation phase, and the type of raw material (e.g. plastic, metal). For instance, (Hopkinson and Dickens, 2006) classified raw materials as liquid, solid, and powder-based, where raw materials that melted and became liquid during the deposition stage were not included in the liquid-based material category. (Wond and Hernandez, 2012)

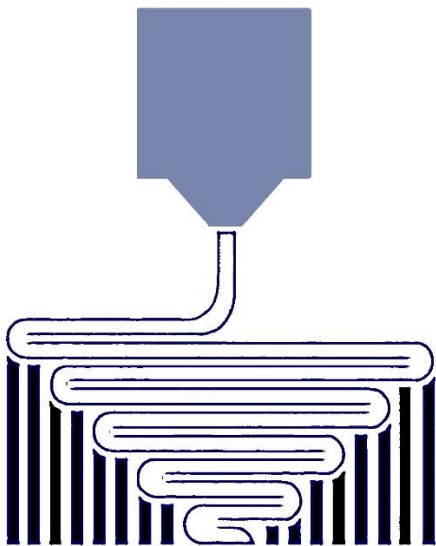
classified raw materials based on their structure at the deposition stage as liquid, solid, and powder-based. On the other hand, (Çelik and Özkan, 2017) categorized additive manufacturing technologies as those using metal materials and those not using metal materials. (Tofail et al., 2018) classified powdered raw materials as solid-based raw materials and divided layered production technologies into liquid and solid-based based on the material used. The literature displays various ways to define and classify raw materials used in additive manufacturing technologies.

Based on the literature studies, it is evident that additive manufacturing is a vast field continuously evolving with ongoing research and developments. This study focuses on the fused deposition modeling method, which is the most popular among additive manufacturing methods and is widely used. The main topics covered in this study include the materials used in production, process parameters, and modeling and optimization studies that examine the effects of process parameters on various output parameters.

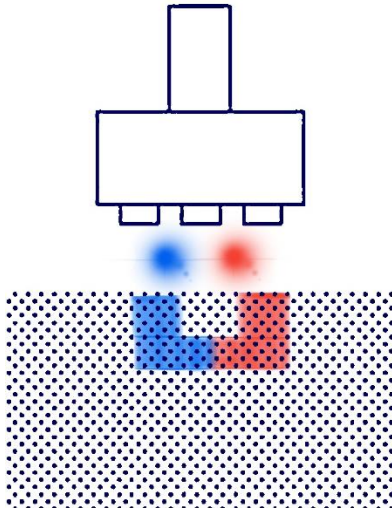
FDM Process

Additive manufacturing technology is an advanced method where parts are manufactured using computer-aided design data. Traditional manufacturing processes can be costly and time-consuming; the part's accuracy depends on the technician's expertise. Moreover, changes in part geometry during the production process can increase the cost of production. Hence, additive manufacturing technologies have emerged as a solution. They can make changes to the geometries of complex parts within a stipulated time and produce them at a low cost ((Singh and Davim, 2018);(Wu et al., 2017)). Fused deposition modeling is one of the material extrusion methods patented by Scott Crump and developed by Stratasys Inc. In this method, the semi-fluid material filament is extruded and layered to produce the desired part. With the invention of low-cost and various fused deposition machines, this production technology has become widespread and is commonly called 3D printing (Calignano et al., 2017).

Table 1. Additive Manufacturing Methods

Sr. No	Type of AM Methods	Working Principle	Material
1	 <p data-bbox="222 964 620 991">Material Extrusion (Ahangar et al., 2019)</p>	<p>Material extrusion is a type of 3D printing that involves the selective distribution of material through a nozzle. The filament is heated in the nozzle and then deposited layer by layer to create the desired shape. The material used is typically a thermoplastic polymer or composite material that becomes liquid when heated and solidifies at room temperature after it is deposited (F42 Committee, 2012).</p>	Polymer Composite

2

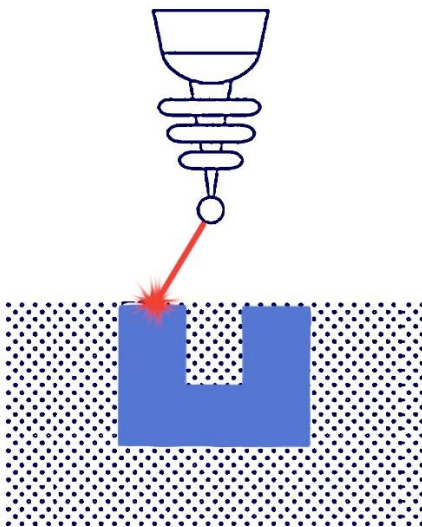


Binder Jetting (Ahangar et al., 2019)

Binder jetting manufacturing is a process where a liquid binding agent is used to bond powder materials selectively. The process involves applying a liquid adhesive to the powder material in layers to form the desired shape. This is repeated by laying a layer of powder material on top, and the process is continued until the final product is formed (F42 Committee, 2012).

Polymer
Composite
Ceramic
Metal
Hybrid

3

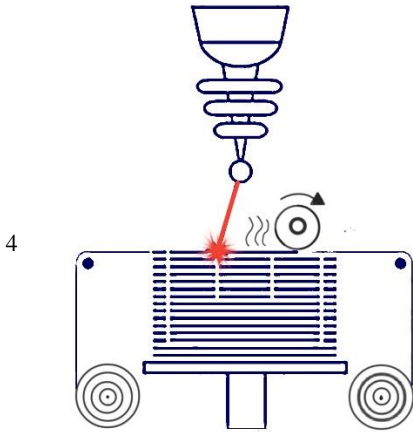


Powder Bed Fusion (Ahangar et al., 2019)

Powder bed fusion is an additive manufacturing technique that selectively combines regions of a powder bed with thermal energy. The process involves laying the powder material in layers and directing the laser onto it to melt and fuse the desired layer shape. The melted layer then acts as the base for the next layer of powder. This process is repeated until the entire desired object is created

Polymer
Composite
Ceramic
Metal
Hybrid

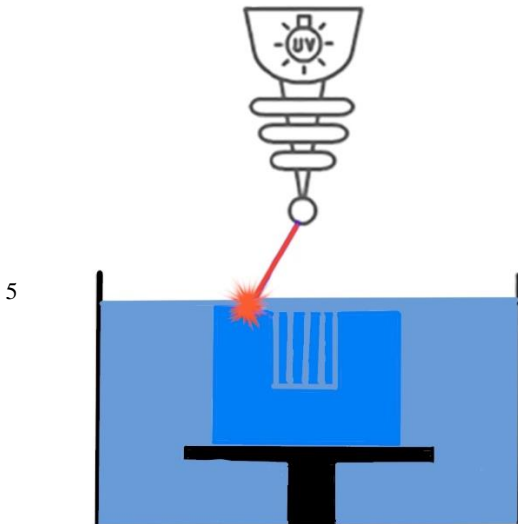
(F42 Committee, 2012).



Laminated Object Manufacturing (Ahangar et al., 2019)

Laminated object manufacturing technology is a type of additive manufacturing process where layers of material are combined to create an object. This is done by joining metal sheets on top of each other using welding or adhesives (F42 Committee, 2012).

- Polymer
- Ceramic
- Metal
- Hybrid

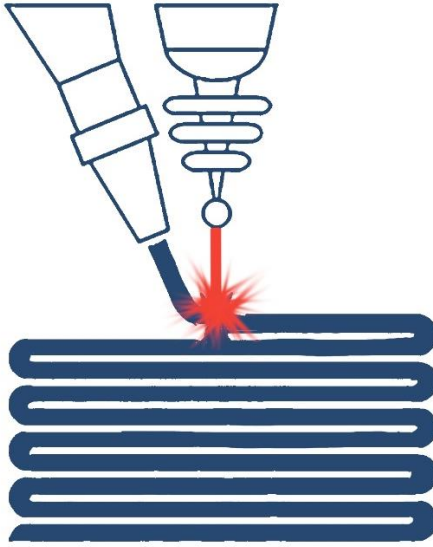


Stereolithography (SLA) (Ahangar et al., 2019)

Stereolithography is additive manufacturing that uses a light-activated polymerization technique to solidify a liquid photopolymer raw material. The process involves reflecting ultraviolet light onto the liquid resin pool's surface in a pattern corresponding to the desired shape. The resin that comes into contact with the light hardens and forms a layer. As the platform moves downward, layers of the desired shape are formed on top of each other (F42 Committee, 2012).

- Polymer
- Ceramic

6

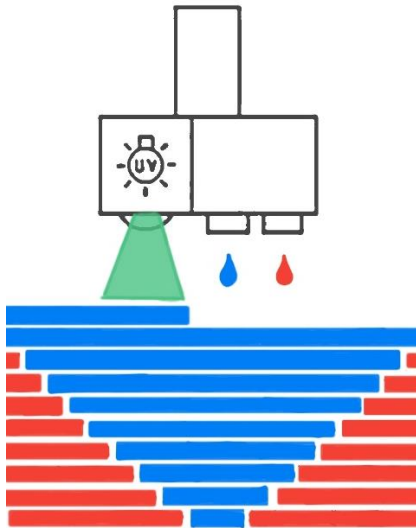


Direct Energy Deposition (DED) (Ahangar et al., 2019)

Direct Energy Deposition (DED) is an advanced additive manufacturing technology that uses thermal energy to melt and combine materials. This process involves melting metal wire or ceramic powder using thermal light and depositing it layer by layer to create a three-dimensional object (F42 Committee, 2012).

Metal
Hybrid

7



Material Jetting (Ahangar et al., 2019)

The material jet method is an additive manufacturing process where droplets of material are deposited selectively to form a structure. In this method, liquid material droplets are sprayed onto a platform in layers, and each layer is hardened using ultraviolet (UV) light to achieve the desired shape. Photopolymers and waxes are examples of materials used in this method (F42 Committee, 2012).

Polymer
Composite
Ceramic
Hybrid
Biological

Part production with fused deposition modeling is divided into three stages: pre-processing, production, and final processing. The pre-processing stage involves converting the computer-aided design data into an appropriate format for the printer to produce the part, selecting the appropriate parameters according

to the desired properties, and determining the layer thickness and model temperature.

The machine's software slices the computer-aided design data into layers and creates a path that the nozzle should follow for production. The software directs the filament material to the heater to form the part in layers, following the path determined by the rollers, and then to the nozzle to be extruded. Production is carried out in a temperature-controlled environment to ensure adhesion between layers (Wiese et al., 2020).

The printer contains the construction material that forms the part, known as filament in the form of wire or thread, and the support material is generally used in perforated and curved structures to produce the part by minimizing errors. The support material may be the same or different from the sample. Support structures should minimize part distortion, be easily removable without damage, and reduce time and cost (Jiang et al., 2018).

In a typical fused deposition modeling printer, semi-fluid filaments are sprayed onto the platform by a nozzle that moves horizontally in the X and Y planes. Conversely, the platform moves downwards in the Z plane to create the next layer. In cases where the table is fixed, the nozzle moves upwards in the Z plane instead. The formed layer cools, and bonds to the layer below it, and this process is repeated until the part is completed. Finally, post-processing techniques are applied to the part, removing support structures (Wiese et al., 2020).

Fused Deposition Modeling (FDM) printers are categorized into different groups in the literature. Some studies divide FDM printers as Cartesian and robotic (Alwi et al., 2013). Meanwhile, some studies suggest three types of FDM printers - Cartesian, delta, and polar (Wakimoto et al., 2018). Finally, some research mentions four types of printers by adding robotic printers ((Alex, 2017);(Yusuf, 2016)).

The linear coordinate system is used in Cartesian-type printers. The print head moves on the Z-axis, determining the height of the form. The printing platform moves linearly according to the position of the form desired to be created on the x and y-axis. It is the most commonly used printer type (Schmitt et al., 2018).

Unlike Cartesian-type printers, the printing platform is fixed in delta-type printers, and the print head moves in all directions. When using the Cartesian coordinate system, the print head moves linearly in the Z axis and sinusoidally in the X and Y axis. The arms, which carry the print head and are connected to form a triangular structure, position the print head according to the layer position of the form to be created. Delta printers have advantages such as higher production

volume, faster printing, and better temperature control compared to Cartesian type printers (Schmitt et al., 2018).

Polar printers use the polar coordinate system for positioning instead of the Cartesian coordinate system. Polar coordinate sets define points in a circular grid rather than a square. The platform moves circularly while the print head moves linearly in all directions. Polar printers are more energy efficient and can print more significant volumes of objects in a smaller space (Alex, 2017).

Robotic printers have articulated joints that enable linear and circular movements of the print head attached to a single robot arm. There is no fixed printing platform. Thanks to the robotic arm, the print head has flexible movement capability, and complex structures are more accessible to produce (Alex, 2017). However, the print quality is lower than others. It is not as cheap and common as other 3D printers but is used for large-scale prints such as building scale.

The advantages of the FDM production process are as follows:

- (i) It enables the production of complex-shaped parts.
- (ii) Low-cost raw materials and a wide variety of thermoplastic materials can be used (Gonzales and Alvarez, 2018).
- (iii) The production process is easier and less expensive than other production methods (Gonzales and Alvarez, 2018).
- (iv) The machines can be installed in the office environment and efficiently operated (Upcraft and Fletcher, 2003).
- (v) Changes in the part geometry can be made in line with customer requests, and these changes can be easily transferred to the production process.

There are several disadvantages of the FDM manufacturing process, which are as follows:

- (i) It is not suitable for mass production.
- (ii) The parts produced by FDM exhibit anisotropic behavior in the Z direction due to low cohesion force between the layers, which means that they offer poor resistance to tensile stresses perpendicular to the direction of the layers.
- (iii) Support structures are required to prevent the sagging of the parts caused by the force of gravity (Gonzales and Alvarez, 2018).
- (iv) Due to low surface quality, additional mechanical and chemical treatments may be necessary after production.

FDM Process Parameters

Determining the proper production parameters for the FDM method is extremely important for the quality and accuracy of the product, preventing and/or reducing waste, reducing production costs and time, and increasing

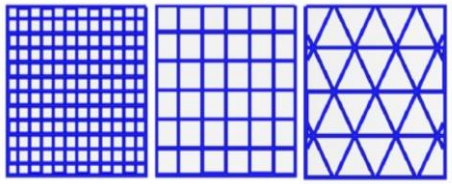
efficiency (Ravikumar et al., 2022). Many different process parameters are examined in studies. However, the most commonly examined and studied parameters are layer thickness, build orientation, infill pattern, infill density, nozzle diameter, print speed, air gap, raster angle, extrusion temperature, raster width, and number of contours. Explanations about these parameters that are effective in production with the FDM process are given in Table 2.

Table 2. Fused Deposition Modeling (FDM) process parameters

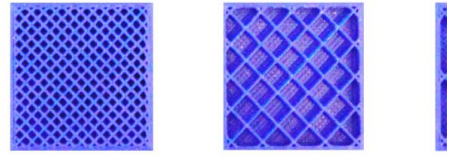
FDM Process Parameters	Description
Layer thickness	The layer thickness refers to the height of each layer that is deposited onto the printing platform by the extrusion nozzle. It is measured in the z-axis direction. Choosing the appropriate thickness for the first layer is crucial to ensure that the part sticks to the platform. If the first layer doesn't adhere well to the printing platform, it may cause the part to warp or deform (Khan et al., 2021);(Doshi et al., 2022). Decreasing the nozzle diameter reduces the layer thickness, leading to a better surface quality but increased time and cost due to the increased number of layers required (Singh and Davin, 2018).
Build Orientation	The part is placed on the printing platform at a certain angle to the horizontal axis, known as the build orientation (Yusuf, 2016). Researchers are conducting various studies on build orientation. According to the research carried out on parts printed at 0°, 45°, and 90° angles, it was found that the mechanical strength, tensile stress, and strain of the part printed at 0° were better than the parts printed at 45° and 90° (Upcraft and Fletcher, 2003). Moreover, it has been observed that the surface quality of parts printed at 0° and 90° angles is advantageous regarding production time and cost. However, at angles between 40° and 60°, the use of support material has increased due to the slope, which has resulted in decreased surface quality and increased cost.
Infill pattern	The infill pattern determines the internal structure of FDM printed parts. Common patterns include diamond, cross, honeycomb, gyroid, triangle, cubic, grid and linear.
Infill density	The infill density, which refers to the amount of filament in a part during production, is an essential factor to consider. While parts can be produced to be 100% filled, this will increase the amount of material used, resulting in a heavier part and increased time and cost of production. However, increasing the infill density can also increase the part's strength. Therefore, it's essential to adjust the infill density based on the functional requirements of the part.
Air Gap	The distance between two adjacent tool paths on a single layer of an FDM printed part. By increasing the air gap, density and production time can be reduced. While the surface quality of the parts generally increases with negative and positive air gap, the surface quality decreases in case of zero air gap.
Printing speed	The speed at which the nozzle moves during printing is called print speed or feed rate (Gao et al., 2022). When the printing speed is low, the material

	filaments adhere better to each other, resulting in increased tensile and bending strength. However, it also increases the printing time (Gao et al., 2022). On the other hand, high printing speeds decrease the production time, but the material filaments don't have enough time to plasticize, which results in weak mechanical properties (Zhang et al., 2008).
Raster Angle	The raster angle refers to the direction of the printed filament about the x-axis. This angle plays a significant role in determining the adhesion and strength of the final product. Research has shown that parts printed at $-45^{\circ}/+45^{\circ}$ have better surface quality, while a raster angle of 30° provides better bending and impact resistance (Singh and Davin, 2018).
Raster width	The raster width refers to the width of the path followed by the filaments on the printing platform, and the size of the nozzle diameter determines it. It has been found that mechanical properties improve when smaller raster widths are used (Singh and Davin, 2018). This also reduces the amount of material used and the production time. However, when the raster width is too large, stress concentration and deterioration in the conductivity of the part may occur. On the other hand, larger raster widths can improve bonding and diffusion (Gao et al., 2022).
Extrusion temperature	During the production process, it is essential to print the material at the lowest possible temperature. If the temperature increases after the material turns fluid, it can cause deterioration in the material structure. This may result in the material inside the nozzle burning, which can lead to a loss of functionality of the nozzle. The burnt material may also mix with the part, affecting its dimensional accuracy (Gibson et al., 2015). On the other hand, if the nozzle temperature is too low, the filament may not melt entirely, which can cause the nozzle to clog (Gao et al., 2022).
Nozzle diameter	Diameter of nozzle tip of the extruder
Number of contours	The number of solid outer layers that enclose the internal infill pattern of an FDM printed part.

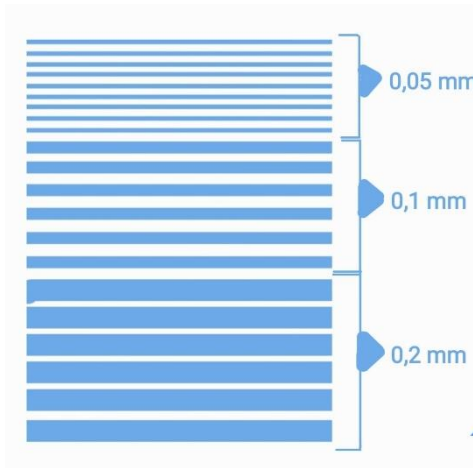
The process parameters that have been thoroughly researched include air gap, number of contour, build orientation, infill density, infill pattern, layer thickness, raster width, and raster angle. These parameters, shown in Figure 2, significantly impact filament bonding and, as a result, affect the mechanical performance of FDM-printed components. Furthermore, the interactions between these parameters play a crucial role in determining the mechanical properties of the printed components.



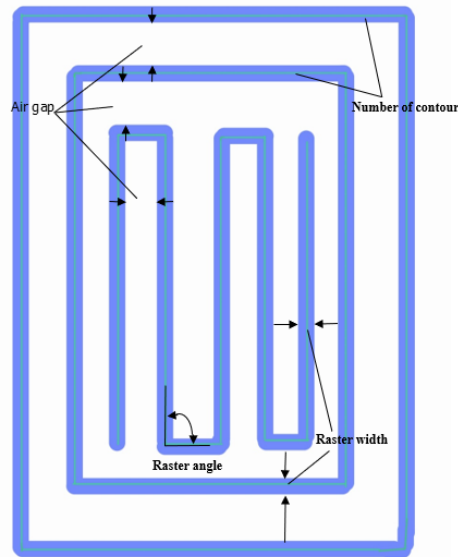
a.) infill pattern



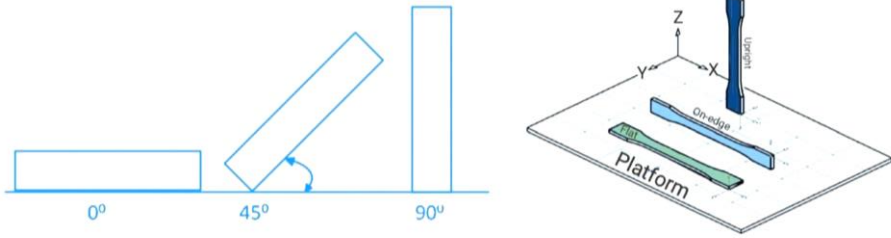
b.) infill density



c.) Layer thickness



d.) air gap, number of contour, raster width, and raster angle



e.) Building orientation

Figure 2. FDM process parameters (air gap, number of contour, build orientation, infill density, infill pattern, layer thickness, raster width, and raster angle)

FDM Process Materials

In 3D FDM printing, the raw material used is called filament. Filaments are made of polymer-based materials that are melted and reshaped to create the desired 3D object. Polymers are large molecules made up of repeating units called monomers. Plastic is commonly used daily due to its flexibility, durability, versatility, and lightness. Plastics are produced using raw materials such as cellulose, salt, natural gas, and oil. There are two main groups of plastics: thermoset and thermoplastic. Thermoplastics can be melted and reshaped, while thermosets cannot be reused once they solidify. A comparison of materials such as ABS, PLA, PC, PETG, TPU and Nylon, which are commonly used in 3D printing, is given in Figure 3.

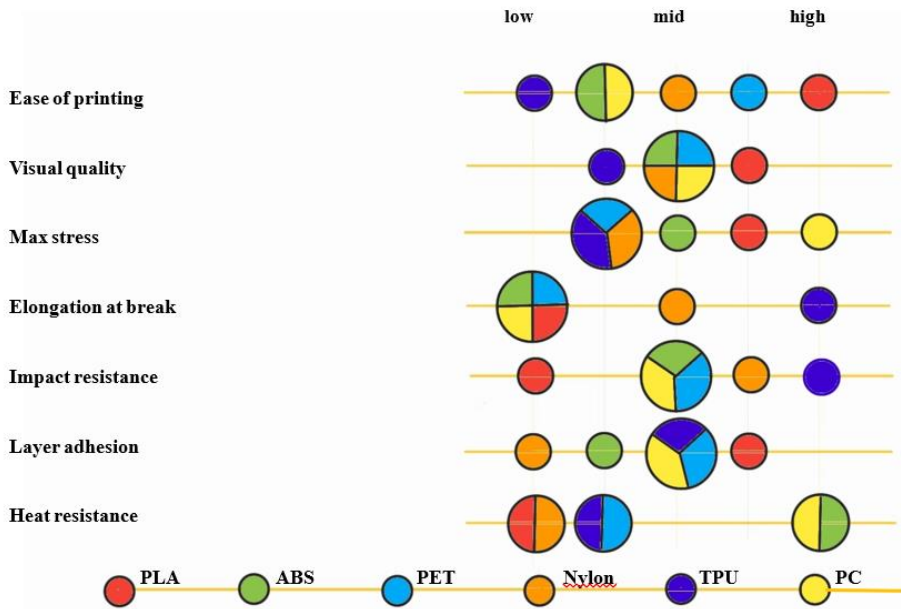


Figure 3. Comparison of material properties of filaments [41]

The most popular among these materials are PLA and ABS. Acrylonitrile Butadiene Styrene (ABS) is a thermoplastic polymer made from petroleum. It is a stiff material and has high impact resistance when compared to other polymers. However, it has limitations. Although the melting temperature of ABS is 105°C, it can deform when used at temperatures above 80°C. Another downside of ABS is that it releases toxic hydrogen cyanide gas during printing. Therefore, it is crucial to use ABS in a well-ventilated environment when printing with 3D printers (Khan et al., 2021).

PLA is a biopolymer made from renewable resources like corn, starch, potatoes, molasses, and sugar cane. It is environmentally friendly and has excellent optical, barrier, and high mechanical properties. Many industries and universities are interested in PLA as a substitute for traditional petroleum-based polymers such as low-density polyethylene (LDPE), polyamide (PA), polypropylene (PP), and polystyrene (PS). However, PLA has some disadvantages, including low toughness and high brittleness, poor processing ability, low service temperature, and foaming. It also has a low melting point and a slow crystallization rate (Çetin, 2022).

Previous Study on FDM Process Parameters Design, Modeling and Optimization

Determining the mechanical properties of parts manufactured with 3D printers is crucial, considering the desired performance and usage area. The mechanical properties of the samples are subject to variations based on several factors, such as the printing process parameters, the type of printer utilized, the material used, and physical events. In this regard, numerous researchers have conducted studies to observe the changes in mechanical properties, including yield strength, tensile strength, bending strength, modulus of elasticity, shear stress, fatigue strength, compressive strength, and impact strength of parts created with different parameters.

In this set of studies, various factors affecting the mechanical properties of parts produced using fused deposition modeling (FDM) were investigated.

(Rajpurohut et al., 2019) studied the effect of raster angle, layer thickness, and raster width on the tensile properties of parts printed using polylactic acid (PLA). They found that the raster angle, raster width, and the interaction of layer thickness and raster width significantly affected the tensile properties. Samples printed with a raster angle of 0° exhibited higher tensile strength than those printed with a 90° raster angle. The study also revealed a close relationship between raster angle and damage mode.

(Ning et al., 2015) examined the effects of adding carbon fiber of different content and lengths to ABS plastic on the mechanical properties of FDM-produced parts. They found that adding carbon fiber increased Young's modulus and tensile strength but reduced toughness, yield strength, and ductility.

(Vakharia et al., 2022) printed different types of ABS materials, with and without carbon fiber and carbon nanotube reinforcement, at different layer thicknesses. They found that ABS materials printed with a layer thickness of 0.1 mm outperformed those printed with a layer thickness of 0.2 mm. Carbon nanotube reinforcements were also shown to improve the strength and elastic modulus of ABS materials significantly.

(Rankouhi et al., 2016) investigated the correlation between the mechanical properties and layer thickness of ABS parts produced using FDM. They found that layer thickness and raster orientation significantly affected the mechanical properties. Samples printed with a layer thickness of 0.2 mm exhibited higher elastic modulus and maximum tensile strength than those printed with a layer thickness of 0.4 mm.

(Valean et al., 2020) examined the effect of orientation (0° , 45° , 90°) and layer thickness on the mechanical properties of polylactic acid (PLA) dogbone tensile specimens printed using FDM. They found that orientation had less effect on

Young's modulus but a higher effect on tensile strength. Increasing the number of layers caused both Young's modulus and tensile strength to decrease.

(Bardiva et al., 2021) investigated the effect of process parameters (layer thickness, infill density, and orientation) on flexural strength, tensile strength, and time taken to produce test specimens. The study found that the optimum parameters for producing high-strength parts in a short time were a layer thickness of 0.3 mm, a part orientation of 0°, and an infill density of 80%.

(Yeşiloğlu, 2022) investigated the mechanical properties of PLA samples produced using FDM with different filling densities and geometries (Octet, Gyroid, and Cross). The study found that mechanical properties deteriorated in all filler geometries with increasing density. The highest tensile strength was seen in the Octet-filled sample, and the highest deformation was seen in the Cross-filled sample. Breaking strength was observed to be highest in the Octet-filled sample and lowest in the Cross-filled sample.

The process parameters significantly influence the quality of parts built using FDM technology. Therefore, researchers usually adopt experimental approaches to obtain the optimal combination of parameters. These approaches include Taguchi design ((Lee et al., 2005);(Kafshgar et al., 2021)), fractional factorial design ((Hikmat et al., 2021);(Mazen et al., 2022)), full factorial design ((Moradi et al., 2021);(Rashet et al., 2022)), and face-centered composites design (FCD) ((Panda et al., 2009);(Baksik et al., 2010)), along with analysis methods such as analysis of variance (ANOVA) ((Kafshgar et al., 2021);(Hikmat et al., 2021)) or signal-to-noise ratio (S/N) ((Lee et al., 2005);(Laeng et al., 2006)). Some researchers also establish a mathematical model between the response and parameters, such as response surface methodology (RSM) ((Equbal et al., 2021);(Saad et al., 2021), and optimize it using various algorithms like particle swarm optimization (PSO) (((Saad et al., 2021);(ShirMohammadi et al., 2021)), artificial neural network (ANN) (Giri et al., 2021), bacterial foraging optimization (BFO) (Panda et al., 2009), genetic algorithm (GA) (Aminzade et al., 2021), surrogate-based optimization (Ulu et al., 2018), naked mole-rat algorithm (NMRA) (Chohan et al., 2021), and other heuristic optimization methods (Liu et al., 2022). Table 3 presents the process parameters, materials, and optimization techniques utilized in recent studies on FDM.

Table 3. Recent studies on FDM process

Study	Material	Process Parameter	Output	Methods
(Alhazmi et al. 2020)	PLA	Infill density, building orientation	Tensile	Full factorial

(Dave et al. 2020)	PLA	Raster angle, raster width, and layer height	Tensile	ANFIS
(Deshwal et al. 2019)	PLA	Infill density, speed, and print temperature	Tensile	RSM, CCD , GA-RSM, GA-ANN , GA-ANFIS
(Heidari et al. 2020)	PLA	Infill density, print speed, and layer thickness	Tensile	Taguchi method, S/N ratio
(Kamaal et al. 2021)	CFR-PLA	Build orientation, infill density, and layer thickness	Tensile, impact	TOPSIS
(Manoharan et al. 2020)	PLA	Layer thickness, infill density, print speed, temperature, and build orientation	Tensile	RSM, CCD, ANN
(Gunasekaran et al. 2020)	PLA	Infill density	Tensile, hardness, impact, flexural	Full factorial
(Son et al. 2020)	PLA, ABS, PETG	Infill density and infill pattern	Tensile	Full factorial
(Pramanik et al. 2020)	ABS	Printing speed, Extruder temperature, infill density, bed temperature, layer thickness	Surface roughness	RSM-CCD-ANOVA
(Divyathej et al. 2016)	ABS	Layer thickness	Flexural strength Compressive strength Surface roughness Impact	Experiment
(Sood et al. 2010)	ABS	Layer thickness, build orientation, raster angle, raster width, air gap	Tensile strength, flexural strength, impact strength	RSM-CCD-ANOVA
(Slonov et al. 2018)	PPSF	Raster width, air gap, raster angle	Tensile strength, elastic modulus, impact strength	Experiment
(Patil et al. 2021)	PLA	Infill patterns, infill density, printing speed and layer thickness	Surface roughness, Printing time and Filament length	Grey Relational Analysis (GRA)

(Abouelmajd et al. 2021)	PLA	Printing speed, extrusion temperature, and raster orientation	bending strength, bending stiffness, and deflection	Taguchi, ANOVA
(Kam et al. 2023)	PA12	layer thickness, extruder temperature, infill density, infill pattern	tensile strength, elongation, and impact strength	Taguchi
(Chinchanikar et al. 2023)	PLA	infill density, layer thickness, print speed, extrusion temperature	Impact, tensile, and flexural strengths	CCD, TOPSIS, NSGA II, RSM, GRA
(Dusanapodi et al. 2023)	ABS	Extrusion multiplier, Temperature, and Layer thickness	Porosity, tensile and compressive strengths	Taguchi, GRA, GA
(Yadav et al. 2023)	PLA	print speed, acceleration, jerk	Surface roughness	FCCD, GA-ANN
(Tayyab et al. 2023)	ABS	nozzle diameter, layer height, infill density, printing speed, raster orientation, infill pattern	Flexural strength, yield strength	Taguchi, GA-ANN

CONCLUSION

This review provides a comprehensive list of the process parameters used in the FDM printing process and their effects on the characteristics and quality of the printed parts, such as tensile and flexural strength, impact resistance, and surface roughness. Researchers have used DOE techniques and statistical optimization tools to identify the FDM process variables that significantly impact the desired output and to determine the optimal combination of these variables. These findings are crucial because the FDM process's efficiency and the quality of the printed parts depend on these process variables. The critical findings of this review and the need for further research are presented below.

- Fused Deposition Modeling (FDM) is a 3D printing technology that is mainly used with thermoplastic materials. Therefore, most of the research on FDM is focused on PLA and ABS thermoplastic materials. However, some studies have also been conducted on other thermoplastics such as PETG, Nylon, and composite materials.
- FDM process parameters such as raster orientation, layer thickness, building orientation, raster width, infill pattern, and infill density have been extensively studied in the literature.

- The most commonly used experimental design methods to observe the effect of FDM process parameters are Taguchi, FCCD, and Full Factorial.
- ANOVA, ANN, RSM are the more preferred methods in the literature for mathematical modeling and optimization.

References

- Abouelmajd, M., Bahlaoui, A., Arroub, I., Zenzami, M., Hmina, N., Lagache, M., & Belhouideg, S. (2021). Experimental analysis and optimization of mechanical properties of FDM-processed polylactic acid using Taguchi design of experiment. *International Journal for Simulation and Multidisciplinary Design Optimization*, 12, 30.
- Ahangar, P., Cooke, M. E., Weber, M. H., & Rosenzweig, D. H. (2019). Current biomedical applications of 3D printing and additive manufacturing. *Applied sciences*, 9(8), 1713.
- Alex, M. (2017). The 4 Types of FFF/FDM 3D Printer Explained (Cartesian, Delta, Polar). <https://www.3dnatives.com/en/four-types-fdm-3d-printers140620174/>
- Alhazmi, M. W., Backar, A., & Backar, A. H. (2020). Influence of infill density and orientation on the mechanical response of PLA+ specimens produced using FDM 3D printing. *Int. J. Adv. Sci. Technol*, 29(6).
- All3DP. (2019, Temmuz 22). 2019 Types of 3D Printing Technology | All3DP.
- Alwi, A., Gardner, M., Karayiannis, S., Reodique, K., Starkey, B., & Varley, T. (2013). MegaScale 3D Printing Group 1—Final Report. Faculty of Engineering and Physical Sciences University of Surrey, 201.
- Aminzadeh, A., Aberoumand, M., Rahmatabadi, D., & Moradi, M. (2021). Metaheuristic approaches for modeling and optimization of fdm process. In *Fused Deposition Modeling Based 3D Printing* (pp. 483-504). Cham: Springer International Publishing.
- Bagsik, A., Schöppner, V., & Klemp, E. (2010, September). FDM part quality manufactured with Ultem* 9085. In *14th international scientific conference on polymeric materials* (Vol. 15, pp. 307-315).
- Bardiya, S., Jerald, J., Satheeshkumar, V. (2021). The impact of process parameters on the tensile strength, flexural strength and the manufacturing time of fused filament fabricated (FFF) parts. *Materials Today: Proceedings*, 39, 1362–1366.
- Buswell, R. A., De Silva, W. L., Jones, S. Z., & Dirrenberger, J. (2018). 3D printing using concrete extrusion: A roadmap for research. *Cement and Concrete Research*, 112, 37-49.
- Calignano, F., Manfredi, D., Ambrosio, E. P., Biamino, S., Lombardi, M., Atzeni, E., ... & Fino, P. (2017). Overview on additive manufacturing technologies. *Proceedings of the IEEE*, 105(4), 593-612.
- Chinchanikar, S., Shinde, S., Shaikh, A., Gaikwad, V., & Ambhore, N. H. (2023). Multi-objective optimization of fdm using hybrid genetic algorithm-based

- multi-criteria decision-making (mcdm) techniques. *Journal of The Institution of Engineers (India): Series D*, 1-15.
- Chohan, J. S., Mittal, N., Kumar, R., Singh, S., Sharma, S., Dwivedi, S. P., ... & Wojciechowski, S. (2021). Optimization of FFF process parameters by naked mole-rat algorithms with enhanced exploration and exploitation capabilities. *Polymers*, 13(11), 1702.
- Çelik, K., & Özkan, A. (2017). Eklemeli imalat yöntemleri ile üretim ve onarım uygulamaları. *Düzce Üniversitesi Bilim ve Teknoloji Dergisi*, 5(1), 107-121.
- Çetin, M. (2022). *Granül termoplastik malzemelerin ekstrüzyon esaslı eklemeli imalat şartlarının incelenmesi ve optimizasyonu* (Master's thesis, Eskişehir Teknik Üniversitesi).
- Dave, H. K., Prajapati, A. R., Rajpurohit, S. R., Patadiya, N. H., & Raval, H. K. (2022). Investigation on tensile strength and failure modes of FDM printed part using in-house fabricated PLA filament. *Advances in Materials and Processing Technologies*, 8(1), 576-597.
- Deng, X., Zeng, Z., Peng, B., Yan, S., & Ke, W. (2018). Mechanical properties optimization of poly-ether-ether-ketone via fused deposition modeling. *Materials*, 11(2), 216.
- Deshwal, S., Kumar, A., & Chhabra, D. (2020). Exercising hybrid statistical tools GA-RSM, GA-ANN and GA-ANFIS to optimize FDM process parameters for tensile strength improvement. *CIRP Journal of Manufacturing Science and Technology*, 31, 189-199.
- Divyathej, M.V., Varun, M., Rajeev, P. (2016). Analysis of mechanical behavior of 3D printed ABS parts by experiment, *International Journal of Scientific & Engineering Research*, Vol. 7, No. 3, 116-124
- Dong, G., Wijaya, G., Tang, Y., & Zhao, Y. F. (2018). Optimizing process parameters of fused deposition modeling by Taguchi method for the fabrication of lattice structures. *Additive Manufacturing*, 19, 62-72.
- Doshi, M., Mahale, A., Kumar Singh, S., and Deshmukh, S. (2022). Printing parameters and materials affecting mechanical properties of FDM-3D printed parts: perspective and prospects. *Materials Today: Proceedings*, 50, 2269–2275.
- Dusanapudi, S., Krupakaran, R. L., Srinivas, A., Nikhil, K. S., & Vamshi, T. (2023). Optimization and experimental analysis of mechanical properties and porosity on FDM based 3D printed ABS sample. *Materials Today: Proceedings*.

- Equbal, A., Sood, A. K., Equbal, M. I., Badruddin, I. A., & Khan, Z. A. (2021). RSM based investigation of compressive properties of fdm fabricated part. *CIRP Journal of Manufacturing Science and Technology*, 35, 701-714.
- F42 Committee. (2012). Terminology for Additive Manufacturing Technologies.
- Fung, E. (2014, Nisan 15). Rapid Construction, China Style: 10 Houses in 24 Hours. WSJ. <https://blogs.wsj.com/chinarealtime/2014/04/15/how-a-chinese-company-built-10-homes-in-24-hours/>
- Gao, G., Xu, F., Xu, J., Tang, G., and Liu, Z. (2022). A survey of the influence of process parameters on mechanical properties of fused deposition modeling parts. *Micromachines*, 13(4), 553.
- Gibson, I., Rosen, D., Stucker, B., Khorasani, M., Gibson, I., Rosen, D., ... & Khorasani, M. (2021). Development of additive manufacturing technology. *Additive manufacturing technologies*, 23-51.
- Giri, J., Shahane, P., Jachak, S., Chadge, R., & Giri, P. (2021). Optimization of FDM process parameters for dual extruder 3d printer using Artificial Neural network. *Materials Today: Proceedings*, 43, 3242-3249.
- González, D. S., and Álvarez A. G. (2018). AM manufacturing feasibility study & technology demonstration EDA AM state of the art & strategic report; European Defence Agency, 16.ESI.OP.144. Brussels. 10-136
- Gunasekaran, K. N., Aravinth, V., Kumaran, C. M., Madhankumar, K., & Kumar, S. P. (2021). Investigation of mechanical properties of PLA printed materials under varying infill density. *Materials Today: Proceedings*, 45, 1849-1856.
- Hague, R., Dickens, P., & Hopkinson, N. (Eds.). (2006). *Rapid manufacturing: an industrial revolution for the digital age*. John Wiley & Sons.
- Heidari-Rarani, M., Ezati, N., Sadeghi, P., & Badrossamay, M. R. (2022). Optimization of FDM process parameters for tensile properties of polylactic acid specimens using Taguchi design of experiment method. *Journal of Thermoplastic Composite Materials*, 35(12), 2435-2452.
- Hikmat, M., Rostam, S., & Ahmed, Y. M. (2021). Investigation of tensile property-based Taguchi method of PLA parts fabricated by FDM 3D printing technology. *Results in Engineering*, 11, 100264.
- <https://all3dp.com/1/types-of-3d-printers-3d-printing-technology/>
- İnternet: FDM yöntemi malzemeleri, URL: <https://www.hubs.com/knowledge-base/fdm-3d-printing-materials-compared/>, Son Erişim Tarihi: 14.12.2022.
- Jiang, J., Stringer, J., Xu, X., and Zhong, R. Y. (2018). Investigation of printable threshold overhang angle in extrusion-based additive manufacturing for

- reducing support waste. *International Journal of Computer Integrated Manufacturing*, 31(10), 961-969.
- Kafshgar, A. R., Rostami, S., Aliha, M. R. M., & Berto, F. (2021). Optimization of properties for 3d printed pla material using taguchi, anova and multi-objective methodologies. *Procedia Structural Integrity*, 34, 71-77.
- Kam, M., Ipekci, A., & Şengül, Ö. (2023). Investigation of the effect of FDM process parameters on mechanical properties of 3D printed PA12 samples using Taguchi method. *Journal of Thermoplastic Composite Materials*, 36(1), 307-325.
- Kamaal, M., Anas, M., Rastogi, H., Bhardwaj, N., & Rahaman, A. (2021). Effect of FDM process parameters on mechanical properties of 3D-printed carbon fibre–PLA composite. *Progress in Additive Manufacturing*, 6, 63-69.
- Khan, S., Joshi, K., and Deshmukh, S. (2021). A comprehensive review on effect of printing parameters on mechanical properties of FDM printed parts. *Materials Today: Proceedings*, 50(9)
- Laeng, J., Khan, Z. A., & Khu, S. Y. (2006). Optimizing flexible behaviour of bow prototype using Taguchi approach. *Journal of Applied Sciences*, 6(3), 622-630.
- Laeng, J., Khan, Z. A., & Khu, S. Y. (2006). Optimizing flexible behaviour of bow prototype using Taguchi approach. *Journal of Applied Sciences*, 6(3), 622-630.
- Lee, B. H., Abdullah, J., & Khan, Z. A. (2005). Optimization of rapid prototyping parameters for production of flexible ABS object. *Journal of materials processing technology*, 169(1), 54-61.
- Lee, B. H., Abdullah, J., & Khan, Z. A. (2005). Optimization of rapid prototyping parameters for production of flexible ABS object. *Journal of materials processing technology*, 169(1), 54-61.
- Lim, S., Buswell, R. A., Le, T. T., Austin, S. A., Gibb, A. G., & Thorpe, T. (2012). Developments in construction-scale additive manufacturing processes. *Automation in construction*, 21, 262-268. <https://doi.org/10.1016/j.autcon.2011.06.010>
- Liu, B., Yang, L., Zhou, R., & Hong, B. (2022). Effect of process parameters on mechanical properties of additive manufactured SMP structures based on FDM. *Materials Testing*, 64(3), 378-390.
- Liu, X., Zhang, M., Li, S., Si, L., Peng, J., & Hu, Y. (2017). Mechanical property parametric appraisal of fused deposition modeling parts based on the gray Taguchi method. *The International Journal of Advanced Manufacturing Technology*, 89, 2387-2397.

- Manoharan, K., Chockalingam, K., & Ram, S. S. (2020, December). Prediction of tensile strength in fused deposition modeling process using artificial neural network technique. In *AIP Conference Proceedings* (Vol. 2311, No. 1). AIP Publishing.
- Mazen, A., McClanahan, B., & Weaver, J. M. (2022). Factors affecting ultimate tensile strength and impact toughness of 3D printed parts using fractional factorial design. *The International Journal of Advanced Manufacturing Technology*, 1-13.
- Mohamed, O. A., Masood, S. H., & Bhowmik, J. L. (2015). Optimization of fused deposition modeling process parameters: a review of current research and future prospects. *Advances in manufacturing*, 3, 42-53.
- Moradi, M., Aminzadeh, A., Rahmatabadi, D., & Rasouli, S. A. (2021). Statistical and experimental analysis of process parameters of 3d nylon printed parts by fused deposition modeling: Response surface modeling and optimization. *Journal of Materials Engineering and Performance*, 30(7), 5441-5454.
- Ning, F., Cong, W., Qiu, J., Wei, J., Wang, S. (2015). Additive manufacturing of carbon fiber reinforced thermoplastic composites using fused deposition modeling. *Composites Part B: Engineering*, 80, 369-378.
- Panda, S. K., Padhee, S., Anoop Kumar, S. O. O. D., & Mahapatra, S. S. (2009). Optimization of fused deposition modelling (FDM) process parameters using bacterial foraging technique. *Intelligent information management*, 1(02), 89.
- Patil, P., Singh, D., Raykar, S. J., & Bhamu, J. (2021). Multi-objective optimization of process parameters of Fused Deposition Modeling (FDM) for printing Polylactic Acid (PLA) polymer components. *Materials Today: Proceedings*, 45, 4880-4885.
- Pramanik, D., Mandal, A., & Kuar, A. S. (2020). An experimental investigation on improvement of surface roughness of ABS on fused deposition modelling process. *Materials Today: Proceedings*, 26, 860-863.
- Rajpurohit, S. R., & Dave, H. K. (2019). Analysis of tensile strength of a fused filament fabricated PLA part using an open-source 3D printer. *The International Journal of Advanced Manufacturing Technology*, 101, 1525-1536.
- Raju, M., Gupta, M. K., Bhanot, N., & Sharma, V. S. (2019). A hybrid PSO–BFO evolutionary algorithm for optimization of fused deposition modelling process parameters. *Journal of Intelligent Manufacturing*, 30, 2743-2758.

- Rankouhi, B., Javadpour, S., Delfanian, F., Letcher, T. (2016). Failure analysis and mechanical characterization of 3D printed ABS with respect to layer thickness and orientation. *Journal of Failure Analysis and Prevention*, 16, 467-481.
- Rashed, K., Kafi, A., Simons, R., & Bateman, S. (2022). Fused filament fabrication of nylon 6/66 copolymer: Parametric study comparing full factorial and Taguchi design of experiments. *Rapid Prototyping Journal*, 28(6), 1111-1128.
- Ravikumar, P., Desai, C., Kushwah, S., and Mangrola, M.H. (2022). A review article on FDM process parameters in 3D printing for composite materials. *Materials Today: Proceedings*, 60(19), 2162-2166.
- Rudenko, A. (2014). 3D Castle Completed. <http://totalkustom.com/3d-castle-completed.html>
- Saad, M. S., Mohd Nor, A., Zakaria, M. Z., Baharudin, M. E., & Yusoff, W. S. (2021). Modelling and evolutionary computation optimization on FDM process for flexural strength using integrated approach RSM and PSO. *Progress in Additive Manufacturing*, 6, 143-154.
- Schmitt, B. M., Zirbes, C. F., Bonin, C., Lohmann, D., Lencina, D. C., & Netto, A. da C. S. (2018). A Comparative Study of Cartesian and Delta 3D Printers on Producing PLA Parts. *Materials Research*, 20(suppl 2), 883-886. <https://doi.org/10.1590/1980-5373-mr-2016-1039>
- Shirmohammadi, M., Goushchi, S. J., & Keshtiban, P. M. (2021). Optimization of 3D printing process parameters to minimize surface roughness with hybrid artificial neural network model and particle swarm algorithm. *Progress in Additive Manufacturing*, 6, 199-215.
- Singh, R., & Davim, J. P. (Eds.). (2018). *Additive manufacturing: applications and innovations*. CRC Press.
- Slonov, A. L., Khashirov, A. A., Zhansitov, A. A., Rzhetskaya, E. V., & Khashirova, S. Y. (2018). The influence of the 3D-printing technology on the physical and mechanical properties of polyphenylene sulfone. *Rapid Prototyping Journal*, 24(7), 1124-1130.
- Son, T. A., Minh, P. S., & Do Thanh, T. (2020). Effect of 3D printing parameters on the tensile strength of products. In *Key Engineering Materials* (Vol. 863, pp. 103-108). Trans Tech Publications Ltd.
- Sood, A. K., Ohdar, R. K., & Mahapatra, S. S. (2010). Parametric appraisal of mechanical property of fused deposition modelling processed parts. *Materials & Design*, 31(1), 287-295.
- Srivastava, M., Rathee, S., Maheshwari, S., & Kundra, T. K. (2018). Multi-objective optimisation of fused deposition modelling process parameters

- using RSM and fuzzy logic for build time and support material. *International Journal of Rapid Manufacturing*, 7(1), 25-42.
- Sürmen, H. K. (2019). Eklemeli İmalat (3b Baskı): Teknolojiler ve uygulamalar. *Uludağ Üniversitesi Mühendislik Fakültesi Dergisi*, 24(2), 373-392.
- Şahin, K., & Turan, B. O. (2018). Üç boyutlu yazıcı teknolojilerinin karşılaştırmalı analizi. *Stratejik ve Sosyal Araştırmalar Dergisi*, 2(2), 97-116.
- Tayyab, M., Ahmad, S., Akhtar, M. J., Sathikh, P. M., & Singari, R. M. (2023). Prediction of mechanical properties for acrylonitrile-butadiene-styrene parts manufactured by fused deposition modelling using artificial neural network and genetic algorithm. *International Journal of Computer Integrated Manufacturing*, 36(9), 1295-1312.
- Tofail, S. A., Koumoulos, E. P., Bandyopadhyay, A., Bose, S., O'Donoghue, L., & Charitidis, C. (2018). Additive manufacturing: scientific and technological challenges, market uptake and opportunities. *Materials today*, 21(1), 22-37.
- Torres, J., Cotelo, J., Karl, J., & Gordon, A. P. (2015). Mechanical property optimization of FDM PLA in shear with multiple objectives. *Jom*, 67, 1183-1193.
- Ulu, E., Korkmaz, E., Yay, K., Burak Ozdoganlar, O., & Burak Kara, L. (2015). Enhancing the structural performance of additively manufactured objects through build orientation optimization. *Journal of Mechanical Design*, 137(11), 111410.
- Upcraft, S., and Fletcher, R. (2003). The rapid prototyping technologies. *Assembly Automation*, 23(4), 318-330.
- Vakharia, V. S., Singh, M., Salem, A., Halbig, M. C., Salem, J. A. (2022). Effect of Reinforcements and 3-D Printing Parameters on the Microstructure and Mechanical Properties of Acrylonitrile Butadiene Styrene (ABS) Polymer Composites. *Polymers*, 14(10), 2105.
- Vălean, C., Marşavina, L., Mărghitaş, M., Linul, E., Razavi, J., Berto, F. (2020). Effect of manufacturing parameters on tensile properties of FDM printed specimens. *Procedia Structural Integrity*, 26, 313-320.
- Wakimoto, T., Takamori, R., Eguchi, S., & Tanaka, H. (2018). Growable Robot with “Additive-Additive-Manufacturing”. *Extended Abstracts of the 2018 CHI Conference on Human Factors in Computing Systems - CHI '18*, 1-6.
- Wiese, M., Thiede, S., & Herrmann, C. (2020). Rapid manufacturing of automotive polymer series parts: A systematic review of processes, materials and challenges. *Additive Manufacturing*, 36, 101582.

- Wong, K. V., & Hernandez, A. (2012). A review of additive manufacturing. *International scholarly research notices*, 2012.
- Wu, B., Myant, C., & Weider, S. (2017). The value of additive manufacturing: future opportunities. *Imperial College London, Briefing Paper*, (2).
- Yadav, K., Rohilla, S., Ali, A., Yadav, M., & Chhabra, D. (2023). Effect of Speed, Acceleration, and Jerk on Surface Roughness of FDM-Fabricated Parts. *Journal of Materials Engineering and Performance*, 1-10.
- Yeşiloğlu, R., (2022). Eklemeli İmalat İle Üretilen Farklı Dolgu Geometrisi Ve Yoğunluğa Sahip Pla Esaslı Yapıların Mekanik Davranışlarının Deneysel Olarak Araştırılması. Yüksek Lisans Tezi, Karabük Üniversitesi Lisansüstü Eğitim Enstitüsü, Karabük.
- Yusuf, B. (2018). 3D printers explained: delta, cartesian, polar, scara. *All 3DP*. <https://all3dp.com/know-your-fdm-3d-printers-cartesian-delta-polar-and-scara>. Accessed, 31.
- Zhang, Y., and Chou, K. (2008). A parametric study of part distortions in fused deposition modelling using three-dimensional finite element analysis. *Proceedings of the Institution of Mechanical Engineers, Part B: Journal of Engineering Manufacture*, 222(8), 959–968.

Chapter 26

Analyzing and Fixing the Grasshopper Optimization Algorithm

Okkes Tolga Altinoz^{1*}

Abstract – Single objective optimization algorithms (SOOA) are designed to solve real-world applications with the single objective (SOOPs). As a method to solve these problems Grasshopper optimization algorithm (GOA) is proposed by modeling to mimic the behavior of the grasshopper swarms. The main disadvantage of the GOA is the tendency to fall on the local optimum. At the same time the stochastic methods which rely on the random operators help to avoid the local optimum problem. For this reason, the behavior of the GOA has constructed again to get a better performance. The improvement on the algorithm demonstrated on both mathematical analysis and the empirical study on the benchmark problems. The results proves that the proposed change in the GOA produce superior values on all benchmark problems.

Keywords – optimization, grasshopper optimization algorithm, numerical calculation

I. INTRODUCTION

In general, the optimization is defined as finding a set of solutions for a particular problem to minimize or maximize an objective function. Even it has a single objective, SOOA still remains importance because of these algorithms is the basis of the most advanced algorithms for multi and many objective optimization problems. For this reason, even currently new SOOA have been developing and improving to get a better result in a short time. The great teacher, nature helps the developers to construct new nature inspired optimization algorithm. Among them GOA is proposed by mimic the behavior of the Grasshopper swarms. At the next subsection the improved GOA have proposed in the literature explained.

A. Literature Review

In the study by Liu et al. [3], the improved inertia weight (to enhance local search ability, the search ability of the GAO coverage around the target as the

¹ Department of Electrical and Electronics Engineering, Ankara University, Turkey
^{*}(taltinoz@ankara.edu.tr) Email of the corresponding author

iteration increases) is introduced to the GOA algorithm for the efficiency of the power system.

Another power optimization problem (optimal power flow (OPF) problem) is considered with GAO in [4] to enhance the exploration and exploitation property of GOA. For this reason to balance exploration and exploitation; two different update rule is replaced in GAO at the initial and at the final steps of the searching process. An adaptive coefficient is defined for this reason (like in harmony search algorithm), the exploration enhancement is replaced with a more random generator update rule and exploitation enhancement is replaced with a more tendency to the global best member.

In [5] the problem of reaching the comfort zone more quickly a slightly modified update rule with a multiplication of a variable is proposed and applied to the feature selection problem.

In [6] the aim is to improve the exploitation capability of GAO with two improvements PCA and inertia weight. As the first improvement, Principal component analysis strategy is applied on minimally correlated variables to improve the exploitation capability of the GOA. The second improvement is the inertia weight to balance exploration and exploitation property of GAO with respect to the average value of the fitness functions of the population.

In the research by Feng et al. [7] three additional mechanisms are added to GAO which are a nonlinear convergence parameter, niche mechanism, and the β -hill climbing techniques. The first mechanism is the nonlinear definition of the control (convergence) parameter where the larger the convergence parameter means the larger step size that effects the exploration property of the GAO (in GAO it is decreases linearly; cannot be balanced that is one of the drawbacks of GAO). In [7] the \tanh function is added as nonlinear convergence parameter as the new function for social interaction between grasshoppers. The second mechanism is the niche mechanism to maintain the diversity of the swarm such that a niche repulsing function is defined to maintain the diversity of the swarm while preserving local optimum. As the third mechanism, β -hill climbing technique is applied as the position update rule.

In [8], random walk (randomly selected grasshopper moves towards another randomly selected grasshopper with a random step size) with a new convergence parameter is applied as improvement of GAO to avoid premature convergence. In [9], the algorithm named fractional grasshopper optimization algorithm (Fractional-GOA) which is defined with the integration of the fractional calculus with GAO. By using the fractional theory, fractional term is added to the position update rule of the GAO.

Zhao et al. in [10] used a evolutionary-like (with a probabilistic mutation mechanism -Cauchy mutation [20] and the diversity of genetic mutation- similarly in the crossover operator -N-point Crossover- integrated on GOA in [12], or more cost efficient version is reported in [19] and [23] considering only crossover operator) GAO improved algorithm which is named as MOLGOA is proposed. Additional to mutation operator orthogonal learning mechanism is defined to improve the convergence speed.

In [11], the enhanced version of GOA is proposed with the aid of new movement update rule so that more randomize position update is changed with the difference between position (position of the randomly selected members) and the best member's position.

In literature related to the optimization algorithms from many similar papers, it is clearly empirically showed that chaotic maps improve the performance of the algorithm and in [13] chaotic tent map is added to GOA (Chaotic Singer is added similarly presented in [21]) that desired to balance between exploration and exploitation property of GOA. Another example is presented in [14] and [24] where a chaotic adaptive arc function integrated as attraction function which isn't a complex computation without expensive modification.

In [15], like other algorithms, to improve the exploration and exploitation properties and their balance, the spiral search method (that is proposed by Mirjalili to mimic population of moths' specific navigation patterns [16] -moving of a moth around a flame-) is added to GOA. This search method is replaced/improved with attraction function.

Gao et al. in [18] improves GOA and hybridize with simulated annealing algorithm and compared them as a part of the study. As a part of the improvement two control parameters f and l are linearly decreasing as a part of the algorithm. The idea is simple to reduce the attraction radius with respect to the iteration. As the iteration increases the smaller area is investigated. For this reason, the attraction which is based on the distance is reduces with respect to the iteration.

In [22], the parameter c is adaptive change with respect to a defined new function. The idea is to present a summation of logarithmic and exponential functions with additional control parameters to get rid of limited development behaviour and slow convergence rate. references.

B. Motivation of the Study

After the discussion of the papers given above, in general, GAO looks promising for single objective problems with the local optimum problem. For this reason, new variants of the GAO are proposed and compared. However, the

algorithm looks not completed and needs to be corrected by analysing GAO. For this reason, two additional improvements are proposed to be finished the GAO design.

The literature review and the motivation of the study is proposed in the first section. Section 2 gives the grasshopper optimization algorithm. Section 3 contains the application and results of the study. Finally in the last section concludes the research.

II. GRASSHOPPER OPTIMIZATION ALGORITHM (GAO)

The Grasshopper Optimization Algorithm (GAO) was proposed by Saremi et al. in [1] in 2017 (and in 2020 [2]). The proposed algorithm is relatively recent optimization method which is a swarm intelligence algorithm that mimics grasshoppers' behaviours. Similar to population-based nature inspired optimization algorithm the position of the individual in the population updates at each iteration. The update rule is given as follows.

$$x_i = c \left(\sum_{j=1}^N s(|x_j - x_i|) \times c \times \frac{u_b - l_b}{2} \times \frac{x_j - x_i}{d_{ij}} \right) + T_d \quad (1)$$

The s function (named as attraction function) that represents the social interaction forces on a member that is calculated as.

$$s(r) = f e^{-\frac{r}{l}} - e^{-r} \quad (2)$$

where f (indicates the intensity of attraction) and l (attractive length scale) are control parameters of the function and r is the distance between the i th and the j^{th} grasshopper ($r = d_{ij}$). When the plot of this s function with respect to the variable r , there is a function with a single maximum. The value 0 of s function is the comfort zone. The distance at this comfort zone is calculated as 2.079 for $f = 0.5$ and $l = 1.5$. There are two social movements inside the distance $[0; 10]$ which are attraction and repulsion movements. The attraction is the value from negative to zero at the s plot. After 0 the repulsion goes to the maximum value of this function. The maximum value is calculated as

$$\frac{ds(r)}{dr} = 0 = -\frac{fr}{l} e^{-\frac{r}{l}} + r e^{-r} \quad (3)$$

$$\frac{f}{l} e^{-\frac{r}{l}} = e^{-r} \quad (4)$$

$$\frac{r}{l} - r = \ln\left(\frac{f}{l}\right) \quad (5)$$

$$r = \ln\left(\frac{f}{l}\right) \left(\frac{l}{1-l}\right) \quad (6)$$

where if $f = 0.5$ and $l = 1.5$ than $\ln\left(\frac{0.5}{1.5}\right) \left(\frac{1.5}{-0.5}\right) = 3.2958$ (and the maximum value of the s function for this value is 18.5185×10^{-3}) which is the maximum point of the attraction function.

III. IMPLEMENTATION OF GRASSHOPPER OPTIMIZATION ALGORITHM (GAO)

The implementation of GOA can be found in [17] by the one of the designers of the GOA S. Mirjalili. The implementation given in [17] has a difference with the published paper GOA [1] that is the definition of the distance between two grasshoppers. In this implementation the distance is reduced to the [2; 4) based on the even or odd distance value. However, the definition of the distance on the paper differs from the implementation. In addition, when the research related to the improvement of the GOA is investigated, the improvement on the s function is common. That has an influence on the distance calculation. For this reason, the evaluation of the distance between grasshoppers differs at different improvements of the GOA. For this reason, the original definition of the GOA algorithm is investigated empirically on benchmark problems by changing the consideration of the distance. The first version is the version of the implementation of GOA in [17], which is abbreviated as GOA24 (since the distance is reduced to [2; 4) with respect to the even or odd value of the distance between grasshoppers). Therefore, in GOA24 the s function takes values in $[-3.5367 \times 10^{-3}; 16.426 \times 10^{-3}]$ for all possible distance. Since nature inspired optimization algorithms presents stochastic behaviour because of random number generator is the algorithm. For this reason, it is possible not to calculate Eq. 2 and the distance $|x_i - x_j|$ but to assign random number generator instead of these two functions. By this way it is possible to decrease the computational complexity of the algorithm and it is named as GOA24-R where instead of s function a uniform random number generator (approximately $s_R = [-3.5 \times 10^{-3}; 16.5 \times 10^{-3}]$) is added to the code. This new function is rearranged by this cost-effective formulation as given in Eq. 7 and in Eq. 8.

$$x_i = c \left(\sum_{j=1}^N s_R \times c \times \frac{u_b - l_b}{2} \times \frac{x_j - x_i}{d_{ij}} \right) + T_d \quad (7)$$

$$x_i = c \left(\sum_{j=1}^N k \times \frac{x_j - x_i}{d_{ij}} \right) + T_d \quad (8)$$

where the stochastic variable $k = s_R \times c \times \frac{u_b - l_b}{2}$. The meaning of the variable given here is to keep the corresponding grasshopper in the group.

Table 1. Performance comparison of the GOA variants on CEC2022 Benchmark Problems

Problem	GOA-RC	GOA-R	GOA
F1	508.7745 (550.9546) +	1.3445e+3 (2.3031e+3) +	6.6351e+3 (5.41e+3)
F2	406.8523 (4.2086) +	414.6378 (19.5847) +	447.8782 (40.7693)
F3	600.7415 (1.1195) +	601.7681 (1.7946) +	612.1355 (4.9724)
F4	817.3590 (12.6762) +	811.9582 (9.3947) +	822.6315 (8.3778)
F5	935.9315 (139.1619) +	958.5463 (138.5538) -	943.2280 (74.2203)
F6	4.3708e+3 (2.0932e+3) +	5.0578e+3 (2.2919e+3) +	6.6856e+3 (1.4764e+3)
F7	2.0386e+3 (37.8797) +	2.0507e+3 (33.7408) ≈	2.0574e+3 (30.8546)
F8	2.2382e+3 (30.1682) +	2.2304e+3 (18.2944) +	2.2644e+3 (55.2254)
F9	2.5555e+3 (45.9037) +	2.5755e+3 (63.3085) +	2.6468e+3 (68.5349)
F10	2.5303e+3 (51.6926) ≈	2.5383e+3 (56.1257) ≈	2.5461e+3 (59.0064)
F11	2.6467e+3 (124.5946) +	2.7080e+3 (184.0545) +	2.8321e+3 (111.3625)
F12	2.8631e+3 (1.9747) ≈	2.8636e+03 (2.2524) ≈	2.8663e+3 (2.4700)
+/- / ≈	10/0/2	8/1/3	

In other words, it shows how much it stays in the group according to the normalized unit distance between two grasshoppers. At the beginning, the group of locusts is spread over a wider area, but thanks to the variable c , it continues to move in a narrower and narrower area. However, if we recall the Pythagorean triangle rule, the lengths in each dimension must be multiplied by 0.707 (This means that $l = \sqrt{2}$ for the hypotenuse to be one in an isosceles triangle in a two-dimensional space. Providing the unit length between locusts and the sum of the changes of each locust in each dimension to change the new position of the locust is the basis of GOA. Therefore, GOA-RC is proposed by adding this multiplier to GOA (Eq. 9).

$$x_i = c \left(\sum_{j=1}^N s_R \times c \times \frac{u_b - l_b}{2\sqrt{2}} \times \frac{x_j - x_i}{d_{ij}} \right) + T_d \quad (9)$$

$$x_i = c \left(\sum_{j=1}^N k' \times \frac{x_j - x_i}{d_{ij}} \right) + T_d \quad (10)$$

$$k = s_R \times c \times \frac{u_b - l_b}{2\sqrt{2}} \quad (11)$$

These two improvements on the GOA will be compared under the same conditions. The improvement on GOA do not needs additional heavy calculations (contrary, it is simplified). For this reason, the execution time will not be discussed in the research.

IV. COMPARISON OF THE IMPROVED GOAS

GOA and two improvements (GOA-R and GOA-RC) which are proposed in this research will be compared on the benchmark problems that are proposed in [25]. The CE2022 benchmark problem set has the random nature that divides variables randomly into subcomponents. Three set of problems are generated in CEC2022 benchmark problems. These are unimodal function (f_1) basic problems (f_2 - f_5), hybrid functions (f_6 - f_8) and composition functions (f_9 - f_{12}). The search range is [-100,100] for all variables.

The implementations are repeated 15 times independently. The mean and standard deviation of the objective values are recorded. In addition, the statistical similarity test rank um test is implemented to demonstrate the similarity of the runs by comparing them with GOA.

Comparison results are given in Table 1. In general, speaking the proposed improvements, especially GOA-RC algorithm produce superior values against GOA. The unimodal benchmark problem f_1 is the simplest problem among these 12 benchmark problems. The optimum value is 300 and unfortunately none of the algorithms can detect this objective value.

Basic Problems:(f_2 - f_5) (Obj=[400,600,800,900]) GOA is reached the approximate optimum for the f_3 problem. Even for the other problems the algorithm converges to the optimum, GOA-R gives better for f_4 problem.

Hybrid Function:(f_6 - f_8)(Obj=[1800,2000,2200]) The improvements is better than the GOA algorithm. Only for f_8 the GOA-R gives better objective values.

Composition Function: (f_9 - f_{12}) (Obj=[2300, 2400, 2600, 2700]) Still the algorithms falls behind the optimum values. The problems f_{10} and f_{12} has almost same values. The improvements could not produce a better distribution for independent runs.

V. CONCLUSION

The GOA has published recently, and it is based on the swarm behaviour of the Grasshoppers on the nature. This behaviour is modelled by mathematical formulation. However, these formulations need simple modification to increase the stochastic behaviour of the algorithm also simplified the calculations. For this reason, two additional improvements are proposed for GOA. These improvements are showed mathematically and empirically. Both analysis showed that the proposed improvements is better than the GOA under benchmark problems. However, the performance of the GOA and improved GOA algorithms still could not find the optimum values of the benchmark problems. For this reason, a new algorithm or a deeply modification on the dynamics of the GOA is needed to be changed or added.

REFERENCES

- S. Saremi, S. Mirjalili, and A. Lewis, "Grasshopper optimisation algorithm: Theory and application," *Advances in Engineering Software*, vol. 105, pp. 30–47, 2017. doi:10.1016/j.advengsoft.2017.01.004
- M. Salami, F. M. Sobhani, and M. S. Ghazizadeh, "A hybrid shortterm load forecasting model developed by factor and feature selection algorithms using improved grasshopper optimization algorithm and principal component analysis," *Electr. Eng.*, vol. 102, no. 1, pp. 437–460, Mar. 2020
- J. Liu, A. Wang, Y. Qu, and W. Wang, "Coordinated operation of multiintegrated energy system based on linear weighted sum and grasshopper optimization algorithm," *IEEE Access*, vol. 6, pp. 42186–42195, 2018.
- M. A. Taher, S. Kamel, F. Jurado, and M. Ebeed, "Modified grasshopper optimization framework for optimal power flow solution," *Electr. Eng.*, vol. 101, no. 1, pp. 121–148, Apr. 2019.
- A. Zakeri and A. Hokmabadi, "Efficient feature selection method using real-valued grasshopper optimization algorithm," *Expert Syst. Appl.*, vol. 119, pp. 61–72, Apr. 2019
- X. Yue and H. Zhang, "Grasshopper optimization algorithm with principal component analysis for global optimization," *J. Supercomput.*, vol. 76, pp. 5609–5635, Jul. 2019
- H. Feng, H. Ni, R. Zhao, and X. Zhu, "An enhanced grasshopper optimization algorithm to the bin packing problem," *J. Control Sci. Eng.*, vol. 2020, pp. 1–19, Mar. 2020
- P. Mishra, V. Goyal, and A. Shukla, "An improved grasshopper optimization algorithm for solving numerical optimization problems," in *Advances in Intelligent Computing and Communication (Lecture Notes in Networks and Systems)*, vol. 109, 2020.
- A. Tanwar, A. K. Sharma, and R. V. S. Pandey, "Fractional-grasshopper optimization algorithm for the sensor activation control in wireless sensor networks," *Wireless Pers. Commun.*, vol. 1, pp. 1–24, Mar. 2020
- H. Zhou, Z. Ding, H. Peng, Z. Tang, G. Liang, H. Chen, C. Ma, and M. Wang, "An improved grasshopper optimizer for global tasks," *Complexity*, vol. 2020, Sep. 2020, Art. no. 4873501
- S.A.A. Ghaleb, M. Mohamad, S. A. Fadzli and W. A. H. M. Ghanem, "Training Neural Networks by Enhance Grasshopper Optimization Algorithm for Spam Detection System," in *IEEE Access*, vol. 9, pp. 116768-116813, 2021, doi: 10.1109/ACCESS.2021.3105914.

- A.A. Ewees, M. A. Gaheen, Z. M. Yaseen and R. M. Ghoniem, "Grasshopper Optimization Algorithm With Crossover Operators for Feature Selection and Solving Engineering Problems," in *IEEE Access*, vol. 10, pp. 23304-23320, 2022,
doi: 10.1109/ACCESS.2022.3153038.
- R. Raja and B. Ashok, "Chaotic Grasshopper Optimization with Wavelet Kernel Extreme Learning Machine for Medical Data Classification," 2021 5th International Conference on Computing Methodologies and Communication (ICCMC), Erode, India, 2021, pp. 958-962, doi: 10.1109/ICCMC51019.2021.9418047.
- G. Wang, A. A. Heidari, M. Wang, F. Kuang, W. Zhu and H. Chen, "Chaotic Arc Adaptive Grasshopper Optimization," in *IEEE Access*, vol. 9, pp. 17672-17706, 2021, doi: 10.1109/ACCESS.2021.3052800.
- Z. Xu et al., "Spiral Motion Mode Embedded Grasshopper Optimization Algorithm: Design and Analysis," in *IEEE Access*, vol. 9, pp. 71104-71132, 2021, doi: 10.1109/ACCESS.2021.3077616.
- S. Mirjalili, "Moth-flame optimization algorithm: A novel natureinspired heuristic paradigm," *Knowl.-Based Syst.*, vol. 89, pp. 228–249, Nov. 2015
- S. Mirjalili, "Grasshopper Optimisation Algorithm (GOA)," (<https://www.mathworks.com/matlabcentral/fileexchange/61421-grasshopper-optimisation-algorithm-go>), MATLAB Central File Exchange. Retrieved August 21, 2023.
- M. Gao, H. Xu, J. Su and L. Yan, "A Modified Grasshopper Optimization Algorithm," 2021 11th IEEE International Conference on Intelligent Data Acquisition and Advanced Computing Systems: Technology and Applications (IDAACS), Cracow, Poland, 2021, pp. 120-123, doi: 10.1109/IDAACS53288.2021.9660892.
- P. Bekana, A. Sarangi and S. K. Sarangi, "Analysis of Crossover Techniques in Modification of Grasshopper Optimization Algorithm," 2021 International Conference in Advances in Power, Signal, and Information Technology (APSIT), Bhubaneswar, India, 2021, pp. 1-5,
doi: 10.1109/APSIT52773.2021.9641242.
- C. N. Ravi, T. S. Karthik, K. Manikandan, P. Kalaivaani, P. N. Chopkar and A. Srivastava, "Cauchy Grasshopper Optimization Algorithm with Deep Learning Model for Cloud Enabled Cyber Threat Detection System," 2023 7th International Conference on Intelligent Computing and Control Systems (ICICCS), Madurai, India, 2023, pp. 202-208, doi: 10.1109/ICICCS56967.2023.10142752.

- M. A. Niloy, F. H. Reevu, A. Yeaser, R. I. Shupty and A. S. Pramanik, "Chaotic Singer Grasshopper Optimization Algorithm for solving Combined Economic and Emission Dispatch," 2021 5th International Conference on Electrical Engineering and Information Communication Technology (ICEEICT), Dhaka, Bangladesh, 2021, pp. 1-6, doi: 10.1109/ICEEICT53905.2021.9667800.
- W. Wang, R. Zhang, Y. Li, G. Lv, Z. Luo and H. Xu, "Fault Diagnosis for Power Transformer Based on Uniform Distribution of Grasshopper Optimization Algorithm Combined with Neural Network," 2022 International Conference on Power Energy Systems and Applications (ICoPESA), Singapore, Singapore, 2022, pp. 225-230, doi: 10.1109/ICoPESA54515.2022.9754384.
- B. Pattanaik and M. Alagirisamy, "Hybrid Energy Dual Storage Systems for EV Powertrain with Enhanced Algorithm GOA and GA," 2022 6th International Conference on Computing Methodologies and Communication (ICCMC), Erode, India, 2022, pp. 675-681, doi: 10.1109/ICCMC53470.2022.9754001.
- A. Nurhayati, J. F. Rusdi, Saepudin, H. Gusdevi, N. Agustina and W. L. Jaelani, "Performance Comparison of Evolutionary Biogeography Based Whale Optimizations with Chaotic Arc Adaptive Grasshopper Optimization Algorithms," 2021 3rd International Conference on Cybernetics and Intelligent System (ICORIS), Makasar, Indonesia, 2021, pp. 1-6, doi: 10.1109/ICORIS52787.2021.9649446.
- A. Kumar, K. V. Price, A. Wagdy Mohamed, A. A. Hadi, P. N. Suganthan, "Problem Definitions and Evaluation Criteria for the 2022 Special Session and Competition on Single Objective Bound Constrained Numerical Optimization," Technical Report, Nanyang Technological University, Singapore, 2021.

Chapter 27

Health Problem Pre-Application System Recommendation for International Transportation Personnel and Passengers and Evaluation of The Proposed System

Orhan GÖNEL¹
Bengisu OLGUN BEKMAN²

1. INTRODUCTION

Workers of the international transportation sector, passengers and other personnel in these vehicles may need to receive health care in their own country or in foreign countries. Many problems were identified (Gonel, 2023) and possible problems were predicted with academic methods related to achievement of proper health care. A system and a program as the core of the system is proposed in order to eliminate these problems and bring the health service received to a better level. Also, specifications of this program have been identified.

Main aim of the system is to create a health problem statement in order to request proper health care. An international and uniform statement that is free from all possible failures will provide better understanding of the health problem of the patient. Better understanding of the problem will lead to directing the patient to the appropriate healthcare service. The system in question was developed for the benefit of personnel working in the international transportation sector, passengers and other people in these vehicles. It is often a problem for patients for to reach healthcare services during the voyages. But, since the system eliminates language problems, it can be used by a much wider audience such as tourists, immigrants and refugees. And due to the additional benefits of the system, it can be used even in cases where patients and healthcare personnel speak the same language.

The experienced and possible problems and the security barriers of the system proposed to be developed were compared with the Swedish Cheese Model (SCM). Results of the study revealed that barriers of the system prevent all failures.

¹ ITU Denizcilik Fakültesi, Öğretim Görevlisi Dr., gonelo@itu.edu.tr, 0000-0002-1298-6175

² Sağlık Bakanlığı Marmara Üniversitesi Pendik Eğitim Araştırma Hastanesi Aile Hekimliği Ana Bilim Dalı Resident, Dr., bengisu.berkarda@saglik.gov.tr, 0000-0002-4187-7031

1.1 Aim of the Study

A passenger, crew member or another person may get into a situation that requires them to receive health care during a voyage in a transportation vehicle. In a situation like this it is necessary to report to the authorities by the responsible personnel or travelers to ensure that health care is received. The thing to be done by the responsible personnel of these vehicles or other people is to report this situation to the necessary authorities and ensure that health care is received. If we consider that this incident took place on a ship,

- A report will be prepared
- The report will be sent to the relevant authorities
- The report will be evaluated
- Efforts will be made to arrange the most appropriate health service according to the conditions.

The most appropriate healthcare service will be arranged based on the assessment and circumstances (refer to Sections 3.1 and 3.2 for details). The aim of this study is to ensure that all patients' complaints are fully understood and that they reach the most appropriate healthcare service as soon as possible.

1.2 Determined Problems

This section includes the problems experienced by patients who may or may not speak the same language as the healthcare personnel or who try to receive healthcare services with an interpreter. The term 'problem' refers to 'failure' in SCM.

Table 1. Problems Encountered in Medical Translations (Gonel, 2023)

No	Determined Problem
1	Incomplete and/or inadequate translation carried out by interpreter
2	Incorrect translation carried out by interpreter
3	Translation errors occurred when the interpreter is not qualified to act as a professional medical interpreter
4	Translation errors caused by the use of digital translation platforms
5	Difficulty in accessing the internet or online translator (If online medical translator is to be used)
6	The patient being in a state that he cannot express himself (due to pain, suffering and similar reasons)
7	The patient being in an unconsciousness state
8	Inability of the patient and the health personnel to speak the same language

- 9 The patient's limited ability to speak the same language as the medical staff but inability in speaking about medical issues
 - 10 The patient that can verbally express himself may not able to read the patient forms written in a complicated medical format.
 - 11 Unavailability of failure to access previous health records of the patient
 - 12 Misunderstanding and or inability to understand the patient's previous health records due to language difference
-

Problems 1, 2 and 3 in Table 1 are the problems experienced during the translation of the patient's health problems to the healthcare personnel by a person who acts as an interpreter. In Articles 1 and 2, these are situations where a person who undertakes the task of interpreting and is not a professional translator (such as the patient's relative, another seafarer) conveys the patient's complaints incompletely, inadequately or incorrectly. Problem 3 is the translation of the patient's health complaints by a professional translator whose expertise is general translation but not medical translation. In this case, the interpreter may not be able to translate medical terms and complex sentences related to medicine. These problems have been observed to occur if a professional medical translator is not used, and it is possible that they may occur again in the future.

Problems Number 4 and 5 are problems that occurred as a result of translation of the patient's complaints over the internet. The difference is that problem 4 is about the use of internet-based general translation programs and problem 5 is about use of online medical translation services accessed over the internet. To access both types of services, it is necessary to have an internet connection, computer, tablet and similar equipment. For problem 5, additional equipment such as microphone, speaker and preferably a camera are is required. Translation services from digital translation platforms can be obtained from any point connected to the internet, but former studies Gonel (2023) showed that, a sentence used to explain a medical complaint was translated on 7 different websites and 5 different translations were encountered. It should be noted that online medical translation service is not always available and may have some additional difficulties.

Problems 6, 7, 8, 9 and 10 are the health problems experienced when the patient communicates one-on-one with the healthcare personnel without using an interpreter. It may be the case that the patient does not speak the same language and cannot communicate with the healthcare personnel (problem 8). Even though the patient and the healthcare personnel can speak the same language, the patient being in an unconscious state (problem 7) or inability to communicate due to extreme pain, suffering, shock and similar situations (problem 6) is also possible.

If the patient and healthcare personnel speak the same language at a limited level, some communication can be established, but problems may arise regarding the details (problems 9 and 10).

There are also problems regarding the submission and translation of records describing the patient's past health status and may have negative effects on the patient's treatment (problems 11 and 12).

1.3 Anticipated Problems

The patient cannot be expected to know the information that healthcare personnel need in order to make an accurate preliminary assessment. The information that the patient provides and thinks is important to explain his or her health problem may cause the healthcare personnel to fail to make the correct preliminary assessment (Table 2).

Table 2. Possible Problems to be Encountered in Medical Translations

No	Anticipated Problem
13	Failure to declare required health information when creating a statement/report regarding a health problem

2. METHOD

In this study, it is aimed to ensure all problems are to be avoided. The method used in this study is based on the SCM however, it differs from standard SCM.

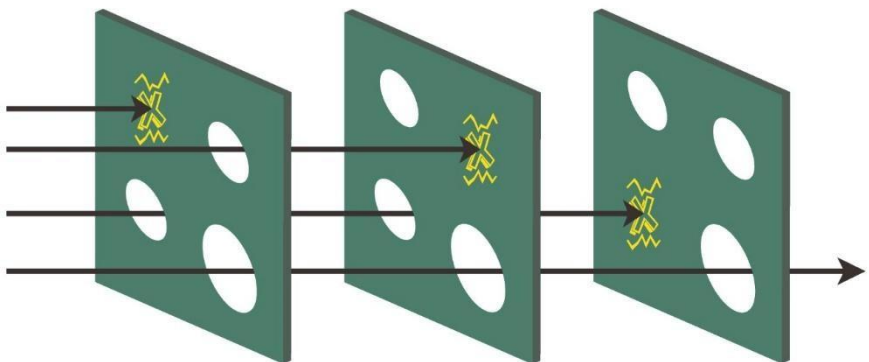


Figure 1. A Basic Illustration of the Swiss Cheese Model

The SCM was first introduced by James Reason in 1990 (Shappell & Wiegmann, 2001). Basically, it is used to reduce or stop all accidents, hazards and any sort of harm. On one side there are hazards/hazard vectors and on one

side there are defense layers. Defense layers may not stop all hazards on their own. But when all defense layers are aligned, hazards can be prevented. The method is generally viewed as being related to accident prevention and modeling. But it is also used to assess risks (Pumar et al., 2023). A basic and standard illustration of the method is shown in Figure 1.

Illustration in Figure 1 is a very generic example of SCM and often used to visually explain SCM. To be more specific and distinguish occurrence and prevention of the failure, Figure 2 and Figure 3 are used. In Figure 2, slices as barriers failed to prevent a failure from happening. However, in Figure 3, although failure managed to overcome several barriers, it was prevented from occurring by another barrier.



Figure 2. A Failure Occurred

Over time, the method has been developed by researchers and different versions and applications have been created. 'Hot cheese: a processed Swiss cheese model' by Li and Thimbleby (2014) is an example for this version. Model may be both applied as Swiss Cheese (Puthillath, et al., 2021) and Reverse Swiss Cheese (Kirwan, et al., 2022) in different aspects. Since the Swiss Cheese model is explained in detail in many academic studies (Wiegmann et al, 2021; Feinstein et al, 2022) no additional explanation related to origins of the model is included in this study. But key components of the system are explained in the following subsections.

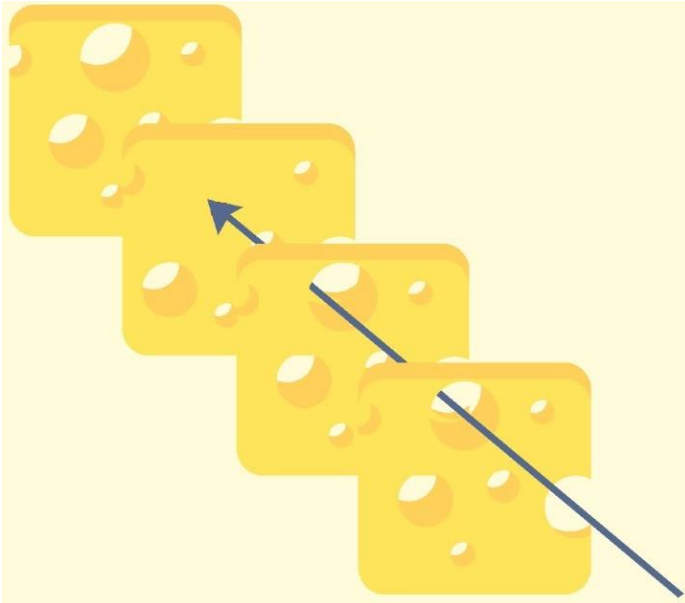


Figure 3. A Failure Prevented

2.1 Eyes and Slices

Any system has defense mechanisms to prevent problems. Generally, the defense mechanism consists of small parts, and these parts also have flaws. The parts of this defense mechanism are identified as ‘slices’ of Swiss cheese, and the defects in the defense mechanism parts are identified as ‘eyes’.

2.2 Active and Latent Failures

In the Swiss cheese method, failures are divided into two as 'active' and 'latent'. Term ‘error’ is used instead of ‘failure’ in some studies. After a certain period of time the model was introduced, the term 'latent conditions' began to be used for a clear definition (Larouzee & Coze, 2020). Active failures are the acts that are leading to accidents in a more direct way. Latent failures on the other hand are more contributory and have less direct effect to accident. An example given by Li and Thimbleby (2014) is, ‘*administering the wrong drug is an active failure, but the latent condition might have been the confusingly similar names of two different drugs*’.

2.3 Some Examples of Swiss Cheese Methods in Academic Studies

Pumar et al. (2023) described slices as homeostatic defenses (age, sex, and hormonal balance and others) and failures as tumor-promoting mechanisms (insults) in their study. Suryoputro et al, (2015) had only one failure in their study

– ‘Train collision’ – and five layers as ‘Fallible decisions’, ‘Line management deficiencies’, ‘Psychological precursors of unsafe acts’, ‘Unsafe acts’ and ‘Inadequate defenses’. As seen in examples, a number of failures and layer may change in different studies and there is no standard in the Swiss Cheese Model.

A very important issue that emerged from the examination of the studies using SCM is that the failures were not divided into 'active' and 'latent' in all studies.

2.3 Method Applied in This Study

In this study, it is aimed to prevent possible failures from occurring rather than analyzing an existing failure or accident. Additionally, barriers specifically created to prevent these failures were used instead of the barriers of an existing system. For these reasons Reverse Swiss Cheese model is applied in this study. Also, failures were not divided into 'active' and 'latent'.

The method was used in Section 4.4 to determine whether the proposed system solves the identified problems.

3. PROPOSED SYSTEM

In this section, the purpose, definition and features of the proposed system are mentioned in order to avoid the problems identified. The current system is also explained here.

3.1 Current System

The system proposed in this study was initially created to find solutions to the problems experienced by seafarers while receiving health care onboard and abroad. It was later modified and developed for use in other international transportation sectors due to the system's advantages. But the existing system is explained and examples are given through seafarers.

If a person needs to receive health care in a normal workplace, the patient reaches the place where he will receive health care either by his own means or by the means of health institutions, depending on the urgency of the health problem. In some cases, health service is brought to the patient. The patient is given the necessary health care or referred to the appropriate place if initial treatment means are not enough. Same system cannot be exercised onboard ships. When a patient requires to receive health care on ships the actions taken are,

- Receiving medical assistance or medical advice services through the Global Maritime Distress Safety System (IMO, 2000),
- For Turkish flagged and other flagged ships with Turkish crew, 'Tele Sağlık' service procurement (T.C. Sağlık Bakanlığı, 2023a),
- Transferring the patient to another sea craft or aircraft (MAIB, 2011),

- Receiving health care when the ship docks at the port (with medical personnel coming on board) (ATSB, 2016),

- Transferring the patient to a shore-based health facility. (MAIB, 2013).

Definitely for the first option and preferably for the second option, communication will be provided by the ship's GMDSS operators. The customary practice for the fifth option is that the patient is accompanied by an officer, preferably with relatively higher foreign language skills (Gonel, 2023). If the ship is under sail, health care is usually requested via a written message, preferably to the ship's agency, port authorities and other relevant parties. In most scenarios for receiving proper healthcare following two are involved;

- Interpreter (or a person transferring health issues),
- A written text.

Current system in a commercial ship is displayed in Figure 4. There are two important problems in the current system. First, when and where the patient will receive health care may not be determined based on sufficient medical data. In this case, it may be delayed for the patient to receive the necessary medical service, and large expenses may be incurred due to misdirection.

The second problem is that the patient may not be properly pre-triaged. Once the patient first reaches medical healthcare, he or she may be referred back to the appropriate healthcare facility. In this case, there will also be a serious loss of time.

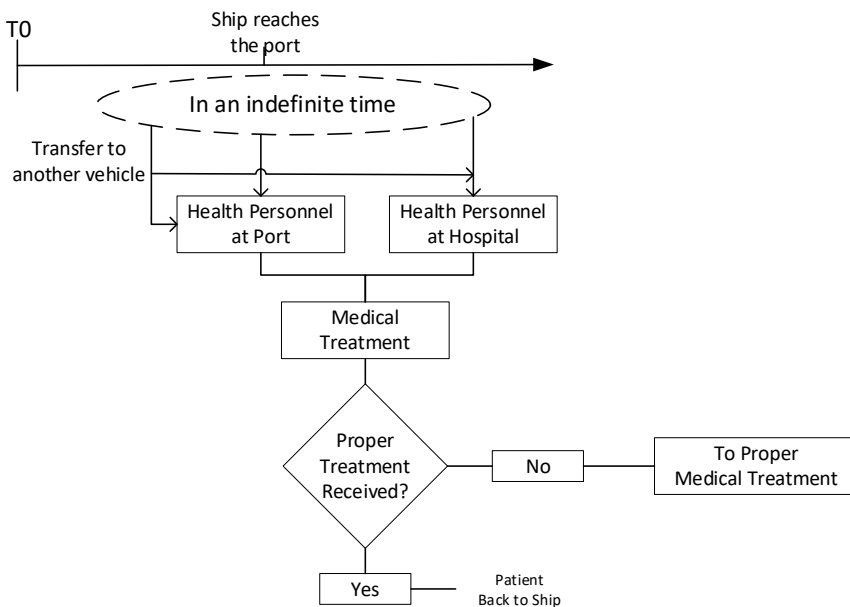


Figure 4. Current System in Commercial Ships

There are online based pre-triage sites already available on the internet. However, the programs used by these sites operate through simple algorithms. Based on the answers given, predetermined results are automatically generated. The patient's health declaration is not determined by medical personnel. Relevant services cannot evaluate a new variant of a known disease, an epidemic disease that has begun to appear in a certain region, or any current situation. In addition, these services work in a single language. A bigger potential problem here is that web browsers translate such pages across languages within their own interfaces. Since such translations are not made by medical translators, it is quite possible for translation errors to occur. 'NeyimVar?' provided by the T.C. Ministry of Health service is one of the best examples of such sites (T.C. Sağlık Bakanlığı, 2023b). The system has detailed visuals and a user-oriented interface. It currently provides services in three languages. It can be thought that there is a similarity between the 'NeyimVar?' and the system proposed in this study. However, 'NeyimVar?' serves for the purpose of guiding the patient, and the system that is the subject of this study is for present the patient's complaints to the healthcare personnel in the most appropriate and accurate way.

There is another version of an online based pre-triage site. These sites provide 'Online Consultant Service' but requires payment. Some of such service providers even provide online consultation by medical personnel. Translation is not included in the service provided in any of the systems examined³. A similar service is provided by family medicine physicians in Turkey. Patients can have examinations via video call from their family medicine physicians. In addition, the 'International Patient Support Unit Translation and Call Center' of Health Ministry of Turkey provides health consultancy services in six languages over the phone 24/7 (T.C. Sağlık Bakanlığı, 2019). These services also are not an alternative to the system that is the subject of this study.

3.2 Purpose of the Proposed System

The purpose of the proposed system is to replace the 'written text' described in the previous section (Section 3.1). Proposed system will create a universal health form that will act only as a pre-triage application. Notification will reach the healthcare personnel more quickly and conveniently. In this way, the most appropriate treatment method and place for the patient will be determined and the patient can be directed to the most appropriate health service. The proposed

³ Some of the services mentioned above are provided by commercial service providers. Publishing permission was not requested from any of such sites that were randomly identified through an internet search. To avoid copyright and similar problems, these sites are not referenced.

system will prevent all errors mentioned in Section 1.2, especially translation errors. It will also ensure that the patient receives health care without an interpreter.

3.3 Area of Use of the Proposed System

The main envisaged areas of use of the proposed system are:

- Personnel working on ships, aircraft, trains and similar transportation sector vehicles
- Passengers and all other persons in these vehicles
- Workers working in foreign countries
- Tourists
- Immigrants, refugees, asylum seekers and those in similar situations
- All patients who need to receive healthcare services - regardless of the language.

Although the system was initially developed for use in places with language differences, it can be used wherever healthcare services will be received. It will direct patients to the right healthcare service and save time and labor. It will eliminate the difficulties experienced when a translator is needed.

3.4 Boundaries of the Proposed System

The proposed system was developed only as a pre-triage application form. This form is intended to be used only for pre-triage and direct the patient to the appropriate healthcare service. This form can neither replace a doctor's examination nor triage service.

3.5 Working Principle of the Proposed System

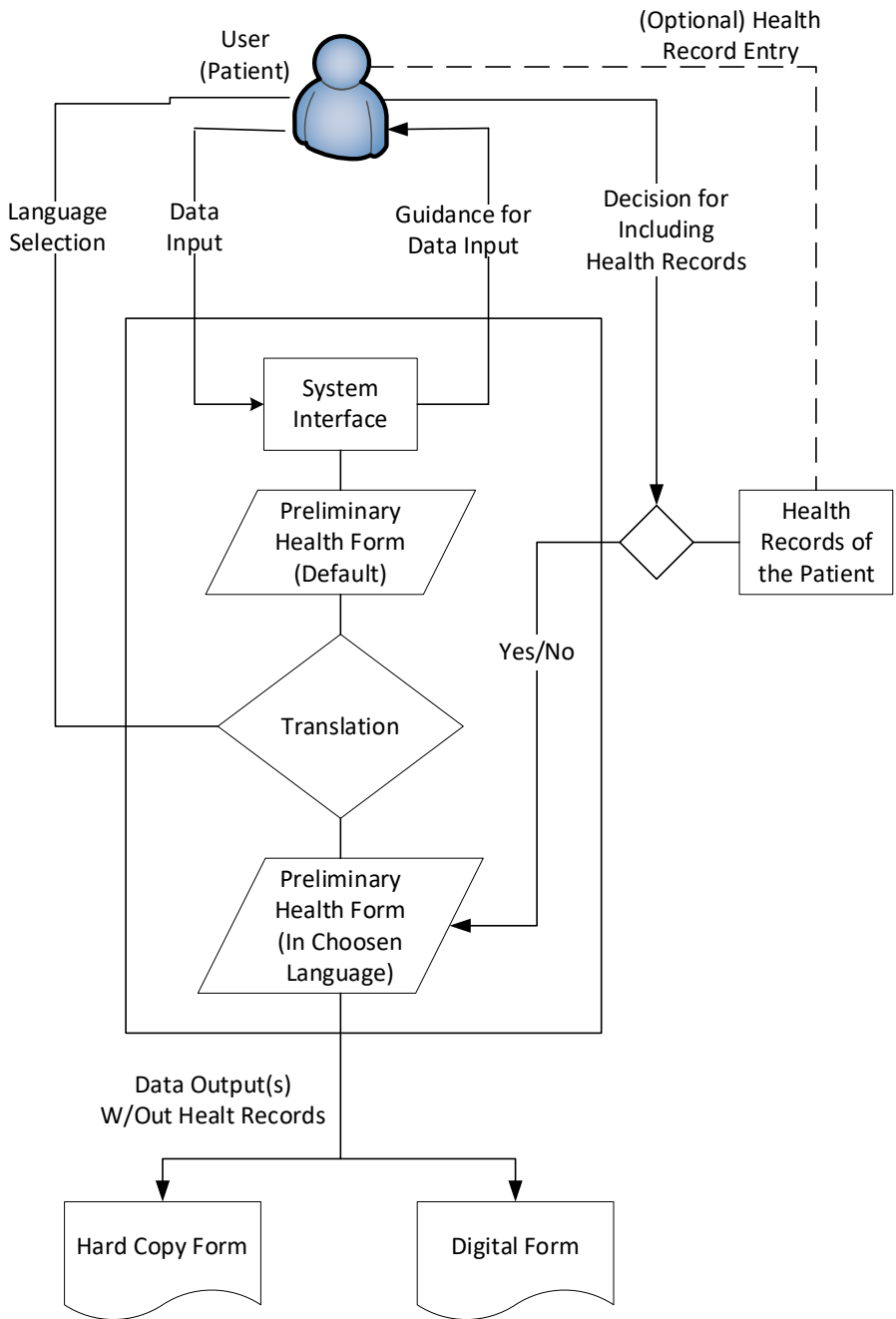


Figure 5. Working Principle of the System

The working principle of the system is explained in detail in Figure 5. The user (patient) logs into the program via a computer, tablet or similar device. A

complaint record begins to be created by following the system's guidance and options. For example, one or more of many options such as 'pain', 'wound' and 'pain' will be selected. The location of the complaint in the body is selected from different human body maps (such as muscle map, bone map). The most important issue at this stage is that the questions that come in order are determined by the physicians and the questions that follow change according to the answers given.

Once all questions are answered, an application draft is created and displayed on the screen for the patient to review. If the patient approves the pre-application registration, the pre-registration will be created and saved on the system. If the patient has entered his past health records into the system at a previous stage or enters them at this stage, he can choose to add his past health records to the health application form at his own discretion.

The patient can translate the record created through the system into the language or languages of his/her choice. He can receive this record digitally in different file types, or he can also print these files if he wishes. All features of the system are explained in detail in Section 4.5.

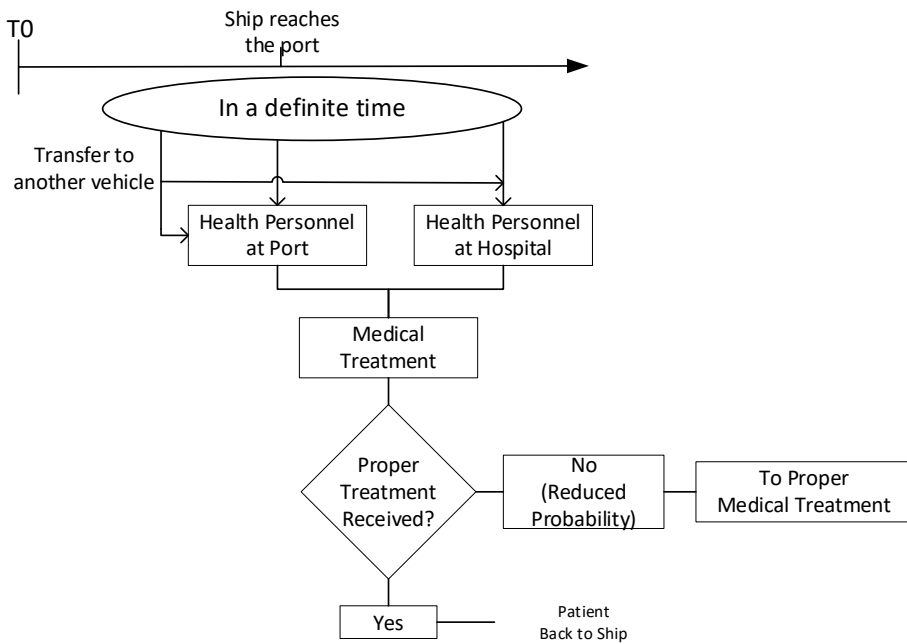


Figure 6. Proposed System in Commercial Ships

Current system and proposed system can be compared by examining Figure 4 and Figure 6.

Proposed system has two major benefits compared to the current system. The first is, the patient is routed to proper medical treatment more properly based on accurate medical information. This will avoid both unnecessary time loss and expanses. Secondly it will be less likely that the patient will be rerouted for another medical treatment due to pre-triage.

4. EVALUATION OF THE SYSTEM

In this section, SCM was used and it was evaluated whether the proposed system could find solutions to the identified problems.

4.1 Categorization of Identified Problems

In Section 1.1, the problems encountered when applying for health care are mentioned in detail. In this section, these problems are divided into categories. Table 1 shows these identified problems, and Table 3 shows the categories of these problems. These categories correspond to failures in SCM and are not divided into 'active' and 'latent'. Possible problems (Table 2) are not added to Table 3.

Table 3. Categories of the Problems Encountered in Medical Translations

Cat. Code	Categories of the Problems
C1	Communication problems due to language differences
C2	Inability of the patient to express himself due to consciousness and other factors
C3	Translation errors
C4	Internet based errors
C5	Problems related to health records

In both Category C1 and C2, the patient cannot express himself. The difference is that in category C1, the patient is in a state that he can communicate but cannot express himself due to the language difference. In category C2, the patient is unable to express himself due to shock, loss of consciousness and similar reasons. In this case, language is not an issue.

It has been observed that incorrect translations made by non-professional translators can cause many medical issues including death of the patient. And even medical translations made by professional interpreters (interpreters who are not medical translators) cause similar medical issues (Gonel, 2023). Category C3 includes all health problems experienced when the patient's health problems are translated by the translator to the medical staff.

An internet connection and other necessary equipment are needed to use general online translation programs and receive professional medical translation services online. All problems experienced in the provision of relevant connections and services are included in category C4.

Health problems experienced due to failure to submit health records or misunderstanding due to language differences are designated as category E.

4.2 Defense Layers

A multi-layered solution network was modeled. Solution layers Lay A, B1, B2, C1, C2, D and E, identified problem categories were produced as solutions (Table 4). Each of the layers provided solutions to each problem category. The auxiliary layer (Aux Lay A) is an additional layer that was not created as a solution to determined problems (Section 1.2) but for anticipated problems (Section 1.3). Solution layers correspond to slices in SCM.

Table 4. Defense Layers

Lay. Code	Defense Layer
A	Interface where the patient can use any language he wants
B1	Creating health form at the time of complaint occurs or complaint is expected
B2	Creating health for the unconscious or uncapable patients by other people
C1	Translations made only by medical doctors and medical translators.
C2	Creating the patient form without entering text
D	Using an offline interference
E	Keeping past health records ready by entering them into the system in advance

The first layer (Lay A) is use of an interface that allows each patient to log in to the system using their native language or any language of their preference. The system interface has also been prepared in a way that does not require any text writing (Lay C2). Translations between languages will be made by medical doctors and medical translators (Lay C1). Another feature of the interface is working without the need for an internet connection (Lay D).

The system in question was developed for personnel and passengers of ships, planes, trains and similar transportation vehicles. Since there is likely to be a time difference between the occurrence of a health complaint and access to healthcare, pre-registration will be created as soon as a health problem occurs during the voyage. Thus, in cases where the patient loses consciousness or similar, the patient's complaints will be conveyed directly to the healthcare personnel through the patient's statement (Lay B1). In cases where the patient suddenly faints, loses

consciousness as a result of an accident, etc., the patient record can be filled in by another person (Lay B2). Performing this process as soon as possible will contribute to the more accurate collection of information about the patient's condition.

If the people who are in question to use the system voluntarily upload their past health records to the system, in case of any emergency, healthcare personnel will be able to access the patient's health records in the language of their choice (Lay E).

4.3 Auxiliary Defense Layers

An additional security layer has been added to the system for the anticipated problem (I13) that is not detected from the actual events but is predicted to occur. The patient will not know the information the medical staff needs for a correct diagnosis. For this reason, each question that the system asks the patient varies according to the previous questions and questions, and all questions and the order of the questions are determined by the physicians (Aux Lay A).

4.4 Evaluation of the System

The identified problems (Section 1.2) were divided into categories (Section 4.1) and the solution layers developed to solve these problems (Section 4.2) were compared with the SCM (Figure 7). As a result, it has been seen that solution layers prevent all problems (detected and potential problems) in theory.

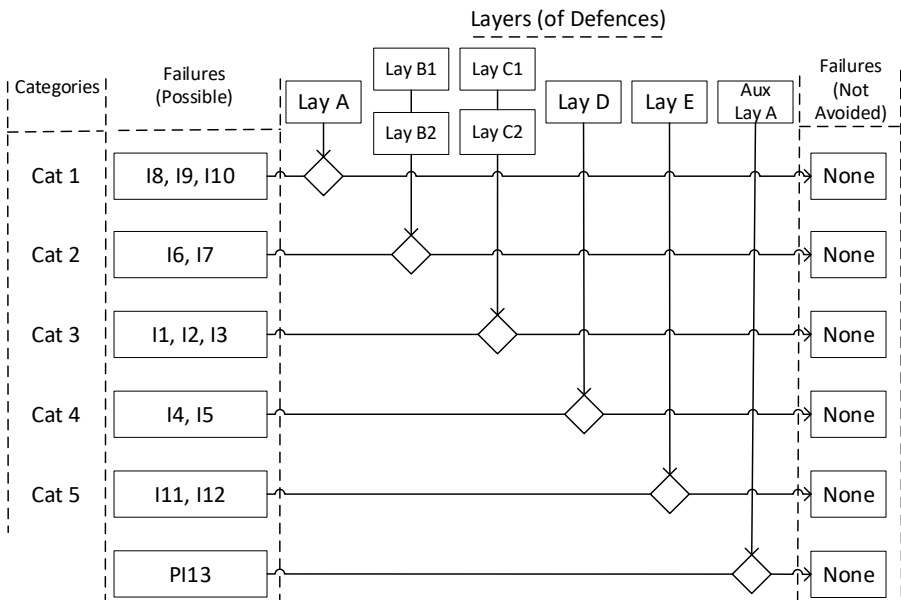


Figure 7. Effects of Defense Layers on Failures

4.5 Benefits of the System

Since the benefits of the system are explained in detail (Gonel, 2023), they are not included in this study to avoid repetition.

5. CONCLUSION

It is quite possible that especially seafarers and also international transport workers and passengers may require healthcare. In these moving vehicles, such as ships, it may not be possible for patients to reach healthcare services in a short time. The patient must be guided in the most appropriate way with the correct preliminary diagnosis. Moreover, correct guidance of the patient is not the only problem. Many problems may occur even when the patient reaches the healthcare personnel and is about to receive healthcare services. Failures may occur due to many different reasons, especially language-related problems. Proposed system will avoid all these problems and thus provide reduced expenses and time loss.

The benefits and additional benefits of the system show that the system can be used not only for transport sector workers and passengers, but also for refugees, immigrants, tourists and many other groups. In addition, it will be appropriate and beneficial to use the system for all patients who will receive healthcare services.

REFERENCES

- ATSB. (2016). Man Overboard Fatality from Hyundai Dangjin, Atsb Transport Safety Report. Canberra: Australian Transport Safety Bureau.
- Feinstein, J., Morley, S., Yang, H. (2015). Swiss cheeses and their applications. *Function Spaces in Analysis*, 99–118. <https://doi.org/10.1090/conm/645/12928>
- IMO. (2000). Medical Assistance at Sea. International Maritime Organization. MSC/Circ.960.
- Larouzee, J., Le Coze, J.-C. (2020). Good and bad reasons: The Swiss cheese model and its critics. *Safety Science*, 126, 104660. <https://doi.org/10.1016/j.ssci.2020.104660>
- Li, Y., Thimbleby, H. (2014). Hot cheese: A processed Swiss Cheese Model. *The Journal of the Royal College of Physicians of Edinburgh*, 44(2), 116–121. <https://doi.org/10.4997/jrcpe.2014.205>
- MAIB. (2011). Fatal injuries to a crewman during mooring operations on FORTH GUARDSMAN South of Jura 13 March 2011. Maritime Accident Investigation Branch.
- MAIB. (2013). Fatal injury to a crew member on board E.R.Athina at anchor off Aberdeen 10 June 2012. Maritime Accident Investigation Branch.
- Puthillath, B., Marath, B., Ayappan, B. C. (2021). Analyzing the cause of human electrical accidents using Swiss cheese model. *Vilakshan - XIMB Journal of Management*, 20(1), 193–208. <https://doi.org/10.1108/xjm-01-2021-0004>
- Suryoputro, M. R., Sari, A. D., Kurnia, R. D. (2015). Preliminary study for modeling train accident in Indonesia using swiss cheese model. *Procedia Manufacturing*, 3, 3100–3106. <https://doi.org/10.1016/j.promfg.2015.07.857>
- Teran Pumar, O. Y., Lathia, J. D., Watson, D. C., Bayik, D. (2023). ‘slicing’ glioblastoma drivers with the Swiss Cheese Model. *Trends in Cancer*. <https://doi.org/10.1016/j.trecan.2023.08.002>
- T.C. Sağlık Bakanlığı (2019). Uluslararası Hasta Destek Birimi Tercümanlık ve Çağrı Merkezi. (Data retrieved 24.09.2023 from <https://aydinism.saglik.gov.tr/TR-18925/uluslararasi-hastadestek-birimi-tercumanlik-ve-cagri-merkezi.html>)
- T.C. Sağlık Bakanlığı (2023a). Gemide Sağlık Danışma Hattı. (Data retrieved 11.09.2023 from <https://www.hssgm.gov.tr/TeleSaglikIletisim>)
- T.C. Sağlık Bakanlığı (2023b). Neyim var? (Data retrieved 22.09.2023 from <https://neyimvar.gov.tr/belirtiler>)

Wiegmann, D. A., Shappell, S. A. (2001). A human error analysis of commercial aviation accidents using the Human Factors Analysis and classification system (HFACS). *PsycEXTRA Dataset*.

<https://doi.org/10.1037/e420582004-001>

Wiegmann, D. A., Wood, L. J., Cohen, T. N., Shappell, S. A. (2021).

Understanding the “swiss cheese model” and its application to patient safety. *Journal of Patient Safety*, 18(2), 119–123.

<https://doi.org/10.1097/pts.0000000000000810>

Chapter 28

Detection and Recognition of Allergic Fruit with Deep Learning Models

Sevinç AY¹

ABSTRACT

The development of artificial intelligence technologies has led to the development of new technologies in many areas of our lives. Health, education, security etc. Artificial intelligence-based technologies that create major changes in fields are becoming increasingly widespread. With artificial intelligence technologies, faster results have been achieved in the diagnosis and treatment of diseases by reducing human interaction in the field of healthcare. Food allergies are one of the most important problems that threaten human health at increasing rates every year. In terms of primary risk factors, family history, age group and other diseases stand out. Although it is known that foods affect people in the primary risk group, there are foods that can be considered allergenic in their own right. Especially allergenic fruits cause mild, moderate or severe allergic cases. The fact that fruits added to children's diets at an early age are allergenic forms the basis of serious nutritional problems. Preliminary detection of allergenic foods can help individuals organize and manage their diets. In addition, the detection of these fruits in artificial intelligence-supported applications can be used to guide allergic individuals about fruit consumption, to teach students about allergenic fruits at an early age, and to determine the type of fruit and present it to customers in shopping places. Within the scope of the study, allergenic fruits were detected and recognized using the deep learning model Faster R-CNN and the ResNet50 backbone network. As a result of the training in this study, 89% success was achieved.

Keywords – Faster R-CNN, ResNet50, Deep Learning, Artificial Intelligence

INTRODUCTION

¹ Lecturer Dr.: Firat University Distance Education Center.say@firat.edu.tr ORCID No: 0009-0001-6309-0889

The capabilities of artificial intelligence are increasing and starting to appear in many areas of life. The health sector also stands out among the areas where artificial intelligence technologies are used. New technologies are frequently used in the diagnosis and treatment of diseases and in improving public health. Reasons such as insufficient healthcare personnel and increasing workload, not every individual having equal rights to receive healthcare, and the availability of different diagnosis and treatment options make the use of artificial intelligence technologies in the field of healthcare necessary (Akalin and Veranyurt, 2021:232).

One of the most important problems in the field of health is allergic diseases, the prevalence of which is increasing in society. Food allergies are considered as abnormal responses of the immune system to a food. Although food allergies are disorders that significantly reduce the quality of life, there is still no definitive treatment. Avoidance of allergenic foods is considered the most important precaution (Ulusoy, 2017:75).

In the study, detection and recognition of allergic fruits was carried out using Faster R-CNN, one of the deep learning architectures. Faster R-CNN is a prominent deep learning model in the field of object detection. Object detection was achieved by training Faster R-CNN with the ResNet50 backbone network.

This paper is organized beginning with the introduction section. After the introduction section at the material and method section the proposed object detection method with the brief explanations of the object detection algorithms and performance measurement metrics are explained. After the implementation section the conclusion is given as the final section.

Literature Review

There are not many studies in the literature on detecting allergenic fruits with deep learning methods. There are many studies in which allergenic foods are classified, food ingredients are determined, or only some types of fruits are identified. Different methods were used in these studies.

According to Koirala (2018:41), knowing the potential allergen in foods becomes very important in the fight against obesity. For this reason, they performed detection via deep learning on digital photographs containing food images. They stated that they use Faster R-CNN in their applications because it stands out among object detection methods. They used a publicly available data set and adapted it to their study. They managed to recognize images with 0,7 AP.

OCR and deep learning methods were used together to detect allergenic nutritional content in fruits and packaged foods. Fruits 360 dataset from Kaggle, which contains a total of 80424 data consisting of 650 images in 116 fruit and vegetable classes, was used. A manually prepared csv file containing allergen information was used. Performance comparison is presented using InceptionV3, VGG16, VGG19, Inception ResNetV2, ResNet50, Xception and MobileNetV2. Models pre-trained using transfer learning were used. In the study, the highest performance was achieved at 96.6% with VGG16 (Rohini et. al., 2021:76)

In a study where allergenic foods were detected using computer vision and deep learning methods, dataset named Allergen30 was used. Data augmentation was carried out by applying pre-processing steps on the dataset. All images in the dataset were resized to 416x416. Object detection was performed on more than 6000 images. Performance comparison of YOLOv5s, YOLOv5m, YOLOv5l and YOLOR-P6 algorithms was made. It was observed that the algorithm showing the highest performance was YOLOR-P6 with 0.811 mAP. YOLOv5s stood out as the fastest algorithm (Mishra et.al., 2022:3078)

Machine learning methods were used to identify the fungi that are considered to be allergenic foods. Naive Bayes, Decision Tree (C4.5), Support Vector Machine (SVM), and Logistic Regression were used in the study classifying mushrooms according to whether they are poisonous or not. In studies conducted on the data set taken from the Kaggle website, a success rate of 9.4% was achieved with the C4.5 algorithm (Kousalya et. al., 2022:6).

Convolutional Neural Network (CNN) was used in a study prepared to detect cinnamon powder, which is considered an allergenic food. Principal Component Analysis (PCA) and using Near-Infrared Spectroscopy (NIRS) were also used to detect cinnamon powder, whose structure was deteriorated during the production process by mixing other substances. In the study comparing NIRS-PCA and CNN, 99.95% and 92.80% performance was achieved, respectively (Ku et. al., 2023:324).

MATERIAL AND METHOD

In this section, the Faster R-CNN algorithm used for allergic fruit recognition is mentioned. Briefly, the ResNet50 backbone network is explained. Finally, the benchmark problems and performance measurements used in this research is presented.

Faster R-CNN

Faster R-CNN is one of the most used deep learning models in the field of object detection. It has better performance than Convolutional neural networks (CNN) developed before it. Additionally, solutions to their limitations have been produced.

Faster R-CNN is a deep learning architecture that emerged as a result of the development of R-CNN models that appeared before it. (Megalingam et al., 2023:684). Although R-CNN, Fast R-CNN and Faster R-CNN are known as region-based networks, they are based on the R-CNN structure. R-CNN and Fast R-CNN use selective search, which is a candidate region recommendation method that cannot meet real-time requirements and consumes a lot of time. Faster R-CNN, developed to prevent this bottleneck, is an architecture with a two-stage network structure. RPN (Region Proposal Network) is used as the first stage to extract candidate regions. Candidate regions are determined using bounding boxes from the input image. In the second stage, Fast R-CNN is used (Li et al., 2022: 4).

ResNet50

ResNet50 is a 50-layer convolutional neural network frequently used in the field of computer vision. It is the abbreviation of residual network. It was introduced in 2015. With ResNet, a solution could be found to the vanishing gradient problem, which is one of the major problems of convolutional neural networks (Alzamily et.al, 2022:6611).

ResNet enabled CNN to work using multiple layers. The residual connection structure used with ResNet prevents the model from learning excessively. With this structure, data transfer between layers becomes easier during learning. In this way, the depth effect of the model is reduced. With the connection skipping method, some layers are skipped and the activation of one layer is connected to the other layer. This structure combines throughout the architecture to form networks. It was inspired by VGG networks. Although it is deeper than VGG networks, it has less complexity and filter usage (He et.al., 2016:772).

Dataset

The Allergic Fruit dataset taken from the Kaggle website was used within the scope of the study. The dataset consists of images containing one or more fruits. In the study, 1635 images containing a single fruit image were selected for training. The dataset contains 316 images for testing. All images in the dataset are 640x640 in size.

Data augmentation was applied to the data in order to increase the data in the dataset. Data was increased by combining multiple fruit images into a single image, horizontal and vertical rotation, and zooming. After data augmentation, 3550 fruit images were obtained. Figure 1 shows sample images of the dataset.

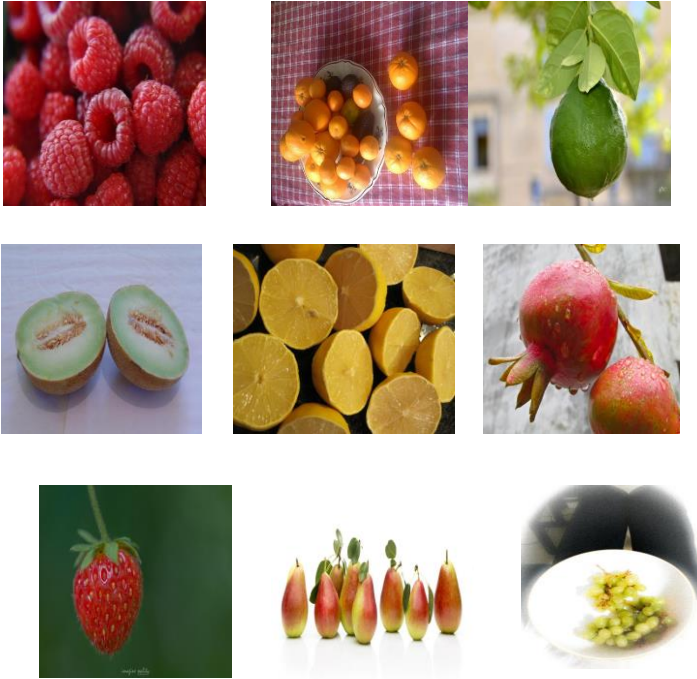


Figure 1: Sample fruit images from Allergic-Fruit dataset

Performance Metrics

Evaluation metrics commonly used to evaluate performance in deep learning and object detection studies are Precision, Recall, Average Precision (AP), and average Average Precision (mAP).

Precision shows the true positive (TP) rate in the prediction results. Its formula is as follows:

$$\text{Precision} = \frac{TP}{TP+FP} \quad (1)$$

Recall expresses the proportion of correct predictions out of all true positives and false negatives as follows:

$$\text{Recall} = \frac{TP}{TP+FN} \quad (2)$$

Mean Average Precision (mAP) is the average AP value over all object classes and is calculated as follows:

$$\text{mAP} = \frac{(\sum AP)}{N_classes} \quad (3)$$

The N_{classes} value in the formula represents the number of classes.

RESULTS AND DISCUSSION

In this section, object detection was performed using Faster R-CNN on the Allergic-Fruit dataset. Faster R-CNN and ResNet50 backbone network were used together.

MATLAB 2021b program was used within the scope of the study. All experiments were carried out on Windows 10 operating system on a computer equipped with Intel(R) Xeon(R) W-2245 CPU @ 3.90GHz processor, 32 GB RAM and NVIDIA Quadro RTX 40000 graphics card. The training results obtained are shown in Table 1.

Table 1: mAP value after training Faster R-CNN with ResNet50

Model	Backbone	mAP	Fps
Faster R-CNN	ResNet50	89.4%	24.2

In object detection studies, precision-recall curve is frequently used to provide information about the performance of the study. Figure 2 shows the precision-recall curve of the ResNet50 backbone network. Also shown is the Loss Average Miss Rate

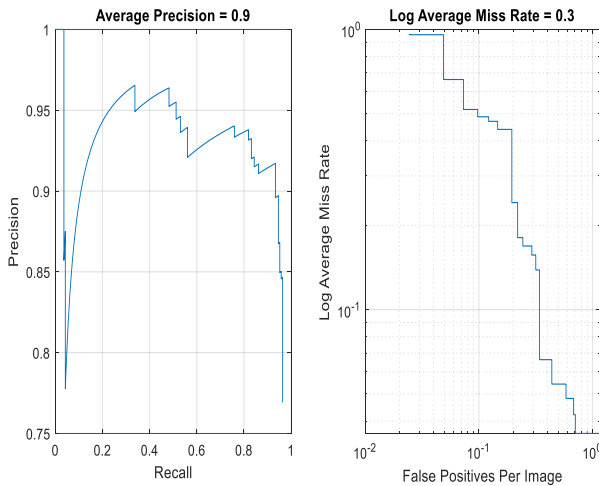


Figure 2: Precision-recall curve for Faster R-CNN

Training was carried out on the allergic fruit dataset using Faster R-CNN and ResNet50 backbone network. The object detector created as a result of the training was tested on test data. Object detection was applied on 316 test

data. Object detection results obtained from the object detection detector are shown in Figure 3.

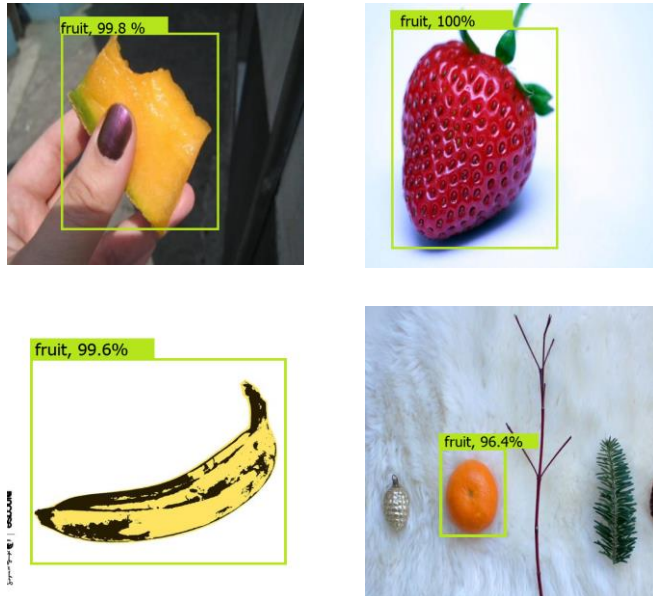


Figure 3: Allergic fruit detection images with Faster R-CNN

CONCLUSION

Allergenic fruits are an important part of the diet from early childhood. Within the scope of the study, these fruits were detected on the allergic fruit dataset. It is thought that this study can be used when regulating individuals' diets against allergenic foods, when introducing allergenic foods to customers in markets, when educating children, and when classifying agricultural products during the production.

Within the scope of the study, object detection was achieved by training the Faster R-CNN deep learning model with the ResNet50 backbone network. As a result of the study, the mAP value, which is one of the most important criteria showing the success of the study, was determined as 89.4%.

The scope of the study can be expanded by running it with different deep learning architectures. Additionally, including different allergenic foods in the study will increase the effectiveness of the study.

ACKNOWLEDGMENT

Allergic-fruit Dataset taken from the Kaggle website was used within the scope of the study.

REFERENCE

- Akalın, B., and Veranyurt, Ü. (2021). Sağlık Hizmetleri ve Yönetiminde Yapay Zekâ. *Acta Infologica*, 5(1), 231-240.
- Alzamily, J. I., Ariffin, S. B., and Abu-Naser, S. S. (2022). Classification of Encrypted Images Using Deep Learning–Resnet50. *Journal of Theoretical and Applied Information Technology*, 100(21), 6610-6620.
- He, K., Zhang, X., Ren, S., and Sun, J. (2016). Deep residual learning for image recognition. In *Proceedings of the IEEE conference on computer vision and pattern recognition* (pp. 770-778).
- Koirala, J. (2018). *Food Object Recognition: An Application of Deep Learning*.
- Kousalya, K., Krishnakumar, B., Boomika, S., Dharati, N., and Hemavathy, N. (2022, January). Edible mushroom identification using machine learning. In *2022 International Conference on Computer Communication and Informatics (ICCCI)* (pp. 1-7). IEEE.
- Ku, H. H., Liao, Y. C. and Chi, C. H. (2023). Deep Learning Applied on Cinnamon Powder Adulteration Detection. In *2023 IEEE 6th International Conference on Knowledge Innovation and Invention (ICKII)* (pp. 324-327). IEEE.
- Li, X., Xie, Z., Deng, X., Wu, Y., and Pi, Y. (2022). Traffic sign detection based on improved faster R-CNN for autonomous driving. *The Journal of Supercomputing*, 1-21.
- Megalingam, R. K., Thanigundala, K., Musani, S. R., Nidamanuru, H., and Gadde, L. (2023). Indian traffic sign detection and recognition using deep learning. *International Journal of Transportation Science and Technology*, 12(3), 683-699.
- Mishra, M., Sarkar, T., Choudhury, T., Bansal, N., Smaoui, S., Rebezov, M., ... and Lorenzo, J. M. (2022). Allergen30: detecting food items with possible allergens using deep learning-based computer vision. *Food Analytical Methods*, 15(11), 3045-3078.
- Rohini, B., Pavuluri, D. M., Kumar, L. N., Soorya, V. and Aravinth, J. (2021, March). A framework to identify allergen and nutrient content in fruits and packaged food using deep learning and OCR. In *2021 7th International conference on advanced computing and communication systems (ICACCS)* (Vol. 1, pp. 72-77). IEEE.
- Ulusoy, E. (2017). Besin alerjilerinin değerlendirilmesi. *Klinik Tıp Pediatri Dergisi*, 9(2), 74-77.

Chapter 29

A Comparative Study on Signal Processing for Harmonics

Sitki AKKAYA¹

ABSTRACT

In power systems, maintaining the fundamental frequency and amplitude at standard values of 50 Hz and 220 V_{rms} in Turkey is crucial. However, these parameters can fluctuate due to various factors such as arc/welding furnaces, nonlinear loads, and switching. Several standards such as IEEE 1159 and IEEE 1459 focus on power quality parameters and meaningful interpretation of power system measurements, while IEC 61000-4-7 and IEC 61000-4-30 provide guidelines for testing disturbances. According to these standards, one of the disturbances of these factors on power systems emerges as harmonics. The most important ones are odd-order harmonics like 3rd, 5th, and 7th, as defined in IEC 61000-4-7, pose significant risks and measurement errors. These can be inphase with- or time-varying on the fundamental component. The importance of periodic tracking and analysis in power systems is not negligible. This tracking must be carried out with a robust method for a correct decision for prevention of impairment on power systems. For this goal, this chapter delves into time- and time-frequency- signal processing methods based on such as Fast Fourier Transform (FFT), Short-Time Fourier Transform (STFT), Continuous Wavelet Transform (CWT), Empirical Mode Decomposition (EMD), and Hilbert Huang Transform (HHT) for harmonics analysis. The discussion covers their performance in cases of in-phase and time variation. This chapter provides a comprehensive understanding of power quality, harmonics, and signal processing methods in different cases such as inphase and time-varying. The researchers can learn the importance of time ranges of harmonic components and determine the optimal method by using the results of this study.

Keywords –Power Quality Analysis, Power Quality Disturbances, Fast Fourier Transform, FFT, Short-Time Fourier Transform, STFT, Continuous Wavelet Transform, CWT, Empirical Mode Decomposition, EMD, Hilbert Huang Transform, HHT, In-phase, Time-varying, Harmonics, IEEE 1159, IEEE 1459, IEC 61000-4-7, IEC 61000-4-30

¹ Asst. Prof. Dr.; Sivas University of Science and Technology, Department of Electrical and Electronics Engineering, sakkaya@sivas.edu.tr ORCID No: 0000-0002-3257-7838

1. INTRODUCTION

In power systems, the fundamental frequency and amplitude are critical components and should be convenient with the standards of 50 Hz and 220 V_{rms} in Turkey [1]–[4]. However, these components are changed on different occasions and system components [5]–[8]. Arc/welding furnaces, nonlinear loads, induction motors, DC motors, lamps, switching, lightning, etc are effective in this variation [9]–[12]. This issue was handled in some studies in detail in terms of analysis and classifications [5]–[13].

IEEE 1159 and IEEE 1459 standards concentrate on power quality parameters and meaningful interpretation of power system measurements, respectively. Guidelines for testing and evaluating disturbances in power systems can be found in IEC 61000-4-7 and IEC 61000-4-30 [1]–[4]. IEC 61000-4-30 offers the window for analysis as 0.2 seconds [2].

The odd-order harmonics like 3rd, 5th, and 7th are the important disturbances as defined in IEC 61000-4-7 [1]. These can emerge singular or multiple, as inphase with the fundamental component, and at different time ranges. These bring about some risks and measurement mistakes for the people and the systems. Measurement mistakes led to other problems like the determination of values of components to be eliminated.

Periodic tracking and analysis of harmonics in power systems are essential. Thus, a robust correction with filtration/compensation is completely dependent on a more robust signal processing. So, the selection of the type of signal processing method is crucial. For this aim in this chapter, a comparison of some signal processing methods like Fast Fourier Transform (FFT), Short-Time Fourier Transform (STFT), Continuous Wavelet Transform (CWT), Empirical Mode Decomposition (EMD), Hilbert Huang Transform (HHT) is done with harmonics in cases of in-phase and time variation.

This chapter is designed as follows. The meaning of power quality and the different types of harmonics are given with definitions and model equations in section 2. 3rd section lets us know signal processing methods based on time and time-frequency domains by using related harmonics. Subsequently, responses of the signal processing methods on the signals with the harmonics are given visually. The summary of this chapter is granted in the last section.

2. POWER QUALITY AND HARMONICS

Within power systems, the fundamental frequency and amplitude stand out as crucial components. In these systems, the ideal signal conforms to the pure sinusoidal form with the fundamental frequency and amplitude should be 50 Hz and 220 V_{rms} in Turkey, respectively. But, they are changed by odd-order

harmonics like 3rd, 5th, and 7th as defined in IEC 61000-4-7. These can emerge singular or multiple, as inphase with the fundamental component, and at different time time ranges. These are defined with models as follows.

Fundamental Frequency Deviation & Voltage Amplitude Variation

The fundamental frequency and voltage amplitude are represented by f_0 and A in Eq. (1). Deviations from these values are undesirable and can lead to detrimental outcomes. However, the intended model for the power system voltage should adhere to this equation.

$$x(t) = A\sin(2\pi f_0 t), \quad f_0 = 50 \text{ Hz}, A = 220 V_{rms} \quad (1)$$

Harmonics

Harmonics persist as the most prevalent disturbances within power systems, and it is essential to minimize their impact as much as possible. The primary culprits among harmonics, namely the 3rd, 5th, and 7th ones, exhibit activity that necessitates continuous monitoring. Owing to the emergence of these components as in-phase and different time ranges, this issue is handled below two subtitles, called in-phase and time-varying harmonics.

a. Inphase harmonics

Considering these harmonics and adhering to standards-based limitations, a signal incorporating inphase harmonics is presented in Eq. (2), where α_3 , α_5 , and α_7 denote the coefficients of the corresponding harmonics.

$$x_1(t) = \sin(2\pi f_0 t) + \alpha_3 \sin(2\pi 3 f_0 t) + \alpha_5 \sin(2\pi 5 f_0 t) + \alpha_7 \sin(2\pi 7 f_0 t), \quad \alpha_n = \frac{1}{n}, n = 3,5,7 \quad (2)$$

b. Time-varying harmonics

A signal with time-varying harmonics has a characteristic as in Eq. (3). In this equation, α_n components are similar to Eq. (2). The unit step function $u(t_i)$ states the start and end times of the harmonics.

$$\begin{aligned}
x_2(t) = & \sin(2\pi f_0 t) \\
& + \alpha_3 \sin(2\pi 3f_0 t)(u(t_1) \\
& - u(t_2)) \\
& + \alpha_5 \sin(2\pi 5f_0 t)(u(t_3) \\
& - u(t_4)) \\
& + \alpha_7 \sin(2\pi 7f_0 t)(u(t_5) \\
& - u(t_6)),
\end{aligned}
\quad
\begin{aligned}
\alpha_n = & \frac{1}{n}, n = 3,5,7 \\
0 \leq t_i, & \leq 0,2 \text{ sec}, \quad i=1:6 \quad (3) \\
u(t_i): & \text{unit step function}
\end{aligned}$$

3. SIGNAL PROCESSING METHODS

Harmonics on power systems must be tracked and analyzed periodically. Selecting an efficient and robust method in the field is important for precious analysis and for designing a filter or a compensation system due to that analysis. There are lots of methods to analyze harmonics in the literature. The most commonly used of them is FFT. It is summarised below.

a. Fast Fourier Transform (FFT)

For x and y of length n , the Fast Fourier Transformation of x is defined as follows:

$$y(k) = \sum_{j=1}^n x(j)W_n^{(j-1)(k-1)}, \quad W_n = e^{(-2\pi i)/n} \quad (4)$$

This method is usable but gives information for only the frequency domain. It has not the ability to give detail inphase of time and frequency. For that reason, the other methods can be usable like STFT, CWT, EMD, and HHT as follows [14].

b. Short-Time Fourier Transform (STFT)

The Short-Time Fourier Transform (STFT) of a signal involves the process of sliding an analysis window $g(n)$ with a length of M over the signal and computing the Discrete Fourier Transform (DFT) for each segment of windowed data. The window moves across the original signal at intervals of R samples, creating an overlap of $L = M - R$ samples between adjacent segments. To prevent spectral ringing, many window functions gradually decrease towards the edges. The DFT of each windowed segment is then accumulated in a complex-valued matrix, encompassing both magnitude and phase information for each point in time and frequency [15].

$$k = \left\lfloor \frac{N_x - L}{M - L} \right\rfloor \quad (5)$$

Columns are formed based on the length of the signal $x(n)$, denoted as N_x , and the $\lfloor \cdot \rfloor$ symbols represent the floor function. The matrix has a number of rows equal to NDFT, the number of DFT points, for centered and two-sided transforms. For one-sided transforms of real-valued signals, the matrix has an odd number of rows, approximately close to NDFT/2. Each column in the Short-Time Fourier Transform (STFT) matrix, represented by the m th column, corresponds to a specific analysis window position or time segment in the signal.

$X(f) = [X_1(f) X_2(f) X_3(f) \dots X_k(f)]$ contains the DFT of the windowed data centered on time mR :

$$X_m(f) = \sum_{n=-\infty}^{\infty} x(n)g(n - mR)e^{-j2\pi fn} \quad (6)$$

c. Continuous Wavelet Transform (CWT)

Continuous Wavelet Transform (CWT) is applied to this signal as follows in (4).

$$W_s(a, b) = \int v(t)a^{-1/2}\overline{\psi\left(\frac{t-b}{a}\right)} dt \quad (7)$$

In this equation, ψ : wavelet window, $\overline{\psi}$: conjugate of ψ , b is time-shifting and a is the coefficient of scaling [16].

d. Empirical Mode Decomposition (EMD)

EMD (Empirical Mode Decomposition) adjusts to the time scale of the signal, unlike CWT and FFT. EMD possesses the capability to break down intricate time series into a collection of signals featuring distinct local properties called intrinsic mode functions (IMFs) and their associated residual values. Each of these decomposed IMFs captures the local characteristics of various time scales present in the original time series [17]. For an IMF generated by the EMD, it must satisfy the following criteria:

- 1) The number of zero-crossings and local endpoints should be equal or differ by at most 1 over the entire time interval.
- 2) At any point in time, the average of the local maximum envelope and the local minimum envelope should be 0.

Find the local extreme values of $x(t)$, and then use an interpolation method to obtain the upper and lower envelope sequence values $x_{max}(t)$ and $x_{min}(t)$ of the original time series $x(t)$.

$$m(t) = \frac{x_{max}(t)+x_{min}(t)}{2} \quad (8)$$

Subtract the instantaneous mean value $m(t)$ from the original time series $X(t)$ to obtain a new series $h(t)$:

$$h(t) = x(t) - m(t) \quad (9)$$

If the number of endpoints and zero crossings are equal or at most one difference, $h(t)$ is the *imf* component. If not, the above steps are repeated until the *imf* condition is obtained.

Subtract $imf_1(t)$ from the original sequence after finding the first natural model function $imf_1(t)$ to obtain the remaining sequence $r_1(t)$:

$$r_1(t) = x(t) - imf_1(t) \quad (10)$$

Then repeat the above steps with $r_1(t)$ as the new original sequence and remove the n^{th} $imf_1(t)$ in turn. Finally, $r_n(t)$ becomes a monotonic sequence.

The original sequence $x(t)$ can be obtained by stacking the components after decomposition.

$$x(t) = \sum_{k=1}^n imf_k(t) + r(t) \quad (11)$$

e. Hilbert Huang Transform (HHT)

Hilbert Transform of each IMF component $imf_k(t)$, $H[imf_k(t)]$ can be written as

$$H[imf_k(t)] = \frac{1}{\pi} P \int_{-\infty}^{+\infty} \frac{imf_k(\tau)}{t-\tau} d\tau \quad (12)$$

where P is the Cauchy principal value of the singular integral [18], [19]. According to the relevant definition of the analysis signal, the analysis form of the time series $imf_k(t)$, can be obtained that

$$z_k(t) = imf_k(t) + jH\{imf_k(t)\} \quad (13)$$

So the instantaneous amplitude and phase of the IMF component can be written as follows, respectively

$$a_k(t) = \sqrt{imf_k(t)^2 + H[imf_k(t)]^2} \quad (14.a)$$

$$\theta_k(t) = \arctan (H[imf_k(t)]/imf_k(t)) \quad (14.b)$$

$$z_k(t) = a_k(t)e^{j\theta_k(t)} \quad (14.c)$$

The instantaneous energy and the instantaneous frequency of the IMF can be obtained as below,

$$|a_k(t)|^2 \quad (15.a)$$

$$w_k(t) = d\theta_k(t)/dt \quad (15.b)$$

The result equation yields the time-amplitude-frequency representation is the Hilbert amplitude spectrum given as the following

$$H(w, t) = Re(\sum_{k=1}^n a_k(t) e^{j \int w_k(t) dt}) \quad (16)$$

4. RESPONSES OF SIGNAL PROCESSING METHODS

In this section, time-series responses for both types of signals are shown. Then, the frequency and time-frequency responses of signals processed with different SP methods are illustrated below.

a. Responses for Inphase Harmonics

The time-series signal with inphase, $x_1(t)$ in Eq. (1), is illustrated in Figure 1. As can be seen from the Figure, the signal changes periodically from start to end due to the coherence. The window for analysis is consistently set to 0.2 seconds [2]. This is also true for the rest of the study.

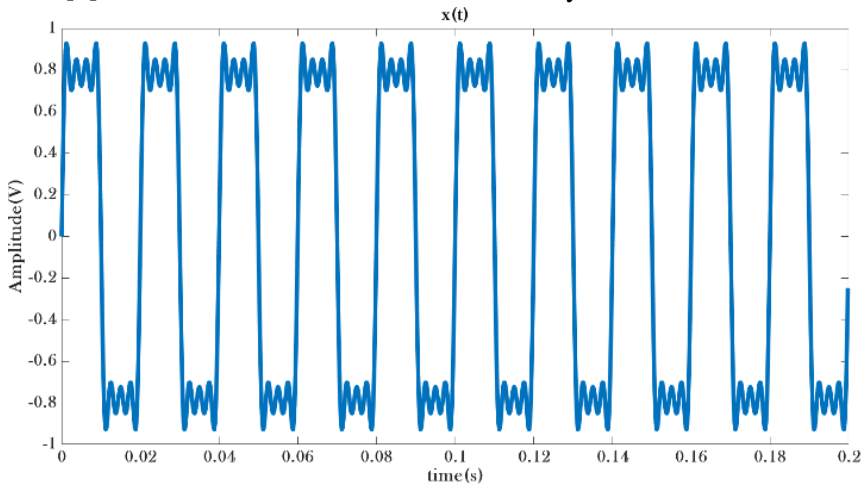


Figure 1: Time series signal $x_1(t)$ with inphase harmonics

- **Response of FFT**

FFT response of $x_1(t)$ is given in Figure 2. This figure shows the amplitudes of the components without any time detail.

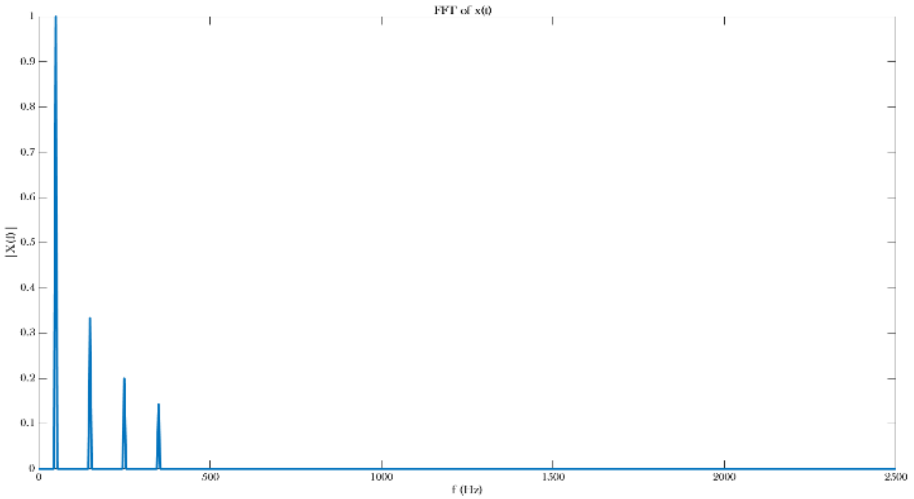


Figure 2: FFT of $x_1(t)$

- **Response of STFT**

STFT response of $x_1(t)$ is shown in Figure 3. This yields some details in terms of time and frequency.

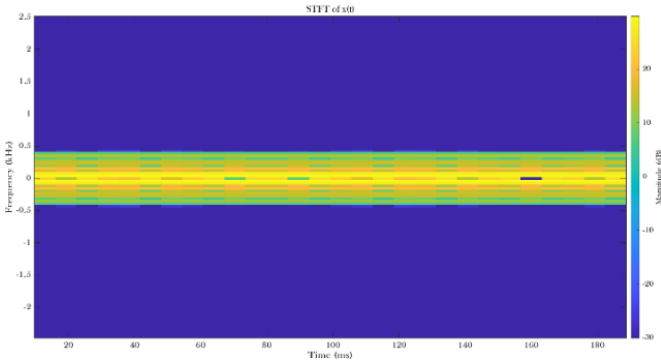


Figure 3: STFT of $x_1(t)$

- **Response of CWT**

CWT response of $x_1(t)$ is shown in Figure 4. This ensures some more robust details than STFT at both time and log frequency.

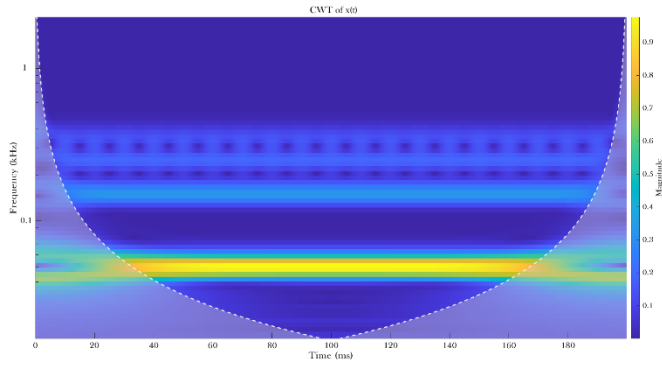


Figure 4: CWT of $x_1(t)$

- **Response of HHT**

HHT response of $x_1(t)$ is shown in Figure 5. This ensures some more robust details than CWT at both time and linear frequency.

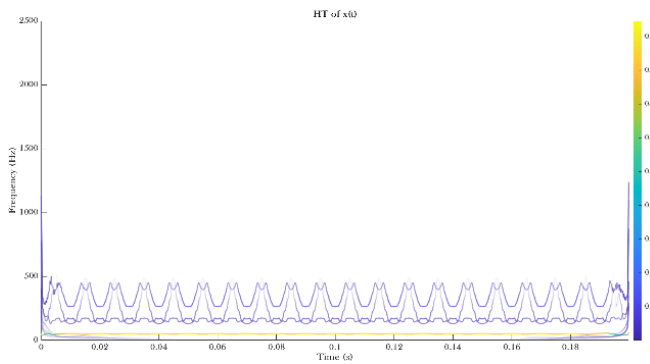


Figure 5: HHT of $x_1(t)$

- **Response of EMD**

$x_1(t)$ and the IMF components of the EMD response are shown in Figure 6. This method allows us to see the components with different frequencies in the time domain.

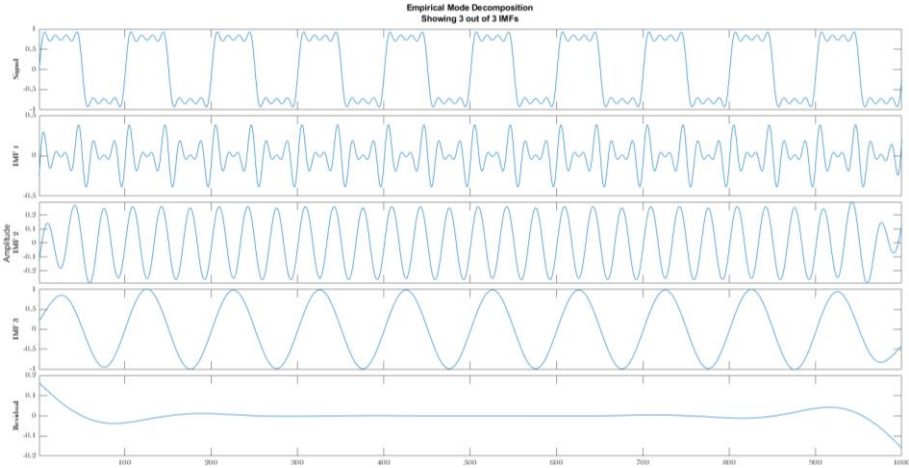


Figure 6: EMD of $x_1(t)$

b. Responses for Time-Varying Harmonics

The time-series signal $x_2(t)$ with time-varying harmonics in Eq. (3) is illustrated in Figure 7. This signal changes periodically in different intervals because of the emergence of harmonics at different times.

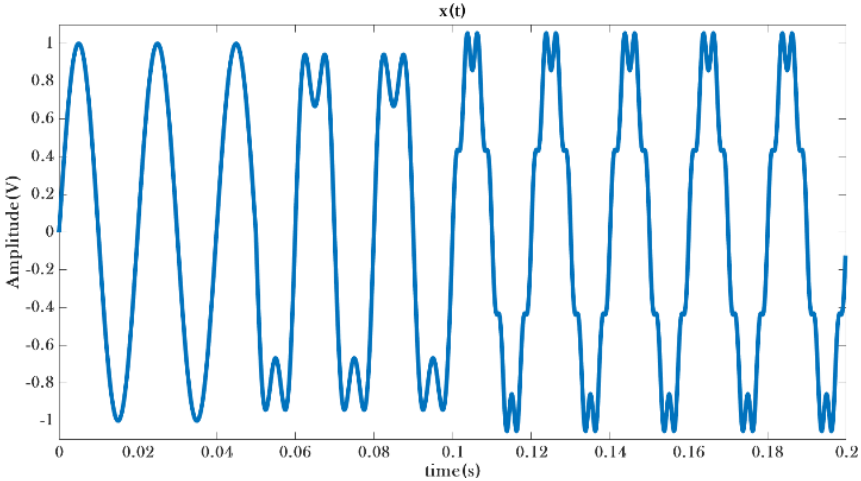


Figure 7: Time series signal $x_2(t)$ with time-varying harmonics

- ***Response of FFT***

FFT response of $x_2(t)$ is given in Figure 8. This figure shows the amplitudes of the components without any time detail.

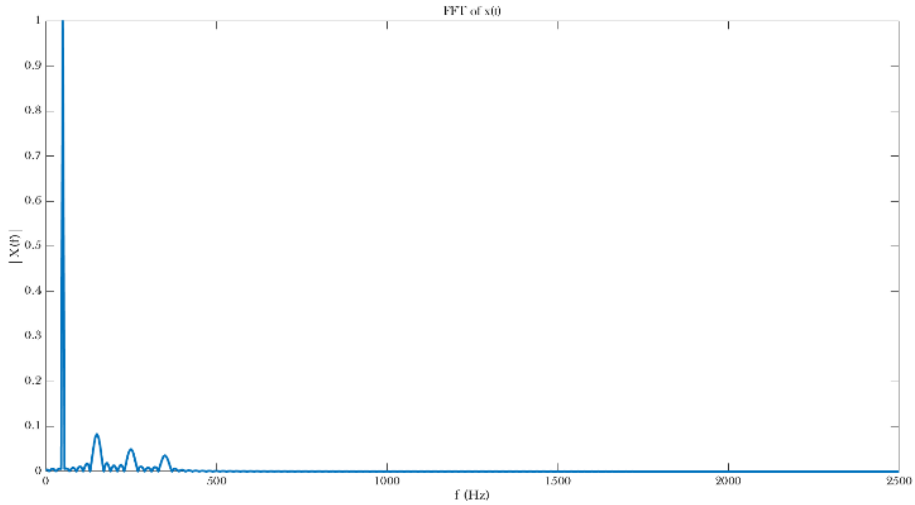


Figure 8: FFT of $x_2(t)$

- **Response of STFT**

STFT response of $x_2(t)$ is shown in Figure 9. This yields some details of the components in terms of start and end time and frequencies with different amplitude values symbolized with the colors.

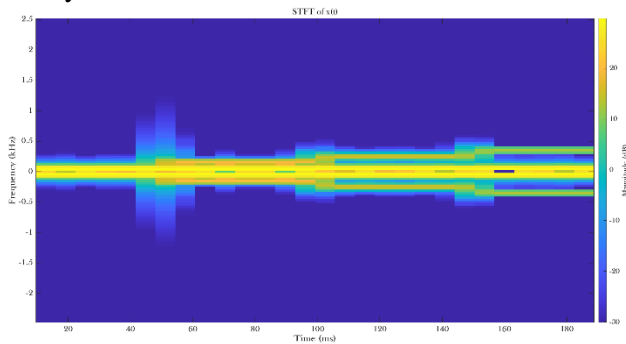


Figure 9: STFT of $x_2(t)$

- **Response of CWT**

CWT response of $x_2(t)$ reveals the different properties of the components in Figure 10. This ensures some more robust details than STFT at both the time and the frequency domain.

- **Response of HHT**

HHT response of $x_2(t)$ is shown in Figure 11. This shows some more details about amplitudes and starts and end times of the components, but that in somewhat oscillation for harmonic components.

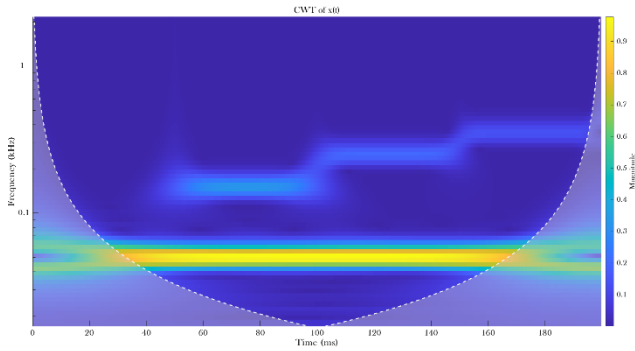


Figure 10: CWT of $x_2(t)$

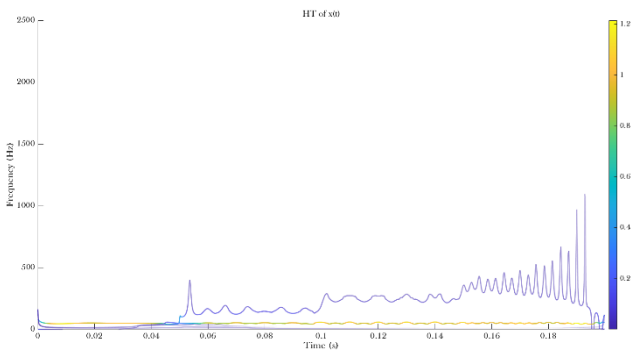


Figure 11: HHT of $x_2(t)$

- **Response of EMD**

$x_2(t)$ and the IMF components of EMD are shown in Figure 12. This method is insufficient for this case because of the amplitudes of harmonic components. However, it determines some points of events approximately.

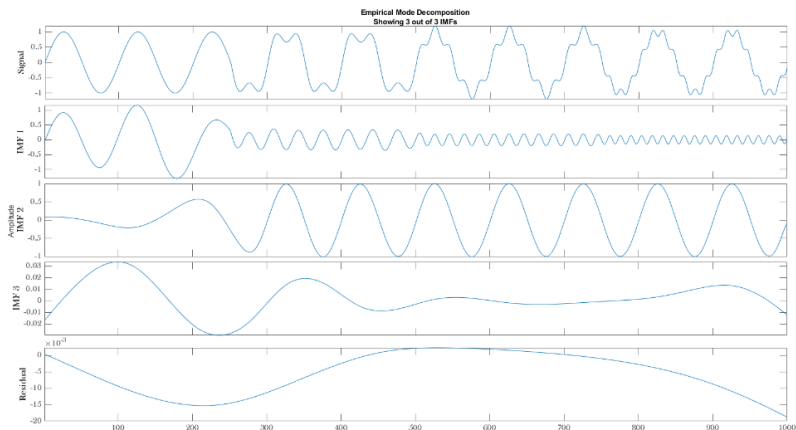


Figure 12: EMD of $x_2(t)$

5. SUMMARY AND DISCUSSION

In summary, harmonics on the power systems are processed with time- and time-frequency- signal processing methods based on such as Fast Fourier Transform (FFT), Short-Time Fourier Transform (STFT), Continuous Wavelet Transform (CWT), Empirical Mode Decomposition (EMD), and Hilbert Huang Transform (HHT) in different cases of emergence time ranges in this chapter. The effects of these were highly notable. FFT only offers frequency domain response except for time domain information. Also, the time ranges of each component affected the amplitudes on the frequency domain. The other methods provide time-frequency domain details almost compatible with each other in the case of inphase harmonics. The considerable differences in responses of time-frequency-based signal processing methods in the case of time-varying harmonics. CWT has the most robust performance meanwhile EMD has the worst because of the end effect. This study ensures that the researchers learn the harmonics with the important parameters on analysis end performances of the signal processing methods on harmonics in different cases.

REFERENCE

- Standard and N. Internationale, "IEC Standard 61000-4-7: General guide on harmonics and interharmonics measurements and measuring instruments for power supply networks and attached devices used for the measurements," vol. 2008. 2008.
- I. E. Commission, "IEC Standard 61000-4-30: Testing and measurement techniques - Power quality measurement methods," vol. 2003, p. 90, 2003.
- I. P. & E. Society, 2010-1459-IEEE Standard Definitions for the Measurement of Electric Power Quantities Under Sinusoidal, Nonsinusoidal, Balanced, or Unbalanced Conditions. 2010.
- I. Power and E. Society, IEEE Recommended Practice for Monitoring Electric Power Quality, vol. 1995, no. 1. 2009.
- S. Akkaya and Ö. Salor, "Flicker Detection Algorithm Based on the Whole Voltage Frequency Spectrum for New Generation Lamps – Enhanced VPD Flickermeter Model and Flicker Curve," *Electric Power Components and Systems*, vol. 0, no. 0, pp. 1–15, 2022, doi: 10.1080/15325008.2021.2011487.
- S. Akkaya and Ö. Salor, "New flickermeter sensitive to high-frequency interharmonics and robust to fundamental frequency deviations of the power system," *IET Science, Measurement and Technology*, vol. 13, no. 6, 2019, doi: 10.1049/iet-smt.2018.5338.
- S. Akkaya and Ö. Salor, "A new flicker detection method for new generation lamps both robust to fundamental frequency deviation and based on the whole voltage frequency spectrum," *Electronics (Switzerland)*, vol. 7, no. 6, 2018, doi: 10.3390/electronics7060099.
- S. Akkaya and Ö. S. Durna, "Enhanced spectral decomposition method for light flicker evaluation of incandescent lamps caused by electric arc furnaces," *Journal of the Faculty of Engineering and Architecture of Gazi University*, vol. 2018, no. 18–2, pp. 987–1005, 2018, doi: 10.17341/gazimmfd.460497.
- S. Akkaya, "A Review of the Experimental Studies on Analysis of Power Quality Disturbances."
- S. Akkaya, "An Overview of the Empirical Investigations into the Classification of Power Quality Disturbances."
- S. Akkaya, "A Conspectus of PQD Analysis." [Online]. Available: <http://as-proceeding.com/:Konya,Turkeyhttps://www.icaens.com/>

- S. Akkaya, "Empirical Investigations: Power Quality Disturbance Classification." [Online]. Available: <http://as-proceeding.com/:Konya,Turkeyhttps://www.icaens.com/>
- S. Akkaya, E. Yükses, and H. M. Akgün, "A New Comparative Approach Based on Features of Subcomponents and Machine Learning Algorithms to Detect and Classify Power Quality Disturbances," *Electric Power Components and Systems*, 2023, doi: 10.1080/15325008.2023.2260375.
- M. , and S. G. J. Frigo, "FFTW: AN ADAPTIVE SOFTWARE ARCHITECTURE FOR THE FFT," *Proceedings of the International Conference on Acoustics, Speech, and Signal Processing*, vol. 3. pp. 1381–1384, 1998.
- B. Sharpe, "Invertibility of overlap-add processing-STFT-accessed Dec 2023", Accessed: Dec. 02, 2023. [Online]. Available: <https://gauss256.github.io/blog/cola.html>
- J. M. Lilly, "Element analysis: A wavelet-based method for analysing time-localized events in noisy time series," *Proceedings of the Royal Society A: Mathematical, Physical and Engineering Sciences*, vol. 473, no. 2200, Dec. 2017, doi: 10.1098/rspa.2016.0776.
- J. Bedi and D. Toshniwal, "Empirical Mode Decomposition Based Deep Learning for Electricity Demand Forecasting," *IEEE Access*, vol. 6, pp. 49144–49156, Dec. 2018, doi: 10.1109/ACCESS.2018.2867681.
- N. E. (Norden E. Huang and S. S. Shen, *Hilbert-Huang transform and its applications*, 2nd Edition. Interdisciplinary Mathematical Sciences, WORLD SCIENTIFIC, 2014.
- Y. Guo et al., "A hilbert-huang transform-based traffic estimation algorithm to power line communications," in *Proceedings - IEEE International Conference on Industrial Internet Cloud, ICII 2019*, Institute of Electrical and Electronics Engineers Inc., Dec. 2019, pp. 132–137. doi: 10.1109/ICII.2019.00035.

Chapter 30

Numerical Analysis of the Effects of Different Fin Geometries on the Performance of Thermoelectric Modules in Channel Configurations

Ali TAŞKIRAN¹

İhsan DAĞTEKİN²

Celal KISTAK³

Nevin ÇELİK⁴

Abstract

Channel flow is frequently encountered in engineering applications. It is utilized in various places where fluid movement occurs, such as in the cooling of electronic devices, heat exchangers, and the heating and cooling of buildings. Therefore, channel flow has attracted the attention of many researchers. One of the methods intensively used in enhancing heat transfer in today's technology is the use of extended heat transfer surfaces. Finned surfaces increase heat and mass transfer through the augmentation of surface area and flow turbulence.

In this study, air was sent into a channel at different velocities ($V = 5$ m/s, 10 m/s, and 15 m/s), and six different types of fins were placed in these channels, namely square, serrated square, circular, serrated circular, flat plate, and serrated flat plate fins, to investigate flow and heat transfer. Among these fin structures, the fin with a high heat transfer coefficient had a thermoelectric module placed on its lower surface. The thermoelectric module facilitated heat transfer in the fin by conducting heat through the fin to the hot surface of the thermoelectric module. The other surface of the thermoelectric module was adjusted to the ambient temperature at 22°C. Results were obtained for channel flow and thermoelectric parameters using Fluent and ANSYS, including temperature,

¹ Arş. Gör. Dr.; Şırnak Üniversitesi Mühendislik Fakültesi Makine Bölümü.
taskiranalii@gmail.com ORCID No: 0000-0001-6810-7291

² Prof. Dr.; Fırat Üniversitesi Mühendislik Fakültesi Makine Bölümü. idagtekin@firat.edu.tr
ORCID No: 0000-0003-0128-7149

³ Arş. Gör. Dr.; Fırat Üniversitesi Mühendislik Fakültesi Makine Bölümü. ckistak@firat.edu.tr
ORCID No: 0000-0003-4621-5405

⁴ Prof. Dr.; Fırat Üniversitesi Mühendislik Fakültesi Makine Bölümü. nevincelik23@gmail.com
ORCID No: 0000-0003-2456-5316

streamlines, pressure, Nusselt, Reynolds, empirical equations, flow, and heat flux.

In light of the numerical results, it was found that the best heat transfer among the six different fin structures occurred in the square fin. The heat transfer coefficient of the square fin was $625 \text{ W/m}^2\text{K}$, while other fin structures varied between 580 and $600 \text{ W/m}^2\text{K}$. Among all fin structures, the best heat transfer occurred at velocities of 15 m/s , 10 m/s , and 5 m/s , respectively. Temperatures varied between 470 and 526 K for different velocities. In comparing the thermoelectrics placed under the fins, the thermoelectric used in the serrated flat plate fin structure exhibited the best physical properties. The temperature, heat flux, current, and results of heat for the thermoelectric were found to be 249.09°C , 9.1852 W/mm^2 , 103.15 mA , and 155.58 W , respectively.

Keywords: Channel flow, fin, heat sink, thermoelectric, numerical simulation.

I. INTRODUCTION

In engineering applications, channel flow is frequently encountered, being used in various scenarios involving fluid movements, such as the cooling of electronic devices, heat exchangers, and the heating and cooling of buildings. The enhancement of heat transfer within duct flows is a common challenge in engineering, necessitating continuous improvement. This is especially critical for the efficient cooling of electronic devices and turbine blades, as it directly impacts their performance. One prevalent method in today's technology for augmenting heat transfer is the utilization of extended heat transfer surfaces, such as finned surfaces. These surfaces play a crucial role in expanding the surface area and intensifying the convective heat and mass transfer turbulence within the flow. Fins have diverse applications, and one notable example is their use in thermoelectric generators to regulate the temperature of small volumes.

Thermoelectric generators harness the thermoelectric effect, also referred to as the Peltier effect, which arises from the characteristics of thermoelectric materials experiencing temperature differentials, enabling the conversion of heat energy into electrical energy. The key components of thermoelectric generators are typically interconnected n-type and p-type semiconductor materials, forming thermoelectric modules. These materials exploit the temperature gradient between hot and cold surfaces to generate electric potential. The principle of operation is based on the concept that one surface remains cold while the other generates heat. This mechanism utilizes the temperature gradient between the hot and cold regions to generate electric potential across the thermoelectric modules.

Due to their ability to operate quietly and quickly, thermoelectric generators are attracting attention, especially in applications with low power requirements and energy recovery projects. In general, a thermoelectric generator is typically composed of a series-connected array of semiconductor elements that are electrically and thermally interconnected in parallel. While a single piece of semiconductor material is theoretically adequate, a series connection is commonly employed to fulfill the high voltage potential needs. To ensure that the carriers are transported in the same direction, p-type and n-type elements are arranged alternately within the setup (Jang and others, 2013).

In a comprehensive survey of the literature, (Tsai and others, 2010) conducted analyses across a range of parameters. They examined four different Reynolds numbers (10000, 20000, 30000, and 40000), three distinct fin sizes (30, 45, and 75 mm), and seven different angle values (45, 60, 75, 90, 105, 120, and 135). For fins with a short wing height of 30 mm, it was observed that increasing the bending angle led to an increase in thermal resistance. Moreover, as the Reynolds number increased from 100 to 100, and the bending angle varied from 45 to 135 degrees, the thermal resistance exhibited a 10% change. Furthermore, it was noted that increasing the thermal resistance was associated with a decrease in pressure. (Karabulut and others, 2013) conducted a numerical investigation aimed at enhancing heat transfer in heat exchangers by examining two different types of wings. They employed a steady-state solution using ANSYS Fluent 3D Navier-Stokes simulations. In their study, for a Reynolds number (Re) of 400, the inlet velocities of the hot and cold air were set at 0.69 m/s and 1.338 m/s, respectively. These conditions were established for inlet temperatures of 300 K and 600 K, respectively. (Jonsson and Moshfegh, 2001) conducted experimental research in a channel tunnel, focusing on heat sinks with seven different types of fins, including plate, strip, and pin fins. They designed and tested a total of 42 different heat sinks, each with a width of 52.8 and varying heights of 10, 15, and 20 for the fins. Their study aimed to establish empirical correlations that illustrate the impact of heat and hydraulic performance on heat receivers. The research covered a range of Reynolds numbers (Re) from 2000 to 16500 and considered different values of fin height relative to the channel height (H / CH), including 1, 0.67, and 0.33. Through their experimentation, they examined how these various factors affected the performance of the heat sinks. Yang et al. systematically explored the impact of heat sink density on heat transfer performance, scrutinizing twelve distinct configurations that included various cross-sectional shapes (circular, elliptical, and square) arranged in both in-line and staggered orientations. Their rigorous analysis revealed that staggered configurations outperformed other arrangements concerning heat transfer coefficients in the

context of pin fin heat sinks, whereas elliptical pin fins were associated with comparatively reduced pressure losses (Yang and others, 2007). This study presents a waste heat recovery simulation technology developed by (Chen and others, 2020) for industrial chimneys. The Thermoelectric Module (TEM) is modeled as a heat sink, utilizing Computational Fluid Dynamics (CFD) and TEM integration. The investigation evaluates the impact of Reynolds number, convection heat transfer coefficient at the cold surface, flue gas inlet temperature, dual TEM, and channel geometry on TEM system performance. Results show that increasing Reynolds number, flue gas inlet temperature, and convection heat transfer coefficient at the cold surface improve TEM performance. In the dual TEM system, the leading TEM performs similarly to a single TEM, while the dual system achieves an additional 43% power.

However, the output power of the trailing TEM decreases by 57%. Modifying channel geometry ($Re = 1,000$) increases TEM output power by 53.5% and efficiency by 25.2%.

Erturun et al. investigated the power generation performance of thermoelectric devices and assessed the potential thermomechanical effects on different thermoelectric leg geometries. They conducted finite element analyses in ANSYS for thermoelectric models with various leg shapes (rectangular prism, trapezoidal prism, cylinder, and octagonal prism) under different temperature gradients (100°C and 300°C). The materials used for the TEG included bismuth telluride and bismuth telluride/cobalt lead. Notably, at 100°C , the maximum stresses for rectangular and cylindrical legs were 49.9 MPa and 43.3 MPa, and at a temperature gradient of 300°C , these values increased to 94.2 MPa and 85.7 MPa, respectively (Erturun and others, 2014). In their study (Erturun and Mossi, 2015) explored the thermomechanical effects on thermoelectric devices, focusing on the impact of different leg structures on power production performance. They developed four distinct designs, including original, rotated, and coaxial-leg configurations. The results revealed that in the concentric leg structure, the maximum temperature decreased by 10%, while the conversion efficiency increased by 7%. In the case of the rotating configuration, thermal resistance decreased by 1.2%, and transport efficiency improved by 0.3%. In their studies, (Quan and others, 2024) propose a polygonal heat exchanger with sickle-shaped fins to enhance the utilization efficiency of exhaust gas in thermoelectric generator (TEG) systems. Demonstrating the effectiveness of embedded sickle fins through the development and validation of a unified fluid-thermal-electric multiphysics numerical model, the researchers identify optimal parameters for maximizing TEG performance. These parameters include a linear fin length of 180 mm, height of 45 mm, arc fin radius of 305 mm, and an end angle of 8° .

Under these specified conditions, the configuration achieves impressive results with an output power of 116.59 W, a temperature uniformity coefficient of 0.99, and a pressure drop of 845 Pa.

Rabari et al. constructed a two-dimensional thermoelectric generator (TEG) system utilizing a nanostructured thermoelectric semiconductor material. The system incorporated p-type nanostructured bismuth antimony tellurium (BiSbTe) and n-type bismuth tellurium (Bi_2Te_3) with the addition of 0.1% by volume of silicon carbide (Rabari and others, 2014). (Liu and others, 2022) conducted an investigation into the efficiency of a waste heat recovery (WHR) system utilizing a thermoelectric generator (TEG) within a bronze ingot casting mold. The integration of a rectangular plate fin heat sink on the TEG's hot side was employed to capture waste heat emitted from the casting mold, with the flue gas flowing perpendicularly to the fin base. The study systematically analyzes the impact of various fin parameters (fin height and number) and flue gas conditions (inlet velocity and temperature) on the TEG system's performance during WHR. Notably, the results indicate a discernible increase in TEG module power with higher fin height, blade number, inlet flue gas velocity, and temperature.

The principal objective of this research is to investigate the impact of square fin structures within a channel on flow dynamics and heat transfer under varying air velocity conditions, specifically at 5, 10, and 15 m/s, while maintaining an elevated air temperature of 573 K. Additionally, the study aims to evaluate the performance of a thermoelectric module integrated beneath the square fin structures. A diverse set of parameters, including temperature, Nusselt number, Reynolds number, electrical current, heat flow, and thermoelectric properties, will be rigorously examined to provide a comprehensive analysis. It is anticipated that numerical simulations will offer invaluable insights into the heat transfer characteristics of square fins at different air velocities, providing a nuanced understanding of their thermal behavior. In summary, this research seeks to offer an in-depth understanding of how square fins can significantly enhance thermal performance and promote energy efficiency. The findings hold significant promise for various engineering applications where optimizing heat transfer and energy conversion are of paramount importance.

II. MATHEMATICAL MODEL AND NUMERICAL METHOD

Figure 1 presents the schematic diagram illustrating the geometry and computational domain. The simulation of thermal and turbulent flow fields involved the application of numerical solutions to solve the turbulent three-dimensional Navier–Stokes and energy equations, along with the continuity equation. The model incorporated an eddy viscosity model to account for

turbulence effects. Assumptions included steady, incompressible, and three-dimensional flow conditions. Buoyancy and radiation heat transfer effects were neglected, and the thermophysical properties of the fluid were treated as constants. The governing equations for mass, momentum, turbulent kinetic energy, turbulent energy dissipation rate, and energy in the steady turbulent main flow utilized the standard k-ε model, as outlined by (Yang and Peng, 2009):

Continuity equation

$$\frac{\partial \rho u_i}{\partial x_i} = 0 \quad (2.1)$$

Momentum equation

$$\rho u_j \frac{\partial u_i}{\partial x_j} = -\frac{\partial P}{\partial x_i} + \frac{\partial}{\partial x_j} \left[\mu_t \left(\frac{\partial u_i}{\partial x_j} + \frac{\partial u_j}{\partial x_i} \right) \right] \quad (2.2)$$

Energy equation

$$\rho u_j \frac{\partial T}{\partial x_j} = \frac{\partial}{\partial x_j} \left[\left(\frac{\mu_L}{\sigma_L} + \frac{\mu_t}{\sigma_t} \right) \frac{\partial T}{\partial x_j} \right] \quad (2.3)$$

Transport equation for k

$$\rho u_j \frac{\partial k}{\partial x_j} = \frac{\partial}{\partial x_j} \left(\frac{\mu_t}{\sigma_k} \frac{\partial k}{\partial x_j} \right) + \mu_t \left(\frac{\partial u_i}{\partial x_j} + \frac{\partial u_j}{\partial x_i} \right) \frac{\partial u_i}{\partial x_j} - \rho \varepsilon \quad (2.4)$$

Transport equation for ε

$$\rho u_j \frac{\partial \varepsilon}{\partial x_j} = \frac{\partial}{\partial x_j} \left(\frac{\mu_t}{\sigma_\varepsilon} \frac{\partial \varepsilon}{\partial x_j} \right) + c_1 \mu_t \frac{\varepsilon}{k} \left(\frac{\partial u_i}{\partial x_j} + \frac{\partial u_j}{\partial x_i} \right) \frac{\partial u_i}{\partial x_j} - c_2 \rho \frac{\varepsilon^2}{k} \quad (2.5)$$

The empirical constants appear in the above equations are given by the following values [9]:

$$c_1 = 1.44, c_2 = 1.92, c_\mu = 0.09, \sigma_k = 1, \sigma_\varepsilon = 1.3, \sigma_t = 0.7$$

The model solution incorporates several key assumptions. Firstly, a three-dimensional analysis was conducted to accurately represent the intricate nature of turbulent flow. The fluid was assumed to exhibit Newtonian behavior, a common simplification in fluid dynamics. Additionally, a gravitational force of -9.81 m/s² was applied in the negative Y-axis direction to account for gravitational effects. The solution was assumed to be in a steady state, implying that both flow and thermal conditions remained constant over time. Lastly, the k-ε turbulence model was employed, utilizing the realizable formulation to enhance the representation of turbulent flow characteristics within the system.

III. RESULT AND DISCUSSION

A. Validation and verification

In order to validate the accuracy of the numerical findings in the present study, a reference study was employed for comparison. The primary focus of this comparison was to assess the precision of the simulated path and the consistency of the obtained results with the reference study. Two specific aspects were considered in this comparative analysis. Firstly, the thermal resistance and Reynolds number of the square fin within the channel were compared, as illustrated in Figure 1. Additionally, the temperature variation within the internal structure of the thermoelectric element, as depicted in Figure 2, was another subject of comparison. The outcome of these comparisons revealed that the results obtained in this study closely aligned with those from the reference work. Consequently, it can be concluded that the numerical methodology employed in this study is indeed accurate and reliable.

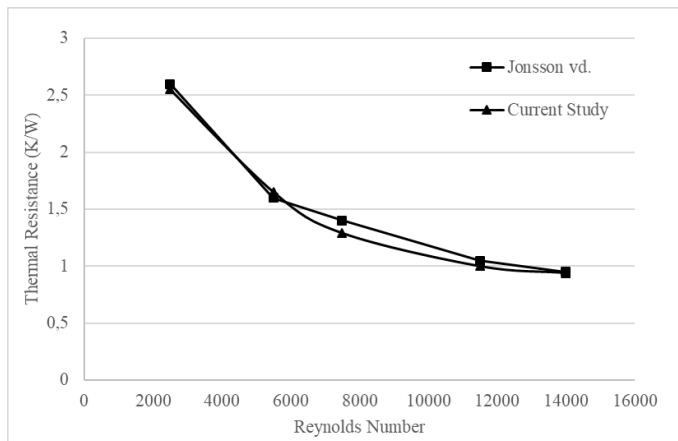


Figure 1. Literature comparison with current study for channel flow (Jonsson and Moshfegh, 2001)

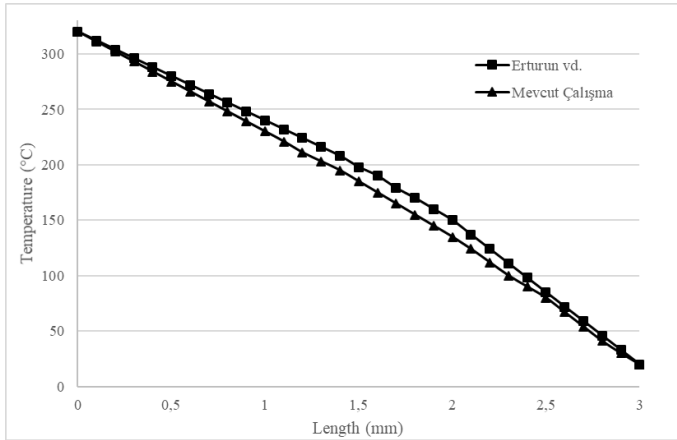


Figure 2. Literature comparison of the thermoelectric structure with the current study (Erturun and others, 2014).

B. Module geometries and material properties

The square fin, measuring 40x40x12 mm in dimensions, is constructed from copper material, and its fin structures have a width of 2x2 mm. Positioned at approximately 210 mm from the channel's edge, it is situated in the center of the channel, as depicted in Figures 3, 4, 5. The overall geometry incorporates a copper plate with dimensions of 50x50x500 mm and a thickness of 2 mm.

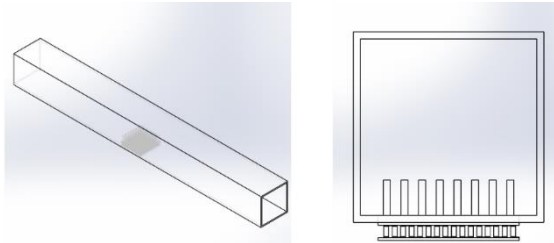


Figure 3. Geometric features of model

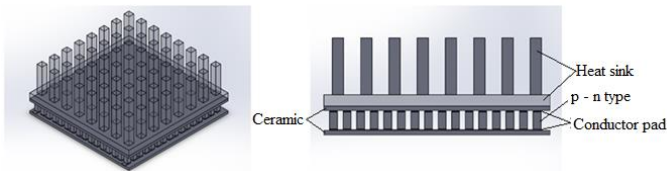


Figure 4. Schematic representation of the fin and thermoelectrics

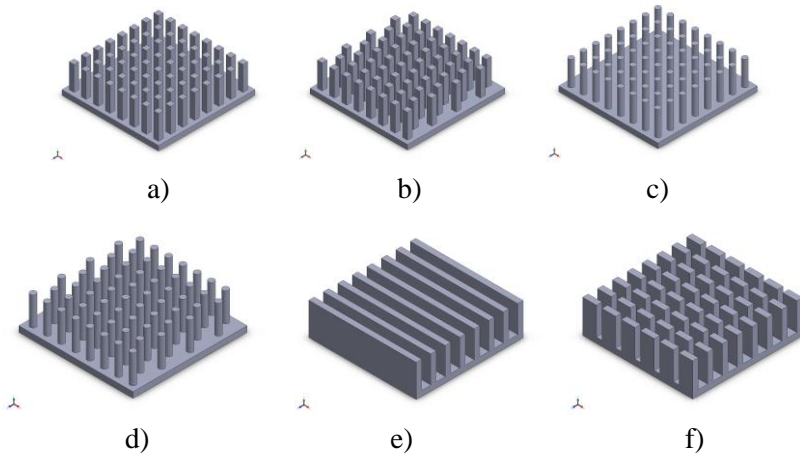


Figure 5. The fin structures utilized in the study include: a) Square fin b) Serrated square fin c) Circular fin d) Serrated circular fin e) Flat plate fin f) Serrated flat plate fin

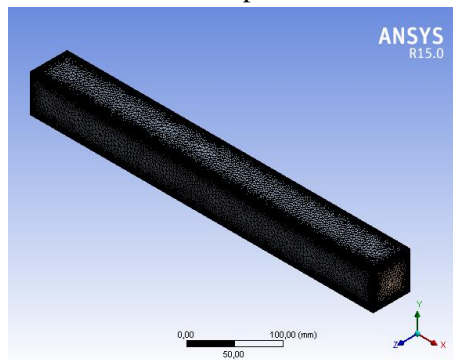


Fig. 6. Mesh structure of model.

After establishing the geometry and mesh structure, the subsequent step involves specifying the boundary conditions essential for the FLUENT simulation and defining the pertinent fluid properties, as illustrated in Figures 6 and 7. In this particular investigation, the incoming air intended for the channel was assumed to have an initial temperature of 573 K. Both the channels and fins were constructed using copper as the material of choice, aligning with the overall design and configuration.

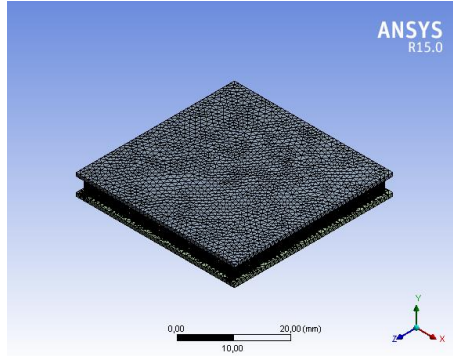


Fig. 7. Thermoelectric mesh structure.

The characteristics of the semiconductors within the thermoelectric module are provided in Table 1. Bismuth telluride (Bi_2Te_3) has been employed as both the p-type and n-type semiconductor materials for this study. A total of 256 semiconductor elements, each with a square geometry measuring $1.4 \times 1.4 \times 3$ mm, were distributed on a 40×40 mm plate.

Table 1: The physical properties of p-n semiconductor materials are detailed in (Erturun and others, 2014).

	p-type semiconductor	n-type semiconductor	Copper	Ceramic (Al_2O_3)	Binding (63Sn-37Pn)
Density (kg/m^3)	6858	7858	8940	3970	8420
Thermal conductivity (W/mK)	5.24	3.5	382	17.2	40
Seebeck Coefficient (V/K)	16.8×10^{-6}	-16.8×10^{-6}	17.6×10^{-6}	6.5×10^{-6}	24×10^{-6}
Electrical Resistivity (Ωm)	25×10^{-6}	9.8×10^{-6}	0.38×10^{-6}	1×10^{12}	0.23×10^{-6}

Copper plates were mounted onto a ceramic plate measuring $40 \times 40 \times 0.8$ mm. These copper plates serve to establish conductivity between the p-n semiconductors. The copper plates have dimensions of $3.8 \times 1.4 \times 0.15$ mm. A connector (63Sn-37Pn) with dimensions of $1.4 \times 1.4 \times 0.1$ mm is used between the copper plate and the p-n semiconductors. The physical properties of the copper, ceramic, and connectors used in the thermoelectric module are provided in Table 1.

C. Performance comparison of square fin

In this study, an experimental setup was designed where air at an initial temperature of 573 K was introduced into a channel at varying velocities of 5, 10, and 15 m/s. Within the channel, a square fin structure was integrated and subsequently modeled for a detailed numerical analysis. The temperature distribution for the square fin under these three distinct flow velocities is visually represented in Figure 8.

It's observed that the temperature of the fluid introduced into the channel decreases as the flow velocity decreases. Moreover, the temperature values within the fin exhibit a decreasing trend from the upper regions that come into contact with the lower surface. For instance, at a flow velocity of 5 m/s, the fin reaches a minimum temperature of 472 K. Consequently, it can be inferred that the heat transfer rate increases with rising flow velocity.

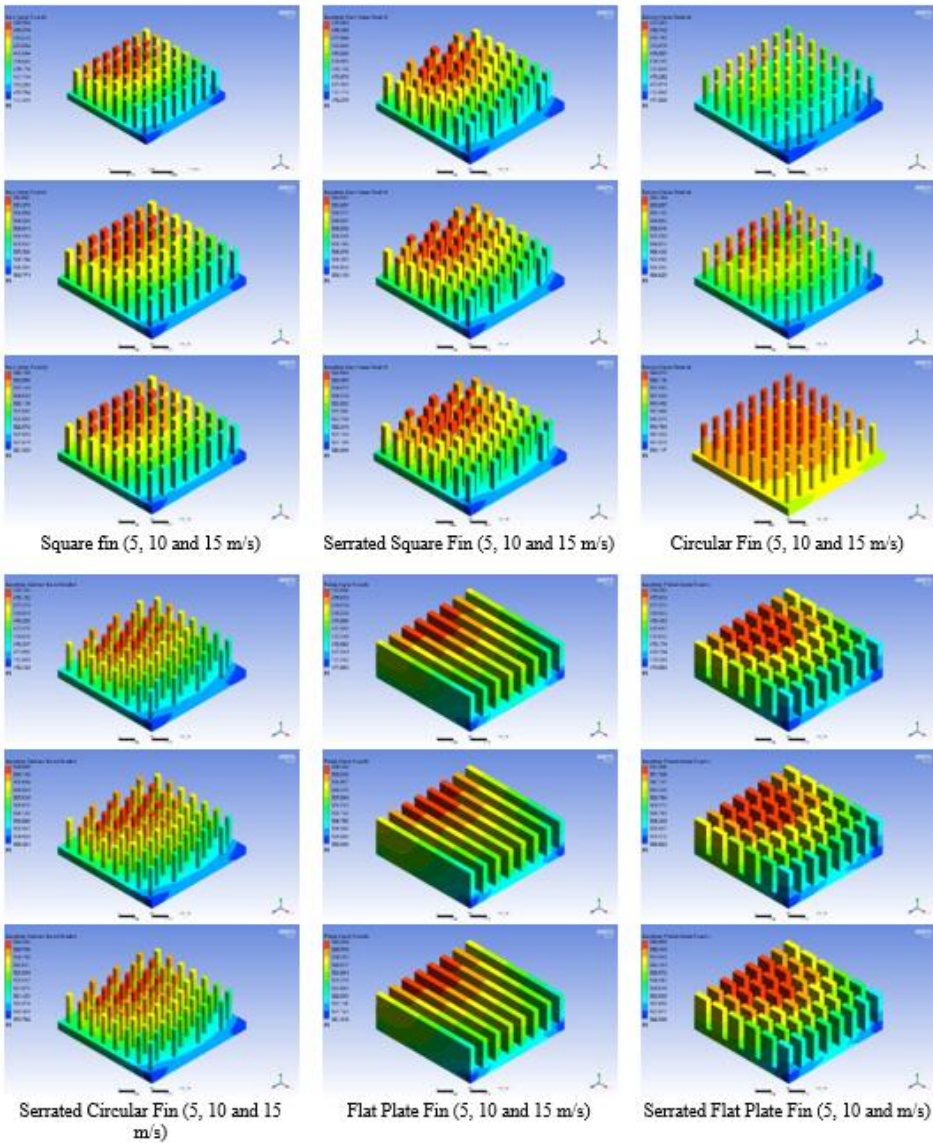


Fig. 8. Temperature distribution of six different fin types based on velocities

In Figure 9, the temperature variation along the channel for a square fin, contingent on the Reynolds number, is depicted. Initially, the air's temperature, at 573 K, undergoes a reduction over a certain length, dependent on the Reynolds number. Subsequently, the temperature remains relatively stable within the 100 - 200 mm region. This stability arises from the uniformity of temperature since the flow encounters no obstacles until it reaches this channel section.

However, once it interacts with the square fin located in the channel, a noticeable temperature rise and decline are observed within the fluid. After passing the fin, the temperature remains consistent and is contingent on the Reynolds number. Depending on the initial temperature, the curve illustrates the lowest temperature drop at $Re = 5247.1$ and the highest temperature drop at $Re = 15741.3$. Notably, the square fin exhibits the most significant temperature increase among the various fin configurations. Figure 10 presents the change in the Nusselt number along the channel for the square fin, relative to the Reynolds number.

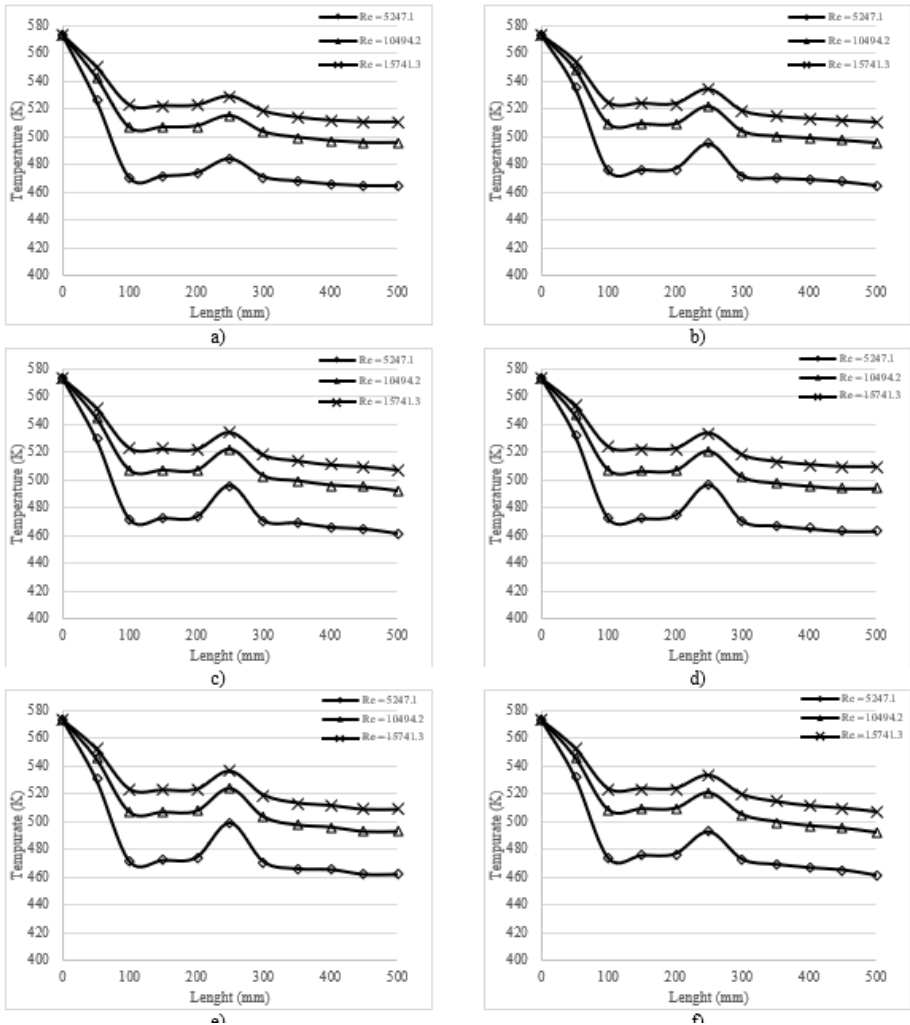


Fig. 9. Variation of temperature across the canal for different Reynolds numbers a) Square fin b) Serrated square fin c) Circular fin d) Serrated circular fin e) Flat plate fin f) Serrated flat plate fin

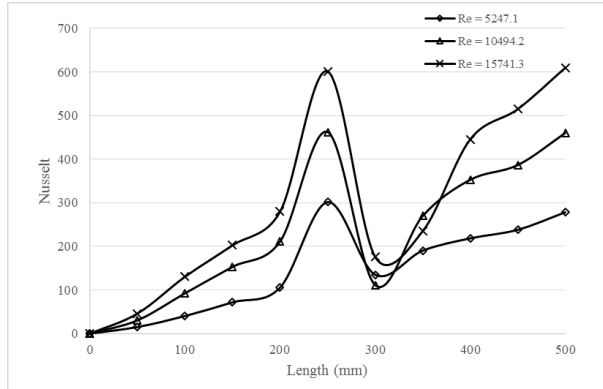


Fig. 10. For different Reynolds numbers, change the local Nusselt numbers along the channel

Figure 11. illustrates the variation of Reynolds-Nusselt numbers for different fin structures. For square, circular, and flat plate fins, the Nusselt number, as a function of Reynolds number, is minimum for flat plate fins. For square and circular fins, the Nusselt number exhibits nearly linear growth. Across all fin structures, an increase in Reynolds number leads to an escalation in the Nusselt number. This correlation arises from the rise in internal energy, and consequently temperature, associated with the increased flow velocity at higher Reynolds values. Similarly, when serrated fins are compared, the least increase is observed in serrated flat plate fins, while the most significant increase is noted in serrated square fins.

Upon comparison of the two graphs, it becomes evident that the most substantial increases occur in square and serrated square fins. At $Re = 15741.3$, the Nusselt values for square and serrated square fins are approximately 550 and 580, respectively. At $Re = 10494.2$, the Nusselt values for square and serrated square fins are around 425 and 445, respectively. At $Re = 5247.1$, the Nusselt values for square and serrated square fins are approximately 275 and 280, respectively.

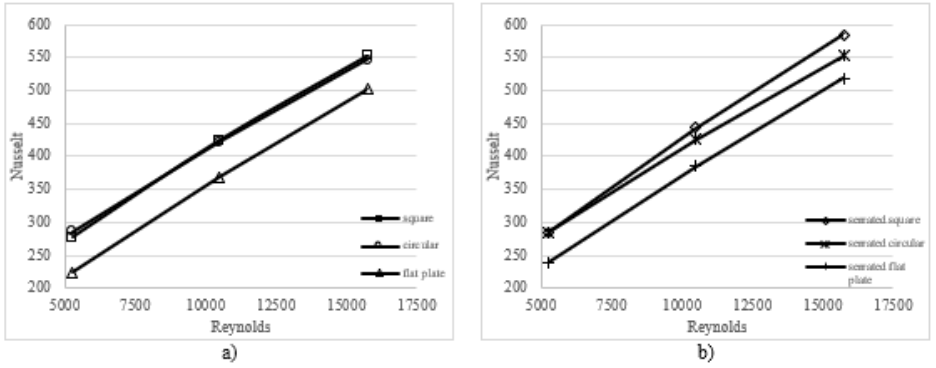


Figure 11. Variation of Reynolds - Nusselt numbers for different fin designs

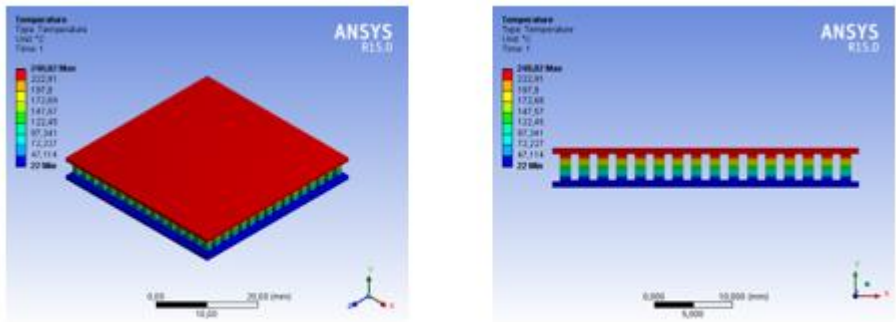


Fig. 12. Temperature distribution of thermoelectric for square fin

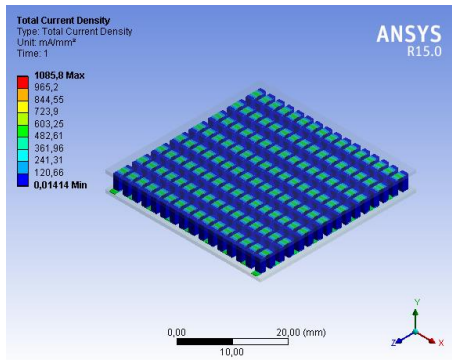


Figure 13. Current distribution of thermoelectric for square fin

The numerical results of the thermo electrical for square fin in ANSYS thermal - electricity are shown in Table 2. The result for thermoelectricity placed

under square fin founded $Re = 15741.3$. Figure 12 and 13 show the temperature and current distribution for the square fin. The results are presented as a table.

Table 2. Numerical results of thermoelectricity for square and staggered square fin

	Temperature (°C)	Heat Flux (W/mm ²)	Current (mA)	Heat (W)
Square fin (5 m/s)	199.3	7.1718	79.375	121.46
Square fin (10 m/s)	232.76	8.5248	95.35	144.39
Square fin (15 m/s)	248.02	9.1422	102.64	154.85
Serrated Square Fin (5 m/s)	199.2	6.693	79.31	121.35
Serrated Square Fin (10 m/s)	232.36	8.5088	95.161	144.11
Serrated Square Fin (15 m/s)	247.62	9.1259	102.45	154.57
Circular Fin (5 m/s)	198.45	7.1372	78.967	120.87
Circular Fin (10 m/s)	231.79	8.532	94.889	143.72
Circular Fin (15 m/s)	247.23	9.1101	102.26	154.3
Serrated Circular Fin (5 m/s)	199.38	7.1748	79.411	121.51
Serrated Circular Fin (10 m/s)	231.21	8.4622	94.61	143.32
Serrated Circular Fin (15 m/s)	246.73	9.09	102.02	153.96
Flat Plate Fin (5 m/s)	198.83	7.1525	79.148	121.13
Flat Plate Fin (10 m/s)	232.58	8.5178	95.267	144.27
Flat Plate Fin (15 m/s)	248.33	9.1545	102.78	155.06
Serrated Flat Plate Fin (5 m/s)	202.82	7.2333	80.101	122.5
Serrated Flat Plate Fin (10 m/s)	233.85	8.569	95.871	145.13
Serrated Flat Plate Fin (15 m/s)	249.09	9.1852	103.15	155.58

The empirical equations for Nusselt and Reynolds numbers are provided in Table 3. The coefficients 'a' and 'b' for the empirical equation $Nu = a \cdot Re^b$ were determined by formulating a corresponding Excel formula. The results indicate a close convergence criterion (R^2 approximately equal to 1), affirming the accuracy and reliability of the obtained outcomes.

Table 3. The empirical equations for Nusselt and Reynolds numbers are as follows:

	a	b	R^2
Square fin	1.2817	0.6275	0.9998
Serrated Square Fin	1.0588	0.653	0.9998
Circular Fin	1.8986	0.585	0.999
Serrated Circular Fin	1.6688	0.5998	0.999
Flat Plate Fin	0.4224	0.7322	0.9998
Serrated Flat Plate Fin	0.5808	0.7024	0.9997

IV. CONCLUSIONS

In this study, the investigation involved introducing air into a channel at different velocities ($V = 5 \text{ m/s}$, 10 m/s , and 15 m/s) and placing six distinct fins—square, serrated square, circular, serrated circular, flat plate, and serrated flat plate fins. A thermoelectric module was strategically positioned on the lower surface of the fin structures. By utilizing Fluent and thermal-electric parameters within ANSYS, various parameters such as temperature, streamlines, pressure, Nusselt, Reynolds, empirical equations, flow, and heat flux were meticulously examined for both channel flow and thermoelectric considerations.

The findings revealed that among the six different fin structures, the square fin exhibited the most efficient heat transfer, with a heat transfer coefficient of $625 \text{ W/m}^2\text{K}$, while other fin structures ranged from 580 to $600 \text{ W/m}^2\text{K}$. The assessment of all fin structures indicated that optimal heat transfer occurred at velocities of 15 m/s , 10 m/s , and 5 m/s , respectively. For the square fin, temperature values varied between 476.934 and 526.169 K for different velocities, demonstrating a 5% increase compared to other fin structures.

The velocity distribution in the channel influenced the pressure, ranging from approximately 11 Pa at 5 m/s to 90 Pa at 15 m/s . Results pointed to the highest temperature, pressure, and heat transfer coefficient transpiring at a Reynolds number of 15741.3. When comparing thermoelectric modules positioned under the fins, the serrated flat plate fin structure exhibited the most favorable physical characteristics. The thermoelectric module demonstrated a temperature of 249.09

°C, heat flux of 9.1852 W/mm^2 , current of 103.15 mA , and heat output of 155.58 W .

While the study primarily focused on a single fin and thermoelectric structure, potential improvements in results could be achieved by strategically placing fins at different locations. Furthermore, alterations to the internal geometry and p-n semiconductor materials of the thermoelectric module hold the potential to yield diverse outcomes.

REFERENCES

- Chen, W. H., Lin, Y. X., Chiou, Y. Bin, Lin, Y. L., and Wang, X. D., (2020). A computational fluid dynamics (CFD) approach of thermoelectric generator (TEG) for power generation: *Applied Thermal Engineering*, 173, 115203.
- Erturun, U., Erermis, K., and Mossi, K., (2014). Effect of various leg geometries on thermo-mechanical and power generation performance of thermoelectric devices: *Applied Thermal Engineering*, 73, 128–141.
- Erturun, U., and Mossi, K., (2015). Thermoelectric devices with rotated and coaxial leg configurations: Numerical analysis of performance: *Applied Thermal Engineering*, 85, 304–312.
- Jang, J. Y., Tsai, Y. C., and Wu, C. W., (2013). A study of 3-D numerical simulation and comparison with experimental results on turbulent flow of venting flue gas using thermoelectric generator modules and plate fin heat sink: *Energy*, 53, 270–281.
- Jonsson, H., and Moshfegh, B., (2001). Modeling of the thermal and hydraulic performance of plate fin, strip fin, and pin fin heat sinks - Influence of flow bypass: *IEEE Transactions on Components and Packaging Technologies*, 24, 142–149.
- Karabulut, K., Buyruk, E., Kılınç, F., and Karabulut, Ö., (2013). Farklı geometrilerden oluşan kanatçıklı plakalı ısı değiştiricileri için ısı transferinin üç boyutlu sayısal olarak incelenmesi. *Tesisat Mühendisliği*, 35–48.
- Liu, J., Yadav, S., and Kim, S. C., (2022). Performance of a thermoelectric generator system for waste heat recovery utilizing plate fin heat sink in bronze ingot casting industry: *Case Studies in Thermal Engineering*, 38, 102340.
- Quan, R., Wang, J., Liang, W., Li, X., and Chang, Y., (2024). Numerical investigation of a thermoelectric generator system with embedded sickle-shaped fins: *Applied Thermal Engineering*, 236, 121741.
- Rabari, R., Mahmud, S., and Dutta, A., (2014). Numerical simulation of nanostructured thermoelectric generator considering surface to surrounding convection: *International Communications in Heat and Mass Transfer*, 56, 146–151.
- Tsai, G. L., Li, H. Y., and Lin, C. C., (2010). Effect of the angle of inclination of a plate shield on the thermal and hydraulic performance of a plate-fin heat sink: *International Communications in Heat and Mass Transfer*, 37, 364–371.

- Yang, K. S., Chu, W. H., Chen, I. Y., and Wang, C. C., (2007). A comparative study of the airside performance of heat sinks having pin fin configurations: *International Journal of Heat and Mass Transfer*, 50, 4661–4667.
- Yang, Y. T., and Peng, H. Sen, (2009). Investigation of planted pin fins for heat transfer enhancement in plate fin heat sink: *Microelectronics Reliability*, 49, 163–169.

Chapter 31

Energy Saving Potentials in Compressed Air Systems

Ergün KORKMAZ¹

ABSTRACT

Compressed air is a highly inefficient process due to the irreversibility of its extraction. In this study, the system components used in compressed air production, process details, and energy-saving potentials are analysed in detail. The place and importance of air leaks and compressor waste heat in saving potentials are emphasized. The study also outlined measures and recommendations that could be taken to increase efficiency in pressure air systems.

Keywords – Compressed air systems, Energy efficiency, Compressors, Energy saving, Pneumatic systems

INTRODUCTION

The industry extensively uses Compressed Air Systems (CASs) because of their excellent portability, safety, purity, cleanliness, storage capacity, and user-friendliness. Between 10% and 30% of the energy used reaches the point of final usage, making them one of the priciest energy sources. Energy loss occurs from heat, leaks, pressure drops, and mishandling. Installing energy efficiency measures in CASs to reduce energy usage and greenhouse gas emissions is crucial.

CASs are one of the most expensive energy storage methods and have a wide range of uses in industry. Air compressors utilize an important portion of the electricity used in industry. In many different sectors, air compressors are utilized to meet instrumentation requirements, power pneumatic tools and equipment, and supply process requirements. Only 10–30% of the energy is used up at the end-use point, with the remaining 70–90% of the prime mover's power being wasted as heat energy and lost to noise, friction, and misuse. Compressed air is an important input used in various stages of production in industrial plants. In the automotive industry, air pressure is the fourth major input facilitating manufacturing processes, after water, electricity, and natural gas (Yuan et al.,

¹ Asst. Prof. Dr.; Isparta University of Applied Sciences, Faculty of Technology, Department of Mechanical Engineering, 32260, Çünür, Isparta, Türkiye. ergunkorkmaz@isparta.edu.tr ORCID No: <https://orcid.org/0000-0003-0565-5914>

2006:293). Furthermore, compressed air accounts for 10% of EU industrial electricity use (Saidur et al., 2010:1135).

Air compressors are among the largest motorized systems in industrial plants. Generally speaking, the highest electricity consumption among industrial motor systems occurs on the side of compressed air systems, following systems connected to pumping and manufacturing machines. Thus, given the high energy consumption, compressed air systems are a priority among the efforts to improve energy efficiency. Energy-saving opportunities range from low-cost/free measures to long-term investment projects for compressed air systems. Industrial users can choose their preferred energy-saving measures from among these energy-saving opportunities, depending on their targeted economic criteria and the availability of their budgets.

The reason for the widespread use of compressed air in the industry is that it is a suitable and flexible power source and Pressure, especially for production processes. Pneumatic equipment can be an alternative to motorized equipment due to lower initial investment costs and lack of maintenance and replacement needs. Pneumatic equipment is widely preferred in environments with flammable substances, which can cause fire because they do not contain electric current. While the energy efficiency is lower, the absence of alternatives in some applications, such as molding, makes high-pressure air one of the main components of the production process. The compressed air industry has many applications, such as pneumatic hand tools, air cylinders and motors, air jets, ventilation and mixing processes, blow molding, air nozzles, and energy storage.

With an average return on investment of less than two years, energy efficiency methods include lowering air inlet temperature, recovering residual heat from the air compressor, lowering compressor pressure, and reducing leakage can result in energy savings of 20% to 60%. (Hernandez et al., 2010:414). Furthermore, detecting and resolving leaks and shutting off compressors when not in use can result in significant cost savings (Kaeser, 2023:29). In conclusion, implementing energy efficiency measures in CASs can save energy and reduce greenhouse gas emissions.

The distribution that results from breaking down the costs into terms of the compressor is depicted in Fig 1. It is commonly known that the approximate sales cost is equivalent to the running costs of a compressor for a year. Consequently, long-term running costs and short-term compressor investment expenditures should be carefully considered. The compressor's costs were assessed over a ten-year operating period and displayed in the graphic seen in Fig 1. 73% of the cost is made up of energy costs, even though the compressor's sales cost is only 18%.

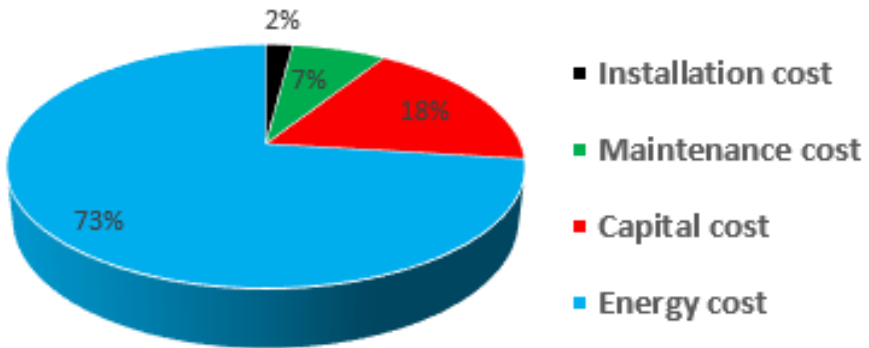


Figure 1: Compressor expenses for a ten-year lifespan (Carbon Trust, 2014:5)

BASIC ELEMENTS OF COMPRESSED AIR SYSTEMS

The compressed air system consists of basic components such as a compressor, a cooler, a dryer, an air storage tank, a filter, and a regulator. Fig 2 shows the basic elements of the industrial pressure air system.

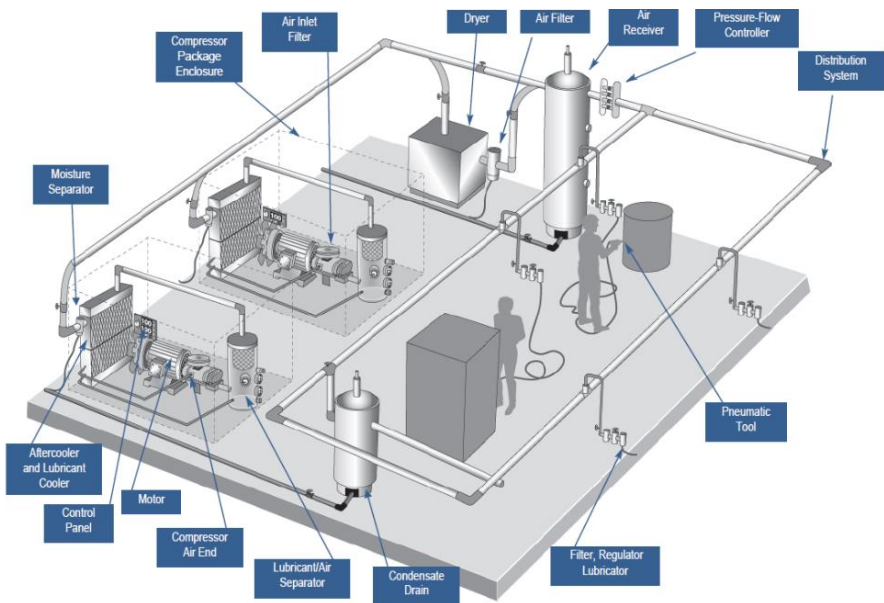


Figure 2: Basic components of industrial CAS (Marshall et al., 2016:4).

Compressors

Compressors are the basic component of a CAS. Compressors compress the air from the suction channel, increase its Pressure and temperature, and store it in the air tank. The air temperature increases to 80–170 °C throughout this

procedure (Kaya et al., 2021:395). Compressors have a 94% recoverable energy potential while transferring 4% of the shaft power to the air (Kaya et al., 2021:398). Fig 3 shows the energy recovery in the compressor schematic.

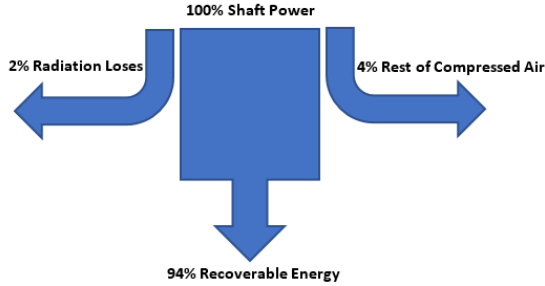
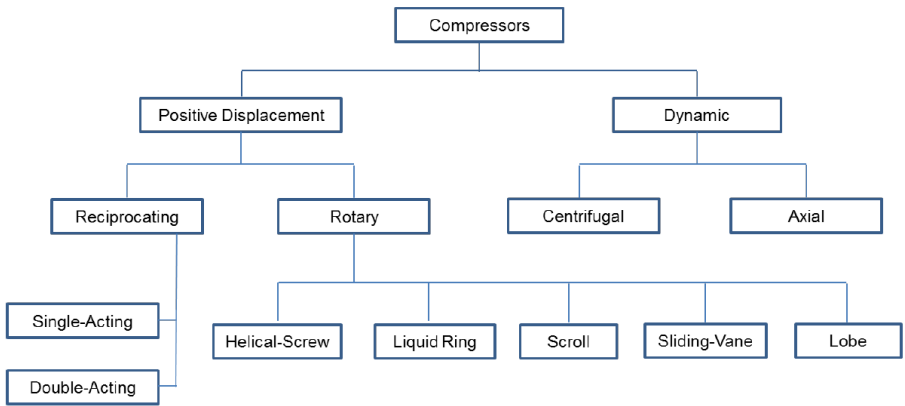
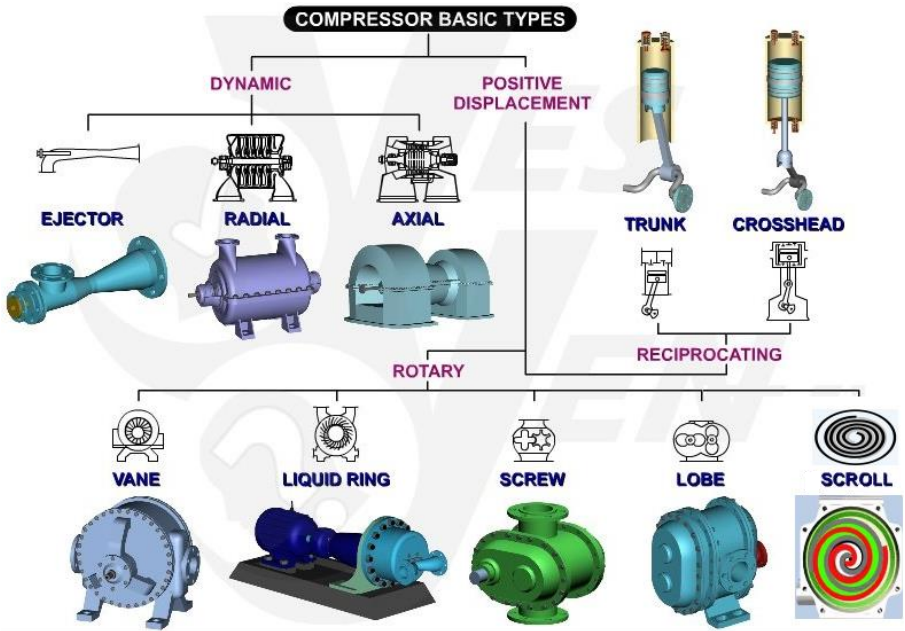


Figure 3: Recoverable energy rates in compressors

Compressors are classified into two main groups, positive displacement and dynamic, according to their methods of generating pressure air. Positive displacement compression and dynamic compression are the two general theories of air compression. Positive displacement compressors comprise many types of rotary compressors, such as screw, tooth, and vane, as well as reciprocating (piston) and orbital (scroll) compressors (Fig 4).



a)



b)

Figure 4: a) Classification of compressors (Marshall et al., 2016:6) and b) The most common compressor types (Yesyen.com, 2023)

During positive displacement compression, one or more compression chambers are filled with air and sealed off from the inlet. Each chamber's volume gradually drops as the air within is compressed. Due to the compression chamber's volume being continuously reduced, a port or valve opens and releases air into the exit system when the pressure reaches the built-in pressure ratio. A dynamic compression impeller rotates quickly, drawing air between its blades

and causing it to accelerate to a high speed. After that, the gas is released via a diffuser, which converts its kinetic energy to static Pressure. Turbocompressors with an axial or radial flow pattern comprise most dynamic compressors. They are all designed to operate at high-volume flow rates. (Marshall et al., 2016:9). Table 1 provides the general selection criteria for the compressor.

Table 1: General compressor selection criteria (BEE, 2007:48)

Compressor Type	Capacity (m ³ /h)		Pressure (Bar)	
	From	To	From	To
Roots blower compressor Single-stage	100	30000	0.1	1
Reciprocating				
Single/Two-stage	100	12000	0.8	12
Multi-stage	100	12000	12.0	700
Screw				
Single stage	100	2400	0.8	13
Two-stage	100	2200	0.8	24
Centrifugal	600	300000	0.1	450

The position of air compressors and the caliber of air they suck in will have a big impact on how much energy is used. Cool, dry, clean air at the intake improves the compressor's function as a breathing machine. The power required by a compressor to compress one liter of compressed air per second is known as specific power consumption (Table 2).

Table 2: Specific Power Consumed by Compressors (Kaya et al., 2021:400).

Compressor type	Specific power consumption (kW/(L/s)) (Working pressure 7 bar)
Screw compressor: small capacity, oil-injected	0.36–0.43
Screw compressor: large capacity, oil-free	0.34–0.40
Rotary channel compressor: oil-injected	0.40–0.43
Small piston compressor	0.36–0.54
Large piston compressor	0.29–0.36

The size and design of the compressor determine the specific power value. Unloaded power consumption is the amount of power the compressor uses while not in use (idle running). The power drawn in screw compressors is dependent upon the system pressure, which is roughly 70%. The power consumed during

unloaded (idle) operation in reciprocating compressors is not dependent on the system pressure.

Reciprocating compressors (Piston compressors)

The reciprocating compressor is one of the most popular air compressors (Fig 5). Their flow output is almost constant throughout various discharge pressures, which defines them. Additionally, the speed and compressor capacity are directly related. But the result is a pulsing output.

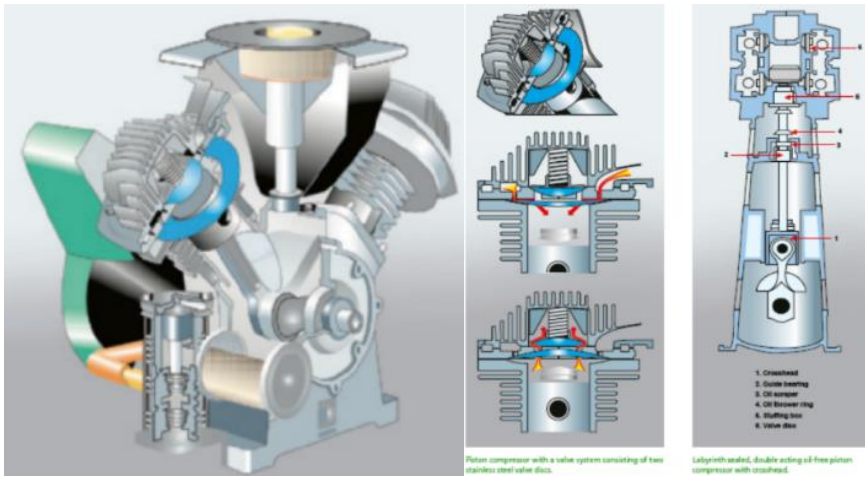


Figure 5: Piston compressor, Used by permission of Atlas Copco. (Atlas Copco, 2019:32-33)

There are numerous configurations for reciprocating compressors; the four most popular ones are tandem, horizontal balance-opposed, vertical, and horizontal. Reciprocating compressors of the vertical type are utilized in the 50 cfm (1.415 m³/min.) – 150 cfm (4.247 m³/min.) capacity range. In multi-stage designs, horizontal balancing opposed compressors are utilized in the capacity range of 200 cfm (5.663 m³/min.) – 5000 cfm (141.584 m³/min.), and in single-stage designs, they can handle up to 10,000 cfm (283.168 m³/min.). A range of types of reciprocating compressors are also accessible:

- Lubricated and non-lubricated
- Single or multiple-cylinder
- Water or air-cooled.
- Single or multi-stage

For lubricated machinery, the discharge air and oil need to be isolated. Compressors without lubrication are particularly helpful in supplying air for processes that need an oil-free discharge and instrumentation. In contrast to

lubricated machines, non-lubricated machines have a greater specific power consumption (kW/cfm). While multi-cylinder machines are often water-cooled, single-cylinder machines are typically air-cooled. However, machines up to 100 kW can be equipped with multi-stage air-cooled models. Systems that are water-cooled use less energy than those that are air-cooled.

Compared to single-stage machines, which have a discharge temperature of 205 to 240°C, two-stage machines are employed for high pressures and have a lower discharge temperature of 140 to 160°C. Occasionally, when running over an identical total pressure difference, single-stage machines may consume more specific power than multi-stage machines. Investment costs for multi-stage machines are often expensive, especially for applications requiring low capacity (less than 25 cfm (0.707 m³/min.)) and high discharge pressure (over 7 bar). Additional advantages of multi-stage include less pressure differential between the cylinders, which lessens the strain and load on compressor parts such as piston rings and valves.

Rotary compressors

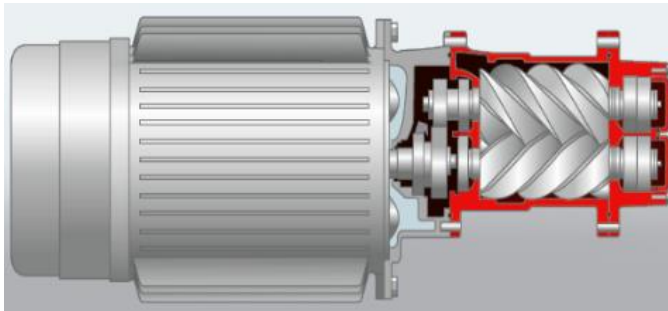
Rather than pistons, rotors are used in rotary compressors to provide a continuous, pulsation-free air discharge. Compared to reciprocating machines, they require less starting torque since they are directly linked to the prime mover. Compared to reciprocating compressors, they often offer better throughput and operate faster. Additionally, they have fewer parts, vibrate less, and require smaller foundations, reducing the likelihood of collapse.

The most popular rotary compressors are screw compressors (Fig 6) and the Roots blower, often known as lobe compressors. The Roots Blower, which can only discharge up to 2.2 bar in a two-stage configuration and up to 1 bar in a single-stage design, is essentially a low-pressure blower.

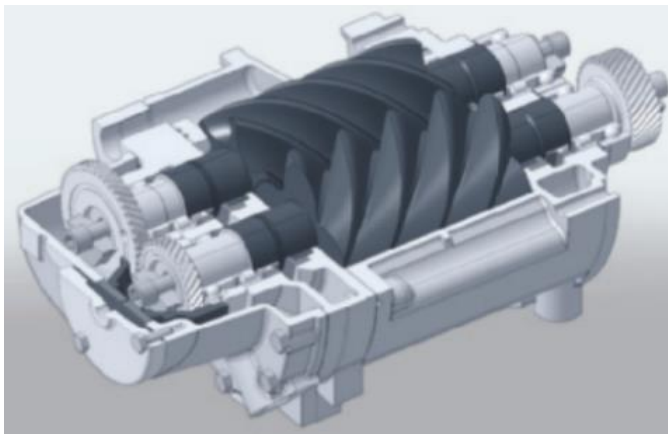
The single-stage helical or spiral lubricating oil-flooded screw air compressor is the most often used rotary air compressor (Fig 6a). These compressors are two rotors that compress air internally within a casing. There are no valves. These systems are oil-cooled, with the oil sealing the internal clearances through air or water-cooled oil coolers. The compressor's internal cooling system ensures that the working parts are never subjected to excessive temperatures. Discharge air and oil must be kept apart. Rotating screw air compressors are simple to install, run, and maintain due to their minimal wear parts and straightforward design (BEE, 2007:47).

True oil-free air is produced by the oil-free rotary screw air compressor (Fig 6b), which compresses air without oil in the compression chamber using

specially-made air ends. These compressors offer the same versatility as oil-flooded rotary compressors and come in air-cooled or water-cooled varieties.



a)



b)

Figure 6: Screw compressor a) Lubricated b) Oil free, Used by permission of Atlas Copco. (Atlas Copco, 2019:36)

The configuration, Pressure, and capacity are all available in a broad range. Dry kinds come in capacities up to 20,000 cfm (566.336 m³/min.) and pressures up to 15 bar, offering oil-free air. Lubricated variants have discharge pressures up to 10 bar and sizes ranging from 100 cfm (2.831 m³/min.) to 1000 cfm (28.316 m³/min.).

Two rotors rotating counter-clockwise inside a compression chamber make up the compression portion of a tooth compressor (Fig 7). Intake, compression, and outflow make up the compression process. Air is forced into the compression chamber during intake until the rotors block the inlet. In the compression phase, while the rotors rotate, the drawn-in air is compressed in the compression chamber, which becomes smaller.

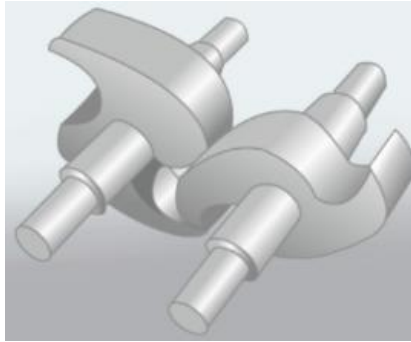


Figure 7: Tooth compressor, Used by permission of Atlas Copco. (Atlas Copco, 2019:38)

A scroll compressor is a kind of orbiting displacement compressor which compresses air into a continuously diminishing volume and is typically oil-free (Fig 8). The compressor element comprises an eccentric spiral that orbits on a motor and a stator spiral that is fixed inside a housing. The spirals are attached with a 180° phase displacement to create air pockets with a progressively changing volume.

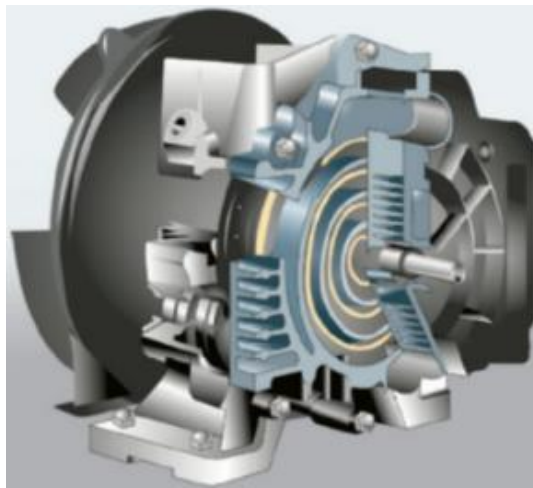


Figure 8: Scroll compressor cross-section, Used by permission of Atlas Copco. (Atlas Copco, 2019:39)

Like many compressed air expansion motors, a vane compressor operates on the same principle. Most vane compressors are oil-lubricated, and the vanes are often made of unique cast alloys. Within a stator housing, a rotor with radial, movable blade-shaped vanes is eccentrically placed. Centrifugal force pushes the

vanes up against the stator walls as it rotates. As the distance between the rotor and stator grows, air is pulled in. The many compressor pockets, whose volumes decrease with rotation, collect the air. The air is released when the vanes pass the outlet port (Fig 9).

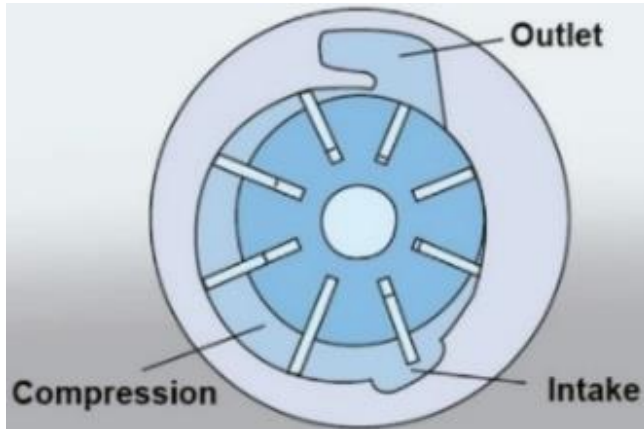


Figure 9: Vane compressor, Used by permission of Atlas Copco. (Atlas Copco, 2019:40)

A Roots blower is an internal compression-free valveless displacement compressor (Fig 10). Compressed air flows back into the housing from the pressure side when the compression chamber and the exit port make contact. Further compression occurs when the compression chamber's volume continues to drop while the rotation continues. As a result, compression occurs in the face of complete counterpressure, leading to low efficiency and overly noise.

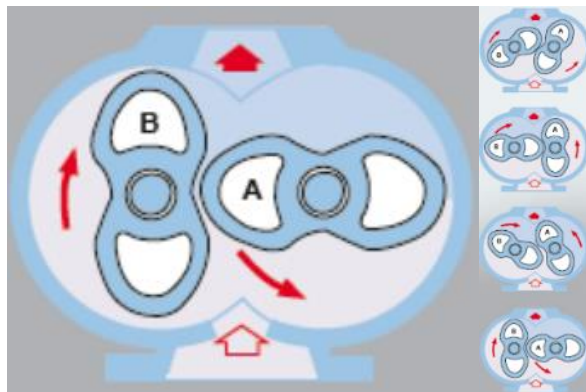


Figure 10: Roots blower, Used by permission of Atlas Copco. (Atlas Copco, 2019:40)

Dynamic compressors

Centrifugal compressors, which comprise most dynamic compressors, function similarly to centrifugal pumps (Fig 11). When compared to reciprocating machines, these compressors have distinctly different features. The output and efficiency of the compressor are significantly altered by even slight changes in the compression ratio. Generally exceeding 12,000 cfm, centrifugal machines are more appropriate for applications needing extremely large capacities.

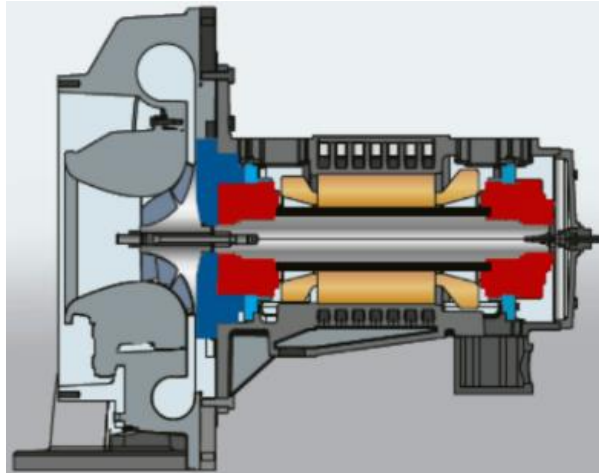


Figure 11: Centrifugal compressor Used by permission of Atlas Copco.
(Atlas Copco, 2019:42)

Energy from a rotating impeller is transferred to the air via the centrifugal air compressor. By altering the air's motion and Pressure, the rotor does this. In a stationary diffuser, this momentum is transformed into useful Pressure by slowing down the airflow. By design, the centrifugal air compressor operates without the use of oil. Shaft seals and atmospheric vents keep the air from the oil-lubricated running gear. With its minimal moving parts and continuous-duty design, the centrifugal compressor is especially well-suited for high-volume applications that require oil-free air.

A single-stage centrifugal machine can achieve the same capacity as a multi-stage reciprocating compressor. There are machines with radial or axial flow impellers. Higher compression ratios can be achieved with axial flow compressors (Fig 12), which are also typically more efficient than radial compressors. Radial machines are usually single-stage designs, whereas axial compressors are frequently multi-stage devices (BEE, 2007:48).

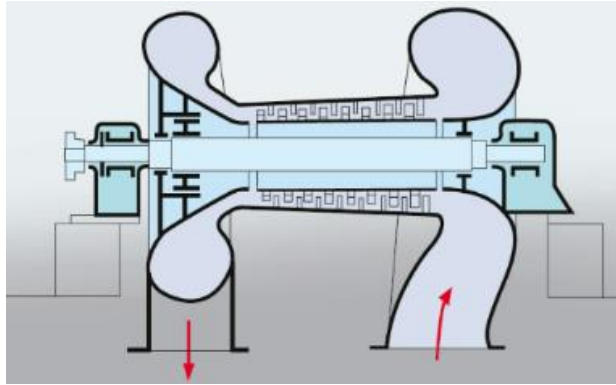


Figure 12: Axial compressor Used by permission of Atlas Copco. (Atlas Copco, 2019:42)

Coolers and Dryers

Reducing the air temperature before moving to the next stage is important in a compressed air system to reduce compression work and increase efficiency. Water-cooled chillers can be used for this. A heat exchanger called an after-cooler cools hot compressed air to cause water that would otherwise condense in the pipe system to precipitate. "After coolers" can remove moisture from the air by reducing temperature in a water-cooled heat exchanger.

In compressors, the temperature of the compressed air rises, and it will cool as it moves on the line after leaving the compression. This will cause condensation and liquid accumulation in the line. This water in the system leads to decreased process efficiencies, corrosion, and increased maintenance costs. Compressed air's water content is called the Pressure Dew Point (PDP). At the current operating pressure, it is the temperature at which water vapor turns into water. Low PDP readings indicate small levels of water vapor in the compressed air.

Most pneumatic instruments and processes cannot tolerate hot-pressure air. So, the air circulating in the pressure airline should be as dry as possible, and a dryer should be used (Fig 13). Air dryers remove residual moisture from the after-cooler since the air used in pneumatic and instrument equipment must be reasonably moisture-free. Adsorbents such as silica gel or activated carbon, refrigerant dryers, or heat from compression dryers remove the moisture.



Figure 13: Air dryer (icskompresor.com, 2023)

Compressed Air Tanks (Air Receivers)

Storage tanks with sufficient volume are an important component of compressed air system design (Fig 14). Storage tanks serve as an air reservoir, ensuring the system pressure remains relatively constant even during increases and fluctuations in air demand. If there is no proper air storage, the compressed air system's sudden increase in air demand during the day may cause sudden pressure drops. To compensate for instantaneous pressure drops, plant managers often increase the discharge pressure settings, which results in the use of more energy than necessary. Therefore, storage tanks are more energy-efficient for meeting instantaneous demand fluctuations. In addition, storage tanks avoid frequent start-up of compressors operating in on/off or load/unload modes. Motor life can be extended by ensuring that compressors operated in start/stop mode are switched on less frequently. Again, longer start-up intervals of compressors operating in load/unload mode provide the time needed to depressurize the oil crankcases and allow the oil crankcases to operate at a lower pressure when the compressors are unloaded, thus saving energy. The crankcase pressure of an air compressor operating properly in load/unload mode can be completely relieved during the unloading cycle (Enerji.gov.tr, 2023:492-493). 60-90 seconds is needed for emptying. Industry sources recommend designing the storage volume to be 10-15 Liter per 1 m³/h of compressor capacity at full load (Abels and Kiscock, 2011).



Figure 14: Compressed air tank (Air receiver) (icskompresor.com, 2023)

Generally, there is no such thing as excessive storage, as more storage provides more benefits. If the operating Pressure is less than 8 bar and there is no excessive compressed air requirement, the tank size can be 1/10 of the compressor capacity. In systems that provide automatic start-stop, selecting the tank size may be considered appropriate so that the compressor is activated 10 times in 1 hour. Storage tanks should be located on the supply side of the system near the compressors to act as a buffer between the compressors and all end uses. A common strategy for positioning the storage tanks is to place one of the storage tanks downstream of the after-cooler so that the condensate can be separated from the saturated air before it enters the air dryer. Another storage tank is usually located downstream of the dryer as the primary system storage. Additional storage tanks installed throughout the system, especially when close to high-end-use points, ensure that the pneumatic equipment receives the appropriate Pressure without interruption.

Using air tanks in compressed air systems ensures the constant and efficient use of air. Inlets and outlets to the air tank must be made in the opposite direction. This prevents the air from circulating easily and the water in the system from being sent back to the line. We can list the benefits of using an air tank in the system as follows:

- It dampens the sudden pressure fluctuations when the compressor is loaded and unloaded.
- It stores the air required for feeding the system. Fluctuations caused by the load/unload operation of the compressor are prevented in this way.
- Due to the manometer and safety valve on them, the compressed air units are kept under control.
- Compressed air tanks are placed at the outlet of the compressor. It is an important system element and requires occupational health and safety attention.

Filters

Compressed air filters are installed in pipes to remove suspended solids and liquids in the air (Fig 15). The filters contain a fine-mesh mesh structure that captures solid particles and liquids by centrifugal action and causes the captured solid and liquid particles to accumulate until they are heavy enough to flow downwards. Filters must be emptied regularly, either manually or by automatic traps. Filters can cause significant pressure loss and air leakage if poorly maintained.

Suction air that contains dust wears moving parts excessively, leading to valve malfunctions from abrasion. It is necessary to have appropriate air filters on the suction side. High dust separation capacity, low-pressure drops, and a sturdy design are necessary for air filters to prevent frequent cleaning and replacement. The impact of the Pressure drop across the air filter on power consumption is seen in Table 3.



Figure 15: Compressed air filter (Ozenkompresor.com, 2023)

Table 3: Power consumption is affected by the pressure drop across the air intake filter (BEE, 2007:52).

Decrease in pressure across the air filter (mmWC)	A rise in the amount of power used (%)
0	0
200	1.6
400	3.2
600	4.7
800	7.0

Installing air filters as close to the compressor as feasible should be done after considering the type of compressor. Generally, "For every 250 mmWC pressure drop increase across at the suction path due to choked filters, etc., the compressor power consumption increases by about 2 percent for the same output." Therefore, it is recommended to regularly clean inlet air filters to reduce pressure drops. Manometers or differential pressure gauges can be used to monitor pressure drops and plan filter-cleaning schedules.

Pressure Regulators

Pressure regulators are valves installed in pipes to reduce the pressure before an end-use point. Fig 16 shows the structure of the pressure regulator with an exhaust hole.

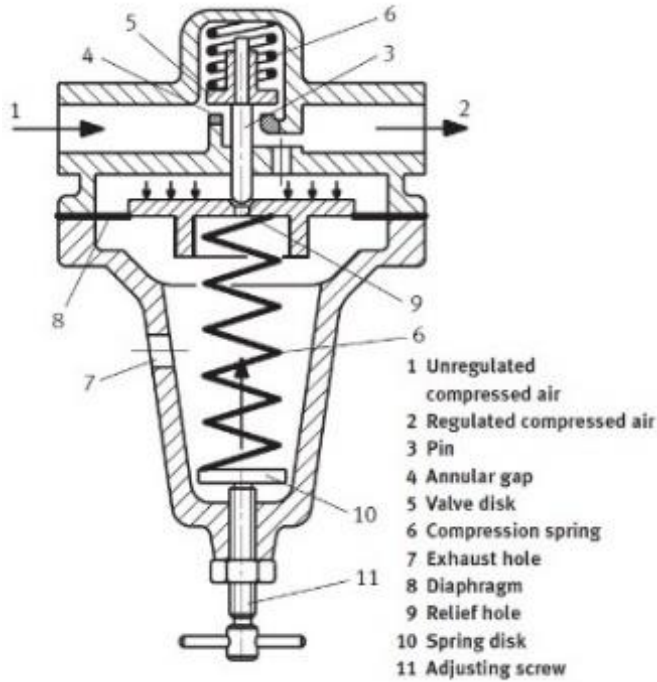


Figure 16: The structure of the pressure regulator (Hesse, 2023:50)

A pressure regulator can be set to any pressure value on the pressure gauge. Pressure regulation ensures that less air is consumed at the point of end use, reduces losses due to leaks downstream of the pressure regulator, and saves energy. However, the generation of air at high pressure and its downstream regulation is inherently inefficient. A better alternative is to produce compressed air at a lower pressure to reduce the need for a pressure regulator. If most of a plant's end uses require low Pressure, a compressed air system design split into high and low Pressure will be more efficient than a single compressed air system design requiring a high-pressure regulation level.

Condensate Drainage Traps

Condensate is collected at several locations throughout the CAS. These locations include dryers, storage tanks, and filters. Drain traps are valves that discharge condensate from the system by opening. The pressure of the compressed air system forces out the condensate. The compressed air line should be built to connect all intake and exit points in the humid region from above or from the side to prevent undefinable condensate flow. Condensate is transported away from the main line by defined condensate outlets that lead downward, also

called "water traps". A water trap (Fig 17) in the humid part of the compressed air system separates condensate and an air receiver when properly built and operates at an airflow velocity of 2 to 3 m/s (Kaeser, 2023:13).

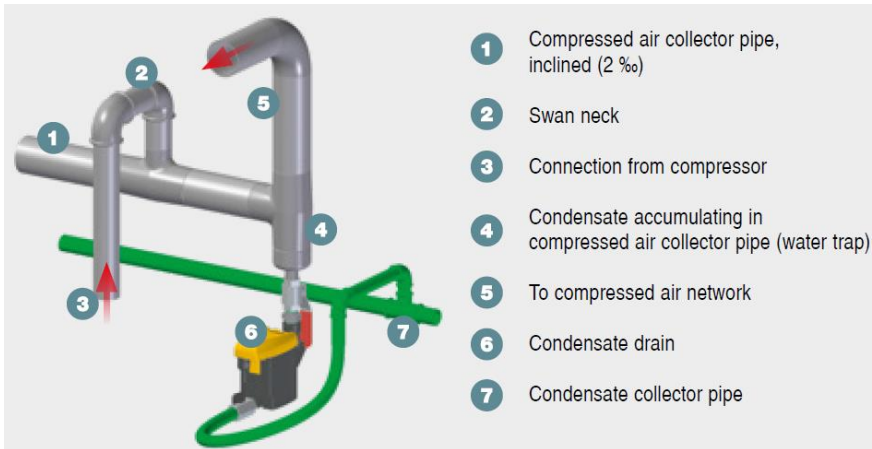


Figure 17: In the humid section of a compressed air system, a water trap with a condensate drain (Kaeser, 2023:13)

A conventional timer-controlled drain trap opens and closes at set intervals in a timed cycle. For example, a timer-controlled drain trap can be set to open for five seconds every two minutes. Often timer-controlled drain traps remain open longer than necessary to drain condensate, especially during periods of low compressed air demand. Compressed air is wasted by leaving a drain trap open longer than necessary.

Lossless condensate drain traps are energy-efficient alternatives designed to drain only condensate without wasting compressed air. Lossless condensate drain traps incorporate a float or level control combined with an electronic or pneumatic actuator to open the valve when a sufficient amount of condensate has accumulated and close the valve when a certain amount of condensate has been reached before causing a loss of compressed air.

ENERGY SAVING APPLICATIONS IN COMPRESSED AIR SYSTEMS

In parallel with the development of the industry, with the increase in the need for energy, environmentally friendly renewable energy sources have taken their place in the alternative energy lane. Considering the negative effects of carbon dioxide gas released by fossil-fuelled power plants on the environment, the

importance of the transition to renewable energy sources is better understood. Today, when energy saving has started to be better understood with the increase in energy demand, efficient use of energy according to the need and saving application policies have gained importance. With the realization and sustainability of these policies, it should be aimed to reduce the carbon footprint significantly. Achieving this goal will give businesses an environmentally friendly green identity. Air compressors are an indispensable pneumatic energy provider for industrial enterprises. This pneumatic energy undertakes important tasks in many industrial fields: textile, electronics, automotive, pharmaceutical, food, beverage, pet bottle etc. It is used for a wide range of different purposes. The cost of this compressed pneumatic energy provided by air compressors is quite expensive. Approximately 70% or more of the lifetime cost of a compressor depends on the use of electrical energy. Considering the losses in the compressed air system, only 7.5% can be used as useful energy. It can be seen that the energy lost in the compression process is quite high. The performance enhancement potential outlined in the fact sheets is depicted in the compressed air system diagram presented in Fig 18. Now let's take a look at the applications that will provide us with energy savings on how we can achieve these important advantages:

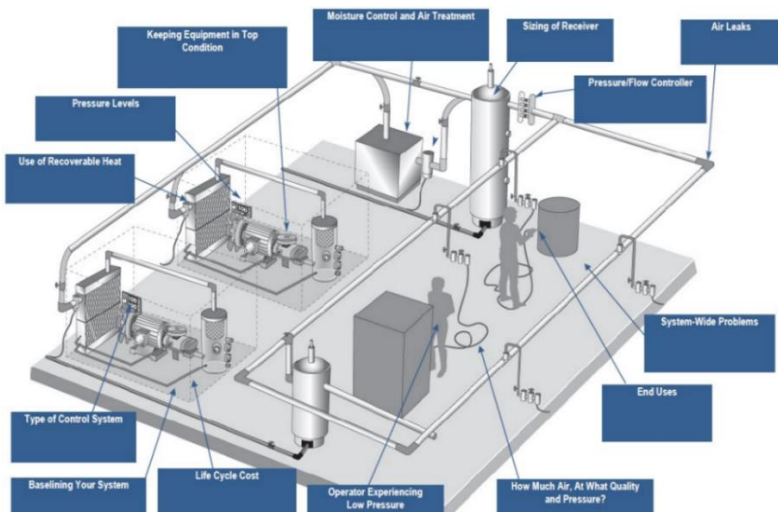


Figure 18: Energy saving opportunities in CASs (Marshall et al., 2016:19).

Correct Selection of Compressor Capacity

The air consumption of the enterprise should be calculated with a good survey study, considering the location conditions, and the compressor's rating should be ensured. This is very important for the compressor to operate at optimal

efficiency. Choosing a compressor with a capacity larger than the calculated air consumption of the enterprise will cause the compressor to operate inefficiently. In this case, the compressor will spend unnecessary energy and often run idle. In this way, energy consumption will increase, and the electricity bills will face high bills. At the same time, this unnecessary operation will shorten the service life of the compressor and increase maintenance costs.

Correct Design of the Compressed Air System

It should be ensured that the compressed air installation is designed correctly by considering the pressure losses. Otherwise, the desired sufficient pressure will not be provided due to pressure losses in the compressed air system. Piping installation should be designed with minimum pressure loss; compressor capacity should be considered when sizing the pipes. Using low friction coefficient aluminium- or plastic-based PPR pipes is especially recommended. These pipes can provide up to 5% energy savings compared to other iron-steel-based pipes.

Regular Maintenance of Compressor and Compressed Air System

Maintenance of compressors should be carried out at the periods specified by the manufacturer without interruption. For the harsh ambient conditions in which the compressors are located, the maintenance times will provide significant advantages for the compressor's efficient operation and service life. Inadequate maintenance causes compressors to operate inefficiently, increase energy consumption, and shorten their service life, resulting in serious maintenance costs. Timely maintenance performed using Original Equipment Manufacturer (O.E.M.) spare parts through authorized services contributes significantly to energy efficiency by ensuring the efficient operation of the compressor.

Control of Air Leaks in Compressed Air System

Air leaks in the compressed air system increase energy consumption by operating the compressors unnecessarily and significantly reduce compressor efficiency. Air leaks affect compressor energy consumption by 20-30% in industrial enterprises where maintenance is not performed regularly. This rate is higher in enterprises where maintenance is rarely performed. Air leaks cause serious pressure drops in the compressed air system and cause inefficient operation of the compressed air system. This situation will adversely affect the efficiency of the production processes by causing a serious decrease in the efficiency of the pneumatic tools and machines used. Air leaks mostly occur at the connection points of the pipework installation. Therefore, an ultrasonic

leakage scan of the compressed air system and implementing a leakage maintenance programme are essential for efficient operation.

Everyone knows that compressed air systems leak. What is not known, however, is how much leakage there is or how much it costs. Through a 3 mm diameter hole with a smooth round orifice, air flows at a flow rate of approximately 0.5 m³/min at a pressure of 6 bar. This leakage totals more than 240,000 cubic meters of air in a year. Table 4 presents the losses corresponding to the airflow escaping from different orifice diameters at an effective pressure of 6 bar in kW.

Table 4: Compressed air flow through the orifice and power loss (McKane et al., 2014:9).

Orifice diameter [mm]	Air consumption at 6 Barg (g=gauge), [m ³ /min]	Loss [kW]
1	0,065	0,3
2	0,24	1,7
4	0,98	6,5
6	2	12,0

In small compressed air systems, switching off all air use and measuring the time it takes for the pressure to drop is sufficient to determine the leakage rate. The formula for this method is presented below:

$$V_L = \frac{V_T \cdot (P_i - P_f)}{T} \quad (1)$$

Here, V_L Leakage volume (m³/min), V_T Tank volume (m³), P_i initial pressure (bar), P_f final pressure [bar], T measurement period or time (min).

In larger systems, the approximate amount of leakage can be found by turning off all air utilization and measuring the load cycle of the supply compressor. The leakage volume formula to be used for this method is given below:

$$V_L = \frac{V_C \cdot t}{T} \quad (2)$$

Where V_C is the volumetric flow rate of the compressor (m³/min), t is the compressor load cycle time (min), and T is the total measurement period-time (min). Table 5 provides estimates of compressed air leakage (m³/min) for the specified operating conditions. These data were obtained using a sharp-edged

orifice with a flow coefficient 0.61. For a smooth round orifice (with a flow coefficient of 0.97), the leakage and cost can increase by up to 60%.

Table 5: Air leakage amounts at different pressures and orifice diameters (m³/min) (McKane et al., 2014:10).

Gauge (effective) pressure before orifice, [bar]	Orifice diameter, mm (For the calculated flow rate (m ³ /min), the orifice coefficient is assumed as 0.61)											
	1	2	3	4	5	6	7	8	9	10	15	20
4	0,03	0,11	0,25	0,45	0,7	1,01	1,38	1,8	2,28	2,82	6,34	11,28
4,5	0,03	0,12	0,28	0,5	0,78	1,12	1,52	1,98	2,51	3,1	6,98	12,4
5	0,03	0,14	0,3	0,54	0,85	1,22	1,66	2,16	2,74	3,38	7,61	13,53
5,5	0,04	0,15	0,33	0,59	0,92	1,32	1,79	2,34	2,97	3,66	8,24	14,65
6	0,04	0,16	0,35	0,63	0,99	1,42	1,93	2,52	3,19	3,94	8,87	15,78
6,5	0,04	0,17	0,38	0,68	1,06	1,52	2,07	2,7	3,42	4,23	9,51	16,9
7	0,05	0,18	0,41	0,72	1,13	1,62	2,21	2,88	3,65	4,51	10,14	18,03
7,5	0,05	0,19	0,43	0,77	1,2	1,72	2,35	3,06	3,88	4,79	10,77	19,15
8	0,05	0,2	0,46	0,81	1,27	1,82	2,48	3,24	4,11	5,07	11,4	20,27
8,5	0,05	0,21	0,48	0,86	1,34	1,93	2,62	3,42	4,33	5,35	12,04	21,4
9	0,06	0,23	0,51	0,9	1,41	2,03	2,76	3,6	4,56	5,63	12,67	22,52
9,5	0,06	0,24	0,53	0,95	1,48	2,13	2,9	3,78	4,79	5,91	13,3	23,65
10	0,06	0,25	0,56	0,99	1,55	2,23	3,03	3,96	5,02	6,19	13,94	24,77

The ambient pressure-to-line pressure ratio in the compressed air system is verified. Assuming that the flow represents a leak, the flow (V_L , m³/s) of air leaving the hole can be computed as follows if this ratio is less than 52%.

$$V_L = \frac{N_L \cdot T_i \cdot \frac{P_L}{P_{amb}} \cdot C_1 \cdot C_d \cdot \frac{\pi \cdot D^2}{4}}{\sqrt{T_L}} \quad (3)$$

Where D is the hole's diameter (meter), T_i is the compressor's air (suction air) temperature (K), P_L is the line pressure where the hole is (kPa), P_{amb} is the ambient pressure at sea level (kPa), C_1 is the volumetric sonic flow constant (13.29), C_d is the square section orifice coefficient (0.8), and T_L is the line's average temperature (K).

Equation (4) calculates the power loss from air leaks (L, kW). $E_a = 0.88$ for a single-stroke piston compressor, $E_a = 0.75$ for a multi-stroke piston compressor, and $E_a = 0.82$ for a screw-type compressor is the compressor adiabatic efficiency in Equation (4).

$$L = \frac{P_i \cdot V_L \cdot \frac{k}{k-1} \cdot N \cdot \left[\left(\frac{P_0}{P_i} \right)^{\frac{k-1}{k \cdot N}} - 1 \right]}{E_a \cdot E_m} \quad (4)$$

Where P_i Atmospheric pressure, N stage number, P_0 Compressor working pressure (kPa), E_m Compressor motor efficiency, V_L the flow rate of leakage air (air leakage) (m^3/s), and k Specific heat ratio of the air ($k=1.4$). Annual Energy Savings (AES) are calculated by equation 5 as follows:

$$\text{AES} = L \cdot H \quad (5)$$

Here, H is expressed as the time (hours) of the year in which the airline is under pressure. Annual Economic Gain (AEG) can be expressed by equation 6.

$$\text{AEG} = \text{AES} \cdot \text{Unit cost of use} \quad (6)$$

Reduction of High Suction Temperature

Compressor suction air temperature has a significant effect on compressor efficiency. Since the suction temperature range of compressors should be between 5 °C and 40 °C, the optimal suction temperature must be ensured; each 5 °C increase in suction air temperature increases energy consumption by approximately 2%. Necessary measures must ensure the suction air temperature does not increase, and the suction air quality is maintained. The waste heat released by the compressor and dryers should be removed from the environment and the ventilation system should be in a way to ensure continuous fresh air flow. For this purpose, the temperature management of the compressor room can be provided by temperature-controlled ventilation system automation in an optimal temperature range. The compressor system must be installed in a suitable room that fulfills the requirements.

Optimization of the operating pressure range of the compressor according to consumption behavior

After studying the consumption behavior of the plant, the optimal operating pressure range of the compressor should be determined. Excessive operating pressure range, which the enterprise does not require, will cause unnecessary energy consumption. Therefore, since it is known that each 1 bar pressure increase in the compressor system increases energy consumption by approximately 7%, energy efficiency should be ensured by optimizing the

operating pressure range according to the desired head at the final consumption point.

By carefully examining the pressure needs of different equipment and the pressure drop in the line between the compressed air generating and usage locations, it is possible to lower (optimize) the delivery pressure settings. Table 6 illustrates typical power savings from pressure reduction. It is necessary to regulate the pressure switches so that the compressor cuts in and out at the best possible times. A 1 bar drop in supply pressure would result in a 6–10% reduction in power usage in a compressor (Table 6).

Table 6: Typical Power Savings by Reducing Pressure (BEE, 2007:54).

Pressure Reduction		Power Savings (%)		
From (Bar)	To (Bar)	Single-stage Water-cooled	Two-stage Water-cooled	Two-stage Air-cooled
6.8	6.1	4	4	2.6
6.8	5.5	9	11	6.5

Optimization of Sequential Operation of Multiple Compressor System

Efficient management of a multi-compressor system is as important as compressor rating. The consumption of businesses can sometimes be very variable, in which case the compressors can operate at part load and sometimes at full load. When a control system does not manage these compressors according to an operating logic, the desired efficiency of the compressor system cannot be obtained; high energy and maintenance costs are inevitable. In a multi-compressor system, the compressor system can be efficiently operated sequentially by programming a suitable operating logic with the compressor intelligent management system against variable air consumption. In this way, it will make a beneficial contribution to both energy efficiency and compressor lifetime.

Recovery of Released Heat Energy

Approximately 76% of the energy supplied to a compressor with oil or fluid cooling, which can be recovered as heat, is present in the compressor cooling medium. Approximately 15% of the total energy is stored in the compressed air, while up to 5% is dissipated as heat through the electric drive motor. With targeted cooling, even the losses from the electric motor can be recovered as heat energy on a fully enclosed fluid-/oil-cooled rotary screw compressor (Kaeser, 2023:23). The supplied energy available for reuse as heat is now at 96%. The

remaining energy is divided between 2% lost through thermal radiation and 2% remaining in the compressed air (Fig 19).

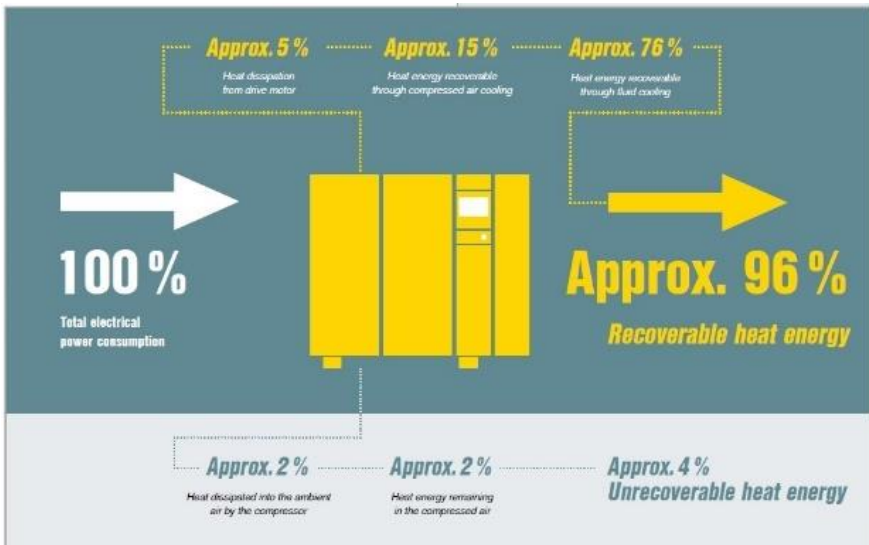


Figure 19: Recoverable waste heat potential (Kaeser, 2023:22).

Compressed air users can choose between different heat recoveries options, such as air and hot water heating, to further increase the efficiency of their supplies. This energy can be recovered at a rate of 91%, especially with a heat exchanger to be added to the lubricated type screw compressor system. This energy can be used for hot water to save energy. Similarly, the waste hot air generated in compressors with fan cooling systems can heat different environments or in the drying and production processes. A significant energy saving can be achieved by converting this waste heat into useful energy.

Selection of Compressor Starting Behaviour

While fixed-speed compressors consume 30-35% of the total power consumption when operating at no load, this ratio is 8-10% in variable speed-controlled compressors. For this reason, it is more advantageous to prefer variable speed-controlled compressors for air consumption below 70-75% of the compressor load rate. If the air consumption of the enterprise is variable and constantly fluctuating, it is more efficient to use variable speed-controlled (inverter) compressors. Otherwise, when fixed-speed compressors are used, load-unload operation frequencies will increase and cause more energy consumption.

Compressed Air Flow Control and Energy Economy

The airflow the compressors provide varies over time based on the parameters necessary for operation. It is crucial to select the appropriate flow control system to ensure maximum efficiency, particularly in energy savings.

The On/Off control: This method involves the compressor operating at full load or being completely unloaded, depending on the air demand. During no-load operation, the compressor continues to rotate. Approximately 30% of the energy consumed at full load is used in no-load operation.

Load control with air inlet damper for compressor: The compressor operates nonstop. The valve in the incoming air duct regulates the compressor's capacity. As per the "on/off control" operating strategy, this approach maintains a more consistent compressor output; nevertheless, it becomes wasteful when the compressor load drops below 90%. This technique uses roughly 50% of the energy required when operating at maximum load, even when no air is required.

Variable Speed Drive Control (VSD): It is well known that the easiest approach to modify the compressor output airflow is to alter the motor speed. The compressor motor's speed can be adjusted using electric systems equipped with frequency converters. The compressor's energy consumption and output air flow are directly related to frequency converter systems. Maintaining a constant air pressure at the compressor exhaust is another option. Fig 10 illustrates the relationship between compressor outlet airflow and energy usage for the three approaches discussed previously.

Applications of Frequency Converters in Compressors: When evaluating an operation's compressors, compressor number one runs at a load almost at full capacity. The second compressor is turned on and off based on the amount of air that is required. There might only need to be one compressor frequency converter application in this compressor room because one of the compressors runs at a load that is almost at full capacity. Variable flow demand may be financially feasible if two compressors are operated alternately at full load, and a compressor frequency converter is used. As illustrated in Fig 20, frequency-controlled compressors offer energy savings of 15-25% compared to full-load operation when operating at low loads (Kaya et al., 2021:416).

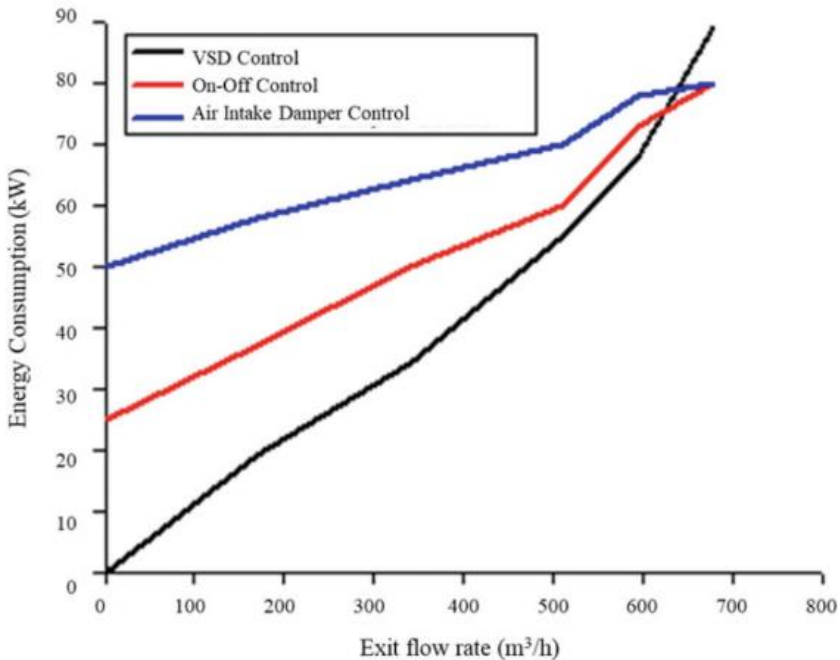


Figure 20: The relationship between energy consumption and compressor outlet airflow for three control techniques (Kaya et al., 2021:416).

Determination of Storage Tank Capacity

The storage tank is an important element of the compressor system and the storage tank where the pneumatic energy is backed up. The compressor's load-unload cycle depends on the storage tank's capacity and the percentage of compressor load. The more often this cycle occurs, the higher the energy consumption. The operating pressure range of the compressor should be optimized by selecting a storage tank with a suitable capacity so that the compressor has fewer load-unload cycles. The correct capacity of the storage tank will reduce the compressor's energy consumption.

Automatic Dischargers

Automatic dischargers play an important role in discharging the condensate water in the air system. Mostly placed under the storage tank, it discharges the condensate with the air at certain intervals. Since automatic drainers operate in a set time cycle, they save energy by discharging air with less loss than manual drainers. On the other hand, instead of working with a time cycle, new automatic evacuators only evacuate condensate water by detecting the condensate water level and operating with zero air loss. These evacuators are more advantageous than automatic evacuators because of their energy efficiency. When the air losses

during an evacuation are calculated, classical automatic evacuators can amortize their investment cost quickly.

RESULTS AND RECOMMENDATIONS

In industrial operations, compressors use more electricity than any other kind of machinery. This indicates that advancements in compressor units might result in extremely significant energy savings. These systems' upgrades also lower maintenance expenses.

Regular compressor and compressed air network maintenance and periodic and timely assessment using shop floor methodologies are necessary for optimal production costs and an early attempt to harvest optimization opportunities. Therefore, to maintain a controlled, optimal functioning, it is strongly advised that you have an expert audit your compressor section/network once and adhere to standard operating practices.

With these applications, a significant advantage will be gained by converting energy losses into useful, usable energy, significantly contributing to energy efficiency and reducing the carbon footprint. Given the continuously rising energy prices, efficient energy use is crucial for the environment and an economic necessity.

As a result, measures, recommendations, and energy-saving potential for CASs are listed below:

Measures and Recommendations for Energy Saving in Compressed Air Systems

Measures and recommendations that can be taken for the effective use and saving of energy in compressed air systems are listed below:

- Compressors must be of the correct type and size.
- The compressed air system should be operated at the lowest possible pressure.
- Pressure regulators should be installed at the points where equipment connects that can run at a pressure lower than mainline pressure,
- If it is economical, the heat of compression should be recovered.
- Air leaks should be reduced.
- Cold, clean, and dry air should be supplied to the compressors. Every 5°C decrease in inlet air temperature causes a 2% reduction in energy consumption, which means a 2% increase in compressor efficiency.

- Air filters should be installed at the air inlet to trap dust and dirt and be cleaned frequently. Every 25 mbar pressure loss at the inlet reduces compressor performance by 2%.
- Compressed air equipment must be regularly maintained.
- Air tank sizes should be selected correctly.
- Use compressors with variable speed drives if variable air flow rates are required.
- Necessary instruments must be provided to ensure system efficiency.
- The speed of the compressed air passing through the main line pipes must be kept below 6 m/sec. For this, mainline pipe diameters must be selected correctly.
- For the water and oil particles in the compressed air to be easily drained from the distribution lines, a 1% slope should be given to the pipes in the flow direction, and a drainage point should be placed every 30 meters.
- In fixed pipe networks, the compressed air from the compressor must be delivered to the end of the line.
- The total pressure drop should not exceed 0.3 bar.
- Service lines should be as close to the pneumatic tools as possible to keep the hose length short.

REFERENCES

- Abels, B. J., and Kissock, K., (2011). Optimizing Compressed Air Storage for Energy Efficiency. *SAE International Journal of Materials and Manufacturing*, 4(1), 477–485. doi:10.4271/2011-01-0323
- Atlas Copco, 2019. *Compressed Air Manual*, 9th Edition. Atlas Copco Airpower NV, ISBN: 9789081535809, 148p., Wilrijk, Belgium.
- BEE, India. (2007). *Compressed air system*. Bureau of Energy Efficiency, Government of India, Ministry of Power. New Delhi, 2007. <https://beeindia.gov.in/sites/default/files/3Ch3.pdf>
- Carbon Trust (2014). *Compressed Air: Opportunities for Businesses*, South Africa, September 2014.
- Enerji.gov.tr, (2023). *Enerji Verimliliği Eğitim Kitabı* (In Turkish). Enerji ve Tabii Kaynaklar Bakanlığı Enerji Verimliliği ve Çevre Dairesi Başkanlığı EVÇED-TEEDB Temmuz 2023-Y.No:49/V01, https://enerji.gov.tr/Media/Dizin/EVCED/tr/EnerjiVerimliliği/Eğitimler/Enerji_verimliliği_ēğitim_kitabi.pdf
- Hernandez-Herrera, H., Silva-Ortega, J. I., Martınez Diaz, V. L., Sanchez, Z. G., Garcıa-a, G. G., Escorcıa, S. M., & Zarate, H. E. (2020). Energy Savings Measures in Compressed Air Systems. *International Journal of Energy Economics and Policy*, 10(3), 414–422.
- Hesse, S. (2002). “Compressed Air as an Energy Carrier”, *Blue Digest on Automation*, Festo AG & Co. 124p.
- icskompresor.com, (2023). <https://www.icskompresor.com.tr/en/ics-compressed-air-tanks>. [Accessed: 16-Dec-2023].
- icskompresor.com, (2023). <https://www.icskompresor.com.tr/en/ics-mke-series-air-dryer>. [Accessed: 16-Dec-2023].
- Kaeser, (2023). *Compressed Air Engineering Basic Principles and Tips*. [Online]. Available: <https://nl.kaeser.com/download.ashx?id=tcm:32-598>. [Accessed: 16-Dec-2023].
- Kaya, D., Çanka Kılıç, F., Öztürk, H.H. (2021). Energy Efficiency in Compressed Air Systems. In: *Energy Management and Energy Efficiency in Industry. Green Energy and Technology*. Springer, Cham. https://doi.org/10.1007/978-3-030-25995-2_13
- Kaya, D., Kılıç, F., Öztürk, H.H. (2021). Energy Efficiency in Compressed Air Systems. In *Energy Management and Energy Efficiency in Industry*; Springer: Cham, Switzerland, pp. 395–418.
- Marshall, R., William, S., Shafer, G., Shaw, P., Sheaffer, P., Stasyshan, R., Ormer, HPV. (2016). *Improving Compressed Air System Performance: A Sourcebook for Industry v3*, 109p., United States.

- McKane, A., Perry, W., and Taranto, T. 2014. Endüstriyel Sistemlerde Optimizasyon/Basınçlı Hava Sistemleri (In Turkish). Sanayide Enerji Verimliliğinin Artırılması Projesi, (UNIDO), YEGM, Aralık 2016, <https://evcedruzgar.enerji.gov.tr/verimlilik/document/Basincli%20Hava%20Sistemleri.pdf>. [Accessed: 16-Dec-2023].
- Ozenkompresor.com, (2023). OFL Serisi Basınçlı Hava Filtreleri. https://ozenkompresor.com.tr/s/2527/i/Basincli_Hava_Sisitemleri_TR.pdf. [Accessed: 16-Dec-2023].
- Saidur, R., Rahim, N., Hasanuzzaman, M. (2010). "A Review on Compressed-Air Energy Use and Energy Savings," *Renewable and Sustainable Energy Reviews*, vol. 14, p. 1135–1153.
- Yesyen.com, (2023). https://yesyen.com/compressor_types.php. [Accessed: 16-Dec-2023].
- Yuan, C., Zhang, T., Rangarajan, A., Dornfeld, D., Ziemba, B., Whitbeck, R. (2006). "A Decision-Based Analysis of Compressed Air Usage Patterns in Automotive Manufacturing," *Journal of Manufacturing Systems*, vol. 25, p. 293-300.

Chapter 32

Investigation of the Effect of Hole Diameter and Aspect Ratio on Elastic Buckling Strength and Determination Buckling Coefficients for Thin Plate Structural Parts in Aerospace Industry with Finite Elements Method

Mert SUBRAN¹

Fatih KARPAT¹²

Abstract – Holes in thin structural plates are widely used in the aerospace industry and other industries for lightening structural parts, access to mechanical and electronic systems, and service and system requirements. However, the hole in the structure affects its buckling strength by changing its stress distribution. In the aviation industry, predicting the buckling behavior of the structure and selecting appropriate geometric dimensions in the designs plays a critical role in terms of the safe usability of the aircraft structure throughout its service life without damage. The buckling strength of thin plates varies depending on parameters such as the shape and size of the hole, geometric dimensions and thickness of the structure, boundary conditions of the structure, and type of loading. In the study's scope, elastic buckling analyses were carried out for uniaxial compression and shear stress loadings of square and different aspect ratios of rectangular plates with circular holes for different boundary conditions, using software based on the finite element method. For each boundary condition and loading examined within the scope of the study, the effect of the change in aspect ratios and hole diameter on the critical buckling force was obtained. From The analysis results also obtained the buckling coefficients required to calculate the theoretical critical buckling load.

Keywords: Plate buckling, Buckling coefficient, Elastic buckling, Perforated plate, Aerospace structures,

¹ 1Mechanical Engineering Department, Uludag University, Türkiye

² Turkish Aerospace Industries Inc, Türkiye

*(mert.subran@tai.com.tr)

² 1Mechanical Engineering Department, Uludag University, Türkiye

I. INTRODUCTION

The use of holes on thin plates in aerospace structures is preferred for different purposes such as lightening of structures, accessibility for service and maintenance, harnesses, hydraulic lines, control connections, etc. [1]. However, the hole or holes added to the structure change the buckling strength because it changes the stress gradient on the structure. Studies in the literature, in case there is a hole on the plate, compared to the plate without a hole, it was concluded that although the hole increases the elastic critical buckling load of the structure in some cases, it significantly reduces the ultimate elastoplastic strength. [2]. Therefore, examining the effect of thin plates with holes exposed to different in-plane loadings on the buckling strength throughout the aircraft's service life is essential. If there is a hole in the plate, plate stresses may concentrate around the hole, increasing the possibility of damage to the structure. Timoshenko conducted the first study on the elastic buckling of a rectangular plate. [3] [4]. Timoshenko found that the critical stress for a plate depends on the plate's dimensions, thickness, elastic modulus, and Poisson's ratio. At the same time, Timoshenko introduced the dimensionless buckling coefficient, which depends on the boundary conditions of the plate, the type of loading and the aspect ratio of the plate, which coefficient is used in analytical solutions for buckling of plates. Buckling is the lateral deformation of the structure that occurs suddenly due to buckling when load is applied. [5]. In the literature, different studies investigate the buckling strength of thin plates containing holes [6] [7]. Some of the studies carried out in recent years on the buckling of plates containing holes are as follows: In the study by Uslu et al., the effect of the change in different parameters for the uniaxial compression load of thin plates containing square and circular holes on the critical buckling load with the finite element method. With the study concluded that more loading is required to buckle the plates with square hole than those containing circular hole on plates for the same hole volume. [8]. In the study carried out by Wang et al., they examined the effect of different parameters of the flange around the hole on the buckling strength of a square plate with a circular hole in its center in the case of uniaxial compression loading with simple supported boundary conditions on each edge. As a result of the study, they concluded that flanged perforated plates have higher buckling strength than non-flanged ones. [9] Ghorbanhosseini et al. examined the effect of changes in different aspect ratios of perforated thin plates under uniaxially compression loading with different boundary conditions on the elastic buckling strength of the structure by the finite element method. In the study, the buckling capacity of two different reinforcement designs was investigated to increase the structure's buckling strength. It has been observed that reinforcement structure significantly

increases the buckling strength of the structure. Additionally, in the study, it was found that the buckling coefficient does not change significantly when the aspect ratio is greater than four, and the buckling coefficient for the four-sided fixed edge boundary condition within the plates is higher than other structures with boundary conditions, and more loading is required to buckle this structure. [3].

Within the scope of our study, The effect of the diameter of the circular hole in the centers of the thin plates and the change in the plate's aspect ratio on the plate's elastic buckling strength was examined. Additionally buckling coefficients were obtained for thin square and rectangular plates with different aspect ratios subjected to in-plane uniaxial compression and shear loads for the fixed support boundary condition on each edge.

II. MATERIALS AND METHOD

A. Analytical Solution

Theoretically, a perforated plate for simple support boundary condition on each edge, the uniaxial compression elastic buckling stress load is calculated with equation 1 [10]. σ_{Cr} in the equation is the minimum critical buckling uniaxial compression stress for the buckling of the structure, K_c is the buckling coefficient, E is the elasticity modulus of the plate material, ν is the Poisson ratio of the part material, t is the thickness of the plate and b is the length of the short side of the plate.

$$\sigma_{Cr} = K_c \frac{\pi^2 E}{12(1-\nu^2)} \left(\frac{t}{b}\right)^2 \quad (1)$$

Buckling stresses of structures exposed to in-plane bending and shear stresses can be calculated with the following formulas [11]

$$\sigma_{BCr} = K_B \frac{\pi^2 E}{12(1-\nu^2)} \left(\frac{t}{b}\right)^2 \quad (2)$$

$$\tau_{SCr} = K_S \frac{\pi^2 E}{12(1-\nu^2)} \left(\frac{t}{\min\{a,b\}}\right)^2 \quad (3)$$

A non-perforated square plate with simply supported boundary conditions for each edge, equation 1 can be converted to the following equation. [1].

$$\sigma_{Cr}^u = 3.62E \left(\frac{t}{b}\right)^2 \quad (4)$$

The buckling coefficient varies depending on variables such as the loading condition of the structure, boundary conditions, aspect ratio, and the geometric changes of the plate.

B. Finite Elements Method

The finite element method represents complex structural problems by dividing complex structural parts into a finite number of small elements and connecting the nodes of the elements. The nodes change places in line with the loads applied to the model. Equation 5 is the linear static analysis solution's finite element method general equation. F in the equation is the external loads applied to the model, K is the stiffness matrix, and u is the unknown displacement amounts. [12].

$$F = Ku \tag{5}$$

The finite element equation for a one-dimensional bar element with two nodes is given below.

$$\begin{Bmatrix} F_{x1} \\ F_{x2} \end{Bmatrix} = \begin{bmatrix} K_{11} & K_{12} \\ K_{12} & K_{22} \end{bmatrix} x \begin{Bmatrix} u_1 \\ u_2 \end{Bmatrix} \tag{6}$$

Buckling of plates is a problem commonly referred to as bifurcation buckling. At the bifurcation point in the load-deformation curve, the deformation change begins to change differently than before buckling. The buckling problem is formulated as an eigenvalue problem and is calculated according to the following equation. [13].

$$\{F\} = [K_0 + \lambda K_\sigma]\{u\} \tag{7}$$

K_0 in the equation is the pre-buckling stiffness matrix. K_σ is the stress stiffness matrix related to the stress on the structure due to buckling. λ is an eigenvalue called the load multiplier. At the buckling point, the determinant of the stiffness matrix is 0.

$$|K_0 + \lambda K_\sigma| = 0 \tag{8}$$

After the determinant solution, eigenvalues, the critical load multipliers, are obtained. In Equation 9, the critical buckling loads required for the buckling that will occur are obtained by multiplying the Eigenvalue factor and the load

magnitude applied to the structure. Buckling loads vary according to buckling modes. i is the number of modes. λ_i is the eigenvalue of mode i . P represents the load value applied to the structure. P_{cri} is the critical buckling load value required for buckling mode i .

$$P_{cri} = \lambda_i P \quad (9)$$

Within the scope of the study, buckling will not occur in the structure if the eigenvalue obtained for the linear elastic buckling obtained in the direction of the load applied to the finite element model through the Hypermesh [14] program is greater than 1. When the initial load is multiplied by the eigenvalue obtained, the critical load required for the structure to buckle will be obtained. When the critical load is exceeded, the eigenvalue will drop below 1. Buckling will occur on the structure.

C. Geometric Model, Material Information and Boundary Conditions

Within the scope of the study, the creation and running of the 2D finite element model was carried out with the Hypermesh Optistruct program. An example of a 2D model is shown in Figure 1.

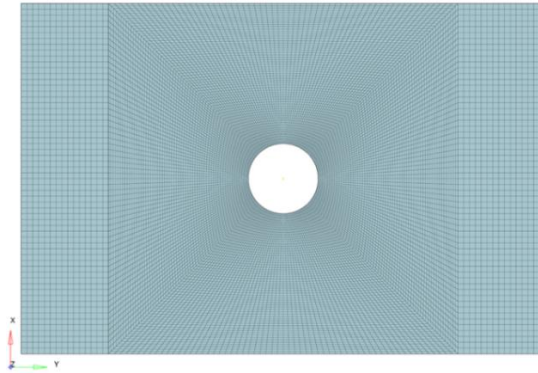


Fig. 1 Two-dimensional finite element model of thin central perforated plate

The geometric properties of the plate are shown in Figure 2. In the study, the plate length (b) is 120 mm. Models were created for aspect ratios (a/b) 1, 1.5, 2, 3, 4, 5 and 6. The plate thickness (t) was kept constant at 2 mm. Hole diameter (d/b) was performed as 0 (non-perforated condition), 0.1, 0.2, 0.3, 0.4, 0.5, 0.6. Geometric parameters are illustrated in Figure 2.

In the study, the plate analysis situations were examined in two-dimensional analysis models according to shear and uniaxial compression loading, with the

boundary condition of each edge being a fixed support. Details of boundary conditions are given in Table 1 and Table 2 according to Figure 2. Those marked at the intersections of rows and columns in the tables represent constrained degrees of freedom.

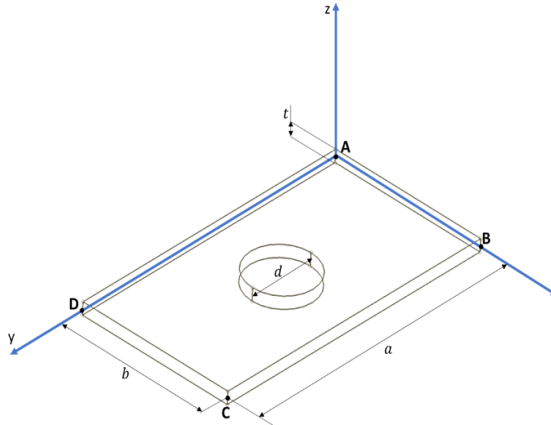


Fig. 2 Representation of geometric parameters of the plate

Table 1 Translational (U_1, U_2, U_3) and rotational (R_1, R_2, R_3) degrees of freedom for fixed supported plate [15]

	U_1	U_2	U_3	R_1	R_2	R_3
Edge AB			x	x		
Edge BC			x		x	
Edge CD			x	x		
Edge DA			x		x	
Point A	x	x	x			
Point B						
Point C		x				
Point D						

Table 2 Translational (U1, U2, U3) and rotational (R1, R2, R3) degrees of freedom for simply supported plate [15]

	U ₁	U ₂	U ₃	R ₁	R ₂	R ₃
Edge AB			x			
Edge BC			x			
Edge CD			x			
Edge DA			x			
Point A	x	x	x			
Point B						
Point C		x				
Point D						

The material of the part used in the analyses was 7050 AMS 4201 aluminum alloy. Properties about the material is given in Table 3. [16].

Table 3 7050 AMS 4201Material Properties [16]

<i>E</i> (MPa)	71015
<i>G</i> (MPa)	27579
<i>v</i>	0.33
ρ (ton/mm³)	2.823x10 ⁻⁹
Yield Strength (<i>L</i>)	455.01MPa
Ultimate Strength (<i>L</i>)	523.97 MPa

Within the scope of the study, investigations were carried out for fixed and simply supported boundary conditions for uniaxial compression stress loading. Investigations were carried out for the fixed supported boundary condition for shear stress loading. Representative illustrations of the examined cases are shown in Figure 3.

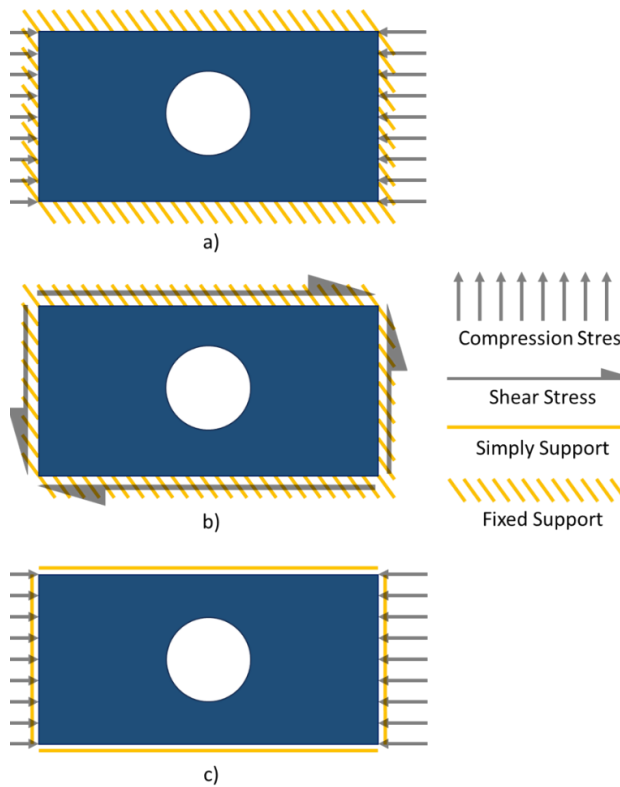


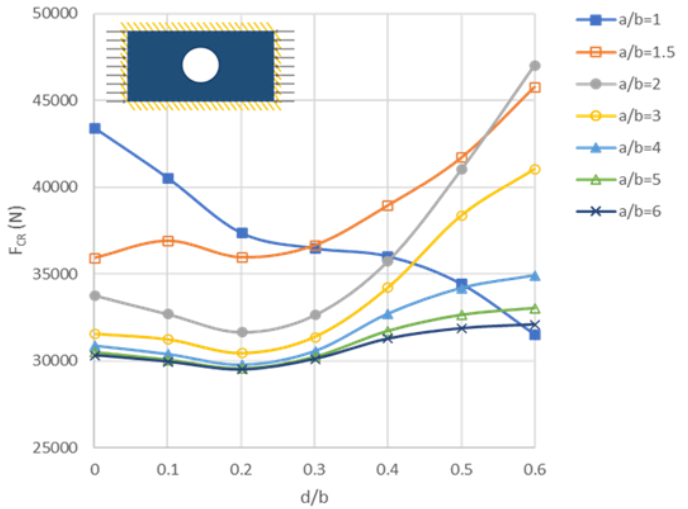
Fig. 3 a) Uniaxial compression stress loading condition of fixed support boundary condition perforated plate b) Shear stress loading condition of fixed support boundary condition perforated plate c) uniaxial compressive stress loading condition of simply support boundary condition perforated plate

In the finite element analyses, 1 N (approximately 0.25 MPa) loading was applied to the short edge nodes of the plate for the uniaxial compression stress condition and to the other edge points of the plate except the corner points for the shear stress condition.

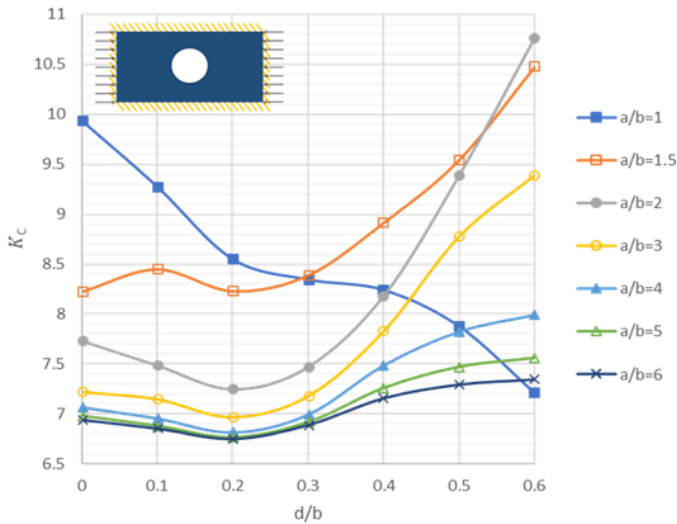
III. RESULTS

According to the analysis results, elastic buckling eigenvalue factors were obtained according to the plates' different a/b ratios and d/b ratios. Critical buckling forces were obtained by multiplying buckling eigenvalues with the force values applied to total the edge nodes. Buckling coefficients were obtained using Equation 1 and Equation 3. In NIU's study (Equation 4), the buckling equivalent coefficient for a square plate with no holes and a simply supported plate was 3.920 [1], and in our study, it is 3.917. The difference amount was found to be

0.08 percent. The results in the study also match the conditions included in El-Sawy study [7].

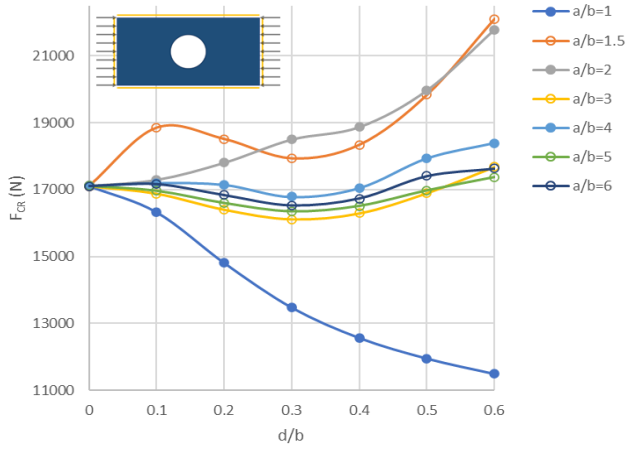


a)

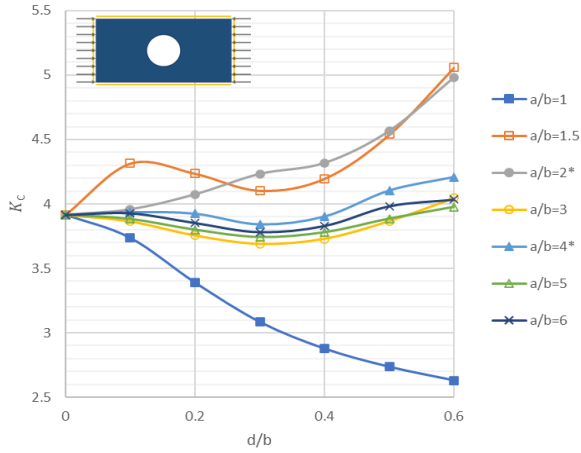


b)

Fig. 4 a) Elastic critical uniaxial compression buckling force for fixed support boundary condition perforated plate b) buckling coefficient uniaxial compression loading for fixed support boundary condition perforated plate

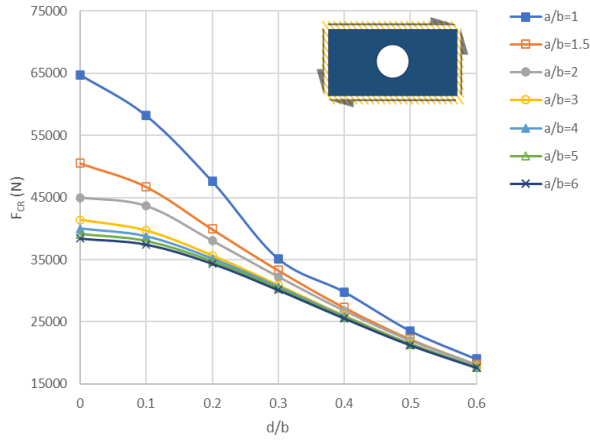


a)

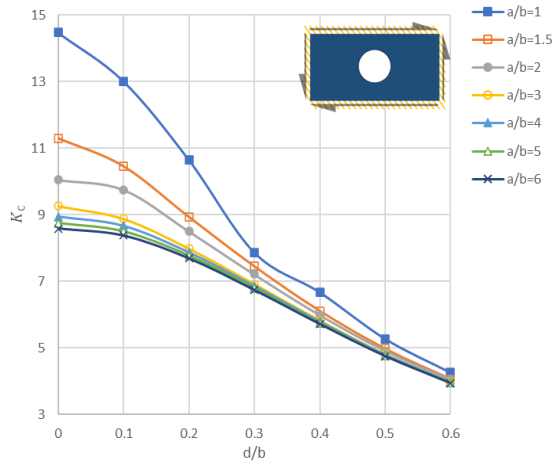


b)

Fig. 5 a) Elastic critical uniaxial compression buckling force for simply support boundary condition perforated plate b) buckling coefficient uniaxial compression loading for simply support boundary condition perforated plate



a)



b)

Fig. 6 Elastic critical shear buckling force for fixed support boundary condition perforated plate b) buckling coefficient shear loading for fixed support boundary condition perforated plate

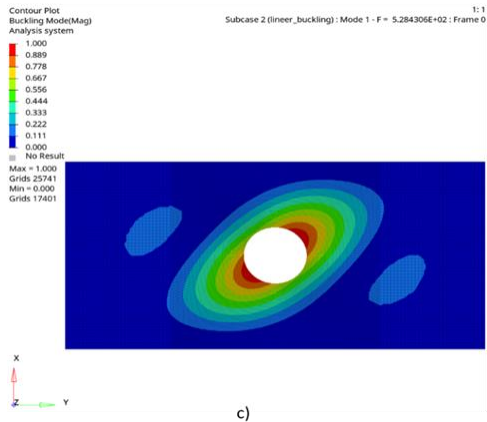
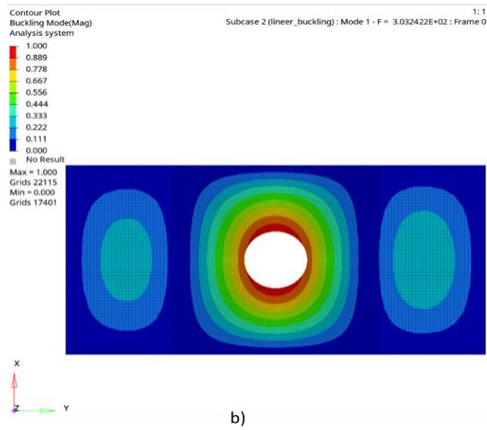
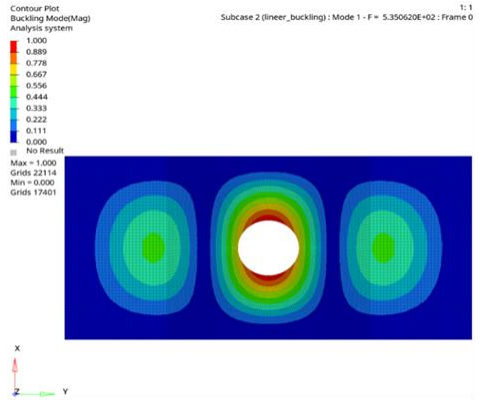


Fig. 7 a) Buckling mode 1 contour plot for uniaxial compression buckling force with fixed support boundary condition perforated plate b) Buckling mode 1 contour plot for uniaxial compression buckling force with simply support boundary condition perforated plate c) Buckling mode 1 contour plot for shear buckling force with fixed support boundary condition perforated plate

IV. CONCLUSION

In the analysis outputs, there was a continuous decrease in the critical buckling force value of square plates in three cases for the boundary conditions and loading cases examined. In thin rectangular perforated plates with uniaxial compression loading under fixed and simply supported boundary conditions, except for plates with $a/b=2$ and simply supported boundary conditions, no consistent increase or decrease in the critical buckling force required for buckling was observed by increasing the hole diameter. Increasing the hole diameter showed that if the a/b ratio was 1.5, a similar curve was observed for uniaxial compression loading and different boundary conditions. However, more force was required to buckle fixed-supported plates. In plates with a fixed support boundary condition where the a/b ratio is 2, the critical buckling force decreases to the d/b ratio of 0.2. At values greater than 0.2, an increase in uniaxial compression critical buckling loading is observed. If the a/b ratio is 3,4,5,6, a similar behavior as the a/b ratio is 2, but less decrease and increase is observed. It has been observed that the elastic pressure critical buckling force is increased by increasing the hole diameter for a/b ratio of 2 in simply supported plates. For simply supported plates, the critical uniaxial compression buckling force is lowest when the a/b ratio is greater than 2 and the d/b ratio is equal to 0.3. In cases where the d/b ratio is greater than 0.3, a slight increase in the critical buckling force is observed. For the fixed-support shear loading case, the critical buckling force in thin plates decreases significantly in all cases.

According to the analysis results, when loadings above the elastic buckling force are carried out, the possible damage areas caused by buckling occur longitudinally around the hole in uniaxial compression loading. In shear loading, it will occur in a diagonal pattern on the plate, depending on the loading direction. (It is illustrated in the figure 7) However, damage to the structure may not only be caused by buckling. If the stress occurring in the structure during loading is greater than the yield strength, permanent deformation and damage may occur. Therefore, damage control in the structure should also be examined in terms of yield strength.

With the study, the effect of a/b ratios and hole diameter changes on the critical buckling force can be predicted. Within the scope of the study, the buckling coefficients required to calculate the theoretical critical buckling load were obtained. For each boundary condition examined within the scope of the study, as the critical buckling load value in square plates decreases with increasing hole diameter, hole diameters that are as low as possible should be preferred. In rectangular plates, as in square plates, hole diameters that are as low as possible should be preferred for the fixed supported boundary condition under

shear loading. In cases where the aspect ratio is different from 1, the hole diameter should be selected for the critical buckling load and uniaxial compression load, considering the stress on the structure and the yield strength.

V. REFERENCES

- [1] M. C. Y. NIU, *Airframe Stress Analysis And Sizing*, 1999.
- [2] B. Cheng and J. Zhao, "Strengthening of perforated plates under uniaxial compression: Buckling analysis," *Thin-Walled Structures* 48, pp. 905-914, 2010.
- [3] S. Ghorbanhosseini, S. Yaghoubi and M. R. Bahrambeigi, "A Comprehensive Study on the Effects of the Boundary Conditions on the Elastic Buckling Capacity of a Perforated Plate," *ADMT Journal* 14(3), pp. 45-53, 2021.
- [4] S. P. Timoshenko and J. M. Gere, *Theory of elastic stability*, New York: ,2rd ed, McGraw-Hill, 1961.
- [5] C. C. C. d. Silva, D. Helbig, M. L. Cunha, E. D. dos Santos, L. A. O. Rocha, M. d. V. Real and L. A. Isoldi, "Numerical buckling analysis of thin steel plates with centered hexagonal perforation through constructal design method," *Journal of the Brazilian Society of Mechanical Sciences and Engineering* (41), pp. 1-18, 2019.
- [6] W. . L. Ko, "Mechanical- and Thermal-Buckling Behavior of Rectangular Plates With Different Central Cutouts," NASA, California, 1998.
- [7] K. . M. El-Sawy and A. S. Nazmy, "Effect of aspect ratio on the elastic buckling of uniaxially loaded plates with eccentric holes," *Thin-Walled Structures* 39, pp. 983-998, 2001.
- [8] F. Uslu, M. H. Saraçoğlu and U. Albayrak, "Buckling of Square and Circular Perforated Square Plates Under Uniaxial Loading," *Journal of Innovations in Civil Engineering and Technology* 4(2), pp. 61-75, 2022.
- [9] W. Wang, H. Ning, H. Wei, Q. Mei and L. Xu, "Influence of flanged-cutout on the buckling behaviors of square plate under uniaxial compression," *AIP Advances*, 13(2), 2023.
- [10] R. Narayanan and F. Y. Chow, "Ultimate Capacity of Uniaxially Compressed Perforated," *Thin-Walled Structures* 2, pp. 241-264, 1984.
- [11] J. Huet, *Static Stress Manual*, Metallic Materials, 1999.

- [12] L. Sabat and C. K. Kundu, "History of finite element method: a review," in *Recent Developments in Sustainable Infrastructure: Select Proceedings of ICRDSI 2019*, Springer, pp. 395-404.
- [13] E.-u. Thammakornbunjut, P. Meelapchotipong, J. Pakpia, S. Tammapattaragul and P. Limpitipanich, "Buckling of Square Plates with Different Central Cutouts," *Journal of Engineering and Digital Technology (JEDT)* 10(2), pp. 13-20, 2022.
- [14] "Altair Engineering, Inc.," 22 12 2023. [Online]. Available: <https://2020.help.altair.com/2020.1/hwdesktop/hm/index.htm>.
- [15] M. Muameleci, *Linear and nonlinear buckling analyses of plates using the finite element method*, Linköping: Master thesis in Solid Mechanics performed at Linköping University, 2014.
- [16] R. C. Rice, J. L. Jackson, J. Bakuckas and S. Thompson, "Metallic Materials Properties Development and Standardization (MMPDS)," FAA/ARMMPDS-01. Technical report., USA: FAA., 2003.

Chapter 33

Energy Consumption of Headlights in Electric Vehicles While Driving

Çiğdem CENGİZ¹,
Metin KAYNAKLI²

Abstract

This study is about the conscious use of headlights to save battery in electric vehicles. Since headlights are one of the most important components of any vehicle, headlight technology has seen a lot of research and development over the last few decades. If headlights are not used correctly, they are the cause of many traffic accidents. That's why researchers are constantly innovating to develop safer and more efficient headlights. These studies show that there is a need for the use of energy-saving and safe headlights. In electric vehicles, fuel directly refers to the battery capacity. Today, instead of gasoline and diesel vehicles, the use of electric vehicles, that is, battery-powered vehicles, is becoming widespread. The main reason for this is that economical fuel is produced from electricity. In this study, a vehicle with basic-level halogen headlights and a premium-segment vehicle with high-end LED headlights are compared. It consumed energy from headlights in equal conditions and at equal time in two vehicles. A Power Meter is installed between the headlights and the battery to measure the energy consumption of the vehicles. The energy consumption of the headlights was recorded using a Power Meter for each headlight. After the measurement, it was determined that the vehicle with LED headlights consumed 59% less battery under equal conditions than the vehicle with Halogen headlights; that is, the vehicle with LED headlights was more economical. In line with these savings, less energy was consumed, and the electric vehicle was enabled to travel more.

Keywords: Lighting, LED, Halogen, Energy consumption.

¹ Bitlis Eren University Bitlis /Turkey, (ORCID: 0000-0002-0010-0795)

² Bitlis Eren University Bitlis /Turkey, (ORCID: 0000-0001-8372-1345)

1. Introduction

The first motor vehicles appeared in the late 19th century. The lighting technology in these vehicles was not taken into account. When the dynamo began to be used in the automotive industry in 1908, automotive bulbs also began to be used. In the first headlights, light was reflected directly on the road thanks to parabolic mirrors. In the following years, the first reflectors were designed. These structures, consisting of parabolic mirrors, made it easier to see the road compared to previous technology. In this type of lighting, which functions more like a flashlight, the light coming from the focal point of the bulb is reflected on the road through reflective parabolic mirrors. It was not possible to adjust the high and low beams in these lighting systems. In 1911, specially coated metal reflectors were developed that increased driving safety and provided a more convenient field of view [1]. With the use of specially coated metal reflectors and new bulb holders, more advanced focusing settings on reflectors have become possible [2]. However, this time, problems such as glare in the driver's eyes have emerged while driving at night. This problem caused accidents, especially when the road was wet. Later, separate reflectors began to be used for low and high beams. With this arrangement, the light distribution problem is partially solved [3,4]. Studies on the production of low-and high-beam light on the same reflector yielded results in 1925. The first stop lamp was used in 1926 [5,6]. The first front fog lights were used in 1931 to better illuminate the road in response to changing weather conditions. Fog lights, with their special optical structure, illuminate the surface, unlike low beam, and can prevent the reflection of the light in the fog. Developments in the automotive sector, the acceleration of vehicles, and increasing traffic density have caused vehicle lighting systems to be inadequate. In particular, light bulb manufacturers competed to find bulbs that could illuminate more. Again, in order not to endanger the flowing traffic in the high-beam lighting area, more light was projected on the right side of the road with the use of asymmetrical light patterns in the low-beam headlights in 1945. In this way, the oncoming traffic is prevented from being disturbed by the light produced [1,2].

The first halogen bulbs in vehicle lighting started to be used in 1962 with the H1 model. As a working principle, it is based on the logic of the wire emitting light by heating as a result of current passing through a tungsten wire. In the meantime, the temperature of the wire rises to 3000°C, and the temperature of the metal socket of the light bulb rises to around 500°C. Then, in 1967, H3 bulbs were produced, and in 1971, the first bi-filament H4 bulbs were produced, respectively. The first progress with adjustable headlights in Europe was seen in France. In 1967, high-beam headlights that could rotate according to the steering direction

began to be used. H4 bi-filament lamps, which began to be used in 1971, began to be used in both low and high beams. While the automotive industry continues to progress within itself, a study conducted in the medical world determined that the third-stop light will better warn the driver behind it. According to the results of this research, automobile lighting systems were introduced to the third stop lamp in 1974 [3,4]. Ellipsoidal headlights were produced in 1983. Free-form headlights were produced in 1988. With the development of bulb technology, H7 bulbs were produced for the first time in 1992, after bi-filament H4 bulbs. During this period, the first Xenon headlights and the 3rd LED taillight were used. In parallel with the development in the automotive field, free-form headlights with transparent windshields were produced in 1993. In 1997, bluish bulbs and high-performance halogen bulbs containing xenon gas were produced. H8, H9, and H11 bulbs were produced in 1999. Bi-Xenon headlights were used for the first time in 2000. The first trials of central lighting systems were made in 2001. The development of static and dynamic rotating headlights was completed in 2002. In this system, the headlights could change direction at an angle of 15° depending on the steering position and cornering situation. In 2003, rotating headlights were approved for use in European countries. LED parking and daytime running lights were used for the first time. In parallel with these developments, static and dynamic rotating headlights were used together for the first time. In 2005, the first legally qualified LED-dipped beam prototype was produced. The headlamp, with its all functions powered by LED, was first used in 2007 [5-7].

After all these developments, the ever-increasing traffic density combined with the increasing vehicle speeds, the constant change in the needs of the drivers, and the driving conditions brought along very detailed work for the companies interested in vehicle lighting. The importance of vehicle lighting systems is gradually increasing, as it is expected from the lighting systems that they should be in continuous development against the change and protection of the potential driving conditions of the drivers, to perform the task of lighting independently of the changing conditions on the road, to protect the driver's vision despite the weather and other conditions, and to be an additional safety element in night driving. Today, vehicle lighting systems, which are divided into two front and rear lighting elements, basically work by the "See and Be Seen" rule. For this reason, vehicle lighting devices have become not only for night vision but also a security element in recent years [5,6]. Lighting systems in terms of design If the front lighting and rear lighting are examined, the primary task of the front lighting is to illuminate the road, to ensure that the driver can see the road according to the changing conditions, and to do all these promptly. It also provides recognition

of the vehicle against oncoming traffic. Backlighting, on the other hand, has the task of creating awareness in the rear traffic and indicating its status [1,4,7].

2. Batteries and Energy Regenerative Braking

One of the most important problems with batteries is that they cannot be charged quickly. To charge batteries quickly, fast charging stations that can provide high energy in a short time are needed. Of course, this is not enough; To prevent batteries from heating up while charging, they need to be carefully monitored through software and the energy flow adjusted accordingly. Charging can be stopped automatically if the voltage exceeds a certain level. Although it is relatively fast for batteries to reach 80% charge, after this point the charging process slows down and it may be necessary to wait longer for the remaining 20%. For this reason, fast charging stations are generally designed to be used to bring batteries to 80% charge. Thus, it may be possible to serve more people. With current technologies, fast charging stations can reach 80% charge in approximately half an hour. This time can reach 8-10 hours on a 220V standard household outlet. Factors such as charging speed, frequency, percentage, and temperature directly affect the total lifespan of the battery. Various alternatives have been developed for fast charging of batteries. One of these is to replace empty batteries with charged batteries. A low-battery electric car approaches a platform at a battery-swapping station. The robotic system on the platform takes the dead battery from under the vehicle and replaces it with the charged battery. The entire process is completed within a few minutes [8,9].

Another way to avoid using so much energy in electric vehicles economically is to use vehicles with energy-saving braking methods. The kinetic energy gained by a car accelerating by consuming energy turns into heat and is wasted when we brake. In electric cars, the vehicle's momentum during braking turns the electric motor, and the electric motor, which works like a dynamo, produces energy and feeds the batteries. In addition, as the load on the brakes decreases, the life of mechanical parts increases, thus the total cost decreases. Due to energy gain, electric cars slow down rapidly instead of slowing down slightly when you take your foot off the gas, like fossil fuel cars. Because as soon as you take your foot off the gas, the electric motor starts charging the batteries. Although this feeling may surprise those who use electric cars for the first time, it does not pose a problem once they get used to it [8,9].

3. Vehicle Road Lighting

Battery Electric vehicles have technology that captures power in a battery pack and uses it for driving. After the batteries run out, they need to be recharged from the grid or renewable charging stations. When offline, the power stored in the vehicle is limited by capacity and is directly affected by space availability and the type of battery used. The power unit is designed for a typical range based on the intended use of the vehicle. In addition to traction power, the vehicle also consumes its power from the battery for auxiliary activities such as lighting, sound systems, internal electrical devices, sensors, and all internal loads. These lights are a must for safe driving during the night.

Automobile lighting and the quality of the light sources used are important for a safe and comfortable ride. Lighting quality is measured by the vehicle's good illumination of the road ahead. For this reason, luminous flux, or, in other words, lumen, as the total amount of light emitted by a certain source, should not be a criterion for the selection of automotive lighting. When talking about lighting quality, the road in front of the vehicle must be well-lit; that is, how the light source in the headlight illuminates certain points on the road should be evaluated. In other words, point light intensity should be taken into account instead of the total light on the road surface. The most important point on the road for the driver's reactions and safety is about 50-75 meters ahead of the road from the driver's side. Bulbs that produce more light illuminate the road better at these points. Also, the color of the light is important. Good contrast is important for good vision. If the contrast is too low, it will be difficult to detect objects and distinguish them from the background. Even if drivers focus their eyes on a roadside traffic sign, pedestrian, or cyclist, they may not understand the danger or make the necessary maneuvers in poor lighting conditions. That's why using the right lighting with the right color temperature is very important. Although the maximum color temperature limit specified in the regulations is 4200 Kelvin, there are halogen lamps with higher color temperatures on the market. The way to get bluish-white light at high color temperatures is to apply a blue filter to the light source (bulb). When this filter is not applied by regulations at the correct rate, it reduces the amount of light transmitted to the road. When the slightest deviation occurs in the light source, the headlight will not be used 100% efficiently, and therefore the road will not be properly illuminated, thus driving safety will not be ensured. It is possible to classify vehicle exterior lighting as front and rear lighting. In Figure 1, the front and rear lighting systems in electric vehicles are shown.

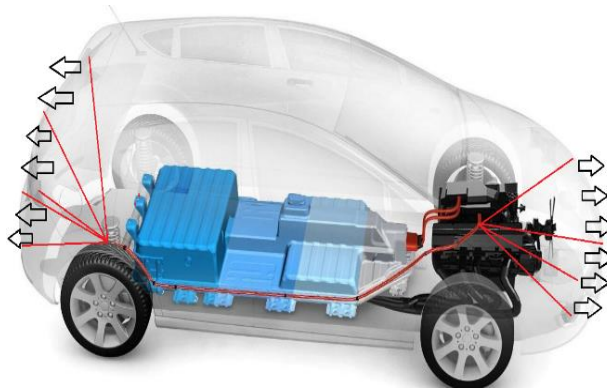


Figure 1. Front and rear lighting systems in electric vehicles.

3.1. Vehicle Front Lighting System

a) High beam: The high beam function is a function that is not always on in traffic. It catches the eyes of the drivers in the opposite traffic and poses a danger. It is the function used to illuminate long distances on intercity roads where there is no lighting in general. High-beam bulbs are powerful bulbs. It is one of the main sources of heat generated in the headlight. Its color is white, and 2 or 4 are used in the vehicle.

b) Low beam: The low beam function is a function that can illuminate less distance than the high beam used when it gets dark and does not dazzle the opposite traffic. A low-beam bulb is a bulb that draws less power than a high-beam bulb. Its color is white, and there are 2 in the vehicle.

c) Position function: The position function is the one that lights up with the headlight and is always on. It ensures that the limits of the traffic vehicle are known. Its color is white, and there are 2 in the vehicle.

d) Signal: The signal function is used to change direction in traffic. The signal function that is not always on can also be in yellow or orange. Its color is white, and there are 2 in the vehicle.

e) Side marker lamp: The function called side marker lamp is the function with more safety features placed at certain angles for the opposite traffic to notice the vehicle in the areas we call dead spots.

3.2. Vehicle Backlight System

a) Position function: The position function is the function that lights up with the headlight and is always on. It is used to notice the car and see its limits. It is red, and there are 2 in the vehicle.

b) Stop function: It is a non-continuous function that warns the traffic behind when braking. The stop function is complemented by an additional function called

the 3rd stop, which is mounted on the tailgate at the rear of the vehicle. Its color is red. There are 3 units in the vehicle, including the 3rd stop.

c) Signal function: This feature enables the vehicle to change lanes without obstructing traffic behind it. It does not light constantly; it flashes at a certain frequency. Its color is yellow. There are 2 in the vehicle.

d) Reverse gear function: It is the function that warns the traffic behind that the reverse gear is active. It is sufficient to have one at the back of the vehicle. Its color is white. There are 1 or 2 in the vehicle.

e) Rear fog function: It is a type of fog lamp placed behind the vehicle. While the front fog lights consist of powerful bulbs, the rear fog lights are only there to create awareness, so it is sufficient to contain only colored light. Its color is red. There are 2 in the vehicle.

f) Reflex function: It is a function that does not contain a bulb and works more efficiently in case of any bulb failure. It is a reflective lens built into the reflex backlight assembly. It creates awareness in the traffic behind by reflecting the light coming from the traffic behind at different angles.

4. Halogen Headlight and LED Headlight

The most commonly used lamp types in headlights are headlights with Halogen lamps, Xenon lamps, and LED lamps. The type with the most disadvantageous energy consumption is the headlights with halogen lamps, and the headlights with the most advantageous consumption are LED headlights. Today, energy consumption has become very important in electric vehicles since there is a trend towards electric vehicles, and the source directly consumed by the headlights is the battery. Because the energy used by the battery directly affects the distance traveled by the vehicle, for this purpose, in this study, halogen bulb headlights and LED source headlights were compared in terms of energy consumption, and a proportional result was tried to be reached. Nowadays, the vehicle fuel in electric vehicles is not gasoline or diesel, but the vehicle battery directly. For this reason, in this study, headlight consumption is investigated for the worst and best scenarios. Figure 2 shows a) a Halogen lamp, b) a Xenon lamp, and c) an LED lamp used for vehicle headlights.

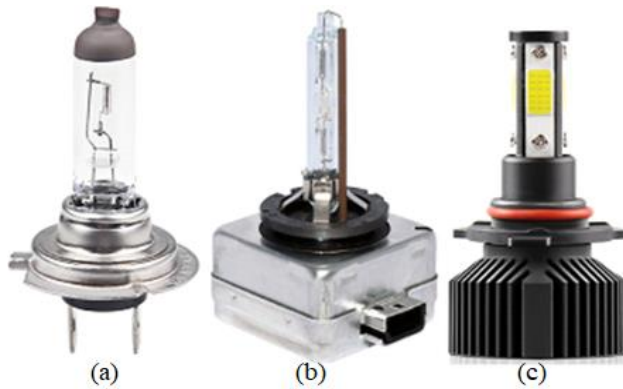


Figure 2. Used for vehicle headlights a) Halogen lamp, b) Xenon lamp, and c) LED lamp.

4.1. Halogen Headlights

The halogen headlight system is the most common headlight type known in the automotive industry. It has a long history and is very economical in terms of costs. The working logic of halogen headlights is the same as the bulbs in our homes that emit yellow light. Halogen headlights work through a tungsten filament that converts this current into light when the electric current from the vehicle's battery passes. This item is surrounded by glass. The glass contains argon and nitrogen gases. Halogen headlights emit light by bringing the electrical energy from the battery to 2500 Celcius. It can be said that it is an improved model of incandescent lamps for halogen headlight bulbs. Although incandescent lamps are still used by some classic cars today, they have been replaced by halogens. Halogens represent monovalent elements that can easily form negative ions. While there are five different halogens in nature, only iodine and bromine elements are used in lighting technology. The reason for this is that the tungsten filament in the bulb prevents breakage and darkening.

One of the most distinctive features of halogen lamps is that they produce a lot of heat and have a yellow hue. Compared to other bulb types, halogen bulbs, which are relatively cheaper, also have some disadvantages. Halogens have a shorter lifespan than others and offer a shorter viewing distance. The most common type of headlight, halogen headlights, has an average lifespan of 1000 hours. Halogen light types complete their lifetime as a result of the evaporation of the gases inside as a result of the cracking of the glass surrounding the tungsten filament or the breaking of the wires inside.

Halogen auto bulbs light up with the glow of the tungsten filament inside. Headlights, taillights, turn signals, license plate lights, and map reading lights in the vehicle are all halogen-based. Xenon or LED lighting is used in the headlights

of new-generation vehicles. Even the interior lighting, license plate lighting, stop, signal, and even headlights of some very new vehicles are completely LED. However, 80% of the vehicles on the market still use halogen-based lighting products.

Halogen bulbs can be found in a variety of forms. The bulbs used in the headlights are usually coded with the H type (such as H1-H3-H4). Vehicle manufacturers determine the most suitable bulb type for headlight designs. Each bulb type has its advantages and disadvantages. In other words, it is not possible to say what the best H4 or H1 type bulb is. Cars generally use 55-watt halogen bulbs. A 55-watt halogen bulb usually gives an average of 1300-1600 lumens (units of light). This value may vary depending on the type of bulb, whether it is a performance or long-life bulb. The front view of a vehicle with halogen headlights is shown in Figure 3.



Figure 3. Front view of a car with halogen headlights.

4.2. LED Headlights

Today, LED headlight lighting has become a mandatory part of modern cars. In the automotive sector, LEDs are used in the headlights, stop lamps, signal lamps, interior lighting, and indicator lights of vehicles. The use of LEDs in vehicles started with the use of taillights and gradually replaced halogen and xenon headlights. Headlights are the most important part of automotive lighting. When LEDs and sensing technologies are used together, smart applications such as matrix LED headlights (headlights in which each LED is controlled separately) are implemented. LEDs used in cars are manufactured from high-quality materials and tested to the highest specifications. In this way, it provides a long service life and eliminates the need for maintenance such as bulb replacement. High-power LEDs are generally preferred in vehicle headlights and signal groups. These LEDs are designed for high performance and a long lifetime. LEDs that can provide high lumens from a small form factor have low thermal

resistance and high operating temperatures. Surface-mounted (SMD) LEDs used in headlights and signal groups are generally produced in white (5000 K - 6500 K) and amber (588 nm - 592 nm) colors. Medium-power LEDs are generally used in the taillights of vehicles. The LEDs used on the stop lamp usually consume less than 1 W and give light with a brightness of 50-60 lumens. The wavelength of these LEDs, which are produced in a red color specific to the automotive industry, is in the range of 610 nm to 620 nm.

LED headlight bulbs have a more advanced technological infrastructure than Halogen and Xenon bulbs. LED technology makes it possible to produce more light with less energy consumption. The instantaneous full brightness of the LEDs ensures high selector performance. Due to this feature, LED headlight bulbs are also known as lightning LED, lightning effect LED, or LED Xenon. LEDs are replacing conventional halogen-incandescent bulbs in modern motor vehicles day by day. It not only offers high luminous efficiency and greater safety but also offers greater design freedom and high energy-saving potential.

LED headlights and LED headlight bulbs have become indispensable parts of modern cars. LED headlight bulbs have a more advanced technological infrastructure than Halogen and Xenon bulbs. LED technology makes it possible to produce more light with less energy consumption. The instantaneous full brightness of the LEDs ensures high selector performance. Due to this feature, LED headlight bulbs are also known as lightning LED, lightning effect LED, or LED Xenon. In the selection of LED headlight bulbs, it is necessary to pay attention to 5 points;

1. Bulb type,
2. Brightness level
3. Light distribution,
4. Color temperature
5. Lifespan.

Car headlights are designed to work with standard types of bulbs. In this way, bulbs belonging to different houses can be easily mounted on the headlight. Although there are usually separate bulbs for low-and high-beam headlights in the headlight, in some vehicles, both low-and high-beam functions are performed with a single bulb. H1, H3, HB3, H4, HB4, H7, and H11 are the most common types of headlight bulbs.

LEDs have a higher light source than Halogen and Xenon bulbs due to their safety. LED headlight bulbs are more than 2 times brighter than Halogen bulbs. This means better lighting and better visibility at night. On the other extreme, inexpensive LED kits may not deliver the expected performance. It is not true

that manufacturers emphasize this value in place of the lumen value for each bulb. Incorrect light spots on LED bulbs, dangerous for other ships, can cause a light distribution. For this reason, the positioning of the LEDs on the headlight bulb is extremely important. In high-quality bulbs, the LED chips are positioned at the most suitable points. Thanks to this light, it has appropriate limitations in its far reflector. The front and rear distant views of a vehicle with LED headlights are shown in Figure 4.



Figure 4. Front and rear headlight view of a vehicle with LED headlights.

4.3. Dot (Matrix) LED Headlights

Matrix LED headlights are headlight systems equipped with a series of individually addressable and controllable LEDs to provide a better driving experience at night. It works with traffic detection devices and electronic control units to optimize lighting scenarios. It provides good road lighting without disturbing oncoming vehicles or vehicles in front. Car headlights are designed to switch between low and high beams depending on traffic and road conditions. The low beam provides short-range illumination delimited by a horizontal line so as not to disturb other vehicles. The high beam, on the other hand, provides a center-weighted light distribution and reaches far distances. In high beams, priority is given to widening the field of view over the comfort of other drivers. LEDs are semiconductor devices that produce light when an electric current is passed through them. By controlling the current flowing through the LEDs, the light intensity can be controlled dynamically and precisely. Unlike filament and gas discharge lamps, LEDs can be turned on instantly. On the other hand, LEDs are extremely resistant to switching. In this way, LEDs become a unique solution for new-generation headlight equipment. Matrix LED headlights consist of multiple LEDs mounted on a common module. Each LED has a special driver circuit for on-off switching and control of light intensity. Thus, the Matrix LED technology can split the high beam into multiple lower beams. Pixel-level digital control over the high beam is provided in Matrix LED headlight systems. In this way, it is aimed at eliminating the negative effects of high-beam headlights on

other drivers. Matrix LED systems constantly monitor the front of the vehicle with the help of a camera and interact with the lighting system in the driving environment. Visible, light-sensitive cameras can detect almost any traffic. The data collected by the camera is evaluated by the electronic control unit and used to manage the control circuitry that regulates the light output of each LED. When another vehicle is detected in front of the vehicle, the distracting glare-producing LEDs are turned off, and the oncoming vehicle is masked. Meanwhile, other LEDs continue to illuminate the road. Figure 5 shows the road lighting of the Matrix LED headlights.

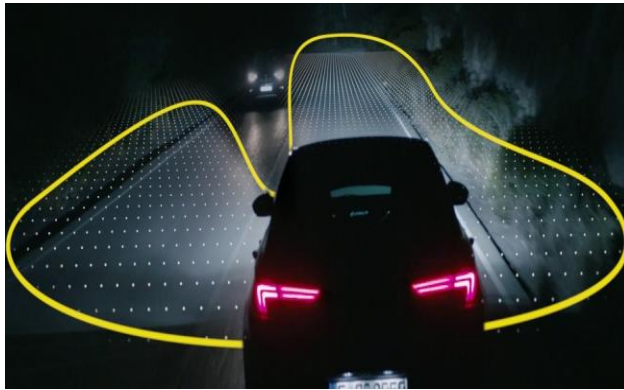


Figure 5. Road illumination of Matrix LED headlights

5. Conclusion and Suggestions

If a voltage is applied to a light-emitting diode, the resistance drops to zero. Light-emitting diodes are extremely sensitive components and can fail if even a small amount exceeds the allowable current. For this reason, it is important to never connect light-emitting diodes directly to a voltage source. They can only be connected if a current limiter or series resistor is installed in the circuit. The high-performance LEDs are controlled via an electronic ballast that provides a constant current. In this case, a series resistor is used as a limiter that controls the current I_F flowing through the LED. To select the appropriate resistor, the UF voltage must be determined beforehand [7]. In this way, excessive current flowing through the LED is prevented, and damage to the LED is prevented [10,11]. Figure 6 shows the electrical circuit necessary for the optimum functional performance of the LED. The R_V resistance of the created measurement circuit is given in Equation 1.

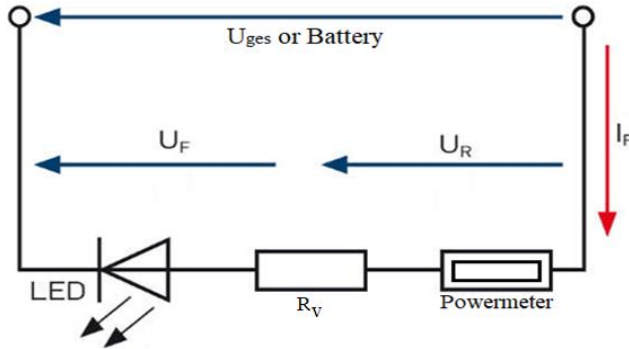


Figure 6. The electrical circuit required for the optimum functional performance of the LED.

$$R_V = \frac{U_{ges} - U_F}{I_F} \quad (1)$$

Although LED has only been used in the premium segment of the automotive industry so far due to its high purchasing costs, it will become the standard in the long run. In addition to the economic aspects, there are also technical reasons for using LEDs in headlights. Light-emitting diodes impress with their functionality, technical performance, and optimum lighting results. They support the conservation of energy resources and provide greater safety in traffic. In addition, the light color similar to daylight provides a pleasant and subjectively enhanced light perception [12-15].

The LED market for lights and headlights continues to evolve in the long run in two directions: On the one hand, the premium segment will become more important, which will require high functionality with excellent light output. On the other hand, the economically and ecologically motivated sector will be further encouraged, which requires not only low energy consumption but also cost-effective solutions. Highly advanced, functional, and economical LEDs will offer many options.

Premium segment models of some automotive brands have been optionally available with full LED headlights since 2010. The front projection lens provides a unique low beam. Daytime running lights also have a unique feature, as they are combined with both a turn signal and a position light. In addition, as LEDs can be turned on or off independently of each other, Adaptive Headlight Systems show successful results in vehicle lighting. For example, in countries where traffic flows from the left, certain LEDs on the left can be turned off.

In Scandinavian countries, daytime running lights have been activated to make vehicles more visible due to the long, dark weather. Today, in many European

countries, the same practice has been followed, and daytime running lights have become a mandatory traffic rule. The activation of daytime running lights is used entirely to make vehicles, motorcycles, and other vehicles more distinctive. From time to time, vehicles that do not notice each other during the day cause serious accidents. Thanks to experiments carried out in empty spaces, it has been determined that accidents can be reduced by using daytime running lights [16-22]. After the acceptance of daytime running lights, it should be determined whether these headlights should be of halogen or LED origin.

6. Material and Method

Environmental protection and rising fuel prices are the two strongest arguments that show that energy saving is more important than ever today. Today, the main focus of new vehicle purchases is fuel consumption. However, today, thanks to both hybrid and fully electric vehicles, fuel means the current drawn from the vehicle battery. For this purpose, the more electricity consumption in the vehicle can be reduced, the more the vehicle's range will increase. That is, attention should be paid to the energy consumption savings potential for vehicle lighting [23-26]. In this study, the energy requirements of a vehicle with incandescent taillights and halogen headlights were determined. For this purpose, measurements were made with a mini-type energy analyzer with a data logger feature. The Power meter connected to the electrical connection to the headlights recorded the total electricity consumption.

For this purpose, fully LED lamp headlights and Halogen headlights were compared in terms of energy consumption. Both vehicles, that is, vehicles with halogen headlights and vehicles with LED headlights, were subjected to the same treatment for equal periods. The results were compared proportionally.

In this study, both the vehicle with complete LED headlights and the vehicle with halogen headlights were exposed to energy consumption for equal periods, respectively. For my headlight-related energy consumption, the right turn signal, left turn signal, daytime running light, high beam, low beam, brake light, fog light, and tail light were operated for 10 minutes each. Vehicle-1 has halogen headlights with basic-level equipment. Vehicle-2 has premium segment-equipped LED headlights. In Table 1, the type of headlights for vehicles can be seen.

Table 1. Type of headlights for vehicles.

Vehicles	Vehicle-1	Vehicle-2
High beam	Halogen	LED
Dipped beam	Halogen	LED
Brake light	Halogen	LED
Rear lights	Halogen	LED
Daytime running light	Halogen	LED
Left turn signal light	Halogen	LED
Right turn signal light	Halogen	LED
Fog lights	Halogen	Halogen
Rear fog light	Halogen	Halogen
Reversing light	Halogen	LED

For this purpose, the energy consumed with the mini Powermeter was recorded. The Powermeter was connected between the headlight and the battery, and the total power passing through the Powermeter was recorded. The power meter is shown in Figure 7.



Figure 7. The power meter connected to the headlight.

The Powermeter used is an easy-to-use DC power analyzer (4-60V 0-100A), and Watt-hours to measure the power flow in a low-voltage circuit. It measures the total current drawn from a battery or the current sent to the battery. The positive/negative (GND) two-wire input (source) and the two-wire output (load) are used for serial addition to the circuit. It updates and records every 0.4 seconds. The % energy consumption of the headlights used in completely equal conditions in terms of duration and function is shown in Table 2.

Table 2. Energy consumption in % of headlights used

Total Energy Consumption From Headlights (%)		
Type of headlight in the vehicle	Halogen	LED
High beam	6%	2%
Dipped beam	61%	33%
Brake light	10%	1%
Rear lights	13%	2.5%
Daytime running light	7%	1%
Left turn signal light	1.5%	0.3%
Right turn signal light	0.5%	0.2%
Fog lights	1%	1%
Rear fog light	-	-
Reversing light	-	-
Total Consumption	100%	41%

It has been observed that the energy consumption of the vehicle using only LED lighting is reduced by 59% compared to the vehicle using Halogen headlights. In electric vehicles that do not use gasoline or diesel fuel, the fuel is the energy provided by the battery. For this reason, the less energy consumed by the battery, the longer distances can be traveled with the energy provided by the battery in the electric vehicle. The energy consumed by the headlights directly affects how many kilometers the vehicle will travel. For this reason, a vehicle with LED headlights, which save 59% energy compared to a vehicle with halogen headlights, will be able to travel more kilometers. Figure 8 shows the distribution of 100 units of energy consumed for halogen headlights according to headlights. Figure 9 shows the distribution of 41 units of energy consumed for LED headlights according to headlights. In other words, in Figure 8, while the car with halogen headlights consumes 100 units of energy, the vehicle with LED headlights consumes 41 units of energy for the same work, and a total of 59 units of energy are saved from the energy used in the headlights.

Halogen Headlights: Total energy consumption of 100 units

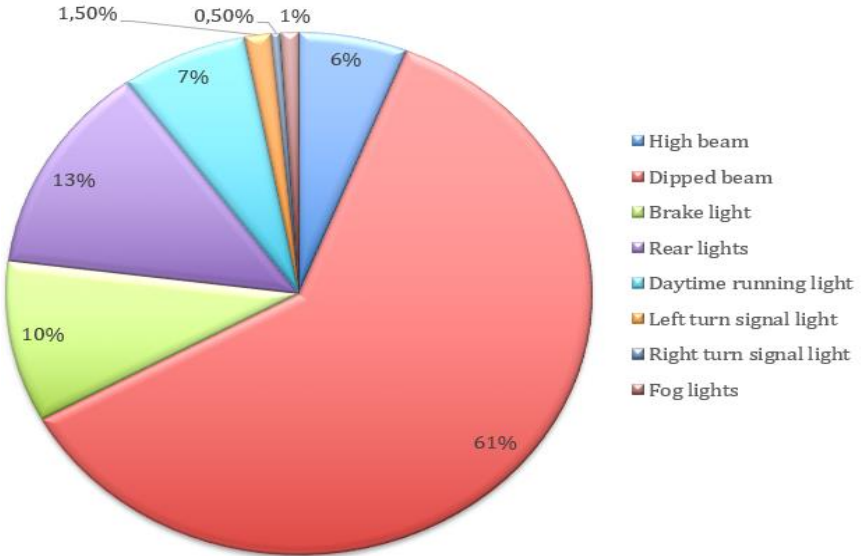


Figure 8. Distribution of 100 units of energy consumed for halogen headlights by headlights.

LED Headlights: Total energy consumption of 41 units

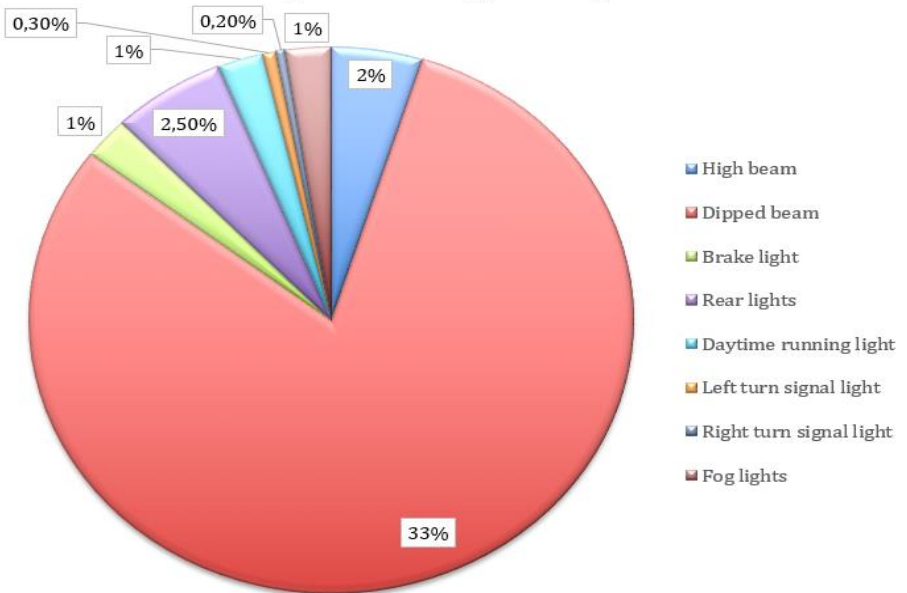


Figure 9. Distribution of 41 units of energy consumed for LED headlights by headlights.

7. Results and Discussion

In the circuit designed to be used in an electric vehicle, the energy consumed from the battery was measured for the High beam, which is used for equal periods under equal conditions. While the ratio of all energy used in the vehicle to the energy used in halogen headlights is 6%, it is recorded as 2% in LED headlights. Accordingly, using LED headlights consumes up to 4% less energy. This means a longer range for the electric vehicle, that is, longer distance travel. The low beam, which is widely used in vehicle road lighting and causes great energy consumption, increases the distance of the electric vehicle while saving energy. While the percentage of energy consumed in dipped headlights is 61% in halogen headlights, the energy consumption in LED headlights is recorded at 33%. Using LED headlights consumes up to 28% less energy. This savings decreased from 10% to 1% on Brake lights. In the rear lights, the energy consumption of the headlights was reduced from 13% to 2.5%, resulting in 10.5% energy savings. Parallel to these results, 6% energy savings were achieved in Daytime Running Lights, 1.2% in Left-Turn Signal Lights, and 0.3% in Right Signal Lights. With the use of LED headlights in total, 59% of energy consumption was achieved while driving, thus increasing the distance of the electric vehicle.

8. Conclusions

With the use of LED headlights in electric vehicles, optimum results can be obtained in terms of energy consumption and savings potential.

First of all, when the halogen headlight features are listed, the first thing that comes to mind is the cost. Halogen headlights have lower production and replacement costs. However, today, the price of LED headlights has decreased and has begun to decline economically. Therefore, the use of LED source headlights will increase in the future. In the application study, the energy consumption of the vehicle with LED headlights provided an advantage of 59% compared to the energy consumption of the vehicle with halogen headlights.

In vehicles with LED headlights, technology compatibility comes to the fore thanks to their ergonomic dimensions and software control possibilities. An important example of this is the adaptive dimming and re-energizing of the matrix headlights based on the position of the oncoming driver.

Another important feature of LED headlights is that they reduce the total amount of power needed in the vehicle. As the amount of power needed increases, the battery sizes are enlarged. Increasing the battery dimensions will increase the vehicle's weight, thus increasing the mass-based energy consumption of the vehicle traveling on the road.

REFERENCES

- [1] Bauer, H., Automotive Electric/Electronic Systems Lighting Technology, Bosch GmbH, Stuttgart, pp. 52, 1999.
- [2] Wulf, J., Reich, A. Temperature loads in headlamps, SAE World Congress and Exhibition, Detroit. 2002.
- [3] Moore, D.W. Headlamp history and harmonization, Michigan, Report No. UMTRI-1998, 98-2, 1998.
- [4] Moore, W.I., Donovan, S.E., Powers, C.R. Thermal analysis of automotive lamps using the ADINA-F coupled specular radiation and natural convection model, Computers and Structure, 72, pp. 17-30, 1999.
- [5] Derlofske, J.V., Bullough, J.D., Gribbin, C. Comfort and visibility characteristics of spectrally tuned high-intensity discharge forward lighting systems, European Journal of Scientific Research, 17(1), pp. 73-84, 2007.
- [6] Honeywill, T. Simulation sees, Automotive Engineer, pp. 32-33, 2007.
- [7] Hella Tech World, <https://www.hella.com/techworld/tr/> [Accessed: Jan. 11, 2023].
- [8] Yılmaz, M., Krein, P.T. Review of battery charger topologies, charging power levels, and infrastructure for plug-in electric and hybrid vehicles. IEEE Transactions on Power Electronics, 28(5), pp. 2151-2169, 2013.
- [9] Sun, X., Li, Z., Wang, X. & Li, C. (2019). Technology development of electric vehicles: A review. Energies, 13(1), 90, 2019.
- [10] Y. Bora, U.B. Önen, N. Umurkan, A review of electric vehicles and their impacts on the grid, International Journal Science Technology Research, 6(10), pp. 251-256, 2017.
- [11] C. Yavuz, E. Yanikoglu, Ö. Guler, Evaluation of Daylight Responsive Lighting Control Systems According to the Results of a Long Term Experiment, Light & Engineering, 20, pp.75, 2012.
- [12] Y. Sayan, Y. Kim J., H. Wu H. Residual Stress Measurement of a Single-step Sintered Planar Anode Supported SC-SOFC Using Fluorescence Spectroscopy, Bitlis Eren Üniversitesi Fen Bilimleri Dergisi, 11(3), pp. 902-910, 2022.
- [13] S. B. Efe, D. Varhan, Interior Lighting of a Historical Building by Using LED Luminaires a Case Study of Fatih Paşa Mosque, Light and Engineering, 28(4), pp. 77–83, 2020.
- [14] Cengiz, M.S. Role of Functional Illumination Urban Beautification: Qatar-Doha Road Illumination Case, Light & Engineering, 30(3), pp. 34-42, 2022.

- [15] Cengiz, M.S. Effects of Luminaire Angle on Illumination Performance in Tunnel Lighting, *Balkan Journal of Electrical & Computer Engineering*, 7(3), pp. 250–256, 2019.
- [16] Onaygil, S., Guler, Ö. Determination of the Energy Saving by Daylight Responsive Lighting Control Systems with an Example from Istanbul, *Building and Environment*, 38(7), pp. 973–977, 2003.
- [17] Yavuz, C. Yanikoglu, E., Güler, Ö. Determination of Real Energy Saving Potential of Daylight Responsive Systems: A Case Study From Turkey, *Light & Engineering*, 18, pp. 99, 2010.
- [18] Buyukkinaci, B., Onaygil, S., Güler, Ö., Yurtseven, M.B. Road lighting automation scenarios depending on traffic speed and volume, *Lighting Research Technology*, 51(6), pp. 910–921, 2019.
- [19] Cengiz, M.S., Cengiz, Ç. Numerical Analysis of Tunnel LED Lighting Maintenance Factor, *IIUM Engineering Journal*. 19(2), pp.154-163, 2018.
- [20] Kıyak, İ., Oral, B., Topuz, V. Smart indoor LED lighting design powered by hybrid renewable energy systems, *Energy and Buildings*, 148, pp. 342–347, 2017.
- [21] Dogruer T., Can, M.S. Design and robustness analysis of fuzzy PID controller for automatic voltage regulator system using genetic algorithm, *Transactions of the Institute of Measurement and Control*. 44(9), pp. 1862-1873, 2022.
- [22] Onaygil, S., Güler, Ö. The Effect of Luminance Uniformity on Visibility Level in Road Lighting, *Lighting Research and Technology*, 35(3), pp. 199–215, 2003.
- [23] Goswamy, A. Hallmark, S., Litteral, T., Pawlovich, T.M. Safety evaluation of destination lighting treatment at stop controlled cross-intersections. *Transp. Res. Rec.* 2672, pp. 113–121, 2018.
- [24] Jawi, Z.M. Prasetijo, J., Kassim, K.A.A., Tan, K.S., Mahyeddin, M.E. Vehicles safety-related impacts of various high beam headlights intensities. *Int. J. Adv. Trends Comput. Sci. Eng.* pp. 59–64, 2020.
- [25] Chen, Y.S. Chiu, S.C. New method of automatic control for vehicle headlights. *Optic*, 157, pp. 718–723, 2018.
- [26] Orynych, O., Tucki, K. Technology management leading to a smart system solution assuring a decrease of energy consumption in recreational facilities. *Energies*, 13, pp. 3425, 2020.

Chapter 34

R-SHINY App As An Interface For Topic Modeling: Rtoptech

Ahmet ALBAYRAK¹

Muammer ALBAYRAK²

ABSTRACT

In this study, R Shiny application was developed for topic modelling. Shiny is an R package for developing interactive web applications. R is used in many different disciplines to fulfill data science processes. Shiny provides great convenience especially for researchers who complain about the difficulty of developing web applications and who are not competent in the field to develop web applications. When searching on Web of Science (Wos) with R Shiny keywords, an increasing number of studies are found every year. In this study, a web application has been developed on topic modelling, which has an important place in natural language processing studies. Topic modelling can be done with different techniques such as deep learning after the execution of natural language processing steps. The deep learning models developed today are of the unsupervised type. After the web application was developed, it was tested on a case study. The data set was prepared for the case study. The data set has been prepared for the Cyber Security program, which provides postgraduate education. The studies of three conferences and four journals with high impact factor in the field of Cyber Security, which have been accepted in the last five years, were collected one by one. Papers and articles were selected by selecting the year, title, keywords, and abstract fields. The prepared data set was evaluated with the developed application, the topic modelling was done, and the results were shared.

Keywords: R Shiny, Data Science, Natural Language Processing, Latent Dirichlet Allocation, Topic Modelling

¹ Düzce Üniversitesi, Mühendislik Fakültesi
ahmetalbayrak@duzce.edu.tr

² Karadeniz Teknik Üniversitesi
m.albayrak@ktu.edu.tr

1. INTRODUCTION

The R language emerged with the 90s and is preferred by researchers in many different disciplines such as statistics, biology, physics, mathematics, economics, and chemistry. The most distinctive feature of the R language is that even for new users, basic statistical analyses on the data and visualizations for understanding the data can be made easily. Thanks to this ease of use, it is preferred even in the fields of machine learning and artificial intelligence today. The R language is built on the S language. Due to the intensity of use of the S language, the R language was announced academically in 1996 with the voluntary contributions of the researchers. In 2000, the first stable version of the R language was officially announced. *Tidyverse* and *ggplot2* packages for data visualization and analysis, which is a very important process for data scientists, were announced in 2007. Over time, various packages have been developed for reading, processing, and modelling all kinds of data. Nowadays R publishes packets over CRAN (Comprehensive R Archive Network). R can now perform many functions such as machine learning, deep learning, natural language processing, statistical analysis, data visualization, for which web applications can be developed. In this way, it has become an indispensable tool for data scientists. R is also used in big data environments where processing intensity and data are high [1, 2].

In the literature, there are about 500 studies when searching (in the topic area) with the keywords R Shiny in the WoS environment. These studies also include articles and conference proceedings. When the results are analysed, an increasing number of Shiny web applications are made every year. The indicator page where Covid-19 data is visualized and analysed was made in 2021. The application has been developed interactively and is designed to follow up the cases in real time [3]. In the R Shiny application called ABCMETA app, basic statistical operations are performed for the meta-analysis process and Bayesian calculations are performed. Especially statistical distributions were analysed in practice [4]. Shiny applications are more common in the healthcare field. To fully understand scientific data visualization, data patterns and trends in nursing, the interactive Shiny application has been developed. The app is intended to assist people in presenting health-related data [5]. Dose adjustment is very difficult and important in toxicological studies. The Shiny application has been developed, which performs mathematical functions to perform dose adjustment [6]. A web application has been developed for marking RNA sequences [7]. In the chemometrics course in the undergraduate chemistry program, students use the Shiny application, which runs multivariate calibration focusing on partial least squares regression as the most widely used data processing tool. Thanks to this software, it has been observed that the performance of the students has increased

[8]. The process of assigning genotypes and phenotypes in the field of bioinformatics has historically been quite challenging. In order to speed up the process, the application has been developed to analyse the relationships between enzymes. The application, which performs the detection of gene clusters and various hypothesis tests, provides a simple, customizable, and user-friendly interface [9].

Estimating ecological processes is a very important and challenging process. Visualization of ecological data has the effect of facilitating the forecasting process. It has been seen that the course and the estimation processes are more understandable and easier with 136 students using the application developed within the scope of the introduction to ecological forecasting course [10]. The Shiny application has been developed for operations such as fertilization, irrigation, crop and soil protection, weather index, yield forecasting, crop classification or bio-indicator of climate change in agriculture [11]. In the study, the data kept since 1993 were analysed on the application. Decision support systems developed for the analysis of environmental problems are used to combat the increasing complexity of environmental problems and to support policy makers [12]. Environmental researchers use R language extensively in decision support systems. In the study, it is explained how to distribute the R Shiny application developed for the analysis of environmental data with Docker [13]. Distributing an application contributes to making that application easier to access and to be used by more researchers [14, 15].

R language and Shiny applications are also encountered in the field of social sciences. In the application developed on behaviour change, factors were adopted as independent variables and behaviour change as dependent variables. Behavioural changes were analysed by sensitivity analysis [16]. Survey studies are processes where the cost of data collection is high, and the process takes a long time. With the developed R Shiny application, reliability tests that expand the scope, ease and cost-effectiveness of online survey research are carried out [17]. There are approximately 670 thousand records in the Digital Theses and Theses Library in Brazil. The developed application is intended to help track metadata and usage statistics. Data visualization tools are used effectively here [18]. An interactive application named shinyReCoR has been developed for natural language processing and analysis of textual data. In practice, it performs steps such as text data compilation, semantic relationship creation, text data pre-processing and clustering. Textual data has increased a lot today with the emergence of big data and social networks. Extracting meaningful information from textual data poses significant challenges for today's researchers [19].

Data science consists of decision support systems that aim from data collection and interpretation to data manipulation, exploration, and modelling, and ultimately to generating insights. Today, the increasing amount of data due to developing technologies is pushing institutions and companies [20]. Companies need data scientists to analyse these large datasets and gain insights. But the breadth and complexity of data science scenarios means that the modern data scientist requires extensive knowledge and experience in a multitude of subjects. With the increasing demand for data analysis skills, the demand for data scientists has increased. However, it is difficult to find data scientists with sufficient experience and knowledge of the field. As a result, it gave rise to the idea of automating some, if not all, of the data science processes [21]. Data science is a complex process driven by the structure and purpose of the data being analysed. At the same time, data science is highly exploratory in nature and repetitive in terms of operations. The process most likely to automate in data science processes is model building. The model includes approaches such as machine learning and deep learning under the artificial intelligence headline [20, 21]. Examples of automating model creation are Auto ML (Auto-WEKA, Amazon Sage Maker, Rapid Miner, IBM Modeler, SAS Enterprise Miner, Bayes DB, Tabular, Flash Extract, Data-Diff, etc.). Data integration has become an important step in data science due to the increasing diversity in data. Weka Knowledge Flows, Clowd flows etc. for data integration. SeeDB, Voyager etc. for data visualization tools have been developed [22]. The R Shiny application developed in this study can be used for the analysis of textual data, which is emerging intensively today, and can be considered as a data science automation tool [23, 24, 25, 26, 27]. The contribution of this study to the literature is that it allows topic modelling with an application in which natural language processing processes are easily performed. The developed application has been tested to determine the content for the graduate Cyber Security program. It is anticipated that this study will contribute to the literature with this aspect. This study continues with the second part where the developed Shiny application is given and then the part where the study is tested.

2. APPLICATION DESIGN AND DEVELOPMENT

In this study, Shiny application is designed as a dashboard. The application, which is structured in tabs where the topic modelling process steps are carried out, consists of four separate parts. These tabs are the section where the data is loaded, the section where the data is visualized, the section where the topic modelling is done, and the sections where the results of the process are given.

A. Tab 1: Home and Dataset Loading

This tab provides the demo page and raw data implementation. Raw data can contain textual and numerical data. Numerical data consists of metadata describing textual data. In this application, which was developed for the purpose of topic modelling, numerical data are processed separately from textual data. Numerical data and textual data are visualized after being implemented in this process step. Scatter plots, bar charts, and histograms are available to visualize numerical data. Word cloud technique is used to visualize textual data. Figure 1 shows the main screen of the application.

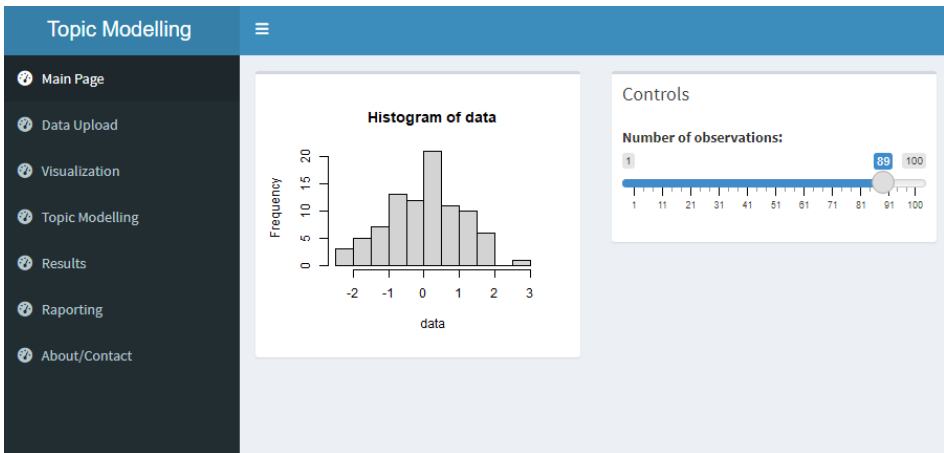


Figure 1. The main screen of the application.

The main screen contains the information and graphics of the application. The screen in Figure 2 has been developed to import and analyse data into the application. In Figure 2, data in csv, excel and other file types can be included in the application.

A scale has been put to create it according to the number of observations in the word cloud data set. The user can interactively configure the word cloud by considering the number of observations. Visualizing textual data by frequency is not a widely used technique academically, but researchers are quite useful [28, 29].

C. Tab 3: Topic Modelling: LDA (Latent Dirichlet Allocation)

Topic modelling is known as an unsupervised machine learning technique used to explore topics in various text documents. These topics are abstract in nature, meaning that interrelated words form a topic. Similarly, a single document can have multiple topics. In this study, LDA technique was used for subject modelling. The LDA subject model creates clusters of similar and related words called subjects. These topics have a specific distribution in a document, and each topic is defined by the ratio of different words it contains. Topic modelling is preferred to bring together related/similar text sources. One of the powerful techniques' researchers can use when they want to automatically organize, understand, search, and summarize large electronic archives is LDA [30]. The third tab architecture is given in Figure 4.

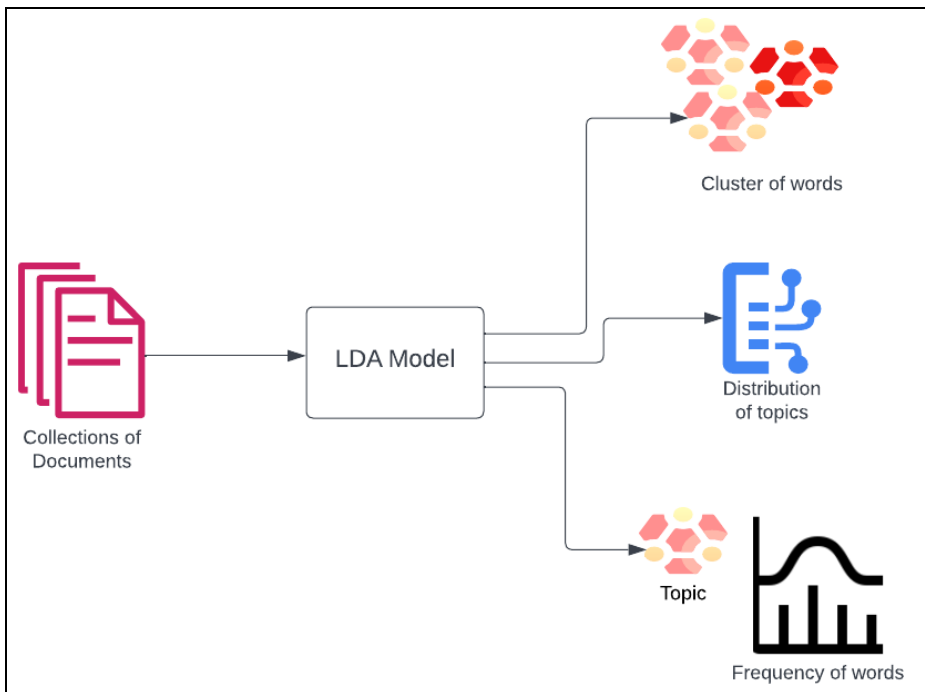


Figure 4. Subject modelling tab architecture.

In natural language processing, in processing textual data, LDA is a statistical model that describes a set of observations through unobserved groups, and each group explains why some parts of the data are similar. Almost 80% of the data produced today is in textual data format. It is the increase in the use of social networks that most affects the textual data format. Textual data is stored in NoSQL databases that do not have a strict schema. These data are in the form of unstructured data. To be processed within a model, they must be converted to structured data format [25, 26]. In this study, topic modelling was performed on the data in the structured data form.

Each document shows a mix of hidden topics, characterized by the distribution of each topic on unique words in the document collection. LDA architecture is given in Figure 5. In the document with textual data, words are represented by $W_{d,n}$. n represents each word ($n=1, \dots, N$), d ($d=1, \dots, D$) represents the document in which the words are kept. Where β_k gives the content of the subject headings, θ_d gives the distribution of each document to the subject headings. $Z_{d,n}$ represents the topic to which each word is attached [31].

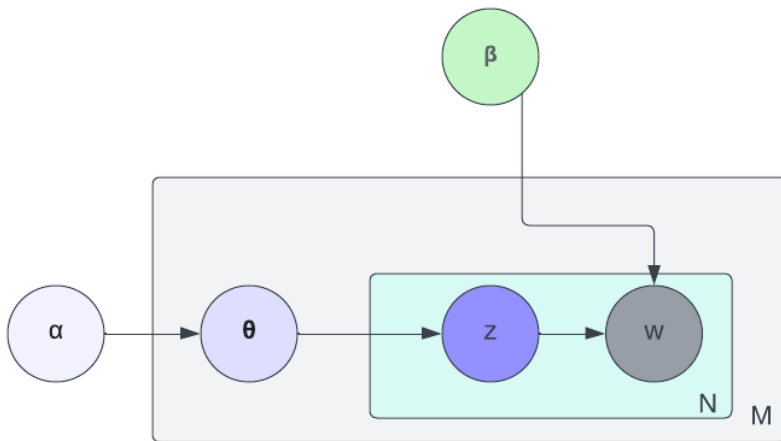


Figure 5. Representation of the LDA architectural structure.

β_k , θ_d , $Z_{d,n}$ represent the values obtained as a result of processing the variable $W_{d,n}$, which were unknown before the operation. In linear representation, K is the number of topics, D is the number of documents, and N is the number of unique words in the documents. It explains how the observed data is produced because of random variables and the spread of these variables. The main purpose in LDA is to explore topics from the document collection. In this process step, only the documents can be observed, the assignment of words to the topics, the

distribution of the topics in the document and the words in the topics are hidden. LDA can work based on the bag of words approach without the need for prior knowledge. While the placement of the words in the document is not considered, the coexistence of the words is used in the LDA technique [32].

In this tab, the user must first prepare the data for the LDA model. To prepare the data, it must be pre-processed (convert to lowercase, remove special characters, remove stopwords and stemming). These processing steps are the steps that should be done in every natural language processing process. Each word is converted to lowercase, then special characters and stopwords are removed from the dataset. In the stemming step, the roots of each word are accessed and the complexity that will arise due to the variations of the words is removed. The next step from the pre-processing step is to obtain the term document matrix. This matrix keeps the frequency of terms found in documents. The document matrix is used as input for LDA. Numerical operations can now be performed on pre-processed words. Appropriate weights should be calculated according to the attribute of each word, and they should be made ready to be sent to the LDA model. For this process, the TF-IDF (Term Frequency — Inverse Document Frequency) transformation, which is frequently used in the literature, is used. TF-IDF is calculated by looking at the frequency of use of each word and the frequency of occurrence in the opposite documents. As a result of this process, D matrix is obtained in $m \times n$ dimensions (m number of documents, n number of different words) [31, 32].

D. Tab 4: Results and Reporting

In the last tab of the application, a report is made to the user about the experimental study. Reporting can be in Html, Word, or Pdf formats. The user should choose and confirm how he wants to see the results of the transaction. Then the reporting process takes place. Reporting is done with R markdown. To use R markdown, the *rmarkdown* package and *pandoc* tool have been installed. The *knitr* R package was used to integrate the code in the R script file into LaTeX, HTML and Markdown documents. Content converted to a Markdown file (.md file) is handled by *Pandoc*, a multipurpose tool designed to convert files from one markdown language to another. YAML metadata is involved at many stages of the creation process. It can affect the most recent document in many ways. YAML metadata is read by each of *Pandoc*, *rmarkdown*, and *knitr* [33, 34].

3. CASE STUDY: TOPIC MODELLING FOR THE CYBER SECURITY MASTER'S PROGRAM

A case study was conducted to test the application developed in this study. The case study was carried out to update the content of the Cyber Security master's program. Cyber Security has become a very important research area due to the increase in communication technologies and types. So much so that security vulnerabilities can affect countries at the national level. Cyber security is a research area within computer science that aims to protect information, computing, or storage systems by providing a set of hardware and software solutions. Although it is within the scope of computer science, it is not limited to this field. Cyber security is defined as the collection of tools, policies, security concepts, security measures, guidelines, risk management approaches, actions, training, best practices, assurance, and technologies that can be used by the International Telecommunication Union (ITU) to protect the cyber environment and user assets. In summary, the concept of cyber security can be defined as protecting internet-connected systems, networks, and programs against internal or external threats [35, 37].

In this study, a topic modelling application was made by taking data from conferences and journals that have an important place in the literature on Cyber Security. At the graduate level, there is Cyber Security department within the body of Düzce University Graduate Education Institute. Cyber Security department accepts students with thesis every semester. When it was first opened, course programs were created with reference to the world's leading universities in Europe and the USA. However, in today's rapidly changing conditions, the need to evaluate the actuality of the courses opened in the department within the scope of the literature has arisen. The conferences and journals selected for subject modelling are.

1. ACM Conference on Computer and Communications Security (CCS)
2. IEEE Symposium on Security and Privacy
3. USENIX Security Symposium
4. Network and Distributed System Security Symposium (NDSS)
4. Computers & Security
5. IEEE Transactions on Information Forensics and Security (TIFS)
6. IEEE Transactions on Dependable and Secure Computing (TDSC)
7. ACM Transactions on Privacy and Security (TOPS)

is in the form. A data set was created using the papers and articles published in these journals and conferences in the last five years (2018-2022 September). The block diagram of the case study is given in Figure 6. The data set was obtained by accessing individual sources. The reasons for choosing these conferences are

that they have high impact factors, intense participation of researchers in the field of cyber security and accessible resources. The four selected journals are widely used by researchers in the field of cyber security and are followed intensively by researchers.

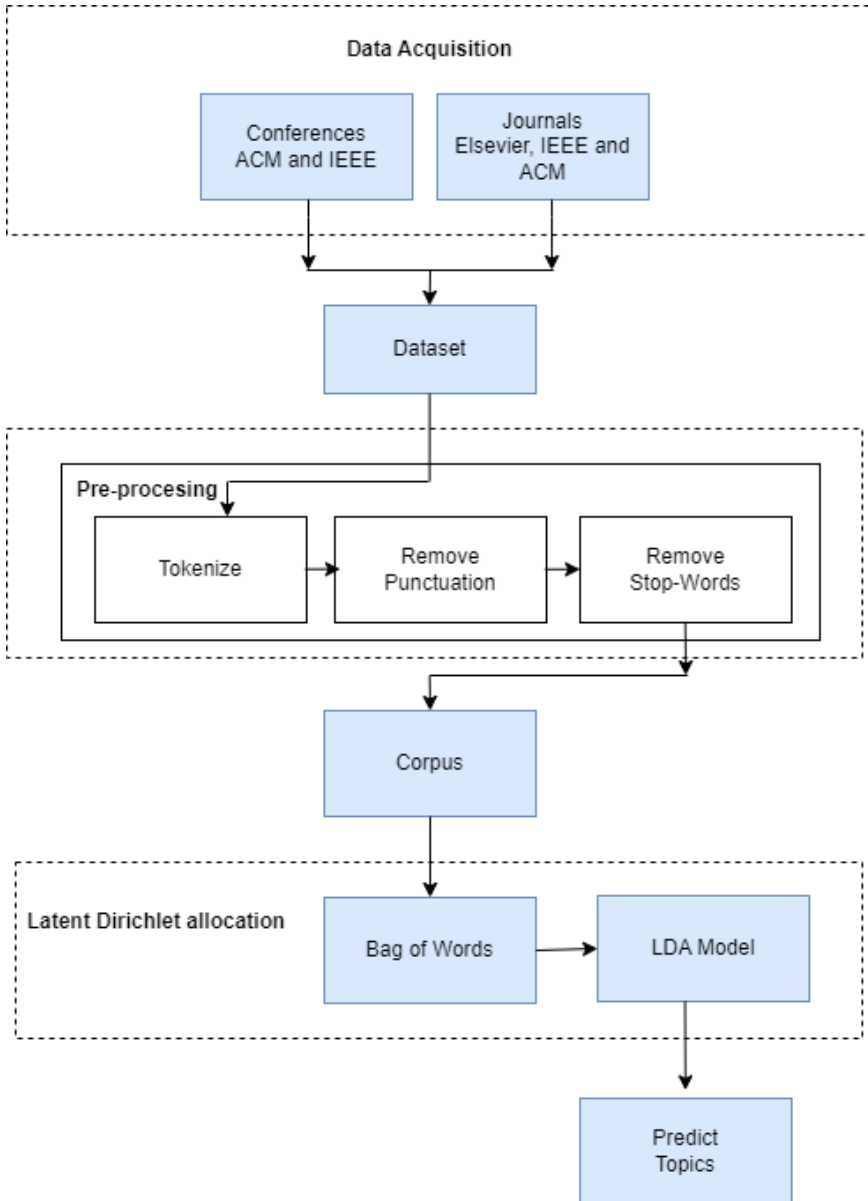


Figure 6. Case study block diagram

While creating the data set, the title, keywords, year, and abstract sections of each article/paper were collected and saved in an excel file. In this way, a total of 6508 records were obtained. While the data set was being collected, some papers/articles could not be accessed, so they could not be saved. After obtaining the raw data, the pre-processing step was started. After the pre-processing step, the data was ready and the LDA technique was applied.

In unsupervised machine learning methods, results are usually given by clustering similar data since the data is not labelled. Experts who will interpret the features of this cluster should understand what the subject is. In the LDA technique, it is necessary to give information about how many different subjects can be in the data set. One of the most important methods to be used to measure how accurate this parameter is the consistency score [38]. In this study, the consistency score probabilities of the subjects were calculated. Coherence' score, which will be in the range of 0 - 1; identified more consistent subjects in high scores and inconsistent subjects in low scores. Thus, the overall performance of the model has emerged. The results for 20 subjects (k) in the study are given in Table 1.

Table 1. LDA results for cybersecurity (k=20)

No.	Topic	Coherence Score
1	cyber security	0,738
2	authentication	0,711
3	malware	0,702
4	phishing	0,698
5	cybercrime	0,696
6	feature extraction	0,654
7	network security	0,641
8	cyber-attack,	0,615
9	cyber-physical systems	0,579
10	critical infrastructure	0,566
11	blockchain	0,536
12	cloud computing	0,520
13	privacy	0,504
14	encryption	0,501
15	Machine learning	0,499
16	cryptography	0,483
17	Intrusion detection	0,480
18	artificial intelligence	0,476
19	anomaly detection	0,474
20	information security	0,470

In this study, 6508 records were analysed. Therefore, it is impossible to show the subject distributions of all interpretations. Many records play an active role during the formation of each subject sub-title. Some entries fit more than one topic. The first twenty of the obtained subjects were selected. Case study results are given in html, pdf, and Word formats with R Markdown in the reporting section of the application. When the subject headings of the courses opened in the Cyber Security department and the results of the LDA are compared, it is concluded that the subject of blockchain is new and that a course related to this subject should be added to the course curriculum.

4. CONCLUSION AND FUTURE WORK

In this study, the processes of data preparation, cleaning, tokenization and creating a corpus are operated on textual data. Then corpus is translated into word bag. The word bag is subject to the subject modelling process with the LDA technique according to the number of subjects to be selected by the user. Each process step is reported with R markdown. The user can complete the process by doing what he wants from the above-given steps on the textual data. The developed application was run on a real scenario for testing. Scenario Cyber Security is about determining how current the courses taught in the department are and whether there is a course that needs to be added. For this purpose, titles, abstracts, and keywords (2018-2022 September) were collected from three conferences and four journals and a dataset was created. The data set consists of 6508 rows of data. Topic modelling study was carried out on the data set with LDA technique. In the experimental studies, it was concluded that choosing 20 subjects would be more meaningful for the data set used. In the case study, it was concluded that the topic of blockchain is new, and that the curriculum should be updated with this new topic. For this purpose, a course on blockchain has been opened as an elective course.

In the next study, in addition to the LDA model, other topic modelling techniques (Latent semantic analysis, Non-Negative Matrix Decomposition) used in the literature will also be included in the study. Thus, the user will be able to try the topic modelling techniques in a comparative way. In this study, the data set was collected as part of the case study. The data set was collected manually one by one. This took about 37 hours. In the future study, it will be ensured that the web scraping technique is used while creating the user's data set. Thus, the user will be able to complete his work much faster. Shiny application has been developed to run locally. In the next version, the Docker image of the Shiny application will be created. Shiny server will be installed on Amazon AWS EC2 server. Multiple Shiny applications will be used on the same port on Docker

containers. The application will thus be taken to live view. The Docker image will be uploaded to Docker Hub to be shared with researchers.

Data Availability Datasets created and/or analysed during the current study will be shared upon communication with the author.

Declarations

Conflict of interest The authors have no relevant financial or nonfinancial interests to disclose. The authors have no competing interests to declare that are relevant to the content of this article. All authors certify that they have no affiliations with or involvement in any organization or entity with any financial interest or non-financial interest in the subject matter or materials discussed in this manuscript. The authors have no financial or proprietary interests in any material discussed in this article.

Ethical approval This article does not contain any studies with human participants or animals performed by any of the authors.

REFERENCES

- [1] Yihui Xie, J.J. Allaire, Garrett Grolemond, R Markdown The Definitive Guide, Florida, USA, CRC Press, 2018.
- [2] Yihui Xie, Christophe Dervieux, Emily Riederer, R Markdown Cookbook, Florida, USA, CRC Press, 2021.
- [3] Salehi M., Arashi M, Bekker A., Ferreira J., Chen D.G., Esmaili F. and Frances M., A Synergetic R-Shiny Portal for Modeling and Tracking of COVID-19 Data, *Frontiers in Public Health*, doi: 10.3389/fpubh.2020.623624.
- [4] Kwon D., Sadashiva Reddy R.R., M. Reis I., ABCMETAapp: R shiny application for simulation-based estimation of mean and standard deviation for meta-analysis via approximate Bayesian computation, *COMPUTATIONAL TOOLS AND METHODS*, <https://doi.org/10.1002/jrsm.1505>.
- [5] Heinsberg L., Koleck T., Ray M., Weeks D., Conley Y., Advancing Nursing Research Through Interactive Data Visualization With R Shiny, *Biological Research for Nursing*, doi: 10.1177/10998004221121109.
- [6] T. Holland-Letz, A. Kopp-Schneider, An R-shiny application to calculate optimal designs for single substance and interaction trials in dose response experiments, *Toxicology Letters* 337 (2021) 18–27.
- [7] H. Atakan Ekiz, Christopher J. Conley, W. Zac Stephens and Ryan M. O’Connell, CIPR: a web-based R/shiny app and R package to annotate cell clusters in single cell RNA sequencing experiments, *BMC Bioinformatics* (2020) 21:191 <https://doi.org/10.1186/s12859-020-3538-2>.
- [8] Tomás M. Antonelli and Alejandro C. Olivieri, Developing and Implementing an R Shiny Application to Introduce Multivariate Calibration to Advanced Undergraduate Students, *J. Chem. Educ.* 2020, 97, 1176–1180, <https://dx.doi.org/10.1021/acs.jchemed.9b00850>.
- [9] Elly Poretsky and Alisa Huffaker, MutRank: an R shiny web-application for exploratory targeted mutual rank-based coexpression analyses integrated with user-provided supporting information, *PeerJ* 8:e10264 DOI 10.7717/peerj.10264.
- [10] Tadhg N. Moore, R. Quinn Thomas, Whitney M. Woelmer and Cayelan C. Carey, Integrating Ecological Forecasting into Undergraduate Ecology Curricula with an R Shiny Application-Based Teaching Module, *Forecasting* 2022, 4, 604–633. <https://doi.org/10.3390/forecast4030033>.
- [11] Seyma Yasar, Ahmet Kadir Arslan, Cemil Colak, Saim Yoloğlu, A Developed Interactive Web Application for Statistical Analysis: Statistical

Analysis Software, Middle Black Sea Journal of Health Science August 2020; 6(2):227-239.

- [12] Tserenpurev Chuluunsaikhan, Ga-Ae Ryu, Kwan-Hee Yoo, HyungChul Rah and Aziz Nasridinov, Incorporating Deep Learning and News Topic Modeling for Forecasting Pork Prices: The Case of South Korea, *Agriculture* 2020, 10, 513; doi:10.3390/agriculture10110513.
- [13] Lihua Jia, Wen Yao, Yingru Jiang, Yang Li, Zhizhan Wang, Haoran Li, Fangfang Huang, Jiaming Li, Tiantian Chen and Huiyong Zhang, Development of interactive biological web applications with R/Shiny, *Briefings in Bioinformatics*, 00(00), 2021,1–15.
- [14] Markus Möllera, Lucas Boutarfaa, Jörn Strassemeyera, PhenoWin – An R Shiny application for visualization and extraction of phenological windows in Germany, *Computers and Electronics in Agriculture* 175 (2020) 105534.
- [15] Yu Li, Towards fast prototyping of cloud-based environmental decision support systems for environmental scientists using R Shiny and Docker, *Environmental Modelling and Software* 132 (2020) 104797.
- [16] Eric S. Kruger, Davood Tofighi, Yu-Yu Hsiao, David P. MacKinnon, M. Lee Van Horn & Katie Witkewitz, An R Shiny App for Sensitivity Analysis for Latent Growth Curve Mediation, *Structural Equation Modeling: A Multidisciplinary Journal*, Volume 29, 2022 - Issue 6.
- [17] Aaron R. Kaufman, Implementing novel, flexible, and powerful survey designs in R Shiny, *PLoS ONE* 15(4): e0232424. <https://doi.org/10.1371/journal.pone.0232424>.
- [18] Lucca de Farias Ramalho and Washington R. de Carvalho Segundo, R-Shiny as an Interface for Data Visualization and Data Analysis on the Brazilian Digital Library of Theses and Dissertations (BDTD), *Publications* 2020, 8, 24. <https://doi.org/10.3390/publications8020024>.
- [19] Nico Andersen and Fabian Zehner, shinyReCoR: A Shiny Application for Automatically Coding Text Responses Using R, *Psych* 2021, 3, 422–446. <https://doi.org/10.3390/psych3030030>.
- [20] Tijn De Bie, Luc De Raedt, José Hernández-Orallo, Holger H. Hoos, Padhraic Smyth, and Christopher K.I. Williams, Automating Data Science, *Communications Of The Acm*, March 2022, Vol. 65. No. 3.
- [21] Federico M. Giorgi, Carmine Ceraolo and Daniele Mercatelli, The R Language: An Engine for Bioinformatics and Data Science, *Life* 2022, 12(5), 648; <https://doi.org/10.3390/life12050648>.
- [22] Chen, J., Jimenez-Ruiz, E., Horrocks, I., and Sutton, C. ColNet: Embedding the semantics of Web tables for column type prediction. In *Proceedings of the 33rd AAAI Conf. on Artificial Intelligence*, 2019.

- [23] Elbattah, M. and Molloy, O. Analytics using machine learning-guided simulations with application to healthcare scenarios. *Analytics and Knowledge Mgmt.* Auerbach Publications, 2018, 277–324.
- [24] Guyon, I., et al. A brief review of the ChaLearn AutoML Challenge: Any-time any-dataset learning without human intervention. In *Proceedings of the Workshop on Automatic Machine Learning 64* (2016), 21–30. F. Hutter, L. Kotthoff, and J. Vanschoren, Eds.
- [25] Hutter, F., Kotthoff, L., and Vanschoren, J., Eds. *Automated Machine Learning—Methods, Systems, Challenges.* Springer, 2019.
- [26] Mansinghka, V., Tibbetts, R., Baxter, J., Shafto, P., and Eaves, B. *BayesDB: A probabilistic programming system for querying the probable implications of data.* 2015; arXiv:1512.05006
- [27] Vartak, M., Rahman, S., Madden, S., Parameswaran, A., and Polyzotis, N. *SeeDB: Efficient data-driven visualization recommendations to support visual analytics.* In *Proceedings of the Intern. Conf. on Very Large Data Bases 8* (2015), 2182.
- [28] Nazabal, A., Williams, C., Colavizza, G., Smith, C., and Williams, A. *Data engineering for data analytics: A classification of the issues, and case studies.* 2020; arXiv:2004.12929.
- [29] Yigit Alisan, and Faruk Serin, *A Computer Assisted Decision Support System for Education Planning,* *International Journal of Information Technology & Decision Making*, Vol. 20, No. 5 (2021) 1383–1407.
- [30] David M. Blei, Andrew Y. Ng, Michael I. Jordan, *Latent Dirichlet Allocation,* *Journal of Machine Learning Research* 3 (2003) 993-1022.
- [31] Volkan Altıntaş, Mehmet Albayrak, Kamil Topal, *Topic modeling with latent Dirichlet allocation for cancer disease posts,* *Journal of the Faculty of Engineering and Architecture of Gazi University* 36:4 (2021) 2183-2196.
- [32] Chen, C. ve Ren, J., *Forum latent Dirichlet allocation for user interest discovery,* *Knowledge-Based Systems*, 126, 1–7, 2017.
- [33] Kristine L.Grayson, Angela K.Hillikera, Joanna R.Wares, *R Markdown as a dynamic interface for teaching: Modules from math and biology classrooms,* *Mathematical Biosciences*, Volume 349, July 2022, 108844.
- [34] Bruno Carius Garrido, Gustavo de Albuquerque Cavalcanti, Marcio Vinícius da Silva Gomes, Juliana Scofano Barrabin, Monica Costa Padilha, Henrique Marcelo Gualberto Pereira, *Assessing limits of detection in qualitative methods: A simple implementation of logistic regression in a web-based R Shiny application environment and its potential in toxicology and doping control,* *Drug Test Anal.* 2022;1–9.

- [35] Žiga Turk, Borja García de Soto, Bharadwaj R.K.Mantha, Abel Maciel, Alexandru Georgescu, A systemic framework for addressing cybersecurity in construction, *Automation in Construction*, Volume 133, January 2022, 103988.
- [36] Charlotte Van Camp, Walter Peeters, A World without Satellite Data as a Result of a Global Cyber-Attack, *Space Policy*, Volume 59, February 2022, 101458.
- [37] Gaurav Dave, Gaurav Choudhary, Vikas Sihag, IlsunYou, Kim-Kwang Raymond Choo, Cyber security challenges in aviation communication, navigation, and surveillance, *Computers & Security*, Volume 112, January 2022, 102516.
- [38] Röder, M., Both, A., and Hinneburg, A., Exploring the Space of Topic Coherence Measures, *Proceedings of the Eighth ACM International Conference on Web Search and Data Mining*, New York-USA 399–408, 2-6 Şubat, 2015.